NASA Conference Publication 2443

Rotordynamic Instability Problems in High-Performance Turbomachinery 1986

Proceedings of a workshop held at
Texas A&M University
College Station, Texas
June 2-4, 1986

NASA

NASA Conference Publication 2443

Rotordynamic Instability Problems in High-Performance Turbomachinery 1986

Proceedings of a workshop sponsored by
Texas A&M University, College Station,
Texas, the U.S. Army Research Office,
Durham, North Carolina, and the
Aeropropulsion Laboratory,
Wright-Patterson Air Force Base, Ohio,
and held at Texas A&M University,
College Station, Texas
June 2-4, 1986

National Aeronautics
and Space Administration

**Scientific and Technical
Information Branch**

1986

ERRATA

NASA Conference Publication 2443

ROTORDYNAMIC INSTABILITY PROBLEMS IN HIGH-PERFORMANCE TURBOMACHINERY 1986

January 1987

Page 33: Replace the figure with the following:

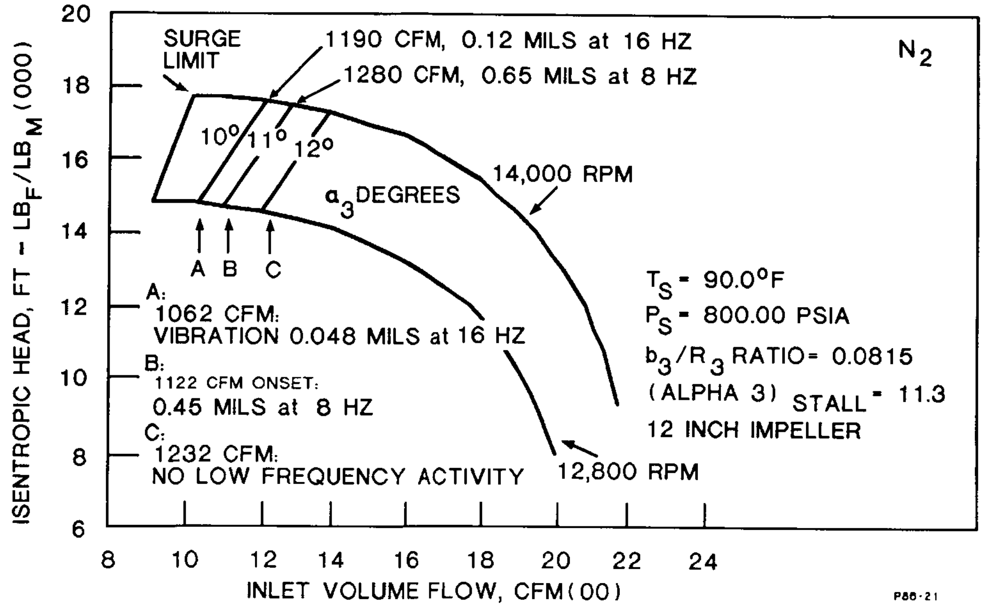

Figure 18. Performance Map with Lines of Constant Alpha 3 versus Shaft Vibration

Page 353: The last sentence in the second paragraph should read ". . . when it can readily be seen from Figs. 3a and 3b that a low value of u/c is desirable on two counts, low vibration amplitude and low transmitted force."

PREFACE

A review of the proceedings from the past workshops and the program for the current workshop shows a continued trend toward a more unified view of rotordynamics instability problems and several encouraging new analytical developments. Test programs that were in existence two years ago continue to yield new reference data. Results from programs developed in the interim are also reported.

Without wishing to slight any authors, the following papers appear to be of particular interest:

(1) Shemeld's paper is useful in conveying the experience and philosophy of "design for stability" from a major high-pressure compressor manufacturer.

(2) Dietzen and Nordmann's paper is the first published effort to merge classical perturbation analysis with computational fluid dynamics (CFD). This approach promises to yield affordable rotordynamic coefficients with the flexability and power of CFD approaches.

(3) Kirk's paper on the influence of the impeller-shroud path on the inlet tangential velocity of compressor wear-ring seals is particularly important given its implications for swirl brakes and seal wear.

(4) Childs and Sharrer's experimental results on labyrinth seals are the first published data that separately identify direct and cross-coupled stiffness and damping coefficients.

(5) San Andres and Vance's paper represents a significant advance in the analysis capability for squeeze-film dampers by accounting for both the convective and temporal acceleration terms, which are traditionally ignored in "Reynolds equation" types of analysis. Their results show that these terms are significant for many damper applications.

(6) As a group, the magnetic-bearing papers are of considerable interest and show the growing commercial interest in this new rotating-equipment development. An expansion of this session is planned for the next workshop.

(7) Childs' paper on impeller-shroud surfaces is the first analytical approach for predicting the shroud influence on impeller forces. Test results at Sulzer Brothers, Ltd., and California Institute of Technology have suggested that the leakage path along the shroud significantly affects dynamic impeller forces.

We are confident that you will find all of the papers in this proceedings to be of interest. Please read them and pick your own favorites.

This workshop was organized to continue addressing the general problem of rotordynamic instability by gathering those persons with immediate interest, experience, and knowledge of this subject for a discussion and review of both past stability problems and present research and development efforts. The

PRECEDING PAGE BLANK NOT FILMED

intent of the workshop organizers and sponsors is that the workshop and this proceedings provide a continuing impetus for an understanding and resolution of these problems.

Chairmen:

Dara W. Childs and
John M. Vance
Turbomachinery Laboratories
Texas A&M University

Robert C. Hendricks
NASA Lewis Research Center

CONTENTS

SESSION I - FIELD EXPERIENCE WITH UNSTABLE TURBOMACHINERY

A HISTORY OF DEVELOPMENT IN ROTORDYNAMICS - A MANUFACTURER'S PERSPECTIVE
David E. Shemeld 1

AN EXAMINATION OF GAS COMPRESSOR STABILITY AND ROTATING STALL
Aziz A. Fozi 19

SUBSYNCHRONOUS VIBRATION OF MULTISTAGE CENTRIFUGAL COMPRESSORS FORCED BY ROTATING STALL
J.W. Fulton 35

INSTABILITY OF MULTISTAGE COMPRESSOR K1501
Zhou Ren-mu 63

SESSION II - LIQUID SEALS FOR TURBOMACHINERY

CALCULATING ROTORDYNAMIC COEFFICIENTS OF SEALS BY FINITE-DIFFERENCE TECHNIQUES
F.J. Dietzen and R. Nordmann 77

STATIC AND DYNAMIC CHARACTERISTICS OF PARALLEL-GROOVED SEALS
Takuzo Iwatsubo, Bo-suk Yang, and Ryuji Ibaraki 99

ROTORDYNAMIC COEFFICIENTS AND LEAKAGE FLOW OF PARALLEL GROOVED SEALS AND SMOOTH SEALS
R. Nordmann, F.J. Dietzen, W. Janson, A. Frei, and S. Florjancic . . . 129

THEORETICAL APPROACH TO OBTAINING DYNAMIC CHARACTERISTICS OF NONCONTACTING SPIRAL-GROOVED SEALS
Takuzo Iwatsubo, Bo-suk Yang, and Ryuji Ibaraki 155

COMPARISON OF HIRS' EQUATION WITH MOODY'S EQUATION FOR DETERMINING ROTORDYNAMIC COEFFICIENTS OF ANNULAR PRESSURE SEALS
Clayton C. Nelson and Dung T. Nguyen 189

SESSION III - LABYRINTH SEALS

DESTABILIZING FORCE OF LABYRINTH SEAL
Hiroshi Kanki and Shigeki Morii 205

INFLUENCE OF DISK LEAKAGE PATH ON LABYRINTH SEAL INLET SWIRL RATIO
R. Gordon Kirk 225

THEORY AND MEASUREMENTS OF LABYRINTH SEAL COEFFICIENTS FOR ROTOR STABILITY OF TURBOCOMPRESSORS
H.R. Wyssmann 237

EXPERIMENTAL ROTORDYNAMIC COEFFICIENT RESULTS FOR TEETH-ON-ROTOR AND TEETH-ON-STATOR LABYRINTH GAS SEALS
Dara W. Childs and Joseph K. Scharrer 259

SESSION IV - DAMPERS

NON-LINEAR IDENTIFICATION OF A SQUEEZE-FILM DAMPER
Roger Stanway, John Mottershead, and Riaz Firoozian 277

ESTIMATION OF SQUEEZE-FILM DAMPING AND INERTIAL COEFFICIENTS FROM EXPERIMENTAL FREE-DECAY DATA
J.B. Roberts, R. Holmes, and P.J. Mason 293

INSTABILITY OF AN INTERSHAFT SQUEEZE FILM DAMPER IN A TWO-SPOOL ROTOR DYNAMICS SIMULATOR
R.G. Alderson 315

A NOVEL FORM OF DAMPER FOR TURBO-MACHINERY
R.D. Brown and J.A. Hart 325

SESSION V - DAMPERS (CONCLUDED)

NON-LINEAR PERFORMANCE OF A THREE-BEARING ROTOR INCORPORATING A SQUEEZE-FILM DAMPER
R. Holmes and M. Dede 349

DYNAMIC PERFORMANCE OF SQUEEZE-FILM BEARINGS
C.R. Burrows, M.N. Sahinkaya, N.C. Kucuk, and D. Taylor 365

EXPERIMENTAL MEASUREMENT OF THE DYNAMIC PRESSURE DISTRIBUTION IN A SQUEEZE FILM BEARING DAMPER EXECUTING CIRCULAR CENTERED ORBITS
L.A. San Andres and J.M. Vance 373

SESSION VI - MAGNETIC BEARINGS

NONLINEAR DYNAMICS OF ATTRACTIVE MAGNETIC BEARINGS
K.V. Hebbale and D.L. Taylor 397

DYNAMICS OF A FLEXIBLE ROTOR IN MAGNETIC BEARINGS
P.E. Allaire, R.R. Humphris, and R.D. Kelm 419

PERFORMANCE OF AN ELECTROMAGNETIC BEARING FOR THE VIBRATION CONTROL OF A SUPERCRITICAL SHAFT
C.D. Bradfield, J.B. Roberts, and R. Karunendiran 431

A MAGNETIC BEARING BASED ON EDDY-CURRENT REPULSION
J.L. Nikolajsen 461

SESSION VIII - PUMPS

ORIGINS OF HYDRODYNAMIC FORCES ON CENTRIFUGAL PUMP IMPELLERS
Douglas R. Adkins and Christopher E. Brennen 467

ON THE EFFECT OF CAVITATION ON THE RADIAL FORCES AND HYDRODYNAMIC STIFFNESS OF A CENTRIFUGAL PUMP
R.J. Franz, C.E. Brennen, A.J. Acosta, and T.K. Caughey 493

FORCE AND MOMENT ROTORDYNAMIC COEFFICIENTS FOR PUMP-IMPELLER SHROUD SURFACES
Dara W. Childs 503

INFLUENCE OF TORSIONAL-LATERAL COUPLING ON STABILITY BEHAVIOR OF GEARED ROTOR SYSTEMS
P. Schwibinger and R. Nordmann 531

N87-22200

A HISTORY OF DEVELOPMENT IN ROTORDYNAMICS -
A MANUFACTURER'S PERSPECTIVE

David E. Shemeld
Dresser Industries, Inc.
Olean, New York 14760

The subject of rotordynamics and instability problems in high performance turbomachinery has been a topic of considerable industry discussion and debate over the last 15 or so years.

This paper reviews an original equipment manufacturer's history of development of concepts and equipment as applicable to multistage centrifugal compressors.

The variety of industry user compression requirements and resultant problematical situations tends to confound many of the theories and analytical techniques set forth. The experiences and examples described herein support the conclusion that the successful addressing of potential rotordynamics problems is best served by a fundamental knowledge of the specific equipment. This in addition to having the appropriate analytical tools. Also, that the final proof is in the doing.

INTRODUCTION

While the subject of "rotordynamics" encompasses a broad range of lateral and torsional considerations, this presentation briefly reviews the manufacturer's efforts to correlate analytical procedures with machine operation including:

- verification of indicated critical speed with analytical results
- the influence of various components on the rotating system's behavior
- aerodynamic influences.

The review continues with the development of rotating system components and their successful application in a variety of services, and compares the results of this development and experience with a previously published graphical representation. (ref. 1, 2).

NOMENCLATURE

Values are given in both SI and U.S. Customary Units. The measurements and calculations were made in U.S. Customary Units.

BHP = power, brakehorsepower
cfm = flow, cubic feet per minute

Hz = frequency, hertz
in. = length, inches
KPa = pressure, kilopascal
kg/m^3 = density, kilogram per cubic meter
kW = power, kilowatt
lbm/ft^3 = density, pound-mass per cubic foot
m^3/hr = flow, cubic meter per hour
mil = vibration, 0.001 inch
mm = length, millimeter
N = running speed
NC = critical speed
NC$_1$ = first bending critical speed
psi = pressure, pound-force per square inch
r/min = speed, revolutions per minute
μm = vibration amplitude, micrometer

ROTORDYNAMICS

Phase One Testing

In the late 1960's a test rig (fig. 1) was established to monitor seal and rotordynamic behavior.

Reviewing the test rig (fig. 2), the casing was a standard multistage centrifugal compressor frame with pressure capability of 34,500 KPa (5000 psi), and speed capability to 14,000 r/min.

The casing was equipped with a rotor consisting of dummy weights installed on a shaft to simulate impellers. The test vehicle configuration allowed installation of a variety of bearing and seal combinations, variable rotor geometry and application of unbalance weights.

In this test rig, rotordynamic influences were monitored through a range of pressures without the influence of aerodynamic effects which normally result from gas compression.

Initial testing evaluated a rotating system configuration representative of components in use at the time. The configuration consisted of a rotor with a 1600 mm (63 in.) bearing span having ten weights installed simulating impellers. The bearings were tilting pad type having five shoes. The seals were standard ring type oil film seals (fig. 7) of low profile geometry (fig. 8).

Bearing vibration results for a speed range through 14,000 r/min are shown on figure 3. Rotor midspan vibration is shown on figure 4. The data definitions for figures 3 and 4 are made in Table 1.

Testing was done using two case (and therefore seal) pressures [1030 KPa (150 psi) and 6900 KPa (1000 psi)] and with a "tight", 0.127 mm (0.005 in.) and "loose", 0.241 mm (0.0095 in.) bearing clearance.

It was evident from reviewing the characteristics of peak locations (fig. 3, curves A vs. B, and C vs. D), and the vibration discontinuity evidenced in figure 3, curve C that both bearing and seal characteristics influence rotordynamic behavior.

Figures 3 and 4 also presented difficulties in data interpretation. For example, in figure 3, note the low [less than 12.7 μm (0.5 mil)] vibration level in the first critical speed range and the difficulty in pinpointing these critical speeds. Also, in figure 4, note the low speed amplitude being an appreciable portion of the full speed amplitude as well as the initial decrease in amplitude as speed increased. Phase data recorded was erratic and inconclusive.

These characteristics suggested a form of runout and the runout to be out of phase with the unbalance. Since rotor instability, as experienced, was associated with vibration at the first bending mode, correct modeling of the parameters influencing the first critical speed was important.

Phase Two Testing

From the foregoing review of data, it was determined that more detailed testing was necessary to overcome the difficulties of data interpretation. Testing during this phase was set up to:

- operate without seals thereby eliminating the apparent seal effects on critical speed;
- intentionally unbalance the rotor at midspan to give a clearer indication of critical speed;
- run with "tight" and "loose" clearance bearings.

This phase of testing would be used to verify the analytical capability to predict rotor response using available bearing and unbalance response programs.

Figures 5A and 5B compare analytical and test results for bearing and midspan vibration vs. speed data for a "tight," 0.102 mm (0.004 in.) clearance bearing.

There is good correlation between the test (solid line) and calculated (dotted line) first critical frequency.

Figures 6A and 6B compare analytical and test results for bearing and midspan vibration respectively for a "loose," 0.241 mm (0.0095 in.) clearance bearing. Note in this data, there are some test coupling unbalance effects and second bending critical speed effects at higher speeds. The calculated values were analyzed with unbalance modeled to compare to only the first critical speed.

The amplitude ratio data of figures 5A and 5B, and 6A and 6B (summarized in Table 2) emphasize the ever present requirement for compromise in compressor component design/application.

From Table 2, while tight bearing provides a lower indicated vibration at running speed, which may be considered advantageous to the user, the ratios at critical speed indicate a more sensitive situation than the loose bearing.

The impact of subtle differences on the design of critical components and the impact on compressor operation must be a prime consideration in revamping or replacing parts.

Phase Three Testing

Having recognized from the first phase of testing that oil film seals had a demonstrated effect on rotordynamics, the third phase of testing was established to evaluate various seal configurations and establish a basis for analytical predictability.

Figure 7 shows a typical ring type oil film seal in cross-section. Due to the axial load associated with the high pressure drop across its unbalance area, the outer ring is the component which influences rotordynamics.

Figure 8 shows several variations in outer ring geometry that result in different seal effects at a given pressure differential.

Testing was conducted with these different, albeit somewhat conventional, seal designs at varying seal pressures and varying levels of rotor unbalance. Test results indicated an unsettling effect of unbalance at low axial loads and indicated highly loaded seals of this geometry to be unpredictable.

Data from tests of these various geometries also provided a plausible explanation for the vibration discontinuity observed in figures 3 and 4. Since predictability is a requirement for reliability, it was determined that a new approach to seal geometry must be taken.

Several seal designs were conceived and tested. The tilt pad seal (fig. 9) evolved as the solution to the problem of predictability of seal effects while eliminating the propensity for oil whirl which had emerged as a problem during testing of other seal geometries.

Verification of the tilt pad seal geometry included testing various oil film clearances enabling this parameter, as well as axial load and unbalance to be included in the analysis as an accurate representation of the rotordynamic system. Upon verification, the tilt pad seal was released to production units and has been providing reliable service for over 12 years.

With the foregoing, the first three phases of the test program were complete. During these phases, over 200 tests were run to evaluate rotordynamic parameters.

ROTOR INSTABILITY

With this progress in analytical capability and machinery experience, the inevitable result was to extend the equipment to higher heads, higher case lift, and higher pressures by design innovations such as back-to-back construction, variable stage spacing, inboard thrust bearings, and high pressure seals. Along the way in this evolution, a vibration problem defined as rotor instability was encountered. The rotor instability was evidenced by a pulsating vibration at subsynchronous frequency, the amplitude of which would increase, resulting in rotor interference with static parts. It was determined that the vibration was aerodynamically excited and the frequency coincided with the rotor's first bending critical speed.

This manufacturer's exposure to the subsynchronous vibration problem first occurred in the early 1970's. The problem surfaced in widespread geographical locations and encompassed both synthesis gas and natural gas compressors in applications at moderate and higher pressures. The approach taken was not to abandon the extended capability and advantages inherent in the design philosophy, but to improve understanding and solve the problem through incorporation of design advances. It was recognized that to accomplish this would require a test vehicle which had experienced a demonstrated, rotor instability in order to verify or evaluate design modifications.

Instability Testing

A compressor that had experienced serious subsynchronous vibration was set up in the test facility (fig. 10) for full pressure, full power operation. A comparison of design and test capability conditions are shown in Table 3.

A series of 30 tests were run on a helium/nitrogen mixture through a range of flows, pressures and speeds.

The first series of tests (one through six) were baseline runs using the compressor as originally built, including five shoe, tilt pad bearings and standard ring type seals. These tests verified the field experience could be duplicated by the shop test. An example of the data which shows the impact of the subsynchronous component on midspan vibration is shown in figure 11. Note the Y-axis of this oscilloscope picture is vibration at 2.54μm/Division (0.1 mil/Division) and the X-axis represents time, in this case, ten seconds. This data represents the maximum speed (9000 r/min) that could be achieved prior to completely unstable operation.

The remainder of the testing applied many of the bearing and seal component configurations to the "real condition" operating environment in combinations which had been shown to be successful in prior testing without aerodynamic influence, and which had already shown promising results when installed in field problem units. In addition, this test program examined a variety of modifications to internal hardware believed to influence the aerodynamic forces on the rotor system, as well as investigation of friction effects of couplings and shrunk on parts.

Figure 12 is indicative of the results of this testing, again showing midspan vibration and data at 2.54 μm/Division. The configuration included in this data included:

- damper, tilt pad bearings, five shoe;
- tilt pad seals;
- aerodynamic adjustments to stationary parts.

The success of these programs is represented by the application of these concepts, analytical techniques and components to a quantity and variety of user compressor requirements. It is important to note these components and concepts have been applied successfully to multistage compression equipment of both back-to-back, as well as straight-through rotor arrangements.

Recent History

With the addition of hydrocarbon gas capability to the existing inert gas full load, full pressure test facilities in LeHavre, France, and Olean, New York, the manufacturer has expanded capability for evaluating rotordynamics/stability behavior in "real-life" conditions.

In 1985, the opportunity was presented to evaluate a compressor's performance under ASME Power Test Code 10, Class 1 conditions. The hydrocarbon gas blend was to match a unique "natural gas" injection application and at the same time, match and verify other aspects of the gas properties and gas behavior.

The compressor configuration was back-to-back, through-flow, without intercooling, having a total of six impellers and fitted with squeeze-film, tilt pad bearings, tilt pad seals, and the special aerodynamic division wall design; all of which had been proven successful on prior development tests and in long-term field operation. Additionally, all internal labyrinths were of conventional design. Bearing span, as well as other geometric parameters, were well within prior experience. Unique to this application was the hydrocarbon 35 mol weight gas being compressed to the 31,030 KPa (4500 psi) design, 33,100 KPa (4800 psi) maximum pressure.

During the full pressure, hydrocarbon performance test, a subsynchronous vibration component appeared and increased in intensity as pressure was increased going back toward surge on the 100 percent speed line. The subsynchronous vibration data during this test, although at very low levels [peaks to 7.6μm, (0.3 mil)], had a pulsation characteristic that would be of potential concern to the operator. It should be noted that later inspection of compressor internals showed absolutely no distress to labyrinth seals or any other internal (or external) components that, if existed, would be indicative of high midspan excursions. Figure 13, Test A, shows representative data at the highest pressure tested during performance testing. The data is bearing vibration shown on a time-sprectrum plot. Table 4, Column A shows basic test conditions at that point. Note for reference, the highest vibration amplitude shown on figure 13 is 12.7μm (0.5 mil) (Test C, 147 Hz).

On this project, two duplicate compressors (units I and II) were being supplied. While the compressor being discussed here (unit I) was being tested on hydrocarbon gas, the sister unit (unit II) was being tested at another facility on an inert gas and had not exhibited the subsynchronous component during its preliminary testing. Based on this, it was decided to run unit I on nitrogen at the highest pressures that could be achieved on that gas (similar to the conditions already experienced by unit II). This test is designated test B on figure 13 and Table 4. The results confirmed units I and II, under these conditions, had very similar operating characteristics free of subsynchronous vibration. This tended to lead the investigation to a detailed review of the compressor design as opposed to suspecting a random type problem such as might have occurred during assembly. This test also confirmed the need to run final verification tests on a gas blend closely duplicating field gas conditions.

Close inspection during disassembly confirmed correct parts assembly. However, scrutiny of the parts and manufacturing drawings revealed the stationary, flow-path components had not received some of the detailed design features that had been applied to other compressors in operation. These stationary components were remachined to conform to prior experience.

Test C (fig. 13 and Table 4) was the final verification test at maximum required pressure and speed. This test verified the adjustments made to the aerodynamic flow path stationary components brought the subsynchronous component to a low amplitude [peaks to 1.9μm, (0.075 mil)], stable condition.

RESULTS

The results of these, and similar test programs, are reflected by the experience in a wide variety of application circumstances. This wide variety of applications, it should be added, reinforces the analytic approach through incorporation of experience data into the evolution of the analytical process.

Based on knowledge gained from these research efforts, and application experiences, the manufacturer is hesitant to embrace as absolute many of the analytical techniques and empirical criteria presently published or available.

One such empirical criterion is represented by figure 14 (ref. 2). This representation plots points based on a compressor's flexibility ratio and average gas density in operation, with flexibility ratio defined as compressor maximum continuous speed divided by the first critical speed on stiff supports. These points are then compared to the "worst case" threshold line with the area above the line indicated as "unstable region" and the area below the line indicated as "safe region". According to the author (ref. 2), "The 'worst case' line given should be a useful rule-of-thumb for indicating a threshold-of-concern for subsynchronous instability in similar industrial centrifugal compressors."

To assist in putting such a chart into perspective, the parameters of figure 14, including the "worst case" line, have been used as a base for plotting a portion of the manufacturer's experience without showing duplicate units (fig. 15).

On figure 15, units numbered 1 through 46, represent a wide range of applications including natural gas (21 units), synthesis gas (12 units), as well as CO_2, air injection and mixed hydrocarbon service. Also represented is a wide range of service pressures from approximately 6900 KPa (1000 psi) through 72,415 KPa (10,500 psi). The period covered is 1969 through 1983. (Since this representation is considered to be only an illustrative tool, later experience has not been added.) As noted, the unit numbers enclosed in squares or boxes represent those units which were full load/full pressure tested prior to shipment. All other units were shipped having received, from a mechanical standpoint, only API-617 testing. For further reference, locations on this plot of test points A, B, and C from fig. 13 are shown.

CONCLUSION

The subject of rotordynamics and stability is a complex, technical issue made more complex by the constantly changing users' compression requirements typical of the multistage compressor industry. This history of development and testing serves to demonstrate that causes of subsynchronous excitations are not particular to any one area of compressor design; i.e., bearings, main seals, internal labyrinths, stationary components, impeller inlets, exits, etc. Nor is the phenomenon unique to a given configuration. Therefore, the solutions to these problems cannot be addressed by close examination of a singular element or component of the compressor assembly.

The described development testing and operating experience has allowed this manufacturer to establish the analytical processes by continual data feedback, as well as to conceive and develop bearing and seal components, and aerodynamic concepts as necessary to address solutions to rotordynamics/stability problems.

Some industry publications (ref.'s 1, 2, 3, 4, 5, 6, 7, 8) covering a span from 1976 through to as recently as 1984, would imply to the reader that when problems arise, solutions requiring major geometry changes to compressor shafting, cases and stationary components are to be considered cost-effective solutions based on current state-of-the-art of theory and application. "Cost-effective" has been described,at least as associated with one reported incident,as between 3 million (ref. 2) to 4 million (ref. 3) Pound Sterling.

To date, problems addressed by this manufacturer have not required the radical solutions implied as necessary by the aforementioned references. More typical of the manufacturer's experience is the Arun, 49,060 KPa (7115 psi) injection experience (ref. 9). Despite such successes, it has been recognized that additional development is necessary. To this end, the test vehicle (fig. 10) has been re-established in the test facility to enable identification and quantification of the mechanisms leading to rotor instability.

REFERENCES

1. Fulton, J. W.: "The Decision to Full Load Test a High Pressure Centrifugal Compressor in its Module Prior to Tow-Out", I. Mech. E., Second European Congress on "Fluid Machinery for the Oil, Petrochemical and Related Industries", The Hague, The Netherlands, March 1984.

2. Fulton, J. W.: "Full Load Testing in the Platform Module Prior to Tow-Out: A Case History of Subsynchronous Instability", NASA Conference Publication 2338, "Proceedings of a Workshop Held at Texas A&M University", College Station, Texas, May 1984.

3. Desmond, A. D.: "A Case Study and Rectification of Subsynchronous Instability in Turbocompressors", I. Mech. E., Second European Congress on "Fluid Machinery for the Oil, Petrochemical and Related Industries", The Hague, The Netherlands, March 1984.

4. Cochrane, W. Winston: "New Generation Compressors Injecting Gas at Ekofisk", The Oil and Gas Journal, May 1976.

5. Geary, C. H. Jr., et al: "Design and Operation of the World's Highest Pressure Gas Injection Compressors", Offshore Technology Conference, Houston, Texas, U.S.A., May 1976.

6. "High Ratio Compression Station In Canada", Turbomachinery International, May-June 1978.

7. Simmons, P. E.: "The Acceptance of a High Speed Centrifugal Compressor Rotor, Based on its Response to Deliberate Unbalance", I. Mech. E. Conference on "Fluid Machinery for the Oil, Petrochemical and Related Industries", The Hague, The Netherlands, March 1984.

8. Evans, B. F.; Smalley, A. J.: "Subsynchronous Vibrations in a High Pressure Centrifugal Compressor: A Case History", NASA Conference Publication 2338, "Proceedings of a Workshop Held at Texas A&M University", College Station, Texas, May 1984.

9. Coletti, N. J.; Crane, M. E. Jr.: "Centrifugal Compression on the Arun High Pressure Injection Project", I. Mech. E. Conference on "Fluid Machinery for the Oil, Petrochemical and Related Industries", The Hague, The Netherlands, March 1981.

TABLE 1

Curve Definitions for Figures 3 and 4

Line	Case (Seal) Pressure		Bearing Clearance	
	KPa	psi	mm	in.
A	6900	1000	0.127	0.005
B	1030	150	0.127	0.005
C	6900	1000	0.241	0.0095
D	1030	150	0.241	0.0095

TABLE 2

Vibration Ratio Comparisons
(Based on Test Data Figures 5 and 6)

1. Midspan to bearing vibration ratio at first critical speed (NC_1):

   tight clearance - 5.20
   loose clearance - 1.70

2. Tight to loose bearing clearance vibration ratio:

   a. midspan vibration
      at NC_1 - 5.20
      at 12000 r/min - 0.56

   b. bearing vibration
      at NC_1 - 1.70
      at 12000 r/min - 0.14

TABLE 3

Operating Conditions

	Field	Test
mol wgt.	11.6	11.0
Flow, m^3/hr	6,540	6,610
ft3/min	3,850	3,890
Inlet pressure, KPa	1,720	1,585
psi	250	230
Discharge pressure, KPa	10,342	10,690
psi	1,500	1,550
Power, KW	10,146	10,205
bhp	13,600	13,680
Speed, r/min	10,436	11,000
Bearing span, mm	1,753	1,753
in.	69	69
Number of impellers	11	11

TABLE 4

Hydrocarbon Test Conditions

Test	A	B	C
Gas	H.C.	N_2	H.C.
Mol weight	34.6	28	35.6
Inlet pressure, KPa	14,135	19,300	14,135
psi	2,050	2,800	2,050
Discharge pressure, KPa	32,910	30,340	33,100
psi	4,773	4,400	4,800
Speed, r/min	8,305	8,800	8,800
Power, KW	5,425	3,540	10,986
BHP	7,273	4,746	14,726

ORIGINAL PAGE IS
OF POOR QUALITY

1969 - SEAL / ROTOR RESPONSE FACILITY TEST RIG

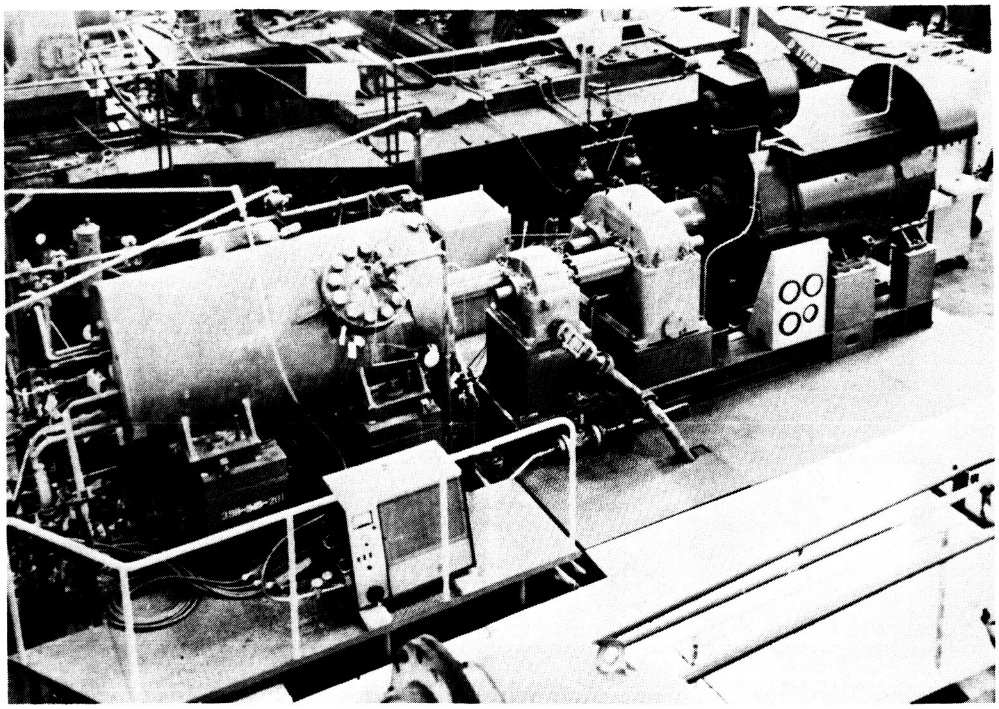

Figure 1

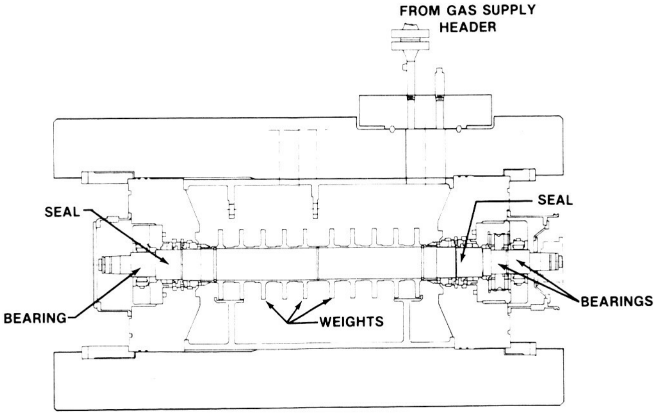
FROM GAS SUPPLY
HEADER
SEAL
SEAL
BEARING
BEARINGS
WEIGHTS

FACILITY - TEST RIG

Figure 2

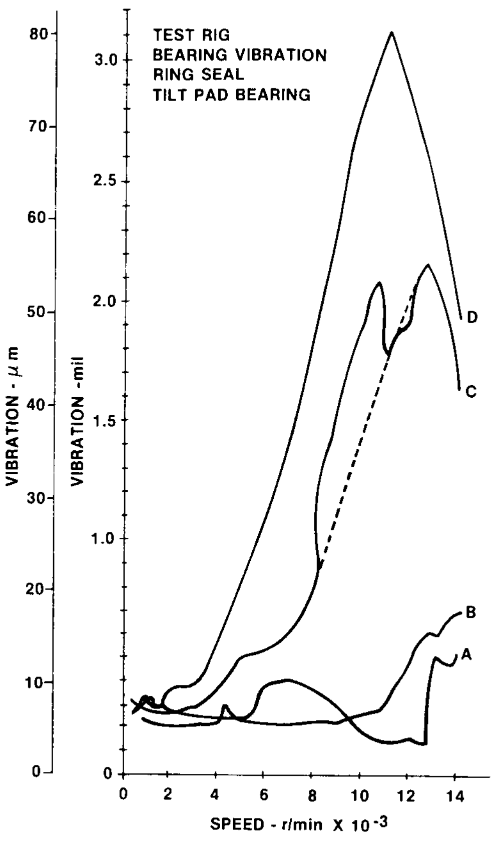

Figure 3

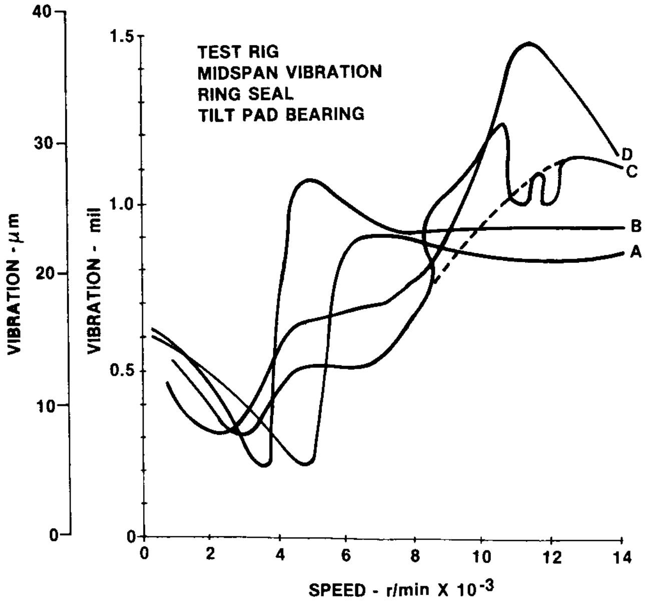

Figure 4

ORIGINAL PAGE IS
OF POOR QUALITY

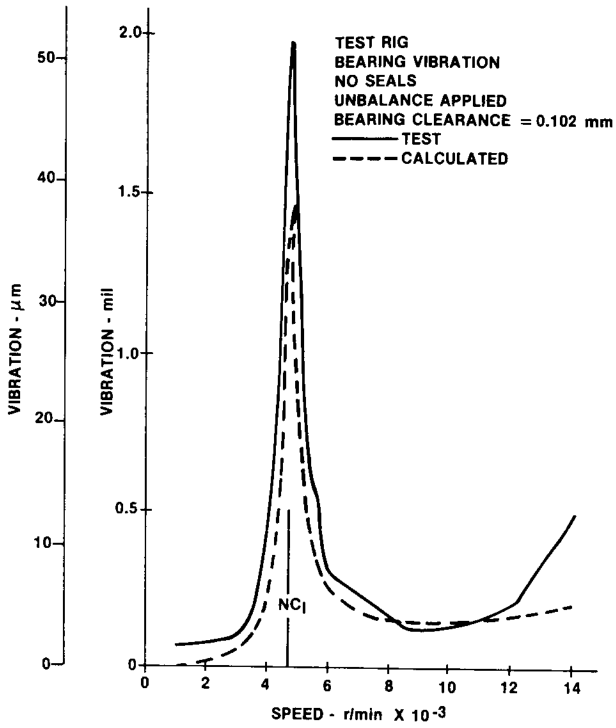

Figure 5A

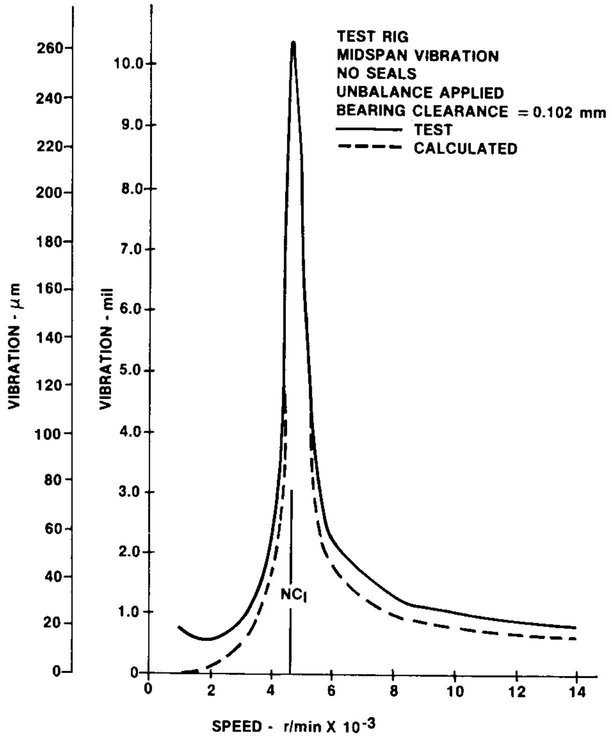

Figure 5B

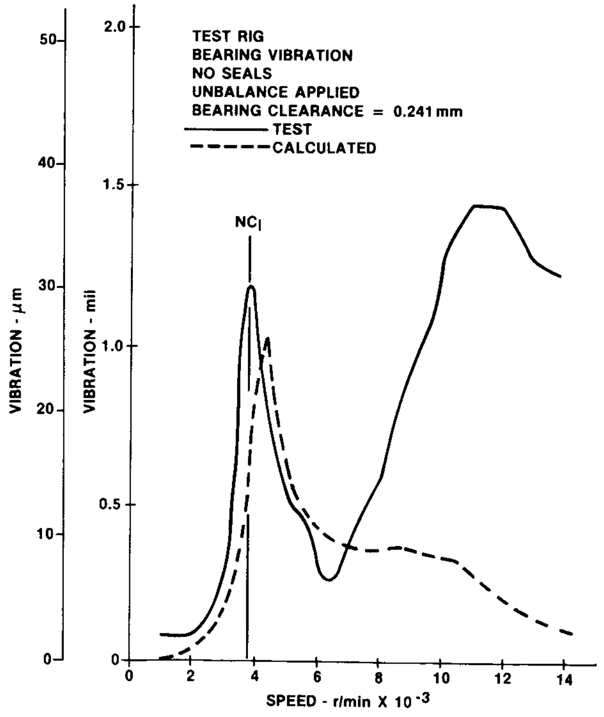

Figure 6A

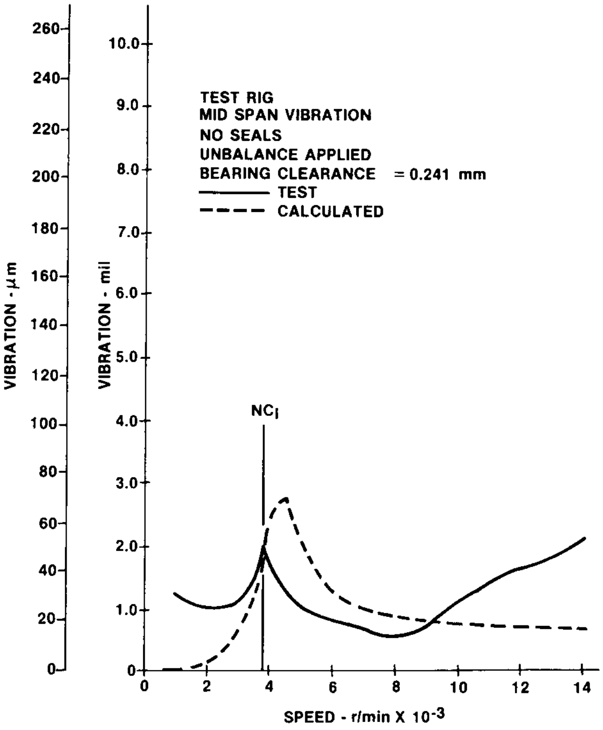

Figure 6B

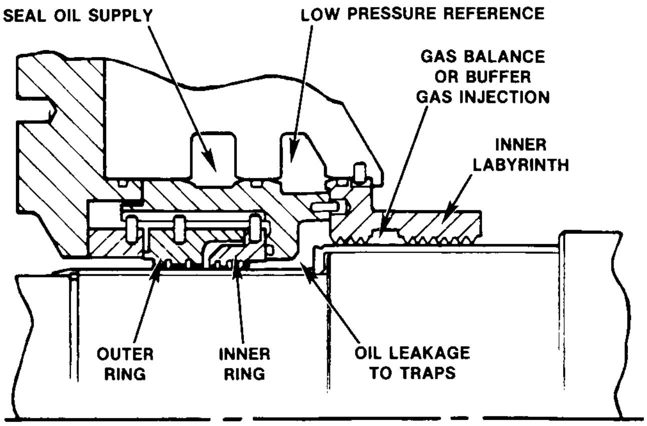
SEAL OIL SUPPLY
LOW PRESSURE REFERENCE
GAS BALANCE OR BUFFER GAS INJECTION
INNER LABYRINTH
OUTER RING
INNER RING
OIL LEAKAGE TO TRAPS

RING TYPE OIL FILM SEAL

Figure 7

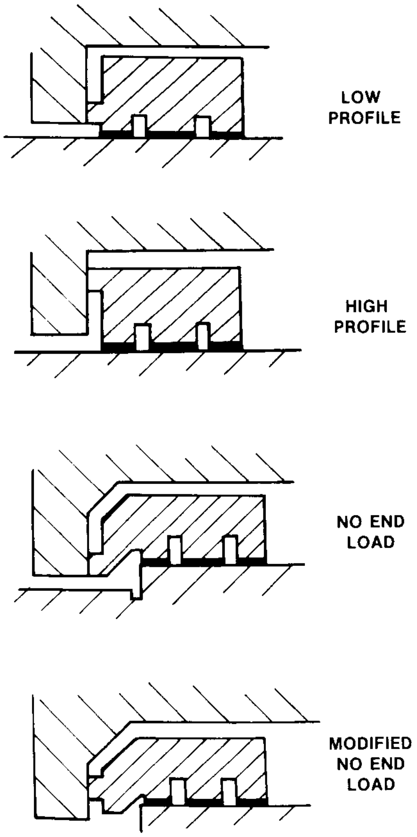
LOW PROFILE
HIGH PROFILE
NO END LOAD
MODIFIED NO END LOAD

OUTER RING GEOMETRY

Figure 8

ORIGINAL PAGE IS
OF POOR QUALITY

TILT PAD SEAL

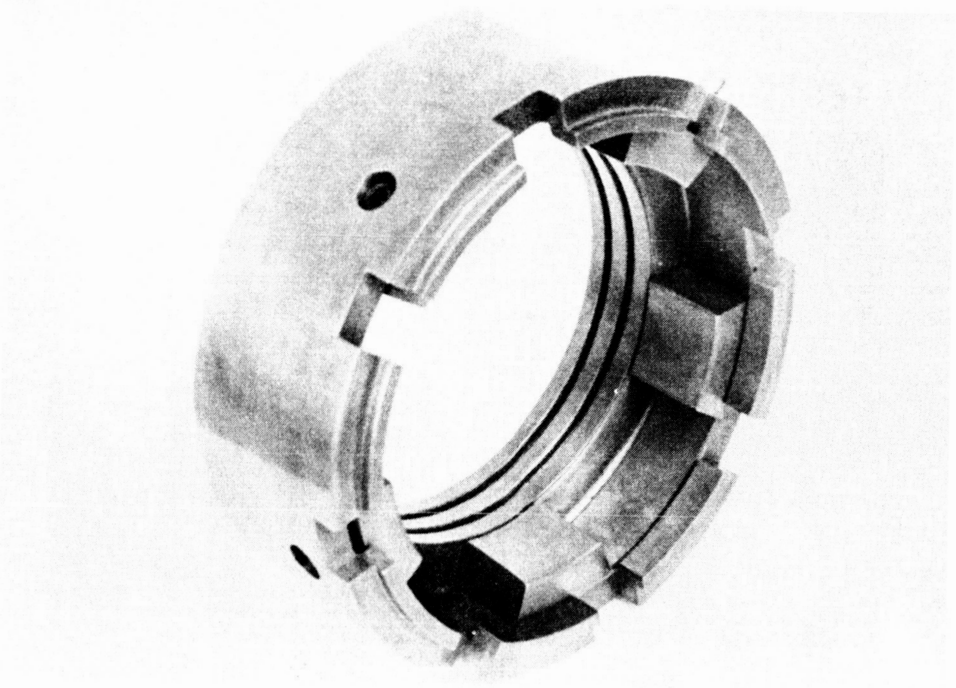

Figure 9

1973 - FULL LOAD / FULL PRESSURE TEST VEHICLE

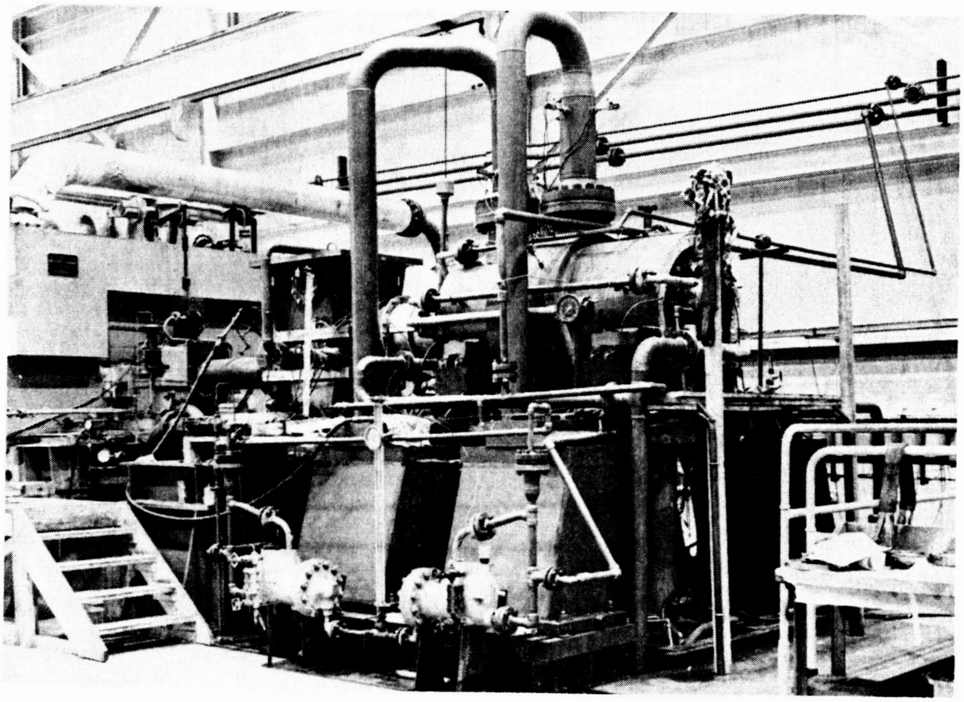

Figure 10

ORIGINAL PAGE IS
OF POOR QUALITY

VIBRATION AMPLITUDE VS TIME

TEST #6 V3H RUN 3

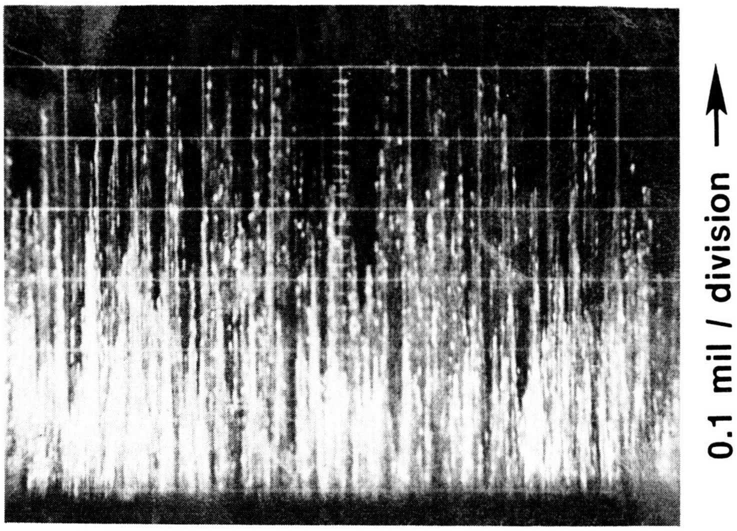

N = 9000 r/min — 10 sec —

Figure 11

VIBRATION AMPLITUDE VS TIME

TEST 22 V3H RUN 8

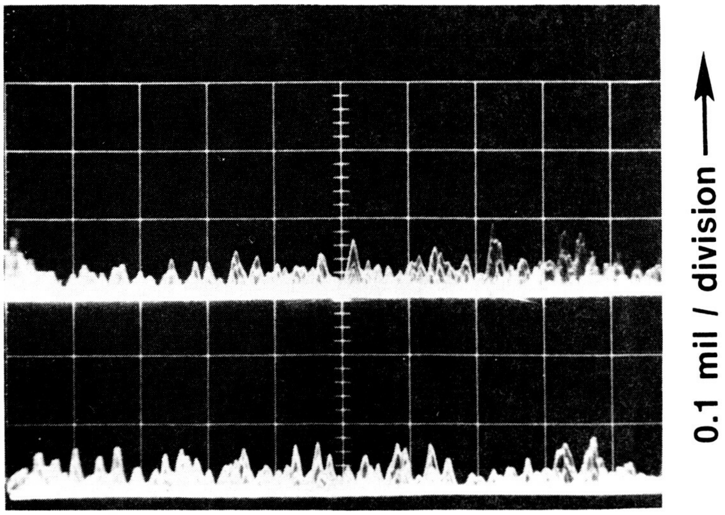

N = 10,900 r/min —10 sec —

Figure 12

ORIGINAL PAGE IS
OF POOR QUALITY

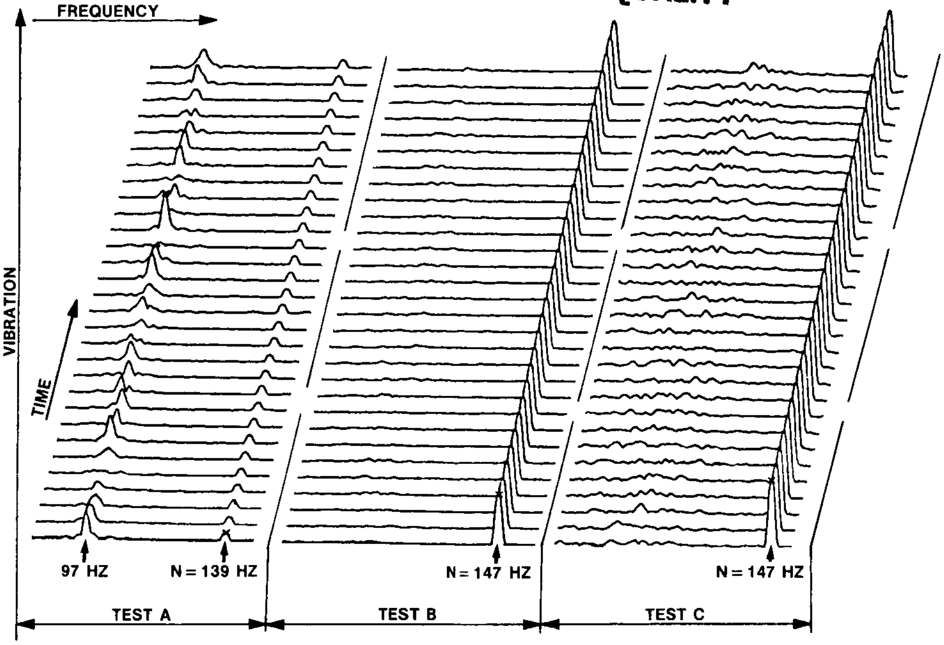

TIME SPECTRUM PLOT

Figure 13

FROM: NASA CONFERENCE PUBLICATION 2338 (1984)

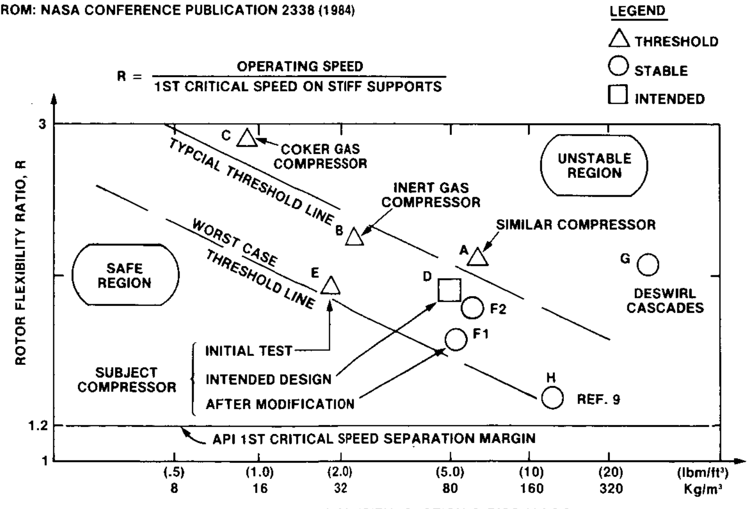

Figure 14

DRESSER CLARK EXPERIENCE

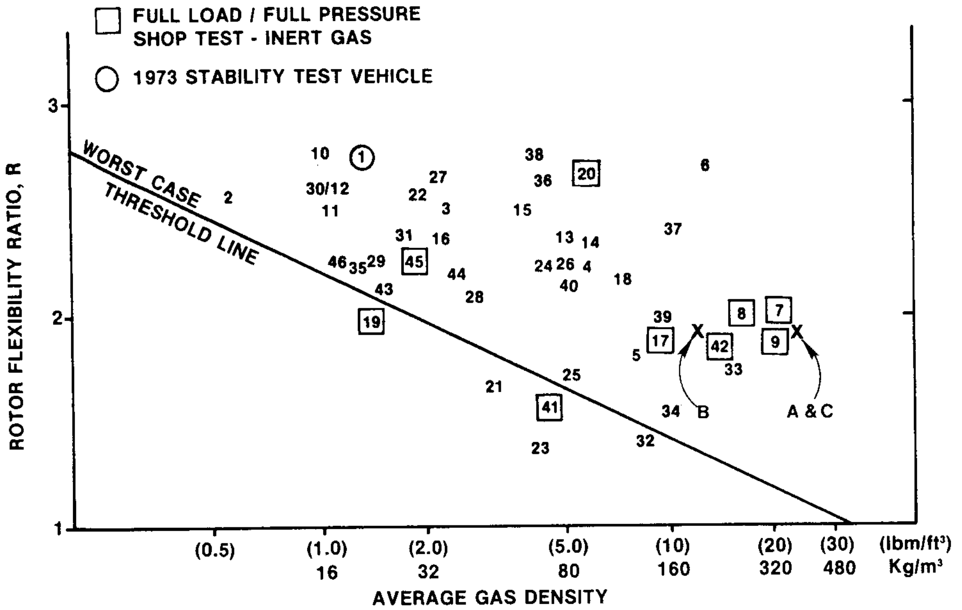

Figure 15

N87-22201

AN EXAMINATION OF GAS COMPRESSOR STABILITY AND ROTATING STALL

Aziz A. Fozi
Solar Turbines Incorporated
San Diego, California 92138

The principal sources of vibration related reliability problems in high pressure centrifugal gas compressors are the re-excitation of the first critical speed or Resonant Subsynchronous Vibration (RSSV), and the forced vibration due to rotating stall in the vaneless diffusers downstream of the impellers. An example of such field problems is documented in reference 1.

This paper describes the results of a test program at the author's company, initiated in 1983 and completed during 1985, that studied the RSSV threshold and the rotating stall phenomenon in a high pressure gas compressor.

SYMBOLS

Values are given in both SI and English units. The measurements and calculations were made in English units.

Alpha 3	Averaged calculated one-dimensional flow angle into the diffuser measured in degrees from tangential
b3	Inlet width of diffuser
N	Speed
Ncr	Rigid Bearing First Critical Speed
R3	Inlet radius of diffuser
RSSV	Resonant Subsynchronous Vibration or re-excitation of the first critical speed (translatory whirl). Stability threshold means conditions at which the RSSV becomes present.

BACKGROUND

The purpose of this test program was to study subsynchronous vibration problems in an offshore gas compressor installation. The plan was to assemble an identical gas compressor and run it at the same pressure and speed conditions in order to create similar instability mechanisms that could be studied and overcome by hardware modifications at the factory.

AREAS OF STUDY

Tests conducted focused on:

1. Stability threshold and how it is influenced by modifications in balance piston hardware.
2. Presence of rotating stall in parallel-wall vaneless diffusers (as a forcing function) and how the development of rotating stall is influenced by diffuser inlet flow angle (ref. 2).

Justification for focusing the test on the balance piston and vaneless diffusers is provided in this section.

The frequency of the subsynchronous vibration matched the first critical speed of the rotor. This indicated a self-excited mechanism. The compressor was designed to operate at 3,100 kPa ab (450 psia) suction and 12,410 kPa ab (1800 psia) discharge pressure. In practice, the compressor was limited to 11,030 kPa ab (1600 psia). Operation above 11,030 kPa ab (1600 psia) was possible but the subsynchronous vibration would cause bearing damage (clearance increase) within a few days.

On account of its sensitivity to discharge pressure, the cause of this instability was thought to be aerodynamic cross-coupling rather than mechanical, such as the influence of oil seals. In fact, the oil seals were not suspect since the seal oil system was referenced to suction pressure and was not a function of the discharge pressure.

Earlier tests conducted on a similar gas compressor at the author's company in 1974 indicated that stability threshold can be increased by relatively simple modifications to the balance piston flow field. The analytical basis for this work was partially drawn from reference 3. Given this background, the test focused on the balance piston as the major source of excitation and its modification to extend the stability limits.

The next step was to identify the cause of vibration occurring at frequencies lower than the RSSV component (around 65 Hz or about 20% running speed) that had become noticeable during tests. The low frequencies involved indicated an aerodynamic forcing function. It is well known that incipient compressor surge is signaled by occurrence of very low frequency vibration (less than 10 Hz is typical). As a matter of fact, during tests under aerodynamic load such as ASME PTC-10 tests, the proximity to surge is announced by the appearance of these low frequencies. It was thus concluded to search for an aerodynamic forcing function as the cause of such low frequency vibration. Rotating stall in the parallel wall vaneless diffusers was the prime candidate. Figure 1 is a typical test spectrum where all these different frequencies are excited.

The test program was divided into two portions. First, the effect of balance piston flow field on stability was studied. Then, the pressure field at the inlet of the last stage diffuser was monitored for rotating stall.

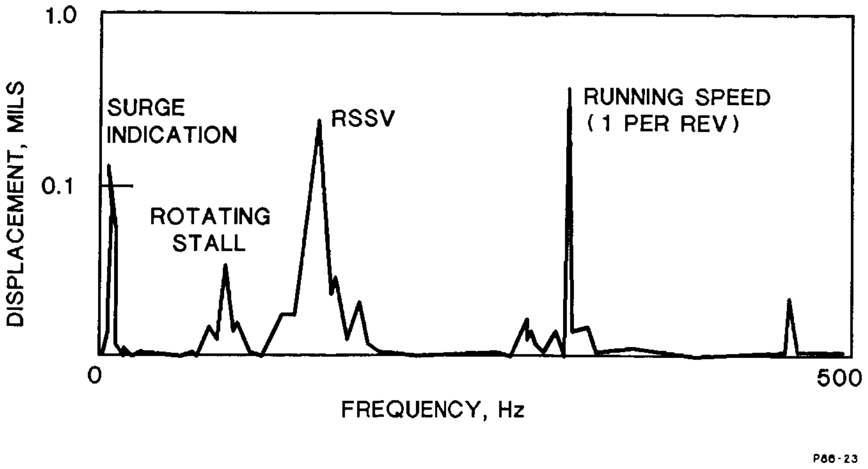

Figure 1. Subsynchronous Vibration Spectrum

TEST PROGRAM DETAILS

Facility

Tests were conducted at the gas compressor closed loop facility of the author's company. This facility in San Diego utilizes a 3200 kW (4300 hp) Centaur gas turbine driver with a step-up gearbox to achieve 24,500 rpm maximum output speed. The gases used were nitrogen or carbon dioxide.

The facility piping is limited to 10,340 kPa gauge (1500 psig) on suction and 31,025 kPa gauge (4500 psig) on discharge. Shell and tube heat exchangers are used to cool the compressed gas.

Compressor

Figure 2 shows a cross section of the gas compressor used for the test. This compressor is capable of 27,580 kPa ab (4000 psia) discharge pressure. The rotor construction features the impellers and suction and discharge stub shafts held together as a monolithic piece by a center tiebolt stretched to provide 311,375 Newtons (70,000 pounds) compressive force. The rotor configuration is straight-through, non-intercooled, with constant impeller hub and shroud labyrinth seal diameter.

The undamped critical speed map (fig. 3) provides rotor-dynamic data. The rigid bearing first critical speed was slightly above 10,000 rpm compared to a typical running speed range of 18,000-23,000 rpm. The rotor weight was 55 kg (122 pounds). Nominal bearing data follow:

ORIGINAL PAGE IS
OF POOR QUALITY

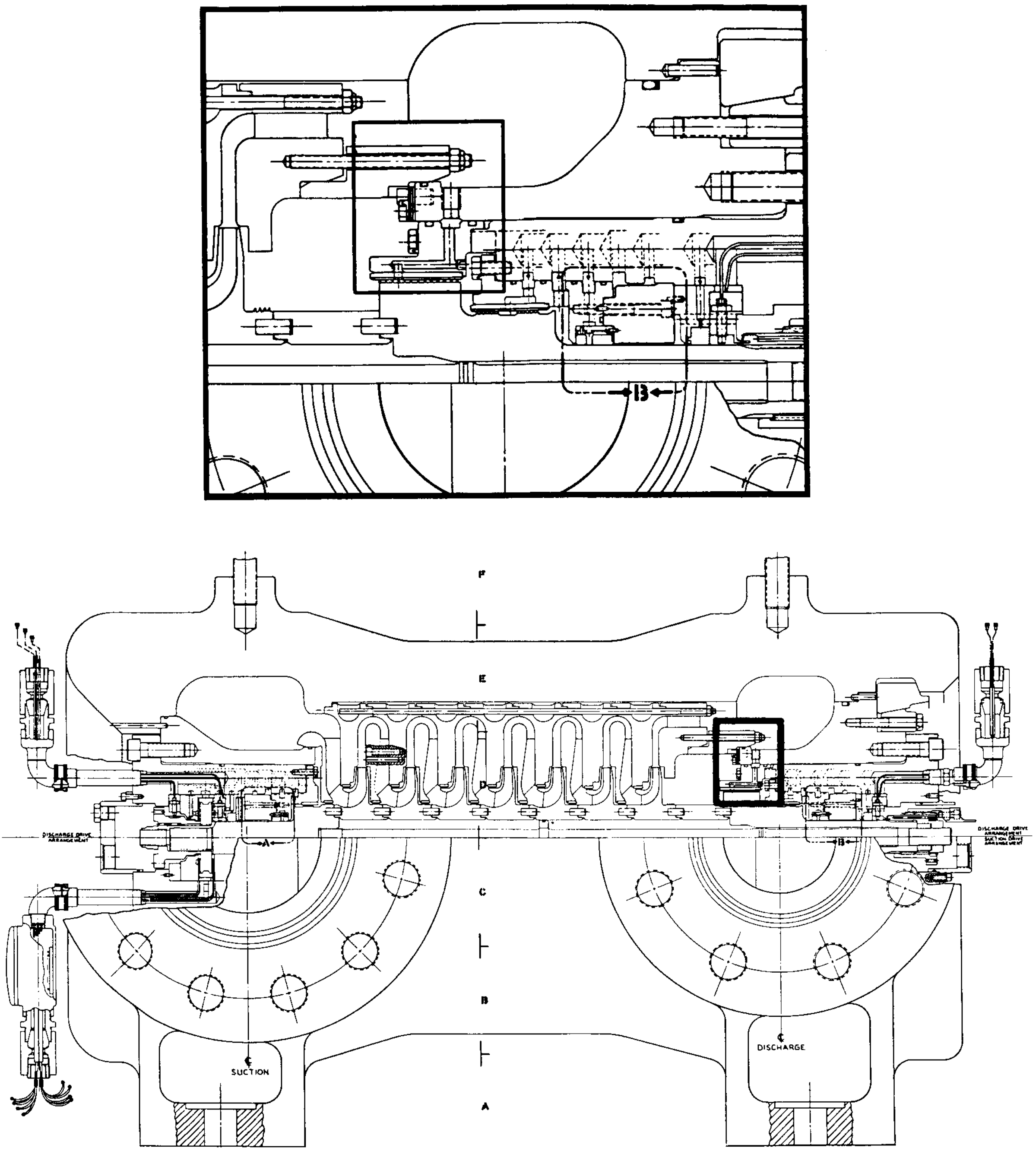
B
F
E
C
B
A
A
B
DISCHARGE DRIVE ARRANGEMENT
DISCHARGE DRIVE ARRANGEMENT
SUCTION DRIVE ARRANGEMENT
℄ SUCTION
℄ DISCHARGE

Figure 2. Cross Section of Test Gas Compressor

• Shaft Diameter	44.5 mm (1.75 in.)
• Bearing Clearance Assembled	0.0686 mm (0.0027 in.) - Diametral
• Bearing Preload	0.7
• Pivot Offset	0.6
• Load Position	Between Pivots
• Length/Diameter	0.25
• Number of Pads	5
• Load on Each Bearing	271 Newtons (61 lb)
• Bearing Span	864 mm (34 in.)

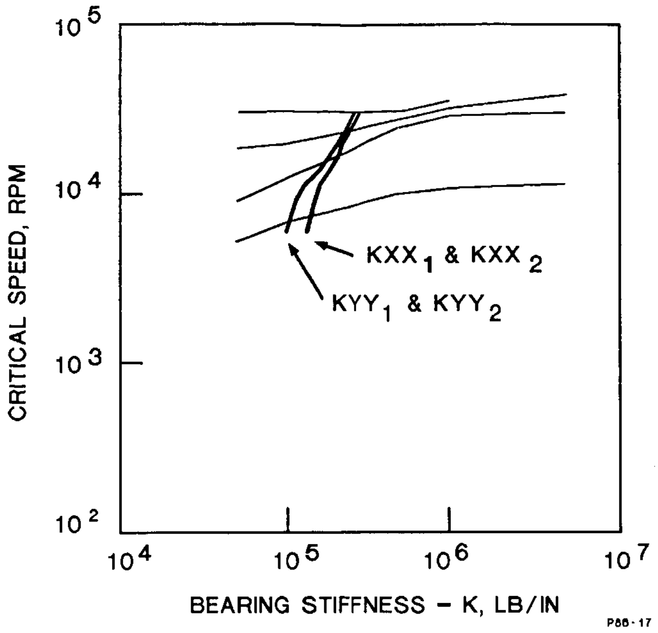

Figure 3. Undamped Critical Speed Map

All the labyrinths used were straight-through with the teeth on the rotating elements. The balance piston and impeller shroud seals had a 127 mm (5 in.) diameter. The hub seals had a 94 mm (3.7 in.) diameter. Shaft seals were conventional oil film-type floating rings with anti-rotation pins.

Test Configurations for Stability Threshold

Three balance piston configurations were tested:

- **I - The Baseline Case** - The balance piston flow was taken from the last stage impeller. This is considered the conventional approach (See fig. 4.)

- **II - The 'P2 Inject'** - This configuration is the same as shown in the cross section. The balance piston flow is derived from the discharge cavity and the gas is injected at the third labyrinth tooth. The flow is established because of the dynamic pressure recovery through the last stage diffuser. A portion of injected gas will recirculate back into the last stage diffuser. See figure 5 for detail.

  The purpose of 'P2 inject' modification is to eliminate the inlet swirl into the balance piston which is believed to be a strong source of aerodynamic cross coupling forces. Reference 4 is cited here as one of the recent sources of analytical justification for this phenomenon.

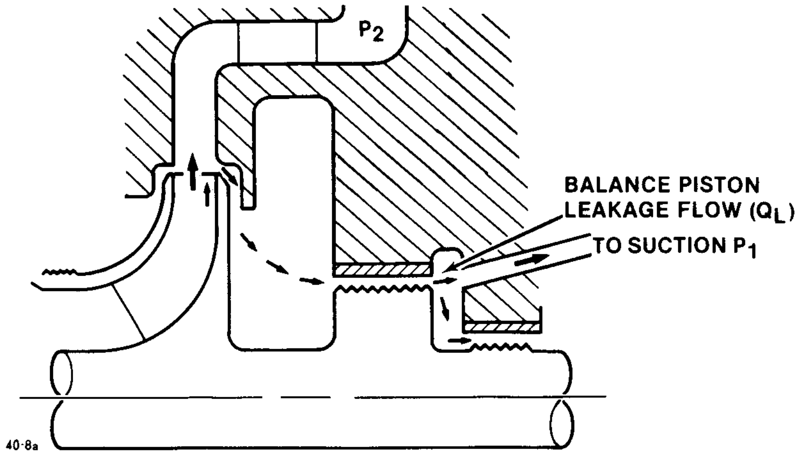
P2
BALANCE PISTON LEAKAGE FLOW (QL)
TO SUCTION P1
40-8a

Figure 4. Conventional Balance Piston Flow

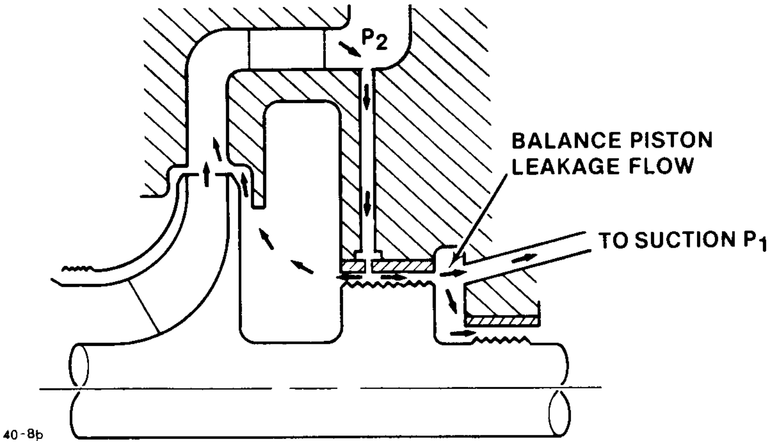
P2
BALANCE PISTON LEAKAGE FLOW
TO SUCTION P1
40-8b

Figure 5. Balance Piston Flow with P_2-Inject Modification

Some thought was given to direct the 'P2 inject' flow against the rotation to delay the re-establishment of tangential velocity field in the balance piston due to viscous forces. However, the available anti-swirl gas velocity at the injection point appeared to be insufficient to derive any significant results.

III - The 'Hub Seal' - This case was a simplified approach where the balance piston flow is derived from the discharge collector, the last impeller being isolated with a seal at the hub. Thus, the impeller induced swirl is avoided. Figure 6 shows the mechanical details.

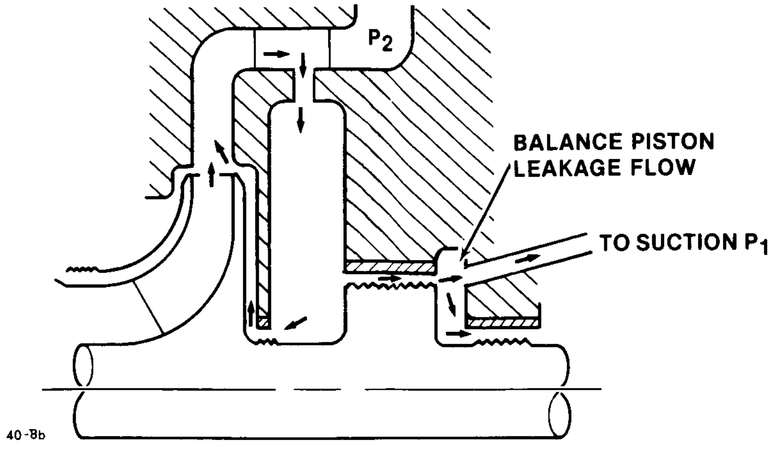
P2
BALANCE PISTON
LEAKAGE FLOW
TO SUCTION P1
40-8b

Figure 6. Balance Piston Flow with Hub Seal Modification

Test Configurations for Rotating Stall

Tests were conducted with two diffusers having inlet width-to-radius ratios (b3/R3) of 0.029 and 0.043 respectively, and results were compared to the criteria proposed in refs. 2 and 5. Figure 7 gives dimensional data for the two vaneless diffusers tested. Note that the only difference between the two geometries is in the inlet width (b3).

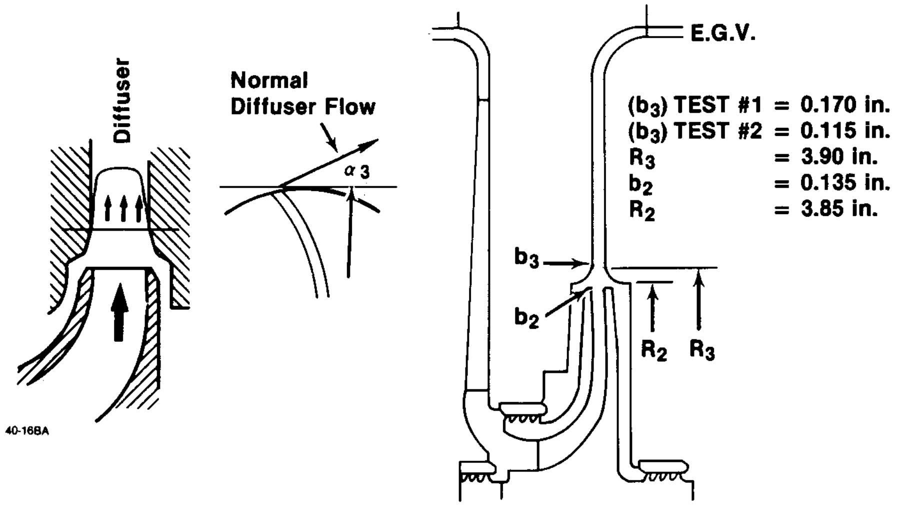
Diffuser
Normal
Diffuser Flow
α 3
40-168A
E.G.V.
(b3) TEST #1 = 0.170 in.
(b3) TEST #2 = 0.115 in.
R3 = 3.90 in.
b2 = 0.135 in.
R2 = 3.85 in.
b3
b2
R2
R3

Figure 7. Vaneless Diffuser Geometry

Tests consisted of operating at any constant speed and traversing the compressor operating map from choke towards surge. The diffuser inlet flow angle (Alpha 3) was calculated in real time and displayed. Formation of stall cells was monitored by pressure transducers and data points were recorded as stall cells developed and changed in shape.

Instrumentation

The instrumentation used included single- and two-channel FFT spectrum analyzers, a 14-channel tape recorder, and speed tracking balance analyzer. The stall cells were detected by quartz crystal dynamic pressure transducers connected to charge amplifiers displayed on dual trace camera oscilloscopes.

Although one transducer is sufficient to detect the presence of pressure fluctuations (stall), with two transducers the number of stall cells can be calculated based on the observed phase difference between the two signals. See reference 5 for details. Figure 8 shows a detail of the transducer installation.

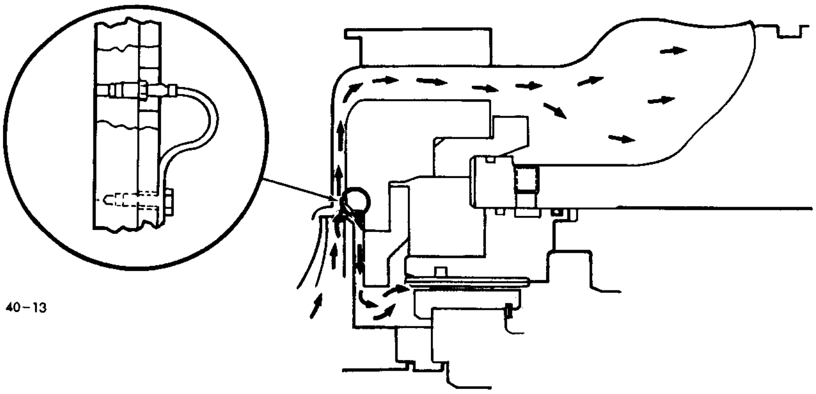

Figure 8. Pressure Transducer Installation at Diffuser Inlet

Oscilloscope traces presented later are numbered 1 and 2 in the direction of rotation to show phase. The typical amplification factor was a 690 kPa ab (100 psia) dynamic signal per volt, or as indicated on the pictures. The horizontal (milliseconds) and vertical (volts) scales are annotated on these pictures for reference.

The time scale selected favored detection of low frequency signals in the area of 10 to 100 Hz. With this scale, the blade passing frequency at about 6000 Hz is compressed on the oscilloscope trace and is not system noise.

TEST RESULTS

Stability tests concentrated on establishing the threshold at which the RSSV component appeared on the spectrum of shaft vibration at either bearing location. The threshold was established in terms of operating pressure and speed conditions and compared to the criteria proposed in reference 6, namely P2 x (P2-P1), herein referred to as P2 Delta P.

A peak-to-peak shaft vibration amplitude value of 1.27 to 2.54 microns (0.05 to 0.1 mils) was selected as the threshold limit. The results indicated that the P2-inject (Case II) provides better stability than the hub seal (Case III), which itself is an improvement over the baseline (Case I) (figs. 9 and 10).

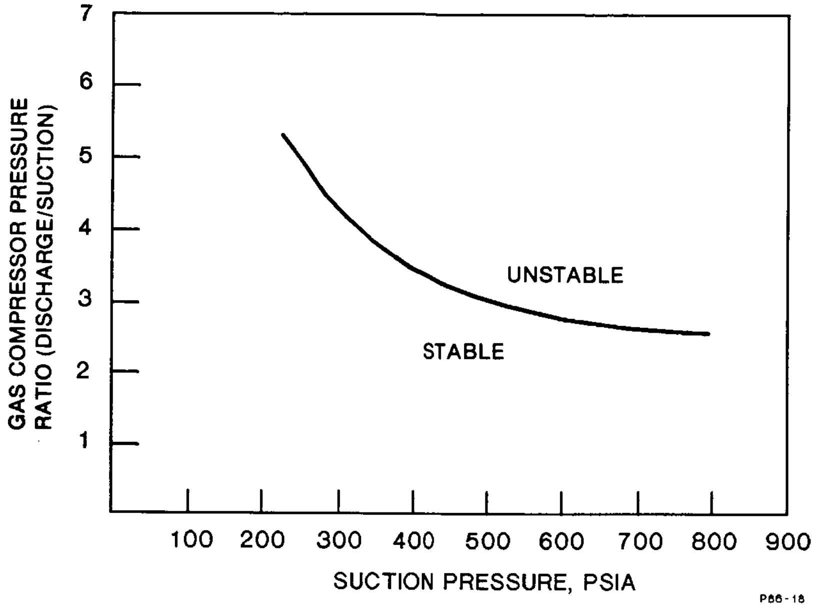

Figure 9. Stability Threshold of Base Case (Case I)

- **Case I** - The stability line for Case I shows the limit where the RSSV component grows to about 1.27 to 2.54 microns (0.05 to 0.1 mils) peak-to-peak. This line is viewed as analogous to a P2 Delta P range of 1 to 2.5 x E6 (psia square) (fig. 11).

- **Case II** - The P2 inject configuration was stable throughout the tested region. Temperature limits of the facility were reached in every case before any evidence of RSSV was observable. Test facility vibration analyzers were set to high sensitivity to detect the onset of RSSV activity; however, none was detected.

- **Case III** - In figure 10, the hub seal stability limit shows considerable improvement over Case I, comparable to a P2 Delta P range of 4 to 7 x E6. The elimination of impeller swirl at the inlet of the balance piston is thought to be responsible for the improvement.

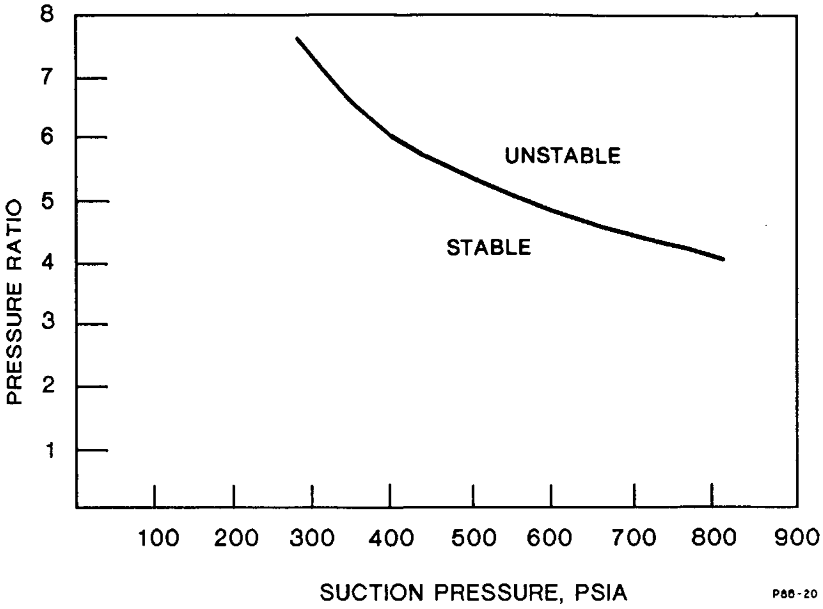

Figure 10. Stability Threshold of Hub Seal Case (Case III)

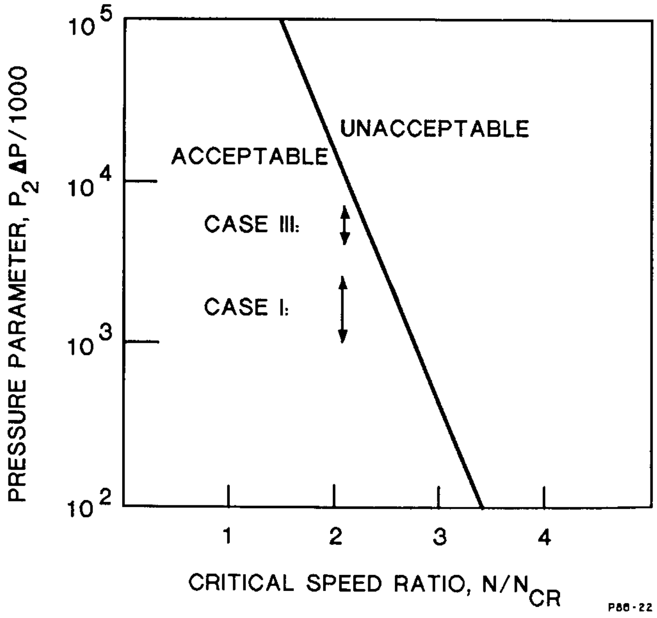

Figure 11. Stability Threshold of Cases I and III

Two observations were made during these tests:

1. The stability threshold for each configuration was defined as a function of suction pressure and pressure ratio, and this threshold was not dependent on the staging selection or speed. It was found that when running on natural gas (S.G. = 0.75) the threshold was the same as when running on nitrogen, although at different speeds. Likewise, two compressors running on the same gas but staged differently (ten stages versus seven stages) gave identical results regardless of speed. (Typical variation: 18,000 versus 21,000 rpm.) This was also noticeable when examining the threshold lines that were obtained in two parts, low suction pressure/high ratio running on carbon dioxide and high suction pressure/low ratio running on nitrogen. The threshold was a continuous line. This led to the conclusion that the speed was not as strong a stability indicator as expected.

2. The RSSV frequency showed dependence on the density of the gas, as evidenced implicitly in the following table:

P1 kPa ab (psia)	Ratio	P2 kPa ab (psia)	Ncr (Hz)	Gas
1,089 (158)	5.8	6,323 (917)	132.5	CO2
1,765 (256)	5.2	9,177 (1,331)	135.0	CO2
2,068 (300)	4.8	9,929 (1,440)	145.0	CO2
3,585 (520)	3.2	11,473 (1,664)	150.0	N2
4,591 (666)	3.0	13,776 (1,998)	152.0	N2
4,964 (720)	2.8	13,900 (2,016)	155.0	N2
5,633 (817)	2.5	14,079 (2,042)	157.5	N2
6,426 (932)	2.2	14,134 (2,050)	160.0	N2

This dependency suggests that labyrinth seals have direct stiffness terms that tend to restore the deflection of the shaft, thus, raising the first critical speed. As the density of the compressed gas increases, the restoring forces become large.

ROTATING STALL

Test Results

The tests showed that the low frequency vibrations on the shaft were indeed induced by rotating stall. Figure 12 shows a case where one stall cell at 65 Hz was observed. The transducer separation in this case was 75 degrees. The 300-Hz signal corresponds to shaft rotation at 18,000 rpm, while the jitter corresponds to blade passing frequency at 18 times running speed.

The test verified the criterion for the onset of rotating stall as being the b3/R3 ratio versus the diffuser gas inlet angle (Alpha 3), as described in references 2 and 5. See figure 13.

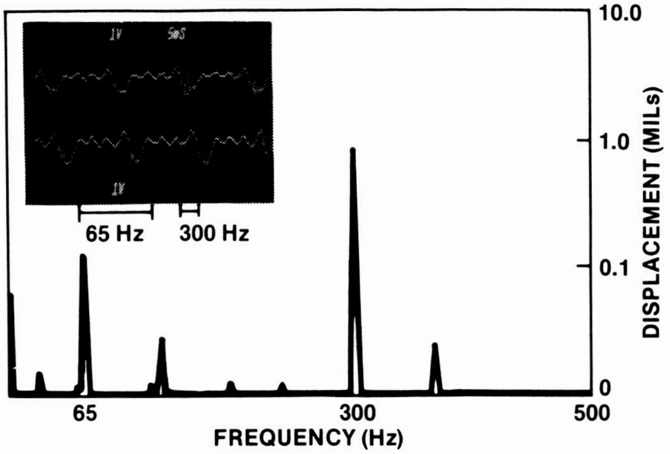

11-21

Figure 12. Shaft Vibration Induced by Rotating Stall

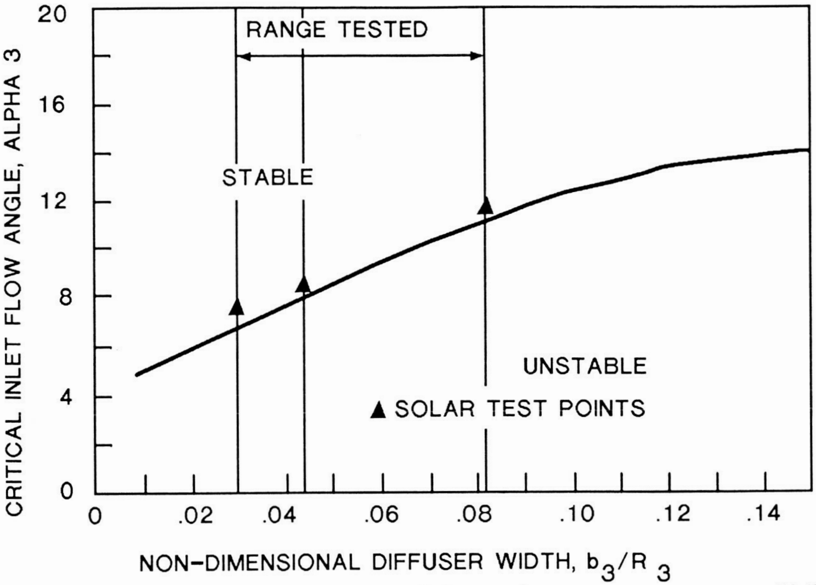

Source: Reference 5

Figure 13. Rotating Stall Criterion, b3/R3 versus Alpha 3

First, the ratio of b3/R3 of 0.043 was tested. Figures 14, 15, and 16 show the development of rotating stall as the Alpha 3 angle was reduced from 9.2 degrees to 7 and then to 5.6 degrees [P2 is at 5068 kPa ab (735 psia)]. The threshold value was obtained at 8.25 degrees, corresponding to the oscilloscope trace in fig. 17. This figure shows the unsteady pressure field as stall develops and dissipates.

For a diffuser b3/R3 ratio of 0.029, a critical alpha angle of 7.5 degrees was obtained. The calculation procedure for alpha angles was based on one-dimensional flow field analysis. The Reynolds number correction was not considered in view of the small b3/R3 values of these tests.

ORIGINAL PAGE IS
OF POOR QUALITY

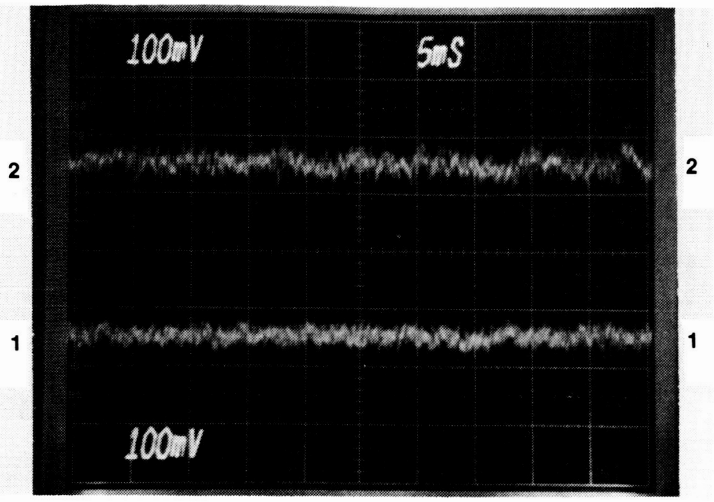

Figure 14. Steady State Pressure Field Prior to Rotating Stall

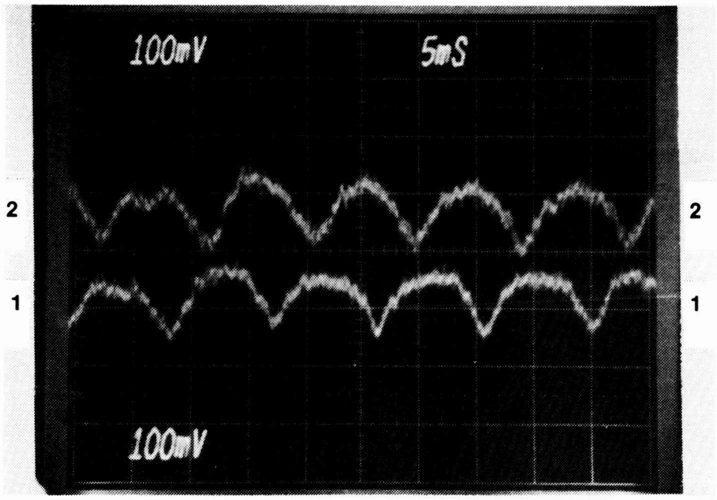

Figure 15. Rotating Stall, Two Cells at 56 Hz Rotational Speed

This correlation between low frequency shaft vibration and rotating stall helped interpret results of another investigation. Low frequency vibration was noted when operating a larger frame gas compressor on a particular area of its operating map close to surge. However, careful operation showed that the unit was not at surge and that the amplitude of vibration would actually decrease as flow was lowered to the surge line. (See the performance map in figure 18).

The impeller diameter of this compressor was 305 mm (12 in.) with a b3/R3 ratio of 0.0815. The last stage diffuser flow angles were calculated and drawn on the performance map. The appearance of vibration closely matched the onset of rotating stall predicted at an Alpha 3 of 11.3 degrees. It is interesting to note the high amplitude of vibration at 8 Hz (single stall cell) compared to 16 Hz (two cells) which apparently indicates the cancellation effect of an even number of stall cells.

ORIGINAL PAGE IS
OF POOR QUALITY

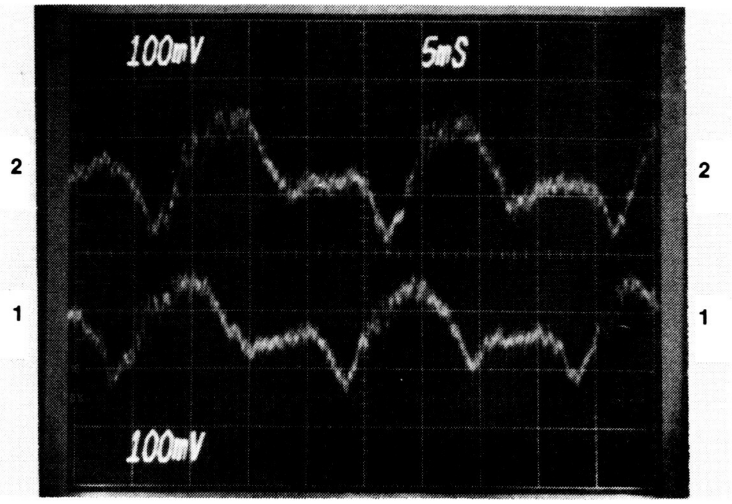

Figure 16. Rotating Stall near Surge

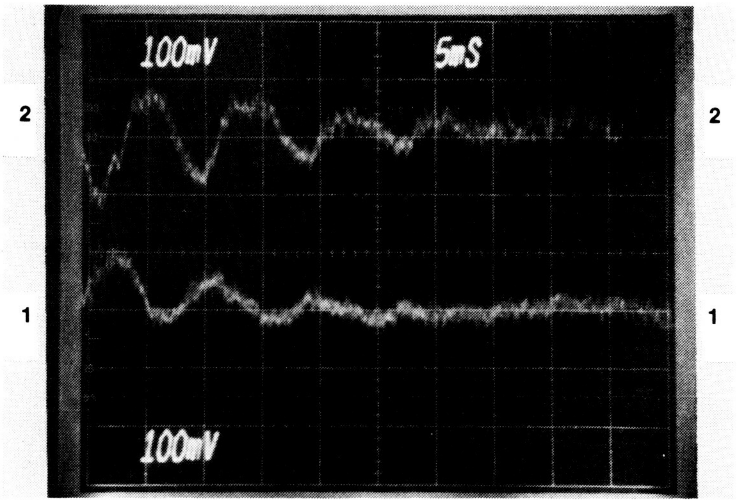

Figure 17. Threshold Where Stall Cell Appears and Dissipates

CONCLUSION AND COMMENTS

The balance piston is a strong excitation source of instability, and modifications to the inlet swirl have great effect in extending the operating limits of the gas compressor. For any given compressor configuration, the stability limit may be defined in terms of suction pressure versus pressure ratio. The P2 Delta P as a function of the critical speed ratio N/Ncr is a useful index but it over-emphasizes the speed sensitivity. Lastly, the rotating stall criterion of Alpha 3 versus b3/R3 was confirmed.

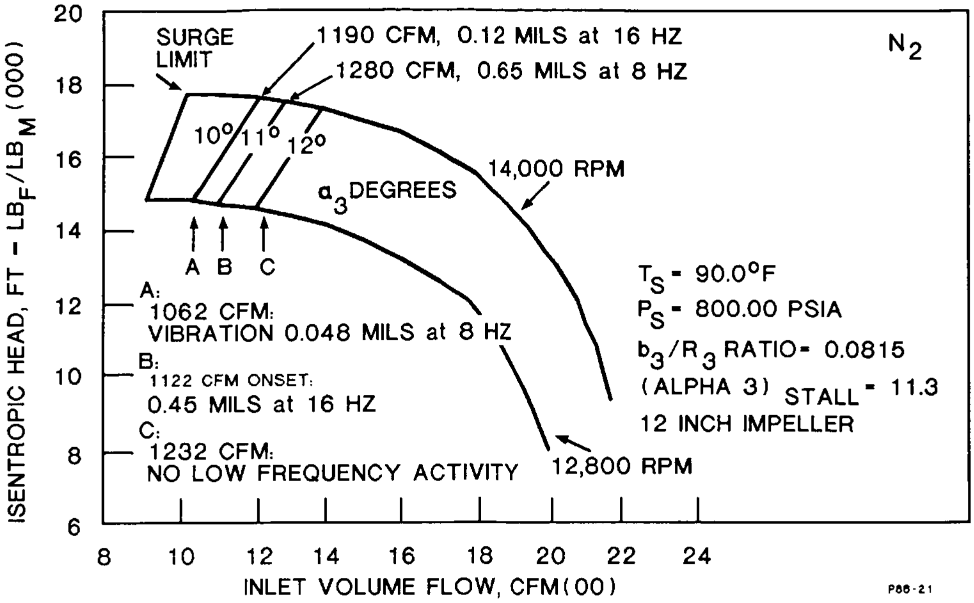

Figure 18. Performance Map with Lines of Constant Alpha 3 versus Shaft Vibration

REFERENCES

1. Fulton, J.W., "Subsynchronous Vibration of a Multistage Centrifugal Compressor Forced by Rotating Stall," Turbomachinery Technology Seminar 1986, Solar Turbines Incorporated, San Diego, California, February 1986.

2. Kinoshita, Y., Senoo, Y., "Rotating Stall Induced in Vaneless Diffusers of Very Low Specific Speed Centrifugal Blowers," ASME 84-GT-203, June 1984.

3. Kostyuk, A.G., "A Theoretical Analysis of the Aerodynamic Forces in the Labyrinth Glands of Turbomachines," Moscow Power Institute (MEI), 1972.

4. Childs, D.W., Scharrer, J.K., "An Iwatsubo-Based Solution for Labyrinth Seals: Comparison to Experimental Results," ASME 85-GT-136, Texas A&M University, College Station, Texas, March 1985.

5. Van Den Braembussche, "Rotating Stall in Vaneless Diffusers of Centrifugal Compressors," Technical Note 145, Von Karman Institute, June 1982.

6. Kirk, R.G., Donald, G.H., "Design Criteria for Improved Stability of Centrifugal Compressors," ASME Publication "Rotor Dynamic Instability," AMD-Volume 55, June 1983.

N87-22202

SUBSYNCHRONOUS VIBRATION OF MULTISTAGE CENTRIFUGAL COMPRESSORS FORCED BY ROTATING STALL

J.W. Fulton
Exxon Research and Engineering Co.
Florham Park, New Jersey 07932

A multistage centrifugal compressor, in natural gas re-injection service on an offshore petroleum production platform, experienced subsynchronous vibrations which caused excessive bearing wear. Field performance testing correlated the subsynchronous amplitude with the discharge flow coefficient, demonstrating the excitation to be aerodynamic. Adding two impellers allowed an increase in the diffuser flow angle (with respect to tangential) to meet the diffuser stability criteria based on factory and field tests correlated using the theory of Senoo (for rotating stall in a vaneless diffuser, Ref. 1). This modification eliminated all significant subsynchronous vibrations in field service, thus confirming the correctness of the solution. Other possible sources of aerodynamically induced vibrations were considered, but the judgment that those are unlikely has been confirmed by subsequent experience with other similar compressors.

INTRODUCTION

This paper describes the joint efforts that a manufacturer and a user made to solve a vibration problem. The vibration was caused by a rotating aerodynamic stall, which created a forced vibration of the rotor resulting in reduced bearing life. The compressor operates at a high pressure typical of natural gas re-injection service. The primary objective of this paper is to provide sufficient engineering information to be useful to others faced with similar problems, in the field, and during design. This objective includes relating the observed phenomena with theories of rotating stall. A secondary objective is to caution purchasers and users of high pressure centrifugal compressors about the potential consequences of rotating stall.

The paper is written from the equipment user's point of view, however it contains technical input from the manufacturer. Except as noted, the calculations of internal flow angles were made by Leon Sapiro of Solar Turbines Inc., who also contributed many valuable insights, and played a major role in solving this problem. Research by the manufacturer is reported in another paper presented at this workshop by Fozi (Ref. 2)

The main parts of the paper describe the following: the equipment, the vibration and its consequences; the method of field diagnosis; the internal analysis to identify the components responsible; the solution and results; an evaluation of the possible causes, including information from a similar case; and finally an empirical guideline indicating when serious vibrations will

PRECEDING PAGE BLANK NOT FILMED

result from rotating stall.

SUBJECT COMPRESSOR RE-INJECTS NATURAL GAS

The problem occurred on the high pressure casings of seven compressor trains used on four oil production platforms located in the South China Sea. Three of the platforms have two trains while the fourth has a single train. The manifestations of the problem were the same on all high pressure casings. The designs of three pairs of trains were similar. The fourth pair of trains were of an earlier type design, which had 178 mm (7 inch) diameter impellers, instead of the 190 mm (7.5 inch) impellers of all the rest. One train, of the newer design, was chosen as a prototype to concentrate efforts toward a solution.

Figure 1 shows the rated conditions of the chosen train. Natural gas, separated from the crude oil produced, enters the low pressure casing at 2070 kPa (300 PSIA). The high pressure casing takes suction at the interstage pressure of 5850 kPa (860 PSIA) and discharges the gas at 14480 kPa (2100 PSIA), to the re-injection wells.

CHARACTERISTICS OF THE VIBRATION

Figure 2 shows the vibration spectrum taken from the shaft proximity probe mounted vertically at the discharge end bearing. The subsynchronous vibration is typical of our case; 33 microns (1.288 mils) peak-to-peak at 27.5 Hertz. The 307 Hertz component is at running speed. All the spectra in this paper, unless otherwise noted, use 16 averages, to give representative amplitudes. The amplitude of the subsynchronous vibration fluctuates appreciably.

The operating conditions for Figure 2 were practically at the rated point of the high pressure casing; the speed 18420 RPM, the suction volume flow 470 cubic meters per hour (277 ACFM), and the suction and discharge pressures 6100 and 14600 kPa (885 and 2121 PSIA) respectively. The molecular weight was 21.4 averaged from several gas samples, compared to 24.0 rated.

The subsynchronous vibration frequency is about 9 percent of RPM, which is typical of the aerodynamically forced type. Bonciani and his co-workers (Ref. 3) provided some of the first descriptions of shaft vibrations in high pressure compressors which were attributable to rotating stall. A comparison of their spectra to Figure 2 showed that it was similar. They emphasized that rotating stall caused a forced subsynchronous vibration as opposed to its being a self-excited resonant subsynchronous vibration.

Figure 3 shows the vibration spectrum taken at the suction end bearing. These data were collected concurrently with Figure 2. The suction end subsynchronous vibration levels were less than 12 microns (0.5 mils) for all operating conditions tested.

The low pressure casing also showed traces of subsynchronous vibration at frequencies associated with "aero-forced" vibration. Figure 4, which uses a logarithmic scale to make the small amplitude vibrations appear more prominently, shows two such frequencies, one with an amplitude of 2 microns (0.08 mil) at 25 Hertz, and another (not marked) next to it with a frequency of 55 Hertz. (The other subsynchronous peak, marked 0.1 mil at 145 Hertz is at a frequency near the first lateral critical speed of the rotor and is probably a "self-excited" vibration.) The subsynchronous vibration of the low pressure casing was always small in amplitude.

CONSEQUENCES OF THE VIBRATION

The subsynchronous vibration was not limited to the 33 microns (1.288 mils) shown in Figure 2. As running time increased the vibration amplitude at the discharge end bearing would increase to the 50 micron alarm level and on to the 63 micron protective shutdown. Forced shutdowns resulted, requiring discharge bearing replacement before starting up again.

To put the magnitude of the problem in proper perspective, it must be pointed out that the subsynchronous vibration was sufficiently limited in amplitude to allow commissioning and operation of the compressor without incident, except for abnormal bearing wear requiring frequent bearing replacement. From the equipment operator's viewpoint, the consequences of such a non-resonant forced response are less severe than the resonant and self-excited type of subsynchronous vibration, which can have a catastrophic consequence on operability. (For instance see Ref. 4.)

Bearing Wore at Pivot Pins

Figure 5 shows the bearing wear pattern. The pivot pin, which supports the pad in the carrier, wears into its mating surface in the back of the bearing pad. The extent of the worn area matches the length of the pin. The depth of the wear into the pad was typically 25 microns (1 mil) on the most severely worn pad, as found when the bearing was removed due to excessive subsynchronous vibration. The overall diametral clearance typically increased to approximately 4 mils at that time compared to the 2.7 mils maximum allowable clearance for a new bearing.

Primarily as a result of the subsynchronous vibration causing bearing wear, the median bearing life was 1000 hours (with a minimum of 88 and a maximum of 2200 hours) for all seven high pressure casings, during the year this problem was under study. This impacted adversely on the availability of the compressor trains and justified considerable effort for correction.

The increase in vibration due to bearing wear can be related to a corresponding reduction in bearing stiffness and damping. The bearing would wear to approximately 4 mils (before a bearing change was required), causing the stiffness and damping of the bearings to decrease substantially. The reduced stiffness allowed the subsynchronous vibration amplitude to increase correspondingly. The manufacturer has performed rotor response analyses which show a 4.4 times increase in response sensitivity when the bearing clearance is increased from 2 to 4 mils (diametral). This reduced stiffness allowed the once-per-revolution component to increase as similarly, but the effect is not so pronounced here because the ratio of increase is partially masked in this case by the presence of a spurious amplitude due to shaft imperfections adding to the once-per-revolution component.

Problem Associated with the Discharge End of the High Pressure Casing

The bearing wear-out, due to the fretting of the tilting pads at the pivot pins, occurred predominantly on the discharge end of the high pressure casing. The subsynchronous vibration also occurred predominantly on the discharge end, as can be seen by comparing Figures 2 and 3. A detailed investigation, including metallurgical laboratory studies of the worn bearings, did not reveal any other supportable cause of the pivot fretting. The suction end pivots did not wear out prematurely.

The bearing life of the low pressure casing has not been a problem. Although detailed records were not kept in the absence of any problem, at least one of the low pressure compressors is still using its original bearings after 17000 hours of service. As the low subsynchronous vibration amplitudes of Figure 4 are typical, the correlation of pivot wear with high subsynchronous vibration amplitudes is thus complete.

Damage Criteria

Because the subsynchronous vibration occurred at low frequency, the shaft vibration velocity, due to this component, was low (about 3.5 millimeters per second, equal to 0.14 inch per second) compared to the 6.3 mm/s (0.25 in./sec.) maximum acceptable for a compressor in good condition. Therefore the manufacturer initially believed that the subsynchronous vibration was not harmful. The manufacturer placed a filter in the vibration monitor system of one of the other compressors of similar design to suppress the subsynchronous vibration signal. Since the compressor was no longer limited by the vibration shutdown from running with high levels of subsynchronous vibration, the result (due to bearing wear) was an increase in both the subsynchronous vibration and the once per revolution vibration, which eventually caused excessive labyrinth wear.

The API 617 limit on non-synchronous components of shaft displacement amplitude (peak-to-peak) specifies that the subsynchronous vibration be less than 4 microns (0.16 mils); the specification limits such components to 10 percent of the overall allowable vibration. The overall allowable vibration in mils equals the square root of [12000 / maximum continuous RPM]. This limit is safe, based on the good experience with the low pressure casings.

Damage Mechanism Hypothesis

The mechanism of the bearing pivot-pin wear is believed to be caused by the subsynchronous vibration breaking down the load-carrying oil film between the pivot-pin and the back of the bearing pad. The subsynchronous vibration tends to hold the the pad against its pivot, thus squeezing out the oil film, while the once-per-revolution component causes the fretting motion. The cause of the fretting is analogous to the wear that occurs on a reciprocating compressor wrist pin having no load reversal.

FIELD DIAGNOSIS

In the field or in testing compressors purchased for a commercial project, transducers for dynamic pressure or velocity usually can not be placed inside the casing. Therefore, diagnosis of aerodynamically induced subsynchronous vibration outside the research laboratory must depend on analysis of commonly available data such as vibration or pressures, temperatures and flows measured outside the casing flange boundaries.

Spectral Characteristics

Field diagnosis is simplified by the distinctive patterns observable in the spectrum. In most cases reported in the literature, rotating stall in stator components has occurred at 4 to 20 percent of RPM. With the spectral analyzer in the real time mode, it can be seen that the component frequency is not locked on to an exact fraction of the rotor speed, but fluctuates slightly, as does the amplitude. In the present case, many distinct frequencies could be produced at will by varying the flow slightly at constant speed. For instance, decreasing the flow from 593 to 562 cubic meters per hour (349 to 331 ACFM) caused the 27.5 Hertz component to split into 12.5 and 40 Hertz components. This phenomena is believed to be due to different numbers of stall cells forming in various stages, but without transducers inside the casing, neither the exact number of cells nor their location can be identified.

Correlation with Flow Coefficients

Once the spectra identified the nature of the problem, we took the second step essential in diagnosis of an aerodynamic stall problem. An aerodynamic performance test was made at full pressure, speed and gas density, measuring the subsynchronous vibration at each point, so that the subsynchronous vibration could be correlated with the performance. The good correlation of subsynchronous vibration with the flow coefficient (proportional to volume flow divided by RPM) showed that the vibration was aerodynamically induced. Later, the results of this test were used to calculate the internal flow angles occurring at the inception of the subsynchronous vibration.

The results of correlating subsynchronous vibration with the flow coefficients from the field test are shown in Figures 6 and 7. Figure 6 shows that the subsynchronous vibration correlates very well with the discharge flow coefficient (based on the discharge flange volume flow). Figure 7 shows that the subsynchronous vibration correlates less well with the suction flow coefficient. The two flow coefficients do not form a constant ratio to each other, because the test was run at two different speeds, causing the volume ratio across the compressor to vary at similar inlet flows. The result of this difference in volume reductions can be seen in Figure 7, where the 17200 RPM data (squares) forms a distinctly different curve from the 18450 RPM data (circles). The better correlation at the discharge end suggests that the suspected stall is in the final stages instead of the initial stages.

The rated flow is indicated on the flow coefficient scale of Figures 6 and 7. It can be seen that the subsynchronous vibration, which is usually associated with operation near the compressor surge line, begins in this case at flows over thirty percent larger than rated (suction basis).

The theory that the final stages are responsible is supported by the predominance of the subsynchronous vibration at the discharge end compared to the suction end. Other investigators (Ref. 3) have used asynchronous vibration response calculations to help identify the location of the stalled stage by comparing the ratio of the subsynchronous vibration at the suction and discharge ends.

INTERNAL ANALYSIS

The result of the field diagnosis was a correlation of the subsynchronous vibration with the exit flow coefficient. Although this demonstrates the cause to be aerodynamic, further analysis is required to determine which component is responsible. The basic strategy for identifying the component is to calculate the flow angles inside the compressor, for the flow measured in the field at the inception of the subsynchronous vibration. These calculated flow angles must then be correlated with the critical flow angle for rotating stall of each of the suspected components. The critical flow angle for rotating stall must be known from calculations based on theory, or from empirical correlations made when sufficient transducers were installed in the compressor flow passages to identify the component which initiated the rotating stall. Even with extensive internal instrumentation, it is not a trivial problem to prove which component is responsible for the rotating stall, as is apparent from References 5, 6 and 7.

Based on internal instrument measurements in another compressor at the manufacturer's plant (Ref. 2), the prime suspect was rotating stall in the diffuser. Other possibilities concerned us, especially rotating stall due to the deswirl vanes after the diffusers, based on a paper by Bonciani (Ref. 8). This and other possible causes of the subsynchronous vibration will be discussed later in this paper. Figure 8 is a cross section of the discharge end of the subject compressor, showing the vaneless diffusers and the deswirl vanes.

Internal Transducer Test Results

The manufacturer tested the other compressor at the factory, with pressure transducers mounted in the last stage diffuser, using full pressure in a closed loop (Ref 2.) Full gas pressure, or more fundamentally, full gas density, is necessary to produce the same gas forces and thus the same shaft vibrations as observed in the field. Of course the same conditions of dynamic similitude (mainly volume flow to speed ratio and volume reduction across the casing) must be observed, as in performance testing, to produce the same flow angles throughout the compressor. Oscilloscope traces of pressure fluctuation versus time from the two transducers are interpreted in Figure 9 for two different flows. At the higher flow, the trace shows mainly high frequency flow noise and impeller vane passing frequencies. As the angle of flow into the diffuser is reduced, with respect to tangential, an 8 psi (peak-to-peak) stall cell is formed. The 75 degree angle between the two transducers shows that a single cell is rotating in the same direction as the shaft. The frequency of the propagation is 10 Hertz (labeled 1/1800 RPM). Although not shown here, as the flow is further reduced to a flow angle of 6.5 degrees, the stall forms two cells of unequal pressure with 80 psi (p-p) at 37.5 Hertz.

Senoo's Theory

This onset of diffuser stall can be correlated to the diffuser inlet flow angle, for a given diffuser aspect ratio b3/R3 (see definitions). Kinoshita and Senoo give such a correlation (Ref. 9), as do Ligrani, Van Den Braembussche and Roustan (Ref. 10). As can be seen in Figure 10, these correlations are very similar and practically identical in our range of interest. These correlations are based on theoretical calculations and compare favorably to empirically determined stability thresholds reported in the literature. Other factors having a secondary influence are radial and tangential distortion of the inlet flow from the impeller, plus the Mach and Reynolds numbers, all of which have been quantified in a theoretical investigation (Ref. 11).

The points labeled with the subsynchronous vibrations amplitudes in Figure 10 compare the last diffuser inlet flow angles, near the inception of subsynchronous vibrations, to two rotating stall criteria. Several points at various flow angles are shown to allow the reader to evaluate the inception point versus the level of vibration he considers significant. Presuming, on the evidence above, that the stall is occurring in the last stage, the agreement is fair. Choosing the smallest vibration shown (5 microns or 0.19 mils) as the inception point, results in the criteria being optimistic by nearly four degrees, with the actual inception occurring at 13 degrees versus 9 predicted.

These flow angle calculations, for the last stage, were made by the author, based on the performance test data from the field. One dimensional compressible flow calculations were used, knowing the state and flow at the discharge flange, the geometry of the impeller tip plus diffuser, and the impeller speed. The diffuser static pressure recovery coefficient was estimated at 0.46, the slip factor at 0.88, and the impeller tip boundary layer (displacement) blockage at 0.95. Labyrinth leakages were calculated. In this compressor, flow is drawn off before the discharge flange and injected into the balance piston labyrinth two teeth away from the last impeller. The draw off and the flow up the back of the impeller, as well as the flow from the tip down the shroud to the eye were accounted for. This calculation method reflects actual volume ratios, but is only possible for the last stage. The vendor used an internal flow analysis refined by many factory tests to calculate the other flow angles quoted in this paper; these were not adjusted for the minor differences in observed volume ratio, but are reliable by virtue of extensive and critical use. The vendor's flow angles were smaller by typically two degrees, thus agreeing with the stall criteria more closely, being about two degrees larger than the predicted critical angle, for the last stage.

The mechanism of rotating stall in a vaneless diffuser is due to unsteady flow in local areas of the diffuser. According to Senoo, it is a phenomena of the boundary layer flow along the diffuser walls. Figure 11 shows the behavior of the boundary layer on the diffuser walls at the threshold of stability according to the theoretical model of Reference 1. The flow angles of the core flow and the boundary layers on the diffuser walls (the walls are identified with respect to the disk and shroud of the preceding impeller) are plotted as a function of the ratio of the local radius to the diffuser inlet radius. The flow angles are defined so that a purely tangential flow would have an angle of zero. It can be seen that, at first, the disk-side boundary layer reverses direction and "falls" back toward the impeller under the influence of the adverse pressure gradient normally existing in the diffuser. Then further along, the shroud-side boundary layer falls back. Reference 1 states "... a reverse flows occurs on the two walls alternately. Such a phenomena has not been observed in two-dimensional or conical diffusers and intuitively it is difficult to understand. The phenomena is related to the complicated nature of the flow, where the two wall boundary layers exchange momemtum so that each boundary layer satisfies the equations of motion in the radial and tangential directions which include the centrifugal force and the wall friction force."

Just as a reminder, rotating stall is not the same as a complete breakdown in flow, which would cause compressor surge. When compressor surge occurs, all areas of the flow reverse. (The flow meter upstream of the suction flange will momentarily show zero flow during a full surge cycle.) For Figure 11 the core flow is still carrying a net flow in the normal direction.

FLOW ANGLES INCREASED BY ADDING STAGES

To solve the rotating stall problem the manufacturer re-staged the high pressure compressor from six impellers to eight, causing the operating point to be much further from surge. This was done by adding two standard modular stages having a reduced design flow coefficient. The new staging caused the flow angles in the diffuser to be more radial, thus avoiding the critical angle for diffuser rotating stall. Another possibility, stall due to the deswirl vanes, was addressed as a contingency measure, and will be discussed later.

Table 1 compares all stages of the original and re-staged high pressure casing to a diffuser stability criterion used by the manufacturer. The manufacturer's flow angles, from an internal flow calculation, are used as well. This criterion is identical to van den Braembussche (Ref. 10), except that 2 degrees are added to the criterion for the last stage, to account for its observed sensitivity. The row labeled "stall" indicates whether each stage is expected to experience diffuser rotating stall at the rated conditions. A dash indicates that the stage is at the threshold of stall.

The flow angles entering the diffuser are given first for the original design at rated flow. The original design had six impellers and diffusers. The flow entered the first diffuser at an actual angle equal to eight degrees. The next stage was a narrower type, which causes the flow angle to be larger, here eleven degrees. The succeeding four diffusers were the same width as well, and the flow angle decreased one degree per stage, due to the compression of gas. The stall criterion angle is twelve degrees for the first diffuser, which is the wider. The criterion gives ten degrees for the stages two through five, which all have the same width. Even though the last stage width is the same as the preceding stage, its criterion is two degrees larger, based on the factory test of the internally instrumented compressor. The actual angles of stages one, four, five, and six fall below the criterion, indicating rotating stall in those stages. The forces due to the stall increase with pressure. Thus the stall induced vibration is predicted to predominate on the discharge end of the compressor.

The solution to the rotating stall was to re-stage by adding two impellers and diffusers. These had narrower flow passages than the preceding stages, thus giving larger flow angles. At rated flow, the actual flow angles for the new stages seven and eight are thirteen and twelve degrees respectively. Because the load is now shared by more impellers, the first six now operate at a somewhat larger flow coefficient. As a result, the actual flow angle increases three degrees on average for the first six stages, compared to the original staging. Now the actual angles exceed the criteria for all stages except the first. Stall of the first stage was not readily avoidable with the staging available, and was accepted on the basis that subsynchronous vibration had not been a practical problem on the suction end of this compressor.

One unusual aspect of the staging used should be mentioned, because it helps explain why these stages exhibit rotating stall at flows considerably in excess of rated flow. The diffuser width is 26 percent greater than the impeller tip width for the stage designated type "A" stage and 15 percent on the type "B". The extra width of these diffusers, compared to more conventional designs, causes the flow angles to be more tangential, and thus more prone to rotating stall. Narrower diffusers are now being manufactured for the high pressure casings on the other three platforms. Among other manufacturers throughout the industry, typical re-injection compressor practice is to design the diffuser widths in the order of 0 to 35 percent less than the impeller tip width.

Results of Re-Stage

The results of the design change were completely successful, as shown by the spectra in Figure 12. The re-stage reduced the subsynchronous vibration to only 2 microns (0.07 mil) at 45 Hertz. These spectra were taken at more than rated pressure and near the actual surge line, which was determined during this test. Operation at 2500 psi discharge pressure and near surge was made as a proof test. No significant subsynchronous vibration was evident at stall frequencies (or any other frequency) on the high pressure casing. Previously 2100 psi with a larger margin to surge had been the limit.

One year (8000 hours operation) has now passed without any indication of reoccurrence of the bearing wear-out problem. Previously 2200 hours operation was the longest bearing life.

SUBSEQUENT CASE CORRECTED BY NARROWING THE DIFFUSERS

After the re-stage, two other compressor trains from the same manufacturer having the same design and frame size were purchased. The train layout was the same as Figure 1; the internal design of the high pressure casing the same as Figure 8. Because of the previous experience, the specified performance test (American Society of Mechanical Engineers Power Test Code - 10) was conducted as near to rated pressure as possible, to detect any significant subsynchronous vibration forced by rotating stall.

Both the high and the low pressure casings of both trains showed vibration typical of rotating stall. On the low pressure casings, the subsynchronous vibration was within the API 617 limit of 3.7 microns (0.15 mils) when operating at rated pressure. On the high pressure casings the subsynchronous vibration was near the API limit, even though the suction pressure of the test was approximately half the rated pressure. Correction was required because there was no way to demonstrate, due to suction pressure limits with this test facility, that the vibration at full suction pressure would be within the API limit. To move the stall inception point to lower flows, the manufacturer installed narrower diffusers in all stages of the high pressure casings.

Table 2A lists the vibrations observed, while Table 2B lists the flow angles of the stage presumed stalled, and the flow as a percentage of the surge flow. In both tables column "A" is the point that encroached on the API limit. Columns "B" are for a flow 29% above surge, near rated flow, which was 32% above surge. Column "B" of Table 2B predicts stall, with the fifth stage 0.9 degrees below the critical flow angle; small stall induced vibrations resulted. The second compressor was not tested with wide diffusers. Column "D" shows that narrow diffusers on the first compressor moved the stall inception from 29% to 19% above surge flow .

The second compressor, with narrow diffusers, had larger subsynchronous vibrations than the first did with wide diffusers, as shown in column "E". However the narrow diffusers on the second restricted the flow where large vibrations occurred to 13% above surge, allowing the surge protection system settings to exclude this stall from the operating range. The inception point, column "F", shows that the stall criteria predicted the stall should not occur for another 0.4 degrees.

The aerodynamic performance was practically unaffected by the narrower diffusers. The head and efficiency were unchanged at the rated point. The head versus flow curve was only slightly changed. Examining the row "Rated flow % above surge" shows that the surge flow is unchanged between columns "A" and "D"; thus surge was unchanged by the narrower diffusers in this case.

Table 3 shows the ratio of the diffuser width (b3) to the impeller tip width (b2) for both the original and revised diffusers. The original diffusers were unusual in being wider than the impellers, with the last stages, which are of a lower specific speed, having the largest ratio. The revised diffusers have a uniform ratios of ordinary proportions.

That the narrower diffusers were successful in eliminating rotating stall in this case is significant. Manipulating the principle variables, diffuser inlet flow angle and diffuser aspect ratio (b3/R3), while making no other changes, supports the theory that the stall criteria in Figure 10 is sufficient to predict diffuser rotating stall inception, (accounting, where necessary, for inlet flow distortion plus Mach and Reynolds number effects.) Other theories were considered, as discussed below, but an evaluation was difficult without the evidence from the narrower diffusers.

WAS DIFFUSER STALL SOLELY RESPONSIBLE?

Both the stator and the rotor can be responsible for rotating stall phenomena in centrifugal stages with vaneless diffusers (Ref. 5 and 6.) Frigne and Van Den Braembussche found five distinct stall characteristics in one single stage test compressor, three due to the impeller and two due to the diffuser. Table 4, adapted from their work (Ref. 6) summarizes these characteristics. Stator components other than the diffuser alone can have an influence, as we shall now discuss.

Influence of Deswirl Vanes Considered

Careful experiments by Bonciani and Terrinoni (Ref. 8) have shown that, in some industrial centrifugal compressor configurations, rotating stall type pulsations in the diffuser area can be induced by the return vanes interacting with the flow. The critical incidence angle with respect to the leading edge of the return vane mean camber line was found to be 6 to 8 degrees for the particular stages tested (defined so the incidence is increasing with decreasing flow).

A photograph of the return vanes, taken during the re-staging of the South China Sea compressor, is given in Figure 13 to show the form of the vane leading edges, which are of a type tolerant to a wide range of incidence. Figure 14 shows the incidence angle, with respect to the leading edge mean camber line, for the fifth stage before re-staging. As can be seen, there is no stall induced vibration for incidences less than 11 degrees, and strong vibrations do not appear until the incidence exceeds 15 degrees. The incidence angles for the preceding stages are similar. No change was made to these vanes, because the vendor did not believe the return vanes were the cause of the rotating stall. Although the re-stage reduced the incidence angle by about two degrees, the angle at the return vanes still greatly exceeded the 6 to 8 degree criterion for rotating stall. Therefore violating this criterion does not cause stall in our case. Perhaps differences in stage geometry, compared to Reference 8, invalidate applying this particular incidence criterion.

Exit Vanes Modified

The last stage has 12 exit vanes, axially configured, indicated as the second set of "deswirl vanes" from the left in Figure 8. A cross section of two of these vanes, drawn to scale for both profile and spacing, is shown in Figure 15. The vanes are required for structural strength, and are not expected to recover any significant amount of energy from the gas tangential velocity before passing the flow to the discharge collector. The incidence angle on them was quite high, being 21 degrees at the rated point, shown as "I" in Figure 15. Due to some concern about the vane stall theory mentioned above, and because nothing was lost by doing so, these vanes were modified to blunt struts, as shown. The elimination of a definite leading edge, and of any flow turning capability, removed all possibility of the influence of these vanes on rotating stall.

The exit vanes were not made blunt on the subsequent case of rotating stall, corrected by narrowing the diffusers. As discussed, narrowing the diffusers, only, was sufficient to eliminate the stall. The incidence angle on the exit vanes was only slightly improved over the case in the previous paragraph. Therefore we conclude that the poor incidence on the exit vanes did not cause the stall.

Inducer Stall Criteria Respected

Following the argument of Kinoshita and Senoo in Reference 9, the impeller inducer inlet incidence and the impeller diffusion ratio (w2/w1) were calculated to evaluate the possibility of the impeller causing the rotating stall. The vendor examined one case, the last stage of the high pressure casing, the one which has 7 inch diameter impellers as mentioned earlier. The principle difference between this design and all the others in this paper is that the hub-to-tip diameter ratio is smaller; 0.36 versus 0.52 on the other compressor designs. The vendor calculates that the incidence angle at the shroud is 2.5

degrees at the rated point of the compressor train and 5.7 at surge. This compressor vibrates due to rotating stall, with the severity increasing as flow is decreased toward the rated point. Our incidence of less than 5 degrees makes it unlikely that last stage impeller stall is responsible for the vibration, based on comparison to the 12 degrees inducer incidence (at the RMS radius) at impeller stall, reported by Frigne and Van Den Braembussche in Reference 11, and the 13 degrees (at shroud) reported by Kammer and Rautenberg in Reference 5. The velocity ratios (w2/w1RMS) are 1.27 at rated flow and 1.43 at surge, which should be within the diffusion capability of the impeller.

The case where the rotating stall was moved to a predictable lower flow by narrowing all the diffusers, with no other changes, gives additional support to the hypotheses that inducer stall is not generally responsible for the rotating stall induced vibrations described in this paper.

PREDICTING VIBRATION AMPLITUDES

Rotating stall should be kept out of the operating range where practical, but in many cases this may be neither necessary nor economic. For instance the low pressure casings discussed above have rotating stall, based on their vibration spectra, but the vibration amplitudes are not harmful, so there is no incentive to eliminate the stall. When purchasing a compressor there is a need to know whether rotating stall will be a potential problem which should be addressed before it runs at rated conditions in an operating plant. For this, and other purposes, a criterion for the vibration amplitude due to stall is useful.

From the equipment user's point of view, such a criterion should indicate where concern about stall induced vibration begins. Therefore the criteria should err toward over-estimating the vibrations amplitude. Although accuracy is advantageous, it is not paramount because once the concern is raised, any particular case will have to be settled by reference to the experience of the particular manufacturer involved. Of course some compressors may then be found acceptable even though they exceed such a criterion.

Criqui has published an empirical criterion for the vibration severity of rotating stall for the compressor designs discussed in this paper (Ref.12.) His plot may not be accurate when applied to dissimilar compressor designs. Figure 16 shows his line, with points added from the cases discussed in this paper. The criterion predicts significant subsynchronous vibrations for stages which operate with diffuser rotating stall (expected where the diffuser entry flow angle fails to meet the criteria in Figure 10) and which have stage pressure ratios and stage discharge pressures plotting above and to the right of the line . The added points are for the compressors discussed in this paper. These points refer to vibration above the limits of API 617, a more stringent standard than Criqui's line, which reflects operator complaints. His criterion does not take into account where the particular stage is located along the shaft, nor how many stages are stalled simultaneously.

TESTING FOR ROTATING STALL INDUCED VIBRATIONS

Compressors specified to petroleum industry standards are not usually tested at the manufacturer's works for rotating stall induced vibrations meeting the previously mentioned API limit. The API 617 mechanical test has nothing to do with aerodynamic similtude. Nor does it specify the correct frequency range to find most rotating stalls. The frequency range inspected is 0.25 to 8 times running speed (API 617 item 4.3.4.4 paragraph 1.). Furthermore the usual aerodynamic performance test, conducted according to ASME PTC-10, cannot be expected to induce significant vibrations because it is usually conducted at reduced pressure compared to rated. Although any stall in the flow range should be present during a performance test, usually no internal instrumentation is provided which would discover rotating stall.

LESSONS LEARNED

The main points of this case can be summarized as follows:

1. Tilt pad bearings can suffer premature wear-out as a result of forced subsynchronous vibration, in spite of the relatively low vibration velocity of the shaft motion. The displacement amplitude of the subsynchronous vibration (0.17 mils) at the start of the wear-out process, when a new bearing was installed (shown in Figure 6), was just slightly less than the API Standard 617 limit for subsynchronous vibration.

2. The Senoo and Van Den Braembussche criteria were closely confirmed by both the field and the factory test correlations of subsynchronous vibration with the diffuser flow inlet angle. When the criteria were respected, then the subsynchronous vibration was eliminated.

3. A rated pressure, rated gas density performance test, maintaining rated ACFM/RPM and rated volume reduction across the casing is required, if this type of subsynchronous vibration problem is to be demonstrated during factory testing of new compressors. The rated pressure and density are required to produce the full subsynchronous vibration amplitude. The aerodynamic similitude is necessary to reproduce the gas flow angles throughout the compressor as required to respect the stall criteria.

The API 617 limits on vibration amplitude should be specified for any such test. However, the frequency range should be revised to include frequencies lower than the arbitrary 25 percent minimum in API 617. Both limits should be required of field operation as well.

The subsynchronous vibration problem does not have the same catastrophic effect on operability as does subsynchronous instability, and in the case described in this paper, merely degraded the compressor's availability. Therefore the cost of such a test should be weighed against the magnitude of the potential problem. The empirical severity criteria may aid the evaluation.

4. Designs of new compressors should be reviewed against the rotating stall criteria, where the stage pressure and pressure ratios approach those of this case. Similar criteria are needed for components, other than diffusers, susceptible to rotating stall.

REFERENCES

1 Senoo, Y., Kinoshita, Y., and Ishida, M., "Asymetric Flow in Vaneless Diffusers of Centrifugal Blowers," ASME Journal of Fluids Engineering, March 1977, pp. 104-114.

2 Fozi, A. A., "An Examination of Gas Compressor Stability and Rotating Stall", Fourth Workshop on Rotor Instability Problems in High Performance Turbomachinery, Texas A&M University, June 1986.

3 Bonciani, L., Ferrara, P.L., and Timori, A., "Aero-Induced Vibrations in Centrifugal Compressors," Quaderni Pignone 29, June 1980 pp. 5-12.

4 Fulton, J. W., "Full Load Testing in the Platform Module prior to Tow-Out: A Case History of Subsynchronous Instablility," NASA Conference Publication 2338, May 28-30, 1984, pp.1-16.

5 Kammer, N., and Rautenberg, M., "A Distinction Between Different Types of Stall in a Centrifugal Compressor Stage," ASME Journal of Engineering for Gas Turbines and Power, Vol. 108, January 1986, pp. 83-92.

6 Frigne, P., and Van Den Braembussche, R., "Distinction Between Different Types of Rotating Stall in a Centrifugal Compressor With Vaneless Diffuser," ASME Journal of Engineering for Gas Turbines and Power, Vol 106, April 1984, pp. 468-474.

7 Abdelhamid, A.N., Colwill, W.H, and Barrows,J.F., "Experimental Investigation of Unsteady Phenomena in Vaneless Radial Diffusers," ASME Journal of Engineering for Power, Vol. 101, January 1979, pp. 52-60.

8 Bonciani, L., and Terrinoni, L., "Influence Of Stationary Components on Unsteady Flow in Industrial Centrifugal Compressors," NASA Conference Publication 2338, May 28-30, 1984, pp. 429-479.

9 Kinoshita, Y., and Senoo, Y., "Rotating Stall Induced in Vaneless Diffusers of Very Low Specific Speed Centrifugal Blowers," ASME Paper No. 84-GT-203, June 1984.

10 Ligrani, P.M., Van Den Braembussche, R., and Roustan, M., "Rotating Stall Measurements in the Vaneless Diffuser of a Radial Flow Compressor," ASME Paper No. 82-GT-257, May 1982.

11 Senoo, Y., and Kinoshita, Y., "Influence of the Inlet Flow Conditions and Geometries of Centrifugal Vaneless Diffusers on Critical Flow Angle for Reverse Flow," ASME Transactions, Vol. 99, No. 3, March 1977, pp. 98-103.

12 Criqui, A. F., "Advancements in Centrifugal Gas Compressor Stability," Solar Technology Seminar '86, San Diego, California, February 5-8, 1986, pp. 40-1 to 10.

13 Fulton, J. W., "Subsynchronous Vibration of a Multistage Centrifugal Compressor Forced by Rotating Stall," Solar Technology Seminar '86, San Diego, California, February 5-8, 1986, pp. 41-1 to 41-12.

NOMENCLATURE

ACFM - actual cubic feet per minute
API - American Petroleum Insitute
b2 - impeller tip width
b3 - diffuser width at the beginning of the parallel wall section
d - impeller diameter in inches
RMS - root mean square
RPM - revolutions per minute
R3 - diffuser radius at the beginning of the parallel wall section
w1 - relative flow velocity entering the impeller
w2 - relative flow velocity leaving the impeller

Flow coefficient = (700/d^3)*(ACFM/RPM)

Calculated Diffuser Flow Angles at Rated Flow

Stage	1	2	3	4	5	6	7	8
Old Staging								
Impeller Type	1C	2B	2B	1B	1B	1B		
Actual	8	11	10	9	8	7		
Criteria	12	10	10	10	10	12		
Stall	Yes	No	-	Yes	Yes	Yes		
New Staging								
Impeller Type	1C	2B	2B	1B	1B	1B	2A	2A
Actual	10	14	12	11	10	10	13	12
Criteria	12	10	10	10	10	10	8	10
Stall	Yes	No	No	No	-	-	No	No

AGX586-32

Table 1. Calculated Diffuser Flow Angles at Rated Flow

Subsequent Case: Wide and Narrow Diffusers
Subsynchronous Vibrations

	A	B	C	D	E	F
Diffuser Width	Wide	Wide	Wide	Narrow	Narrow	Narrow
Compressor No.	1	1	2	1	2	2
Discharge (mils)	0.14	0.04	Not	0.05	0.28	0.07
Suction (mils)	0.012	0.001	tested	0.001	0.05	0.023
Frequency (Hertz)	41	33		37	26	55
% Running speed	15.7	12.7		14.2	9.7	20.4

AGXF586-37

Table 2A. Subsequent Case: Vibrations Observed

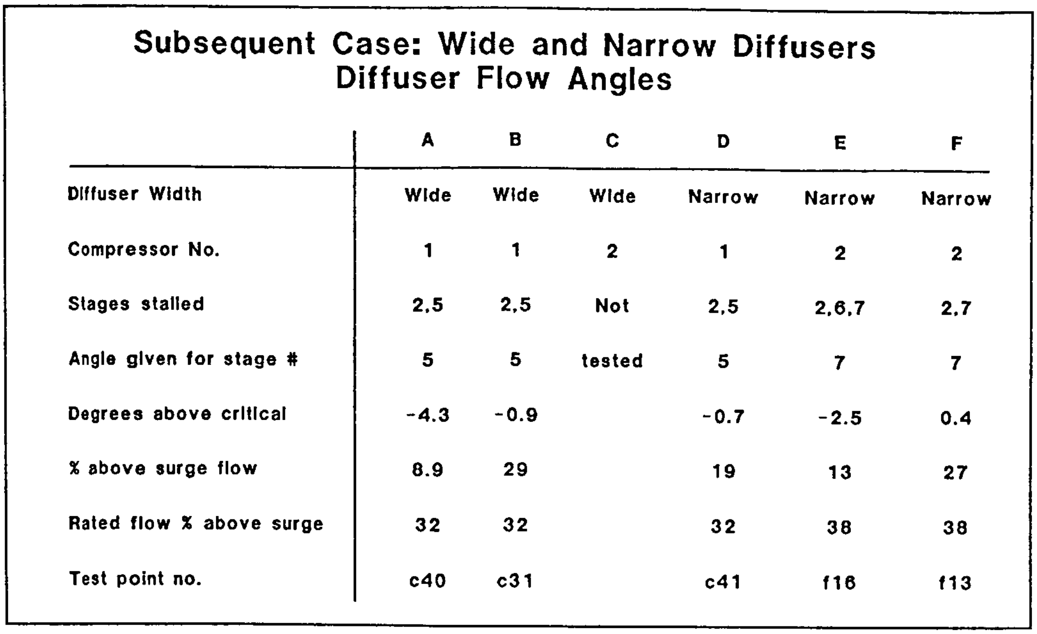

Subsequent Case: Wide and Narrow Diffusers
Diffuser Flow Angles

	A	B	C	D	E	F
Diffuser Width	Wide	Wide	Wide	Narrow	Narrow	Narrow
Compressor No.	1	1	2	1	2	2
Stages stalled	2,5	2,5	Not	2,5	2,6,7	2,7
Angle given for stage #	5	5	tested	5	7	7
Degrees above critical	-4.3	-0.9		-0.7	-2.5	0.4
% above surge flow	8.9	29		19	13	27
Rated flow % above surge	32	32		32	38	38
Test point no.	c40	c31		c41	f16	f13

AGXF586-38

Table 2B. Subsequent Case: Corresponding Flow and Diffuser Inlet Angles

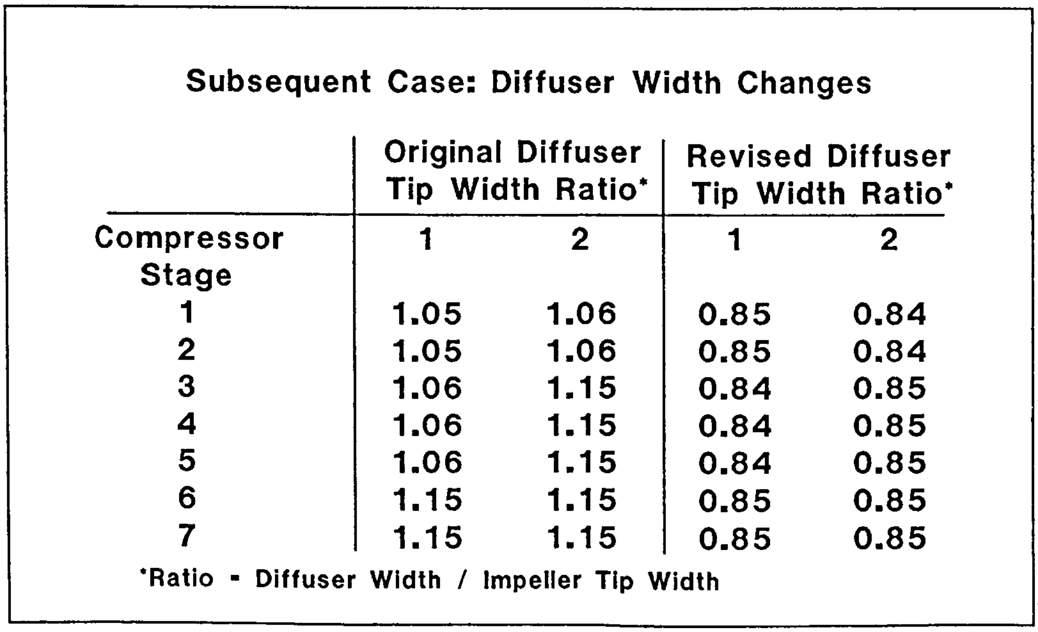

Subsequent Case: Diffuser Width Changes

	Original Diffuser Tip Width Ratio*		Revised Diffuser Tip Width Ratio*	
Compressor Stage	1	2	1	2
1	1.05	1.06	0.85	0.84
2	1.05	1.06	0.85	0.84
3	1.06	1.15	0.84	0.85
4	1.06	1.15	0.84	0.85
5	1.06	1.15	0.84	0.85
6	1.15	1.15	0.85	0.85
7	1.15	1.15	0.85	0.85

*Ratio - Diffuser Width / Impeller Tip Width

AGSF586-33

Table 3. Subsequent Case: Diffuser Width Changes

Rotating Stall Characteristics

Type	Character	Amplitude*	No. of Calls	Harmonics	Freq. Ratio
Impeller	Mild	0.065	3,4,5	No	0.14
Impeller	Abrupt	0.30	1,2,3	N/A	0.26-0.31
Impeller	Progressive	0.10	1,2,3	Yes	0.67-0.81
Diffuser	High Freq.	0.10	3	No	0.17-0.21
Diffuser	Low Freq.	N/A	2	No	0.13-0.16

* Amplitude (in diffuser) = (Max. Vel.) / (2*RMS velocity

AGX586-34

Table 4. Characteristics of the Different Types of Rotating Stall as Tested on a Single Impeller Air Test Facility (Measured by Frigne and Van Den Braembussche, Ref. 6)

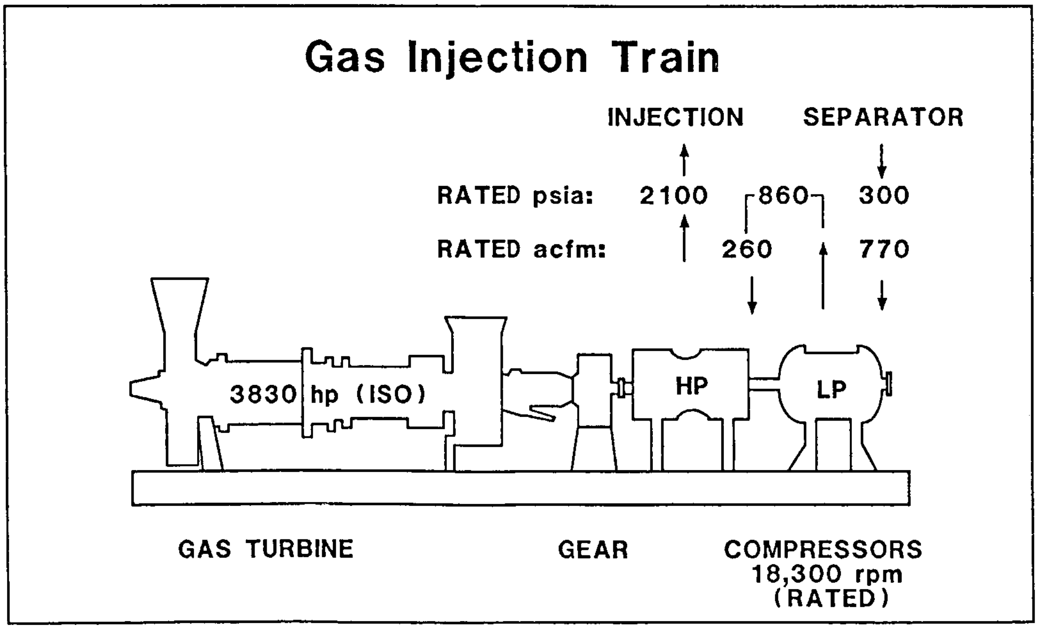
Gas Injection Train
INJECTION
SEPARATOR
RATED psia:
2100
860
300
RATED acfm:
260
770
3830 hp (ISO)
HP
LP
GAS TURBINE
GEAR
COMPRESSORS
18,300 rpm
(RATED)

AGXF586-1

Figure 1. Compressor Train

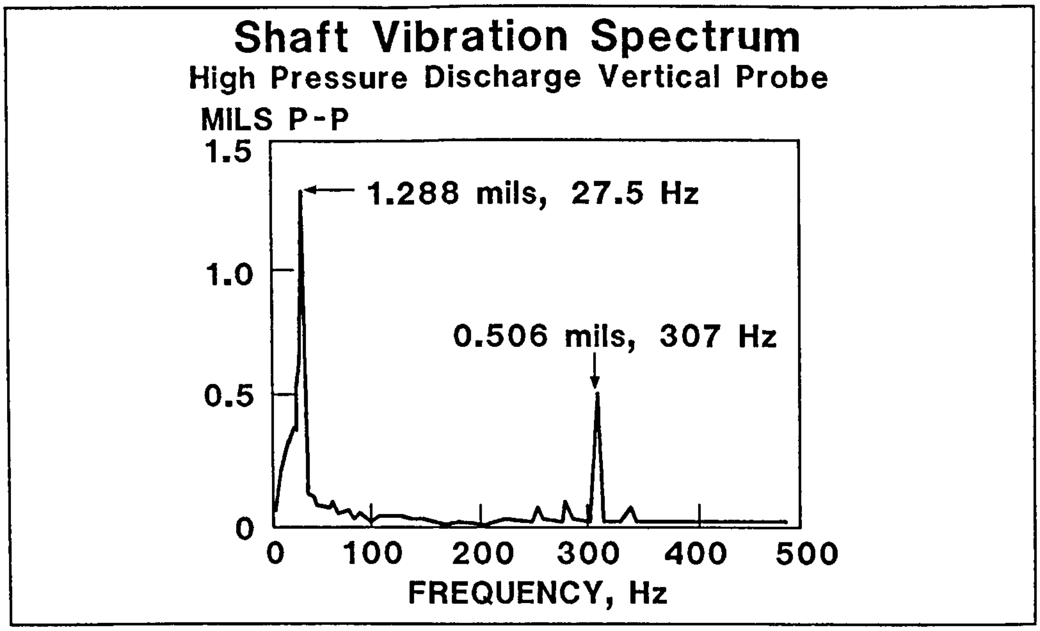

AGXF586-2

Figure 2. Proximity Probe Spectrum of the Problem Vibration

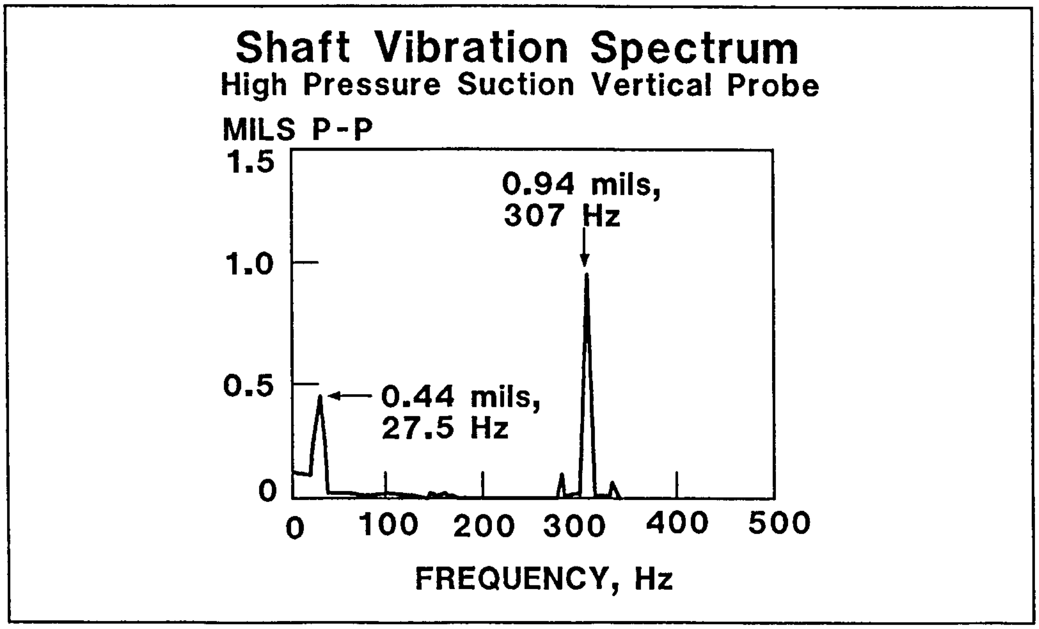

AGXF585-3-20

Figure 3. Spectrum at Suction End

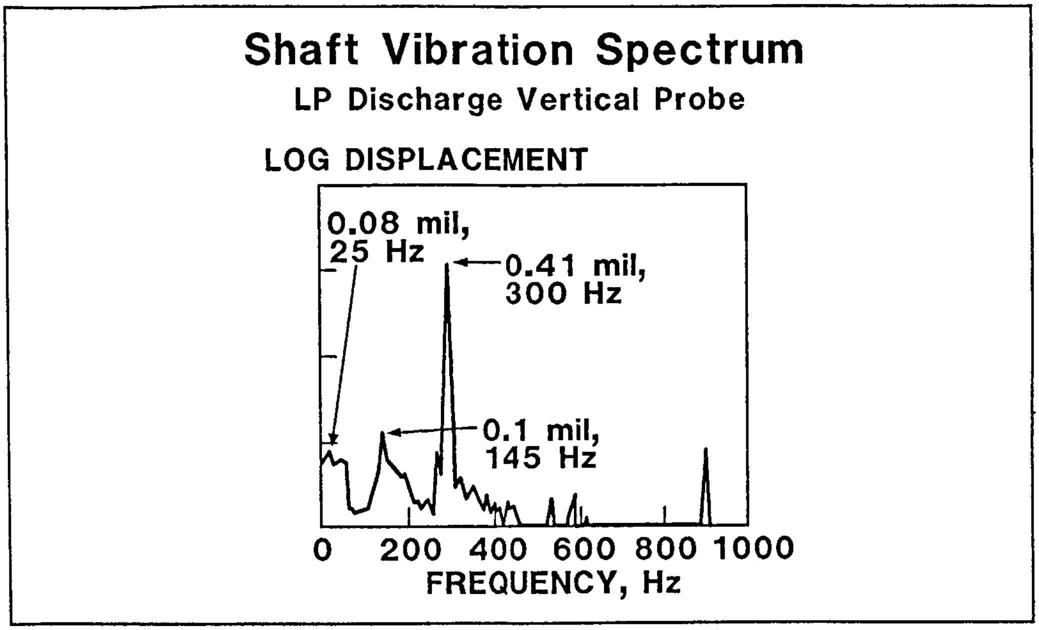

AGXF586-4-15

Figure 4. Spectrum from the Low Pressure Casing

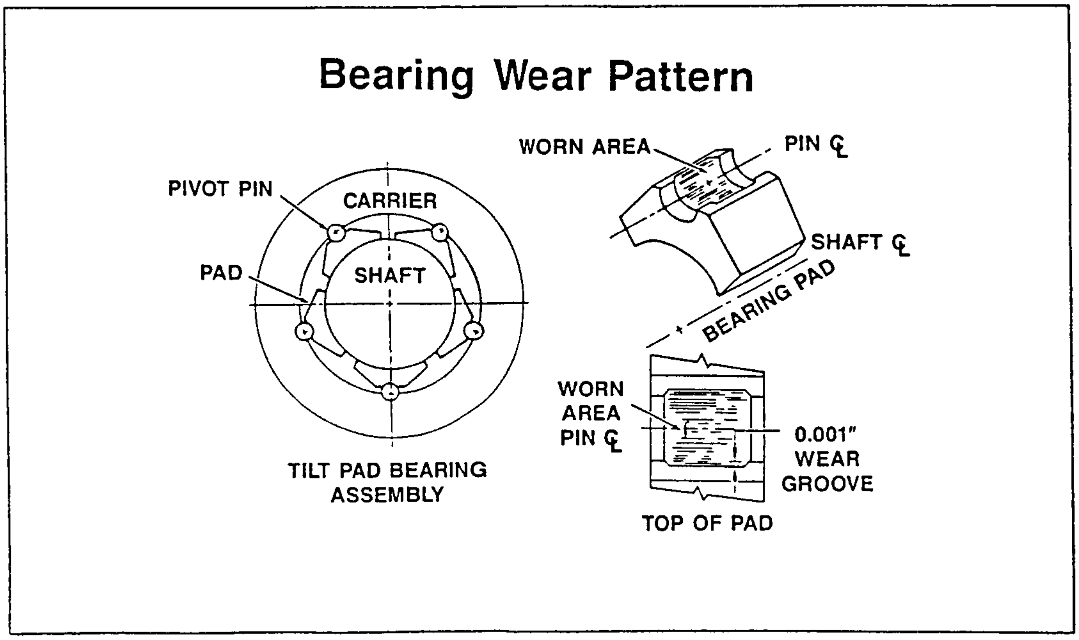
Bearing Wear Pattern
WORN AREA
PIN ℄
PIVOT PIN
CARRIER
PAD
SHAFT
SHAFT ℄
BEARING PAD
WORN
AREA
PIN ℄
0.001"
WEAR
GROOVE
TOP OF PAD
TILT PAD BEARING
ASSEMBLY

0586-46-050

Figure 5. Bearing Wear Pattern

ORIGINAL PAGE IS
OF POOR QUALITY

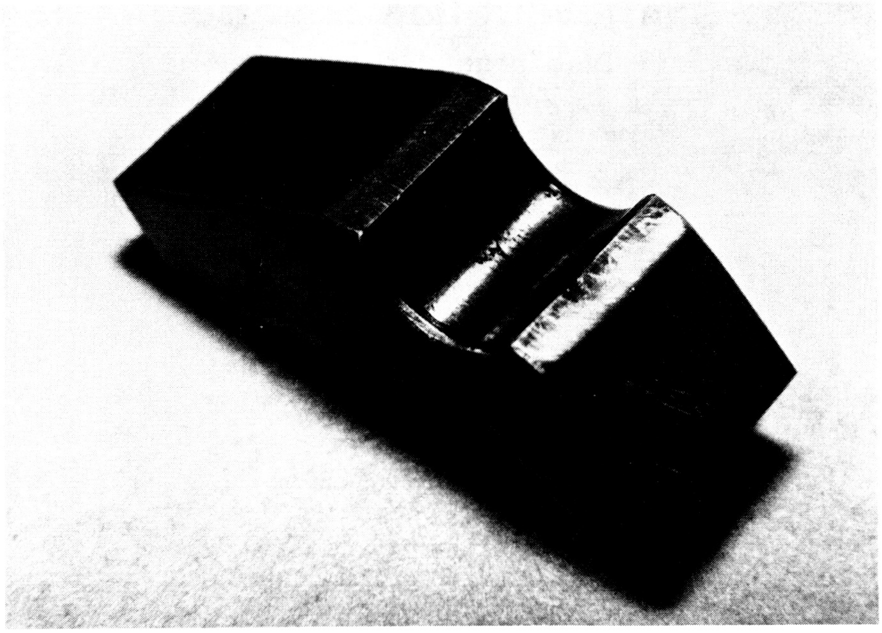

Figure 5A. Photograph of Bearing Pivot Wear Pattern

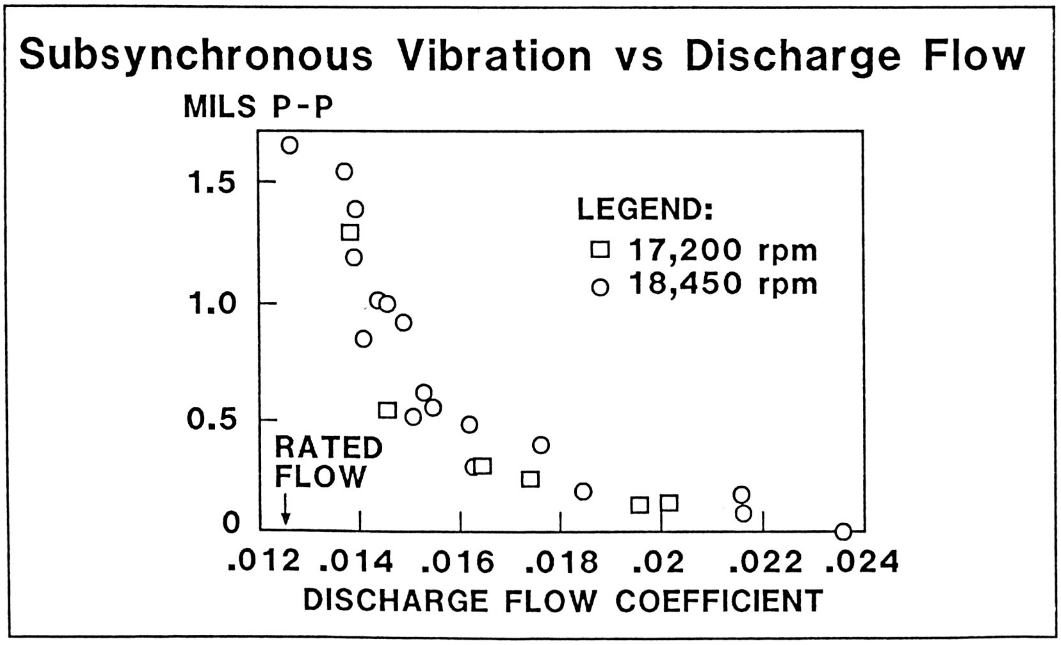

AGXF586-6-4

Figure 6. Correlation of Vibration with Discharge Flow

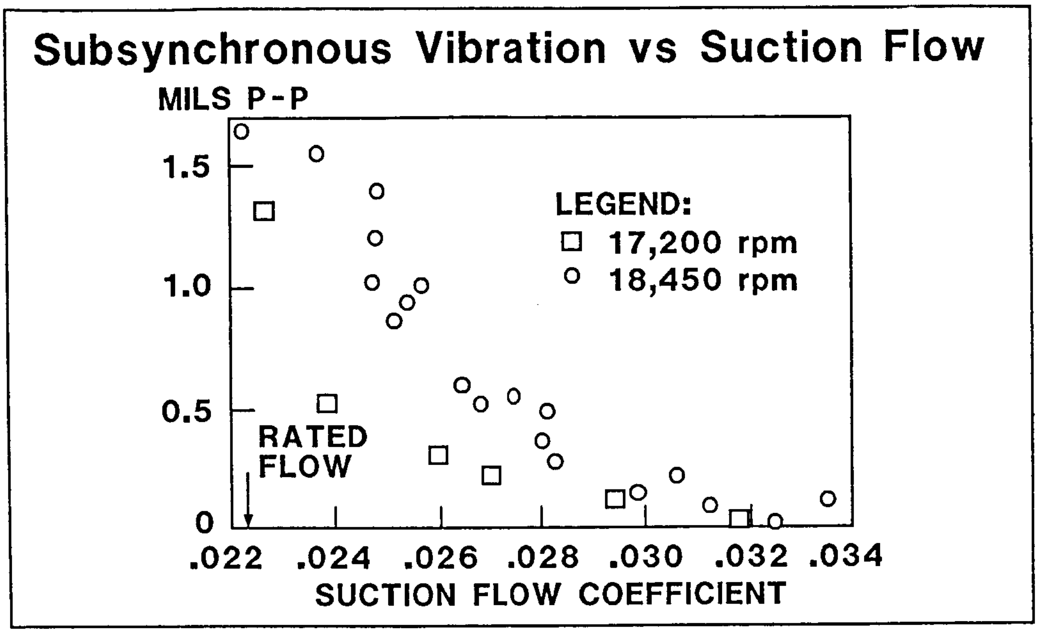

AGXF6-86-7-5

Figure 7. Correlation of Vibration with Suction Flow

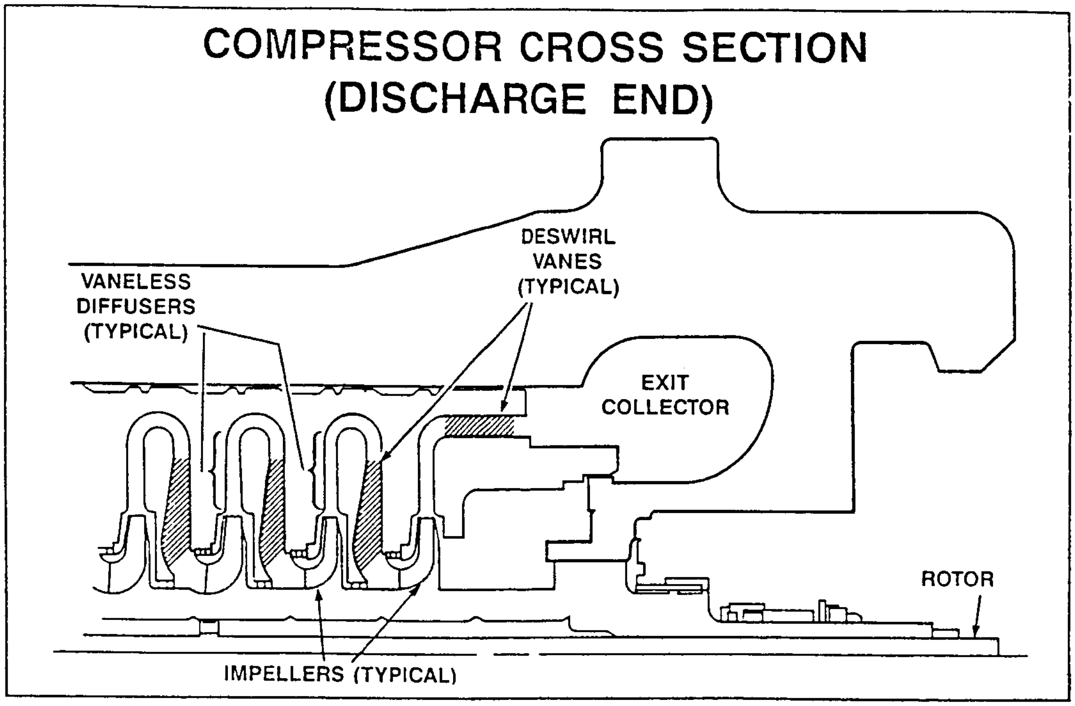
COMPRESSOR CROSS SECTION (DISCHARGE END)
DESWIRL VANES (TYPICAL)
VANELESS DIFFUSERS (TYPICAL)
EXIT COLLECTOR
ROTOR
IMPELLERS (TYPICAL)

0586-46-051

Figure 8. Compressor Cross Section (Discharge End)

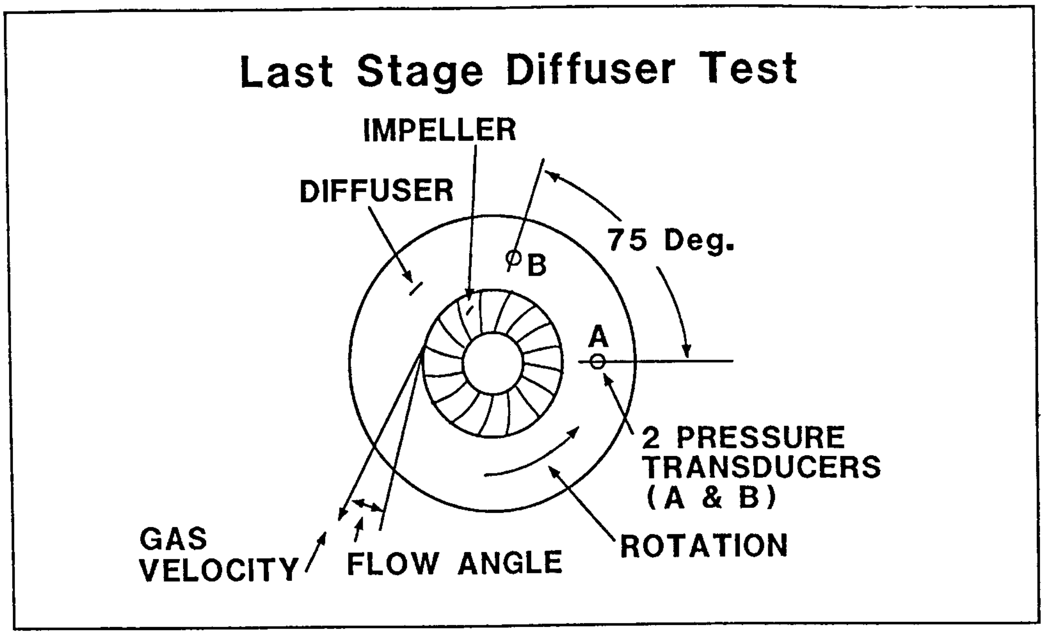
Last Stage Diffuser Test
IMPELLER
DIFFUSER
B
75 Deg.
A
2 PRESSURE TRANSDUCERS (A & B)
GAS VELOCITY
FLOW ANGLE
ROTATION

AGXF586-9-17

Figure 9A. Factory Test Arrangement

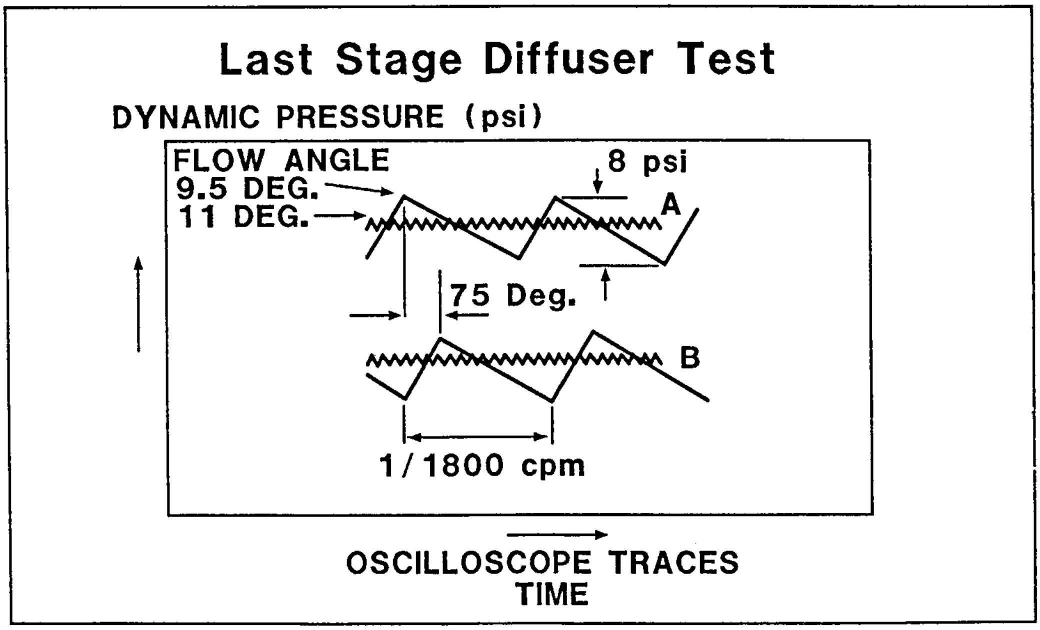

AGXF586-10-19

Figure 9B. Factory Test with Diffuser Wall Pressure versus Time

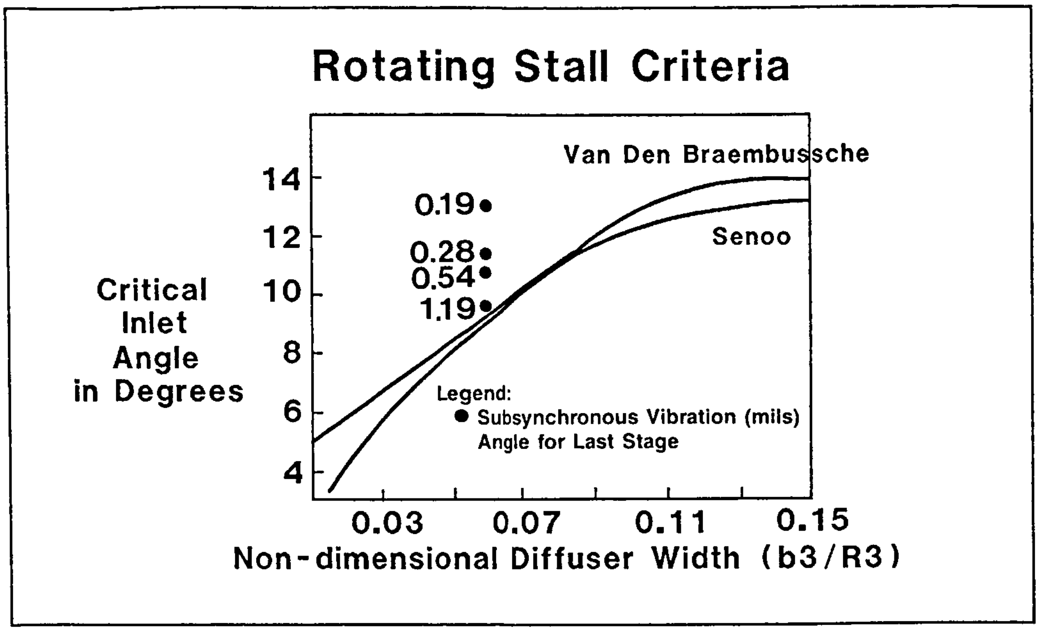

AGXF586-35

Figure 10. Rotating Stall Criteria Compared to Field Test

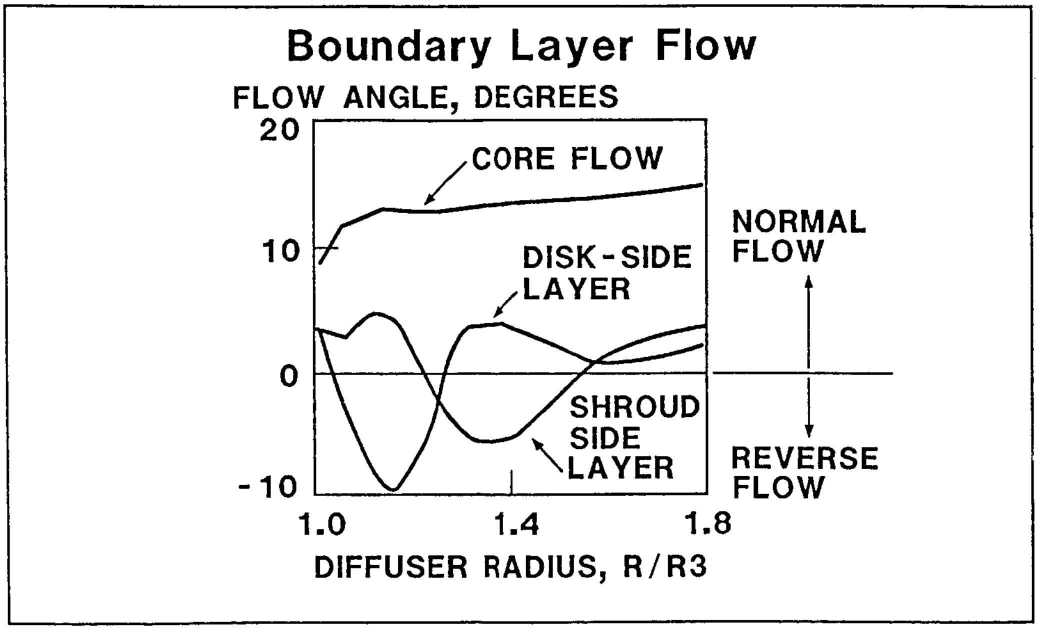

AGXF586-11-16

Figure 11. Diffuser Boundary Layers (Adapted from Senoo, Ref. 1)

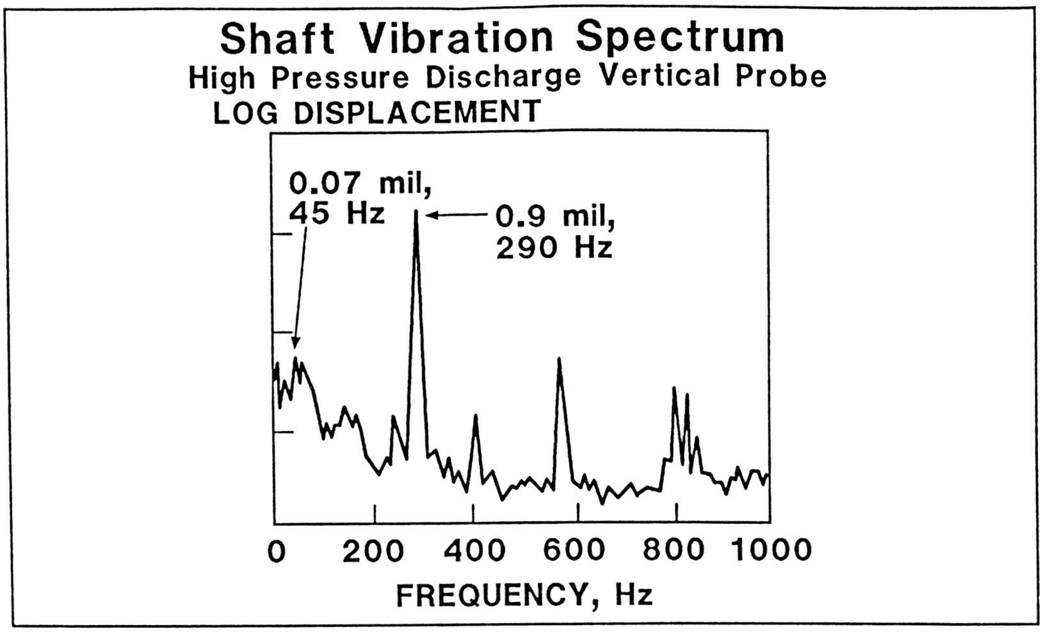

AGXF586-12-18

Figure 12. Spectrum after Modifications

ORIGINAL PAGE IS
OF POOR QUALITY

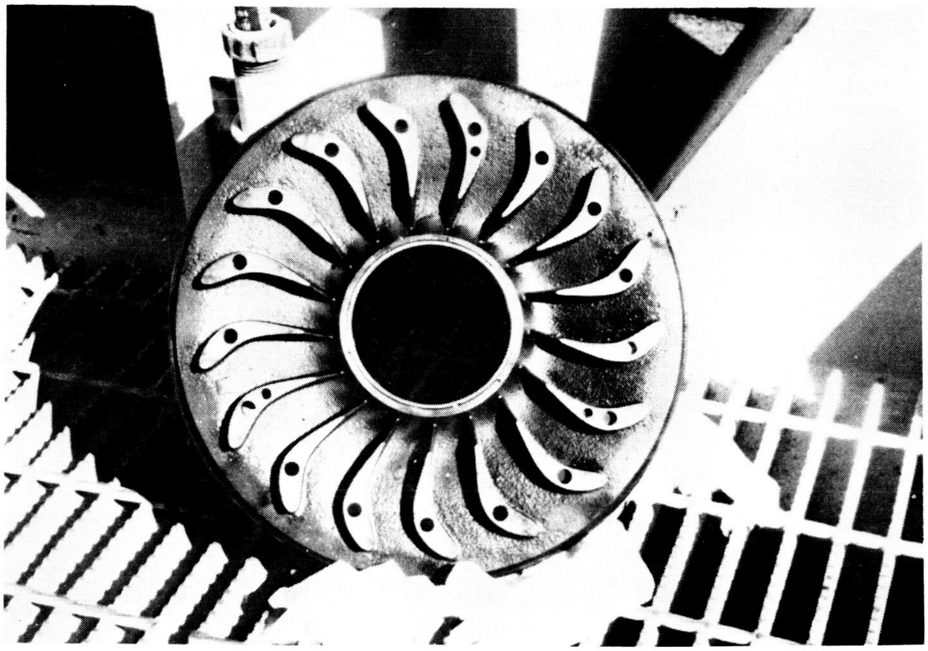

Figure 13. Return Vanes

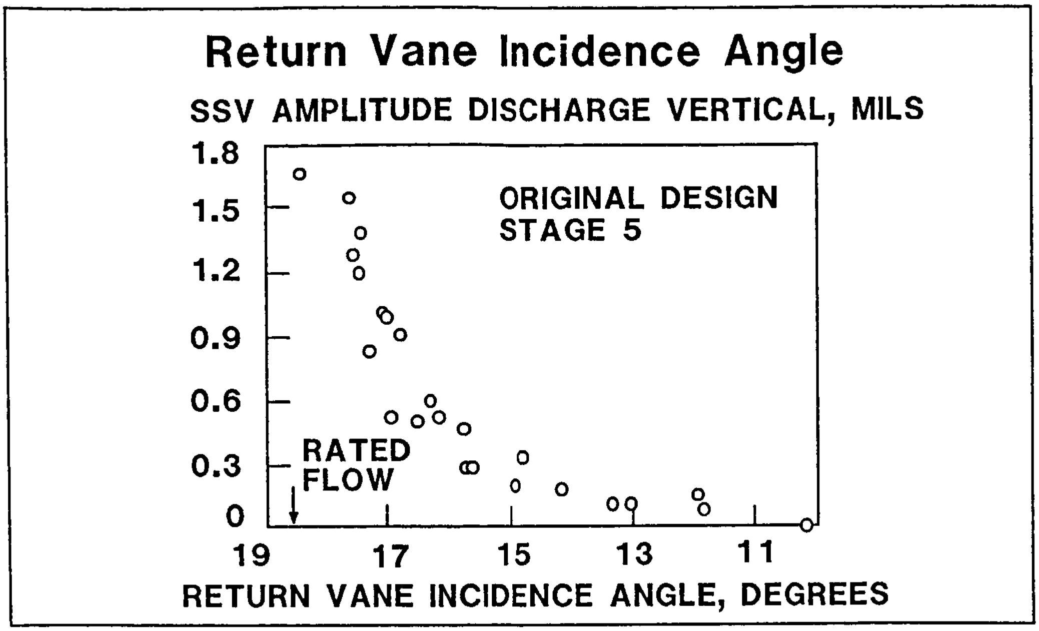

AGXF586-14-13

Figure 14. Return Vane Incidence versus Subsynchronous Vibration

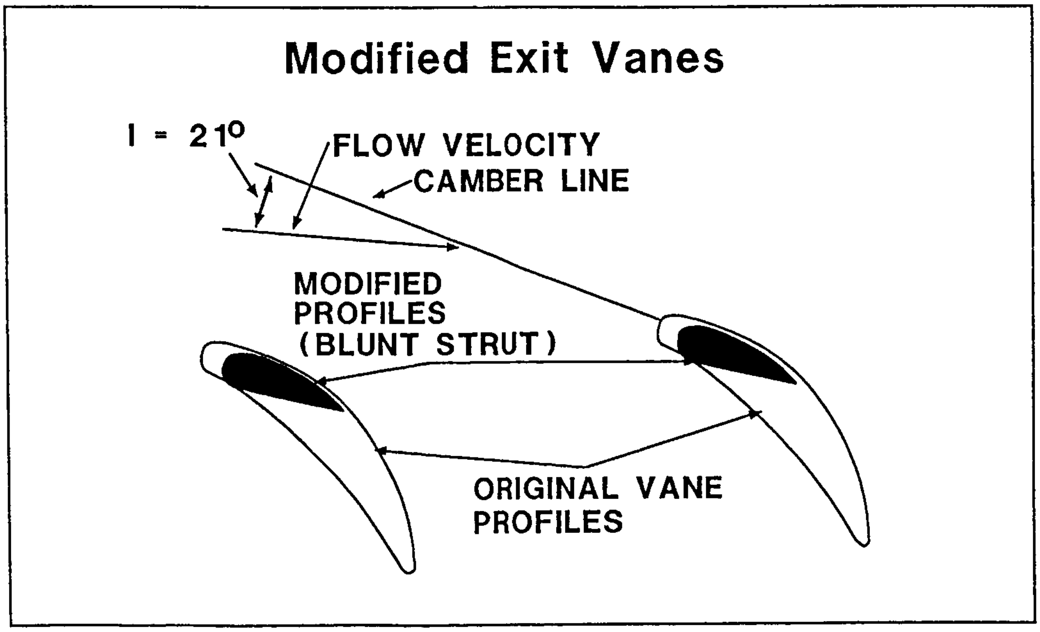
Modified Exit Vanes
I = 21°
FLOW VELOCITY
CAMBER LINE
MODIFIED
PROFILES
(BLUNT STRUT)
ORIGINAL VANE
PROFILES

AGXF586-15-11

Figure 15. Exit Vane Modification

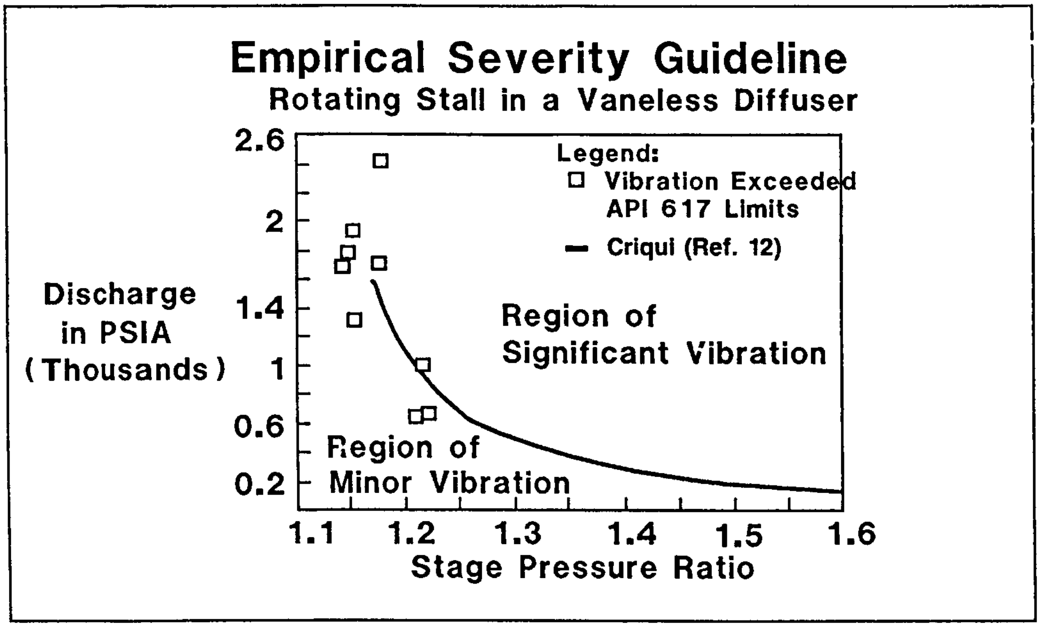

AGX566-36

Figure 16. Empirical Severity Guideline

N87-22203

INSTABILITY OF MULTISTAGE COMPRESSOR K1501

Zhou Ren-mu
Hangzhou Steam Turbine Works
Hangzhou Zhejiang, People's Republic of China

The K1501 compressor, driven by a steam turbine, is used to transport synthetic gas in fertilizer plants of 1000 tons daily production. The turbocompressor set, which had been in operation since 1982, vibrated rather intensely, and its maximum load was only about 95 percent of the normal value. Damaging vibration to pads and gas-sealing labyrinths occurred three times from 1982 to 1983 and resulted in considerable economic loss. From the characteristics of the vibration, we suspected its cause to be rotor instability due to labyrinth-seal excitation. But, for lack of experience, the problem was not addressed for two years. Finally, we determined that the instability was indeed produced by labyrinth-seal excitation and corrected this problem by injecting gas into the middle-diaphragm labyrinths.

This paper primarily discusses the failure and the remedy described above.

INTRODUCTION

In recent years, China imported many large chemical plants that have various kinds of compressors. Unacceptable vibration has occurred in some running compressors. The most serious occurrence was with the KT1501-K1501 set that transported synthetic gas for a fertilizer-producing process (at 1000 tons a day). Figure 1 shows the KT1501-1501 set, which consists of one steam turbine (including two cylinders) and three compressors. Its maximum power is 19 786 kW and its maximum continuous speed is 11 230 rpm. It has a traditional concrete construction pad.

Intensive vibration originated from the low-pressure compressor, K1501LP. Figure 2 shows the longitudinal section of its rotor. Table I shows the parameters of the tilting pad of both bearings. Figure 3 shows the gas labyrinth construction of the middle diaphragm. Figure 4 provides a critical speed map and mode shapes for the rotor.

Vibration occurred suddenly each time. The first accident took place on May 7, 1982, when the speed was 10 800 rpm. The following characteristics were observed:

(1) The vibration of the shaft exceeded 80 μm suddenly.
(2) The vibration accompanied intensive sound radiation (over 95 dB).
(3) Sealing oil oozed out of the gas exit tube.
(4) Intense floor vibration followed.

When the cylinders were opened and examined, the following damages were observed:

(1) The pads of radial bearing 074 were obviously deformed because of intensive journal vibration.

(2) The gas labyrinth of the middle diaphragm and the ends of the cylinder were worn out. Some wear scars remained on the surface of the shaft.

When only the damaged parts were replaced, the vibration and damage reoccurred when the speed reached 10 820 rpm.

There are three identical sets of this kind in our nation - in Nanking, Anqing, and Guangzhou. This type of failure occurred in all three compressors. The most serious failure was in Nanking. Because the failures were clearly not accidental, the Chemical Engineering Ministry began and directly guided experimental research in Nanking. (All the phenomena described above occurred in Nanking.) The following is a description of the whole test, which was divided into three steps.

FIRST OF STEP OF TEST (May 1982 - January 1983)

At first we did what we could to minimize downtime and production losses. The origin of the vibration was rotor instability as will be detailed. Although the labyrinth-seal excitation was considered to be the cause of the instability, the possibility of oil whip had not been dismissed at that time. Therefore the following measures were adopted:

(1) Six teeth in the middle of the diaphragm labyrinth were removed.

(2) The ratio of bearing width to diameter was decreased from 0.40 to 0.39 mm.

(3) Additional displacement transducers were installed on bearings 074 and 075 (fig. 1) to improve vibration monitoring.

Because none of these measures eliminated the rotor instability, a large quantity of measurements and analyses were then made. This work was performed mainly by Zhejiang University. Because vibration was monitored closely during the experiments, no serious damage occurred.

Figure 5 shows frequency spectra of the shaft vibration in direction x on bearings 074 and 075 at a speed of 10 220 rpm as measured by a transducer on November 19, 1982. From figure 5, the rotating speed was 170.3 Hz, and the frequency of fractional frequency whirl (FFW) was 80 Hz. The frequency ratio η_F equalled 0.47. The vibration amplitudes of the components in this figure are almost equal. Figure 6 shows a frequency spectra of the shaft vibration in direction y on bearing 074 and in direction x on bearing 075 at 9460 rpm on November 19, 1982. Again, the vibration amplitudes were almost equal. The frequency of FFW was 77 Hz (measured), the rotating frequency was 157.7 Hz, and the frequency ratio η_F equalled 0.488. So obviously the FFW appeared at 9460 rpm.

Figure 7, which gives a speed-spectrum map from an experimental recording, indicates that the FFW appeared just at 8000 rpm and that η_F equalled 0.5. Amplitude increased rapidly with increasing speed, but frequency dropped slightly.

Figure 8 shows an evolution of the shaft center orbit measured on bearing 074 at 9200 to 9480 rpm on December 18, 1982. It was photographed from the cathode oscilloscope.

All of the test results fully demonstrated that the vibration came from the instability of the rotor, but the nature of the instability was not determined. So a power spectrum referring to the vibration of bearing 074 and to the pulse pressure of the gas outlet was made. The transfer function and the coherent function were also calculated. However, the nature of the instability was still not evident.

The following additional changes were performed in this step:

(1) The inlet temperature of the lubricant oil was changed from 40 to 45 °C.

(2) The opening level of the compressor-protecting valve was changed from 40 to 100 percent.

(3) The inlet gas temperatures and pressures of the compressor were changed.

Yet no consistent, useful results were obtained.

At the same time, some temporary measures were taken during the tests:

(1) A middle vertical slipping pin was added on the body of the compressor to prevent motion caused by expansion of the cylinder.

(2) The supports were packed with insulation to prevent the cold current heat losses from influencing them.

Attention was also paid to the pads and oil-sealing slipring of the cylinder, but no effects were obtained.

SECOND STEP OF TEST (February - October 1983)

To clarify the nature of the instability, we decided to observe the dynamic properties of the rotor K1501LP on a balancing machine. This test was performed by Hangzhou Steam Turbine Works (ref. 1). The test included the following:

(1) High-speed balancing of the rotor
(2) Observation of the critical speed and its insensitivity to other parameters
(3) Increasing the number of the oil-inlet holes in the bearings
(4) Increasing the clearance in the bearings

Figure 9 shows the Nyquist tracks before and after the balancing correction. Before the correction the severity of the bearing vibration increased quickly when the speed exceeded 9000 rpm. For the sake of safety the pedestal stiffness was increased from 820 to 2250 N/μm. When the speed reached 11 230 rpm, the two bearings were vibrating at 6.5 and 2.2 mm/sec, respectively. This result indicated poor balancing. We found that the mixed vibration of the second and third modes appeared before the second critical speed was reached. Using the method of modal separation, we corrected the unbalance of the rotor. The bearings were vibrating at only 0.3 and 0.35 mm/sec, respectively, when the pedestal stiffness was restored to 820 N/μm. The first critical speed was 4000 rpm and the second was 10 700 rpm; these speeds are in agreement with the results of our calculation. The results of our experiment on insensitivity indicate that the rotor is sensitive to unbalance at 11 230 rpm. (This does not conform to American Petroleum Institute (API) standards.)

The Nyquist tracks of the rotor with one and with five oil-inlet holes (one hole for each pad) in the bearing are shown in figure 10. The dotted lines in the figure show a change of rotor vibration for one oil-inlet hole. However, oil whip did not take place. The oil clearance was increased from 0.15 to 0.20 mm, but the state of the shaft vibration did not change. It was impossible to test the labyrinth-seal excitation, for the rotor was driven in a vacuum chamber.

In brief, high-speed balancing showed clearly that the instability of the rotor did not come from the oil whip.

THIRD STEP OF TEST (November 1983)

To eliminate the vibration failure rapidly, we cooperated with Mitsubishi in completing a series of tests on November 5-8, 1983. The test speeds were to 10 222 rpm on the first day, and to 10 550 rpm on the third day. All the tests were within specifications. The test procedure for the fourth day is shown in figure 11. After reaching 10 750 rpm and running for an hour, the shaft vibrated intensely.

Figure 12 shows a real-time analysis of the shaft vibration during stable operation. Figure 13 shows the same analysis during a period of instability. Figure 14 gives a three-dimensional spectrum analysis of the shaft vibration in direction x on bearing 075. Figure 15 shows an orbit of the shaft center during instability.

The tests just described make clear the inevitability of rotor instability. But comparisons between figures 7 and 14 show that the latter tests did not produce considerable FFW before instability appeared, and the amount was less than that of the operational speed-frequency map by 25 dB (fig. 12). Just before the rotor became unstable (fig. 14), the frequency of the FFW was 74 Hz/sec (which is the same as in fig. 12). This frequency suddenly rose to 80 Hz after 5 sec (which is in agreement with fig. 13). The frequency ratio η_F equalled 0.4465.

MEASURES TAKEN

Although much important data on the dynamic properties of the rotor were acquired through the three steps of the tests, the nature of this instability has not been directly determined. According to the information and inference, however, the origin of the instability is labyrinth-seal excitation. The compressor manufacturer also provided some suggestions for improvements.

Finally, a decision was made that gas should be injected into the labyrinths of the middle diaphragm. The new construction is shown in figure 16. After this measure was taken, the instability was eliminated. Figure 17 shows a frequency spectrum of the shaft vibration on bearing 074 at 10 690 rpm before corrective measures were taken, and figure 18 shows this spectrum after corrective measures were taken. It can be seen that the FFW was eliminated.

The same results were obtained in Anquing immediately after the Nanking tests.

CONCLUDING REMARKS

The following are some of the author's viewpoints included only for reference:

1. Instability of compressor K1501 was excited by the labyrinth seal without regard to bearings, oil seal, and other factors.

2. The fractional frequency whirl (FFW) resulting from the labyrinth-seal excitation was a positive precession rather than negative precession as usually observed (ref. 2).

3. Comparisons between figure 7 and 14 show that the evidences of instability appearing after high-speed balancing of the rotor differed from those before balancing. Evidently the rotating speed at which the visual FFW occurred increased.

4. The middle-diaphragm labyrinth with gas injection as shown in figure 16 effectively eliminated the excitation existing in it, so that the method presented by Kirk (ref. 3) was again proved to be reliable.

REFERENCES

1. Zhou, Ren-mu: High-Speed Dynamic Balancing of Multistage Rotor of Compressor. Jour. of Applied Mechanics, vol. 1, no. 1, 1984 (Chinese).

2. Traupel, W.: Thermische Turbomaschinen, zweiter Band, 3. Auflage, S. 475, 1982.

3. Kirk, R.G.; et al.: Analysis and Identification of Subsynchronous Vibration for a High Pressure Parallel Flow Centrifugal Compressor. Rotordynamic Instability Problems in High-Performance Turbomachinery, NASA CP-2133, 1980, pp. 45-63.

TABLE I. - PARAMETERS OF TILTING PAD BEARING

	Bearing	
	074	075
Diameter of journal, mm	101.6	114.3
Width of bearing, mm	41	47
Specific load, N/cm^2	59.3	48.7
Clearance, mm	0.11 to 0.14	0.14 to 0.17
Number of oil-inlet holes	1	1

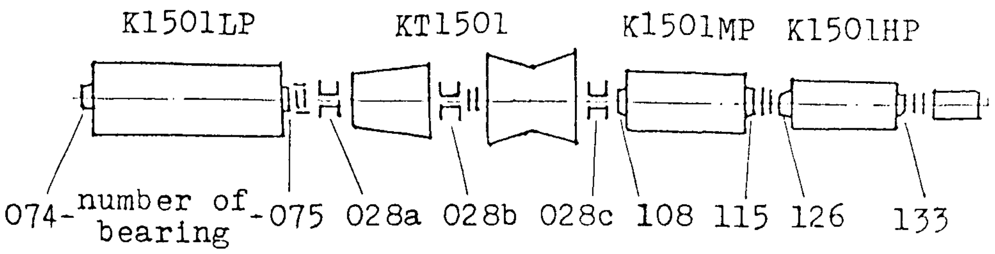
K1501LP
KT1501
K1501MP
K1501HP
074-number of bearing-075
028a
028b
028c
108
115
126
133

Figure 1. - Steam turbine compressor set of KT150-K1501.

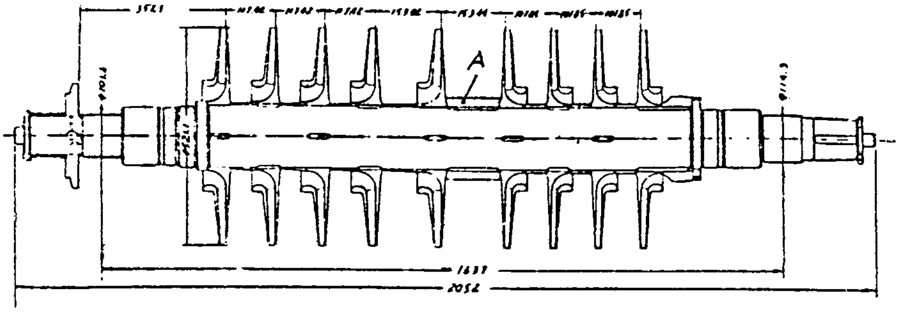

Figure 2. - Rotor of K1501LP.

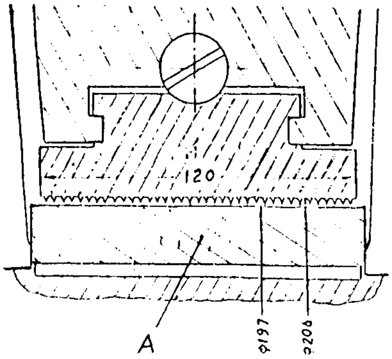
120
A
φ197
φ206

Figure 3. - Labyrinth construction.

ORIGINAL PAGE IS
OF POOR QUALITY

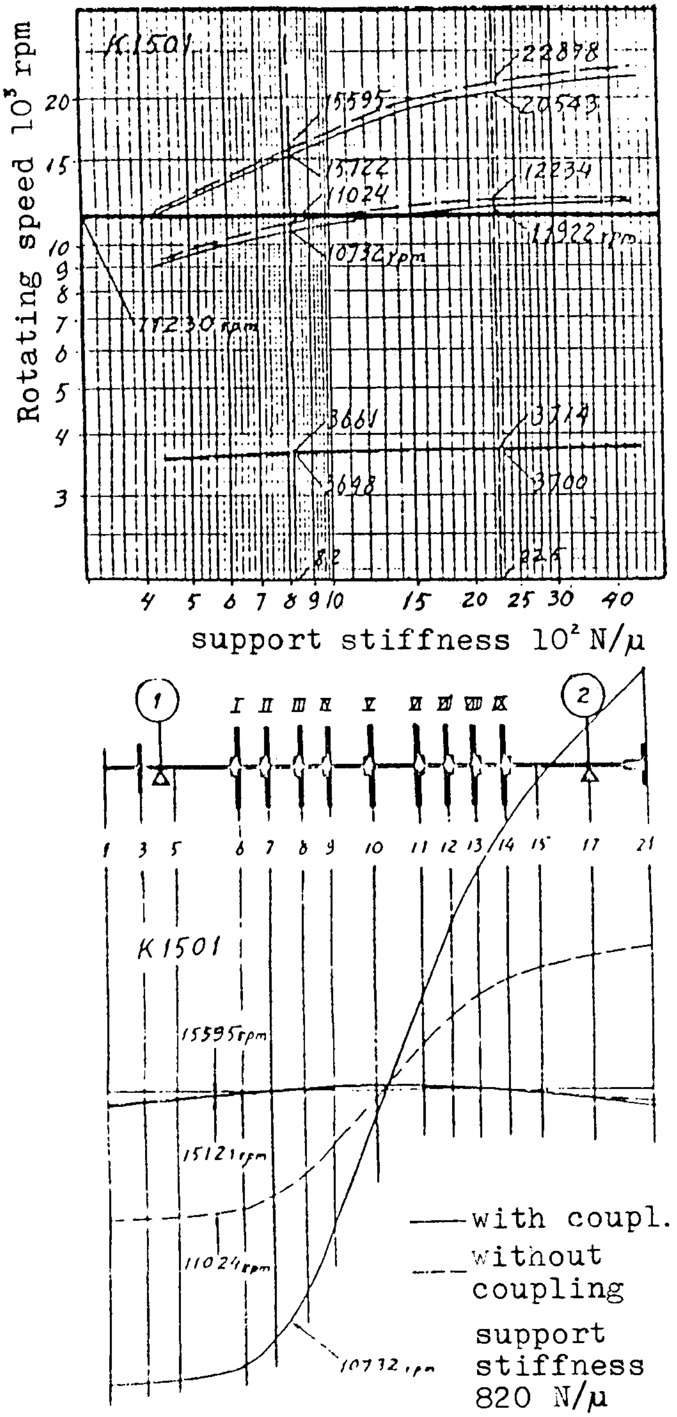

Figure 4. - Critical speed and mode shape of rotor K1501LP.

ORIGINAL PAGE IS
OF POOR QUALITY

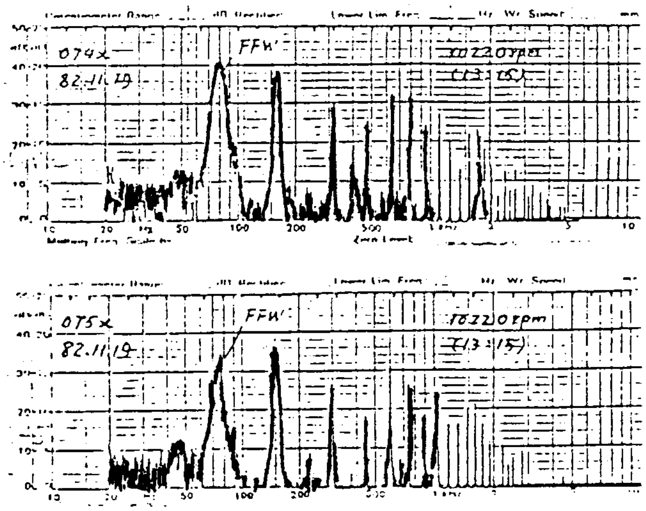

Figure 5. - Frequency spectrum of shaft vibration in bearings 074x and 075x at 10 220 rpm (Nov. 19, 1982).

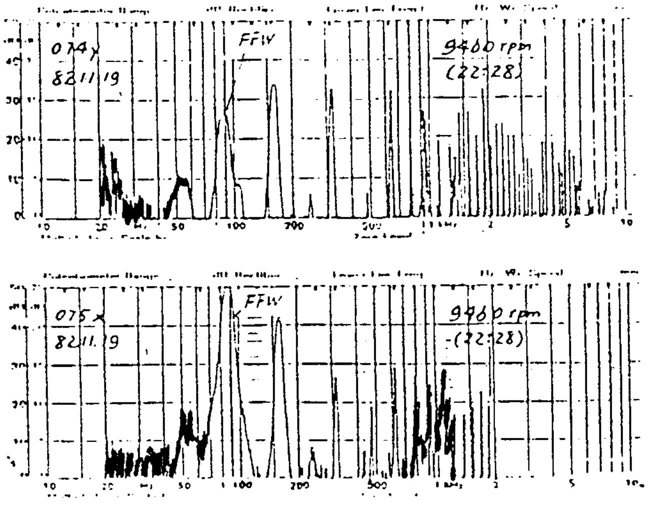

Figure 6. - Frequency spectrum of shaft vibration in bearings 074y and 075y at 9460 rpm (Nov. 19, 1982).

ORIGINAL PAGE IS
OF POOR QUALITY

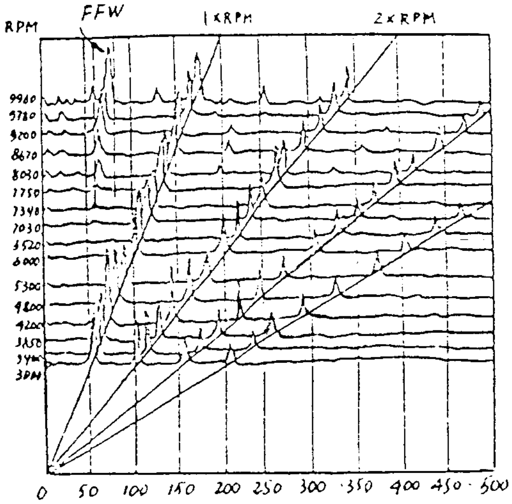

Figure 7. - Vibration speed-spectrum map.

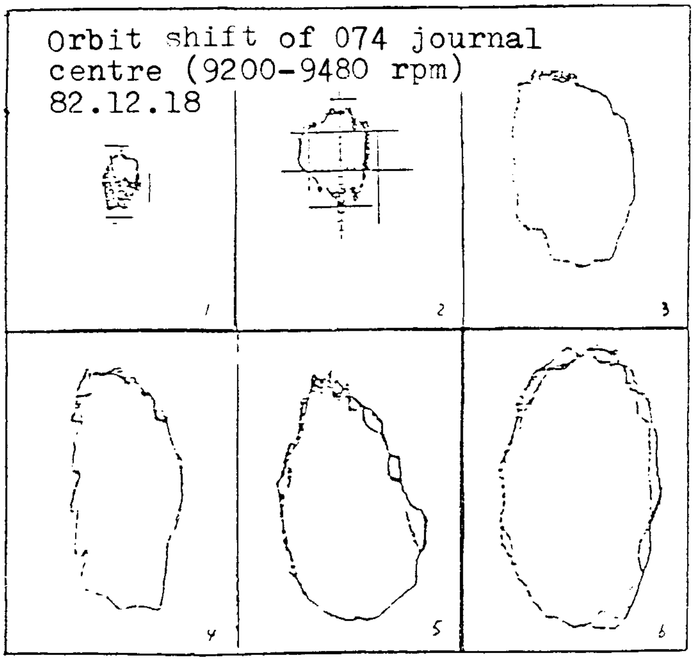

Figure 8. - Orbit of shaft center on bearing 074 from 9200 to 9600 rpm.

ORIGINAL PAGE IS
OF POOR QUALITY

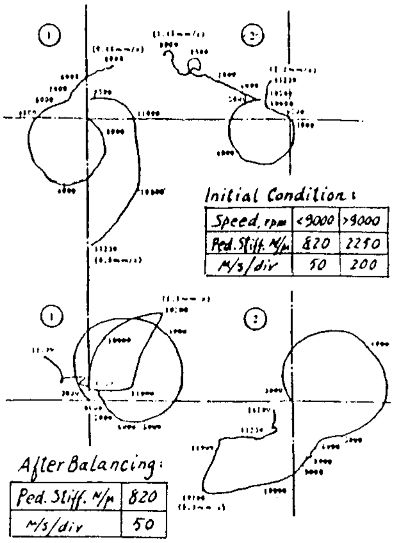

Figure 9. - Nyquist tracks before and after rotor balancing correction.

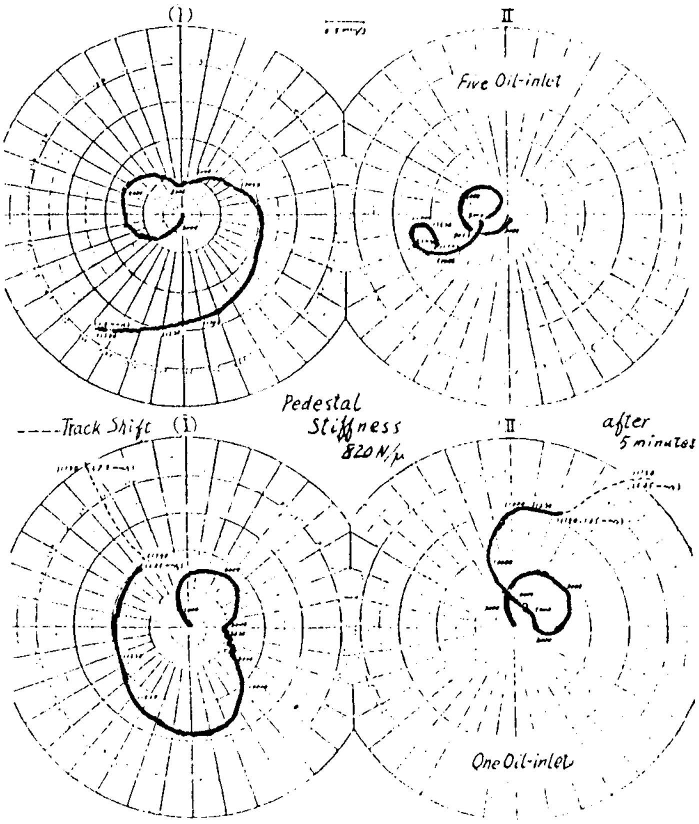

Figure 10. - Influence of number of oil-inlet holes on shaft vibration.

ORIGINAL PAGE IS
OF POOR QUALITY

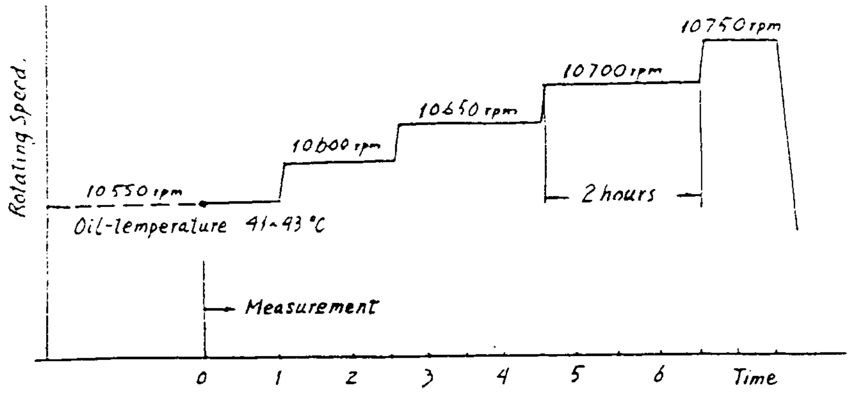

Figure 11. - Test procedure for November 8, 1983.

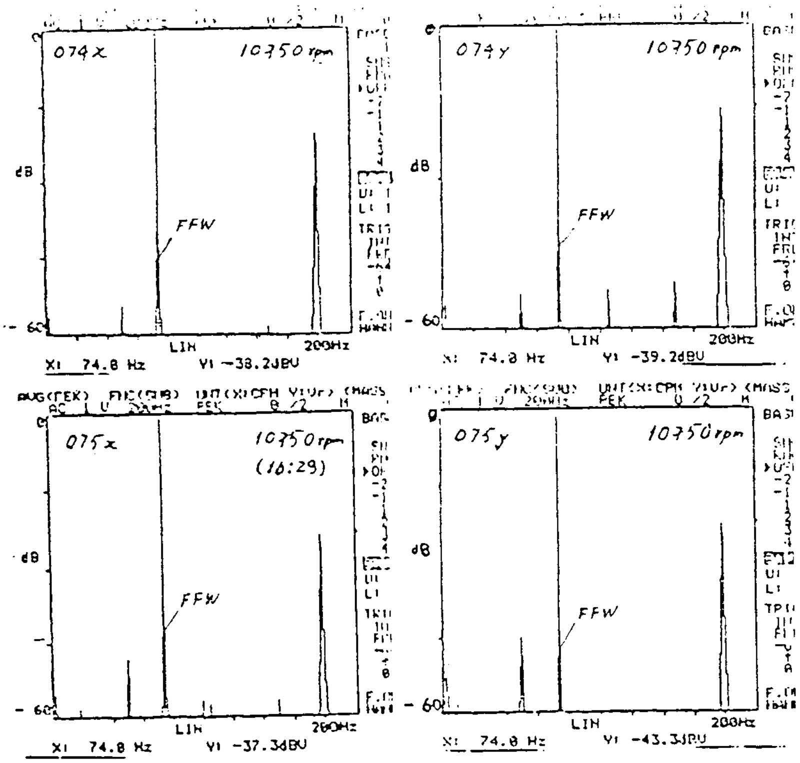

Figure 12. - Real-time analysis of shaft vibration at 10 750 rpm before rotor instability.

ORIGINAL PAGE IS
OF POOR QUALITY

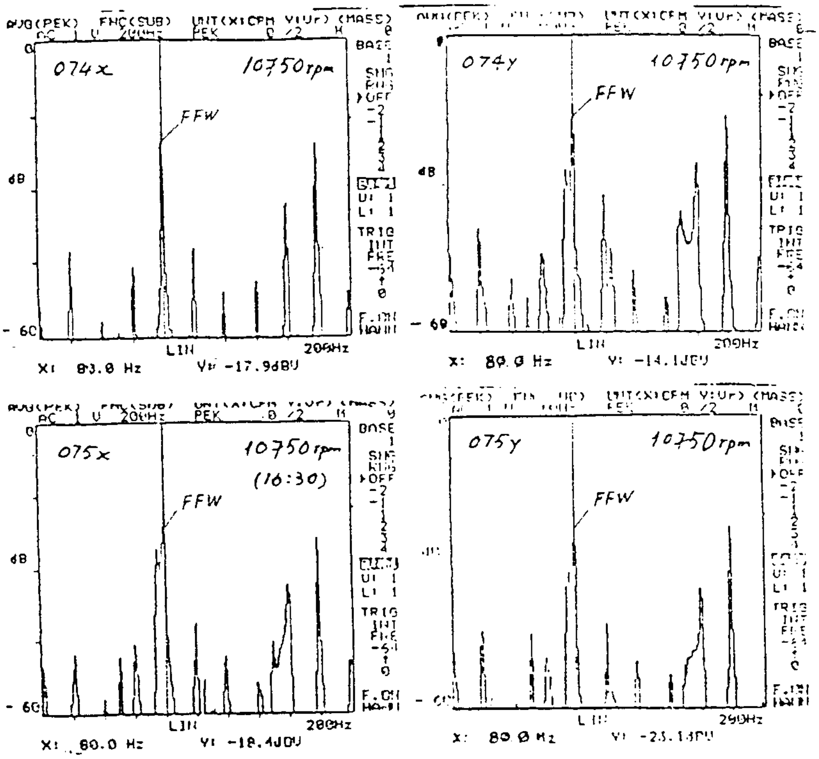

Figure 13. - Real-time analysis of shaft vibration at 10 750 rpm during rotor instability.

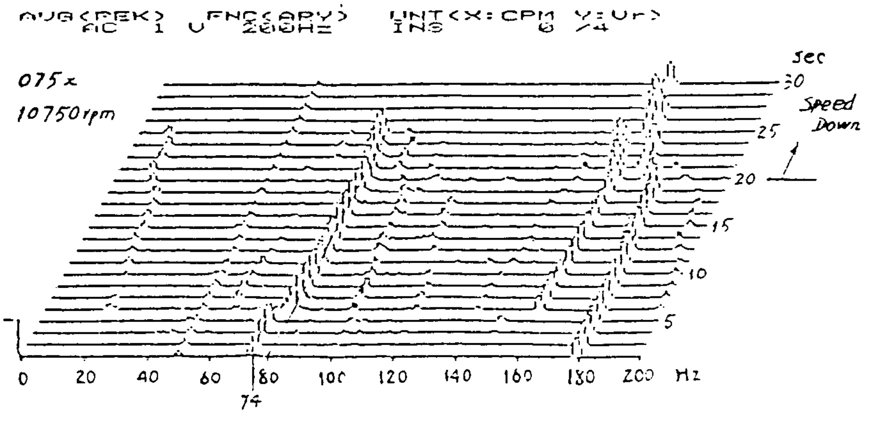

Figure 14. - Three-dimensional spectrum of shaft vibration in bearing 075 at 10 750 rpm during instability.

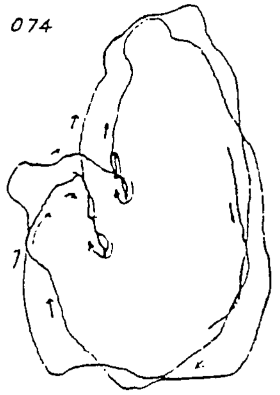

Figure 15. - Orbit of shaft center on bearing 074 at 10 750 rpm during instability.

ORIGINAL PAGE IS
OF POOR QUALITY

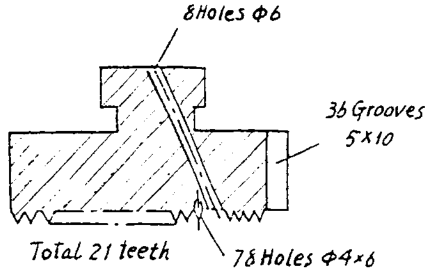
8Holes Φ6
36 Grooves
5x10
Total 21 teeth
78 Holes Φ4x6

Figure 16. - Construction of new labyrinth.

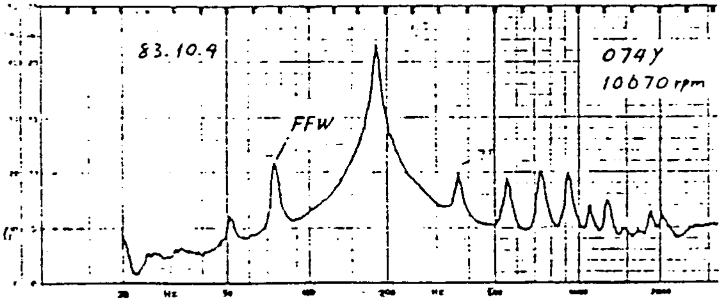

Figure 17. - Frequency spectrum of shaft vibration on bearing 074y taken with old labyrinth.

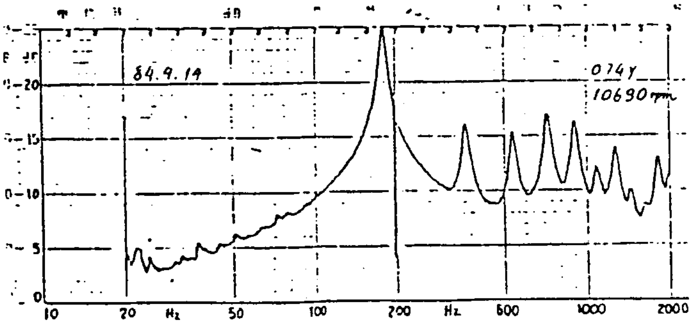

Figure 18. - Frequency spectrum of shaft vibration on bearing 074y taken with new labyrinth.

N87-22204

CALCULATING ROTORDYNAMIC COEFFICIENTS OF SEALS BY FINITE-DIFFERENCE TECHNIQUES

F.J. Dietzen and R. Nordmann
University of Kaiserslautern
Kaiserslautern, Federal Republic of Germany

For modelling the turbulent flow in a seal the Navier-Stokes equations in connection with a turbulence model (k-ε-model) are solved by a finite-difference method. A motion of the shaft round the centered position is assumed. After calculating the corresponding flow field and the pressure distribution, the rotordynamic coefficients of the seal can be determined. These coefficients are compared with results obtained by using the bulk flow theory of Childs [1] and with experimental results.

INTRODUCTION

It is well known that the fluid forces in seals, which are described by equation (1)

$$-\begin{bmatrix} F_z \\ F_y \end{bmatrix} = \begin{bmatrix} K & k \\ -k & K \end{bmatrix} \cdot \begin{bmatrix} z \\ y \end{bmatrix} + \begin{bmatrix} D & d \\ -d & D \end{bmatrix} \cdot \begin{bmatrix} \dot{z} \\ \dot{y} \end{bmatrix} + \begin{bmatrix} M & m \\ -m & M \end{bmatrix} \cdot \begin{bmatrix} \ddot{z} \\ \ddot{y} \end{bmatrix} \qquad (1)$$

have a strong influence on the dynamic behaviour of rotating turbo-machinery. While there exist some good theories for calculating the coefficients of straight seals [1], no satisfactory model is known to describe the effects of grooved seals. Reference [2] presents a survey and comparison of results of existing theories. The authors' opinion is that the existing methods are not at all satisfactory. The main weakness of these theories is the fact, that they are using so called 'bulk-flow-theories' which connect the wall shear stress with the mean flow-velocity relative to this wall. However, in the region of a groove there occur stresses in the fluid which cannot be neglected. Calculating the flow by using the Navier-Stokes equations in connection with a turbulence model eliminates this disadvantage. Therefore, a finite difference model is presented which allows the calculation of the coefficients by using these equations.

PRECEDING PAGE BLANK NOT FILMED

Nomenclature:

F_z, F_y	Forces on the shaft in z and y direction
K, k	direct and cross-coupling stiffness in eq. (1, 24)
D, d	direct and cross-coupling damping in eq. (1,24)
M, m	direct and cross-coupling inertia in eq. (1, 24)
u, v, w	axial, radial and circumferential velocity
p	pressure
k	turbulence energy
ε	energy dissipation
μ_e, μ_l, μ_t	effective, laminar and turbulent viscosity
ρ	density
t	time
x, r, θ	axial, radial and circumferential coordinate
η	radial coordinate after transformation
σ_k, σ_ε, κ	Constants od the k-ε-model
C_μ, C_1, C_2	Constants of the k-ε-model
ϕ	general variable standing for u, v, w, p, k or ε
S_ϕ	general source term
C_o	seal clearance by centric shaft position
δ	seal clearance by eccentric shaft position
r_o	radius of the precession motion of the shaft
$e = \frac{r_o}{c_o}$	perturbation parameter
ω	rotational frequency of the shaft
Ω	precession frequency of the shaft
ξ	entrance lost-coefficient
L	Length of the seal

r_i	radius of the rotor (shaft)
r_a	radius of the stator

Subscripts

0	zeroth order variables
1	first order variables
R	rotor
S	stator

MATHEMATICAL MODEL

To describe turbulent flow by the Navier-Stokes equations the velocities and the pressure are separated into mean and fluctuating quantities.

$$u = \bar{u} + u' \qquad v = \bar{v} + v'$$
$$w = \bar{w} + w' \qquad p = \bar{p} + p'$$

Time-averaging of the Navier-Stokes equations leads to terms of the following form: $\overline{u'v'}$, $\overline{v'w'}$, $\overline{u'w'}$.

To substitute these terms one can use the Boussinesq's eddy-viscosity concept. For example:

$$\overline{u'v'} = -\frac{\mu_t}{\rho}\left(\frac{\partial\bar{u}}{\partial y} + \frac{\partial\bar{v}}{\partial x}\right) \qquad (2)$$

μ_t is the turbulent viscosity, which is not a fluid property but depends strongly on the state of flow. Summing up the laminar and turbulent viscosity to an effective viscosity

$$\mu_e = \mu_l + \mu_t \,, \qquad (3)$$

one obtains the following time-averaged Navier-Stokes equations for turbulent flow. (In the following the overbars are omitted.)

1. axial momentum:

$$\rho\frac{\partial u}{\partial t} + \frac{\partial}{\partial x}(\rho uu) - \frac{\partial}{\partial x}(\mu_e\frac{\partial u}{\partial x}) + \frac{1}{r}\frac{\partial}{\partial r}(r\rho vu) - \frac{1}{r}\frac{\partial}{\partial r}(r\mu_e\frac{\partial u}{\partial r}) + \frac{1}{r}\frac{\partial}{\partial \Theta}(\rho wu) - \frac{1}{r}\frac{\partial}{\partial \Theta}(\frac{1}{r}\mu_e\frac{\partial u}{\partial \Theta}) =$$

$$-\frac{\partial p}{\partial x} + \frac{\partial}{\partial x}(\mu_e\frac{\partial u}{\partial x}) + \frac{1}{r}\frac{\partial}{\partial r}(r\mu_e\frac{\partial v}{\partial x}) + \frac{1}{r}\frac{\partial}{\partial \Theta}(\mu_e\frac{\partial w}{\partial x}) \qquad (4)$$

2. radial momentum:

$$\rho\frac{\partial v}{\partial t} + \frac{\partial}{\partial x}(\rho uv) - \frac{\partial}{\partial x}(\mu_e\frac{\partial v}{\partial x}) + \frac{1\partial}{r\partial r}(r\rho vv) - \frac{1\partial}{r\partial r}(r\mu_e\frac{\partial v}{\partial r}) + \frac{1\partial}{r\partial\Theta}(\rho wv) - \frac{1\partial}{r\partial\Theta}(\frac{1}{r}\mu_e\frac{\partial v}{\partial\Theta}) =$$

$$-\frac{\partial p}{\partial r} + \frac{1\partial}{r\partial r}(r\mu_e\frac{\partial v}{\partial r}) + \frac{\partial}{\partial x}(\mu_e\frac{\partial u}{\partial r}) + \frac{1\partial}{r\partial\Theta}(r\mu_e\frac{\partial}{\partial r}(\frac{w}{r})) - \frac{2}{r^2}\mu_e\frac{\partial w}{\partial\Theta} - \frac{2}{r^2}\mu_e v + \frac{\rho}{r}w^2 \qquad (5)$$

3. tangential momentum

$$\rho\frac{\partial w}{\partial t} + \frac{\partial}{\partial x}(\rho uw) - \frac{\partial}{\partial x}(\mu_e\frac{\partial w}{\partial x}) + \frac{1\partial}{r\partial r}(r\rho vw) - \frac{1\partial}{r\partial r}(r\mu_e\frac{\partial w}{\partial r}) + \frac{1\partial}{r\partial\Theta}(\rho ww) - \frac{1\partial}{r\partial\Theta}(\frac{1}{r}\mu_e\frac{\partial w}{\partial\Theta}) =$$

$$-\frac{1\partial p}{r\partial\Theta} + \frac{1\partial}{r\partial r}(\mu_e\frac{\partial v}{\partial\Theta}) + \frac{\partial}{\partial x}(\frac{1}{r}\mu_e\frac{\partial u}{\partial\Theta}) + \frac{1}{r^2}\mu_e\frac{\partial v}{\partial\Theta} - \frac{w}{r^2}\frac{\partial}{\partial r}(r\mu_e) + \frac{1\partial}{r\partial\Theta}(\frac{2}{r}\mu_e v) + \frac{1\partial}{r\partial\Theta}(\frac{1}{r}\mu_e\frac{\partial w}{\partial\Theta}) - \frac{\rho}{r}vw \qquad (6)$$

4. continuity equation

$$\frac{\partial}{\partial x}(\rho u) + \frac{1\partial}{r\partial r}(r\rho v) + \frac{1\partial}{r\partial\Theta}(\rho w) = 0 \qquad (7)$$

To describe μ_t we use the k-ε turbulence model [3, 4]. This model determines μ_t as a function of the kinetic energy k of the turbulent motion and the energy dissipation ε. It is relative simple and often used to calculate the turbulent flow in seals [12, 13, 14, 15]. Stoff [12], for example, compares his flow measurements in a labyrinth seal with calculations on base of the k-ε model. He observes that both agree well.

$$\mu_t = c_\mu\ \rho\ \frac{k^2}{\varepsilon} \qquad (8)$$

The equations for k and ε can be derived in exact form from the Navier-Stokes equations

5. turbulence energy k

$$\rho\frac{\partial k}{\partial t} + \frac{\partial}{\partial x}(\rho uk) - \frac{\partial}{\partial x}(\frac{\mu_e\partial k}{\sigma_k\partial x}) + \frac{1\partial}{r\partial r}(r\rho vk) - \frac{1\partial}{r\partial r}(r\frac{\mu_e\partial k}{\sigma_k\partial r}) + \frac{1\partial}{r\partial\Theta}(\rho wk) - \frac{1\partial}{r\partial\Theta}(\frac{1\mu_e\partial k}{r\sigma_k\partial\Theta}) =$$

$$G - \rho\varepsilon \qquad (9)$$

6. energy dissipation ε

$$\rho\frac{\partial\varepsilon}{\partial t} + \frac{\partial}{\partial x}(\rho u\varepsilon) - \frac{\partial}{\partial x}\left(\frac{\mu_e}{\sigma_\varepsilon}\frac{\partial\varepsilon}{\partial x}\right) + \frac{1}{r}\frac{\partial}{\partial r}(r\rho v\varepsilon) - \frac{1}{r}\frac{\partial}{\partial r}\left(r\frac{\mu_e}{\sigma_\varepsilon}\frac{\partial\varepsilon}{\partial r}\right) + \frac{1}{r}\frac{\partial}{\partial\Theta}(\rho w\varepsilon) - \frac{1}{r}\frac{\partial}{\partial\Theta}\left(\frac{1}{r}\frac{\mu_e}{\sigma_\varepsilon}\frac{\partial\varepsilon}{\partial\Theta}\right) =$$

$$C_1\frac{\varepsilon}{k}G - C_2\rho\frac{\varepsilon^2}{k} \qquad (10)$$

$$G = \mu_e\left\{ 2\left(\left(\frac{\partial v}{\partial r}\right)^2 + \left(\frac{\partial u}{\partial x}\right)^2 + \left(\frac{1}{r}\frac{\partial w}{\partial\Theta} + \frac{v}{r}\right)^2\right) + \left(\frac{\partial v}{\partial x} + \frac{\partial u}{\partial r}\right)^2 + \left(\frac{1}{r}\frac{\partial v}{\partial\Theta} + \frac{\partial w}{\partial r} - \frac{w}{r}\right)^2 + \left(\frac{\partial w}{\partial x} + \frac{1}{r}\frac{\partial u}{\partial\Theta}\right)^2\right\}$$

$$C_\mu = 0.09 \qquad C_1 = 1.44 \qquad C_2 = 1.92$$

$$\kappa = 0.4187 \qquad \sigma_k = 1. \qquad \sigma_\varepsilon = \frac{\kappa}{C_\mu^5(C_1 - C_2)} \qquad (11)$$

To model the flow in the case of a shaft moving on an eccentric orbit, a coordinate-transformation [5, 6] is made. (Fig. 1)

$$\eta = r_a - \frac{r_a - r}{\delta} C_o \qquad (12)$$

$\delta(\theta,t)$ is the seal clearance, varying with angle θ and time t. By this transformation the eccentric moving shaft is reduced to a shaft rotating in the centre of the seal.

We must note that the following relations of the transformation must be used.

$$\left(\frac{\partial\phi}{\partial\Theta}\right)_r = \left(\frac{\partial\phi}{\partial\Theta}\right)_\eta + \left(\frac{\partial\phi}{\partial\eta}\right)_\Theta\left(\frac{\partial\eta}{\partial\Theta}\right)_r$$

$$\left(\frac{\partial\phi}{\partial t}\right)_r = \left(\frac{\partial\phi}{\partial t}\right)_\eta + \left(\frac{\partial\phi}{\partial\eta}\right)_t\left(\frac{\partial\eta}{\partial t}\right)_r \qquad (13)$$

$$\left(\frac{\partial\phi}{\partial x}\right)_r = \left(\frac{\partial\phi}{\partial x}\right)_\eta$$

PERTURBATION ANALYSIS

The rotordynamic coefficients of a seal are in a wide range independent of the shaft eccentricity. Therefore we can assume small shaft motions around the centered position which allow us to use a perturbation analysis.

$$\delta = C_0 - eh_1$$

$$u = u_0 + eu_1 \qquad v = v_0 + ev_1$$

$$w = w_0 + ew_1 \qquad p = p_0 + ep_1$$

With these expressions and the coordinate-transformation equation (12) the equations (4), (5), (6), (7), (9), (10) change themselves.

This is demonstrated in the following examples.
From equation (12) we obtain:

$$r = \eta + e\frac{h_1}{C_0}(r_a - \eta) \tag{14}$$

$$\frac{\partial}{\partial r} = \frac{C_0\partial}{\delta\ \partial\eta} = \frac{1}{1 - e\frac{h_1}{C_0}}\frac{\partial}{\partial\eta} \tag{15}$$

and so:

$$\frac{1\partial}{r\partial\Theta}(r\rho vu) = \frac{1}{\eta + e\frac{h_1}{C_0}(r_a - \eta)}\ \frac{1}{1 - e\frac{h_1}{C_0}}\frac{\partial}{\partial\eta}\{\rho(\eta + e\frac{h_1}{C_0}(r_a - \eta))(v_0 + ev_1)(u_0 + eu_1)\}$$

$$= \frac{1\partial}{\eta\partial\eta}(\eta\rho v_0u_0) + e\frac{1\partial}{\eta\partial\eta}\{\eta\rho(u_0v_1 + v_0u_1)\} + e\frac{h_1}{C_0}\{\frac{\partial}{\partial\eta}(\rho u_0v_0) + (1 - \frac{r_a}{\eta})\frac{1}{\eta}\rho u_0v_0\} \tag{16}$$

$$\frac{1}{r}\frac{\partial}{\partial\Theta}(\rho uw) = \frac{1}{\eta + e\frac{h_1}{C_o}(r_a - \eta)}\{\frac{\partial}{\partial\Theta}(\rho(u_o + eu_1)(w_o + ew_1))$$

$$+ \frac{\partial}{\partial\Theta}(\rho(u_o + eu_1)(w_o + ew_1)\frac{\partial}{\partial\Theta}(r_a - \frac{r_a - r}{\delta} C_o))\} \tag{17}$$

$$= e\frac{1}{\eta}\frac{\partial}{\partial\Theta}(\rho u_o w_1 + \rho w_o u_1) + e(\eta - r_a)\frac{1}{\eta}\frac{\partial}{\partial\eta}(\rho u_o w_o)\frac{1}{C_o}\frac{\partial h_1}{\partial\eta}$$

$$\rho\frac{\partial u}{\partial t} = \rho(\frac{\partial u_o}{\partial t} + \frac{\partial u_1}{\partial t}) + \rho\frac{\partial(u_o + eu_1)}{\partial\eta}\frac{\partial}{\partial t}(r_a - \frac{r_a - r}{\delta} C_o) \tag{18}$$

$$= e\rho\frac{\partial u_1}{\partial t} + e\rho\frac{\partial u_o}{\partial\eta}(\frac{\eta - r_a}{C_o})\frac{\partial h_1}{\partial t}$$

One obtains a set of zero-order equations for u_o, v_o, w_o, p_o, k_o, ε_o and a set of first-order equations for u_1, v_1, w_1, p_1. It is assumed that the viscosity μ_e remains constant for small motions. Therefore the k_1 and ε_1 equations can be dropped.

The variation of the seal clearance for an eccentric shaft can be described by the following equation

$$h_1 = \frac{z}{e}\cos\theta + \frac{y}{e}\sin\theta$$

So we establish the same assumptions as in [1], that the velocities and the pressure in circumferential direction can be described by sin- and cos-functions, in our first order equations

$$u_1 = u_{1c}\cos\theta + u_{1s}\sin\theta \qquad v_1 = v_{1c}\cos\theta + v_{1s}\sin\theta$$

$$w_1 = w_{1c}\cos\theta + w_{1s}\sin\theta \qquad p_1 = p_{1c}\cos\theta + p_{1s}\sin\theta$$

By separating in the resulting equations the terms with sinθ and cosθ we obtain two real equations of every 1. order equation. These equations are then arranged in a new form by introducing complex variables.

$\bar{u}_1 = u_{1c} + iu_{1s}$ $\qquad$ $\bar{v}_1 = v_{1c} + iv_{1s}$

$\bar{w}_1 = w_{1c} + iw_{1s}$ $\qquad$ $\bar{p}_1 = p_{1c} + ip_{1s}$

$\bar{h}_1 = z + iy$

We now assume that the shaft is moving on a circular orbit with frequency Ω around the centered position. Also $\bar{h}_1$ takes the form:

$$\bar{h}_1 = r_o e^{i\Omega t}$$

and similary

$\bar{u}_1 = \hat{u}_1\, e^{i\Omega t}$ $\qquad$ $\bar{v}_1 = \hat{v}_1\, e^{i\Omega t}$

$\bar{w}_1 = \hat{w}_1\, e^{i\Omega t}$ $\qquad$ $\bar{p}_1 = \hat{p}_1\, e^{i\Omega t}$

In the following we assume that t = 0; this means that the shaft is just moving through the z-axis in the y-direction.

The resulting equations for u_o, v_o, w_o, p_o, k_o, ε_o and $\hat{u}_1$, $\hat{v}_1$, $\hat{w}_1$ have all the same form.

$$\frac{\partial}{\partial x}(\rho u_o \phi) - \frac{\partial}{\partial x}(\Gamma_\phi \frac{\partial \phi}{\partial x}) + \frac{1}{\eta}\frac{\partial}{\partial \eta}(\eta \rho v_o \phi) - \frac{1}{\eta}\frac{\partial}{\partial \eta}(\Gamma_\phi \eta \frac{\partial \phi}{\partial \eta}) = S_\phi \qquad (19)$$

Zeroth Order Equations

ϕ	Γ_ϕ	S_ϕ
u_o	μ_e	$-\frac{\partial p_o}{\partial x} + \frac{\partial}{\partial x}(\mu_e \frac{\partial u_o}{\partial x}) + \frac{1}{\eta}\frac{\partial}{\partial \eta}(\mu_e \eta \frac{\partial v_o}{\partial x})$
v_o	μ_e	$-\frac{\partial p_o}{\partial \eta} + \frac{\partial}{\partial x}(\mu_e \frac{\partial u_o}{\partial \eta}) + \frac{1}{\eta}\frac{\partial}{\partial \eta}(\mu_e \eta \frac{\partial v_o}{\partial \eta}) - \frac{2}{\eta^2}\mu_e v_o + \frac{\rho}{\eta} w_o^2$
w_o	μ_e	$-\frac{w_o}{\eta^2}\frac{\partial}{\partial \eta}(\eta \mu_e) - \frac{\rho}{\eta} v_o w_o$
1	0	0
k_o	$\frac{\mu_e}{\sigma_k}$	$G - \rho\varepsilon$
ε_o	$\frac{\mu_e}{\sigma_\varepsilon}$	$C_1 \frac{\varepsilon}{k} G - C_2 \rho \frac{\varepsilon^2}{k}$

ORIGINAL PAGE IS
OF POOR QUALITY

First Order Equations

ϕ	Γ_ϕ	S_ϕ
$\hat{u}_1$	μ_e	$-\frac{\partial\hat{p}_1}{\partial x}+\frac{\partial}{\partial x}(\mu_e\frac{\partial\hat{u}_1}{\partial x})+\frac{1}{\eta}\frac{\partial}{\partial\eta}(\eta\mu_e\frac{\partial\hat{v}_1}{\partial x})-\frac{\partial}{\partial x}(\rho u_o\hat{u}_1)-\frac{1}{\eta}\frac{\partial}{\partial\eta}(\eta\rho u_o\hat{v}_1)$
		$-\frac{\mu_e}{\eta^2}\hat{u}_1+i\rho(-\Omega+\frac{w_o}{\eta})\hat{u}_1+i\frac{\rho}{\eta}u_o\hat{w}_1-i\frac{\mu_e}{\eta}\frac{\partial\hat{w}_1}{\partial x}+D_1+iD_2$
$\hat{v}_1$	μ_e	$-\frac{\partial\hat{p}_1}{\partial\eta}+\frac{\partial}{\partial x}(\mu_e\frac{\partial\hat{u}_1}{\partial x})+\frac{1}{\eta}\frac{\partial}{\partial\eta}(\eta\mu_e\frac{\partial\hat{v}_1}{\partial x})-\frac{\partial}{\partial x}(\rho v_o\hat{u}_1)-\frac{1}{\eta}\frac{\partial}{\partial\eta}(\eta\rho v_o\hat{v}_1)$
		$-i\mu_e\frac{\partial}{\partial\eta}(\frac{\hat{w}_1}{\eta})-3\frac{\mu_e}{\eta^2}\hat{v}_1+i\rho(\frac{w_o}{\eta}-\Omega)\hat{v}_1+(2\frac{\rho}{\eta}w_o+i2\frac{\mu_e}{\eta^2}+i\frac{\rho}{\eta}v_o)\hat{w}_1+D_3+iD_4$
$\hat{w}_1$	μ_e	$i\frac{\hat{p}_1}{\eta}-i\frac{\partial}{\partial x}(\frac{\mu_e}{\eta}\hat{u}_1)-i\frac{1}{\eta}\frac{\partial}{\partial\eta}(\mu_e\hat{v}_1)-\frac{\partial}{\partial x}(\rho w_o\hat{u}_1)-\frac{1}{\eta^2}\frac{\partial}{\partial\eta}(\rho\eta^2 w_o\hat{v}_1)$
		$-2\frac{\mu_e}{\eta^2}\hat{w}_1-i3\frac{\mu_e}{\eta^2}\hat{v}_1-(\frac{\rho}{\eta}v_o+i\rho\Omega+\frac{1}{\eta^2}\frac{\partial\eta\mu_e}{\partial\eta}-i2\frac{\rho}{\eta}w_o)\hat{w}_1+D_5+iD_6$

Only the first order continuity-equation to determine $\hat{p}_1$ shows a slightly modified form.

$$\frac{\partial}{\partial x}(\rho\hat{u}_1)+\frac{1}{\eta}\frac{\partial}{\partial\eta}(\eta\rho\hat{v}_1)=i\frac{\rho}{\eta}\hat{w}_1+D_7+iD_8 \tag{20}$$

The parameters D_1 - D_8 do not depend on $\hat{u}_1$, $\hat{v}_1$, $\hat{w}_1$, $\hat{p}_1$ and result from the coordinate-transformation. (D_1 - D_8 are shown in the appendix.)

FINITE-DIFFERENCE METHOD

For solving these equations a finite-difference procedure is used which is based on a method published by Gosman and Pun [7]. The seal is discretized by a grid (Fig. 2) and the variables are calculated at the nodes. The velocities u, v are determined at points which lie between the nodes where the variables p, w, k, ε are calculated (Fig. 3). Because of its general convergence a 'hybrid - difference' method is used, which means that the convective terms are calculated by a 'upwind'- or a 'central-difference' method as a function of flow-velocity and grid-distance.

Because there is no explicit equation to calculate p we use the continuity equation. Starting by a guess for p, the momentum-equations are solved; with the resulting values u, v ($\hat{u}_1$, $\hat{v}_1$, $\hat{w}_1$) the flow through the control-area around a point for the pressure p ($\hat{p}_1$) is calculated. If the difference between the entrance- and the exit-flow rate is less than 0, p must be reduced; in the opposite case p must be increased. This is done by the 'SIMPLE'-procedure [8] or better by the more modern version 'PISO' [9].

However one has to respect in the determination of $\hat{p}_1$ with these procedures that the equation for $\hat{w}_1$ has not the same form as for $\hat{u}_1$ and $\hat{v}_1$. Also we have to notice that u_0, v_0, p_0, w_0, k_0, ε_0 are real-, while $\hat{u}_1$, $\hat{v}_1$, $\hat{w}_1$, $\hat{p}_1$ are of complex type. The mesh to calculate u, v doesn't extend all the way to the boundary wall, and the component u, w is allowed to slip in accordance with the logarithmic law of the wall.

LEAKAGE FLOW AND DYNAMIC COEFFICIENTS

Leakage flow, Centered Position

For centered shaft position the values u_0, v_0, p_0, w_0, k_0 ε_0 are determined.

Boundary conditions:

$$u_{0S} = 0 \qquad v_{0S} = 0 \qquad w_{0S} = 0$$

$$u_{0R} = 0 \qquad v_{0R} = 0 \qquad w_{0R} = \omega \cdot r_i$$

The leakage results from the calculated axial velocity u_0.

Dynamic Coefficients, Eccentric Shaft Motion

For calculating the dynamic coefficients the following assumptions are made:

1. The shaft rotates on a circular orbit around the centered position.
2. At time $t = 0$ the shaft is located at: $z = r_0$, $y = 0$
3. The viscosity μ_e remains constant in spite of the eccentric motion.

Boundary conditions: (Fig. 4, 5)

Stator: $\hat{u}_{1S} = (0., 0.)$ $\hat{v}_{1S} = (0., 0.)$ $\hat{w}_{1S} = (0., 0.)$

Rotor: $\hat{u}_{1R} = (0., 0.)$ $\hat{v}_{1R} = (0., (\Omega - \omega) \cdot C_0)$ $\hat{w}_{1R} = (\Omega C_0, 0.)$

Entrance: $p_A = \frac{1}{2} \rho u^2 (1 + \xi) + p_B$

$$\hat{p}_{1B_j} = - \rho u_{0B_j} (1 + \xi) \hat{u}_{1B_j}$$

Exit: $\hat{p}_{1C_j} = (0., 0.)$

To satisfy the entrance condition we make use of the iterative character of the finite-difference method. This means that we start with a pressure $\hat{p}_{1B_j}$ at the entrance and after every iteration step we check if the calculated $\hat{u}_{1B_j}$ satisfy condition (21). If not, the pressure $\hat{p}_{1B_j}$ will be corrected.

The resulting forces on the shaft are calculated by a pressure integration for the five precession frequencies: $\Omega = 0\omega,\ 0{,}5\ \omega,\ 1{,}0\ \omega,\ 1{,}5\ \omega,\ 2\ \omega$.

$$- F_z = \frac{\pi r_i}{C_0} \int_L p_{1C}\, dx \tag{22}$$

$$- F_y = \frac{\pi r_i}{C_0} \int_L p_{1S}\, dx \tag{23}$$

By a 'Least-Square-Fit' we obtain the rotor-dynamic coefficients of (1) from the following equations

$$\begin{aligned} - F_z &= K + C\Omega - M\Omega^2 \\ - F_y &= -k + C\Omega + m\Omega^2 \end{aligned} \tag{24}$$

The precession frequencies can be arbitrarily chosen, because the dynamic coefficients are mostly independent of them. We take the same as in [1].

RESULTS FOR AN ANNULAR SEAL

To test the theory, calculations are made for a straight smooth seal. The results are compared with the experimental values of Massmann [10] and the results of Childs theory [1].

C-2

Seal Data:

$L = 23{,}5$ mm
$r_i = 23{,}5$ mm
$C_o = 0{,}2$ mm
$\mu_1 = 0{,}7 \cdot 10^{-3}$ Ns/m^3
$\rho = 996$ kg/m^3
$\xi = 0{,}5$

A fully developed turbulent axial and circumferential flow at the entrance of the seal is assumed. As in [10] flowrates are measured, in the presented calculation we suppose that the axial flow velocity is known:

$u_{\text{average}} = 16{,}46$ m/s

and that the average circumferential velocity at the entrance is half the shaft-speed.

For a known mass flow the pressure difference between entrance and exit of the seal can be calculated. The results of this theory are compared with Childs theory in Fig. 6.

In Fig. 7, 8, 9, 10, 11 results of the presented theory, Childs theory [1] and experimental data from Massmann [10] are shown.

Both theories are in good agreement with each other and with the measurements. For calculation a mesh with 15 x 5 nodes in x-r direction was applied. The CPU time was about 30 sec on a Siemens 7.561 computer.

RESULTS FOR A GROOVED SEAL

We also made some calculations, for the grooved seal, whose geometry and seal data are shown in Fig. 12. In Fig. 13 the leakage for a given pressure difference is presented as a function of the groove depth. First the leakage decreases and then slightly increases again. This behaviour agrees with the measurements of Black [11].

In Fig. 14, 15, 16, 17 the stiffness K, k and the damping D, d are shown. The coefficients K, k, D decrease with growing groove depth. Only the damping d increases. Although we haven't yet any experimental results for this seal the tendencies seem to be right.

CONCLUSION

It is shown that it is possible to calculate the dynamic coefficients of seals with a finite-difference method, based on the Navier-Stokes equation in connection with a turbulence model. Although application on straight seals is possible, it was not our aim to develop a procedure for this seal configuration but to present a method which will be applicable on grooved seals. The superiority of the theory versus other methods is the simplicity in use for grooved seals by only neglecting the terms D_1 - D_8 in the equations for $\hat{u}_1$, $\hat{v}_1$, $\hat{w}_1$, $\hat{p}_1$ in the grooves, while there exists no mesh displacement.

Appendix:

Transformation-constants for first order equations

$$D_1 = \frac{\partial}{\partial\eta}(\mu_e\frac{\partial v_o}{\partial x} + \mu_e\frac{\partial u_o}{\partial\eta} - \rho v_o u_o) + (1 - \frac{r_a}{\eta})\frac{1}{\eta}(\mu_e\frac{\partial v_o}{\partial x} - \rho v_o u_o) + (1 - \frac{r_a}{\eta})\frac{\mu_e}{\eta}\frac{\partial u_o}{\partial\eta}$$

$$D_2 = (\frac{r_a}{\eta} - 1)\{\frac{\partial}{\partial\eta}(\mu_e\frac{\partial w_o}{\partial x}) - \frac{\partial}{\partial\eta}(\rho u_o w_o)\} - \Omega\rho\frac{\partial u_o}{\partial\eta}(\eta - r_a)$$

$$D_3 = (1 - \frac{r_a}{\eta})(\frac{\rho}{\eta}w_o w_o - \frac{\rho}{\eta}v_o v_o - 2\frac{\mu_e}{\eta^2}v_o + 2\frac{\mu_e}{\eta}\frac{\partial v_o}{\partial\eta}) - \frac{\partial}{\partial\eta}(\rho v_o v_o) - \frac{\partial p_o}{\partial\eta} + 2\frac{\partial}{\partial\eta}(\mu_e\frac{\partial v_o}{\partial\eta})$$

$$D_4 = (\frac{r_a}{\eta} - 1)\{\frac{\partial}{\partial\eta}(\mu_e\eta\frac{\partial}{\partial\eta}(\frac{w_o}{\eta})) - \frac{\partial}{\partial\eta}(\rho w_o v_o)\} - \Omega\rho\frac{\partial v_o}{\partial\eta}(\eta - r_a)$$

$$D_5 = \frac{1}{\eta}\frac{\partial}{\partial\eta}(\mu_e\eta\frac{\partial w_o}{\partial\eta}) - \frac{1}{\eta}\frac{\partial}{\partial\eta}(\mu_e w_o) + (1 - 2\frac{r_a}{\eta})\mu_e\frac{\partial}{\partial\eta}(\frac{w_o}{\eta}) - \frac{\partial}{\partial\eta}(\rho v_o w_o) + 2\frac{\rho}{\eta}v_o w_o(\frac{r_a}{\eta} - 1)$$

$$D_6 = (1 - \frac{r_a}{\eta})\{\frac{\partial}{\partial\eta}(\rho w_o w_o) - \frac{\partial}{\partial\eta}(2\frac{\mu_e}{\eta}v_o) + \frac{\partial p_o}{\partial\eta}\} - \Omega\rho\frac{\partial w_o}{\partial\eta}(\eta - r_a)$$

$$D_7 = \frac{\rho}{\eta}v_o(\frac{r_a}{\eta} - 1) - \rho\frac{\partial v_o}{\partial\eta}$$

$$D_8 = (1 - \frac{r_a}{\eta})\rho\frac{\partial w_o}{\partial\eta}$$

With, for example:

$$\frac{1}{r}\frac{\partial}{\partial r}(r\mu_e\frac{\partial u}{\partial r}) + \frac{1}{r}\frac{\partial}{\partial r}(r\mu_e\frac{\partial v}{\partial x}) = \frac{1}{r}\frac{\partial}{\partial r}(r\ \tau_{xr}) \Longrightarrow \frac{1}{\eta}\frac{\partial}{\partial\eta}(\eta\ \tau_{xr_o}) + e\frac{1}{\eta}\frac{\partial}{\partial\eta}(\eta\ \tau_{xr_1}) +$$

$$e\frac{h_1}{C_o}\{\frac{1}{\eta}\frac{\partial}{\partial\eta}(\eta(\frac{r_a}{\eta} - 1)\tau_{xr_o}) + (2 - \frac{r_a}{\eta})\frac{1}{\eta}\frac{\partial}{\partial\eta}(\eta\tau_{xr_o})\}$$

References

/1/ Childs, D.W.: Finite Length solutions for rotordynamic coefficients of turbulent annular seals. Journal of Lubrication Technology, ASME-Paper, No 82 Lub. 42, 1982.

/2/ Atkins, K.E.; Tison, J.D. and Wachet, J.C.: Critical speed analysis of an eight-stage centrifugal pump. Proceedings of the second international pump symposium.

/3/ Launder, B.E.; Spalding, D.B.: The numerical computation of turbulent flows. Computer methods in applied mechanics and engineering. 3 (1974) 269 - 289.

/4/ Rodi, W.: Turbulence models and their application in hydraulics. Presented by the IAHR-Section on Fundamentals of Division II. Experimental and methematical Fluid Dynamics.

/5/ Yao, L.S.: Analysis of heat transfer in slightly eccentric annuli. ASME Journal of Heat Transfer May 198o Vol. lo2 p 279 - 284.

/6/ Ockendon, J.R.; Hodgkins, W.R.: Moving boundary problems in heat flow and diffusion. Being the proceedings of the conference held at the university of Oxford 25-27 March 1974.

/7/ Gosman, A.D.; Pun, W.: Lecture notes for course entitled: 'Calculation of recirculating flows'. Imperial College London, Mech. Eng. Dept., HTS/74/2.

/8/ Patankar, S.V.: Numerical heat transfer and fluid flow. Mc Graw Hill Book Company (198o).

/9/ Benodekar, R.W,; Goddard, A.J.H.; Gosman, A.D.; ISSU R.I.: Numerical prediction of turbulent flow over surfacemounted ribs. AIAA Journal Vol. 23, No 3, March 1985.

/10/ Massmann, H.: Ermittlung der dynamischen Parameter axial turbulent durchströmter Ringspalte bei inkompressiblen Medien. Dissertation, Universität Kaiserslautern, 1986.

/11/ Black, H.F.; Cochrane, E.A.: Leakage and hybrid bearing properties of serrated seals in centrifugal pumps.
6th International Conference on Fluid Sealing, February 27th - March 2nd, 1973. Munich, German Federal Republic.

/12/ Stoff, H.: Calcul et mesure de La turbulence d'un écoulement incompressible dans le Labyrinthe entre un arbre en rotation et un cylindre stationaire. Thesis No. 342 (1949) Swiss Federal College of Technology, Lausanne, Juris Verlag Zürich, 1979.

/13/ Wyssmann, H.R.; Pham, T.C.; Jenny, R.J.: Prediction of stiffness and damping coefficients for centrifugal compressor labyrinth seals. ASME Journal of Engineering for Gas Turbines and Power, Vol. lo6, Oct. 1984.

/14/ Rhode, D.L.; Demko, J.A.; Traegner, U.K.; Morrison, G.L.; Sobolik, S.R.: Prediction of incompressible flow in labyrinth seals. ASME Journal of Fluids Engineering, Vol. 1o8, March 1986.

/15/ Wittig, S.; Jackobsen, K.; Schelling, U.; Dörr, L.; Kim, S.: Wärmeübergangszahlen in Labyrinthdichtungen. VDI-Verichte 572.1, Thermische Strömungsmaschinen '85, p. 337 - 356.

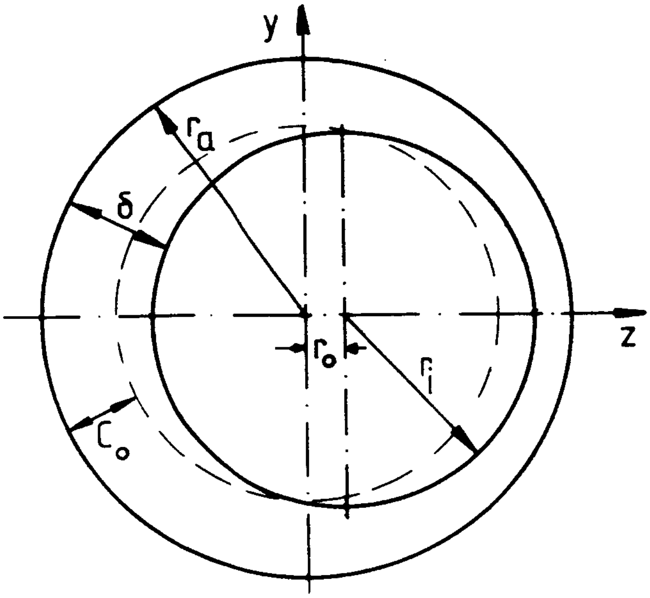

Fig. 1 Geometry of the eccentric shaft

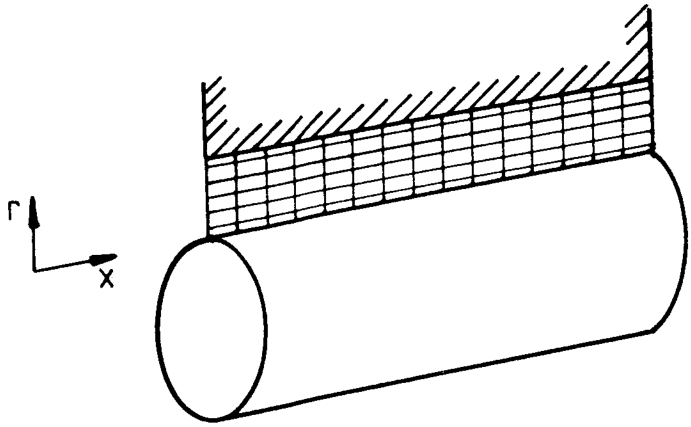

Fig. 2 Mesh arrangement in the seal

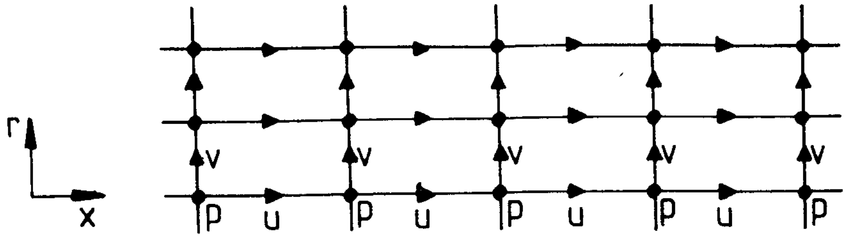
r
x
v
v
v
v
v
p
u
p
u
p
u
p
u
p

Fig. 3 Velocities and pressure in a staggered grid

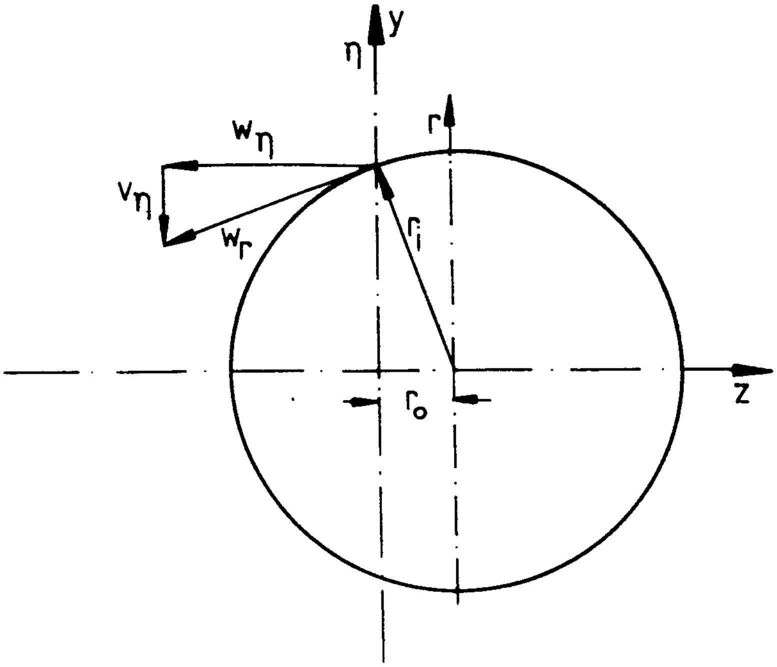
η
y
w_η
r
v_η
w_r
r_i
z
r_o

Fig. 4 Change of the velocities due to the coordinate transformation

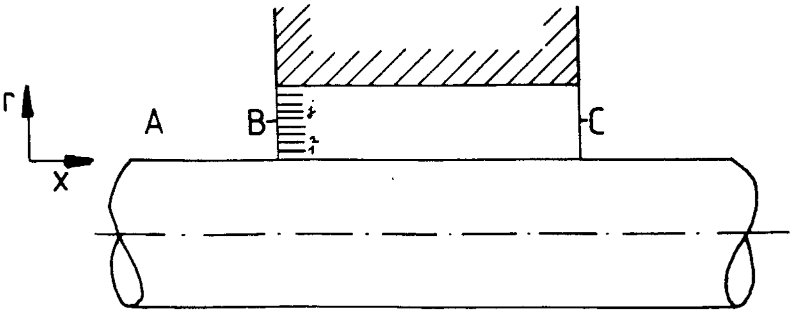

Fig. 5 Locations where the boundary-conditions must be specified

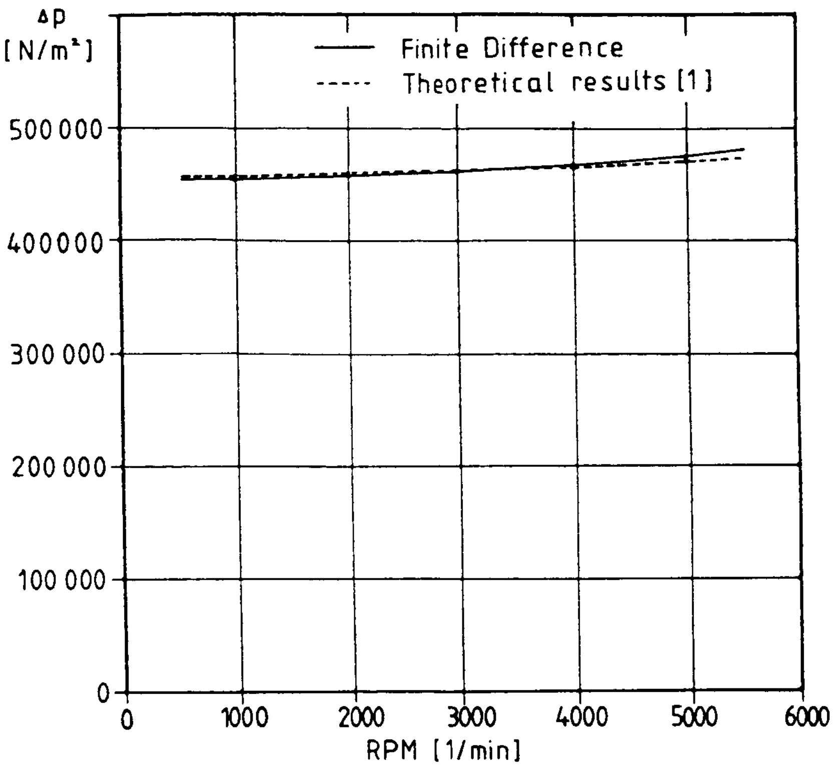

Fig. 6 Pressure difference as a function of the shaft speed for an annular seal

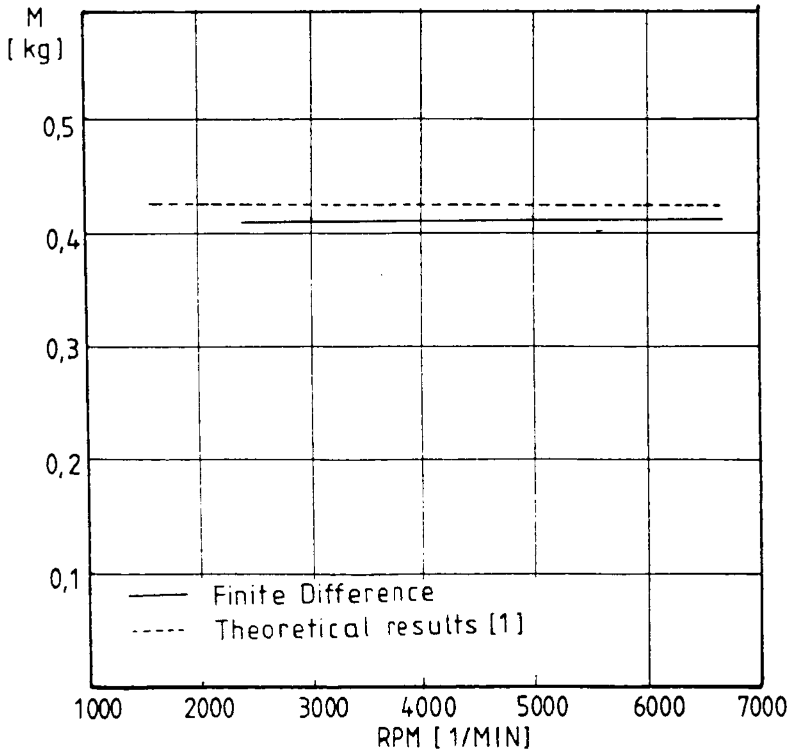

Fig. 7 Direct-inertia as a function of the shaft speed for an annular seal

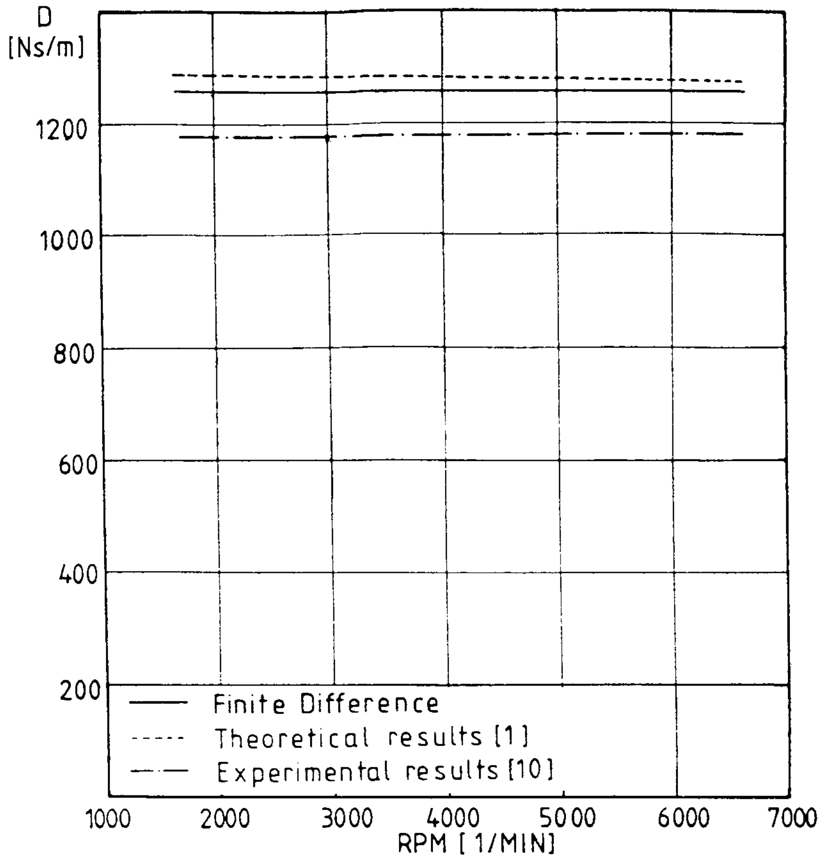

Fig. 8 Direct damping as a function of the shaft speed for an annular seal

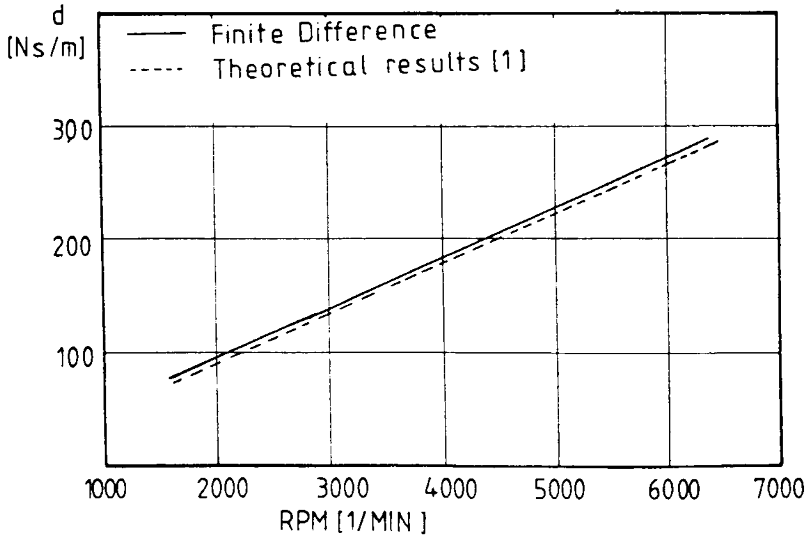

Fig. 9 Cross-coupling damping as a function of the shaft speed for an annular seal

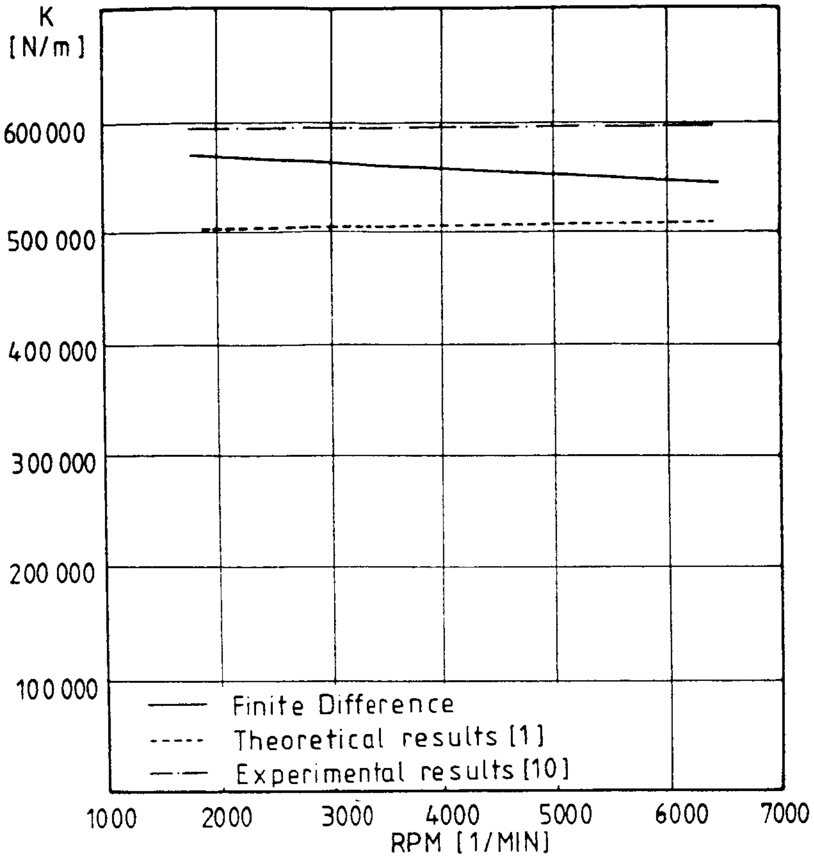

Fig. 10 Direct stiffness as a function of the shaft speed for an annular seal

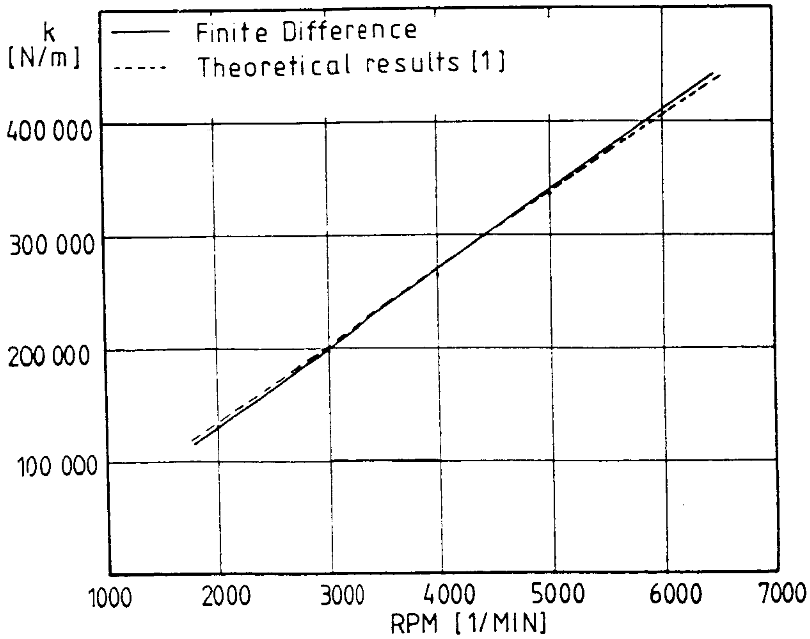

Fig. 11 Cross-coupling stiffness as a function ot the shaft speed for an annular seal

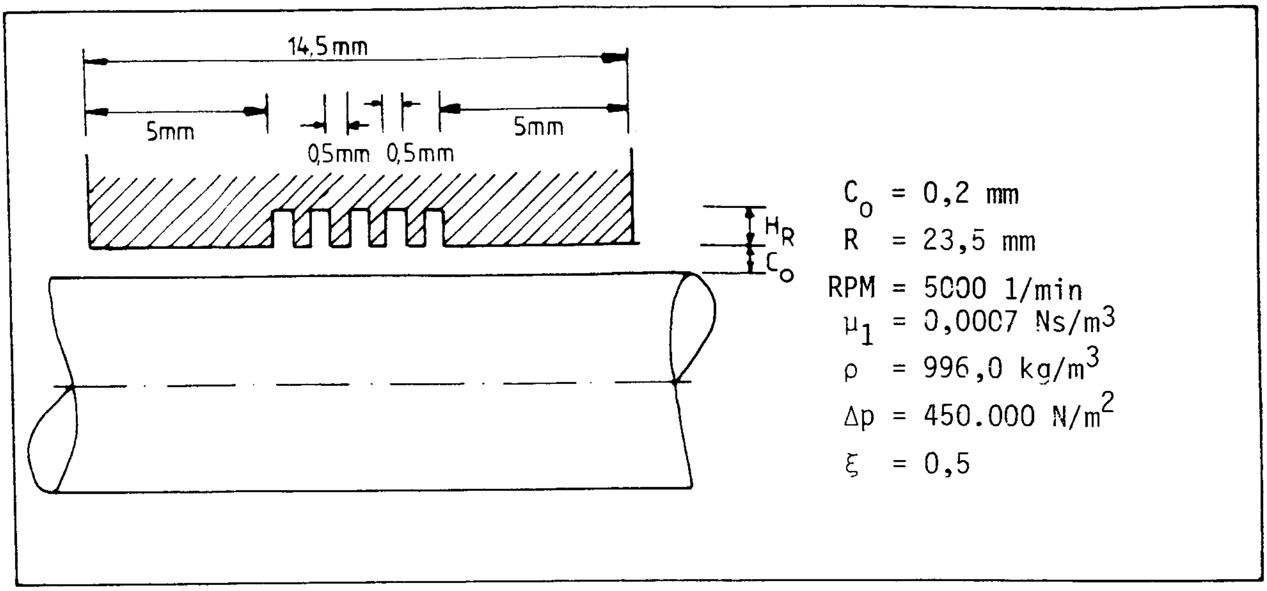
14,5 mm
5mm
0,5mm
0,5mm
5mm
H_R
C_o

C_o = 0,2 mm

R = 23,5 mm

RPM = 5000 1/min

μ_1 = 0,0007 Ns/m^3

ρ = 996,0 kg/m^3

Δp = 450.000 N/m^2

ξ = 0,5

Fig. 12 Geometry of the grooved seal

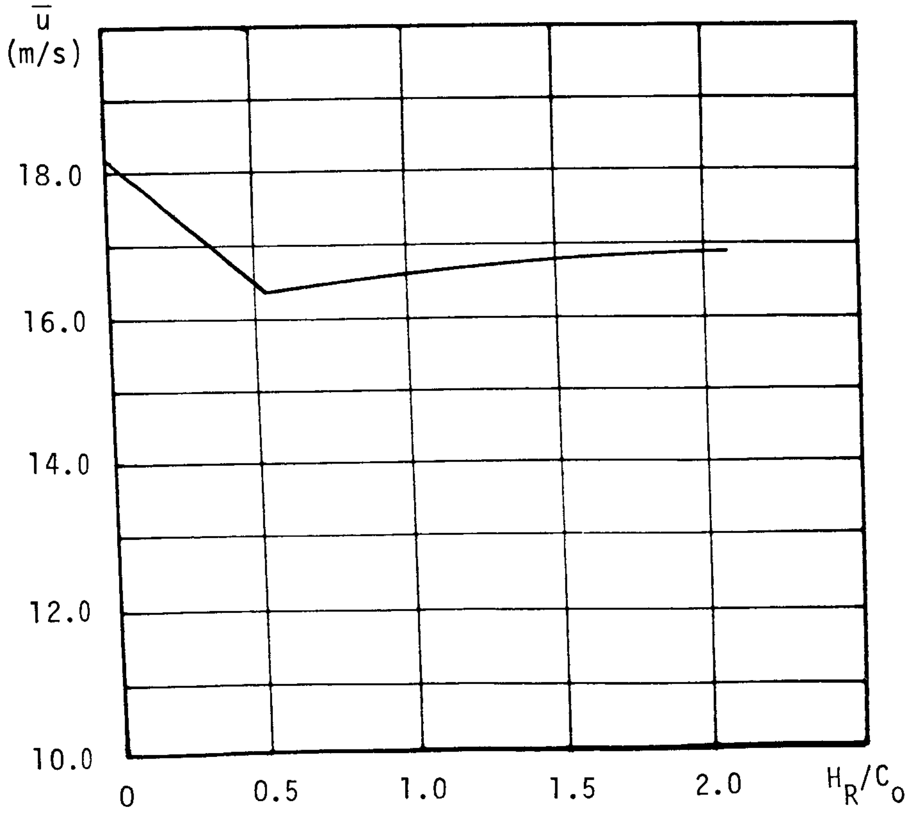

Fig. 13 Leakage of grooved seals for a given pressure as a function of the groove depth

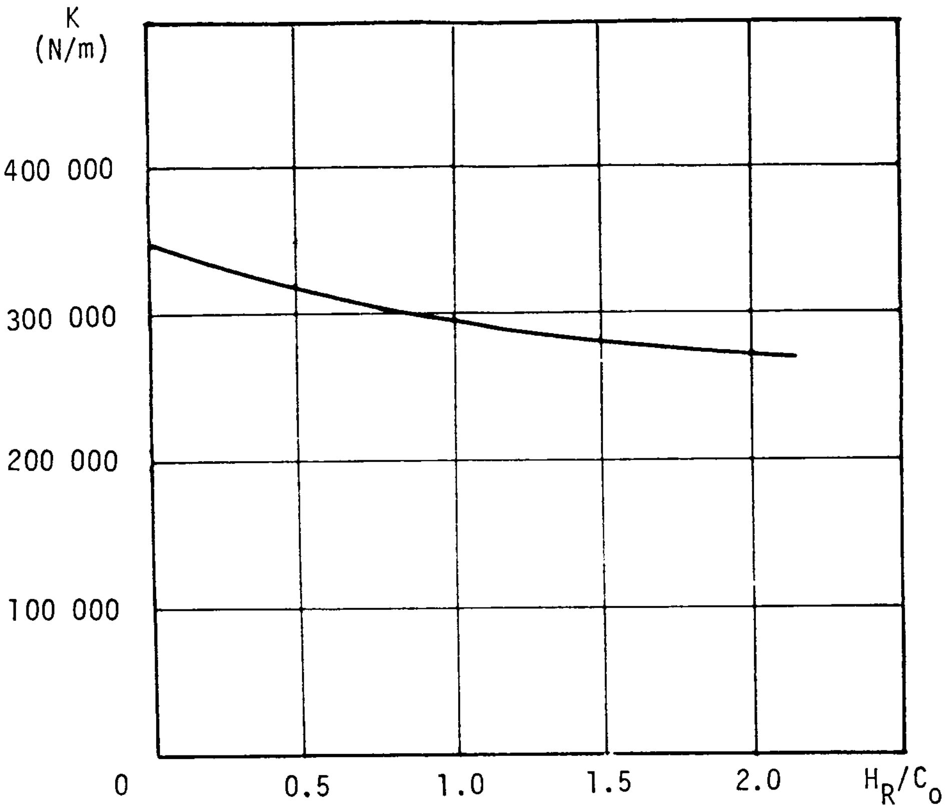

Fig. 14 Direct stiffness of grooved seals as a Function of the groove depth

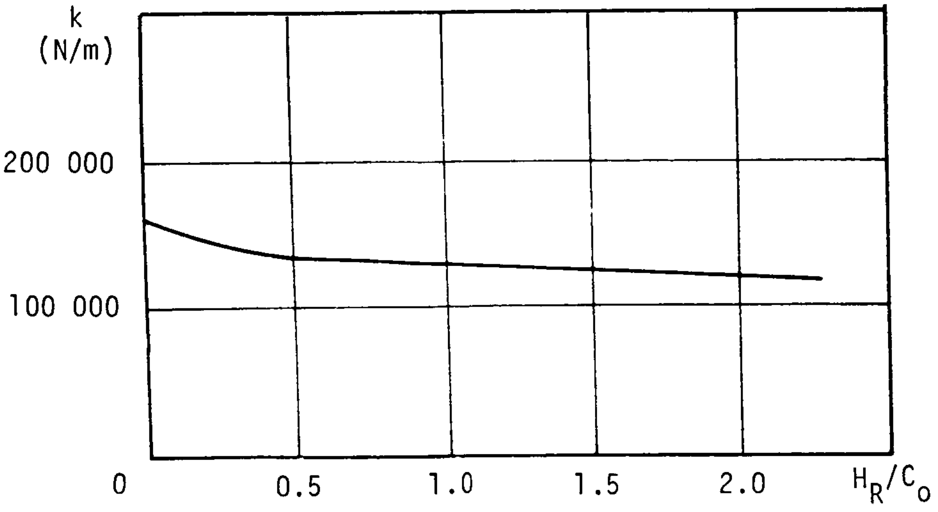

Fig. 15 Cross-coupling stiffness of grooved seals as a function of the groove depth

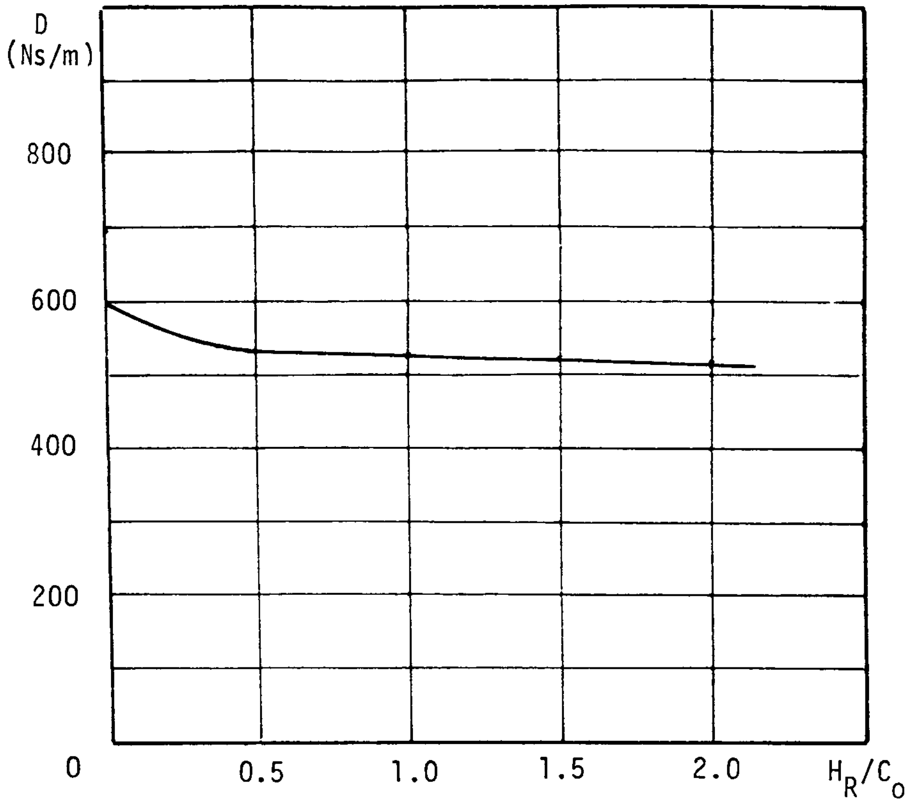

Fig. 16 Direct damping of grooved seals as a function of the groove depth

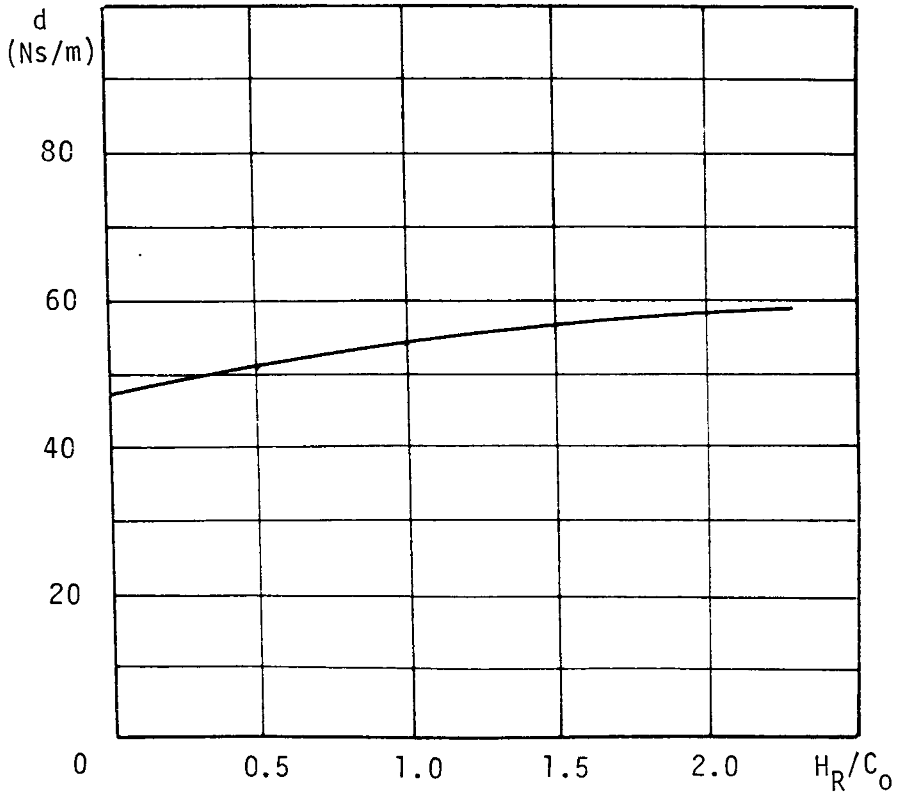

Fig 17 Cross-coupling damping of grooved seals as a function of the groove depth

N87-22205

STATIC AND DYNAMIC CHARACTERISTICS
OF PARALLEL-GROOVED SEALS

Takuzo Iwatsubo
Kobe University
Rokko, Nada, 657, Japan

Bo-suk Yang
The National Fisheries University of Pusan
599, Daeyon-dong, Nam-ku, Pusan, Korea

Ryuji Ibaraki
Toyota Motor Corporation
1, Toyota-cho, Toyota, 471, Japan

This paper presents an analytical method to determine static and dynamic characteristics of annular parallel-grooved seals. The governing equations were derived by using the turbulent lubrication theory based on the law of fluid friction. Linear zero- and first-order perturbation equations of the governing equations were developed, and these equations were analytically investigated to obtain the reaction force of the seals. An analysis is presented that calculates the leakage flow rate, the torque loss, and the rotordynamic coefficients for parallel-grooved seals. To demonstrate this analysis, we show the effect of changing number of stages, land and groove width, and inlet swirl on stability of the boiler feed water pump seals. Generally, as the number of stages increased or the grooves became wider, the leakage flow rate and rotordynamic coefficients decreased and the torque loss increased.

INTRODUCTION

Annular pressure seals can significantly influence the dynamic behavior of rotating machinery by the presence of a high-pressure difference in the close clearance spaces of the leakage path.

Black and Jenssen (refs. 1 to 3) have explained the influence of seal forces on the rotordynamic behavior of pumps. Childs has analyzed the short seal (ref. 4) and has made finite-length analyses (ref. 5) based on Hirs' governing equation, which yields an analytical expression for the seal dynamic coefficients incorporating all of Black and Jenssen's various developments.

Although these results apply only for small seal motion about a centered position, Allaire, et al. (ref. 6), the authors (ref. 7) have expanded these analyses to calculate dynamic coefficients at large eccentricities.

Fleming (ref. 8) has developed an analysis for gas seals with a constant clearance or with convergently tapered geometries. Child (ref. 9) investigated dynamic coefficients for convergently tapered seals both analytically and experimentally.

Previous analytical and experimental developments have generally examined dynamic characteristics of the annular straight seal and the tapered seal. But the dynamic characteristics of the parallel-grooved seal have not been analyzed theoretically. Bolleter (ref. 10) experimentally investigated stability limits for balance pistons with two different types of serration. He showed that serrations that are deep and wide prevent seizure.

In this paper the static and dynamic characteristics of the multistage parallel-grooved seal operating within the turbulent flow region are analyzed theoretically with consideration of the inertia effect. The present analysis combines the previous analysis of the straight seal with the analysis of the labyrinth seal performed by the authors. Namely, land analysis is used for the straight seal and groove analysis is used for the labyrinth seal.

SYMBOLS

C_{lo}	nominal seal radial clearance, cm
C_{xx}, C_{yx}	seal damping coefficients, N s/m
D	journal diameter, cm
F	fluid force, N
H	seal radial clearance, cm
K_{xx}, K_{yx}	seal stiffness coefficients, N/m
L	seal length, cm
L_l	land width, cm
lg	groove width, cm
M_{xx}, M_{yy}	seal add mass coefficients, N s^2/m
MG	fluid mean depth, cm
P	fluid pressure, MPa
Q	rate of leakage, m^3/s
R	seal radius, cm
R_a	axial Reynolds number
R_r	circumferential Reynolds number
S	number of stages
T	groove depth, cm
t	time, s

Torq	torque, N m
u, w	tangential and axial fluid velocity components, m/s
V	journal surface velocity, m/s
x	circumferential coordinate
y	radial coordinate
z	axial coordinate
ε	small eccentricity ratio
θ	diverging angle of stream behind land section
λ	friction loss coefficient
μ	fluid viscosity, mPa s
ν	fluid kinematic viscosity, m^2/s
ξ	loss coefficient
ρ	fluid density, kg/m^3
τ	shear stress, Pa
ω	journal angular velocity, rad/s

Subscripts:

a	axial direction
c	radial direction
d	groove defined in equation (13)
ex	exit
f	between clearance flow and cavity flow
g	groove
in	inlet
j	journal
l	land
r	circumferential direction
s	casing

$(\dot{\ })$ d( )/dt

m mean

GOVERNING EQUATION AND ANALYSIS

Governing Equation

Figure 1 illustrates the geometry of the parallel-grooved seal. Under the usual assumptions for problems of throughflow across annuli with a fine clearance, the momentum and continuity equations are, respectively, as follows:

$$\rho\{\frac{\partial\bar{u}}{\partial t}+\bar{u}\frac{\partial\bar{u}}{\partial x}+\bar{w}\frac{\partial\bar{u}}{\partial z}\}=-\frac{\partial\bar{P}}{\partial x}+\mu\frac{\partial^2\bar{u}}{\partial y^2}-\rho\frac{\partial\overline{u'v'}}{\partial y} \quad \text{(x-direction)} \tag{1}$$

$$\rho\{\frac{\partial\bar{w}}{\partial t}+\bar{u}\frac{\partial\bar{w}}{\partial x}+\bar{w}\frac{\partial\bar{w}}{\partial z}\}=-\frac{\partial\bar{P}}{\partial z}+\mu\frac{\partial^2\bar{w}}{\partial y^2}-\rho\frac{\partial\overline{v'w'}}{\partial y} \quad \text{(z-direction)} \tag{2}$$

$$\frac{\partial\bar{u}}{\partial x}+\frac{\partial\bar{v}}{\partial y}+\frac{\partial\bar{w}}{\partial z}=0 \tag{3}$$

The fluid velocities u and w are integrated across the film and are transformed into the mean velocities u_m and w_m.

$$u_m=\frac{1}{H}\int_0^H\bar{u}\,dy \qquad w_m=\frac{1}{H}\int_0^H\bar{w}\,dy \qquad \int_0^H\frac{\partial\bar{w}}{\partial t}dy=\frac{\partial}{\partial t}\int_0^H\bar{w}\,dy=\frac{\partial}{\partial t}(Hw_m)$$

$$\int_0^H\bar{w}\frac{\partial\bar{w}}{\partial z}dy=\frac{\partial}{\partial z}\int_0^H\bar{w}^2dy=\frac{\partial}{\partial z}(\Gamma_{aa}Hw_m) \qquad \int_0^H\frac{\partial\bar{u}}{\partial t}dy=\frac{\partial}{\partial t}\int_0^H\bar{u}\,dy=\frac{\partial}{\partial t}(Hu_m)$$

$$\int_0^H\bar{u}\frac{\partial\bar{u}}{\partial x}dy=\frac{\partial}{\partial x}\int_0^H\bar{u}^2dy=\frac{\partial}{\partial x}(\Gamma_{rr}Hu_m^2) \qquad \int_0^H\frac{\partial\bar{u}}{\partial x}dy=\frac{\partial}{\partial x}\int_0^H\bar{u}\,dy=\frac{\partial}{\partial x}(Hu_m)$$

$$\int_0^H\bar{w}\frac{\partial\bar{u}}{\partial z}dy=\frac{\partial}{\partial z}\int_0^H\overline{wu}\,dy=\frac{\partial}{\partial z}(\Gamma_{ar}Hu_mw_m) \qquad \int_0^H\frac{\partial\bar{w}}{\partial z}dy=\frac{\partial}{\partial z}\int_0^H\bar{w}\,dy=\frac{\partial}{\partial z}(Hw_m)$$

$$\int_0^H\bar{u}\frac{\partial\bar{w}}{\partial x}dy=\frac{\partial}{\partial x}\int_0^H\overline{uw}\,dy=\frac{\partial}{\partial x}(\Gamma_{ra}Hu_mw_m) \qquad \int_0^H\frac{\partial\bar{v}}{\partial t}dy=\frac{\partial H}{\partial t}$$

For a fully developed turbulent flow regime the velocity profile shape becomes flat, and the quantity is close to unity as shown in Burton's experiments (ref. 11).

$$\Gamma_{rr}=\Gamma_{ar}=\Gamma_{ra}=\Gamma_{aa}=1 \tag{4}$$

Equations (1) to (3) can be rewritten as

$$\frac{\partial (Hu_m)}{\partial t} + \frac{\partial (Hu_m^2)}{\partial x} + \frac{\partial (Hu_m w_m)}{\partial z} = -H\frac{\partial P}{\partial x} + \tau_{tr}\Big|_0^H \tag{5}$$

$$\frac{\partial (Hw_m)}{\partial t} + \frac{\partial (Hu_m w_m)}{\partial x} + \frac{\partial (Hw_m^2)}{\partial z} = -H\frac{\partial P}{\partial z} + \tau_{ta}\Big|_0^H \tag{6}$$

$$\frac{\partial H}{\partial t} + \frac{\partial (Hu_m)}{\partial x} + \frac{\partial (Hw_m)}{\partial z} = 0 \tag{7}$$

Assumptions for Analysis

The assumptions for this analysis are as follows:

(1) The fluid is liquid and incompressible.

(2) The fluid flows into the groove chamber with a constantly diverging angle (ref. 12). This is illustrated in figure 2.

(3) For a small motion of the seal journal about a centered position, the streamline in the groove moves with the journal.

(4) The groove cross section is rectangular.

DERIVATION OF SHEAR STRESS IN MOMENTUM EQUATION

The shear stress terms of equations (4) and (5) are discussed here.

Land. - The axial components τ_{lsa}, τ_{lja} of shear stress at the casing and journal are given by

$$\tau_{lsa} = -\tau_{lja} = \tau_{la} = \frac{1}{2}\rho\lambda_{la}w_{lm}^2 \tag{8}$$

where λ_{la} defines the friction coefficient between the flow and the wall surface:

$$\lambda_{la} = 0.0665\left(\frac{w_{lm}H_l}{\nu}\right)^{-0.25}\left\{1+\left(\frac{7V}{16w_{lm}}\right)^2\right\}^{3/8} \tag{9}$$

The circumferential components τ_{lsr}, τ_{ljr} of shear stress at the casing and journal are given by

$$\tau_{lsr} = \tau_{la}\frac{u_{lm}}{w_{lm}} = \frac{1}{2}\rho\lambda_{la}w_{lm}u_{lm}$$

$$\tau_{ljr} = \tau_{la}\frac{R\omega - u_{lm}}{w_{lm}} = \frac{1}{2}\rho\lambda_{la}w_{lm}(R\omega - u_{lm}) \tag{10}$$

This equation is strictly applicable only for $R_a \gg R_r$. Therefore the shear stress of the land can be written as follows:

$$\left.\begin{aligned} \tau_{tr}\Big|_0^H &= \tau_{ljr} - \tau_{lsr} = -\rho\lambda_{la}w_{lm}\left(u_{lm} - \frac{1}{2}R\omega\right) \\ \tau_{ta}\Big|_0^H &= \tau_{lja} - \tau_{lsa} = -\frac{12\mu_a w_{lm}}{H} \end{aligned}\right\} \tag{11}$$

Where the effective viscosity μ_a (ref. 13) is

$$\mu_a = 0.01(7-3\beta)R_a\lambda_{la}\mu \qquad\qquad \beta = \left(\frac{7V}{16w_{lm}}\right)\Big/\left\{1+\left(\frac{7V}{16w_{lm}}\right)^2\right\}$$

Groove. - The crossflow in the groove is considered to be the cavity flow plus the clearance flow (fig. 2). The exchange of energy within a small mixing area between both flows is influenced by the entrance velocity and the geometric shape of the groove. The clearance flow can be described by a stream tube if this mixing area is replaced by a separating layer. The cavity flow assumes that the momentum that is supplied from the journal is balanced by the sum of the momentum lost by fluid friction at the separating layer and the momentum due to cavity flow. If the cavity flow is replaced with flow through a circular pipe, the fluid mean depth of groove MG is given as

$$MG = \frac{L_g\left\{T+(T-L_g\tan\theta)\right\}}{2\left(L_g+T+\ T-L_g\tan\theta+L_g/\cos\theta\right)} \tag{12}$$

The friction coefficient between the groove wall and the fluid is

$$\lambda_d = 0.0791\left(\frac{u_{dm}\cdot 4MG}{\nu}\right)^{-0.25} \tag{13}$$

Therefore the momentum that is supplied from the side and root of the groove is expressed, where

$$\frac{1}{2}\rho\lambda_d\left\{\left(R-T+\frac{4MG}{2}\right)\omega-u_{dm}\right\}^2\times\left\{T+(T-L_g\tan\theta)+L_g\right\} \tag{14}$$

And the momentum that is lost from the fluid friction between the clearance flow and the cavity flow is

$$\frac{1}{2}\rho\lambda_f(u_{dm}-u_{gm})^2 \cdot L_g/\cos\theta \tag{15}$$

where λ_f defines the fluid friction loss coefficient between the cavity flow and clearance flow, and $\lambda_f = 0.1$ (ref. 14). Using equations (14) and (15), one can calculate the circumferential fluid velocity of the cavity flow U_{dm}. The axial component of shear stress is given by

$$\tau_{gsa} = \frac{1}{2}\rho\lambda_{ga}w^2_{gm}, \quad \tau_{gfa} = \frac{1}{2}\rho\lambda_f(w_{gm}-w_{dm})^2 = \frac{1}{2}\rho\lambda_f(w_{gm}-0.5w_{gm})^2 \tag{16}$$

and the circumferential component by

$$\left.\begin{aligned} \tau_{gsr} &= \tau_{gsa}\frac{u_{gm}}{w_{gm}} = \frac{1}{2}\rho\lambda_{ga}w_{gm}u_{gm} \\ \tau_{gfr} &= \tau_{gfa}\frac{u_{dm}-u_{gm}}{w_{gm}} = \frac{1}{8}\rho\lambda_f w_{gm}(u_{dm}-u_{gm}) \end{aligned}\right\} \tag{17}$$

where

$$\lambda_{ga} = 0.0665\left(\frac{w_{gm}H_g}{\nu}\right)^{-0.25}\left\{1+\left(\frac{7u_{dm}}{16w_{gm}}\right)^2\right\}^{3/8}$$

Therefore the shear stress of the groove can be written as

$$\left.\begin{aligned} \tau_{tr}\Big|_0^H &= \tau_{gfr} - \tau_{gsr} = \frac{1}{2}\rho 0.25\lambda_f w_{gm}(u_{dm}-u_{gm}) - \frac{1}{2}\rho\lambda_{ga}w_{gm}u_{gm} \\ \tau_{ta}\Big|_0^H &= \tau_{gfa} - \tau_{gsa} = -\frac{1}{2}\rho(\lambda_{ga}+0.25\lambda_f)w^2_{gm} \end{aligned}\right\} \tag{18}$$

Derivation of Static Characteristics

Axial fluid velocity. - The pressure loss is stated as follows: The inlet loss at the land entrance is

$$\Delta P_{lin} = \frac{1}{2}\rho\xi_1 w^2_{lo} \tag{19}$$

where

$\xi_1 = 1.5$ (at 1st stage)

$$\xi_1 = 1+0.824\delta_2-(1+0.824\delta_1)\left(\frac{H_2}{H_1}\right)^2 \quad \text{(after 2nd stage)}$$

$$\delta_1 = 1.95\left(\frac{w_{lo}\ H_1}{\nu}\right)^{-0.43} \qquad \delta_2 = 1.95\left(\frac{w_{lo}\ H_2}{\nu}\right)^{-0.43}$$

$$H_1 = C_{lo}+L_g\tan\theta \qquad H_2 = C_{lo}$$

The wall friction loss in the land is

$$\Delta P_l = 2\,\frac{L_{lo}}{C_{lo}}\cdot\frac{1}{2}\,\rho\lambda_{la}w_{lo}^2 \tag{20}$$

The exit loss due to diverging flow behind the land is

$$\Delta P_{lex} = \frac{1}{2}\,\rho\xi_2 w_{lo}^2 \tag{21}$$

where ξ_2 is the exit loss coefficient

$$\xi_2 = \left(1-\frac{C_{lo}}{C_{lo}+L_g\tan\theta}\right)^2 \quad \text{(at each stage)}$$

$$\xi_2 = \left(1-\frac{C_{lo}}{C_{lo}+T}\right)^2 \quad \text{(at seal exit)}$$

The friction loss at the wall and the separating layer of the groove is

$$\Delta P_g = \frac{1}{2}\,\rho w_{lo}^2(\lambda_{ga}+0.25\lambda_f)\left(\frac{C_{lo}}{C_{lo}+L_g/2\cdot\tan\theta}\right)^2\frac{L_g}{C_{lo}+L_g\tan\theta} \tag{22}$$

The pressure restoration due to deceleration at the groove is

$$\Delta P_{gup} = \frac{2C_{lo}}{C_{lo}+L_g\tan\theta}\left(1-\frac{C_{lo}}{C_{lo}+L_g\tan\theta}\right)\frac{1}{2}\,\rho w_{lo}^2 \tag{23}$$

The pressure drop across the seal is equal to the sum of each pressure loss and is stated as follows:

$$\begin{aligned}
P_{in}-P_{ex} &= \Delta P'_{lin} + S(\Delta P_{l}+\Delta P_{lex}+\Delta P_{g}-\Delta P_{gup}+\Delta P_{lin})+\Delta P_{l}+\Delta P'_{lex} \\
&= \frac{1}{2}\rho\xi'_{1}w^{2}_{lo} + S\Bigg[\frac{1}{2}\rho w^{2}_{lo}\frac{2L_{l}}{C_{lo}}\lambda_{la} + \frac{1}{2}\rho w^{2}_{lo}\left(1-\frac{C_{lo}}{C_{lo}+L_{g}\tan\theta}\right)^{2} \\
&\qquad + \frac{1}{2}\rho w^{2}_{lo}(\lambda_{ga}+0.25\lambda_{f})\left(\frac{C_{lo}}{C_{lo}+L_{g}/2\ \tan\theta}\right)^{2}\frac{L_{g}}{C_{lo}+L_{g}/2\cdot\tan\theta} \\
&\qquad - \frac{1}{2}\rho w^{2}_{lo}\frac{2C_{lo}}{C_{lo}+L_{g}\tan\theta}\left(1-\frac{C_{lo}}{C_{lo}+L_{g}\tan\theta}\right) \\
&\qquad + \frac{1}{2}\rho w^{2}_{lo}\,\xi_{1}\Bigg] \\
&\qquad + \frac{1}{2}\rho w^{2}_{lo}\frac{2L_{l}}{C_{lo}}\lambda_{la} + \frac{1}{2}\rho w^{2}_{lo}\left(1-\frac{C_{lo}}{C_{lo}+L_{g}\tan\theta}\right)^{2} \qquad (24)
\end{aligned}$$

Rate of leakage. - The main advantage of the grooved seal is that leakage flow can be minimized but seal components need never rub. Seal leakage flow may also be denoted by Q, where

$$Q = \int_{R}^{R+T} w_{lo}\ 2\pi r\ dr = \pi w_{lo}C_{lo}(2R+C_{lo}) \qquad (25)$$

Figure 3 shows the calculated results of leakage flow. As the number of stages increased or the land became narrower, the leakage flow decreased.

Circumferential fluid velocity. - From the momentum equation (5) for the land

$$\frac{\partial u_{lo}}{\partial z} + \frac{1}{l}u_{lo} = \frac{1}{l}\cdot\frac{V}{2} \qquad (26)$$

where $l = C_{lo}/\lambda_a$ and $V = R\omega$. The boundary condition is $z = z_{n-1/2}$; $u_{lo} = u_{lo(z_{n-1/2})}$. The circumferential fluid velocity u_{lo} at the land is

$$u_{lo} = \frac{V}{2} - \left\{\frac{V}{2} - u_{lo(z_{n-\frac{1}{2}})}\right\}\cdot e^{-z/l} \qquad (27)$$

From the momentum equation (5) for the groove

$$\frac{\partial u_{go}}{\partial z} + \frac{u_{go}}{2C_{go}}(\lambda_{ga}+0.25\lambda_{f}) = \frac{\lambda_{f}u_{dm}}{8C_{go}} \qquad (28)$$

where u_{dm} can be calculated from equations (14) and (15) and the boundary condition is

$$z = z_n \qquad u_{go} = u_{go(z_n)}$$

The circumferential fluid velocity u_{go} at the groove is

$$u_{go} = u_z - u_{ug} C_{go}^{-A/\tan\theta} \tag{29}$$

where

$$u_{ug} = u_z - u_{go(z_n)} \qquad A = \lambda_{ga} + 0.25\lambda_f \qquad u_z = \frac{\lambda_f u_{dm}}{8\ A}$$

Figure 4 shows the axial distribution of circumferential fluid velocity ΔP = 0.49 MPa, N = 4000 rpm, L = 55 mm, and S = 20. The results indicate that the circumferential velocity approaches one-half of the shaft angular velocity exponentially.

Torque loss. - The method for estimating the torque loss in a grooved seal treats the loss as frictional dissipation by viscous shear in an annulus. From equation (10) the torque loss of the land is

$$\begin{aligned} Torq_l &= \int_0^{2\pi}\int_0^{L_l} \tau_{ljr} \times R \times R d\phi dz \\ &= \rho\pi R^2 \lambda_{la} \omega_{lo} \left(\frac{V}{2} L_l + \left\{ \frac{V}{2} - u_{lo(z_{n-1/2})} \right\} \cdot l (e^{-L_l/l} - 1) \right) \end{aligned} \tag{30}$$

The torque loss of the groove assumes that the groove is divided into four parts as shown in figure 5. The shear stress of part 1 is

$$\tau_{g1} = \frac{1}{2} \rho \lambda_d u_{dm}^2 \tag{31}$$

Therefore the torque loss of part 1 is given as follows:

$$\tau_{g1} = \int_0^{2\pi}\int_{R-T}^{R} \tau_{g1} \times r \times r d\phi dr = \frac{2\pi}{3} \left\{ R^3 - (R-T)^3 \right\} \cdot \frac{1}{2} \rho \lambda_d u_{dm}^2$$

Similarly

$$T_{g2} = \int_0^{2\pi}\int_0^{L_g} \tau_{g2} \times (R-T) \times (R-T) d\phi dz = \rho\pi (R-T)^2 L_g \lambda_d u_{dm}^2$$

$$T_{g3} = \int_0^{2\pi}\int_{R-T}^{R-L_g\tan\theta} \tau_{g3} \times r \times r d\phi dr = \frac{2\pi}{3}\left\{(R-L_g\tan\ )^3-(R-T)^3\right\}\frac{1}{2}\rho\lambda_d u_{dm}^2$$

$$T_{g4} = \int_0^{2\pi}\int_{R-L_g\tan\theta}^{R} \tau_{g4} \times r \times r d\phi dr$$

$$= \frac{2\pi}{3}\left\{R^3-(R-L_g\tan\theta)^3\right\}\frac{1}{2}\rho\lambda_{ga}\frac{C_{lo}w_{lo}}{C_{lo}+L_g\tan\theta}u_{go(z_{n+1/2})}$$

Therefore the torque loss of the groove is

$$Torq_g = T_{g1} + T_{g2} + T_{g3} + T_{g4} \tag{32}$$

And the total torque loss of the parallel-grooved seal is defined by the following equation:

$$\Delta T = \sum_{i=1}^{S+1} Torq_l + \sum_{i=1}^{S} Torq_g \tag{33}$$

Figure 6 shows the torque loss of the parallel-grooved seal for ΔP = 0.49 MPa and L = 55 mm without inlet swirl. As the number of stages increased or the seal clearance decreased, the torque loss increased.

Derivation of Pressure Distribution

For a small motion about a centered position the clearance, pressure, and velocity are expanded in the perturbation variables as follows:

$$H = C_o + \epsilon\psi \qquad P = P_o + \epsilon P_1 \qquad w_m = w_o + \epsilon w_1 \qquad u_m = u_o + \epsilon u_1 \tag{34}$$

where C_0, P_0, ω_0, u_0 are steady-state values and ψ, P_1, w_1, u_1 are small perturbations. The short-bearing solution (ref. 4) is developed for the first-order equation by neglecting u_1, the pressure-induced circumferential velocity component.

Static pressure distribution. - The steady-state equation described is static, has zero eccentricity, and is solved analytically. Substitution of equation (6) into equations (11), (18), and (34) yields steady-state, axial-direction momentum equations for the land

$$\frac{\partial P_{lo}}{\partial z} = -\frac{12\mu_a w_{lo}}{C_{lo}^2} \tag{35}$$

and for the groove

$$\frac{\partial P_{go}}{\partial z} = -\frac{\rho C_{lo}^2 w_{lo}^2 \lambda_{sa}}{2(C_{lo}+z\tan\theta)^2} \tag{36}$$

where λ_{sa} defines the equivalent friction coefficient of the groove.

$$\lambda_{sa} = \lambda_{ga}+0.25\lambda_f-2\tan\theta$$

Pressure distribution of nonsteady state. - Substitution of the perturbation variables of equations (6) and (7) yields the following perturbation equation for the land:

$$\begin{aligned}\frac{\partial P_{l1}}{\partial z} &= -\frac{\psi}{C_{lo}}\cdot\frac{\partial P_{lo}}{\partial z} - \frac{12\mu_a w_{l1}}{C_{lo}^2} \\ &\quad -\rho\left(\frac{\partial w_{l1}}{\partial t} + \frac{w_{lo}}{C_{lo}}\cdot\frac{\partial\psi}{\partial t} + u_{lo}\frac{\partial w_{l1}}{\partial x} + \frac{u_{lo}w_{lo}}{C_{lo}}\cdot\frac{\partial\psi}{\partial x} + 8w_{lo}\frac{\partial w_{l1}}{\partial z}\right)\end{aligned} \tag{37}$$

$$\frac{\partial w_{l1}}{\partial z} = -\frac{1}{C_{lo}}\left(\frac{\partial\psi}{\partial t} + u_{lo}\frac{\partial\psi}{\partial x}\right) \tag{38}$$

Equation (38) can be integrated by using the boundary condition $z = z_{n-1/2}$, $w_{l1} = w_{l1}(z_{n-1/2})$ as follows:

$$w_{l1} = w_{l1(z_{n-\frac{1}{2}})} - \frac{1}{C_{lo}} f_l(x,t)(z - z_{n-{}^1{}_2}) - \frac{l}{C_{lo}} u_{ul}\frac{\partial\psi}{\partial x}(e^{-z/l}-1) \tag{39}$$

where

$$f_l(x,t) = \frac{\partial\psi}{\partial t} + \frac{V}{2}\cdot\frac{\partial\psi}{\partial x} \qquad u_{ul} = \frac{V}{2} - u_{lo(z_{n-\frac{1}{2}})}$$

Equation (19) yields the following perturbation-variable boundary condition at the seal inlet:

$$P_{l1(z_{n-\frac{1}{2}})} = -\rho\xi_1 w_{lo} w_{l1(z_{n-\frac{1}{2}})} \tag{40}$$

The perturbation-variable boundary condition at the seal exit is given as

$$z = z_n \; ; \; P_{l1(z_n)} = 0 \tag{41}$$

The complete solution for the perturbation pressure is obtained as

$$P_{l1} = \frac{12\mu_a w_{lo}\psi}{C_{lo}^3} \, PRL1 + \frac{6\mu_a}{C_{lo}^3} f_l(x,t) \cdot PRL2$$

$$- \frac{12\mu_a u_{ul} l}{C_{lo}^2} \cdot \frac{\partial \psi}{\partial x} \, PRL6 + \frac{\rho}{2C_{lo}} \left(\frac{\partial}{\partial t} + \frac{V}{2} \cdot \frac{\partial}{\partial x} \right) f_l(x,t) \, PRL2$$

$$- \frac{\rho u_{ul} l}{C_{lo}} \left(\frac{\partial}{\partial t} + \frac{V}{2} \cdot \frac{\partial}{\partial x} \right) \left(\frac{\partial \psi}{\partial x} \right) PRL6 + \frac{\rho u_{ul} l}{C_{lo}} \cdot \frac{\partial}{\partial x} f_l(x,t) \, PRL7$$

$$- \frac{\rho u_{ul}^2 l^2}{C_{lo}} \frac{\partial}{\partial x} \left(\frac{\partial \psi}{\partial x} \right) PRL8 + \frac{\rho w_{lo}}{C_{lo}} f_l(x,t) \, PRL1 + \frac{\rho w_{lo} u_{ul} l}{C_{lo}} \cdot \frac{\partial \psi}{\partial x} \, PRL2 \tag{42}$$

where PRL1 to PRL8 are provided in appendix A.

Similarly for the groove the axial-momentum equation and the continuity equation reduce to

$$\frac{\partial P_{g1}}{\partial z} = - \frac{\psi}{C_{go}} \cdot \frac{\partial P_{go}}{\partial z} - \frac{\rho}{C_{go}} (\lambda_{ga} + 0.85\lambda_f) w_{go} w_{g1}$$

$$- \rho \left(\frac{\psi w_{go}}{C_{go}} \cdot \frac{\partial w_{go}}{\partial z} + \frac{\partial w_{g1}}{\partial t} + u_{go} \frac{\partial w_{g1}}{\partial x} + w_{go} \frac{\partial w_{g1}}{\partial z} + w_{g1} \frac{\partial w_{go}}{\partial z} \right) \tag{43}$$

$$u_{go} \frac{\partial \psi}{\partial x} + \psi \frac{\partial w_{go}}{\partial z} + C_{go} \frac{\partial w_{g1}}{\partial z} + w_{g1} \frac{\partial C_{go}}{\partial z} + \frac{\partial \psi}{\partial t} = 0 \tag{44}$$

Substitution of equation (29) and the boundary condition $z = z_n$, $w_{g1} = w_{g1(z_n)}$ into equation (44) yields

$$w_{g1} = w_{g1(z_n)} \frac{C_{lo}}{C_{go}} - f_g(x,t) \frac{z - z_n}{C_{go}}$$

$$- \frac{u_{ug}}{A - \tan\theta} \cdot \frac{C_{go}^{-a+1} - C_{lo}^{-a+1}}{C_{go}} \cdot \frac{\partial \psi}{\partial x} + \frac{\psi w_{lo} (z - z_n) \tan\theta}{C_{go}^2} \tag{45}$$

where

$$f_g(x,t) = \frac{\partial \psi}{\partial t} + u_z \cdot \frac{\partial \psi}{\partial x} \qquad a = A/\tan\theta$$

The pressure boundary condition is

$$z = z_n \qquad P_{g1} = P_{g1(z_n)} \tag{46}$$

The perturbation-variable boundary condition is obtained as

$$P_{g1(z_n)} = -\rho\xi_2\omega_{lo}\omega_{g1(z_n)} \tag{47}$$

The complete solution for the perturbation pressure is obtained as

$$\begin{aligned} P_{g1} = & -\frac{\rho C_{lo}^2\omega_{lo}^2\lambda_{sa}\psi}{6\tan\theta}\cdot PRG1 + \rho C_{lo}\omega_{lo}\lambda_{sa}\cdot f_g(x,t)\cdot PRG14 + \frac{\rho C_{lo}\omega_{lo}u_{ug}}{A+\tan\theta}\cdot\frac{\partial\psi}{\partial x}\cdot PRG6 \\ & -\frac{\rho u_{ug}\omega_{lo}\tan\theta}{A+\tan\theta}\cdot\frac{\partial\psi}{\partial x}\ PRG18 - \frac{\rho C_{lo}\omega_{lo}}{\tan\theta}\cdot f_g(x,t)\cdot PRG2 + \frac{\rho u_{ug}}{A-\tan\theta}\cdot\frac{\partial}{\partial x}\left(\frac{\partial\psi}{\partial x}\right) PRG21 \\ & +\rho\left(\frac{\partial}{\partial t} + u_z\cdot\frac{\partial}{\partial x}\right) f_g(x,t)\cdot PRG16 + \frac{\rho C_{lo}\omega_{lo}u_{ug}\lambda_{sa}}{A-\tan\theta}\cdot\frac{\partial\psi}{\partial x}\cdot PRG19 \\ & -\rho C_{lo}\omega_{lo}^2\tan\theta\lambda_{sa}\cdot PRG13 - \frac{\rho u_{ug}}{A-\tan\theta}\left(\frac{\partial}{\partial t} + u_z\cdot\frac{\partial}{\partial x}\right)\left(\frac{\partial\psi}{\partial x}\right) PRG17 \\ & +\frac{\rho u_{ug}}{A}\cdot\frac{\partial}{\partial x} f_g(x,t)\cdot PRG20 - \rho\omega_{lo}\tan\theta\ f_g(x,t)\cdot PRG15 \end{aligned} \tag{48}$$

where PRG1 to PRG2 are provided in appendix B.

Dynamic Force

For a small motion about a centered position the clearance function is defined in terms of the radial seal displacement (ΔX,ΔY).

$$\varepsilon\psi = -\Delta X\cos\phi - \Delta Y\sin\phi \tag{49}$$

The components of the reaction force acting on the seal journal are defined by the integrals

$$\left.\begin{aligned} F_X &= -\left[\sum_{n=1}^{S}\int_0^{2\pi}\left\{\int_{z_{n-\frac{1}{2}}}^{z_n}\varepsilon P_{l1} + \int_{z_n}^{z_{n+\frac{1}{2}}}\varepsilon P_{g1}\right\} + \int_0^{2\pi}\int_{z_{S+\frac{1}{2}}}^{z_{S+1}}\varepsilon P_{l1}\right]\cos\phi R\,d\phi\,dz \\ F_Y &= -\left[\sum_{n=1}^{S}\int_0^{2\pi}\left\{\int_{z_{n-\frac{1}{2}}}^{z_n}\varepsilon P_{l1} + \int_{z_n}^{z_{n+\frac{1}{2}}}\varepsilon P_{g1}\right\} + \int_0^{2\pi}\int_{z_{S+\frac{1}{2}}}^{z_{S+1}}\varepsilon P_{l1}\right]\sin\phi R\,d\phi\,dz \end{aligned}\right\} \tag{50}$$

Substituting for ψ and its derivatives into equations (42) and (48) yields the following form for the seal coefficients:

$$-\begin{bmatrix} F_X \\ F_Y \end{bmatrix} = \begin{bmatrix} K_{XX} & K_{XY} \\ K_{YX} & K_{YY} \end{bmatrix}\begin{bmatrix} X \\ Y \end{bmatrix} + \begin{bmatrix} C_{XX} & C_{XY} \\ C_{YX} & C_{YY} \end{bmatrix}\begin{bmatrix} \dot{X} \\ \dot{Y} \end{bmatrix} + \begin{bmatrix} M_{XX} & M_{XY} \\ M_{YX} & M_{YY} \end{bmatrix}\begin{bmatrix} \ddot{X} \\ \ddot{Y} \end{bmatrix} \tag{51}$$

Because the seal coefficients of each stage are different, the following definitions are used. The dynamic coefficients of the parallel-grooved seal become

$$\left.\begin{aligned}
K_{XX} &= \sum_{n=1}^{S+1} K_{XXl} + \sum_{n=1}^{S} K_{XXg} & \qquad K_{YX} &= \sum_{n=1}^{S+1} K_{YXl} + \sum_{n=1}^{S} K_{YXg} \\
C_{XX} &= \sum_{n=1}^{S+1} C_{XXl} + \sum_{n=1}^{S} C_{XXg} & \qquad C_{YX} &= \sum_{n=1}^{S+1} C_{YXl} + \sum_{n=1}^{S} C_{YXg} \\
M_{XX} &= \sum_{n=1}^{S+1} M_{XXl} + \sum_{n=1}^{S} M_{XXg} & \qquad M_{YX} &= \sum_{n=1}^{S+1} M_{YXl} + \sum_{n=1}^{S} M_{YXg} = 0
\end{aligned}\right\} \tag{52}$$

where

$$K_{XX} = K_{YY} \qquad K_{YX} = -K_{XY} \qquad C_{XX} = C_{YY}$$

$$C_{YX} = -C_{XY} \qquad M_{XX} = M_{YY} \qquad M_{YX} = -M_{XY} = 0$$

The dynamic seal coefficients for the land are

$$K_{XXl} = -\frac{\pi R}{C_{lo}}\left[\frac{12\mu_a \omega_{lo}}{C_{lo}^2} IPRL1 - \frac{\rho V^2}{8R^2} IPRL2 \right.$$

$$\left. + \frac{\rho u_{ul} l V}{2R^2}(IPRL4 - IPRL7) + \frac{\rho u_{ul}^2 l^2}{R^2} IPRL8 \right] = K_{YYl}$$

$$K_{YXl} = \frac{\pi}{C_{lo}}\left[\frac{6\mu_a}{C_{lo}^2}\cdot\frac{V}{2} IPRL2 - \frac{12\mu_a u_{ul} l}{C_{lo}^2} IPRL4 \right.$$

$$\left. + \frac{\rho \omega_{lo} V}{2} IPRL1 + \rho \omega_{lo} u_{ul} l \; IPRL3 \right] = -K_{XYl}$$

$$C_{XXl} = -\frac{\pi R}{C_{lo}}\left[\frac{6\mu_a}{C_{lo}^2} IPRL2 + \rho \omega_{lo} \; IPRL1 \right] = C_{YY}$$

$$C_{YXl} = \frac{\;}{C_{lo}} \frac{V}{2} IPRL2 - u_{ul} l \; IPRL4 + u_{ul} l \; IPRL7 = -C_{XYl}$$

$$C_{YXl} = \frac{\rho\pi}{C_{lo}} \left[\frac{V}{2} IPRL2 - u_{ul} l (IPRL4 - IPRL7) \right] = -C_{XYl}$$

$$M_{XXl} = -\frac{\rho\pi R}{2C_{lo}} \cdot IPRL2 = M_{YYl} \qquad M_{YXl} = M_{XYl} = 0$$

where IPRL1 to IPRL8 are provided in appendix C. The dynamic seal coefficients for the groove are

$$\begin{aligned} K_{XXg} = \rho\pi R \Bigg[& \frac{C_{lo}^2 \omega_{lo}^2 \lambda_{sa}}{6 \tan\theta} IPRG1 + C_{lo} \omega_{lo}^2 \tan\theta \lambda_{sa} \cdot IPRG13 \\ & + \frac{u_z^2}{R^2} IPRG16 - \frac{u_{ul} u_z}{(A - \tan\theta) R^2} \cdot IPRG17 \\ & + \frac{u_{ul} u_z}{A \; R^2} IPRG20 + \frac{u_{ul}^2}{(A - \tan\theta) R^2} IPRG21 \Bigg] = K_{YYg} \end{aligned}$$

$$\begin{aligned} K_{YXg} = \rho\pi C_{lo} \omega_{lo} \Bigg[& u_z \lambda_{sa} \; IPRG14 + \frac{u_{ul} \lambda_{sa}}{A - \tan\theta} IPRG19 \\ & - \frac{u_z \tan\theta}{C_{lo}} IPRG15 - \frac{u_{ul} \tan\theta}{C_{lo} (A + \tan\theta)} \cdot IPRG18 \\ & - \frac{u_z}{\tan\theta} IPRG2 + \frac{u_{ul}}{A + \tan\theta} IPRG8 \Bigg] = -K_{XYg} \end{aligned}$$

$$C_{XXg} = \rho\pi R C_{lo}\omega_{lo}\left[-\lambda_{sa}\ IPRG14 + \frac{\tan\theta}{C_{lo}}\ IPRG15 + \frac{1}{\tan\theta}\ IPRG2\right] = C_{YYg}$$

$$C_{YXg} = \rho\pi\left[2u_z\ IPRG16 - \frac{u_{ul}}{A-\tan\theta} IPRG17 + \frac{u_{ul}}{A}\ IPRG20\right] = -C_{XYg}$$

$$M_{XXg} = -\rho\pi R \cdot IPRG16 = M_{YYg}$$

$$M_{YXg} = M_{XYg} = 0$$

where IPRG1 to IPRG21 are provided in appendix C.

NUMERICAL EXAMPLE

Seal coefficients were calculated for a pump seal with the characteristics shown in table I. The dynamic coefficients decreased with an increase in the number of stages (fig. 7); that is, the axial Reynolds number became small because the pressure loss increased with an increase in the number of stages. The cross-coupling terms were relatively sensitive to swirl at the seal entrance; as the inlet swirl was propagated right through, the mean circumferential fluid velocity approaches one-half the journal speed exponentially (ref. 15).

Figure 8 illustrates the influence of the ratio L_{lg} of land width L_l to groove width plus land width $(L_l + L_g)$ for $N = 4000$ rpm and $L/D = 0.25$. As the clearance ratio C_l/C_g became small, the dynamic coefficients became large with an increase in the ratio L_{lg}.

CONCLUSIONS

The static and dynamic characteristics of the annular parallel-grooved seal were theoretically investigated with consideration for the effect of the turbulent flow and the inertia term.

As the number of stages increases or the land becomes narrower, the dynamic coefficients and the leakage flow rate decrease. But torque loss increases rapidly.

APPENDIX A

$$q_{l1} = \rho w_{lo}\left\{1+0.824\delta_2 - (1+0.824\delta_1)\left(\frac{H_2}{H_1}\right)^2\right\} + \frac{12\mu_a L_l}{C_{lo}^2}$$

$$q_{l2} = \rho w_{lo}\left\{1+0.824\delta_2 - (1+0.824\delta_1)\left(\frac{H_2}{H_1}\right)^2\right\}$$

$$m = \frac{1}{q_{l1}}\left(q_{l2} + \frac{12\mu_a}{C_{lo}}(z - z_{n-1/2})\right)$$

$$PRL1 = z - z_{n-1/2} - m\,L_l$$

$$PRL2 = (z - z_{n-1/2})^2 - m\cdot L_l^2$$

$$PRL3 = e^{-z/l} - 1 - m\cdot(e^{-L_l/l} - 1)$$

$$PRL4 = e^{-2z/l} - 1 - m\cdot(e^{-2L_l/l} - 1)$$

$$PRL5 = (z - z_{n-1/2})\cdot e^{-z/l} - m\,L_l\cdot e^{-L_l/l}$$

$$PRL6 = PRL1 + l\,PRL3$$

$$PRL7 = l\cdot PRL3 + PRL5$$

$$PRL8 = PRL3 - \frac{1}{2}PRL4$$

APPENDIX B

$$q_{g1} = \rho\omega_{lo}\left\{\left(1-\frac{C_{lo}}{C_1}\right)^2 - \frac{C_{lo}\lambda_{sa}}{2\tan\theta}\left(\frac{1}{C_1^2} - \frac{1}{C_{lo}^2}\right)\right\}$$

$$q_{g2} = \rho\omega_{lo}\left\{\left(1-\frac{C_{lo}}{C1}\right)^2 + \frac{\lambda_{sa}}{2\tan\theta}\right\}$$

$$m = \frac{1}{q_{g1}}\left\{q_{g2} - \frac{\rho\omega_{lo}C_{lo}\lambda_{sa}}{2\tan\theta}\cdot\frac{1}{C_{go}}\right\}$$

$J1 = 1/C_1 - 1/C_{lo}$ $\quad$ $J2 = 1/C_1^2 - 1/C_{lo}^2$

$J3 = 1/C_1^3 - 1/C_{lo}^3$ $\quad$ $J4 = ln(C_1/C_{lo})$

$J5 = C_1^{-a-1} - C_{lo}^{-a-1}$ $\quad$ $J6 = C_1^{-a+2} - C_{lo}^{-a+2}$

$J7 = C_1^{-a+1} - C_{lo}^{-a+1}$ $\quad$ $J8 = C_1^{-a} - C_{lo}^{-a}$

$$J9 = C_1^{-2a+1} - C_{lo}^{-2a+1}$$

$$J10 = \frac{1}{q_{g1}}\ \rho\omega_{lo}\left\{\left(1-\frac{C_{lo}}{C_{go}}\right)^2 + \frac{\lambda_{sa}}{2\tan\theta}\right\}$$

$$J11 = \frac{1}{q_{g1}}\cdot\frac{\rho C_{lo}\omega_{lo}\lambda_{sa}}{2\tan\theta}$$

$$J12 = (J10\cdot L_g + J11\cdot J1)$$

$$J13 = C_1^{-a+3} - C_{go}^{-a+3}$$

$$J14 = C_1^{-2a+2} - C_{go}^{-2a+2}$$

$$PRG1 = \frac{1}{C_{go}^{3}} - \frac{1}{C_{lo}^{3}} - m \cdot J3 \qquad PRG2 = \frac{1}{C_{go}} - \frac{1}{C_{lo}} - m \cdot J1$$

$$PRG3 = \frac{1}{C_{go}^{2}} - \frac{1}{C_{lo}^{2}} - m \cdot J2 \qquad PRG4 = \ln(C_{go}/C_{lo}) - m \cdot J4$$

$$PRG5 = z - z_{n} - m \cdot L_{g} \qquad PRG6 = C_{go}^{-a-1} - C_{lo}^{-a-1} - m \cdot J5$$

$$PRG7 = C_{go}^{-a+2} - C_{lo}^{-a+2} - m \cdot J6$$

$$PRG8 = (z - z_{n})\, C_{go}^{-a-1} - m\, L_{g} \cdot C_{1}^{-a-1}$$

$$PRG9 = C_{go}^{-a+1} - C_{lo}^{-a+1} - m \cdot J7 \qquad PRG10 = C_{go}^{-a} - C_{lo}^{-a} - m \cdot J8$$

$$PRG11 = (z - z_{n})\, C_{go}^{-a} - m\, L_{g} \cdot C_{1}^{-a}$$

$$PRG12 = C_{go}^{-2a+1} - C_{lo}^{-2a+1} - m \cdot J9$$

$$PRG13 = \frac{1}{\tan^{2}\theta}\left(\frac{C_{lo}}{3}\, PRG1 - \frac{1}{2}\, PRG3\right)$$

$$PRG14 = \frac{1}{\tan^{2}\theta}\left(-\, PRG2 + \frac{C_{lo}}{2}\, PRG3\right)$$

$$PRG15 = \frac{1}{\tan^{2}\theta}\left(C_{lo}\, PRG2 + PRG4\right)$$

$$PRG16 = \frac{1}{\tan^{2}\theta}\left(-C_{lo}\, PRG4 + \tan\theta \cdot PRG5\right)$$

$$PRG17 = \frac{1}{A - \tan\theta}\, PRG9 + \frac{C_{lo}^{-a+1}}{\tan\theta}\, PRG4$$

$$PRG18 = PRG8 + \frac{1}{A}\, PRG10$$

$$PRG19 = -\frac{1}{A+\tan\theta} PRG6 + \frac{C_{lo}^{-a+1}}{2\tan\theta} PRG3$$

$$PRG20 = PRG11 + \frac{1}{A-\tan\theta} PRG9$$

$$PRG21 = \frac{1}{2A-\tan\theta} PRG12 - \frac{C_{lo}^{-a+1}}{A} PRG10$$

APPENDIX C

$$I1 = \frac{1}{q_{l1}}\left(q_{l2}\, L_l + \frac{6\mu_a L_l}{C_{lo}^2}\right)$$

$$IPRL1 = L_l^2/2 - L_l \cdot I1 \qquad IPRL2 = L_l^3/3 - L_l^2/2 \cdot I1$$

$$IPRL3 = -l(\, e^{-L_l/l} - 1) - L_l - (\, e^{-L_l/l} - 1) \cdot I1$$

$$IPRL4 = l\ IPRL3 + IPRL1$$

$$IPRL5 = -l \cdot L_l e^{-L_l/l} - l^2(e^{-L_l/l} - 1) - L_l e^{-L_l/l} \cdot I1$$

$$IPRL6 = -\frac{l}{2}(e^{-2L_l/l} - 1) - L_l - (e^{-2L_l/l} - 1) \cdot I1$$

$$IPRL7 = l \cdot IPRL3 + IPRL5 \qquad IPRL8 = IPRL3 - \frac{1}{2} IPRL6$$

$$C_1 = C_{lo} + L_g \tan\theta \qquad IPRG1 = -\frac{J2}{2\tan\theta} - \frac{L_a}{C_{lo}^3} - J3 \cdot J12$$

$$IPRG2 = \frac{J4}{\tan\theta} - \frac{L_g}{C_{lo}} - J1 \cdot J12$$

$$IPRG3 = -\frac{J1}{\tan\theta} - \frac{L_g}{C_{lo}^2} - J2 \cdot J12$$

$$IPRG4 = \frac{C_1}{\tan\theta} J4 - L_g \quad - J4 \cdot J12$$

$$IPRG5 = \frac{L_g^2}{2} - L_g \cdot J12$$

$$IPRG6 = -\frac{J8}{A} - L_g C_{lo}^{-a-1} \quad - J5 \cdot J12$$

$$IPRG7 = -\frac{J13}{A - 3\tan\theta} - L_g C_{lo}^{-a+2} \quad - J6 \cdot J12$$

$$IPRG8 = -\frac{L_g}{A} C_1^{-a} - \frac{J7}{A(A - \tan\theta)} - L_g C_1^{-a-1} \cdot J12$$

$$IPRG9 = -\frac{J6}{A - 2\tan\theta} - L_g C_{lo}^{-a+1} \quad - J8 \cdot J12$$

$$IPRG10 = -\frac{J7}{A - \tan\theta} - L_g C_{lo}^{-a} - J8 \cdot J12$$

$$IPRG11 = -\frac{L_g C_1^{-a+1}}{A - \tan\theta} - \frac{J6}{(A - \tan\theta)(A - 2\tan\theta)} - L_g C_1^{-a} \cdot J12$$

$$IPRG12 = -\frac{J14}{2(A - \tan\theta)} - L_g C_{lo}^{-2a+1} \quad - J9 \cdot J12$$

$$IPRG13 = \frac{1}{\tan^2\theta}\left(\frac{C_{lo}}{3} IPRG1 - \frac{1}{2} IPRG3\right)$$

$$IPRG14 = \frac{1}{\tan^2\theta}\left(-IPRG2 + \frac{C_{lo}}{2} IPRG3\right)$$

$$IPRG15 = \frac{1}{\tan^2\theta}\left(C_{lo} \, IPRG2 + IPRG4\right)$$

$$IPRG16 = \frac{1}{\tan^2\theta}\left(-C_{lo} \, IPRG4 + \tan\theta \cdot IPRG5\right)$$

$$IPRG17 = \frac{1}{A - \tan\theta} \cdot IPRG9 + \frac{C_{lo}^{-a+1}}{2\tan\theta} \cdot IPRG4$$

$$IPRG18 = IPRG8 + \frac{1}{A} IPRG10$$

$$IPRG19 = - \frac{1}{A+\tan\theta} IPRG6 + \frac{C_{1o}^{-a+1}}{2\tan\theta} \cdot IPRG3$$

$$IPRG20 = \frac{1}{A-\tan\theta} IPRG9 + IPRG11$$

$$IPRG21 = \frac{1}{2A-\tan\theta} \cdot IPRG12 - \frac{C_{1o}^{-a+1}}{A} \cdot IPRG10$$

REFERENCES

1. Black, H.F.: Effects of Hydraulic Forces in Annular Pressure Seals on the Vibration of Centrifugal Pump Rotors. J. Mech. Eng. Sci., vol. 11, no. 2, 1969, pp. 206-213.

2. Black, H.F.; and Jenssen, D.N.: Dynamic Hybrid Properties of Annular Pressure Seals. Proc. J. Mech. Eng., vol. 184, 1970, pp. 92-100.

3. Black, H.F.; and Jenssen, D.N.: Effects of High-Pressure Ring Seals on Pump Rotor Vibration. ASME Paper 71-WA/FF-38, 1971.

4. Child, D.W.: Dynamic Analysis of Turbulent Annular Seals Based on Hir's Lubrication Equation. J. Lubr. Technol., vol. 105, no. 3, 1983, pp. 429-436.

5. Child, D.W.: Finite-Length Solutions for Rotordynamic Coefficients of Turbulent Annular Seals. J. Lubr. Technol., vol. 105, no. 3, 1983, pp. 437-445.

6. Allaire, P.E.; Lee, C.C.; and Gunter, E.J.: Dynamics of Short Eccentric Plain Seals with High Axial Reynolds Number. J. Spacecraft, vol. 15, no. 6, 1978, pp. 341-347.

7. Yang, B.S.; Iwatsubo, T.; and Kawai, R.: A Study on the Dynamic Characteristics of Pump Seal (1st Report, In Case of Annular Seal with Eccentricity). Bull. JSME, vol. 27, 1984, pp. 1047-1053.

8. Fleming, D.F.: Damping in Seals for Compressible Fluids. Rotordynamic Instability Problems in High-Performance Turbomachinery. NASA CP-2133, 1980.

9. Childs, D.W.; Dressman, J.B.: Convergent-Tapered Annular Seals: Analysis and Testing for Rotordynamic Coefficients. ASME Winter Annular Meeting, 1981, pp. 35-41.

10. Bolleter, U.; and Florjancic, D.: Predicting and Improving the Dynamic Behavior of Multistage High Performance Pumps. 1st Int. Pump Symposium, 1984, pp. 1-8.

11. Burton, R.A.: Approximation in Turbulent Film Analysis. J. Lubr. Technol., vol. 96, no. 1, 1974, pp. 168-173.

12. Komotori, K.; and Mori, H.: Leakage Characteristics of Labyrinth Seals. 5th Int. Conf. on Fluid Sealing, Paper E4, 1971.

13. Black, H.F.: On Journal Bearing with High Axial Flows in the Turbulent Regime. J. Mech. Eng. Sci., vol. 12, no. 4, 1970, pp. 301-303.

14. Hauck, L.: Exciting Forces due to Swirl-Type Flow in Labyrinth Seals. IFToMM Paper, 1982, pp. 361-368.

15. Black, H.F., et al.: Inlet Flow Swirl in Short Turbulent Annular Seal Dynamics. 9th Int. Conf. on Fluid Sealing, BHRA Fluid Enrg., 1981.

TABLE I. - NUMERICAL CALCULATION MODEL

Working fluid	Water
Fluid temperature, K	293.15
Density, ρ, kg/m^3	9.982×10^2
Viscosity, μ, mPa s	1.009
Kinematic viscosity, ν, m^2/s	1.006×10^{-6}
Journal radius, R, mm	100.0
Seal radial clearance, C_0, mm	0.4
Seal length, L. mm	55 to 205
Groove depth, T, mm	3.0
Divergent flow angle, θ, deg	4.0
Journal rotating frequency, N, rpm	2000 to 8000
Pressure difference, ΔP, MPa	0.49 to 4.9

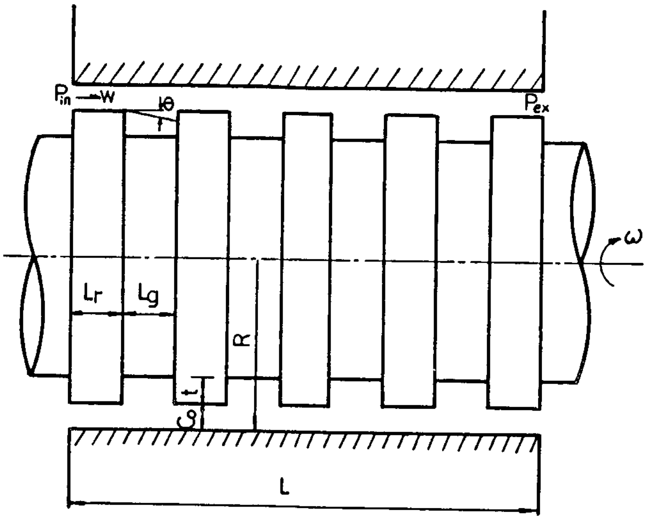
P_{in}
W
θ
P_{ex}
ω
Lr
Lg
R
T
Cg
L

Figure 1. - Geometry of parallel-grooved seal.

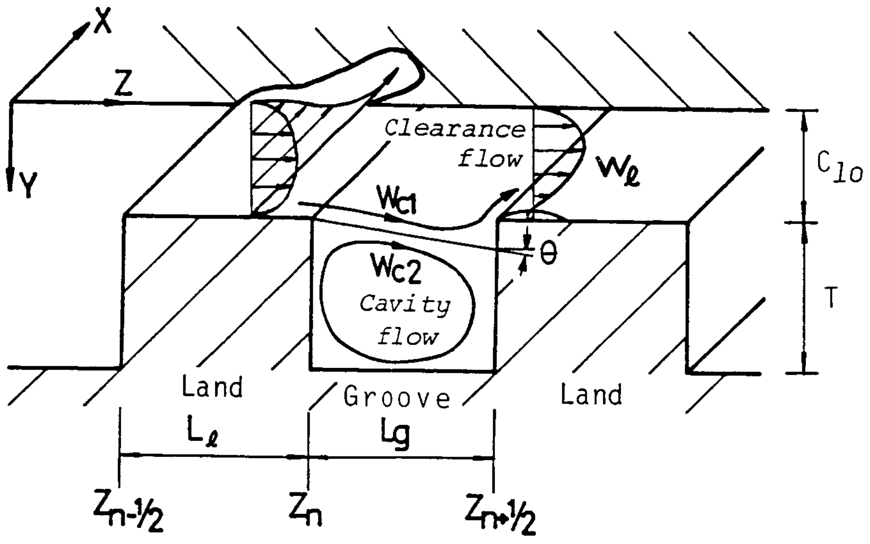
X
Z
Y
Clearance flow
W_ℓ
W_{c1}
W_{c2}
Cavity flow
θ
C_{lo}
T
Land
Groove
Land
L_ℓ
Lg
$Z_{n-1/2}$
Z_n
$Z_{n+1/2}$

Figure 2. - Streamlines and coordinate system for seal analysis.

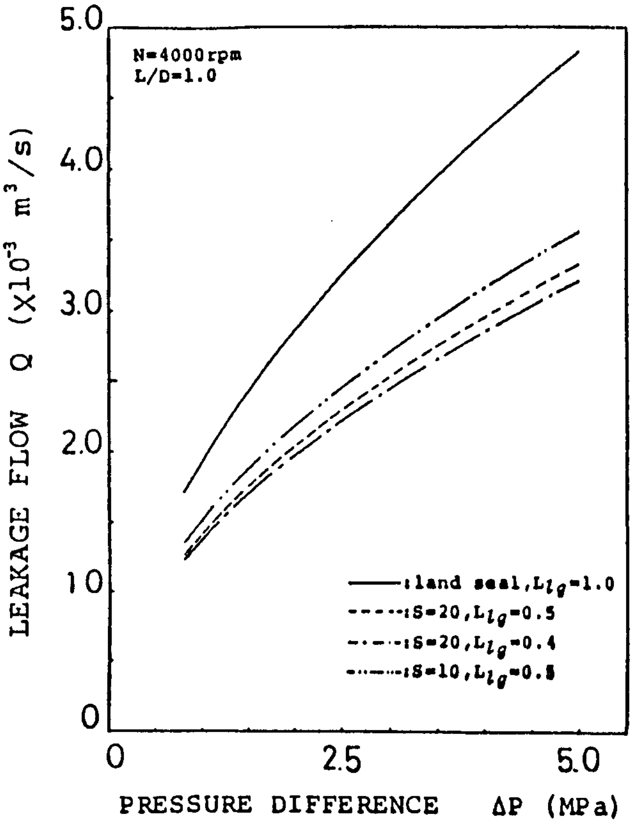

Figure 3. - Leakage flow rate.

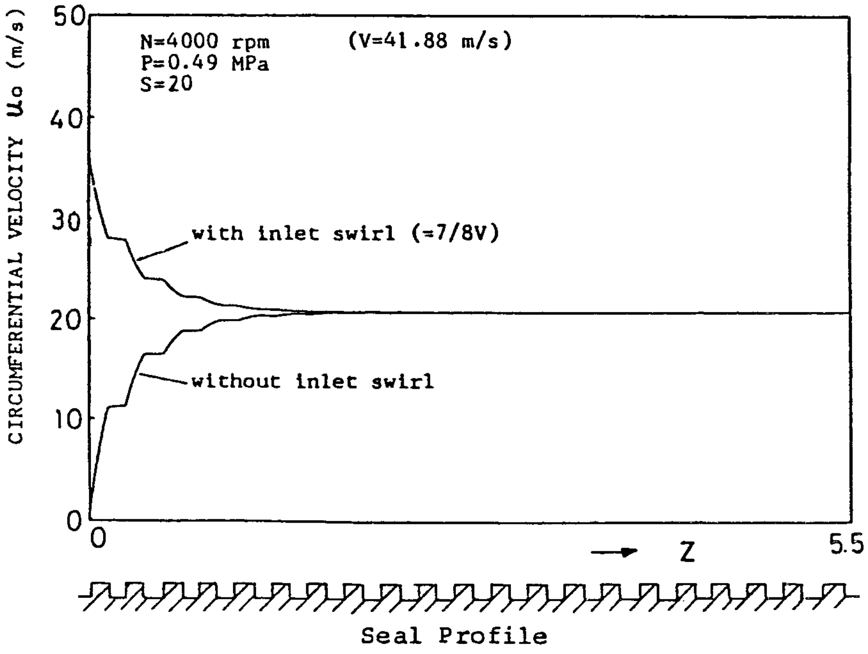

Figure 4. - Axial distribution of circumferential fluid velocity.

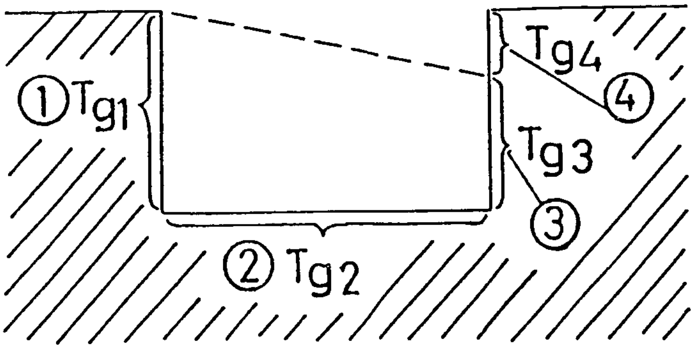
①Tg1
②Tg2
Tg3
③
Tg4
④

Figure 5. - Torque loss of groove.

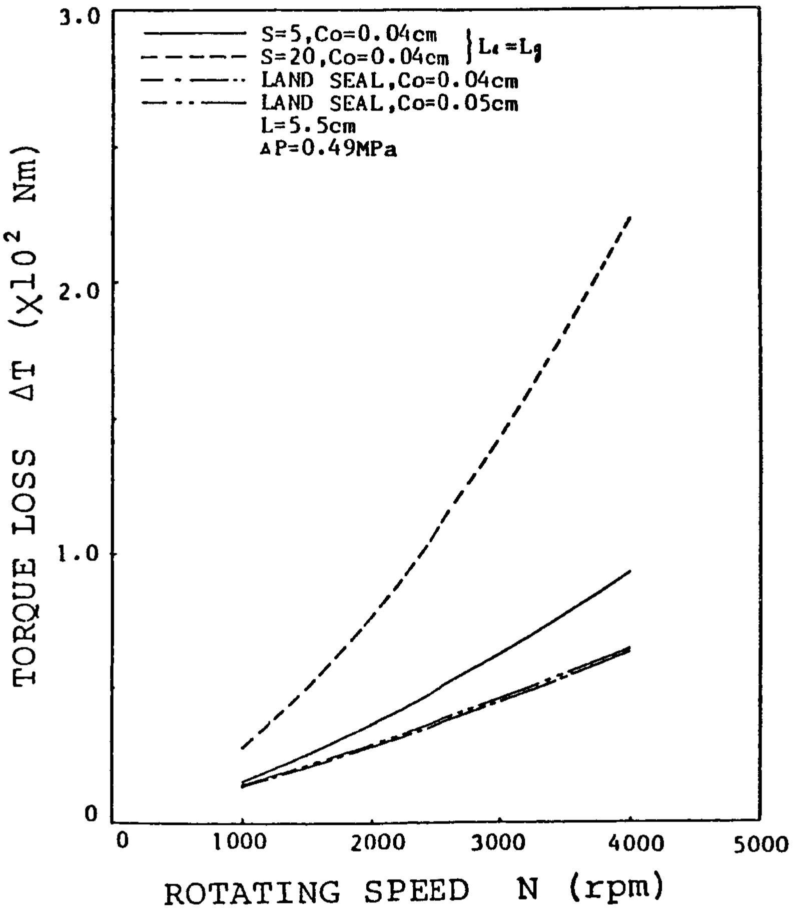

Figure 6. - Torque loss.

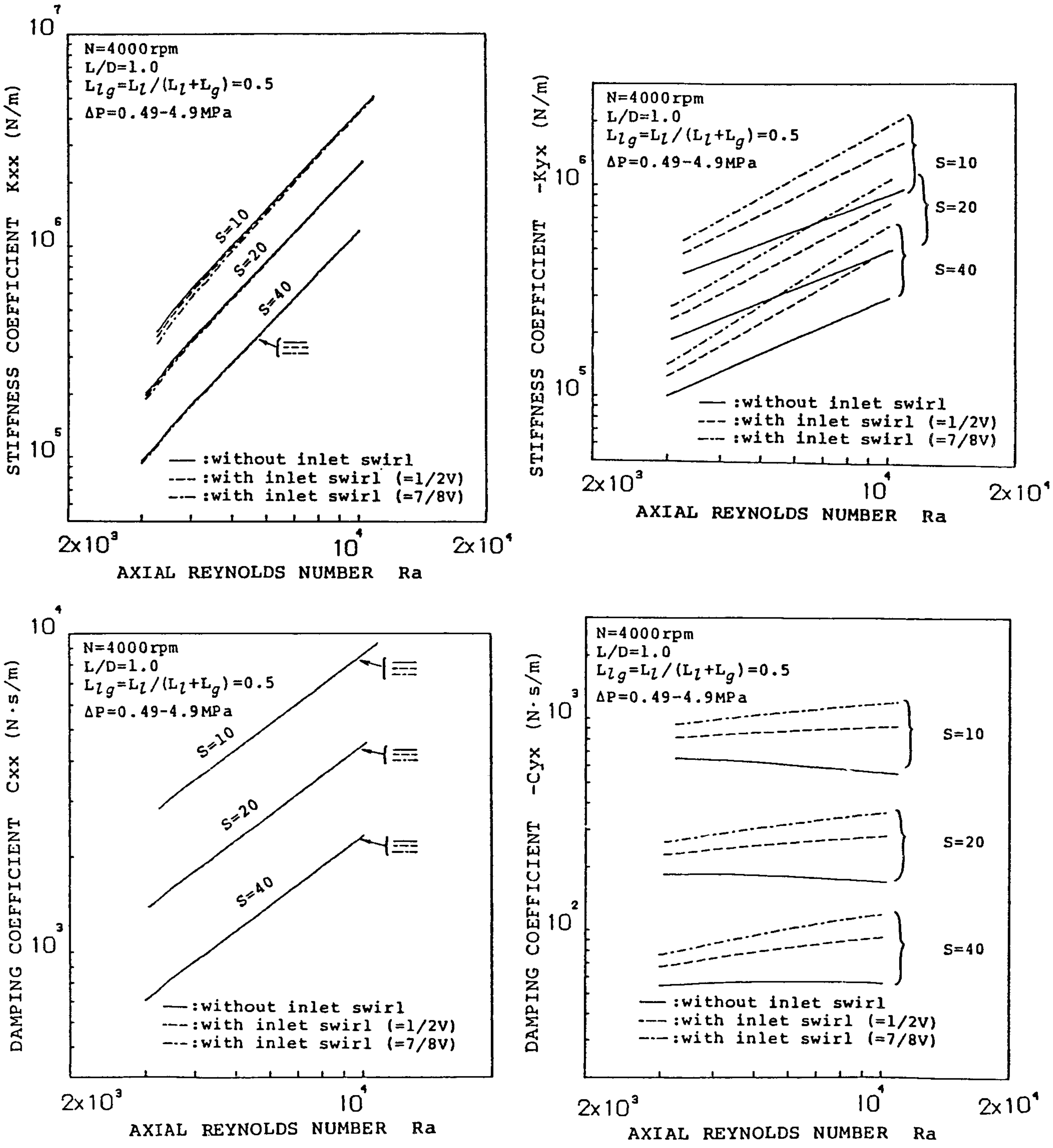

Figure 7. - Influence of number of stages.

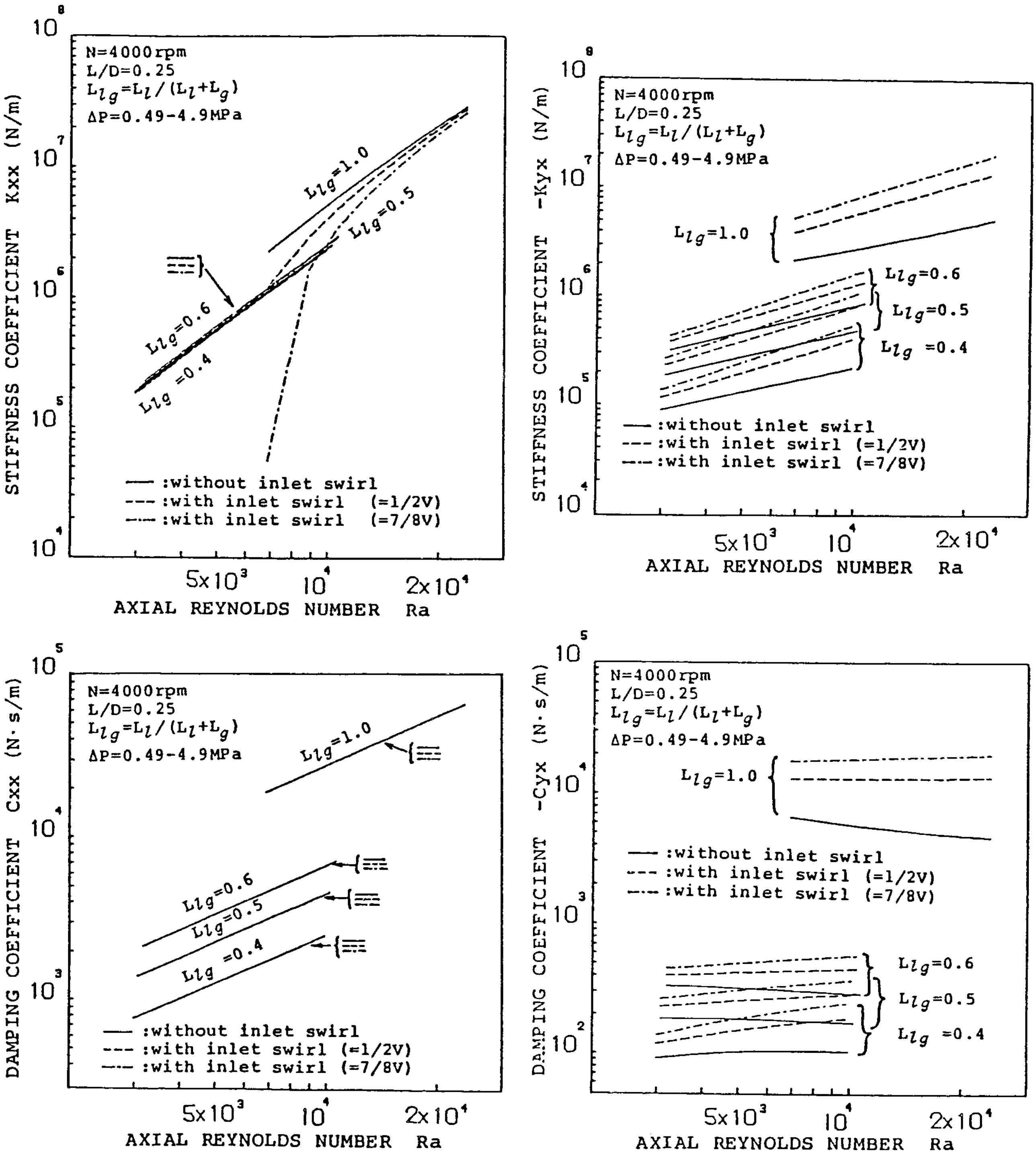

Figure 8. - Influence of ratio of land width to groove width plus land width L_{lg}.

ORIGINAL PAGE IS
OF POOR QUALITY

N87-22206

ROTORDYNAMIC COEFFICIENTS AND LEAKAGE FLOW OF PARALLEL GROOVED SEALS AND SMOOTH SEALS

R. Nordmann, F.J. Dietzen, and W. Janson
University of Kaiserslautern
German Federal Republic

A. Frei and S. Florjancic
Sulzer Brothers
Winterthur, Switzerland

Based on Childs finite length solution (ref. 1) for annular plain seals an extension of the bulk flow theory is derived to calculate the rotordynamic coefficients and the leakage flow of seals with parallel grooves in the stator. Hirs turbulent lubricant equations are modified to account for the different friction factors in circumferential and axial direction. Furthermore an average groove depth is introduced to consider the additional circumferential flow in the grooves. Theoretical and experimental results are compared for the smooth constant clearance seal and the corresponding seal with parallel grooves. Compared to the smooth seal the direct and cross-coupled stiffness coefficients as well as the direct damping coefficients are lower in the grooved seal configuration. Leakage is reduced by the grooving pattern.

INTRODUCTION

An important assumption for the reliability of high speed centrifugal pumps is a good rotordynamic behavior. Connected to this problem hydraulic forces acting on the rotor are of major importance. It is well known that neck or wear-ring seals as well as interstage seals (fig. 1) may have a large influrence on the bending vibrations of a pump rotor. Besides their designed function of reducing the leakage flow between the impeller outlet and inlet or two adjacent pump stages, respectively, the contactless seals have the potential to develop significant forces. This type of forces created by lateral rotor vibrations can be described by stiffness-, damping- and mass coefficients in a linearized model

$$\begin{bmatrix} F_x \\ F_y \end{bmatrix} = \begin{bmatrix} M & m \\ -m & M \end{bmatrix} \cdot \begin{bmatrix} \ddot{x} \\ \ddot{y} \end{bmatrix} + \begin{bmatrix} C & c \\ -c & C \end{bmatrix} \cdot \begin{bmatrix} \dot{x} \\ \dot{y} \end{bmatrix} + \begin{bmatrix} K & k \\ -k & K \end{bmatrix} \cdot \begin{bmatrix} x \\ y \end{bmatrix} \qquad (1)$$

For rotordynamic calculations of multistage pumps the machine designer needs to know this dynamic characteristics of the actual seal configuration. For smooth seals, where both stator and rotor elements have the same smooth surfaces, analytical and experimental investigations have been carried out (ref. 1,3,4,5). The results confirm the validity of equation (1) and dynamic coefficients can be predicted by the finite length solution derived in ref. 1 with sufficient accuracy. A finite length solution is also available for seals with different but directionally-homogeneous

PRECEDING PAGE BLANK NOT FILMED

surface roughness for the rotor and stator elements (ref. 2).

The subject of this investigation is a seal type with parallel grooves in the stator element and a smooth surface in the rotor element. Concerning the leakage flow, this type of seal is more effective than the pure smooth seal, because of higher friction in the axial direction. However, if pump rotordynamics is important the dynamic seal coefficients have to be known. Up to now the stiffness and damping characteristics of grooved seals and their influence to the stability and unbalance response of pump rotors is not well investigated and there is a need for additional research in this area.

At the present time, there are only a few techniques available in the technical literature. Black and Cochrane (ref. 6) have improved their earlier theory for smooth seals by introducing an equivalent length for the grooved section to reduce the circumferential pressure gradients. Recently, Childs and Kim (ref. 7) have extended their analysis procedure (ref. 2) to predict rotordynamic coefficients of grooved turbulent annular seals.

In the present paper an extension of the bulk flow theory (ref. 1) is given, to calculate rotordynamic coefficients and leakage for seals with parallel grooves in the stator. The theoretical results obtained by the developed procedure are correlated to experimental results, measured at a seal test rig. Furthermore the grooved seal results are compared with corresponding data of the smooth seal configuration.

BULK FLOW MODEL FOR SEALS WITH PARALLEL GROOVES

Seal geometry

Fig. 2 shows the type of seal, which is considered in our investigation. It consists of a smooth rotor and a circumferentially grooved stator. The seal has the radius R, the length L and may have different clearances at the entrance C_o and the exit C_1, respectively. The groove geometry is described by the groove depth H_R and the groove length L_G and land length L_L. We assume, that the groove depth H_R has approximately the same order of magnitude as the seal clearances C_o, C_1.
In the following derivations the groove geometry is described simply by an average value H_R^* for the groove depth (fig. 2).

Bulk flow velocities

In Childs finite length analysis (ref. 1) for plain seals a bulk flow model was used. Following this procedure we introduce the bulk flow velocities U_Z in the axial Z-direction and U_Θ in the circumferential direction. The axial velocity U_Z is considered only in the region of the actual seal clearance H. Although there is a fluid circulation in the grooves: in the Z-direction, this part of the flow is neglected in our model (fig. 3). In circumferential direction the real velocity distribution (fig. 3) is replaced by a constant bulk flow U_Θ, which is assumed to act in the area of the average seal clearance $H^* = H + H_R^*$. At the rotor surface the fluid velocity is $R\omega$ with the shaft angular velocity ω.

Fig. 4 points out the variables of the bulk flow model for a seal location with coordinates Z and Θ: the two mentioned velocities U_Z, U_Θ, the fluid pressure p and

ORIGINAL PAGE IS
OF POOR QUALITY

the local clearances H, $H^* = H + H_R^*$. All quantities depend on the coordinates Z and Θ and the time t, as well.

Wall shear stresses

Concerning the wall shear stresses at the rotor and the stator we refer to Hirs formulation, expressing the shear stresses by an empirical function of the bulk flow velocity relative to the wall. First we apply this relation for the rotor assuming a smooth surface in the two directions. With the bulk flow velocity $V_R = [(U_\Theta - R\omega)^2 + U_Z^2]^{1/2}$ relative to the rotor surface (fig. 5), we obtain

$$\tau_R = n_R \left(\frac{2H\,V_R}{\nu}\right)^{m_R} \frac{\rho}{2} V_R^2 = C_R \frac{\rho}{2} V_R^2 \qquad (2)$$

n_R, m_R are empirical turbulence coefficients, ρ is the fluid density and ν the kinematic viscosity of the fluid.
With the relations of figure 5 we can determine the components of the rotor wall shear stress

$$\tau_{R\Theta} = \tau_R (U_\Theta - R\omega)/V_R \quad ; \quad \tau_{RZ} = \tau_R\, U_Z/V_R \qquad (3)$$

Contrary to the definition of $\tau_{R\Theta}$ in equation (3) we use a slightly different form and define $\tau_{R\Theta}$ with the seal clearance H* instead of H, which is used for τ_{RZ} in the axial direction. After some steps we obtain from equations (2) and (3)

$$\tau_{R\Theta} = \frac{n_R}{2} \rho\, U_Z (U_\Theta - R\omega) \left(\frac{H^*}{H}\right)^{m_R} R_a^{m_R} \left\{1 + \left(\frac{U_\Theta - R\omega}{U_Z}\right)^2\right\}^{(1+m_R)/2} \qquad (4a)$$

$$\tau_{RZ} = \frac{n_R}{2} \rho\, U_Z^2\, R_a^{m_R} \left\{1 + \left(\frac{U_\Theta - R\omega}{U_Z}\right)^2\right\}^{(1+m_R)/2} \qquad (4b)$$

with the axial Reynolds number $R_a = \frac{2H\,U_Z}{\nu}$.

Caused by the parallel grooves the stator has different friction characteristics in the two directions. In axial direction it behaves like a rough surface. For the circumferential direction we assume a smooth surface. Again we refer to Hirs formulation and express the wall shear stress τ_S in dependence of the bulk flow velocity $V_S = (U_\Theta^2 + U_Z^2)^{1/2}$

$$\tau_S = C_S \frac{\rho}{2} V_S^2 \qquad (5)$$

In the case of the grooved stator the triangle ratios of figure 5 are not quite correct. Nevertheless, we still use the relations and express the shear stress components approximately by

$$\tau_{S\Theta} = \tau_S\, U_\Theta/V_S \quad ; \quad \tau_{SZ} = \tau_S\, U_Z/V_S \qquad (6)$$

The resultant friction factor C_S (eq. 5) can be introduced by the following superposition rule

$$\begin{aligned} C_S &= (C_{S\Theta}^2 \cos^2\varphi + C_{SZ}^2 \sin^2\varphi)^{1/2} \\ C_{S\Theta} &= n_{S\Theta} \left(\frac{2H^*V_S}{\nu}\right)^{m_{S\Theta}} \\ C_{SZ} &= n_{SZ} \left(\frac{2H\, V_S}{\nu}\right)^{m_{SZ}} \end{aligned} \tag{7}$$

$n_{S\Theta}$, n_{SZ}, $m_{S\Theta}$, m_{SZ} are empirical turbulence coefficients.

Formula (7) describes the change of the resultant stator friction factor C_S in dependence of the local flow angle φ (figs. 5,6). If we consider one of the special cases, e.g. a pure flow in axial direction, we obtain

$$U_Z = V_S, \quad U_\Theta = 0, \quad \varphi = \pi/2, \quad \sin\varphi = 1, \quad \cos\varphi = 0$$

$$C_S = C_{SZ}, \ \tau_{S\Theta} = 0, \ \tau_{SZ} = C_{SZ} \frac{\rho}{2} U_Z^2 .$$

From equations (5), (6), (7) we finally end up with the two shear force components

$$\tau_{S\Theta} = C_S'' \left(\frac{H^*}{H}\right)^{m_{S\Theta}} \frac{n_{S\Theta}}{2} \rho\, U_Z U_\Theta R_a^{m_{S\Theta}} \left\{1 + \left(\frac{U_\Theta}{U_Z}\right)^2\right\}^{(1+m_{S\Theta})/2} \tag{8a}$$

$$\tau_{SZ} = C_S' \frac{n_{SZ}}{2} \rho\, U_Z^2 R_a^{m_{SZ}} \left\{1 + \left(\frac{U_\Theta}{U_Z}\right)^2\right\}^{(1+m_{SZ})/2} \tag{8b}$$

C_S', C_S'' are defined in the Appendix. (8a) and (8b) can be compared with prior results from Childs and Kim (ref. 2). They differ only in the coefficients C_S', C_S''.

BULK FLOW MOMENTUM AND CONTINUITY EQUATIONS

Figures 7 and 8 show a differential element of the fluid having the dimensions $Rd\Theta$, dZ, $H(Z,\Theta,t)$ or $H^*(Z,\Theta,t)$ respectively. The upper and lower surfaces correspond to the rotor and stator seal elements and have the velocities $R\omega$ and zero. Figure 7 points out the bulk flow velocity components U_Z and U_Θ with their changes in axial and circumferential direction along the element. For the derivation of the momentum equations the wall shear stresses τ_s, τ_r and the pressure p at the different seal surfaces have to be taken in account (fig. 8). Summing forces in the two directions for the free body diagram leads to the axial and circumferential momentum equations 9 and 10, respectively

$$- H \frac{\partial p}{\partial Z} = \tau_{SZ}+\tau_{RZ} + \rho H \left(\frac{\partial U_Z}{\partial t} + U_Z \frac{\partial U_Z}{\partial Z} + U_\Theta \frac{\partial U_Z}{R\partial_\Theta}\right) - \rho H_R^* \, U_Z \frac{\partial U_\Theta}{R\partial_\Theta} = 0 \qquad (9)$$

$$- \frac{H^*}{R} \frac{\partial p}{\partial \Theta} = \tau_{S\Theta}+\tau_{R\Theta} + \rho H^* \left(\frac{\partial U_\Theta}{\partial t} + \frac{U_\Theta}{R} \frac{\partial U_\Theta}{\partial \Theta} + U_Z \frac{\partial U_\Theta}{\partial Z}\right) - \rho H_R^* \, U_Z \frac{\partial U_\Theta}{\partial Z} = 0 \qquad (10)$$

In comparison to the derivations of reference 2 both equations have an additional term with the average groove depth H_R^*, expressing an added momentum change caused by the grooves. Furthermore the shear stresses are different as described in equations (4) and (8). Note that H^* is used in the circumferential momentum equation.

The bulk flow continuity equation (11) also has

$$\frac{\partial H}{\partial t} + \frac{1}{R} \left(\frac{\partial \, HU_\Theta}{\partial \Theta}\right) + \left(\frac{\partial \, HU_Z}{\partial Z}\right) + \frac{1}{R} H_R^* \frac{\partial U_\Theta}{\partial \Theta} = 0 \qquad (11)$$

an added term resulting from the flow difference in circumferential direction in the area of the grooves. If we substitute the shear stresses τ_{SZ}, τ_{RZ}, $\tau_{S\Theta}$, $\tau_{R\Theta}$ by the velocity-dependent formulas (4) and (8) we obtain the complete bulk flow equations (see Appendix A), which can be used for further analysis. By introducing the following variables

$u_z = U_z/\bar{V}$, $u_\Theta = U_\Theta/R\omega$, $\tilde{p} = p/\rho\bar{V}^2$

$h = H/\bar{C}$, $\tau = t/T$, $z = Z/L$, $C = (C_o + C_1)/2$

$T = L/\bar{V}$, $b = \bar{V}/R\omega$, $\bar{V}$ average axial velocity

the equations can be treated also in nondimensional form.

PERTURBATION ANALYSIS

In the further analysis we follow strictly ref. 2. The governing equation (9), (10), (11) or the corresponding equations in non-dimensional form define the bulk flow velocity components u_Θ, u_z and the pressure $\tilde{p}$ as a function of the variables $R\Theta$, z and the time τ. The expansion of this equations in the perturbation variables

$$\begin{aligned} u_z &= u_{zo} + \varepsilon \, u_{z1} & \qquad u_\Theta &= u_{\Theta o} + \varepsilon \, u_{\Theta 1} \\ h &= h_o + \varepsilon \, h_1 & \qquad \tilde{p} &= \tilde{p}_o + \varepsilon \, \tilde{p}_1 \end{aligned} \qquad (12)$$

with the eccentricity ratio $\varepsilon = e/\bar{C}$ yields zeroth-order and first-order perturbation equations.

Zeroth - Order - Equations

The eccentricity ratio $\varepsilon = 0$ describes the centered position of the rotor in the stator element. If we introduce u_{zo}, $u_{\Theta o}$, h_o and p_o in the nondimensional bulk flow equations, we obtain the following zeroth order perturbation equations.
Axial Momentum Equation:

$$\frac{\partial \tilde{p}_o}{\partial z} = - \frac{1}{2f^3} \{\sigma_R \, a_{oR} + \sigma_{sz} \, a_{osz} \, De + 4q\} \qquad (13a)$$

Circumferential Momentum Equation:

$$\frac{\partial u_{\Theta o}}{\partial z} = - \frac{1}{2f} \{(\frac{h_o{}^*}{h_o})^{m_R} \sigma_R \, a_{oR} \, (u_{\Theta o}-1) + (\frac{h_o{}^*}{h_o})^{m_{s\Theta}} \sigma_{s\Theta} a_{os\Theta} \, Da \, u_{\Theta o}\} \qquad (13b)$$

Contuniity Equation:

$$u_{z\Theta} = \frac{1}{h_o} \qquad (13c)$$

The parameters of these equations are defined in Appendix B. $h_o = f$ is the dimensionless clearance function for the centered position and $q = (C_o - C_1)/(C_o + C_1)$ is a measure of the degree of taper in a seal. For the constant clearance seal, treated later in this paper, it follows $q = 0$ and $h_o = 1$. The quantities σ_R, σ_{sz} and $\sigma_{s\Theta}$ are defined by

$$\sigma_R = (\frac{L}{\bar{C}}) \lambda_R \ ; \quad \sigma_{sz} = (\frac{L}{\bar{C}}) \lambda_{sz}; \quad \sigma_{s\Theta} = (\frac{L}{\bar{C}}) \lambda_{s\Theta} \qquad (14)$$

with the wall friction factors

$$\lambda_R = n_R \, R_{ao}{}^{m_R} \, (1 + \frac{1}{4b^2})^{(1+m_R)/2}$$

$$\lambda_{sz} = n_{sz} \, R_{ao}{}^{m_{sz}} \, (1 + \frac{1}{4b^2})^{(1+m_{sz})/2} \qquad (15)$$

$$\lambda_{s\Theta} = n_{s\Theta} \, R_{ao}{}^{m_{s\Theta}} \, (1 + \frac{1}{4b^2})^{(1+m_{s\Theta})/2}$$

The solution of the zeroth order equations define the steady state leakage and the development of the circumferential velocity $u_{\Theta o}(z)$ due to wall shear. In general the coupled and nonlinear equations have to be solved iteratively to determine the leakage flow corresponding to a specified pressure drop. A leakage coefficient C_d can be introduced for the leakage/pressure drop relationship

$$\Delta p_0 = C_d \frac{\rho}{2} \bar{V}^2 \tag{16a}$$

In formula (16a) the pressure drop at the entrance

$$\Delta p_0' = \frac{1+\xi}{(1+q)^2} \frac{\rho}{2} \bar{V}^2 \tag{16b}$$

is included. For the special case of a constant clearance seal without fluid rotation we obtain the simple relation

$$\frac{\partial p_0}{\partial z} = -(\sigma_R + \sigma_{sz}) \frac{\rho}{2} \bar{V}^2 \tag{17}$$

which can be used to determine the empirical coefficients n_R, m_R, n_{sz}, m_{sz}

First order equations

The first order equations describe the pressure and flow conditions due to a small seal motion about the centered position. Their derivation is relatively extensive, therefore we mention only some important steps in the solution procedure, following again references 1,2. To find results for the first order quantities u_{z1}, $u_{\Theta 1}$, p_1, the time and Θ-dependency is eliminated by the assumption of a harmonic pressure and velocity distribution in circumferential direction and by introducing a circular harmonic seal motion with the relative radius $r_0 = R_0/\bar{C}$ and the frequency Ω. In this way the first order equations are reduced to a system of three coupled, complex ordinary differential equations for the complex unknowns u_{z1}, $u_{\Theta 1}$ and p_1, which now depend only on the axial coordinate z.

$$\frac{\partial}{\partial z} \begin{Bmatrix} u_{z1} \\ u_{\Theta 1} \\ p_1 \end{Bmatrix} + \begin{bmatrix} a_{11} & a_{12} & a_{13} \\ a_{21} & a_{22} & a_{23} \\ a_{31} & a_{32} & a_{33} \end{bmatrix} \begin{Bmatrix} u_{z1} \\ u_{\Theta 1} \\ p_1 \end{Bmatrix} = \left(\frac{r_0}{\varepsilon}\right) \begin{Bmatrix} g_1 \\ g_2 \\ g_2 \end{Bmatrix} \tag{18}$$

The 3x3-matrix A has the following elements

$$a_{11} = -2q/f \quad ; \quad a_{12} = -j\,\omega T\, f^*/f \quad ; \quad a_{13} = 0$$

$$a_{21} = f^* A_{3\Theta} \quad ; \quad a_{22} = f^*(A_{2\Theta} + j\Gamma T) \quad ; \quad a_{23} = -jf^* b(L/R)$$

$$a_{31} = A_{3z} + 2q/f^2 + j\Gamma T; \quad a_{32} = A_{2z} + j\omega T f^*/f^2 + j(L/R)H^*_R/(bf^2); \quad a_{33} = 0$$

with $\Gamma = \Omega - \omega u_{\Theta o}(z)$, $T = L/\bar{V}$

and the right hand sight consists of

$$g_1 = 2q/f^3 + j\Gamma T/f$$

$$g_2 = -f^* A_{1\Theta}$$

$$g_3 = -(A_{1z} + 2q/f^4 + j\Gamma T/f^2)$$

The parameters $A_{1\Theta}$, $A_{2\Theta}$, $A_{3\Theta}$, A_{1z}, A_{2z}, A_{3z} are expressed in Appendix B.

With the boundary conditions of ref. 1 the equations (18) can be solved and yield the solution for the velocity and pressure field of the form

$$\begin{bmatrix} u_{z1} \\ u_{\Theta 1} \\ p_1 \end{bmatrix} = \left(\frac{r_o}{\varepsilon}\right) \cdot \begin{Bmatrix} f_{1c} + j\, f_{1s} \\ f_{2c} + j\, f_{2s} \\ f_{3c} + j\, f_{3s} \end{Bmatrix} \tag{19}$$

Dynamic Coefficients

From the pressure field solution of (19) the reaction force components acting on the rotor due to the circular shaft motion can be determined by integration of the pressure along the seal and in circumferential direction. As pointed out in ref. 1 the nondimensional form of eq. (1)

$$\frac{1}{\pi R \Delta p} \cdot \begin{Bmatrix} F_x \\ F_y \end{Bmatrix} = \begin{bmatrix} \tilde{K} & \tilde{k} \\ -\tilde{k} & \tilde{K} \end{bmatrix} \begin{Bmatrix} x \\ y \end{Bmatrix} + T \begin{bmatrix} \tilde{C} & \tilde{c} \\ -\tilde{c} & \tilde{C} \end{bmatrix} \begin{Bmatrix} \dot{x} \\ \dot{y} \end{Bmatrix} + T^2 \begin{bmatrix} \tilde{M} & \tilde{m} \\ -\tilde{m} & \tilde{M} \end{bmatrix} \begin{Bmatrix} \ddot{x} \\ \ddot{y} \end{Bmatrix} \tag{20}$$

can be used in the definition for the radial and circumferential components of the reaction force

$$-\frac{F_r(\Omega T)}{\pi R \Delta p R_o} = \tilde{K} + \tilde{c}\,(\Omega T) - \tilde{M}\,(\Omega T)^2 = \frac{2}{C_d}\left(\frac{L}{\bar{C}}\right) \int_o^1 f_{3c}(z)\, dz$$

$$\frac{F_\Theta(\Omega T)}{\pi R \Delta p R_o} = \tilde{k} - \tilde{C}\,(\Omega T) - \tilde{m}\,(\Omega T)^2 = \frac{-2}{C_d}\left(\frac{L}{\bar{C}}\right) \int_o^1 f_{3s}(z)\, dz \tag{21}$$

Finally the dynamic seal coefficients K, k, C, c, M, m can be found by a least square curve-fit-procedure applied to the right hand side of equation (21).

Applicability of the derived equations

The presented equations can be applied for smooth as well as grooved seals. Furthermore it is possible to investigate constant clearance and tapered seals. All equations are expressed in a form corresponding to prior derivation from Childs (ref. 1,2). Therefore it is easy to reduce the general form into simpler expressions and to compare them with prior equations. In the special case of a smooth constant clearance seal it follows $H_R = H_R^* = 0$; $H = H^*$; $n_R = n_{sz} = n_{s\theta}$; $m_R = m_{sz} = m_{s\theta}$; $C_s = C''_s = 1$, $q = 0$ and $h_o = 1$.
All further parameters, especially those defined in the Appendix are changing for this special case and the resultant equations coincide with the equations in ref. 1.

THEORETICAL AND EXPERIMENTAL RESULTS FOR SMOOTH AND GROOVED SEALS

The objective of the theoretical and experimental investigations is to check the usefulness of the developed model for grooved seals. For this task predicted and measured dynamic coefficients for grooved seals are compared. It is of further interest to point out differences of leakage and rotordynamic coefficients for smooth and grooved seals.

Geometry of the Test-Seals

The two seals which have been investigated are shown in fig. 9. Seal ① is a smooth constant clearance seal without any grooves, seal ② has eight parallel grooves in the stator. The rotor elements are considered to be smooth. Both seals have the following data: radius R = 23,5 mm, length L = 23,5 mm, constant clearance $\bar{C}$ = 0,2 mm. For the grooved seal the groove depth is H_R = 0,5 mm with L_G = 0,7 mm and L_L = 1,5 mm.

Test Rig for Seal Investigations

With the test rig shown in fig. 10 the leakage flow as well as the dynamic seal coefficients can be determined by measurements. The cross section shows two seal inserts integrated symmetrically in a very rigid housing. A stiff shaft, driven by an ac-motor, rotates inside the housing and acts as the second part of the seal. The housing is flexibly supported by eight beamlike springs and therefore a pure lateral motion relative to the shaft is specified. In the operating condition water with 30°C is entering the housing in the center, flows through the two test seals and is exiting the housing at both ends.

To characterize the fluid state several pressure and temperature pickups are distributed at the test apparatus. The fluid velocity, determined from the mass flow rate, was measured in the supply line. The housing can be excited by test forces, which are measured by a force transducer. To detect the resultant motion of the housing relative to the shaft eddy current-pickups were used.

For the steady-state leakage measurement the housing is fixed in a centered position and the mass flow rate and the pressure drop are taken by measurements. With this test data and additional informations concerning the fluid the leakage flow and the empirical turbulence coefficients can be found.

The experimental determination of the seal dynamic coefficients works with a parameter identification procedure. In the measurement step test forces are applied to the housing in radial direction and with the measured relative motions between the two seal surfaces mobility frequency response functions can be calculated by Fast Fourier Transformation. Corresponding frequency response curves of a seal test rig-model are fitted to the measured functions by variation of the seal dynamic coefficients. The identification procedure is described in more detail in ref. 4,5.

Leakage Performance

To compare the leakage flow of different seal stators the leakage coefficient C_L is defined as follows

$$\dot{Q} = C_L \, 2\pi R^2 \sqrt{\frac{2\Delta p_o}{\rho}} \tag{22}$$

$\dot{Q}$ is the volumetric steady state flow rate measured at the test rig and Δp the corresponding pressure drop. C_L is a nondimensional relative measure of the leakage expected trough seals with the same radius. Fig. 11 illustrates measured values C_L for the two seals without grooves and with grooves. The grooved seal ② has a leakage coefficient, which is about 15 % lower than that of seal ① without grooves. Both leakage coefficients increase slightly with the pressure drop Δp.

Empirical Turbulence Coefficients

In the described analysis the friction factors λ_R, λ_{sz}, $\lambda_{s\Theta}$ were characterized in terms of the empirical turbulence coefficients (eq. 15). These empirical coefficients have to be determined from static test data before a theoretical prediction for the seal dynamic coefficients is possible. Leakage rates and pressure gradients are measured for this task. The steady state axial pressure gradient is described by eq. (17)

$$\frac{\partial p_o}{\partial z} = -(\sigma_R + \sigma_{sz}) \frac{\rho}{2} \bar{V}^2 \tag{17}$$

With the measured pressure gradient, the velocity $\bar{V}$ and the density ρ the combined σ-values in parantheses can be calculated. We start with the smooth seal configuration and suppose that σ_R can be applied for both the smooth rotor and the smooth stator. From eq. (17) we obtain $2 \cdot \sigma_R$ and the friction factor λ_R, respectively. The second test is carried out with the smooth rotor and the grooved stator. From the measured quantities for this case first of all only the combined friction factor $(\sigma_R + \sigma_{sz})$ is known. With the value σ_R from the first test σ_{sz} and the corresponding λ_{sz} can be calculated. Fig. 12 shows the two friction factors λ_R and λ_{sz} in dependence the axial Reynolds number R_{ao}. The grooved seal ② has approximately the double friction factor compared to the smooth stator of seal ① .

From the λ versus R_{ao} data the empirical turbulence coefficients n_R, m_R, n_{sz}, m_{sz} are calculated with a least square procedure, based on equations (15). The following values were obtained (fig. 14):

$$\begin{aligned} n_R &= 0{,}062 \;;\quad m_R = -\,0{,}22 \\ n_{sz} &= 0{,}058 \;;\quad m_{sz} = -\,0{,}13 \end{aligned} \qquad (23)$$

Concerning the values $n_{s\Theta}$, $m_{s\Theta}$, we assume, that the smooth surface constants are relevant.

Dynamic Coefficients, Influence of the Groove depth

With the presented analysis we can now calculate the dynamic seal coefficients. The numerical procedure is applied to determine especially the stiffness and damping coefficients K, k, C, c for seal ② in dependence of the rotational speed and the average groove depth. The axial Reynolds number R_{ao} is kept constant in this investigation. Besides the seal geometry (fig. 9) further input data are as follows:

Fluid data for water with 30°C
Axial average velocity $\bar{V} = 16{,}46$ m/sec
Entry swirl $U_{\Theta o} = 0{,}2\ R\omega$
Inlet pressure loss $\xi_o = 0{,}5$

Describing the friction behavior, the empirical coefficients from (23) are used (fig. 14).

To point out the influence of the groove depth, different values of H_R^* are assumed (figs. 13,14). Taking the average depth from a geometrical approximation (sum of the upper areas equal the sum of the lower areas) we obtain $H_R^* \cong 0{,}1$ mm. The selected values for the calculations are $H_R^* = 0;\ 0{,}1;\ 0{,}2$ mm. Note that the empirical constants are held constant in this investigation.

Fig. 13 illustrates that the direct stiffness and damping as well as the cross coupled stiffness are reduced by H_R^*, there is a weak influence to the cross coupled damping. An increase of H_R^* from 0 to 0,2 mm reduces K about 50 % and C about 37 %, respectively.

In Fig. 14 the direct stiffness K and the direct damping C are compared for the two seal types ① and ② . All presented values are related to the coefficients K and C of seal ① without grooves. The results correspond to $R_{ao} = 8419$ and a rotational speed 4000 rpm. All other data are the same as in the example before. Starting with the reference seal ① with empirical constants for smooth surfaces the stiffness ratio as well as the damping ratio are equal to 1 by definition. Seal ② with grooves has other constants (fig. 14). If we consider only this influence (change in friction) and keep the average groove depth constant ($H_R^* = 0$), direct stiffness as well as damping increase to 1,12 and 1,19 respectively. Taking now the empirical values of seal ② constant, an increase of H_R^* reduces both stiffness and damping, as was shown already in fig. 13. If we compare with corresponding measurement results, we recognize that the calculation with $H_R^* = 0{,}1$ mm yields good results for stiffness but 15 % too high values for the damping.

Dynamic Coefficients, Comparison of Test Results and Theoretical Results

As described before the dynamic seal coefficients can be measured at the seal test rig. For one working condition with constant rotational speed, axial velocity and constant fluid temperature four frequency response functions are measured by exciting the dynamic seal test rig and picking up the response in the two directions. A computer takes over the measured data and calculates the dynamic seal coefficients by means of a least square identification procedure (references 4,5). Several measurements were carried out for different rotational speeds but constant axial Reynolds number R_{ao} and fluid temperature. Fig. 15 illustrates for the two seals with and without grooves the identified stiffness and damping coefficients versus the rotational speed. The test results show, that neither the direct coefficients nor the cross coupled coefficients are equal in amount, as expected from theory (eq. 1). Each of the two coefficients, which should be equal in magnitude, are shown in the diagram as found out by the identification process. The scatter of the measurement points is very different. The added mass terms are much higher than predicted by theory. They are not presented in the diagram.

The fitting curves show the tendency as expected from theory, a slightly parabolic decrease of K with the rotational speed, constant direct damping and a linear increase with the rotational speed for the cross coupled terms k and c.

Seal ① without grooves has higher direct stiffness and damping terms compared to seal ② with grooves. The cross coupled stiffness of seal ① is also greater than of seal ② . There is no clear difference in the cross coupled damping values. Basicly, the different measurement results for the two seal types show the expected influence of the grooves (see also fig. 13), reducing especially K, C and k.

In fig. 16 the identified stiffness and damping coefficients of seal ② are refered to the corresponding predictions from the grooved seal model. There are two parameters in the model, which can be changed slightly, to obtain a better correlation between measured and theoretical results: the average groove depth H_R* and fluid entry swirl at the seal entrance. It was found, that values for the entry swirl between $U_{\Theta o} = 0{,}1\ R\omega$ for low rotational speeds and $U_{\Theta o} = 0{,}3\ R\omega$ for higher rotational speeds and a average groove depth of $H_R^* = 0{,}1$ mm were best suited to fit the theoretical values to the test results. The predicted direct stiffnesses are slightly lower, the direct damping values about 20 % higher than the measured quantities.

The influence of the axial Reynolds number for a constant rotational speed of 4500 rpm is pointed out in fig. 17. Measured as well as predicted parameters show the similar trend for the different seal coefficients. K is increasing in a parabolic curve, C depends linear on the Reynolds number and the cross coupled terms k and c behave indifferent.

Finally in fig. 18 the seal model predictions for the two seal types are compared, in accordance to the measurement results in fig. 15. The results are as follows, an expected decrease of both stiffness coefficients from seal ① to seal ② but a weak difference of the damping parameters for the two seals.

CONCLUDING REMARKS

A theoretical model, based on Childs finite length solution, is presented to determine rotordynamic coefficients and the leakage flow of seals with parallel grooves in the stator. Calculated and measured stiffness and damping values for the investigated seal with eight grooves show, that the developed model is useful for the prediction of this seal type.

Concerning the pump efficiency seals with grooves have the advantage of a lower leakage flow compared to the smooth seal. But the direct and cross coupled stiffness coefficients as well as the direct damping are reduced in the grooved seal configuration. This has to be considered when rotordynamic problems are important.

APPENDIX A: COMPLETE BULK FLOW EQUATIONS

$$-H\frac{\partial p}{\partial z} = \frac{n_R}{2}\rho U_z^2\left(\frac{2HU_z}{\nu}\right)^{m_R}\cdot\left\{1+\left(\frac{U_\theta - R\omega}{U_z}\right)^2\right\}^{(1+m_R)/2} +$$

$$+ C_s' \frac{n_{sz}}{2}\rho U_z^2\left(\frac{2HU_z}{\nu}\right)^{m_{sz}}\cdot\left\{1+\left(\frac{U_\theta}{U_z}\right)^2\right\}^{(1+m_{sz})/2}$$

$$+ \rho H\left(\frac{\partial U_z}{\partial t} + U_z\frac{\partial U_z}{\partial z} + U_\theta\cdot\frac{\partial U_z}{R\partial\theta}\right) - \rho H_R^* U_z \frac{1}{R}\frac{\partial U_\theta}{\partial\theta}$$

$$-\frac{H^*}{R}\frac{\partial p}{\partial\theta} = \frac{n_R}{2}\rho\left(\frac{H^*}{H}\right)^{m_R} U_z(U_\theta - R\omega)\left(\frac{2HU_z}{\nu}\right)^{m_R}\left\{1+\left(\frac{U_\theta - R\omega}{U_z}\right)^2\right\}^{(1+m_R)/2}$$

$$+ C_s'' \frac{n_{s\theta}}{2}\rho\cdot\left(\frac{H^*}{H}\right)^{m_{s\theta}} U_z U_\theta\left(\frac{2HU_z}{\nu}\right)^{m_{s\theta}}\left\{1+\left(\frac{U}{U_z}\right)^2\right\}^{(1+m_{s\theta})/2}$$

$$+ \rho H^*\left(\frac{\partial U_\theta}{\partial t} + \frac{U_\theta}{R}\frac{\partial U_\theta}{\partial\theta} + U_z\frac{\partial U_\theta}{\partial z}\right) - \rho H_R^* U_z\frac{\partial U_\theta}{\partial z}$$

$$\frac{\partial H}{\partial t} + \frac{1}{R}\frac{\partial(HU_\theta)}{\partial\theta} + \frac{\partial(HU_z)}{\partial z} + \frac{1}{R}H_R^*\cdot\frac{\partial U_\theta}{\partial\theta} = 0$$

$$C_s' = \sqrt{\frac{U_z^2}{U_z^2+U_\theta^2} + \left(\frac{n_{s\theta}}{n_{sz}}\right)^2\frac{H^{*\,2m_{s\theta}}}{H^{\,2m_{sz}}}\left(\frac{2}{\nu}\right)^{2(m_{s\theta}-m_{sz})}\left(U_z^2+U_\theta^2\right)^{m_{s\theta}-m_{sz}-1}\cdot U_\theta^2}$$

$$C_s'' = \sqrt{\frac{U_\theta^2}{U_\theta^2+U_z^2} + \left(\frac{n_{sz}}{n_{s\theta}}\right)^2\left(\frac{2}{\nu}\right)^{2m_{sz}-2m_{s\theta}}\cdot\frac{H^{2m_{sz}}}{H^{*2m_{s\theta}}}\left(U_z^2+U_\theta^2\right)^{m_{sz}-m_{s\theta}-1}\cdot U_z^2}$$

APPENDIX B: PERTURBATION COEFFICIENTS

$$B_{sz}\, a_{osz} = \{ 1 + (u_{\theta 0}/b u_{z0})^2 \}^{(1+m_{sz})/2} ; \quad B_{sz} = (1 + 1/4b^2)^{(1+m_{sz})/2}$$

$$B_{s\theta}\, a_{os\theta} = \{ 1 + (u_{\theta 0}/b u_{z0})^2 \}^{(1+m_{s\theta})/2} ; \quad B_{s\theta} = (1 + 1/4b^2)^{(1+m_{s\theta})/2}$$

$$B_R\, a_{oR} = \{ 1 + ([v_{\theta 0}-1]/b u_{z0})^2 \}^{(1+m_R)/2} ; \quad B_R = (1 + 1/4b^2)^{(1+m_R)/2}$$

$$A_{1\theta} = -\{ \alpha_1 [[(m_R-1)(u_{\theta 0}-1) \frac{1}{h_0^*}] + \alpha_2 [v_{\theta 0}((m_{s\theta}-1)\frac{1}{h_0} + D_{a3} + (1-m_{s\theta})\frac{H_R^*}{h_0 h_0^*})] + \frac{u_{z0} H_R^*}{h_0^{*2}} \frac{\partial v_{\theta 0}}{\partial z} \}$$

$$A_{2\theta} = \{ \alpha_1 [1 + (u_{\theta 0}-1)(m_R+1) \frac{v_{\theta 0}-1}{b^2 v_{z0}^2 + (v_{\theta 0}-1)^2}] + \alpha_2 [1 + u_{\theta 0} D_{a2} + \frac{(m_{s\theta}+1) u_{\theta 0}^2}{b^2 u_{z0}^2 + u_{\theta 0}^2}] \}$$

$$A_{3\theta} = \{ \alpha_1 [(u_{\theta 0}-1)(m_R+1) \frac{b^2 u_{z0}}{b^2 u_{z0}^2 + (u_{\theta 0}-1)^2}] + \alpha_2 [u_{\theta 0} (\frac{(m_{s\theta}+1) b^2 u_{z0}}{b^2 u_{z0}^2 + u_{\theta 0}^2} + D_{a1})] + \frac{\partial v_{\theta 0}}{\partial z} \cdot \frac{h_0}{h_0^*} \}$$

$$A_{1z} = -\{ \alpha_3 \frac{u_{z0}}{h_0} (m_R-1) + \alpha_4 (u_{z0} (m_{sz}-1) \cdot \frac{1}{h_0} + D_{e3} u_{z0}) \}$$

$$A_{2z} = \{ \alpha_3 u_{z0} (m_R+1) \frac{v_{\theta 0}-1}{b^2 u_{z0}^2 + (u_{\theta 0}-1)^2} + \alpha_4 (\frac{u_{z0}(m_{sz}+1) u_{\theta 0}}{b^2 u_{z0}^2 + (u_{\theta 0})^2} + D_{e2} u_{z0}) \}$$

$$A_{3z} = \{ \alpha_3 (1 + \frac{u_{z0}(m_R+1) b^2 u_{z0}}{b^2 u_{z0}^2 + (u_{\theta 0}-1)^2} + \alpha_4 (1 + \frac{u_{z0}(m_{sz}+1) b^2 u_{z0}}{b^2 u_{z0}^2 + u_{\theta 0}^2} + D_{e1} u_{z0}) + \frac{2g}{f^2} \}$$

$$\alpha_1 = (\frac{h_0^*}{h_0})^{m_R-1} \cdot \alpha_3 ; \quad \alpha_3 = \frac{1}{2f^2} b_R a_{oR} ;$$

$$\alpha_2 = \frac{1}{2f^2} (\frac{h_0^*}{h_0})^{m_{s\theta}-1} b_{s\theta} a_{os\theta} D_a ; \quad \alpha_4 = \frac{1}{2f^2} b_{sz} a_{osz} D_e ;$$

The parameters D_e, D_a, D_{ei}, D_{ai} are very extensive and therefore not presented. If desired, they can be obtained by the authors.

REFERENCES

1. Childs, D.W., "Finite Length Solutions for Rotordynamic Coefficients of Turbulent Annular Seals", Journal of Lubrication Technology, ASME-Paper No. 82-Lub 42, 1982

2. Childs, D.W. and Chang-Ho Kim, "Analysis and Testing for Rotordynamic Coefficients of Turbulent Annular Seals Different, Directionally Homogeneous Surface-Roughness Treatment for Rotor and Stator Elements", Journal of Tribology, ASME-Paper No. 84-Trib-31, 1985

3. Childs, D.W. and Dressmann J.B., "Testing of Turbulent Seals for Rotordynamic Coefficients", NASA-Conference Publication 2250, Rotordynamic Instability Problems of High Performance Turbomachinery, Proc. of a workshop 1982, pp. 157-171, 1982

4. Nordmann, R. and Maßmann, H., "Identification of Dynamic Coefficients of Annular Turbulent Seals", NASA Conference Publication 2338, Rotordynamic Instability Problems in High Performance Turbomachinery, Proc. of a workshop 1984, pp. 295-311, 1984

5. Maßmann, H. and Nordmann, R., "Some New Results Concerning the Dynamic Behavior of Annular Turbulent Seals", NASA-Conference Publication 2409, Instability in Rotating Machinery, Proceedings of a Symposium held in Carson City, pp. 179-194, 1985

6. Black, H.F. and Cochrane, E.A., "Leakage and Hybrid Bearing Properties of Serrated Seals in Centrifugal Pumps", Paper G5, 6-th International Conference on Fluid Sealing, Munich 1973, pp. G5-61 - G5-70

7. Chang-Ho Kim and Childs D.W., "Analysis and Testing for Rotordynamic Coefficients of Grooved Turbulent Annular Seals", Turbomachinery Report Texas A&M University, June 1985.

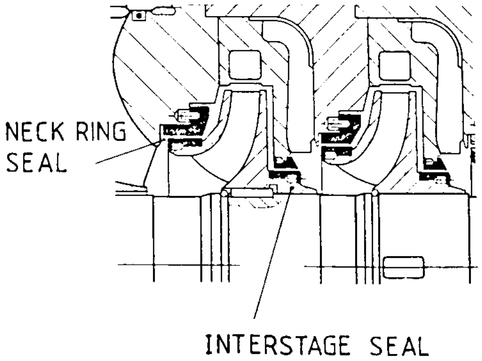

Figure 1. - Seal types in turbopumps

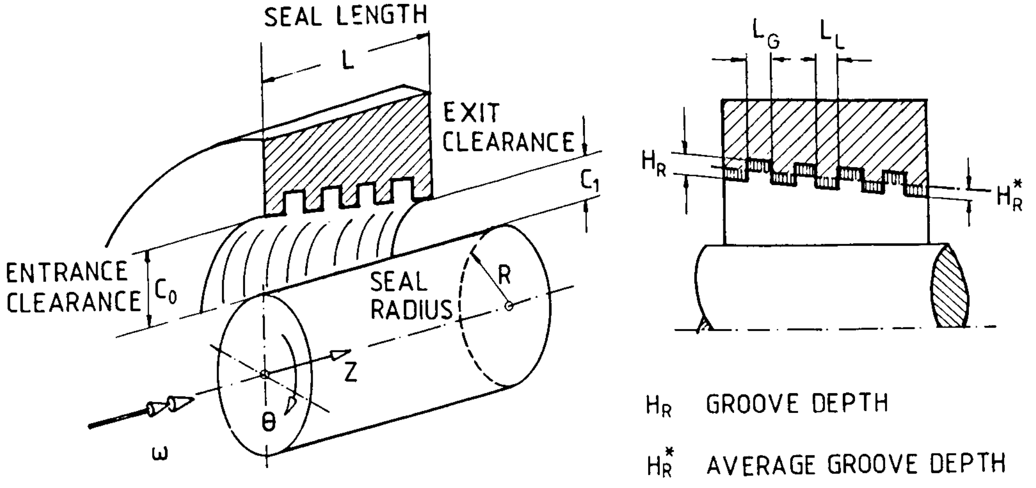
SEAL LENGTH
L
EXIT CLEARANCE
C_1
ENTRANCE CLEARANCE
C_0
SEAL RADIUS
R
Z
θ
ω
L_G
L_L
H_R
H_R^*
H_R GROOVE DEPTH
H_R^* AVERAGE GROOVE DEPTH

Figure 2. - Seal with parallel grooves in the stator

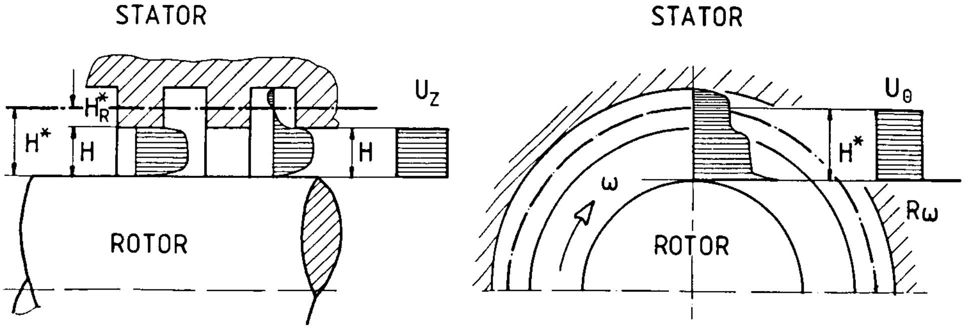
STATOR
H_R^*
H^*
H
H
U_Z
ROTOR
STATOR
U_θ
H^*
ω
$R\omega$
ROTOR

BULK FLOW FLUID VELOCITY U_Z IN AXIAL DIRECTION

BULK FLOW FLUID VELOCITY U_θ IN CIRCUMFERENTIAL DIRECTION

Figure 3. - Bulk flow velocities

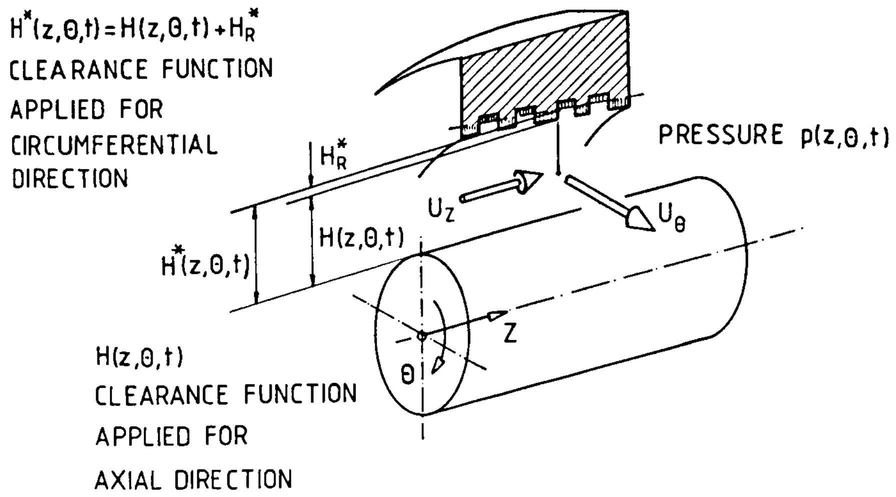
$H^*(z,\theta,t) = H(z,\theta,t) + H_R^*$
CLEARANCE FUNCTION
APPLIED FOR
CIRCUMFERENTIAL
DIRECTION
H_R^*
PRESSURE $p(z,\theta,t)$
U_Z
U_θ
$H(z,\theta,t)$
$H^*(z,\theta,t)$
Z
θ
$H(z,\theta,t)$
CLEARANCE FUNCTION
APPLIED FOR
AXIAL DIRECTION

Figure 4. - Variables of the bulk flow model

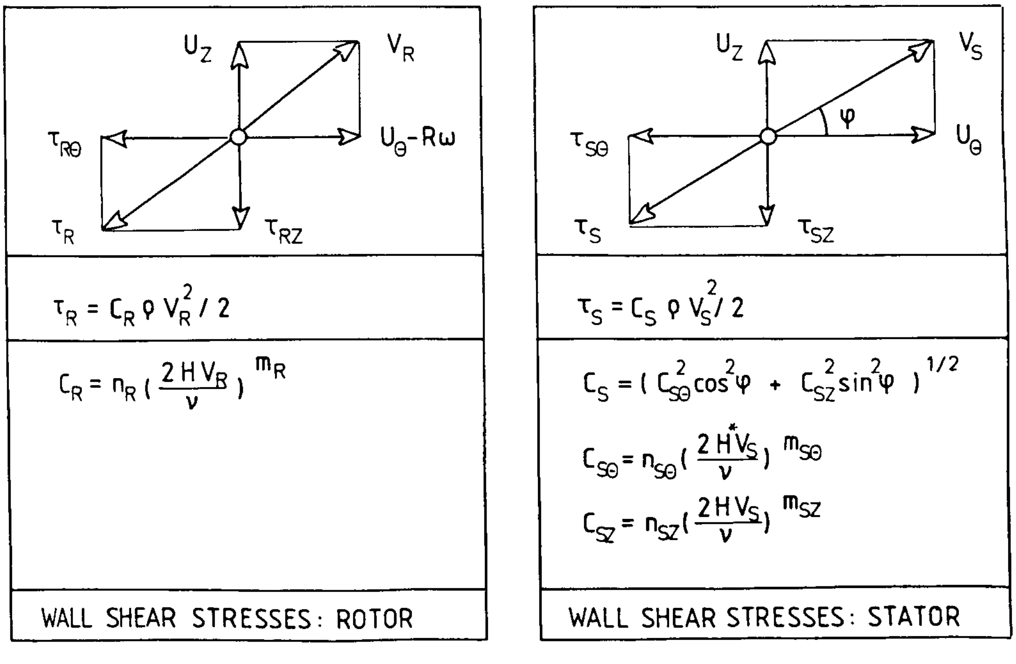
U_Z
V_R
$\tau_{R\theta}$
$U_\theta - R\omega$
τ_R
τ_{RZ}
U_Z
V_S
φ
$\tau_{S\theta}$
U_θ
τ_S
τ_{SZ}
WALL SHEAR STRESSES: ROTOR
WALL SHEAR STRESSES: STATOR

$$\tau_R = C_R \rho V_R^2 / 2$$

$$C_R = n_R \left(\frac{2 H V_R}{\nu} \right)^{m_R}$$

$$\tau_S = C_S \rho V_S^2 / 2$$

$$C_S = \left(C_{S\theta}^2 \cos^2\varphi + C_{SZ}^2 \sin^2\varphi \right)^{1/2}$$

$$C_{S\theta} = n_{S\theta} \left(\frac{2 H^* V_S}{\nu} \right)^{m_{S\theta}}$$

$$C_{SZ} = n_{SZ} \left(\frac{2 H V_S}{\nu} \right)^{m_{SZ}}$$

Figure 5. - Wall shear stresses

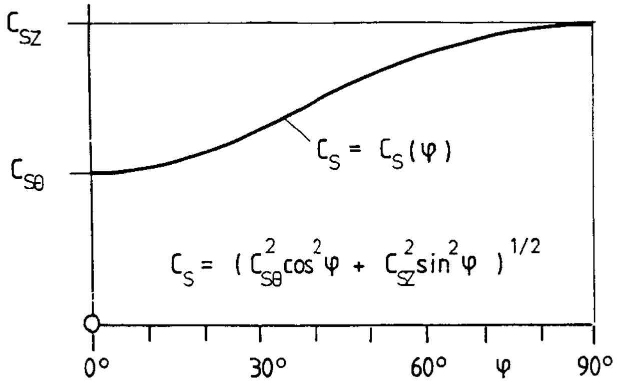

Figure 6. - Stator friction factor in dependence of the flow angle

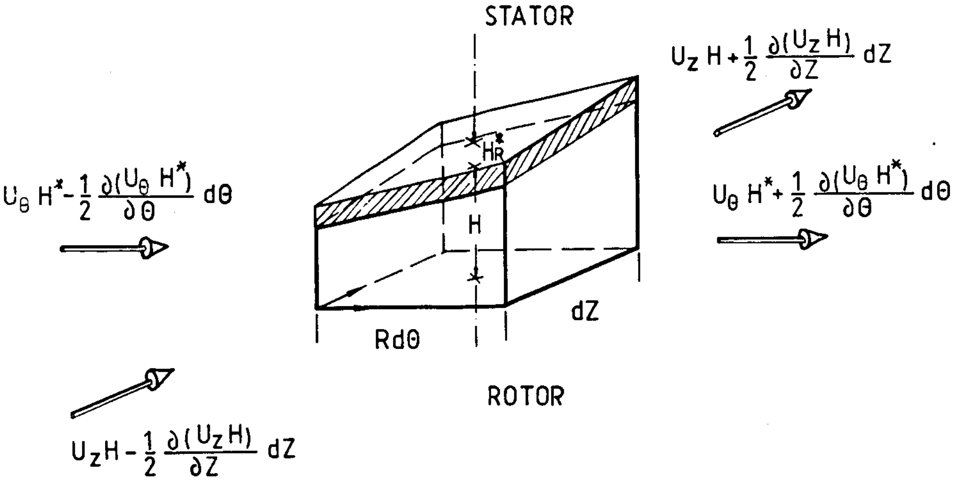
STATOR
$U_Z H + \frac{1}{2}\frac{\partial(U_Z H)}{\partial Z} dZ$
$U_\theta H^* - \frac{1}{2}\frac{\partial(U_\theta H^*)}{\partial \theta} d\theta$
H_R^*
H
$U_\theta H^* + \frac{1}{2}\frac{\partial(U_\theta H^*)}{\partial \theta} d\theta$
dZ
Rdθ
ROTOR
$U_Z H - \frac{1}{2}\frac{\partial(U_Z H)}{\partial Z} dZ$

Figure 7. - Bulk flow velocities at differential element

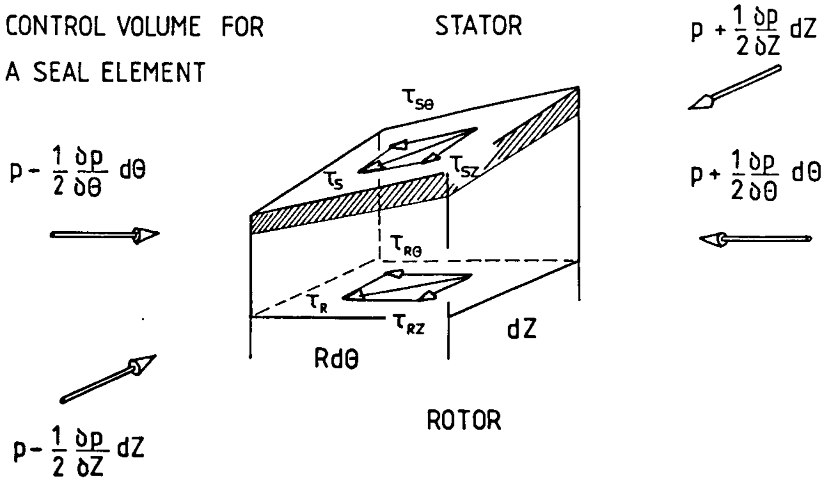
CONTROL VOLUME FOR
A SEAL ELEMENT
STATOR
$p+\frac{1}{2}\frac{\delta p}{\delta Z}dZ$
$\tau_{S\theta}$
$p-\frac{1}{2}\frac{\delta p}{\delta \theta}d\theta$
τ_S
τ_{SZ}
$p+\frac{1}{2}\frac{\delta p}{\delta \theta}d\theta$
$\tau_{R\theta}$
τ_R
τ_{RZ}
dZ
Rdθ
ROTOR
$p-\frac{1}{2}\frac{\delta p}{\delta Z}dZ$

Figure 8. - Control volume for a seal element with pressure and shear stresses

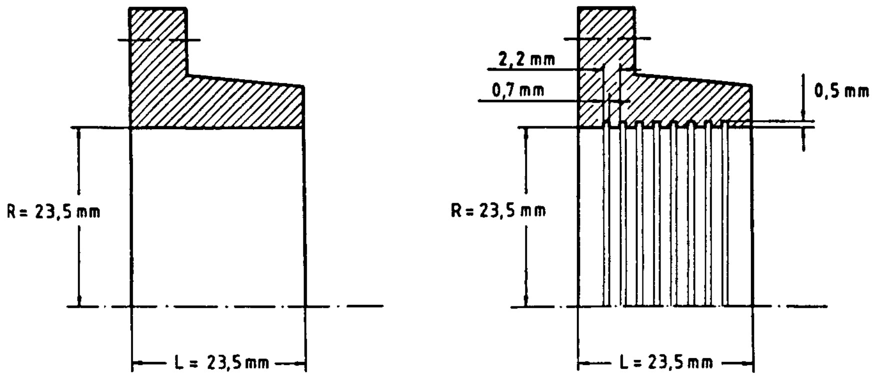
R = 23,5 mm
L = 23,5 mm
2,2 mm
0,7 mm
0,5 mm
R = 23,5 mm
L = 23,5 mm

STATOR OF SEAL ① WITHOUT
PARALLEL GROOVES

STATOR OF SEAL ② WITH
8 PARALLEL GROOVES

Figure 9. - Investigated seals with and without grooves

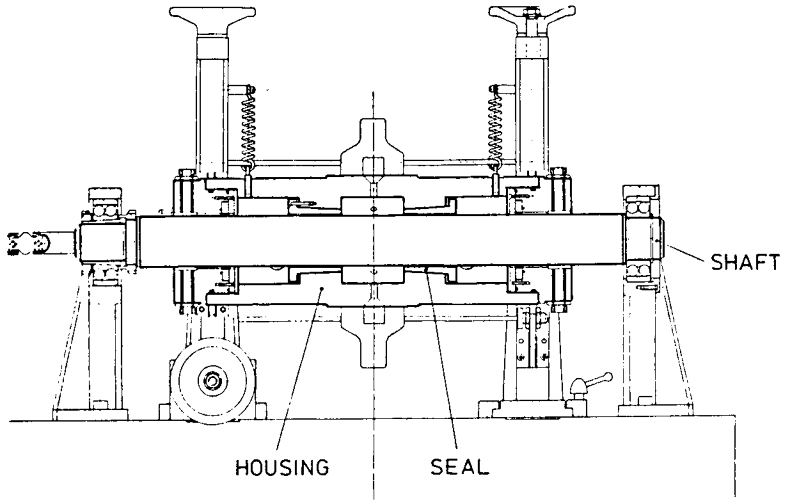
SHAFT
HOUSING
SEAL

Figure 10. - Seal test rig

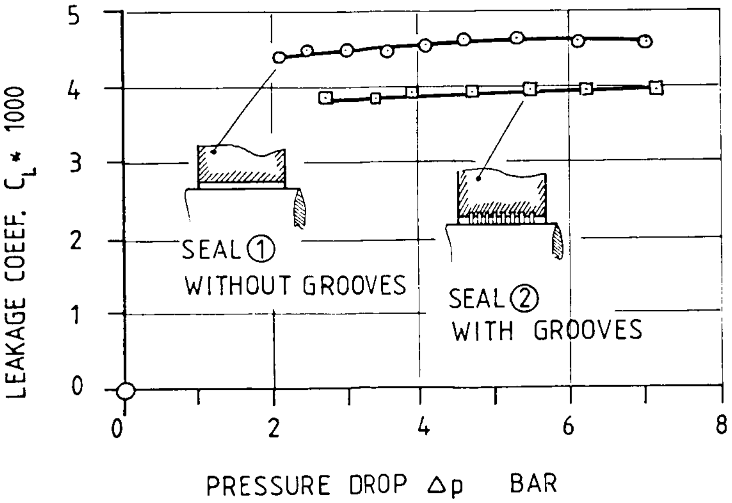

Figure 11. - Leakage coefficients for seal 1 and seal 2

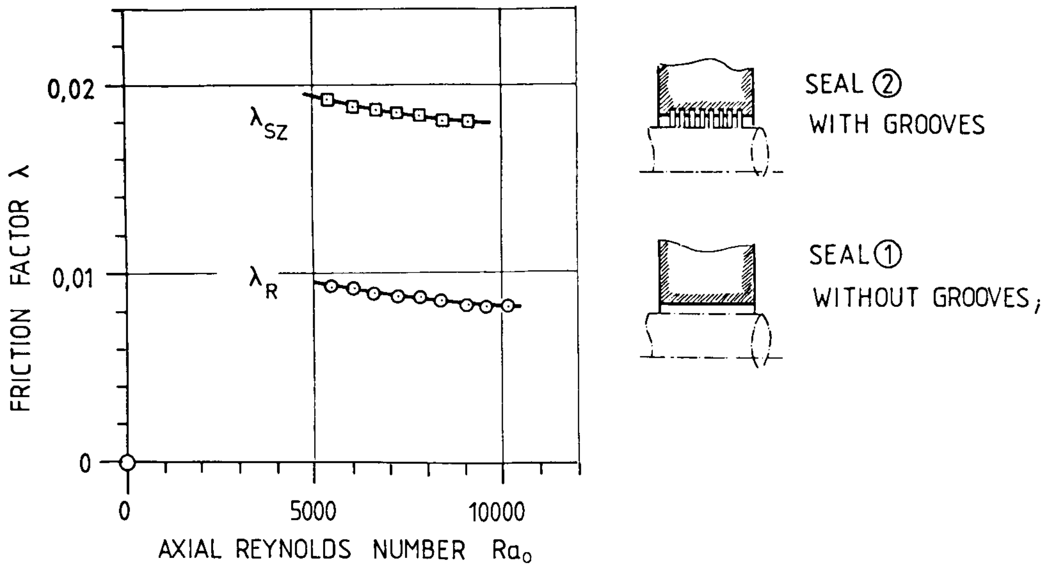

Figure 12. - Friction factors for the stators of seal 1 and seal 2

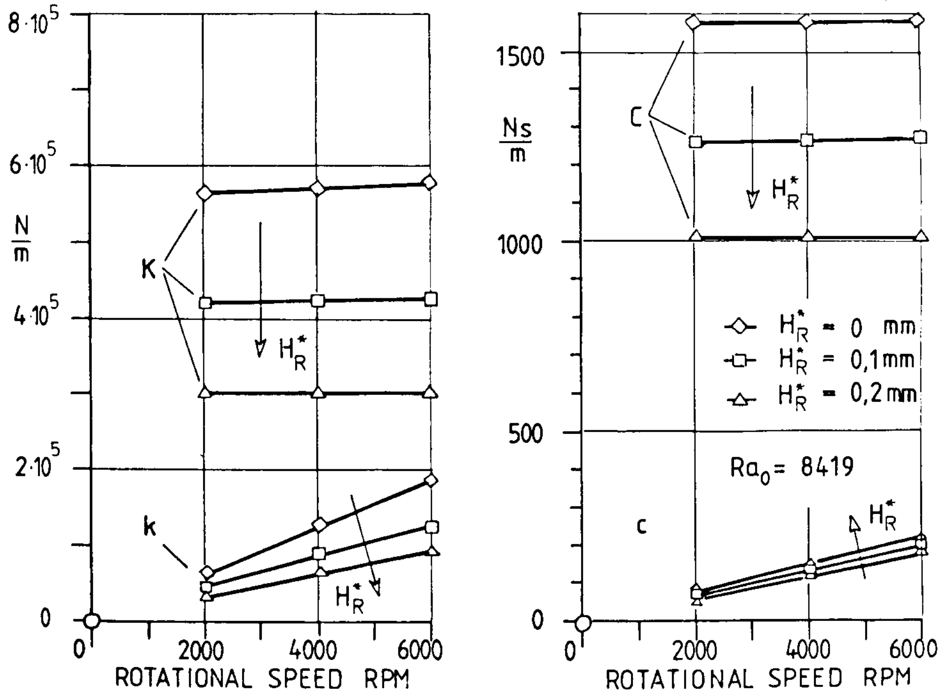

Figure 13. - Calculated stiffness and damping coefficients of a grooved seal in dependence of the rotational speed and the average groove depth

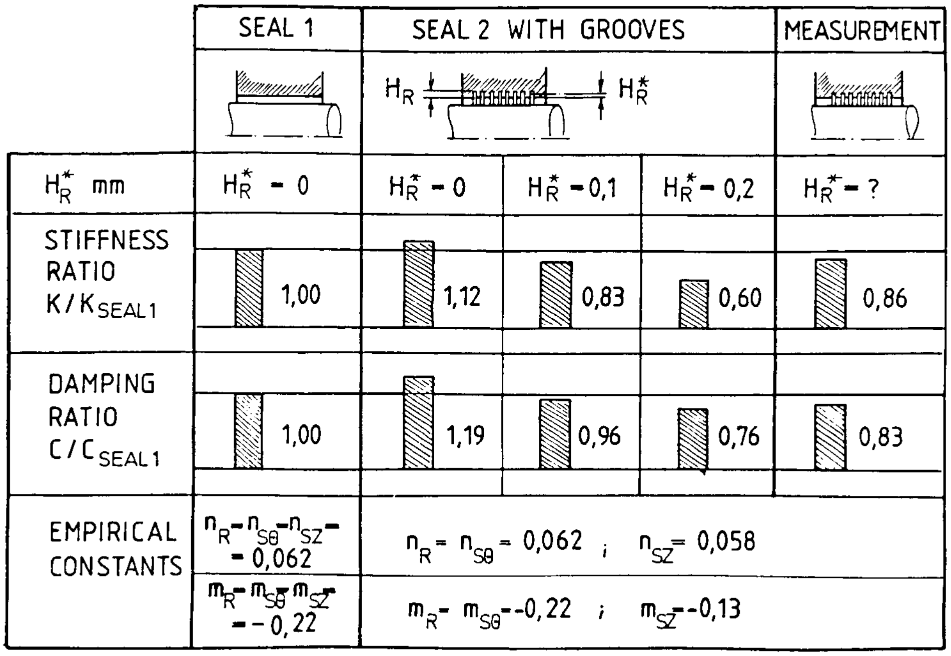

	SEAL 1	SEAL 2 WITH GROOVES			MEASUREMENT
H_R^* mm	$H_R^* = 0$	$H_R^* = 0$	$H_R^* = 0{,}1$	$H_R^* = 0{,}2$	$H_R^* = ?$
STIFFNESS RATIO K/K_{SEAL1}	1,00	1,12	0,83	0,60	0,86
DAMPING RATIO C/C_{SEAL1}	1,00	1,19	0,96	0,76	0,83
EMPIRICAL CONSTANTS	$n_R = n_{S\theta} = n_{SZ} = 0{,}062$	$n_R = n_{S\theta} = 0{,}062$; $n_{SZ} = 0{,}058$			
	$m_R = m_{S\theta} = m_{SZ} = -0{,}22$	$m_R = m_{S\theta} = -0{,}22$; $m_{SZ} = -0{,}13$			

Figure 14. - Comparison of calculated and measured direct stiffness and damping coefficients for seals 1 and 2

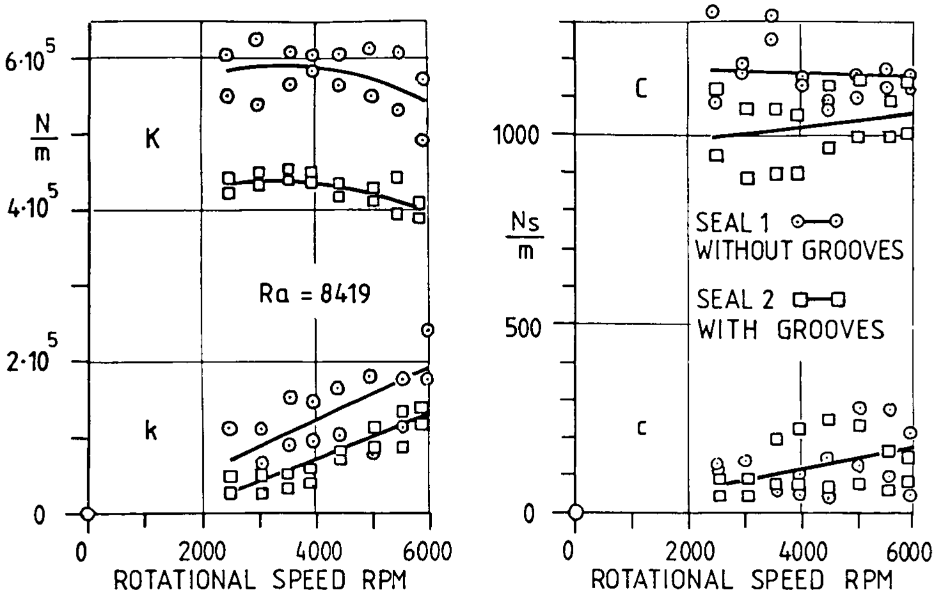

Figure 15. - Measured stiffness and damping coefficients in dependence of rotational speed for seals 1 and 2

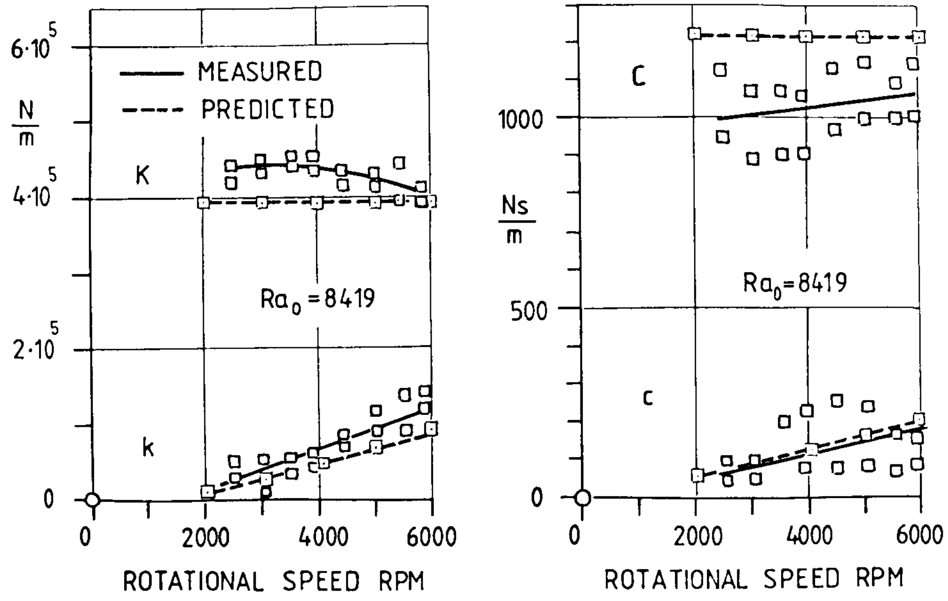

Figure 16. - Measured and predicted stiffness and damping coefficients in dependence of rotational speed for the grooved seal 2

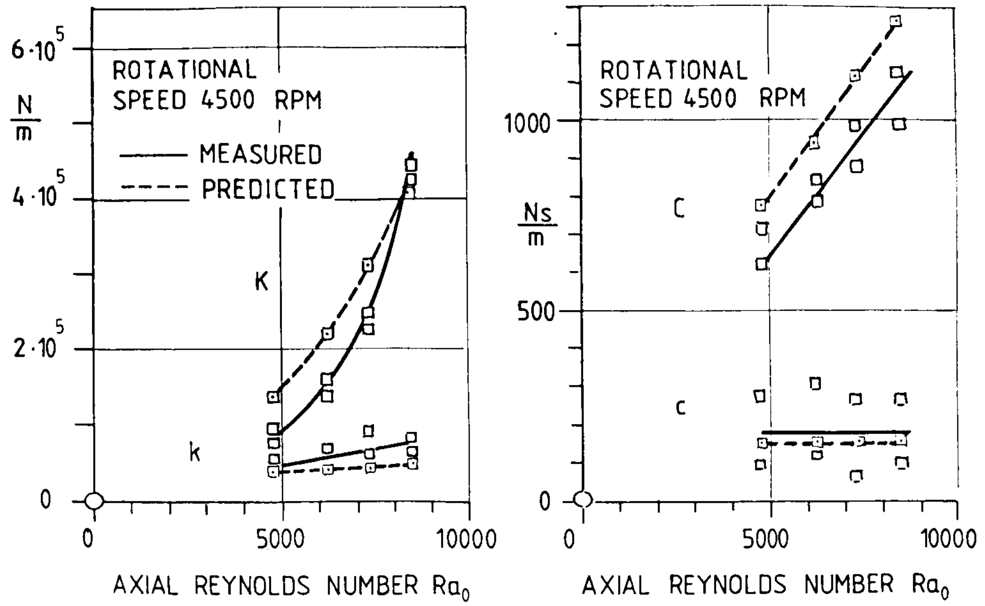

Figure 17. - Measured and predicted stiffness and damping coefficients in dependence of the axial Reynolds number for the grooved seal 2

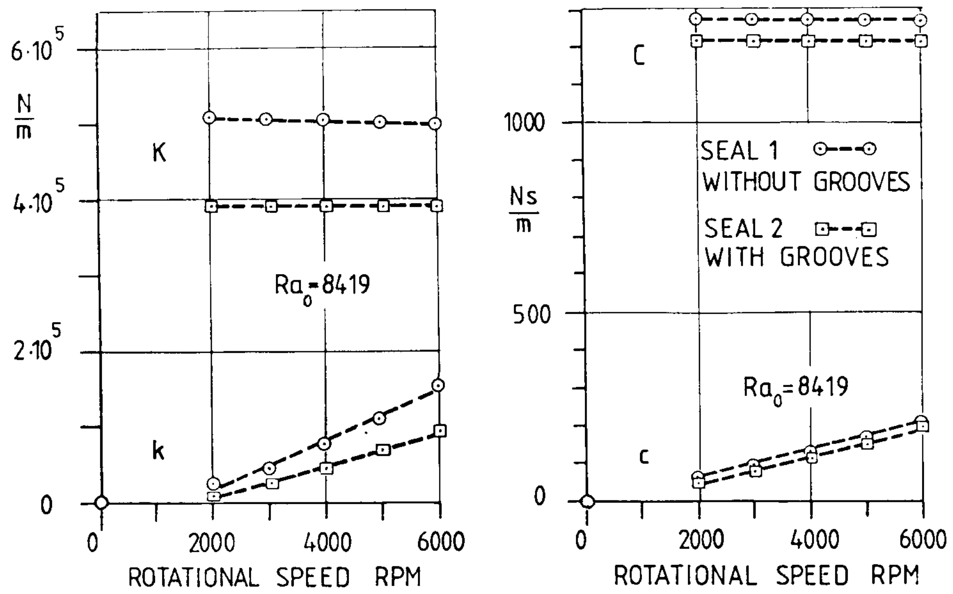

Figure 18. - Predicted stiffness and damping coefficients in dependence of rotational speed for seals 1 and 2

N87-22207

THEORETICAL APPROACH TO OBTAINING DYNAMIC CHARACTERISTICS OF NONCONTACTING SPIRAL-GROOVED SEALS

Takuzo Iwatsubo
Kobe University
Rokko, Nada, Kobe, 657, Japan

Bo-suk Yang
The National Fisheries University of Pusan
599, Daeyon-dong, Nam-ku, Pusan, Korea

Ryuji Ibaraki
Toyota Motor Corporation
1, Toyota-cho, Toyota, 471, Japan

In this paper the dynamic characteristics of spiral-grooved seals are theoretically obtained by using the Navier-Stokes equation. First, with the inertia term of the fluid considered, the flow and pressure in the steady state are obtained for the directions parallel to and perpendicular to the groove. Next, the dynamic character is obtained by analyzing the steady state by analyzing the labyrinth seal.

As a result, the following conclusions were drawn:

(1) As the land width becomes shorter or the helix angle decreases, the cross-coupling stiffness, direct and cross-coupling damping, and add mass coefficients decrease.

(2) As the axial Reynolds number increases, the stiffness and damping coefficients increase. But the add mass coefficient is not influenced by the axial Reynolds number.

(3) The rotational Reynolds number influences greatly the direct and cross-coupling stiffness and direct damping coefficients.

(4) As the journal rotating frequency increases, the leakage flow decreases. Therefore zero net leakage flow is possible at a particular rotating frequency.

INTRODUCTION

High-performance pumps, (i.e., those operating at high rotating speed and high pressure) are used in chemical plants, rocket engines, etc.. These pumps sometimes yield nonsynchronous vibration that is induced by the journal bearings or noncontacting seals. The instability of rotors supported by a journal bearing has been studied very well. However the noncontacting seal, which sometimes induces a nonsynchronous vibration or instability to the pumps, has not been investigated.

PRECEDING PAGE BLANK NOT FILMED

The dynamic characteristics of some noncontacting pump seals (the annular plain seal, the tapered seal, and the stepped seal) have been theoretically investigated by Black (refs. 1 and 2), Childs (refs. 3 and 4), and Yang et al. (ref. 5), but there have been no investigations using the theory of fluid dynamics on the parallel-grooved and spiral-grooved seals. Childs studied the parallel-grooved seal by using only a rough approximation. On the other hand, the parallel-grooved labyrinth seal has been investigated by Kostyuk (ref. 6) and Iwatsubo, et al. (ref. 7). For the investigation of the spiral-grooved seal, we studied steady-state characteristics from the viewpoint of leakage. This study was based on investigations of the spiral journal bearing; that is, Whipple (ref. 8) presents a basic idea to analyze the characteristics of the thrust spiral-grooved bearing, Vohr (refs. 9 and 10) and Passera (ref. 11) present an approximate method using creeping flow analysis (which assumes that the groove number is infinitely large), and Zuk (ref. 12) analyzes the static characteristics of the spiral-grooved seal by solving the Navier-Stokes equation with a finite difference method. But all these analyses are for the static characteristics and there are no investigations of the dynamic characteristics.

This paper presents an analytical method to obtain the dynamic characteristics by solving a Navier-Stokes equation with the perturbation method. First the steady-state flow and pressure distribution in the axial direction are obtained by considering the pumping effect due to the spiral groove. Then the dynamic characteristics are obtained at the steady-state condition, and the dynamic force is represented by the matrix form.

SYMBOLS

$C_{\ell o}$	mean clearance
D	seal diameter
F	flow induced force
H	thickness of fluid film
I_s	thread number
L	seal length
L_g	groove width
L_ℓ	land width
$L_{\ell g}$	L_ℓ/L_g
L_s	number of lands for one thread
NN	number of land and groove sections
P	pressure
ΔP	pressure difference
Q	leakage flow rate

R	journal radius
R_a	axial Reynolds number
R_e	Reynolds number
R_r	circumferential Reynolds number
T	depth of ditch
t	time
u	circumferential fluid velocity
w	axial fluid velocity
x, y, z	coordinates (see fig. 2)
α	spiral angle
ε	perturbation coefficient
θ	divergent flow angle
λ	friction coefficient
μ	viscous coefficient
ξ	loss factor
ξ, η, ζ	coordinates (see fig. 2)
ρ	density
τ	shear stress

Subscripts:

a	axial direction
c	radial direction
d	ditch (mainly used for vortex in ditch)
ex	exit
f	between clearance flow and cavity flow
g	groove
in	inlet
j	journal
l	land

m	mean velocity
r	circumferential direction
s	casing
$(\bar{\cdot})$	time mean

GOVERNING EQUATION AND MODELING OF SPIRAL-GROOVED SEAL

Governing Equation

Figure 1 illustrates the geometry of the spiral-grooved seal. Under the usual assumptions for problems of through flow across annuli with fine clearances, the continuity and momentum equations are represented as follows (ref. 13):

Continuity equation,

$$\frac{\partial H}{\partial t} + \frac{\partial (H u_m)}{\partial x} + \frac{\partial (H w_m)}{\partial z} = 0 \tag{1}$$

where u_m and w_m are mean fluid velocity components in the tangential and axial directions.

Momentum equation in the x-direction,

$$\rho H \left\{ \frac{\partial u_m}{\partial t} + u_m \frac{\partial u_m}{\partial x} + w_m \frac{\partial u_m}{\partial z} \right\} = -H \frac{\partial P}{\partial x} + \left. \tau_{tr} \right|_0^H \tag{2}$$

Momentum equation in the z-direction,

$$\rho H \left\{ \frac{\partial w_m}{\partial t} + u_m \frac{\partial w_m}{\partial x} + w_m \frac{\partial w_m}{\partial z} \right\} = -H \frac{\partial P}{\partial z} + \left. \tau_{ta} \right|_0^H \tag{3}$$

Modeling

There are three kinds of spiral-grooved seals, (1) those with the groove on the journal (fig. 1), (2) those with the groove on the casing, and (3) those with grooves on both journal and casing. In this paper the seal with the groove on the journal is analyzed. Figure 2 is an expanded figure of the spiral-grooved seal. Configuration parameters are indicated on this figure; these are spiral angle α, land width L_l, groove width L_g, seal diameter D, and thread number I_s. These parameters are related as follows:

$$\left.\begin{aligned} L = \pi D \tan\alpha \times L_s \qquad L_g &= \frac{\pi D \sin\alpha}{I_s} \times (1 - L_{lg}) \\ L_l &= \frac{\pi D \sin\alpha}{I_s} \times L_{lg} \end{aligned}\right\} \tag{4}$$

where L_s is number of lands for one thread in the axial direction and $L_{lg} = L_l/L_g$. For the analysis two coordinates are used: one is the η-y-ζ coordinate, which is used for the static analysis and the other is the x-y-z coordinate, which is used for the analysis of dynamic characteristics.

For the analysis the following are assumed:

(1) The fluid is liquid and noncompressible.

(2) Flow in the land in the η-direction is assumed to be a flow between two parallel plates, and flow in the groove is assumed to be a flow in a rectangular cross section and is approximated to the flow in a circular tube.

(3) Flow in the ζ-direction diverges with the angle θ and goes to the next land.

(4) The vortex is formed in the ξ-direction of the groove. But the heat energy is negligibly small.

(5) When the journal deviates a little from the center, the streamline in the groove deviates in the same manner.

DERIVATION OF SHEAR STRESS IN MOMENTUM EQUATION

The shear stress term of equation (3) is derived for the spiral-grooved seal. The friction coefficient of the annular seal is represented by a Reynolds number (ref. 14). But it is very difficult to represent the friction coefficient of the spiral-grooved seal in the same way because the groove is spiral. So the friction coefficient equation derived by Hirs (ref. 15) is used in this analysis. The equation of the friction coefficient between two plates is represented as

$$\lambda = 0.066\ Re^{-0.25} \tag{5}$$

where the velocity used in the Reynolds number is the equivalent mean velocity that includes the pumping action of the spiral-grooved seal. This equivalent mean velocity is used to obtain the shear stress.

Land

The shear stresses of the casing and journal parts in the axial direction (z-direction) τ_{lsa}, τ_{lja} are represented by the formula for the flow between two parallel plates,

$$\tau_{lsa} = -\tau_{lja} = \frac{1}{2}\rho\lambda_{la}w^2_{lm} \qquad \lambda_{la} = 0.066\left(\frac{w_{lm}H_l}{\nu}\right)^{-0.25} \tag{6}$$

Therefore the shear stress term of equation (3) becomes as

$$\tau_{ta}\Big|_0^H = \tau_{lja} - \tau_{lsa} = -2\cdot\frac{1}{2}\rho\lambda_{la}w^2_{lm} \tag{7}$$

Groove

In the groove, flow is divided into two regions: the jet flow region and the vortex region. The shear stress of the casing part of the jet region in the axial direction τ_{gsa} is represented by the formula of the flow between two parallel plates,

$$\tau_{gsa} = \frac{1}{2}\rho\lambda_{ga}w^2_{gm} \qquad \lambda_{ga} = 0.066\left(\frac{w_{gm}H_g}{\nu}\right)^{-0.25} \tag{8}$$

It is assumed that the energy loss in the groove vortex region is represented by the friction loss between the clearance flow and vortex flow. Assuming that the friction between the vortex and the jet flow λ_f is 0.1 and that the axial velocity component of the vortex w_{dm} is set to one-half of the jet flow w_{gm} (ref. 16), the shear stress of the flow τ_{gfa} becomes

$$\tau_{gfa} = -\frac{1}{2}\rho\lambda_f\,(\,w_{gm} - w_{dm}\,)^2 = -\frac{1}{2}\rho 0.25\lambda_f w^2_{gm} \tag{9}$$

Therefore the shear stress term in the groove is obtained from equations (8) and (9) as

$$\tau_{ta}\Big|_0^H = \tau_{gfa} - \tau_{gsa} = -\frac{1}{2}\rho 0.25\lambda_f w^2_{gm} - \frac{1}{2}\rho\lambda_{ga}w^2_{gm}$$

$$= -\frac{1}{2}\rho(\lambda_{ga} + 0.25\lambda_f)w^2_{gm} \tag{10}$$

DERIVATION OF STEADY FLOW AND STATIC CHARACTERISTICS

Axial and Circumferential Velocity of Steady Flow

As described before, the η-y-ζ coordinate system is used for the analysis of static characteristics. References 10 and 11 describe investigations of the static characteristics of the spiral-grooved seal. In these investigations, the residual seal pressure is obtained when seal leakage becomes zero because of the pressure induced by spiral pumping action. This residual pressure is a function of the seal configuration, and the seal coefficient can be represented by the nondimensional form. Boon et al. (ref. 17) obtained the seal coefficient of laminar flow, and Mori, et al. obtained the same by experiment. The seal coefficient $S.C._{laminar}$ for the laminar flow is

$$S.C._{laminar} = \left(\frac{6\mu R\omega}{C_{lo}^2}\right) \Bigg/ \left(\frac{\Delta P_{laminar}}{L}\right)$$

$$= \frac{\kappa^3(1+\tan^2\alpha)+L_{lg}(1-L_{lg})(\kappa^3-1)^2\tan^2\alpha}{L_{lg}(1-L_{lg})(\kappa^3-1)(\kappa-1)\tan\alpha} \tag{11}$$

where $\kappa = H_g/H_e$. THe pressure induced by the spiral pumping action ΔPlaminar for the laminar flow is

$$\Delta P_{laminar} = \frac{6\mu R\omega L}{C_{lo}^2} \cdot \frac{L_{lg}(1-L_{lg})(\kappa^3-1)(\kappa-1)\tan\alpha}{\kappa^3(1+\tan^2\alpha)+L_{lg}(1-L_{lg})(\kappa^3-1)^2\tan^2\alpha} \tag{12}$$

Vohr (ref. 10) compared the seal coefficient for turbulent flow with that for laminar flow by experiment. He obtained the pressure ratio C_t of the seal coefficient of the turbulent and laminar flow as

$$C_t = \frac{\Delta P_{turbulent}}{\Delta P_{laminar}} = 0.0159\ R_r^{0.778} \tag{13}$$

Then the pressure $\Delta P_{turbulent}$ induced by the spiral pumping action in turbulent flow is

$$\Delta P_{turbulent} = \frac{0.0951\mu R\omega L R_r^{0.778}}{C_{lo}^2}$$

$$\times \frac{L_{lg}(1-L_{lg})(\kappa^3-1)(\kappa-1)\tan\alpha}{\kappa^3(1+\tan^2\alpha)+L_{lg}(1-L_{lg})(\kappa^3-1)^2\tan\alpha} \tag{14}$$

Since the pressure difference equation (14) acts to resist the pressure difference in the seal ΔP, the pressure difference in the seal becomes smaller than the pressure difference between both seal ends. This pressure difference is called the apparent pressure difference $\Delta P'$; that is,

$$\Delta P' = \Delta P - \Delta P_{turbulent} \tag{15}$$

This apparent pressure difference acts on the seal and on the fluid flow in the seal. This flow is separated into η- and ζ-directions and the fluid velocities in each direction and in each part are derived in order to calculate the dynamic-flow-induced force in each stage. Then total force is obtained by summing up the lateral force of each stage.

Fluid velocity parallel to groove direction for land. - The relation between the pressure and velocity within the two parallel plates is also considered in the land region;

$$\Delta P' = \frac{1}{2}\rho(1+\xi_{l\eta in})w^2_{l\eta o} + \frac{1}{2}\rho\lambda_{l\eta}w^2_{l\eta o}\cdot\frac{2L}{C_{lo}\sin\alpha} + \frac{1}{2}\rho\left(1-\frac{C_{lo}}{C_{lo}+T\infty}\right)^2 w^2_{l\eta o} \tag{16}$$

The first term on the right-hand side of equation (16) represents the inlet pressure loss. The inlet pressure loss of the land is larger than that of the groove because the inlet clearance of the land is smaller than that of the groove and because the fluid flows into the groove. The second term on the right-hand side of equation (16) represents the pressure loss due to wall friction. The third term represents the outlet pressure loss. The value $\lambda_{l\eta}$ is obtained using equation (5), and $\xi_{l\eta in}$ is the inlet pressure loss coefficient, which is 0.5 for the first stage and is represented as follows after the second stage:

$$\left.\begin{aligned} \xi_{l\eta in} &= 1+0.824\delta_2 - (1+0.824\delta_1)(H_2/H_1)^2 \\ \delta_1 &= 1.95(w_{lO}H_1/\nu)^{-0.43} \\ \delta_2 &= 1.95(w_{lO}H_2/\nu)^{-0.43} \end{aligned}\right\} \tag{17}$$

Therefore if equation (14) is iteratively calculated so that $w_{l\eta 0}$ in function λ coincides with $w_{l\eta 0}$ in equation (16), the flow velocity of the land $w_{l\eta}$ is obtained.

Fluid velocity parallel to the groove direction for groove. - Since the groove is deep enough, the groove is considered to be a rectangular pipe and can be approximated as a circular pipe. The equivalent radius of the rectangular pipe MG (ref. 18) is

$$MG = \frac{L_g(C_{lo}+T)}{2(L_g+C_{lo}+T)} \tag{18}$$

The friction coefficient of the turbulent circular pipe λ_d (ref. 18) is

$$\lambda_d = 0.791\left(\frac{w_{g\eta o}\cdot 4MG}{\nu}\right)^{-0.25} \tag{19}$$

Therefore the apparent pressure difference $\Delta P'$ is written as follows:

$$\Delta P' = \frac{1}{2}\rho(1+\xi_{g\eta in})w_{g\eta o}^2 + \frac{1}{2}\rho\lambda_d w_{g\eta o}^2 \frac{L_g}{\sin\alpha}\cdot\frac{1}{MG} + \frac{1}{2}\rho\left(1-\frac{C_{lo}+T}{C_{lo}+T_\infty}\right)^2 w_{g\eta o}^2 \tag{20}$$

In this equation the first term on the right-hand side represents the inlet pressure loss of the groove. This inlet pressure loss is smaller than that of the land, because the groove has a larger cross section than the land and because the liquid flows mainly into the groove. The second term represents the pressure loss due to wall friction, and the third term represents the outlet pressure loss of the seal. After $\xi_{g\eta in}$ is obtained by using equation (17), the velocity in the groove in the η-direction $w_{g\eta 0}$ is similarly obtained by iteratively calculating equation (20).

Fluid velocity perpendicular to groove direction. - The flow in the ζ-direction is derived by a method similar to that used to obtain the steady flow of the parallel-grooved seal. Conventional evaluation of the loss of the groove region was not clear. Yamada (ref. 19) obtained the friction coefficient of both the land and the groove by experimental methods. According to his results, as the groove region increases in relation to the land region, the friction coefficient increases as shown in figure 3. This friction coefficient is represented by using the results of reference 19

$$\lambda = 0.26\cdot Re^{-0.24}\cdot 3.31^{1-L_{lg}} \tag{21}$$

From the pressure drop relation the following is obtained:

$$\lambda(L_l+L_g) = \lambda_l L_l + \lambda_g L_g \tag{22}$$

where λ_l is a friction coefficient of flow between two parallel plates. Then the friction coefficient of the groove λ_g is obtained from equations (21) and (22),

$$\lambda_g = 0.26\ Re^{-0.24}\left\{3.31^{1-L_{lg}} + \frac{L_l}{L_g}\left(3.31^{1-L_{lg}} - 1\right)\right\} \tag{23}$$

Therefore the apparent pressure difference in the ζ-direction is obtained by summing each stage of the land and groove, respectively,

$$\Delta P' = \frac{1}{2}\rho(1+\xi_{\zeta in})w^2_{l\zeta o} + NN\cdot\frac{1}{2}\rho\lambda_{l\zeta}w^2_{l\zeta o}\frac{2L_l}{C_{lo}}$$

$$+ (NN-1)\cdot\frac{1}{2}\cdot\rho\lambda_g w^2_{l\zeta o}\frac{L_g}{2C_{lo}} + \frac{1}{2}\rho\left(1-\frac{C_{lo}}{C_{lo}+T\infty}\right)^2 w^2_{l\zeta o} \qquad (24)$$

In this equation the first term on the right-hand side represents the inlet pressure loss of the seal, the second and the third terms represent the pressure loss due to wall friction, and the fourth term represents the outlet pressure loss of the seal. The term $\lambda_{l\zeta}$ in this equation is defined in equation (5), $\xi_{\zeta in}$ is defined in equation (17) and NN is the number of the land and groove sections in the ζ-direction. Then the velocity in the ζ-direction $w_{l\zeta 0}$ is obtained by a similar iterative calculation.

Fluid velocity in circumferential and axial directions. - The steady-flow velocity in the x- and z-directions is obtained from the previously calculated steady-flow velocities $w_{l\eta o}$, $w_{g\eta o}$, and $w_{l\zeta o}$ by translating the coordinate system as

$$\begin{pmatrix} u'_{lo} \\ w_{lo} \end{pmatrix} = \begin{pmatrix} \cos\alpha & -\sin\alpha \\ \sin\alpha & \cos\alpha \end{pmatrix}\begin{pmatrix} w_{l\eta o} \\ w_{l\zeta o} \end{pmatrix} \qquad \begin{pmatrix} u'_{go} \\ w_{go} \end{pmatrix} = \begin{pmatrix} \cos\alpha & -\sin\alpha \\ \sin\alpha & \cos\alpha \end{pmatrix}\begin{pmatrix} w_{g\eta o} \\ w_{g\zeta o} \end{pmatrix} \qquad (25)$$

where u'_{lo} and u'_{go} are the velocities relative to the journal. Therefore the absolute velocities in the circumferential direction become

$$u_{lo} = V - u'_{lo} \qquad u_{go} = V - u'_{go} \qquad (26)$$

Leakage Flow Rate

Because the leakage flow rates of the land and groove are different, they are considered separately. The leakage flow rate for the land is represented by the relation of the cross-sectional area and velocity,

$$Q_l = I_s \times \frac{L_{lg}}{I_s}\int_{R+T}^{R+T+C_{lo}} w_{lo}2\pi r dr = \pi C_{lo}\left\{2(R+T)+C_{lo}\right\}L_{lg}w_{lo} \qquad (27)$$

The leakage flow rate for the groove is derived by separating the clearance flow from the cavity flow. The leakage flow rate of the clearance flow in the axial direction is represented as

$$Q_{gc} = I_s \int_0^{L_g/\sin\alpha} w_{go} c_{go} dx$$

$$= I_s \left[\frac{1}{2} L_g (2C_{lo} + L_g \tan\theta) w_{g\eta o} \sin\alpha + \frac{C_{lo} L_g}{\tan\theta} w_{l\zeta o} \right] \quad (28)$$

The leakage flow rate in the cavity is represented by the axial component of cavity flow as

$$Q_{gd} = I_s \times \frac{1 - L_{lg}}{I_s} \int_R^{R+T} w_{go} 2\pi r dr$$

$$= \pi (T + C_{lo})(2R + T + C_{lo})(1 - L_{lg}) w_{go} \quad (29)$$

Therefore the total leakage flow rate for the groove is

$$Q_g = Q_{gc} + Q_{gd} \quad (30)$$

and the total leakage flow rate Q becomes

$$Q = Q_l + Q_g = \pi C_{lo} \left\{ 2(R+T) + C_{lo} \right\} L_{lg} w_{lo}$$

$$+ I_s \left[\frac{1}{2} L_g (2C_{lo} + L_g \tan\theta) w_{g\eta o} \sin\alpha + \frac{C_{lo} L_g}{\tan\theta} w_{l\zeta o} \right]$$

$$+ \pi (T + C_{lo})(2R + T + C_{lo})(1 - L_{lg}) w_{go} \quad (31)$$

Figure 4 shows the leakage flow rate for three types of seal and for L/D = 1.0, a rotating speed of 4000 rpm, and a radial clearance of 0.5 mm. The leakage flow rate for each seal type increased as the pressure difference increased. The leakage flow rate for the parallel-grooved seal was less than that of the land seal. For the spiral-grooved seal, if the spiral angle was small, the leakage flow rate was less than that of the parallel-grooved seal, but if the spiral angle was large, the leakage flow rate was greater than it was for the parallel-grooved seal. For the spiral-grooved seal, if the spiral angle was small and the land width was large, or if the spiral angle was large and the land width was large, the leakage flow rate decreased. For this reason the groove is important for the screw pumping action.

Figure 5 compares the calculated leakage flow rate with experimental results (ref. 20). The groove was on both the journal and casing in this experiment. In the low-speed range the calculated and experimental values were very close, and in the high-speed range the leakage flow rate tended to zero because of gas ingestion phenomenon.

DERIVATION OF PRESSURE DISTRIBUTION

To linearize the equations, a first-order approximation is performed. It is assumed in the linearization that the center of the journal coincides with the center of the casing and that the journal perturbs close to the center. Then the values of fluid film thickness H, pressure P, mean velocity in the z-direction w_m, and mean velocity in the x-direction u_m are written as follows:

$$\left.\begin{aligned} H &= C_o + \varepsilon\psi & \qquad P &= P_o + \varepsilon P_1 \\ w_m &= w_o + \varepsilon w_1 & \qquad u_m &= u_o + \varepsilon u_1 \end{aligned}\right\} \tag{32}$$

where C_o, P_o, w_o, and u_o are the steady-state values and ψ, P_1, w_1, and u_1 are the perturbations. The perturbation term in the circumferential direction is neglected because the spiral angle α is usually small and u_1 is sufficiently smaller than w_1.

Pressure Distribution in Steady-State

The steady-state pressure distribution is obtained by substituting equations (7), (10), and (32) into equation (3) and taking the zeroth-order approximation. The pressure gradient of the land in the axial direction is given by

$$\frac{\partial P_{lo}}{\partial z} = -\frac{0.132}{C_{lo}} \cdot \frac{1}{2} \cdot \rho w_{lo}^2 \left(\frac{C_{lo} w_{lo}}{\nu}\right)^{-0.25} \tag{33}$$

The pressure gradient of the groove in the axial direction is given by

$$\frac{\partial P_{go}}{\partial z} = -\frac{1}{2C_{go}} \rho(\lambda_{ga} + 0.25\lambda_f) w_{go}^2 - \rho\left\{u_{go}\frac{\partial w_{go}}{\partial x} + w_{go}\frac{\partial w_{go}}{\partial z}\right\} \tag{34}$$

where C_{go} and w_{go} are functions of z and are represented as

$$C_{go} = C_{lo} + z\tan\theta\cos\alpha \qquad\qquad w_{go} = \frac{C_{lo} w_{lo}}{C_{lo} + z\tan\theta\cos\alpha} \tag{35}$$

Therefore equation (31) is written as

$$\frac{\partial P_{go}}{\partial z} = -\frac{1\,\rho(C_{lo}w_{lo})^2\lambda_{sa}}{2(C_{lo}+z\tan\theta\cos\alpha)^3} - \frac{\rho C_{lo}u_{go}w_{lo}\tan\theta\cos\alpha}{(C_{lo}+z\tan\theta\cos\alpha)^2} \tag{36}$$

where λ_{sa} is the apparent friction coefficient because its dimension is the same as friction; that is,

$$\lambda_{sa} = \lambda_{ga} + 0.25\lambda_f - 2\tan\theta\cos\alpha \tag{37}$$

Dynamic Pressure Distribution

The dynamic pressure distribution is obtained by substituting equations (7), (10), and (32) into the equation of momentum (3) and taking the first-order approximation. For the continuity equation (1) the first-order approximation is also obtained in the same manner. The momentum equation in the axial direction for the land is

$$\begin{aligned}\frac{\partial P_{l1}}{\partial z} = &-\frac{\psi}{C_{lo}}\cdot\frac{\partial P_{go}}{\partial z} + \frac{1}{2C_{lo}^2}\rho 0.033\left(\frac{C_{lo}w_{lo}}{\nu}\right)^{-0.25}\cdot w_{lo}^2\psi \\ &+\frac{1}{2C_{lo}}\rho 0.033\left(\frac{C_{lo}w_{lo}}{\nu}\right)^{-0.25}\frac{w_{l1}}{w_{lo}}\cdot w_{lo}^2 \\ &-\rho\left\{\frac{\partial w_{l1}}{\partial t} + u_{lo}\frac{\partial w_{l1}}{\partial x} + w_{go}\frac{\partial w_{go}}{\partial z}\right\}\end{aligned} \tag{38}$$

The continuity equation is

$$\frac{\partial w_{l1}}{\partial z} = -\frac{1}{C_{lo}}\left(\frac{\partial\psi}{\partial t} + u_{lo}\frac{\partial\psi}{\partial x}\right) \tag{39}$$

Pressure distribution is obtained by solving equations (38) and (39) simultaneously. Equation (39) is the first-order ordinary equation in w_{l1}, and it is solved by setting the boundary condition $w_{l1} = w_{l1}(0)$ at $z = 0$.

$$w_{l1} = w_{l1(0)} - \frac{1}{C_{lo}}\cdot f_l(x,t)\cdot z \tag{40}$$

where

$$f_l(x,t) = \frac{\partial\psi}{\partial t} + u_{lo}\frac{\partial\psi}{\partial x}$$

Substituting equation (40) into equation (38) and setting the boundary condition $P_{l1} = P_{l1}(0)$ at $z = 0$ yield a solution of equation (38). In this boundary condition $P_{l1}(0)$ is the perturbed pressure at the land inlet which is obtained by a first-order approximation of the equation

$$\Delta P = -(1/2)\rho\xi_1 w_m^2 \tag{41}$$

that is,

$$P_{l1(0)} = -\rho\xi_1 w_{lo} w_{l1(0)} \tag{42}$$

The term $w_{l1}(0)$ is obtained by neglecting the perturbed pressure at the outlet of the land, (i.e., $z = L_l/\cos\alpha$, $P_{l1}(0) = 0$). Then the dynamic pressure of the land P_{l1} is obtained as

$$\begin{aligned} P_{l1} = {} & \frac{1}{2C_{lo}^2}\rho w_{lo} 0.165\left(\frac{C_{lo}w_{lo}}{\nu}\right)^{-0.25}\psi\cdot SPL1 - \frac{1}{2C_{lo}^2}\rho w_{lo} 0.033\left(\frac{C_{lo}w_{lo}}{\nu}\right)^{-0.25} \\ & \times\frac{1}{2w_{lo}}\cdot f_l(x,t)\cdot SPL2 + \frac{1}{C_{lo}}\rho w_{lo}\cdot f_l(x,t)\cdot SPL1 \\ & + \frac{1}{2C_{lo}}\rho\left(\frac{\partial}{\partial t} + u_{lo}\frac{\partial}{\partial x}\right)f_l(x,t)\ SPL2 \end{aligned} \tag{43}$$

where SPL1 and SPL2 are as written in appendix A.

The momentum equation in the axial direction for the groove is

$$\begin{aligned} \frac{\partial P_{g1}}{\partial z} = {} & -\frac{\psi}{C_{go}}\cdot\frac{\partial P_{go}}{\partial z} - \frac{\rho}{C_{go}}(\lambda_{ga} + 0.25\lambda_f)w_{go}w_{g1} \\ & -\rho\left\{\frac{\partial w_{g1}}{\partial t} + w_{go}\frac{\partial w_{g1}}{\partial z} \times\tan\alpha + u_{go}\frac{\partial w_{g1}}{\partial x} + w_{g1}\frac{\partial w_{go}}{\partial z}\right. \\ & \left. + \frac{\psi w_{go}}{C_{go}}\cdot\frac{\partial w_{go}}{\partial z} + \frac{\psi u_{go}}{C_{go}}\cdot\frac{\partial w_{go}}{\partial z} \times\tan\alpha\right\} \end{aligned} \tag{44}$$

The continuity equation is

$$\frac{\partial\psi}{\partial t} + u_{go}\frac{\partial\psi}{\partial x} + \psi\frac{\partial w_{go}}{z} + w_{g1}\frac{\partial C_{go}}{\partial z} + C_{go}\frac{\partial w_{g1}}{\partial z} = 0 \tag{45}$$

Substituting equation (36) into equation (45) and setting the boundary condition $w_{g1} = w_{g1}(0)$ at $z = 0$ yield the solution of equation (45):

$$w_{g1} = w_{g1(0)} \cdot \frac{C_{lo}}{C_{lo}+z\tan\theta\cos\alpha} - \frac{z}{C_{lo}+z\tan\theta\cos\alpha} \cdot f_g(x,t) + \frac{\psi w_{lo} \; z\tan\theta\cos\alpha}{(C_{lo}+z\tan\theta\cos\alpha)^2} \tag{46}$$

where

$$f_g(x,t) = \frac{\partial\psi}{\partial t} + u_{go}\frac{\partial\psi}{\partial x}$$

Substituting equations (36) and (46) into equation (44) and setting the boundary condition $P_{g1} = P_{g1}(0)$ at $z = 0$ yield the solution of equation (44), where $P_{g1}(0)$ is the pressure loss at the inlet of the groove: that is, the outlet loss of the land. The outlet loss of the land is represented by

$$\Delta P_{lex} = \frac{1}{2}\rho\xi_2 w_{lo}^2 \tag{47}$$

where ξ_2 is the outlet loss coefficient

$$\xi_2 = \left(1 - \frac{C_{lo}}{C_{lo}+L_g\tan\theta}\right)^2 \tag{48}$$

The first approximation of equation (47) is represented as

$$P_{g1}(z_n) = -\rho\xi_2 w_{1O} w_{g1}(z_n) \tag{49}$$

The term $w_{g1}(0)$ is obtained by neglecting the perturbed pressure at the groove outlet; that is, $z = Lg/\cos\alpha$, $Pg1 = 0$. Then the dynamic pressure of the groove is obtained as

$$P_{g1} = -\frac{\rho C_{lo}^2 w_{lo}^2 \lambda_{sa}}{6\tan\theta\cos\alpha} \cdot \psi \cdot SPG3 - \frac{\rho C_{lo} w_{lo}}{\tan\theta\cos\alpha} f_g(x,t) \cdot SPG1$$

$$-\frac{\rho C_{lo} w_{lo}^2 \lambda_{sa}}{\tan\theta\cos\alpha} \psi \cdot SPG6 + \frac{\rho C_{lo} w_{lo} \lambda_{sa}}{(\tan\theta\cos\alpha)^2} f_g(x,t) \cdot SPG7$$

$$-\frac{\rho w_{lo}}{(\tan\theta\cos\alpha)} f_g(x,t)\cdot SPG8$$

$$+\frac{\rho}{(\tan\theta\cos\alpha)^2}\left(\frac{\partial}{\partial t}+u_{go}\frac{\partial}{\partial x}\right)f_g(x,t)\cdot SPG9 \qquad (50)$$

where SPG1 to SPG9 are represented in appendix B.

DYNAMIC FORCE

The small displacements in the X- and Y-directions at the center, ΔX and ΔY respectively, are as follows:

$$\varepsilon\psi = -\Delta X\cos\phi - \Delta Y\sin\phi \qquad (51)$$

The flow-induced forces in the X- and Y-directions at the beginning of a land ϕ_n, at the beginning of a groove $\phi_{n+1/2}$, and at the beginning of the next land section ϕ_{n+1} are represented by equations (52) and (53).

$$F_X = -\sum_{n=1}^{I_s}\Bigg[\int_{\phi_n}^{\phi_{n+1/2}}\Bigg\{\int_{L_l/\cos\alpha-R(\phi-\phi_n)\tan\alpha}^{L_l/\cos\alpha}\varepsilon P_{l1in}\,dz$$

$$+L_s\cdot I_s\int_0^{L_g/\cos\alpha}\varepsilon P_{g1}\,dz+(L_s\cdot I_s-1)\int_0^{L_l/\cos\alpha}\varepsilon P_{l1}\,dz$$

$$+\int_0^{L_l/\cos\alpha-R(\phi-\phi_n)\tan\alpha}\varepsilon P_{l1ex}\,dz\Bigg\}\times R\cos\phi\,d\phi$$

$$+\int_{\phi_{n+1/2}}^{\phi_{n+1}}\Bigg\{\int_{L_g/\cos\alpha-R(\phi-\phi_{n+1/2})\tan\alpha}^{L_g/\cos\alpha}\varepsilon P_{g1in}\,dz$$

$$+L_s\cdot I_s\int_0^{L_l/\cos\alpha}\varepsilon P_{l1}\,dz+(L_s\cdot I_s-1)\int_0^{L_g/\cos\alpha}\varepsilon P_{g1}\,dz$$

$$+\int_0^{L_g/\cos\alpha-R(\phi-\phi_{n+1/2})\tan\alpha}\varepsilon P_{g1ex}\,dz\Bigg\}\times R\cos\phi\,d\phi\Bigg] \qquad (52)$$

$$
\begin{aligned}
F_Y = - \sum_{n=1}^{I_s} \Bigg[& \int_{\phi_n}^{\phi_{n+1/2}} \Bigg\{ \int_{L_l/\cos\alpha - R(\phi-\phi_n)\tan\alpha}^{L_l/\cos\alpha} \varepsilon P_{l1in}\, dz \\
& + L_s \cdot I_s \int_0^{L_g/\cos\alpha} \varepsilon P_{g1}\, dz + (L_s \cdot I_s - 1) \int_0^{L_l/\cos\alpha} \varepsilon P_{l1}\, dz \\
& + \int_0^{L_l/\cos\alpha - R(\phi-\phi_n)\tan\alpha} \varepsilon P_{l1ex}\, dz \Bigg\} \times R\sin\phi\, d\phi \\
& + \int_{\phi_{n+1/2}}^{\phi_{n+1}} \int_{L_g/\cos\alpha - R(\phi-\phi_{n+1/2})\tan\alpha}^{L_g/\cos\alpha} \varepsilon P_{g1in}\, dz \\
& + L_s \cdot I_s \int_0^{L_l/\cos\alpha} \varepsilon P_{l1}\, dz + (L_s \cdot I_s - 1) \int_0^{L_g/\cos\alpha} \varepsilon P_{g1}\, dz \\
& + \int_0^{L_g/\cos\alpha - R(\phi-\phi_{n+1/2})\tan\alpha} \varepsilon P_{g1ex}\, dz \Bigg\} \times R\sin\phi\, d\phi \quad \Bigg]
\end{aligned}
\tag{53}
$$

This force may be represented in the following matrix form:

$$
-\begin{bmatrix} F_X \\ F_Y \end{bmatrix} = \begin{bmatrix} K_{XX} & K_{XY} \\ K_{YX} & K_{YY} \end{bmatrix} \begin{bmatrix} X \\ Y \end{bmatrix} + \begin{bmatrix} C_{XX} & C_{XY} \\ C_{YX} & C_{YY} \end{bmatrix} \begin{bmatrix} \dot{X} \\ \dot{Y} \end{bmatrix} + \begin{bmatrix} M_{XX} & M_{XY} \\ M_{YX} & M_{YY} \end{bmatrix} \begin{bmatrix} \ddot{X} \\ \ddot{Y} \end{bmatrix}
\tag{54}
$$

The following coefficients are obtained from equations (52) to (54). The dynamic coefficients are different for the land and the groove.

$$\left.\begin{aligned}
K_{XXl} &= \frac{\rho\pi R}{2C_{lo}}\left[-\frac{w_{lo}^{2}}{C_{lo}}\,0.165\left(\frac{C_{lo}w_{lo}}{\nu}\right)^{-0.25}\cdot ISPL1+\left(\frac{u_{lo}}{R}\right)^{2} ISPL2\right] = K_{YYl}\\
K_{YXl} &= \frac{\rho\pi u_{lo}w_{lo}}{C_{lo}}\left[-\frac{1}{4C_{lo}}\,0.033\left(\frac{C_{lo}w_{lo}}{\nu}\right)^{-0.25}\cdot ISPL2+ISPL1\right] = -K_{XYl}\\
C_{XXl} &= \frac{\rho\pi R w_{lo}}{C_{lo}}\left[+\frac{1}{4C_{lo}}\,0.033\left(\frac{C_{lo}w_{lo}}{\nu}\right)^{-0.25}\cdot ISPL2-ISPL1\right] = C_{YYl}\\
C_{YXl} &= +\frac{\rho\pi u_{lo}}{C_{lo}}\cdot ISPL2 = -C_{XYl} \qquad M_{XXl} = -\frac{\rho\pi R}{2C_{lo}}\cdot ISPL2 = M_{YYl}\\
M_{YXl} &= M_{XYl} = 0
\end{aligned}\right\} \tag{55}$$

$$\left.\begin{aligned}
K_{XXg} &= \frac{\rho\pi R}{\tan\theta\cos\alpha}\left[\frac{C_{lo}^{2}w_{lo}^{2}\lambda_{sa}}{6}\cdot ISPG3+C_{lo}w_{lo}^{2}\lambda_{sa}\cdot ISPG6\right.\\
&\qquad\left.+\frac{1}{\tan\theta\cos\alpha}\left(\frac{u_{go}}{R}\right)^{2}\cdot ISPG9\right] = K_{YYg}\\
K_{YXg} &= -\frac{\rho\pi C_{lo}w_{lo}u_{go}}{\tan\theta\cos\alpha}\left[ISPG1-\frac{\lambda_{sa}}{\tan\theta\cos\alpha}\cdot ISPG7+\frac{1}{C_{lo}}\cdot ISPG8\right] = -K_{XYg}\\
C_{XXg} &= \frac{\rho\pi R C_{lo}w_{lo}}{\tan\theta\cos\alpha}\left[ISPG1-\frac{\lambda_{sa}}{\tan\theta\cos\alpha}\,ISPG7+\frac{1}{C_{lo}}\,ISPG8\right] = C_{YYg}\\
C_{YXg} &= \frac{2\rho\pi u_{go}}{(\tan\theta\cos\alpha)^{2}}\cdot ISPG9 = -C_{XYg}\\
M_{XXg} &= -\frac{\rho\pi R}{(\tan\theta\cos\alpha)^{2}}\,ISPG9 = M_{YYg} \qquad M_{YXg} = M_{XYg} = 0
\end{aligned}\right\} \tag{56}$$

where ISPL2 to ISPG9 are represented in appendix C.

The coefficient matrix represents the summation of the coefficients of the land and the groove.

NUMERICAL EXAMPLE

Data for the seal model are shown in table I. Figure 6 shows the relation between the axial Reynolds number (pressure difference between the inlet and outlet of the seal) and the spiral angle α, where $L/D = 1.0$, rotating speed is 3000 rpm, and pressure difference between inlet and outlet is 0.49 to 4.9 MPa. As Reynolds number in the axial direction increases, K_{xx}, K_{yx}, C_{xx}, and C_{yx} increase, but M_{xx} is almost constant. For the 3-thread 2.6° spiral-angle spiral-grooved seal and the 20-thread 17.66° spiral-angle spiral-grooved seal, the dynamic coefficient decreases as the spiral angle decreases.

Figure 7 shows the effects of the Reynolds number in the axial direction and the ratio of the land width to the groove width. It is known that as the land width increases, the coefficients K_{xx}, K_{yx}, C_{xx}, C_{yx}, and M_{xx} increase and that, if the land is narrow, the spring coefficient K_{xx} becomes negative.

Figure 8 shows the effect of the circumferential Reynolds number for two kinds of spiral-grooved and parallel-grooved seals, where $L/D = 1.0$, the pressure difference between the inlet and outlet is 0.49 to 4.9 MPa, and rotating speed is 2000 to 8000 rpm. Coefficient K_{xx} of the spiral-grooved seal shows a negative value for a low circumferential Reynolds number, but that of the parallel-grooved seal does not show a negative value until a high circumferential Reynolds number is obtained. The reason is that the pressure difference between the inlet and outlet of the spiral groove seal affects the circumferential velocity; that is, the pressure difference and the high rotating speed induce the pumping action, and the apparent pressure difference becomes small. The characteristics of the coefficients K_{xy} and C_{xx} can be illustrated in the same way. The values of the coefficients K_{yx}, C_{xx}, C_{yx}, and M_{xx} for the spiral-grooved seal are larger than those for the parallel-grooved seal.

CONCLUSIONS

From this study of the dynamic characteristics of noncontacting spiral-grooved seals, the following conclusions are drawn:

1. Except for K_{xx}, coefficients become small as the spiral angle and the land width decrease.

2. As the axial Reynolds number increases, coefficients K_{xx}, K_{yx}, C_{xx}, and C_{yx} become large but M_{xx} remains constant.

3. As the circumferential Reynolds number increases, K_{xx} decreases, K_{yx} and C_{xx} increase once and then decrease, C_{yx} increases, and M_{xx} is almost constant.

4. The coefficient K_{xx} becomes negative when the circumferential Reynolds number is large and the axial Reynolds number is small.

5. Leakage flow decreases as the rotating speed becomes large. If the spiral angle is small, leakage flow decreases as the groove width becomes large, and if the spiral angle is large, the leakage flow decreases as the groove width becomes small.

6. Comparing the coefficients of the spiral-grooved seal with those of the parallel-grooved seal, yields the following conclusions:

a. K_{xx} of the spiral-grooved seal is smaller than that of the parallel-grooved seal.

b. K_{yx} and C_{xx} of the spiral-grooved seal are smaller (larger) than they are for the parallel-grooved seal for low (high) circumferential Reynolds numbers, respectively.

c. C_{yx} and M_{xx} of the spiral-grooved seal are larger than they are for the parallel-grooved seal.

d. Leakage flow of the spiral-grooved seal is larger (smaller) than that of the parallel-grooved seal for low (high) rotating speeds, respectively.

APPENDIX A

$$q_l = \rho w_{lo} \xi_1 - \frac{1}{2C_{lo}} \rho w_{lo} 0.033 \left(\frac{C_{lo} w_{lo}}{\nu}\right)^{-0.25} \cdot \frac{L_l}{\cos\alpha}$$

$$q_{l1} = \rho w_{lo} \xi_1$$

$$q_{l2} = \frac{1}{2C_{lo}} \rho w_{lo} 0.033 \left(\frac{C_{lo} w_{lo}}{\nu}\right)^{-0.25}$$

$$SPL1 = z - \frac{1}{q_l}\left\{q_{l1} - q_{l2} \cdot z\right\} \frac{L_l}{\cos\alpha}$$

$$SPL2 = z^2 - \frac{1}{q_l}\left\{q_{l1} - q_{l2} \cdot z\right\} \left(\frac{L_l}{\cos\alpha}\right)^2$$

APPENDIX B

$$C_{gl} = C_{lo} + L_g \tan\theta$$

$$q_{gl} = \rho w_{lo} (1 - C_{lo}/C_{gl})^2$$

$$q_{g2} = -\frac{\rho C_{lo}^2 w_{lo} \lambda_{sa}}{2 \tan\theta \cos\alpha}$$

$$m = \frac{1}{q_g}\left\{q_{gl} + q_{g2}\left(\frac{1}{C_{go}^2} - \frac{1}{C_{lo}^2}\right)\right\}$$

$$SPG1 = 1/C_{go} - 1/C_{lo} - m \cdot K1$$

$$SPG2 = 1/C_{go}^2 - 1/C_{lo}^2 - m \cdot K2$$

$$SPG3 = 1/C_{go}^3 - 1/C_{lo}^3 - m \cdot K3$$

$$SPG4 = \ln(C_{go}/C_{lo}) - m \cdot K4$$

$$SPG5 = C_{go} - C_{lo} - m \cdot K5$$

$$SPG6 = -\frac{1}{2} SPG2 + \frac{C_{lo}}{3} SPG3$$

$$SPG7 = -SPG1 + \frac{C_{lo}}{2} SPG2$$

$$SPG8 = C_{lo} \cdot SPG1 + SPG4$$

$$SPG9 = -C_{lo} \cdot SPG4 + SPG5$$

$$K1 = 1/C_{g1} - 1/C_{lo} \qquad K2 = 1/C_{g1}^2 - 1/C_{lo}^2$$

$$K3 = 1/C_{g1}^3 - 1/C_{lo}^3 \qquad K4 = \ln(C_{g1}/C_{lo})$$

$$K5 = C_{g1} - C_{lo} \qquad K6 = C_{g1}^2 - C_{lo}^2$$

$$K7 = q_{g1}/q_g \qquad K8 = q_{g2}/q_g$$

APPENDIX C

$$ISPL1 = \frac{1}{2}\left(\frac{L_l}{\cos\alpha}\right)^2 + \frac{q_{l2}}{2q_l}\left(\frac{L_l}{\cos\alpha}\right)^3 - \frac{q_{l1}}{q_l}\left(\frac{L_l}{\cos\alpha}\right)^2$$

$$ISPL2 = \frac{1}{3}\left(\frac{L_l}{\cos\alpha}\right)^3 + \frac{q_{l2}}{2q_l}\left(\frac{L_l}{\cos\alpha}\right)^4 - \frac{q_{l1}}{q_l}\left(\frac{L_l}{\cos\alpha}\right)^3$$

$$ISPG1 = \frac{K4}{\tan\theta\cos\alpha} + \frac{K8 \cdot K1^2}{\tan\theta\cos\alpha} - \left(\frac{1}{C_{lo}} + K7 \cdot K1 - \frac{K8 \cdot K1}{C_{lo}^2}\right)\frac{L_g}{\cos\alpha}$$

$$ISPG2 = -\frac{K1}{\tan\theta\cos\alpha} + \frac{K8 \cdot K1 \cdot K2}{\tan\theta\cos\alpha} - \left(\frac{1}{C_{lo}^2} + K7 \cdot K2 - \frac{K8 \cdot K2}{C_{lo}^2}\right)\frac{L_g}{\cos\alpha}$$

$$ISPG3 = -\frac{K2}{2\tan\theta\cos\alpha} - \frac{K8 \cdot K1 \cdot K3}{\tan\theta\cos\alpha} - \left(\frac{1}{C_{lo}^3} + K7 \cdot K3 + \frac{K8 \cdot K3}{C_{lo}^2}\right)\frac{L_g}{\cos\alpha}$$

$$ISPG4 = \frac{1}{tan\theta cos\alpha}\left\{ln(C_{g1}^{C_{g1}}/C_{lo}^{C_{lo}})-K5\right\}-\frac{K8\cdot K1\cdot K4}{tan\theta cos\alpha}$$

$$-\left(lnC_{lo}+K7\cdot K4+\frac{K8\cdot K4}{C_{lo}^{2}}\right)\frac{L_g}{cos\alpha}$$

$$ISPG5 = \frac{K6}{2tan\theta cos\alpha}-\frac{K8\cdot K1\cdot K5}{tan\theta cos\alpha}-\left(C_{lo}+K7\cdot K5+\frac{K8\ K5}{C_{lo}^{2}}\right)\frac{L_g}{cos\alpha}$$

$$ISPG6 = -\frac{1}{2}ISPG2 + \frac{C_{lo}}{3} ISPG3$$

$$ISPG7 = -ISPG1 + \frac{C_{lo}}{2} ISPG2$$

$$ISPG8 = C_{lo}\ ISPG1 + ISPG4$$

$$ISPG9 = -C_{lo}\ ISPG4 + ISPG5$$

REFERENCES

1. Black, H.F.: J. Mech. Sci., 12-4, 1970, 301.
2. Black, H.F.: Proc. 9th Int'l. Conf. Fluid Sealing, 1981, D4-141.
3. Childs, D.W.: Trans. ASME, Ser. F, 105-3, 1983, 429.
4. Childs, D.W.: Trans. ASME, Ser. F, 105-3, 1983, 437.
5. Yang, B., et al.: Trans. JSME, Ser. C, 49-45, 1983, 1636.
6. Kostyuk, A.G.: Teploenergetica, 1975, Vol. 22, No. 3, 41.
7. Iwatsubo, T., et al.: Flow Induced Force of Labyrinth Seal. Rotordynamic Instability Problems in High-Performance Turbomachinery. NASA CP-2250, 1982, pp. 205-222.
8. Whipple, R.T.P.: AERE Report T/R 622, 1958.
9. Vohr, J.H.: Trans. ASME, Ser. D, 87-3, 1965, 568.
10. Vohr, J.H.: Proc. 4th Int'l. Conf. Fluid Sealing, 1969, 311.
11. Passera, W.: Proc. 5th Int'l. Conf. Fluid Sealing, 1971, B6-89.
12. Zuk, J.: NASA TN D-3635, 1966.

13. Iwatsubo, T., et al.: Rotordynamic Instability Problems in High-Performance Turbomachinery Workshop, 1986.

14. Yamada, Y.: Trans. JSME, 26-180, 1961, 1267.

15. Hirs, G.G.: Trans. ASME, Ser. F, 96-1, 1974, 118.

16. Hauck, L.: IFTOMM paper, 1982, 361.

17. Boon, E.F.: Chemie. Ing. Tech., 31-3, 1959, 202.

18. Edited by JSME, Fluid Resistance in Pipe and Duct, 1980, 48.

19. Yamada, Y.: Trans. JSME, 25-171, 1960, 1514.

20. Kawakami, T., Kanki, H.: Private Information.

TABLE I. - DATA FOR NUMERICAL CALCULATION

Working fluid	water
Fluid temperature, K	293.15
Density, ρ, Kg/m^3	9.982×10^2
Viscosity, μ, mPa s	1.009
Kinematic viscosity, ν, m^2/s	1.006×10^{-6}
Journal radius, R, mm	100.0
Seal radial clearance, C_{l0}, mm	0.4
Seal length, L, mm	200.0
Groove depth, T, mm	1.18
Helix angle, α, deg	1.30 to 17.66
Journal rotating frequency, N, rpm	2000 to 8000
Pressure difference, ΔP, MPa	0.49 to 4.9

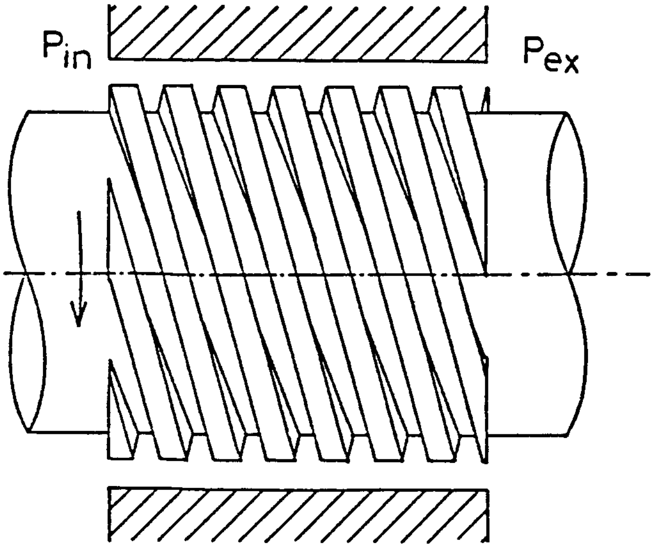

Figure 1. - Spiral-grooved seal.

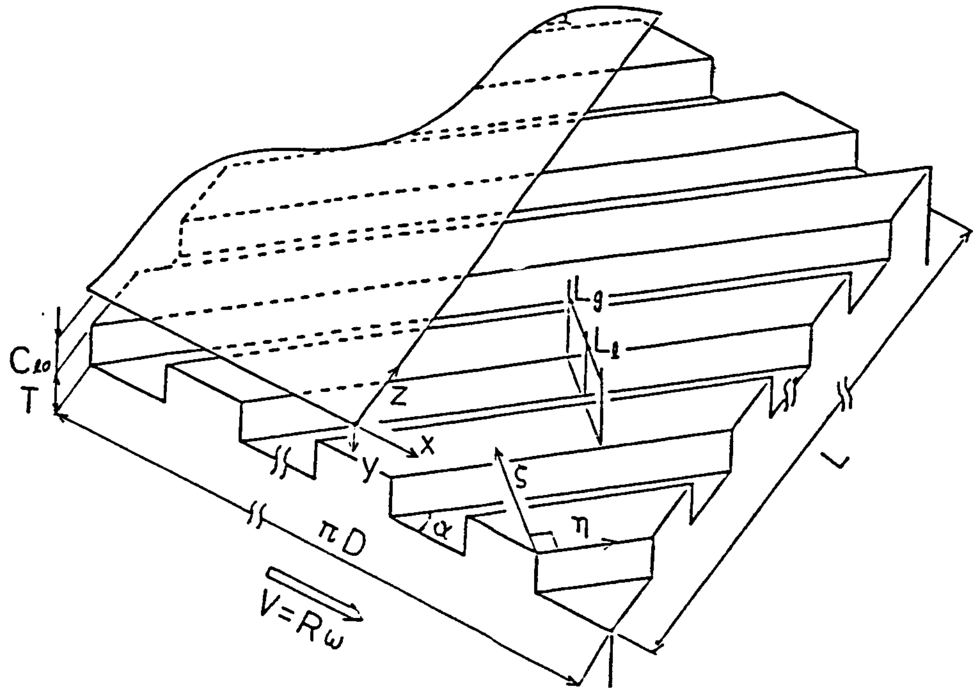

C_{l0}
T
z
x
y
L_g
L_l
ζ
η
α
πD
V=Rω
L

Figure 2. - Illustration of spiral-grooved seal.

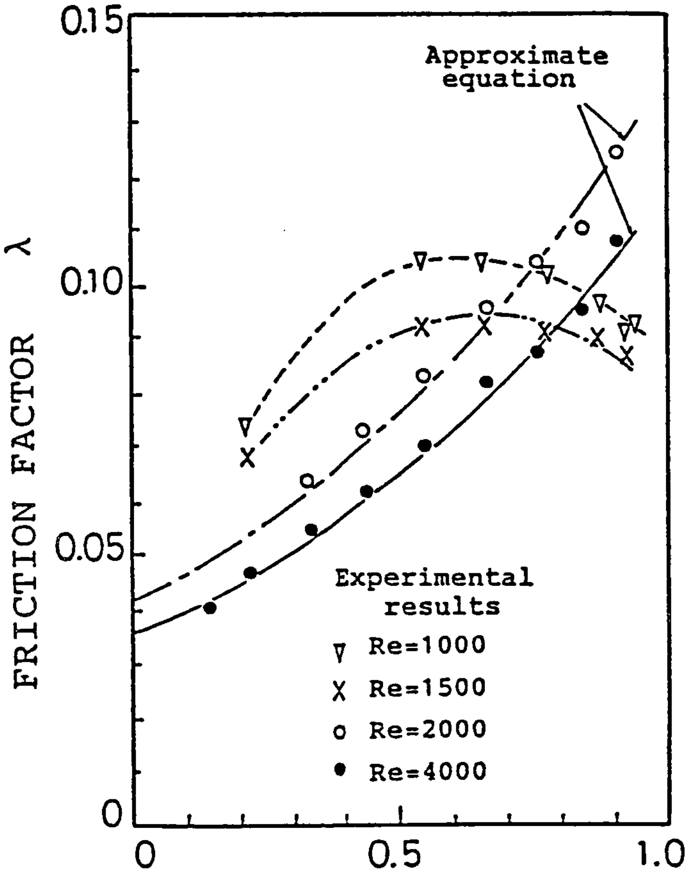

Figure 3. - Friction coefficients.

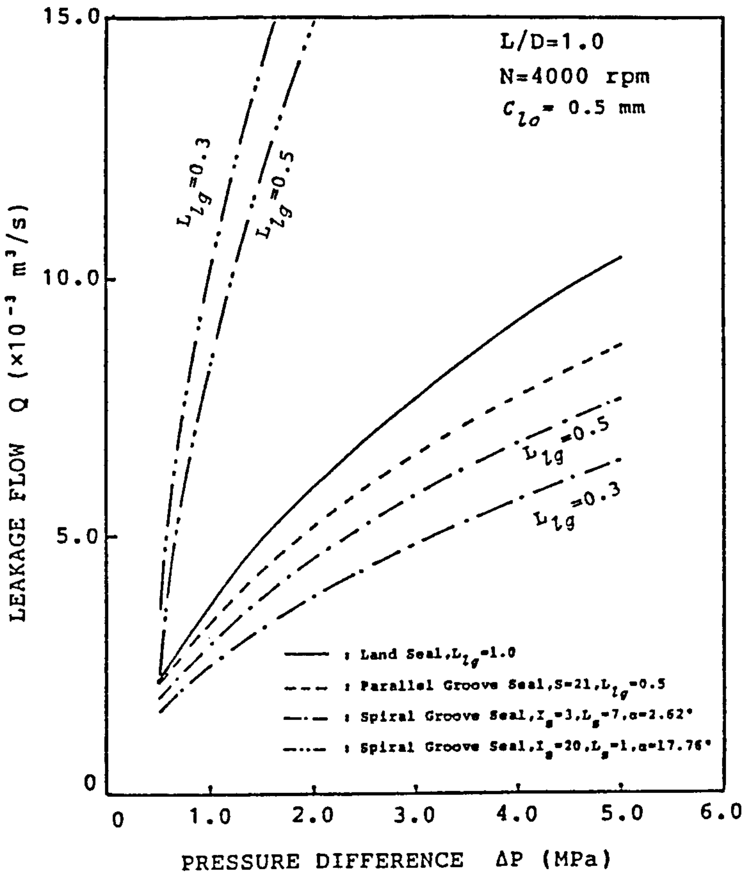

Figure 4. - Leakage flow versus pressure difference.

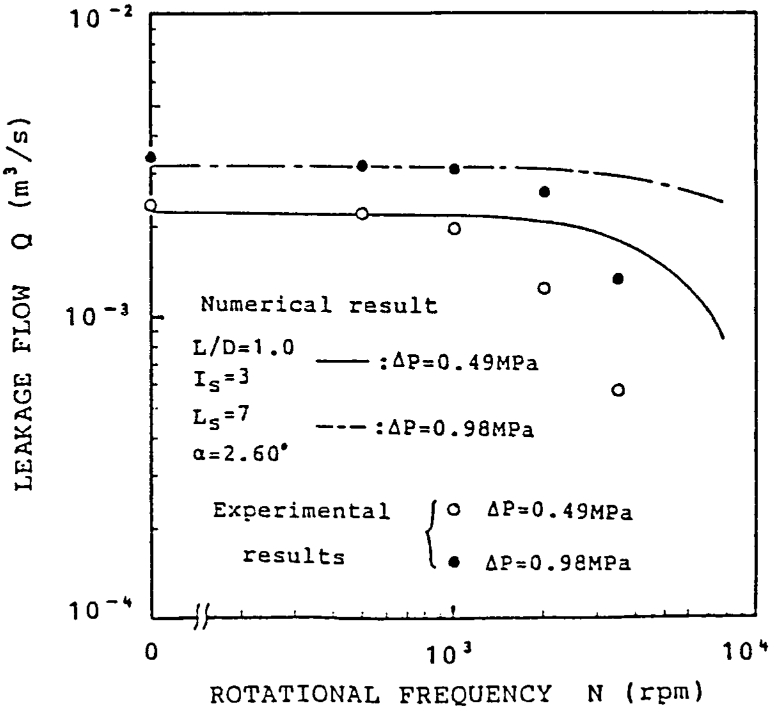

Figure 5. - Leakage flow versus rotating speed.

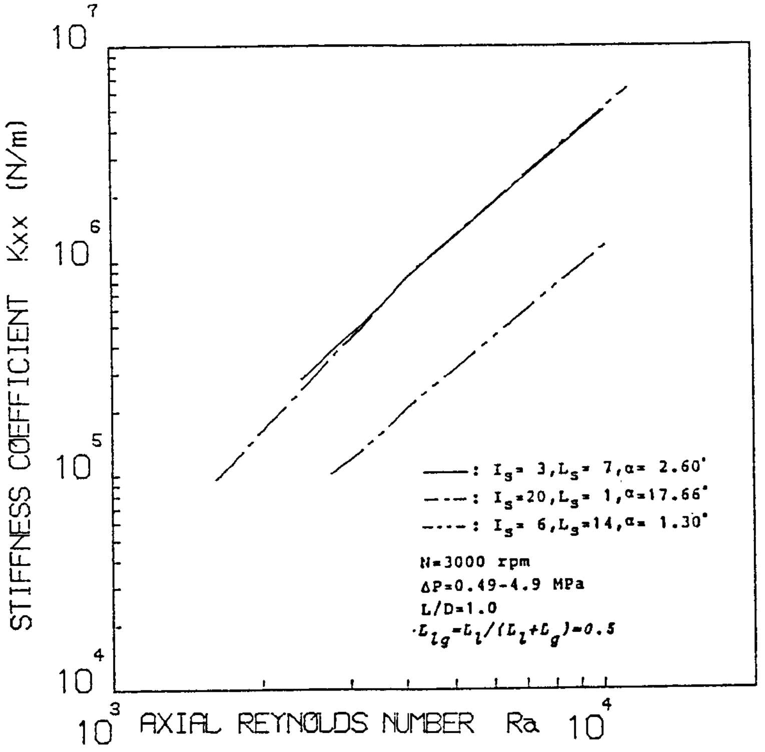

(a) Stiffness coefficient, K_{xx}.

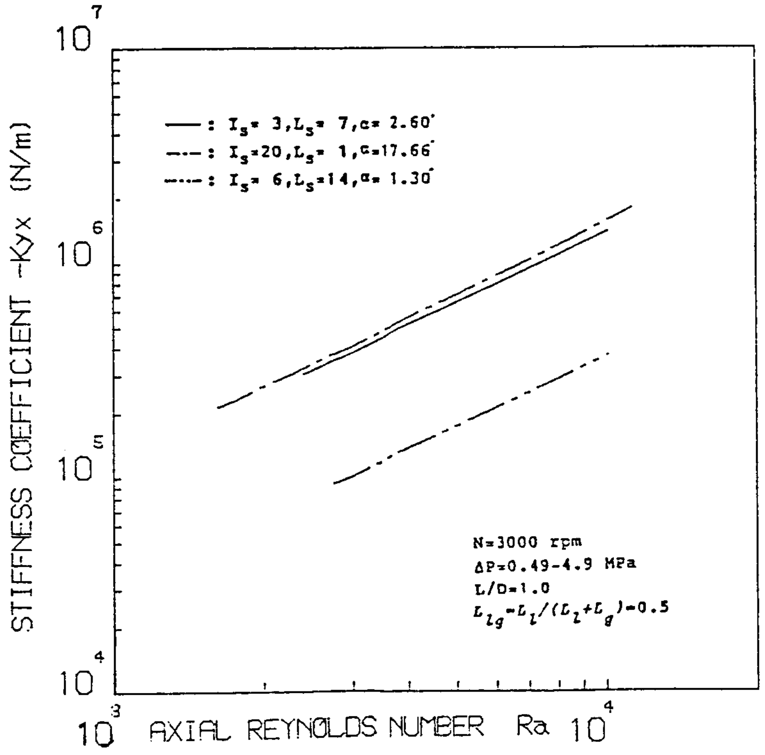

(b) Stiffness coefficient, K_{yx}.

Figure 6. - Effects of axial Reynolds number and spiral angle.

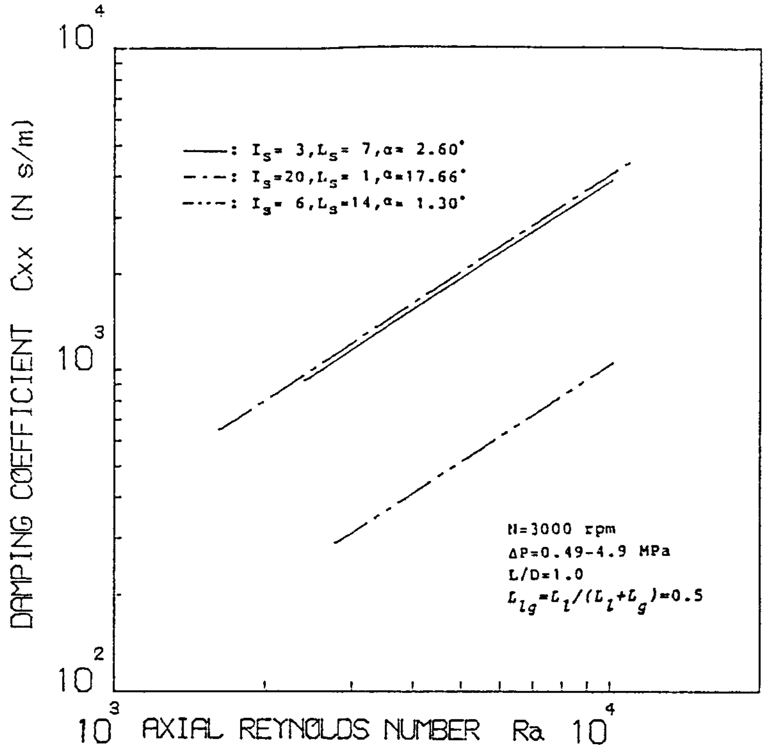

(c) Damping coefficient, C_{xx}.

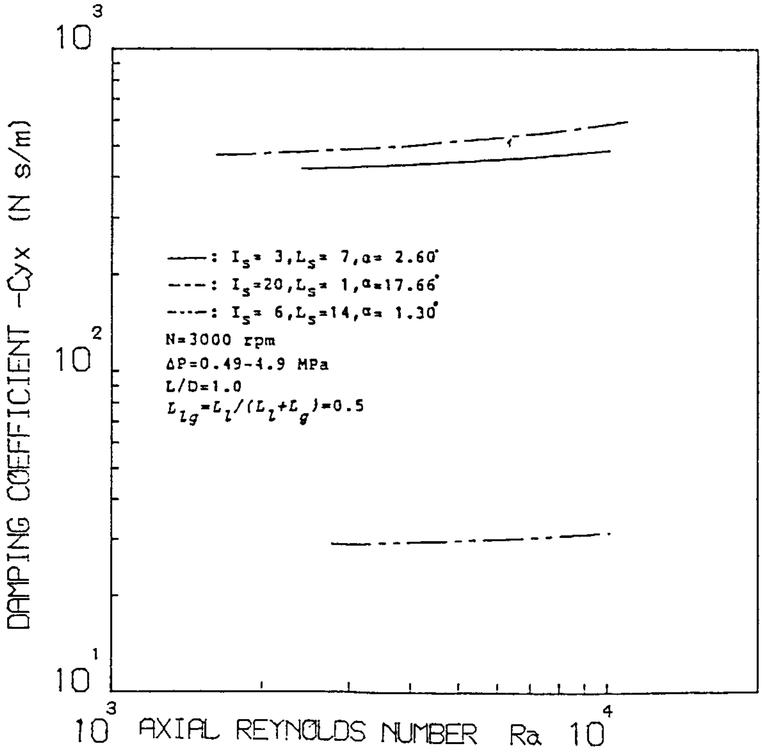

(d) Damping coefficient, C_{yx}.

Figure 6. - Continued.

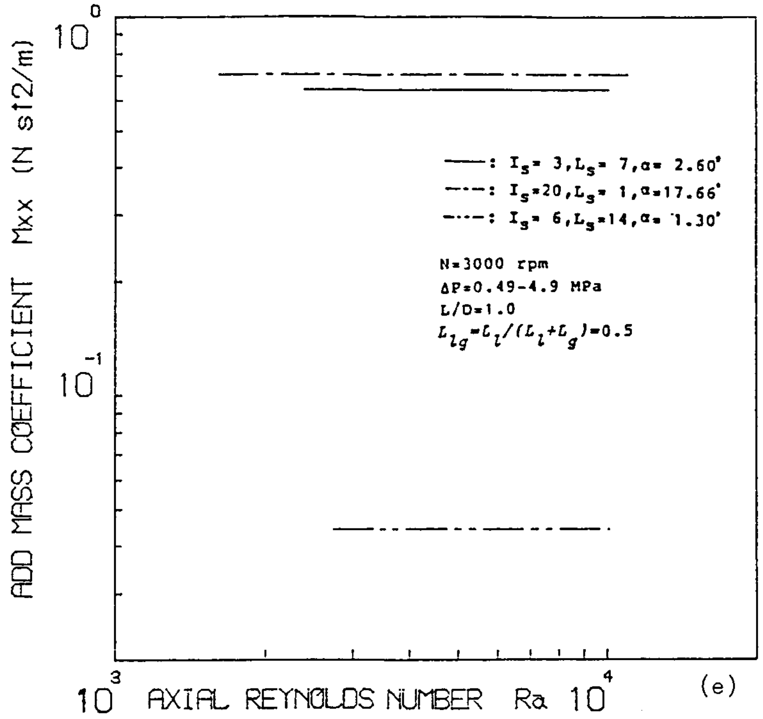

(e) Add mass coefficient, M_{xx}.

Figure 6. - Concluded.

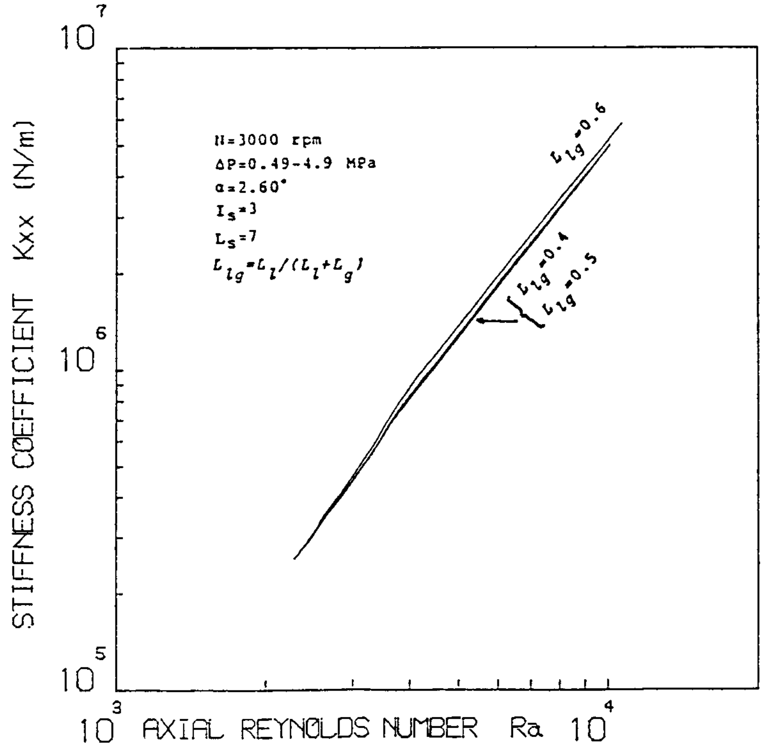

(a) Stiffness coefficient, K_{xx}.

Figure 7. - Effects of axial Reynolds number and ratio of land width to groove width.

C-3

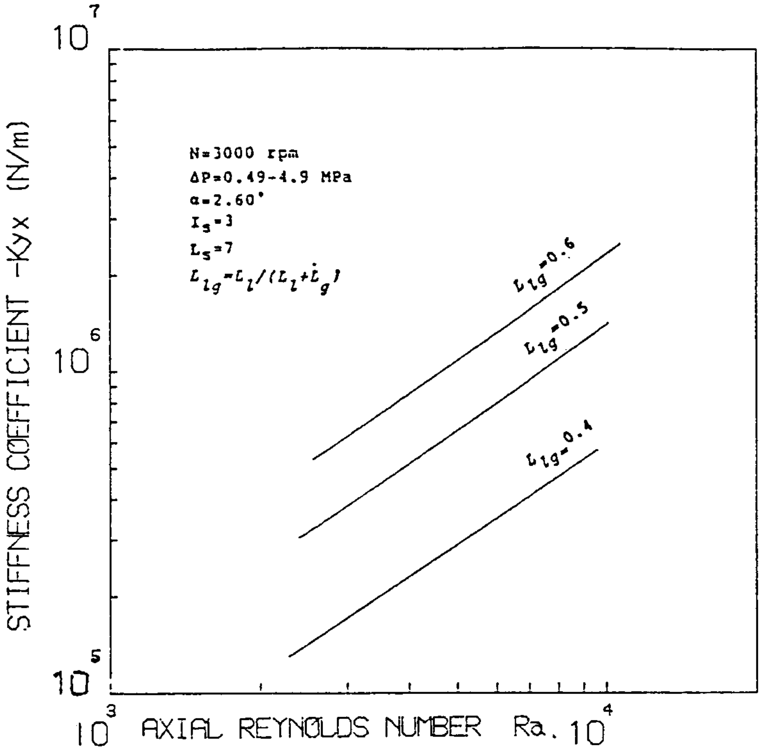

(b) Stiffness coefficient, K_{yx}.

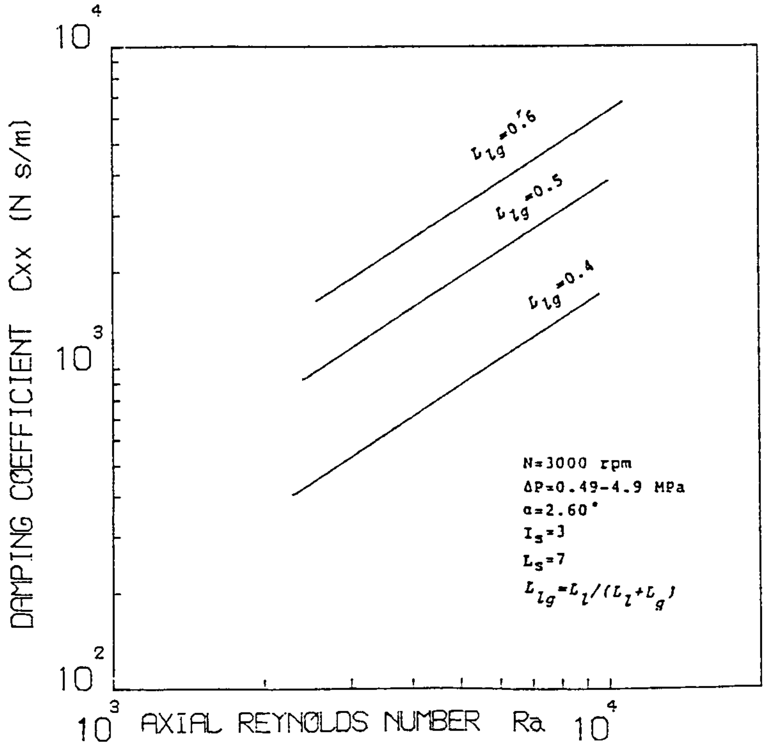

(c) Damping coefficient, C_{xx}.

Figure 7. - Continued.

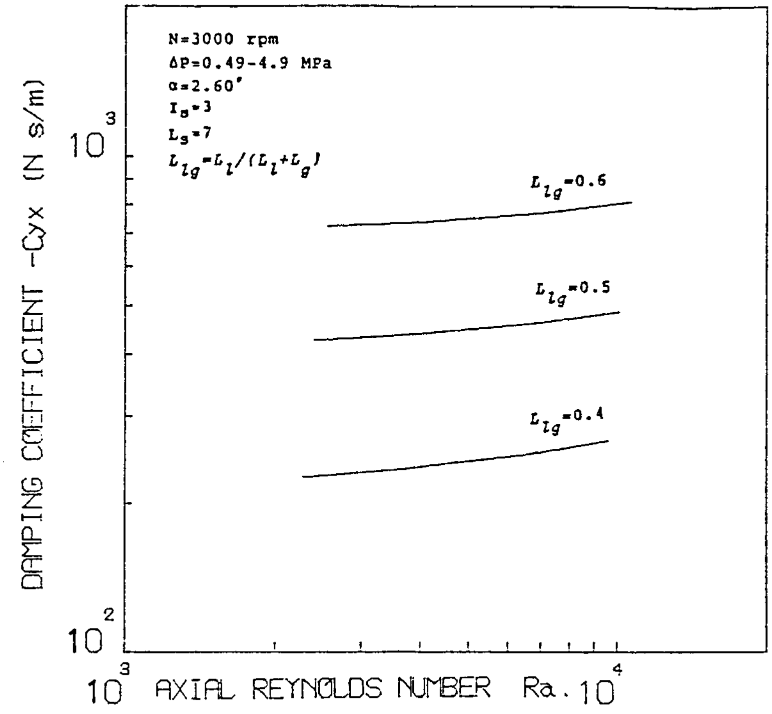

(d) Damping coefficient, C_{yx}.

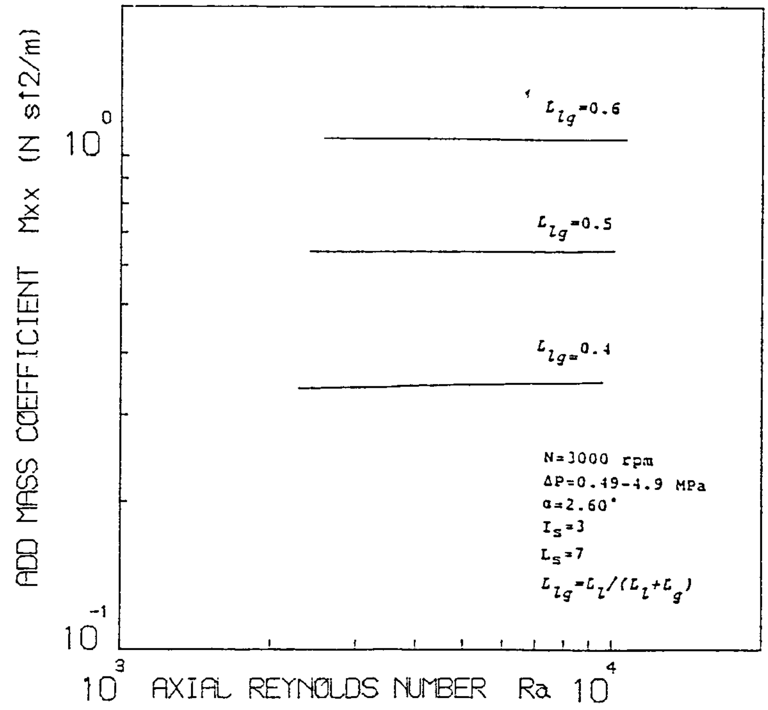

(e) Add mass coefficient, M_{xx}.

Figure 7. - Concluded.

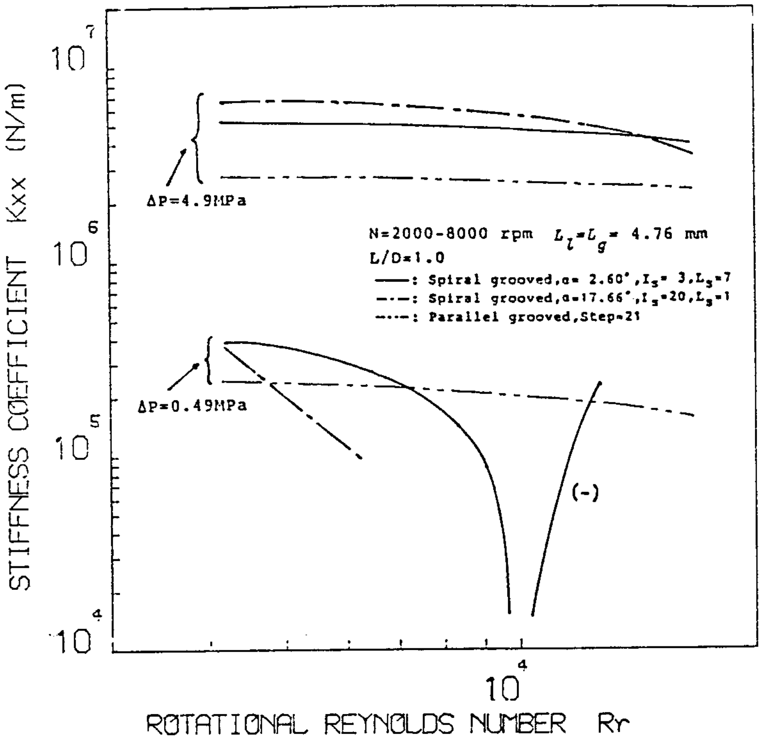

(a) Stiffness coefficient, K_{xx}.

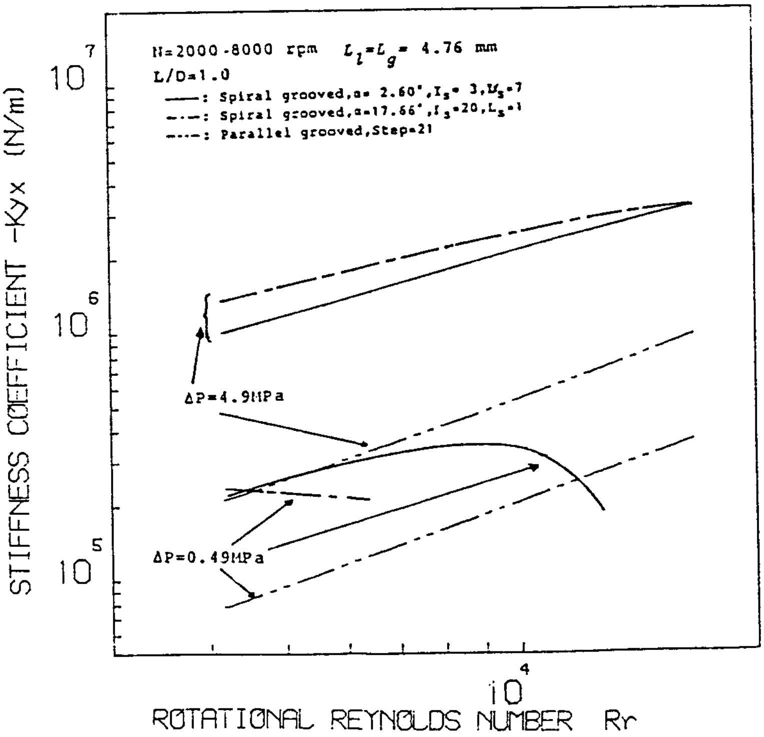

(b) Stiffness coefficient, K_{xx}.

Figure 8. - Effects of circumferential Reynolds number.

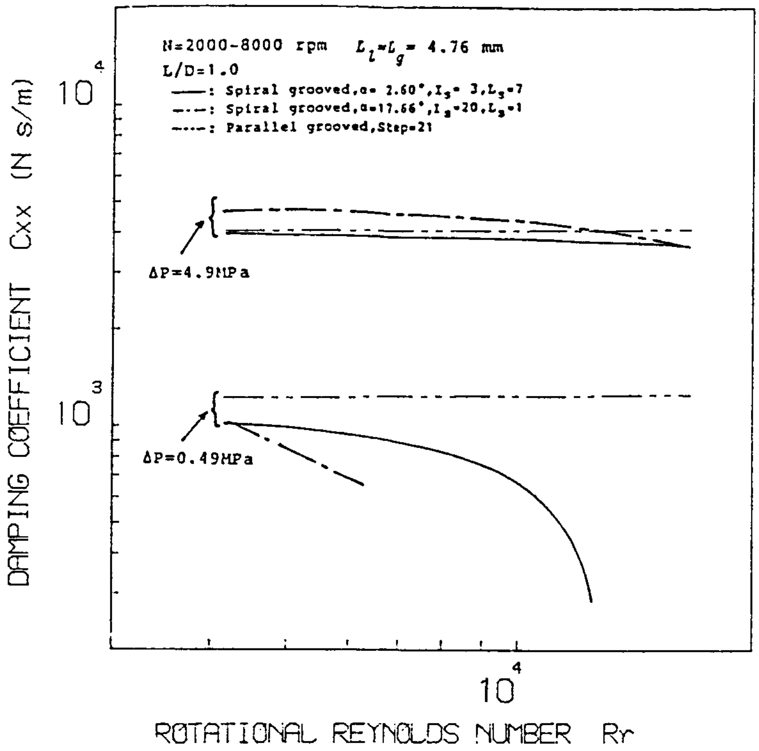

(c) Damping coefficient, C_{xx}.

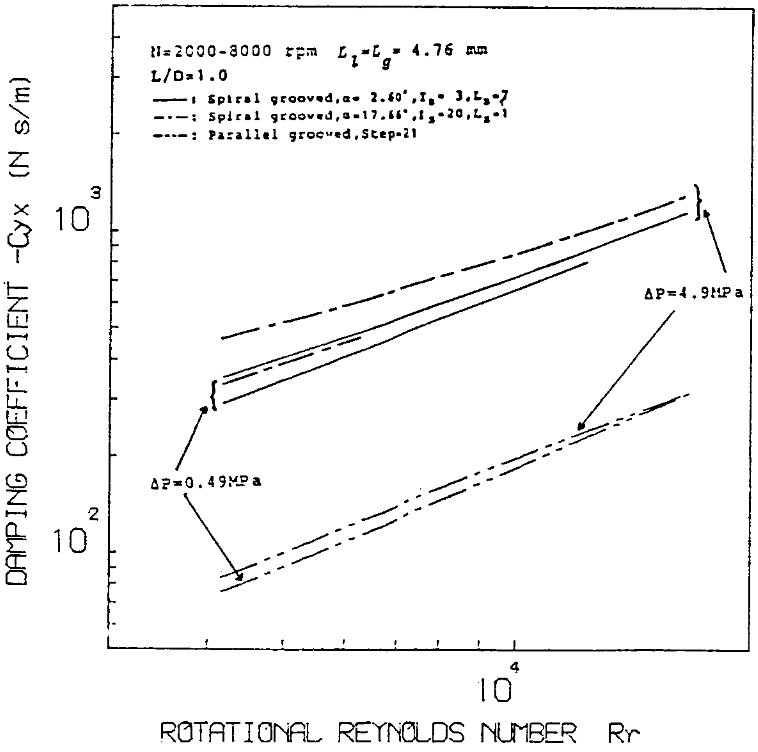

(d) Damping coefficient, C_{yx}.

Figure 8. - Continued.

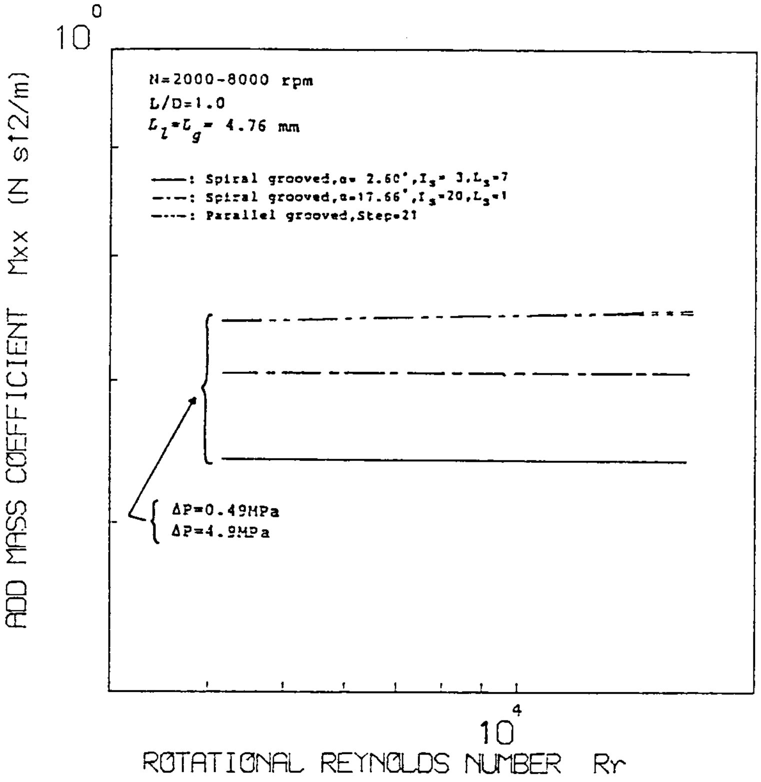

(e) Add mass coefficient, M_{xx}.

Figure 8. - Concluded.

N87-22208

COMPARISON OF HIRS' EQUATION WITH MOODY'S EQUATION FOR DETERMINING ROTORDYNAMIC COEFFICIENTS OF ANNULAR PRESSURE SEALS[†]

Clayton C. Nelson and Dung T. Nguyen
Texas A&M University
College Station, Texas 77843

The rotordynamic coefficients of an incompressible-flow annular pressure seal were determined using a bulk-flow model in conjunction with two different friction factor relationships. The first, Hirs' equation, assumes the friction factor is a function of Reynolds number only. The second, Moody's equation, approximates Moody's diagram and assumes the friction factor is a function of both Reynolds number and relative roughness. For each value of relative roughness, Hirs' constants were determined so that both equations gave the same magnitude and slope of the friction factor. For smooth seals, both relationships give the same results. For rough seals ($e/2H_o = 0.05$) Moody's equation predicts 44% greater direct stiffness, 35% greater cross-coupled stiffness, 19% smaller cross-coupled damping, 59% smaller cross-coupled inertia, and nominally the same direct damping and direct inertia.

NOMENCLATURE

C, c = direct and cross-coupled damping coefficients
D = diameter
e = surface roughness height
F_x, F_y = components of the seal reaction force
f = Friction factor
H = seal clearance
K, k = direct and cross-coupled stiffness coefficients
L = seal length
M, m = direct and cross-coupled inertia coefficients
m,n = Hirs' constants
p = pressure
Δp = pressure drop across the seal
$\mathbf{R}$ = Reynold number ($= 2\rho V H/\mu$)
r = seal radius
t = time
U_z, U_θ = fluid velocity in the z and θ direction
V = fluid velocity
X, Y = rotor displacement from its geometric center

Z, θ = axial and circumferential seal coordinates
ϵ = eccentricity perturbation
μ = viscosity
ρ = density
ω = shaft angular velocity

Subscripts

$0, 1$ = zeroth and first-order perturbations
x, y = rectangular coordinate directions
s, r = shaft and rotor
z, θ = axial and circumferential coordinate directions

INTRODUCTION

The design and safe operation of today's high-performance turbomachinery require accurate predictions of the hydrodynamic forces developed by annular pressure seals. For small orbital motion of the rotor about its geometric center, the hydrodynamic forces are quantified by specifying a set of linearized rotordynamic coefficients as shown in the following equation.

$$-\begin{Bmatrix} F_x \\ F_y \end{Bmatrix} = \begin{bmatrix} K & k \\ -k & K \end{bmatrix} \begin{Bmatrix} X \\ Y \end{Bmatrix} + \begin{bmatrix} C & c \\ -c & C \end{bmatrix} \begin{Bmatrix} \dot{X} \\ \dot{Y} \end{Bmatrix} + \begin{bmatrix} M & m \\ -m & M \end{bmatrix} \begin{Bmatrix} \ddot{X} \\ \ddot{Y} \end{Bmatrix} \tag{1}$$

In this equation, (X, Y) define the motion of the seal rotor relative to its stator; (F_x, F_y) are the components of the hydrodynamic reactive force acting on the rotor; and (K, k), (C, c), and (M, m) are stiffness, damping and inertia coefficients respectively.

Extensive efforts have been made in the last two decades to theoretically predict, and to experimentally measure these rotordynamic coefficients. Lomakin [1] first demonstrated and explained the characteristic "hydrostatic" stiffness of annular seals for a small displacement from the centered position. Most of the subsequent theoretical developments have been made by Black, Jenssen, Allaire, Fleming, Childs, and Nelson [2-16]. The most recent of these developments by Childs [11-14] (liquid seals) and Nelson [15,16] (gas seals) include the effects of fluid prerotation, convergent-tapered geometry, and different surface roughness treatments for the stator and rotor. Both of these analyses proceed from a single set of governing equations which are based on Hirs' turbulent bulk-flow model [17,18].

Comparison between theoretical and experimental results shows moderately good agreement. However, the theory generally tends to underpredict the experimentally measured direct stiffness. Furthermore, this underprediction appears to get substantially worse as the relative roughness, $e/2H_o$, of the seal increases. This has been found to be true both for liquid seals [13,14,19] and for gas seals [22]. There is, however, a specific need to accurately predict rotordynamic coefficients of seals with very rough stators and/or rotors. To retard leakage, soften the effects of rub, increase damping, and decrease the destabilizing effect of the cross-coupled stiffness, various kinds of intentionally roughened surfaces are being tested and used in liquid and gas seal designs [14,16,23].

Failure of the analysis to predict the correct stiffness may, in part, be due to inadequacies in Hirs' equation for the friction factor. For a given set of Hirs' constants, Hirs' equation can accurately reflect the change in the friction factor for small changes in the Reynolds number, but has no functional dependence on the relative roughness. Nevertheless, the relative roughness does change in the circumferential direction when the rotor is displaced from its centered position.

The results presented in this paper compare the theoretical rotordynamic coefficients obtained by using a bulk-flow analysis in conjunction with two different friction factor relationships. The first relationship is Hirs' equation. The second, Moody's equation, assumes the friction factor is a function of both Reynolds number and relative roughness.

GOVERNING EQUATIONS

Figure 1 illustrates the basic geometry and coordinate system used for the annular pressure seal. Using a bulk-flow model and the control volume shown in Fig. 1, a complete derivation of the governing for compressible flow is given in reference [15]. For incompressible flow, these equations reduce to the following form.

$$\frac{\partial H}{\partial t} + \frac{1}{r}\frac{\partial (HU_\theta)}{\partial \theta} + \frac{\partial (HU_z)}{\partial z} = 0 \tag{2}$$

$$\begin{aligned} -\frac{H}{\rho}\frac{\partial p}{\partial z} = \frac{U_z}{2}\left(U_z^2 + U_\theta^2\right)^{1/2} f_s + \frac{U_z}{2}\left[U_z^2 + (U_\theta - r\omega)^2\right]^{1/2} f_r \\ + H\left(\frac{\partial U_z}{\partial t} + \frac{U_\theta}{r}\frac{\partial U_z}{\partial \theta} + U_z\frac{\partial U_z}{\partial z}\right) \end{aligned} \tag{3}$$

$$-\frac{H}{\rho r}\frac{\partial p}{\partial \theta} = \frac{U_\theta}{2}\left(U_z^2 + U_\theta^2\right)^{1/2} f_s + \frac{(U_\theta - r\omega)}{2}\left[U_z^2 + (U_\theta - r\omega)^2\right]^{1/2} f_r + H\left(\frac{\partial U_\theta}{\partial t} + \frac{U_\theta}{r}\frac{\partial U_\theta}{\partial \theta} + U_z\frac{\partial U_\theta}{\partial z}\right) \tag{4}$$

Hirs' Equation

In the governing equations, f_s and f_r represent the friction factors relative to the stator and the rotor respectively. Hirs' turbulent bulk-flow model assumes that these friction factors can be written as:

$$f = \mathrm{n}\mathbf{R}^{\mathrm{m}} \tag{5}$$

where $\mathbf{R}$ is the Reynolds number relative to the surface upon which the shear stress is acting, and the constants n and m are generally empirically determined from static pressure flow experiments. Substitution of the parameters for the annular pressure seal yields the following equations for the friction factors:

$$f_s = \mathrm{n}_s\left[\frac{2\rho H\left(U_z^2 + U_\theta^2\right)^{1/2}}{\mu}\right]^{\mathrm{m}_s} \tag{6}$$

$$f_r = \mathrm{n}_r\left\{\frac{2\rho H\left[U_z^2 + (U_\theta - r\omega)^2\right]^{1/2}}{\mu}\right\}^{\mathrm{m}_r} \tag{7}$$

Moody's Equation

Figure 2 shows a simplified version of Moody's diagram. Moody produced the following approximate equation for the friction factor [24].

$$f = 0.001375\left[1 + \left(20000\frac{e}{D} + \frac{10^6}{\mathbf{R}}\right)^{1/3}\right] \tag{8}$$

This equation gives values within +5% for Reynolds numbers between 4000 and 10^7 and values of e/D up to 0.01. For $e/D > 0.01$, it significantly underestimates the friction factor. Substituting in the parameters of the annular pressure seal, f_s and f_r become:

$$f_s = 0.001375 \left[1 + \left(10^4 \frac{e}{H} + \frac{5(10)^5 \mu}{\rho H (U_z^2 + U_\theta^2)^{1/2}}\right)^{1/3}\right] \tag{9}$$

$$f_r = 0.001375 \left\{1 + \left[10^4 \frac{e}{H} + \frac{5(10)^5 \mu}{\rho H \left[U_z^2 + (U_\theta - r\omega)^2\right]^{1/2}}\right]^{1/3}\right\} \tag{10}$$

Solution Procedure

Assuming small motion of the rotor about its geometric center, the pressure, density, axial velocity, circumferential velocity, and local seal clearance can be expanded in terms of zeroth-order and first-order perturbation variables.

$$H = H_o + \epsilon H_1, \qquad p = p_o + \epsilon p_1, \qquad U_z = U_{z_o} + \epsilon U_{z1}, \qquad U_\theta = U_{\theta_o} + \epsilon U_{\theta 1} \tag{11}$$

Substitution of these expanded variables into the governing equations (2-4) and either (6, 7) or (9, 10) yields a set of zeroth-order and first-order equations. The nonlinear zeroth-order equations are numerically integrated using a bisection method to obtain matched boundary conditions. The linear first-order equations are expanded from three partial differential equations to twelve ordinary differential equations by assuming that the shaft moves in an elliptical orbit. These twelve ordinary differential equations are then numerically integrated using standard numerical integration techniques. A further integration of the first-order pressures circumferentially and axially over a range of orbital speeds yield the rotordynamic coefficients. Complete details of the solution procedure are given in references [15] and [16].

RESULTS

Seal Parameters

To compare the results of these two friction factor equations, rotordynamic coefficients were determined for a high-pressure water seal defined by the following parameters.

Geometry

length: $L = 5.08$ cm (2.00 in)
radius: $r = 7.62$ cm (3.00 in)
nominal clearance: $H_o = 0.381$ mm (15.0 mil)
nominal relative roughness: $e/2H_o = 0 \rightarrow 0.05$

Fluid Properties

density: $\rho = 1000\ \mathrm{kg/m^3}$ ($1.94\ \mathrm{slug/ft^3}$)
viscosity: $\mu = 1.30(10)^{-3}\ \mathrm{N\text{-}s/m^2}$ ($2.72(10)^{-5}\ \mathrm{lb\text{-}s/ft^2}$)

Operating Conditions

Reynolds number: $\mathbf{R}_o = 30{,}000$
pressure drop: $\Delta p = 3.5 \rightarrow 7.0$ MPa ($508 \rightarrow 1015$ psi)
shaft angular speed: $\omega = 3000$ rpm
preswirl ratio: $U_\theta(0,\theta)/(r\omega) = 0.25$

As indicated above, the stator and rotor nominal relative roughness, $e/2H_o$, was varied from 0 to 0.05. To maintain a constant nominal Reynolds number of $\mathbf{R}_o = 30000$, the pressure drop, Δp, was increased along with the roughness. From Moody's diagram, it can be seen that the friction factor varies from $\simeq 0.0056$ to 0.018. This variation is shown by the bold vertical line drawn on the diagram (Figure 2).

For each nominal relative roughness value, a new set of Hirs' constants was determined. These constants were evaluated so that the magnitude and slope of the friction factor from Hirs' equation matched that of Moody's equation. For example, the dashed line on Moody's diagram shows the results of Hirs' friction factor for $e/2H_o = 0.01$.

Rotordynamic Coefficients

The resulting rotordynamic coefficients for the two solutions are shown in Figures 3 - 8. Results from Hirs' equation are shown by the dashed lines, and results from Moody's equation are shown by the solid lines. For smooth seals ($e/2H_o \simeq 0$) both models predict nearly the same values. This result can be explained by observing Moody's diagram. For smooth surfaces, the friction factor curves are close together. That is, changes in relative roughness for a smooth surface cause only minor changes in the friction factor. Thus, circumferential changes in relative roughness due to rotor displacement are not significant.

As the nominal relative roughness is increased, the most striking difference in the predictions is for the direct stiffness and cross-coupled inertia coefficients. For rough seals, use of Moody's equation results in predicted stiffness coefficients which are 44% greater, and cross-coupled inertia coefficients which are 59% smaller. (Cross-coupled inertia terms are, however, so small that their effect on rotordynamic calculations is rather insignificant.)

The physical explanation for the increase in predicted direct stiffness can easily be seen from Figure 9. As shown, stiffness in annular seals is accounted for by the increase in the axial pressure gradient on the near side of a non-centered rotor. When using Moody's equation, the increased relative roughness on the near side results in a larger friction factor then when using Hirs' equation. This in turn, leads to an even larger pressure gradient.

Finally, use of Moody's equation results in predictions which are 35% greater for cross-coupled stiffness and 19% smaller for cross-coupled damping. Direct damping and direct inertia predictions remain nominally the same.

CONCLUSIONS

As stated in the introduction, there is a specific need to accurately predict rotordynamic coefficients of seals with very rough stators and/or rotors. Annular pressure seals are being tested and used which have surfaces that are honeycombed, grooved, knurled, or contain various sizes and shapes of holes and projections. The ratio of the height of these surface irregularities to the clearance is often close to unity (i.e., $e/2H_o \simeq 1.0$). For these rough seals, the theoretically predicted direct stiffness based on Hirs' equation has been substantially smaller than the measured direct stiffness.

In this analysis, it has been shown that for rough seals, the use of Moody's equation gives significantly larger predictions for direct stiffness than use of Hirs' equation. This occurs even though the magnitude and slope of the nominal friction factors from the two equations are the same. This difference can be explained by the fact that Moody 's equation is a function of both roughness and Reynolds number, while Hirs' equation is a function of Reynolds number only. Thus, Moody's equation can account for the effect of the circumferential changes in relative roughness on the friction factor of a non-centered rotor.

From these results, it would appear that reliable predictions of direct stiffness for rough seals must be based on a more sophisticated model than Hirs' equation. This does not, however, imply that the Moody equation used in this paper is the answer. This equation underestimates the friction factor given in Moody's diagram when $e/2H_o > 0.01$, and the diagram itself gives no values for friction factors when $e/2H_o > 0.05$. Furthermore, the equation does not account for the effect of size, shape, and spacing of large surface irregularities on the friction factor. It is possible, however, that some type of modified Moody's equation could be used. That is, for each type of surface irregularity, friction factor relationships could be determined experimentally and/or analytically. From these relationships, a new set of *Moody constants* could be determined and replace those in Moody's original equation.

REFERENCES

1. Lomakin, A.A., "Calculation of Critical Speed and Securing of Dynamic Stability of Hydraulic High-Pressure Pumps with Reference to the Forces Arising in the Gap Seals," *Energomashinostroenie*, Vol. 4, No. 1, p. 1158.

2. Black, H.F., "Effects of Hydraulic Forces in Annular Pressure Seals on the Vibration of Centrifugal Pump Rotors," *J. Mech. Engr. Sci.*, Vol. 11, No. 2, 1969, pp. 206-213.

3. Jenssen, D.N., "Dynamics of Rotor Systems Embodying High Pressure Ring Seals," *Ph.D. disseration, Heriot-Watt University*, Edinburgh, Scotland, July 1970.

4. Black, H.F., and Jenssen, D.N., "Dynamic Hybrid Properties of Annular Pressure Seals," *Proc. J. Mech. Engr.*, Vol. 184, 1970, pp. 92-100.

5. Black, H.F., and Jenssen, D.N., "Effects of High-Pressure Ring Seals on Pump Rotor Vibrations," ASME Paper No. 71-WA/FF-38, 1971.

6. Black, H.F., Allaire, P.E., and Barrett, L.E., "The Effect of Inlet Flow Swirl on the Dynamic Coefficients of High-Pressure Annular Clearance Seals," Ninth International Conference in Fluid Sealing, BHRA Fluid Engineering, Leeuwenhorst, The Netherlands, Apr. 1981.

7. Allaire, P.E., Gunter, E.J., Lee, C.P., and Barrett, L.E., "The Dynamic Analysis of the Space Shuttle Main Engine-High Pressure Fuel Turbopump. Part II - Load

Capacity and Hybrid Coefficients for the Turbulent Interstage Seals," University of Virginia, Report No. UVA/528140/ME76/103.

8. Fleming, D.P., "High Stiffness Seals for Rotor Critical Speed Control," ASME Paper 77-DET-10, Design Technical Engineering Conference, Chicago Ill., Sept. 26-30, 1977.

9. Fleming, D.P., "Stiffness of Straight and Tapered Annular Gas Seals," ASME Paper 78-LUB-18, ASME-ASLE Joint Lubrication Conference, Minneapolis, Minn., Oct. 24-26, 1978.

10. Fleming, D.P., "Damping in Ring Seals for Compressible Fluids," NASA CP2133, Rotordynamic Instability Problems, in High-Performance Turbomachinery, proceeding of workshop held at Texas A&M University, May 12-14, 1980, pp. 169-188.

11. Childs, D.W., "Dynamic Analysis of Turbulent Annular Seals Based on Hirs' Lubrication Equation," *ASME Trans. J. of Lub. Tech.*, Vol. 105, July 1983, pp. 429-436.

12. Childs, D.W., "Finite-Length Solutions for Rotordynamic Coefficients of Turbulent Annular Seals," *AMSE Trans. J. of Lub. Tech.*, Vol. 105, July 1983, pp. 437-444.

13. Childs, D.W., "Finite-Length Solutions for the Rotordynamic Coefficients of Constant-Clearance and Convergent-Tapered Annular Seals," Third International Conference on Vibrations and Rotating Machinery, York, England, Sept. 10-12, 1984.

14. Childs, D.W., and Kim, C.H., "Analysis and Testing for Rotordynamic Coefficients of Turbulent Annular Seals with Different Directionally Homogeneous Surface Roughness Treatment for Rotor and Stator Elements," accepted for publication, *ASME Trans., J. of Lub. Tech.*

15. Nelson, C. C., "Rotordynamic Coefficients for Compressible Flow in Tapered Annular Seals," *ASME Journal of Tribology*, Vol. 107, No. 3, July 1985, pp 318-325.

16. Nelson, C. C., "Analysis for Leakage and Rotordynamic Coefficients of Surface Roughened Tapered Annular Gas Seals," *ASME Journal of Engineering for Power*, Vol. 106, No. 4, Oct. 1984, pp. 927-934.

17. Hirs, G.G., "Fundamentals of a Fulk-Flow Theory for Turbulent Lubrication Films," *Ph.D. dissertation, Delft Technical University*, The Netherlands, July 1970.

18. Hirs, G.G., "A Bulk-Flow Theory for Turbulence in Lubricant Films," *AMSE J. of Lub. Tech.*, April 1973, pp. 137-146.

19. Childs, D.W., and Dressman, J., "Convergent-Tapered Annular Seals: Analysis and Testing for Rotordynamci Coefficients," accepted for publication in *ASME Trans. J. of Lub. Technology.*

20. Childs, D. W., Nelson, C. C., Nicks, D., Scharrer, J., Elrod, D., Hale, K., "Theory Versus Experiment for the Rotordynamic Coefficients of Annular Gas Seals: Part 1, Test Facility and Apparatus," accepted for publication in *ASME J. of Tribology.*

21. Nelson, C. C., Childs, D. W., "Theory Versus Experiment for the Rotordynamic Coefficients of Annular Gas Seals: Part 2, Constant-Clearance and Convergent- Tapered Geometry," accepted for publication in *ASME J. of Tribology.*

22. Elrod, D., Nicks, C., Childs, D.W, and Nelson, C.C., "A Comparison of Experimental and Theoretical Results for Rotordynamic Coefficients of Four Annular Gas Seals," Progress Report for NASA Lewis Research Center Contract NAS8-33716 prepared by Texas A&M University, #TRC-Seals-5-85.

23. Childs, D. W. and Kim, C. H., "Test Results for Round-Hole Pattern Damper Seals: Optimum Configurations and Dimensions for Maximum Net Damping," ASME Paper No. 85-Trib-16.

24. Massey, B.S., *Mechanics of Fluids*, 4th Ed., Van Nostrand Reinhold Co., New York, 1979.

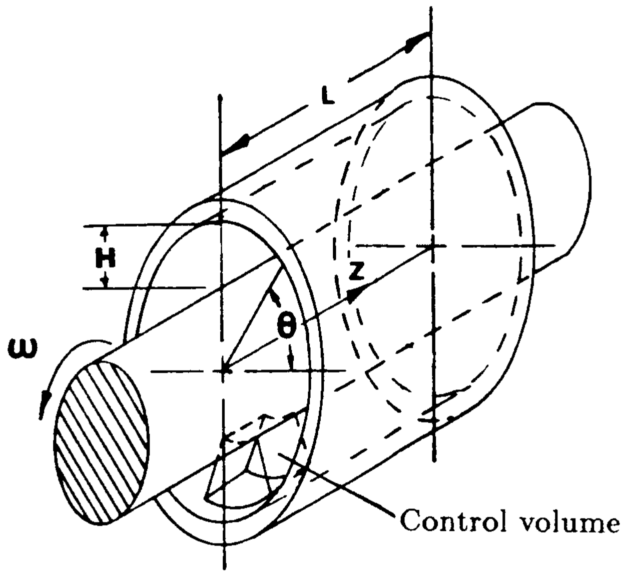
L
H
ω
z
θ
Control volume

Figure 1. Basic Geometry of the annular pressure seal.

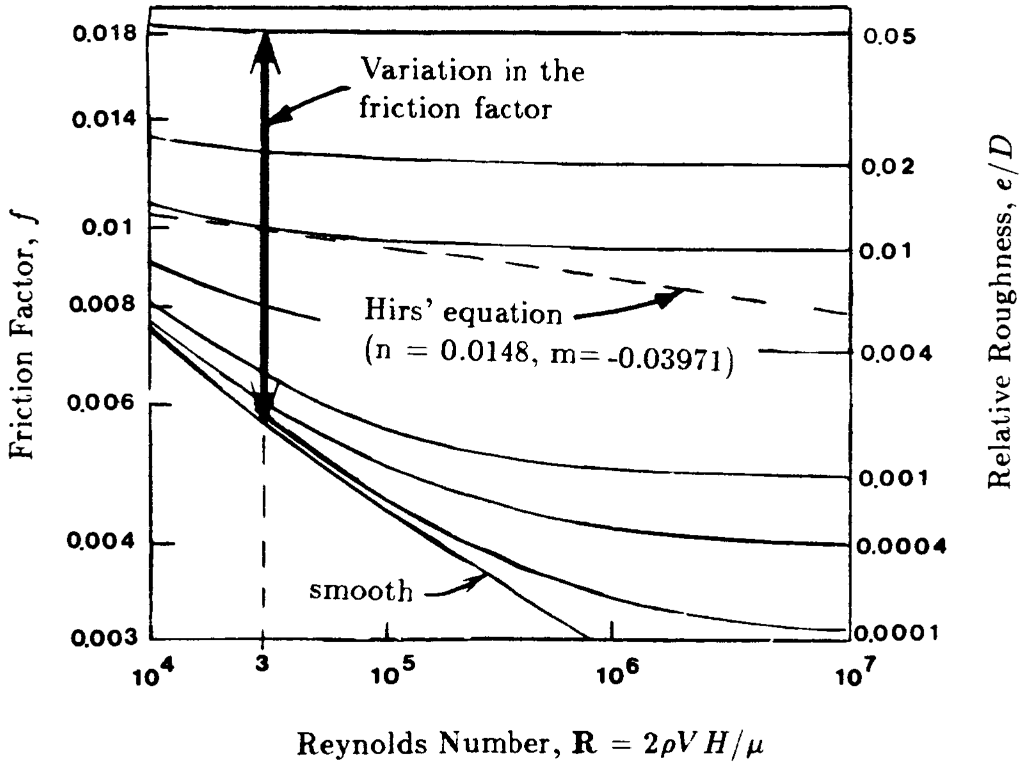

Figure 2. Moody's diagram.

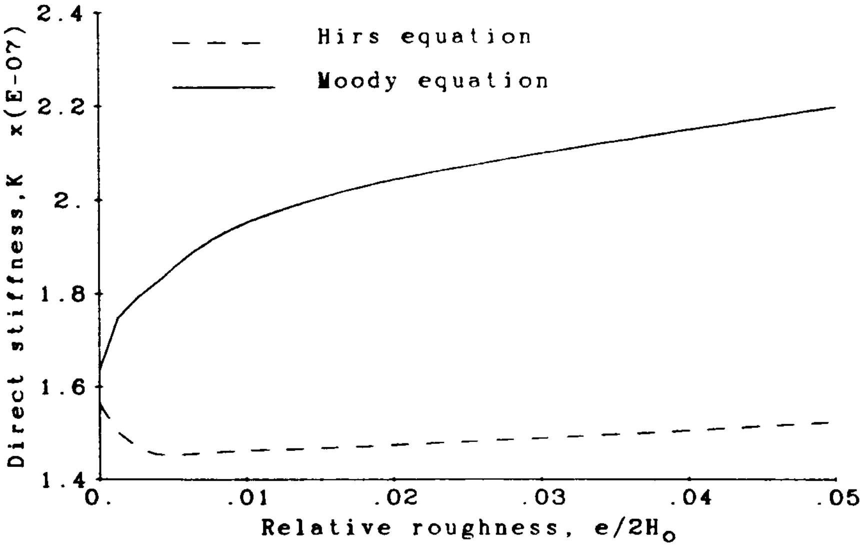

Figure 3. Direct stiffness vs. relative roughness

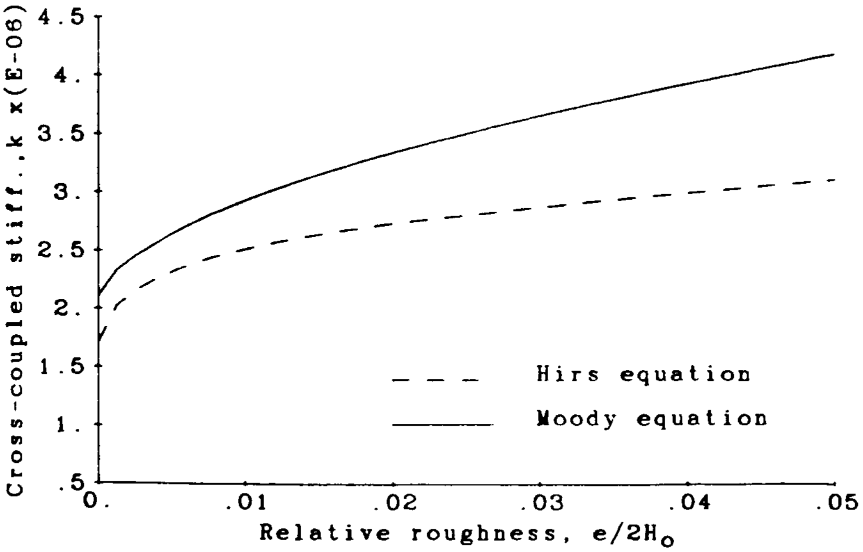

Figure 4. Cross-coupled stiffness vs. relative roughness

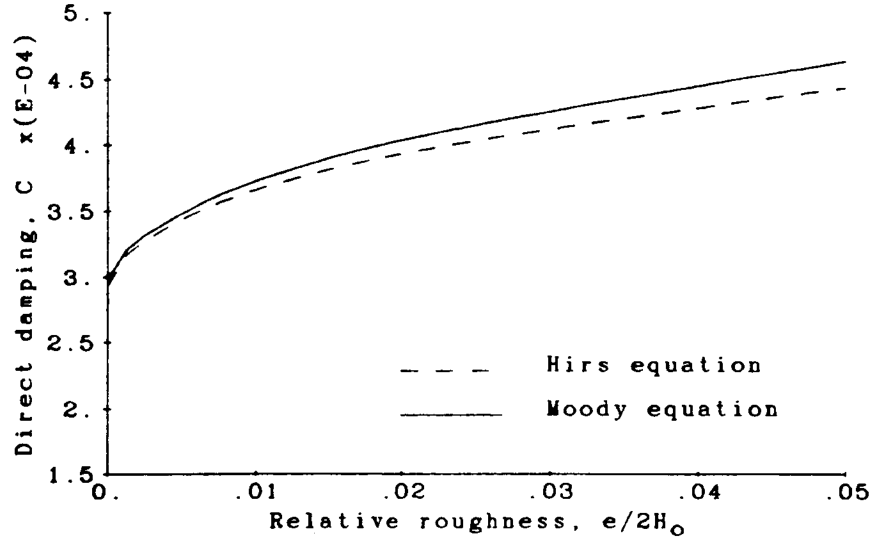

Figure 5. Direct damping vs. relative roughness

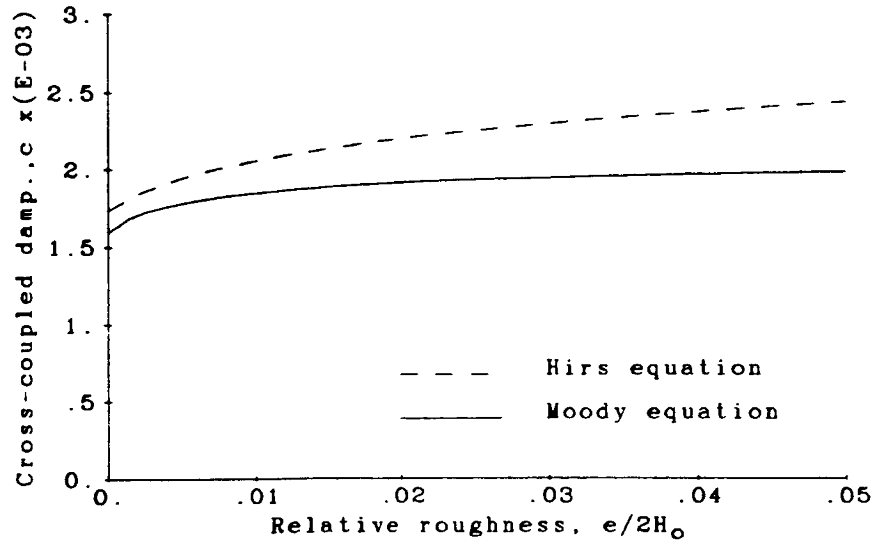

Figure 6. Cross-coupled damping vs. relative roughness

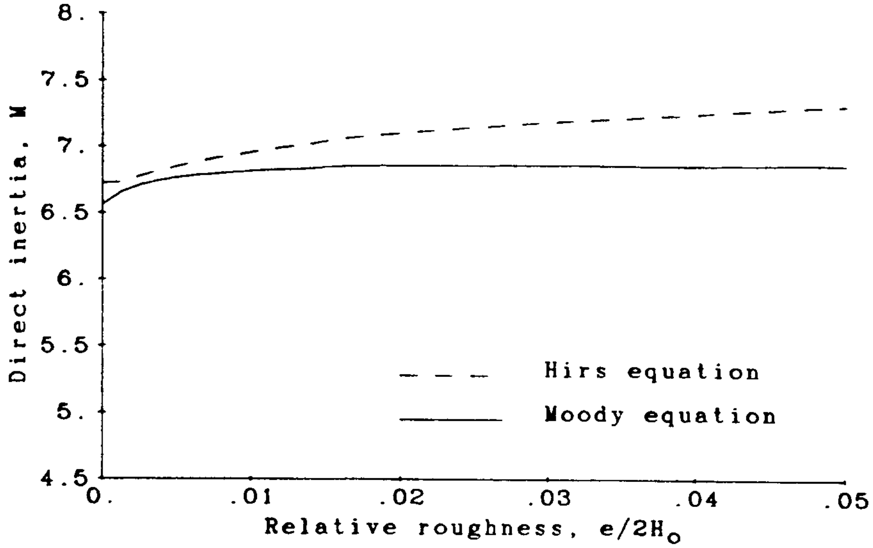

Figure 7. Direct inertia vs. relative roughness

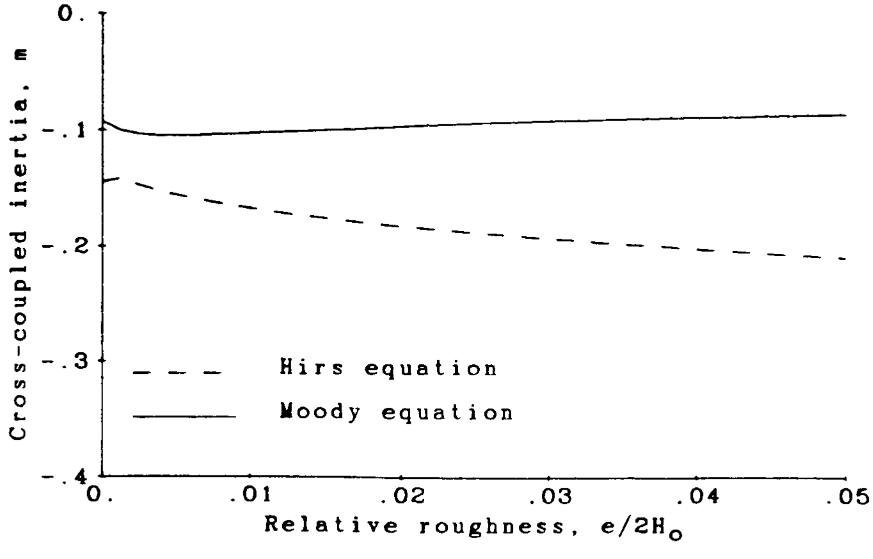

Figure 8. Cross-coupled inertia vs. relative roughness

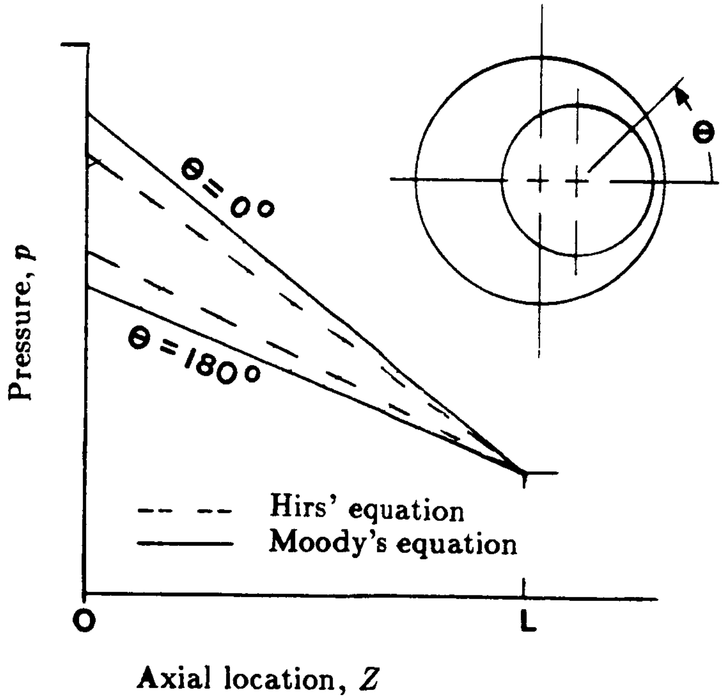

Figure 9. Axial pressure gradient for non-centered rotor.

N87-22209

DESTABILIZING FORCE OF LABYRINTH SEAL

Hiroshi Kanki
Mitsubishi Heavy Industries, Ltd.
Takasago, Japan

Shigeki Morii
Mitsubishi Heavy Industries, Ltd.
Hiroshima, Japan

A great deal of research has recently been conducted to solve the subsynchronous rotor vibration problems in high-performance turbomachinery. Particularly, the destabilizing effect of the labyrinth seal on compressors or turbines has been investigated for many years (refs. 1 to 9). In spite of many efforts the dynamic effect of the labyrinth seal had not been fully determined from qualitative and quantitative points of view. But from our theoretical and experimental work, we have determined completely the dynamic characteristics of the labyrinth seal.

This paper presents the results of recent theoretical and experimental works.

We developed a theoretical study and a numerical calculation program to obtain the dynamic coefficients based on Iwatsubo's perturbation method (ref. 3) and Jenny's tangential momentum effect evaluation method (ref. 9). The simplified formulation was programmed for practical design use. Qualitative and quantitative evaluations of the computer program have been done in several published works. Our experimental study also evaluated damping coefficients and considered inlet swirl effects.

Experimental studies on the labyrinth seal have been performed to improve blading efficiency and to analyze rotor dynamics. For example, the basic labyrinth seal test was done in 1970 to verify Alford's theory, and static and semistatic tests were performed to improve design, to reduce leakage, and to evaluate cross-coupled stiffness. In 1984-1985, to confirm the phenomena, the theoretical analysis of dynamic coefficients, and the swirl effect of the labyrinth seal, we continued seal dynamic model tests. This paper presents primarily the results of the dynamic test.

SYMBOLS

a,b	displacement
C	peripheral velocity
f	cross section of seal chamber
g	gravity acceleration
h	strip height

PRECEDING PAGE BLANK NOT FILMED

L	length of labyrinth seal
l	length of strip pitch
n	ratio of specific heat
P	pressure
q	mass flow rate in axial direction
R	gas constant
R_S	radius of labyrinth seal
T	absolute temperature of gas in seal
t	time
U'	length of acting surface of shear (stator)
U''	length of acting surface of shear (rotor)
u	peripheral velocity of labyrinth seal, $R_S \cdot \Omega$
w	peripheral unit length, $R_S \cdot \psi$
δ	radial clearance of seal
θ_a, θ_b	angular displacement
λ'	friction coefficient (stator)
λ''	friction coefficient (rotor)
μ	strip flow coefficient
ρ	density of gas
τ'	friction shear stress of stator surface
τ''	friction shear stress of rotor surface
Ω	rotating speed of rotor
ω	whirling speed of rotor

Subscripts:

a	outlet
e	entry
F	strip
i	seal chamber number or strip

x	axial
Z	strip number
*	steady state

THEORETICAL STUDY OF DESTABILIZING FORCE CAUSED BY LABYRINTH SEAL

To investigate the destabilizing force caused by the labyrinth seal, an analytical model of the labyrinth seal was established for calculating eight dynamic coefficients (four stiffness coefficients and four damping coefficients) considering inlet swirl effects.

Modeling the Labyrinth Seal

In the flow model of the labyrinth seal Kostyuk introduced one peripheral velocity variable C in the core flow of each labyrinth chamber and developed a simple equation (ref. 5). The developed analytical method uses the modified Kostyuk equation on the labyrinth seal shown in figure 1.

The following fundamental equations are developed for the differential element of unit length showed in figure 2:

Mass Flow Rate Passing Through Strip

$$q_i^2 = \mu_i^2 \cdot \delta_i^2 \cdot (P_{i-1}^2 - P_i^2) \tag{1}$$

Mass Flow Rate Rectified in Chamber

$$\begin{aligned} 2\pi R_{SFi} \cdot q_i &= 2\pi R_{Si} \cdot q_{ei} \\ 2\pi R_{SFi+1} \cdot q_{i+1} &= 2\pi R_{Si} \cdot q_{ai} \end{aligned} \tag{2}$$

Continuous Flow Rate in Chamber

$$\frac{\partial(\rho_i f_i)}{\partial t} + f_i \cdot \frac{\partial(\rho_i C_i)}{\partial W_i} + (q_{ai} - q_{ei}) = 0 \tag{3}$$

Circumferential Momentum in Chamber

$$\frac{\partial(\rho_i f_i C_i)}{\partial t} + f_i \cdot \frac{\partial(\rho_i C_i^2)}{\partial w_i} + (q_{ai} C_{ai} - q_{ei} C_{ei}) + \tau_i' U_i - \tau_i'' U_i'' = -f_i \cdot \frac{\partial P_i}{\partial w_i} \tag{4}$$

Equation of State

$$\begin{aligned} P_i &= g\rho_i \cdot R_i \cdot T_i \\ P_i &= \rho_i^{-n_i} = \text{Const.} \end{aligned} \tag{5}$$

These equations were established for each strip and chamber. And the inlet and outlet conditions of the seal were given as follows:

$$P_o = P_{*o} = P_e \qquad P_Z = P_{*Z} = P_a \qquad T_o = T_e$$
$$P_Z = T_a \qquad C_o = C_{*o} = C_e \tag{6}$$

Method of Solution

To solve equations (1) to (5), we applied Iwatsubo's method (ref. 3), that is, the perturbation linealized method, as follows. The following nondimensional variables ξ, n, ζ, and ψ were introduced as

$$P_i = P_{*i}(1 + \xi_i), \quad C_i = C_{*i}(1 + \eta_i)$$
$$C_{ei} = C_{e*i}\,(1 + \eta_{ei}), \quad C_{ai} = C_{e,\,i+1} = C_{e*i+1}\,(1 + \eta_{e,\,i+1}) \tag{7}$$
$$q_i = q_{*i}\cdot(1+\zeta_i), \quad \delta_i = \delta_{*i}(1 + \psi_i)$$

and, assuming that the rotor is whirling along an elliptical orbit, ψ_i is represented as

$$\psi_i = \frac{a_i}{\delta_{*i}}\cos\omega t\cdot\cos\varphi + \frac{b_i}{\delta_{*i}}\sin\omega t\cdot\sin\varphi \tag{8}$$

Rotor displacement a_*, b_* and angular displacement θ_a, θ_b have the following relation:

$$a_i = a_* + \theta a\cdot\sum_{j=1}^{i-1}\ell_j \qquad b_i = b_* - \theta_b\cdot\sum_{j=1}^{i-1}\ell_j \tag{9}$$

Then these equations were divided into the steady-state equations and the dynamic-state equations shown in table I. As the number of variables was greater than the number of equations, the following two assumptions were made:

(1) Steady-State Tangential Momentum Parameter K_s

The parameter K_s, suggested by Jenny (ref. 9), is defined as follows:

$$C_{e*i} - C_{a*i} - Ks\cdot(C_{e*i} - C_{*i}) \tag{10}$$

This parameter is the one most important to the destabilizing force and depends on the labyrinth seal geometry.

(2) Dynamic-State Tangential Momentum Parameter K_D

In the dynamic state, a parameter K_D, different from Jenny's K_s parameter (ref. 9) as

$$\eta_{ei} = K_o \cdot \eta_i \tag{11}$$

These steady state and dynamic state differential equations yield to the algebraic linear equations with eight coefficients K_{xx}, K_{xy}, K_{yx}, K_{yy}, C_{xx}, C_{xy}, C_{yx}, and C_{yy} by Iwatsubo's method (ref. 3).

And assuming that the rotor is at the center of the labyrinth seal, the coefficients satisfy the next condition

$$\circ\ K_{xx} = K_{yy}, \quad K_{xy} = -K_{yx}, \quad C_{xx} = C_{yy}, \quad C_{xy} = -C_{yx} \tag{12}$$

Numerical Analysis and Comparison Between Theory and Published Experimental Results

Two experiments on labyrinth seal destabilizing force have been published: Wright's (ref. 1), on the effect of bore taper; and Benckert's (ref. 12), which clarified the effect of entry swirl. First, the analytical results of using the preceding method are compared with Wright's experimental results. The configuration of the seal is shown in figure 3. The calculated and measured dynamic coefficient data are shown in figures 4 and 5. The calculation was performed with respect to the experimental data on the effects of taper bore. The taper bore effect is summarized in table II.

The second step compares the calculated results with Benckert's experimental results for the full labyrinth seal. As shown in figure 6, the calculated results and Benckert's experimental results are compared using Benckert's nondimensional variables K^*_0, E^*_0 as follows.

$$K_o^* = \frac{K_{xy}}{\dfrac{(P_z - P_o)\cdot R_s \cdot L}{\delta}} \tag{13}$$

$$E_o^* = \frac{\rho_o}{2} C_o^2 \Big/ \left(P_z - P_o + \frac{\rho_o}{2} C_{axo}^2\right) \tag{14}$$

The calculation and experiment have a good agreement. The calculated entry swirl effect is also shown in table II.

EXPERIMENTAL STUDY OF SMALL LABYRINTH SEAL MODEL

A small labyrinth seal model was tested to qualitatively confirm labyrinth seal dynamics. The experimental model is shown in figure 7. The model casing had four nozzles attached to the annular chamber of the labyrinth seal in the tangential direction (ref. 7). The inlet swirl could be alternated by nozzle selection for each test condition. The dimensions of the model labyrinth seal are summarized in table III. The model was designed to demonstrate the occurrence of whirl at relatively low pressure.

The main test items are summarized in table IV. The tests measured system damping for each test condition. The effect of shaft rotation is very small because of the size of the model and the limit of the rotating speed. Therefore most tests were preformed in nonrotating conditions. System damping was measured by perturbing test working conditions. The free vibration decay was measured for each test. The following results were obtained from this series of tests.

Effect of Labyrinth Seal on Rotor Stability

Figure 8 shows the typical test results for the original straight seal. System damping varied according to nozzle inlet pressure. The nozzle inlet pressure represents the seal inlet swirl velocity. The seal inlet pressure was about one-half of the nozzle inlet pressure.

The measured damping ratio tended to increase up to 0.2 kgf/cm^2, to decrease as pressure increased, and to fall into the unstable region for pressure over 0.5 kgf/cm^2. The vibration waves in figure 8 clearly show the change of system damping.

Effect of the Labyrinth Seal on Damping

Figure 9 shows test results at the no-swirl condition for the original straight seal. The damping increased with inlet pressure and the natural frequency slightly decreased. This shows that the seal has a direct effect on damping.

Effect of Tapered bore

Figure 10 shows the test results for the simplified tapered-bore seal. The clearances were changed for half the number of seal fins so that the seal would simulate both a convergent and a divergent seal. For this model the convergent seal showed more stable characteristics than the divergent seal. However, the differences between them were very small.

Effect of Swirl Breaker

To reduce the destabilizing effect of inlet swirl, two types of swirl breaker were tested. The one had radial bypass holes and the other had antiswirl bypass holes. The results (fig. 11) show a significant increase in stability limit for both cases, and with the antiswirl breaker the stable condition could be maintained to about four times the inlet pressure.

Comparison of Test Results with Calculated Results

Figure 12 shows the nondimensional destabilizing effect (by Benckert's method) for swirl test results and analytical values for conditions associated with the original straight seal model and with tapered-bore seal models. The figure shows fairly good agreement between the theory and the experiment for both the qualitative and quantitative points of views.

EXAMPLE OF APPLICATION

The method of calculating labyrinth seal dynamics was applied to solve compressor vibration problems (ref. 10).

When the compressor was replaced by a new machine with improved performance the machine experienced severe unstable subsynchronous whirl over 90 percent load. The stability characteristics were analyzed by the Mitsubishi rotor dynamics program (ref. 11). The middle of figure 13 shows the stability graph of this rotor system; the graph includes the labyrinth seal destabilizing effects calculated by this work.

After lengthy discussions of the analytical results and the observed phenomena, we decided on a countermeasure, the installation of a damper bearing. A one-day shutdown of the compressor allowed the damper bearing to be installed without unbolting the compressor casing. When the compressor was run with the damper bearing, the subsynchronous vibration completely disappeared. The top and bottom figure of figure 13 compare vibration records from before and after damper bearing installation.

CONCLUSIONS

Our theoretical and experimental study of the destabilizing force of the labyrinth seal confirmed the following dynamic characteristics:

1. The unstable vibration phenomena of labyrinth seals are clearly demonstrated by a simple model rotor system.

2. The existence of the damping effect in labyrinth seals is confirmed in the absence of inlet swirl.

3. For this model the tapered clearance of the labyrinth seal has little effect on the destabilizing force.

4. The special swirl breaker showed a reasonable reduction of the destabilizing effect of the labyrinth seal.

5. Application of the results of the stability analysis gave a reasonable interpretation for actual turbomachinery vibration phenomena.

REFERENCES

1. Benckert, H.; and Wachter, J.: Flow Induced Spring Constants of Labyrinth Seals. I. Mech. E, Sept. 1980. (See also NASA CP-2338, pp. 189-212.)

2. Childs, D.; and Dressman, J.: Testing of Turbulent Seals for Rotordynamic Coefficients. Rotordynamic Instability Problems in High-Performance Turbomachinery, NASA CP-2250, 1982, pp. 157-171.

3. Iwatsubo, T.; et al.: Flow Induced Force of Labyrinth Seal. Rotordynamic Instability Problems in High-Performance Turbomachinery, NASA CP-2250, 1982, pp. 205-222.

4. Kurohashi, M.; et al.: Spring and Damping Coefficients of Labyrinth Seals. Proceedings I. Mech. E., 1980.

5. Kostyuk, A.: Theoretical Analysis of Aerodynamic Forces in Labyrinth Glands of Turbomachines. Teploenergetika, 1972.

6. Wright, D.V.: Air Model Test of Labyrinth Seal Forces on a Whirling Rotor. ASME, Eng. Power, Oct. 1978.

7. Leong, Y.M.M. Salman; Brown, R.D.: Experimental Investigations of Lateral Forces Induced by Flow through Model Labyrinth Glands. Rotordynamic Instability Problems in High-Performance Turbomachinery, NASA CP-2338, 1984, pp. 187-210.

8. Miller, E.H.; and Vohr, J.H.: Preliminary Investigation of Labyrinth Packing Pressure Drops at Onset of Swirl-Induced Rotor Instability. Rotordynamic Instability Problems in High-Performance Turbomachinery, NASA CP-2338, 1984, pp. 281-294.

9. Jenny, R.: Labyrinths as a Cause of Self-excited Rotor Oscillations in Centrifugal Compressors. Sulzer Technical Review 4, 1980.

10. Morii, S.; Nishimoto, K.; and Kanki, H.; et al.: On the Subsynchronous Whirl in the Centrifugal Compressor. ICVPE, 1986. To be published.

11. Shiraki, K.; and Kanki, H.: A New Vibration Criteria for High Speed Large Capacity Turbomachinery. Proceeding of the Eighth Turbomachinery Symposium.

12. Wright, D.V.: Labyrinth Seal Forces on a Whirling Rotor. ASME, AMD-Vol. 55, 1983.

TABLE I. - LINEALIZED EQUATION OF LABYRINTH SEAL

Circumferential Momentum Equation

$$\frac{f_{*i}}{n}\frac{\partial \xi_i}{\partial t} + f_{*i}\frac{\partial \eta_i}{\partial t} + \frac{f_{*i}}{R_{si}}\left(\frac{gR_iT_i}{C_{*i}} + \frac{C_{*i}}{n}\right)\frac{\partial \xi_i}{\partial \varphi} + \frac{2f_{*i}C_{*i}}{R_{si}}\frac{\partial \eta_i}{\partial \varphi}$$

$$- \frac{gR_iT_iP_{*i+1}^2\mu_{i+1}^2\delta_{*i+1}^2C_{e*i+1}R_{sFi+1}^2}{q_{e*i}P_{*i}C_{*i}R_{si}^2}\xi_{i+1}$$

$$+ \Big[\frac{gR_iT_iP_{*i}}{q_{e*i}C_{*i}R_{si}^2}(\mu_{i+1}^2\delta_{*i+1}^2C_{e*i+1}R_{SFi+1}^2 + \mu_i^2\delta_{*i}^2C_{e*i}R_{SFi}^2)$$

$$+ \frac{1}{2}\{\lambda_i'U_i'|C_{*i}| - \lambda_i''U_i''|u_i - C_{*i}|(\frac{u_i}{C_{*i}} - 1)\}\Big]\xi_i$$

$$- \frac{gR_iT_iP_{*i-1}\mu_i^2\delta_{*i}^2C_{e*i}R_{sFi}^2}{q_{e*i}P_{*i}C_{*i}R_{si}^2}\xi_{i-1} + \frac{gR_iT_iq_{e*i}C_{e*i+1}}{P_{*i}C_{*i}}\eta_{ei+1}$$

$$+ \{\lambda_i'U_i'|C_{*i}| + \lambda_i''U_i''|u_i - C_{*i}|\}\eta_i - \frac{gR_iT_iq_{e*i}C_{e*i}}{P_{*i}C_{*i}}\eta_{ei}$$

$$= \frac{gR_iT_i}{2q_{e*i}P_{*i}C_{*i}R_{si}^2}\{\mu_{i+1}^2\delta_{*i+1}C_{e*i+1}R_{SFi+1}^2(P_{*i}^2 - P_{*i+1}^2) - \mu_i^2\delta_{*i}C_{e*i}R_{SFi}^2(P_{*i-1}^2 - P_{*i}^2)\}$$

$$\{a_*\cos(\varphi + \omega t) + a_*\cos(\varphi - \omega t) - b_*\cos(\varphi + \omega t) + b_*\cos(\varphi - \omega t)\}$$

$$+ \frac{\omega \ell_i}{2}\{-a_*\sin(\varphi + \omega t) + a_*\sin(\varphi - \omega t) + b_*\sin(\varphi + \omega t) + b_*\sin(\varphi - \omega t)\}$$

$$+ \frac{gR_iT_i}{2q_{e*i}P_{*i}C_{*i}R_{si}^2}\{\mu_{i+1}^2\delta_{*i+1}^2C_{e*i+1}R_{SFi+1}^2(P_{*i}^2 - P_{*i+1}^2)\sum_{j=1}^{i}\ell_j$$

$$- \mu_i^2\delta_{*i}C_{e*i}R_{SFi}^2(P_{*i-1}^2 - P_{*i}^2)\sum_{j=1}^{i-1}\ell_j\}$$

$$\{\theta_a\cos(\varphi + \omega t) + \theta_a\cos(\varphi - \omega t) - \theta_b\cos(\varphi + \omega t) + \theta_b\cos(\varphi - \omega t)$$

$$+ \frac{\omega \ell_i}{2}(\sum_{j=1}^{i}\ell_j - S_i\ell_i)\{-\theta_a\sin(\varphi + \omega t) + \theta_a\sin(\varphi - \omega t) + \theta_b\sin(\varphi + \omega t) + \theta_b\sin(\varphi - \omega t)\}$$

TABLE I. - CONCLUDED.

Steady State Equation

- Mass Flow Rate Equation

$$\frac{q_i^2}{\mu_i^2 \delta_i^2} = P_{i-1}^2 - P_i^2$$

- Continuous Equation

$$R_{SFi} q_i = R_{si} q_{ei} = R_{SFi+1} q_{i+1}$$

- Circumferential Momentum Equation

$$q_{e*i}(C_{e*i+1} - C_{e*i}) + \frac{1}{2} \frac{\lambda_{\acute{i}} u_{\acute{i}}}{g R_i T_i} P_{*i} |C_{*i}| C_{*i}$$

$$- \frac{1}{2} \frac{\lambda_{\bar{i}} u_{\bar{i}}}{g R_i T_i} P_{*i} |u_i - C_{*i}| (u_i - C_{*i}) = 0$$

Dynamic State Equation

- Continuous Equation

$$\frac{f_{*i}}{n} \frac{\partial \xi_i}{\partial t} + \frac{C_{*i} f_{*i}}{R_{si} \cdot n} \frac{\partial \xi_i}{\partial \varphi} + \frac{C_{*i} f_{*i}}{R_{si} \cdot n} \frac{\partial \eta_i}{\partial \varphi} - \frac{g R_i T_i P_{*i+1}^2 \mu_{i+1}^2 \delta_{*i+1}^2 R_{SFi+1}^2}{q_{e*i} P_{*i} R_{si}^2} \xi_{i+1}$$

$$+ \frac{g R_i T_i P_{*i}}{q_{e*i} R_{si}^2} (\mu_{i+1}^2 \delta_{*i+1}^2 R_{SFi+1}^2 + \mu_i^2 \delta_{*i}^2 R_{SFi}^2) \xi_i - \frac{g R_i T_i P_{*i-1}^2 \mu_i^2 \delta_{*i}^2 R_{SFi}^2}{q_{e*i} P_{*i} R_{si}^2} \xi_{i-1}$$

$$= \frac{u\, g R_i T_i}{2 q_{e*i} R_{*i} R_{si}^2} \{\mu_{i+1}^2 \delta_{*i+1} R_{SFi+1}^2 (P_{*i}^2 - P_{*i+1}^2) - \mu_i^2 \delta_{*i} R_{SFi}^2 (P_{*i-1}^2 - P_{*i}^2)\}$$

$$\{a_* \cos(\varphi + \omega t) + a_* \cos(\varphi - \omega t) - b_* \cos(\varphi + \omega t) + b_* \cos(\varphi - \omega t)\}$$

$$+ \frac{\omega \ell_i}{2} \{-a_* \sin(\varphi + \omega t) + a_* \sin(\varphi - \omega t) + b_* \sin(\varphi + \omega t) + b_* \sin(\varphi - \omega t)\}$$

$$+ \frac{g R_i T_i}{2 q_{e*i} P_{*i} R_{si}^2} \{\mu_{i+1}^2 \delta_{*i+1} R_{SFi+1}^2 (P_{*i}^2 - P_{*i+1}^2) \sum_{j=1}^{i} \ell_j - \mu_i^2 \delta_{*i} R_{SFi}^2 (P_{*i-1}^2 - P_{*i}^2) \sum_{j=1}^{i-1} \ell_j\}$$

$$\{\theta_a \cos(\varphi + \omega t) + \theta_a \cos(\varphi - \omega t) - \theta_b \cos(\varphi + \omega t) + \theta_b \cos(\varphi - \omega t)\}$$

$$+ \frac{\omega \ell_i}{2} \left(\sum_{j=1}^{i} \ell_j - S_i \ell_i\right) \{-\theta_a \sin(\varphi + \omega t) + \theta_a \sin(\varphi - \omega t) + \theta_b \sin(\varphi + \omega t) + \theta_b \sin(\varphi - \omega t)\}$$

TABLE II. - SUMMARY OF CASE STUDY

	Tapered bore seal (Diverging - straight - converging)	Entry swirl (backward - forward)
K_{xx}	⟶ Rigid	- - - - → A little rigid
K_{xy}	⟶ Destabilizing for forward swirl	(-) ⟶ (+) Destabilizing for forward swirl
C_{xx}	⟶ Stabilizing	Positive and almost independent of entry swirl
C_{xy}	Rigid for forward swirl ⟵	Positive and almost independent of entry swirl

TABLE III. - SPECIFICATION OF TEST MODEL

Seal diameter, mm	100
Seal radial clearance, mm	0.25
Height of seal fin, mm	2.75
Pitch of seal fin, mm	4.00
Numbers of fins	15x2
Inlet pressure, atm, absolute	1 to 3.2
Discharge pressure, atm, absolute	1
Critical speed, rpm	930

TABLE IV. - TEST ITEMS AND OBJECTIVES

Test items		Objective
Original	Swirl effect	Effect of inlet swirl
	Rotation effect	Effect of rotation of rotor
	Clearance effect	Effect of seal clearance of same configuration
	Tapered clearance effect	Effect of convergent and divergent clearance configuration
With swirl breaker	Swirl breaker effect	Effect of specially designed swirl breaker

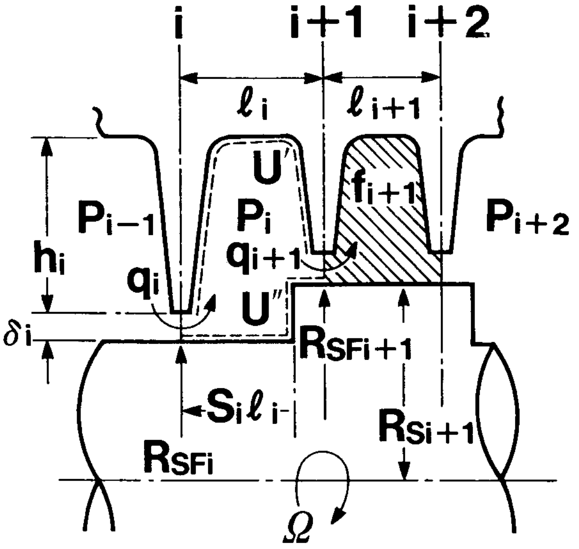
i
i+1
i+2
ℓi
ℓi+1
U′
fi+1
Pi−1
Pi
Pi+2
hi
qi
qi+1
U″
δi
RSFi+1
Siℓi
RSi+1
RSFi
Ω

Figure 1. - Labyrinth seal.

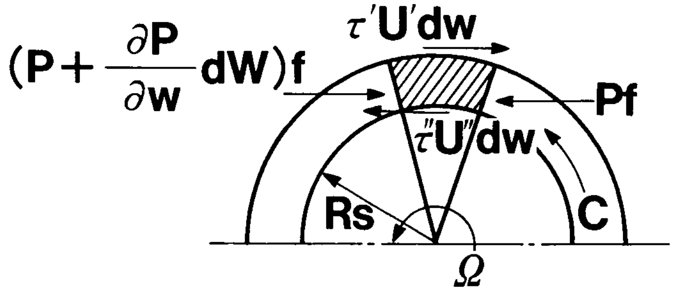
(P+∂P/∂w dW)f
τ′U′dw
Pf
τ″U″dw
Rs
C
Ω

Figure 2. - Cross section of chamber.

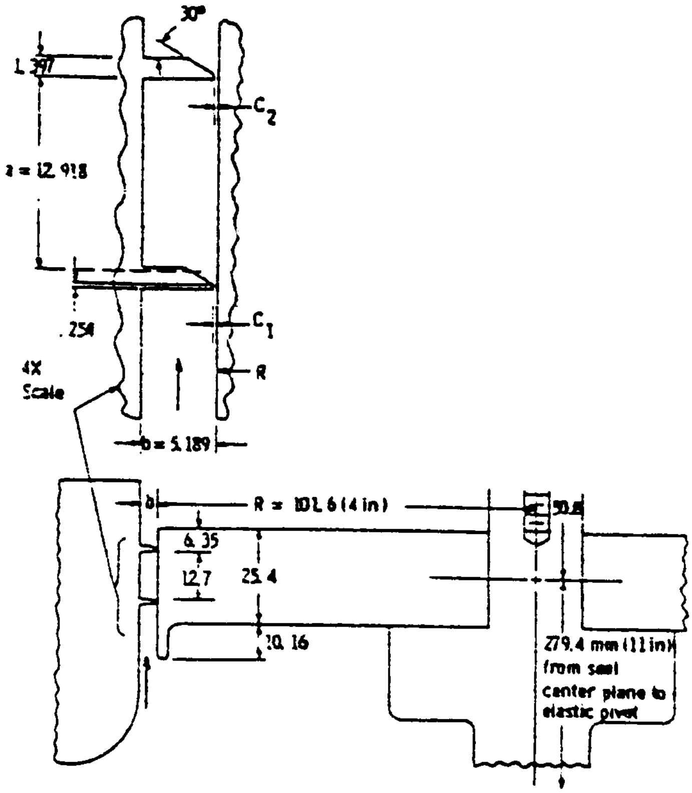
30°
1.397
a = 12.918
C2
C1
.254
R
4X Scale
b = 5.189
b
R = 101.6 (4 in)
50.8
6.35
12.7
25.4
10.16
279.4 mm (11 in) from seal center plane to elastic pivot

Revolution Speed : 1800rpm

Seal Type	C_2/C_1	C_1 (mm)	C_2 (mm)
Diverging	1.4973	0.1311	0.1963
Straight	1.0	0.1585	0.1585
Converging	0.6642	0.1915	0.1272

Outlet Pressure : 1.076kgf/cm^2

Figure 3. - Seal configurations by Wright's test (ref. 12).

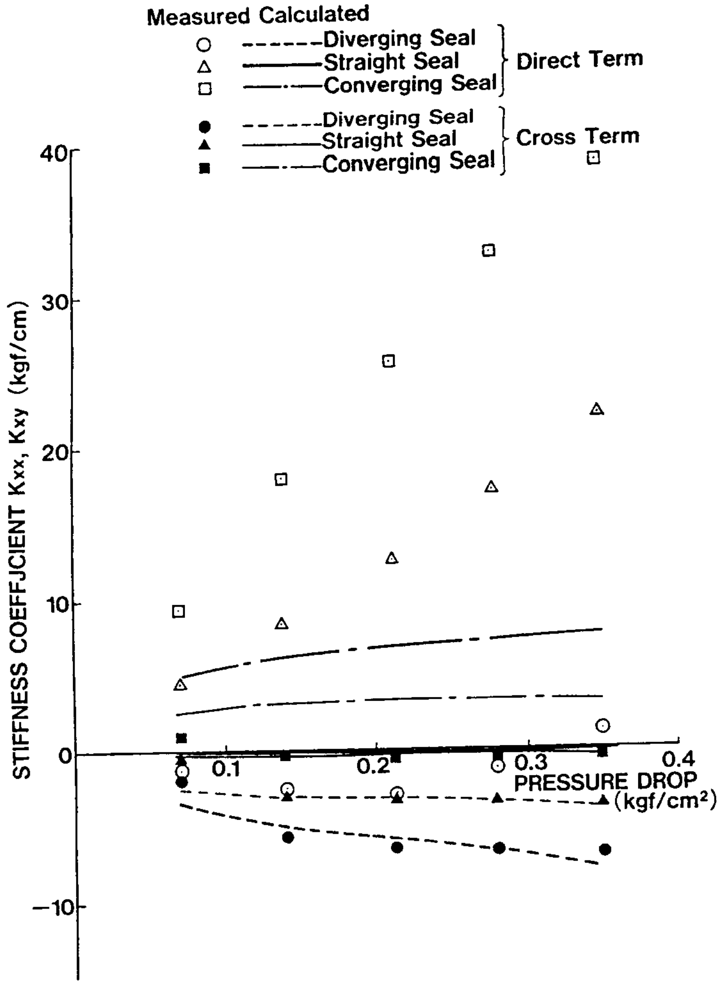

Figure 4. - Comparison of calculated and measured stiffness coefficients.

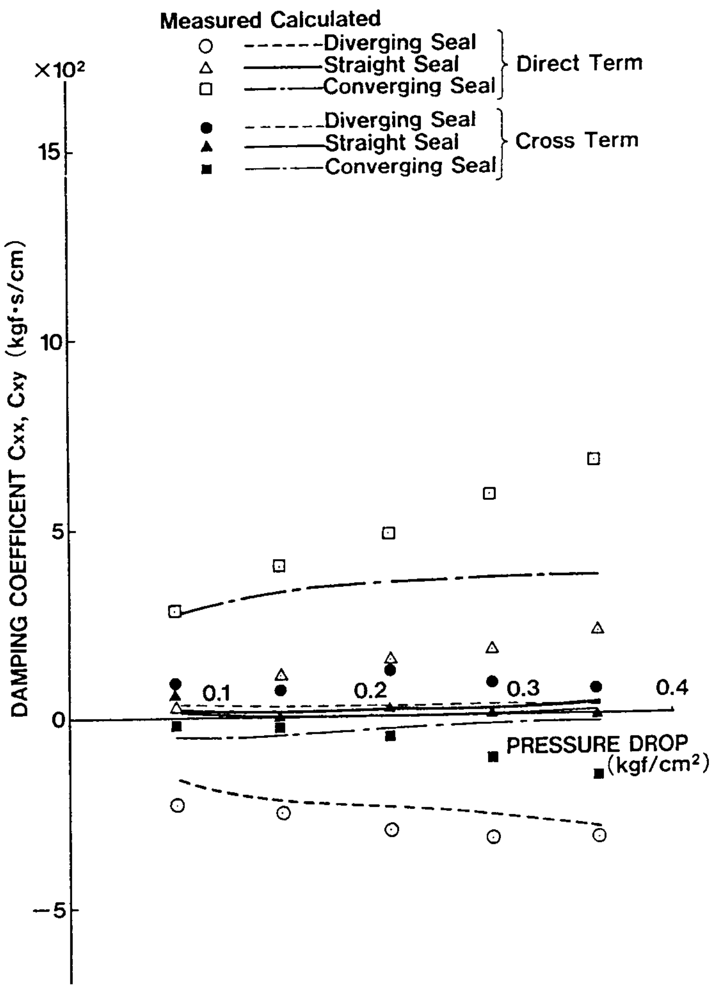

Figure 5. - Comparison of calculated and measured damping coefficients.

ORIGINAL PAGE IS
OF POOR QUALITY

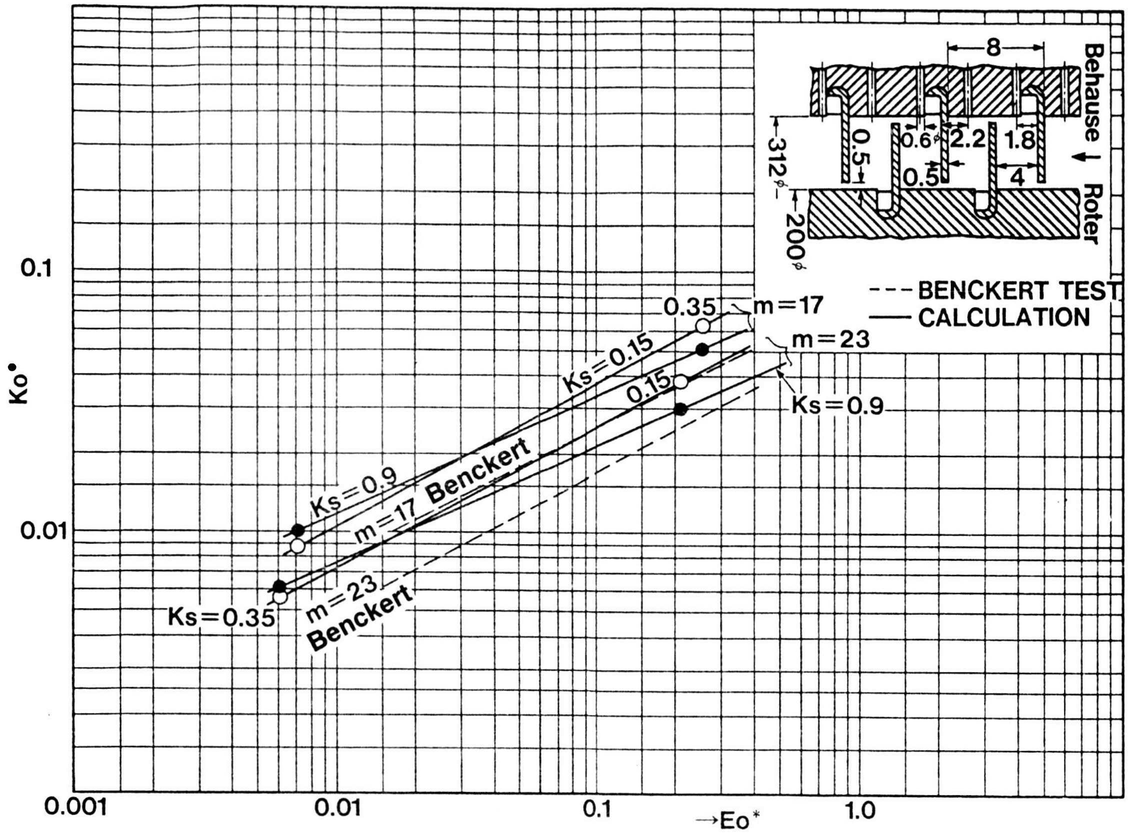

Figure 6. - Comparison of calculated cross-coupling coefficient with that measured by Benckert's test (ref. 1).

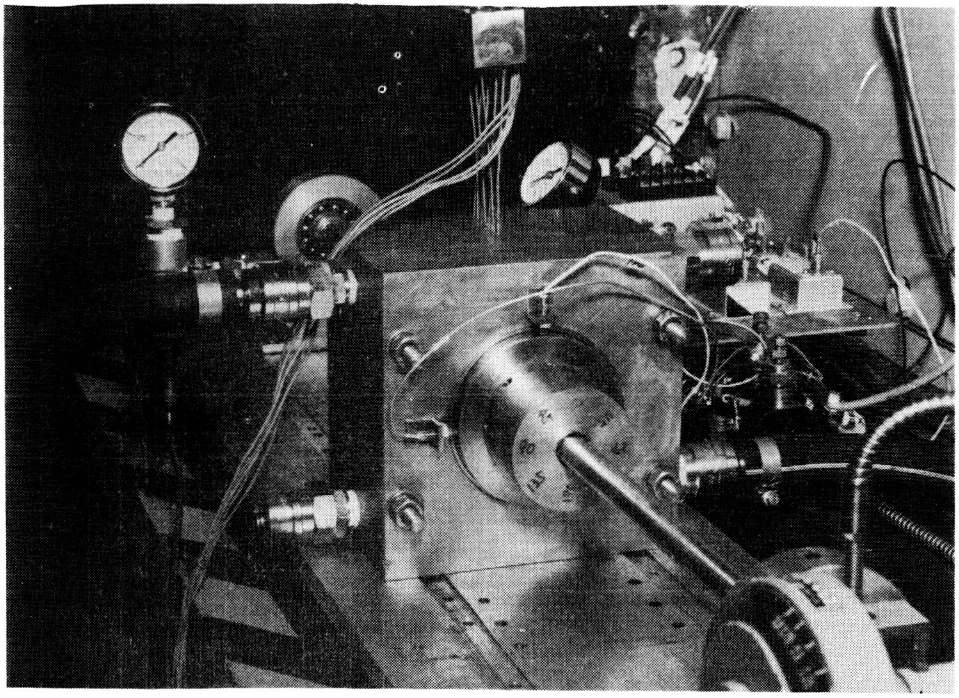

Figure 7. - Test model.

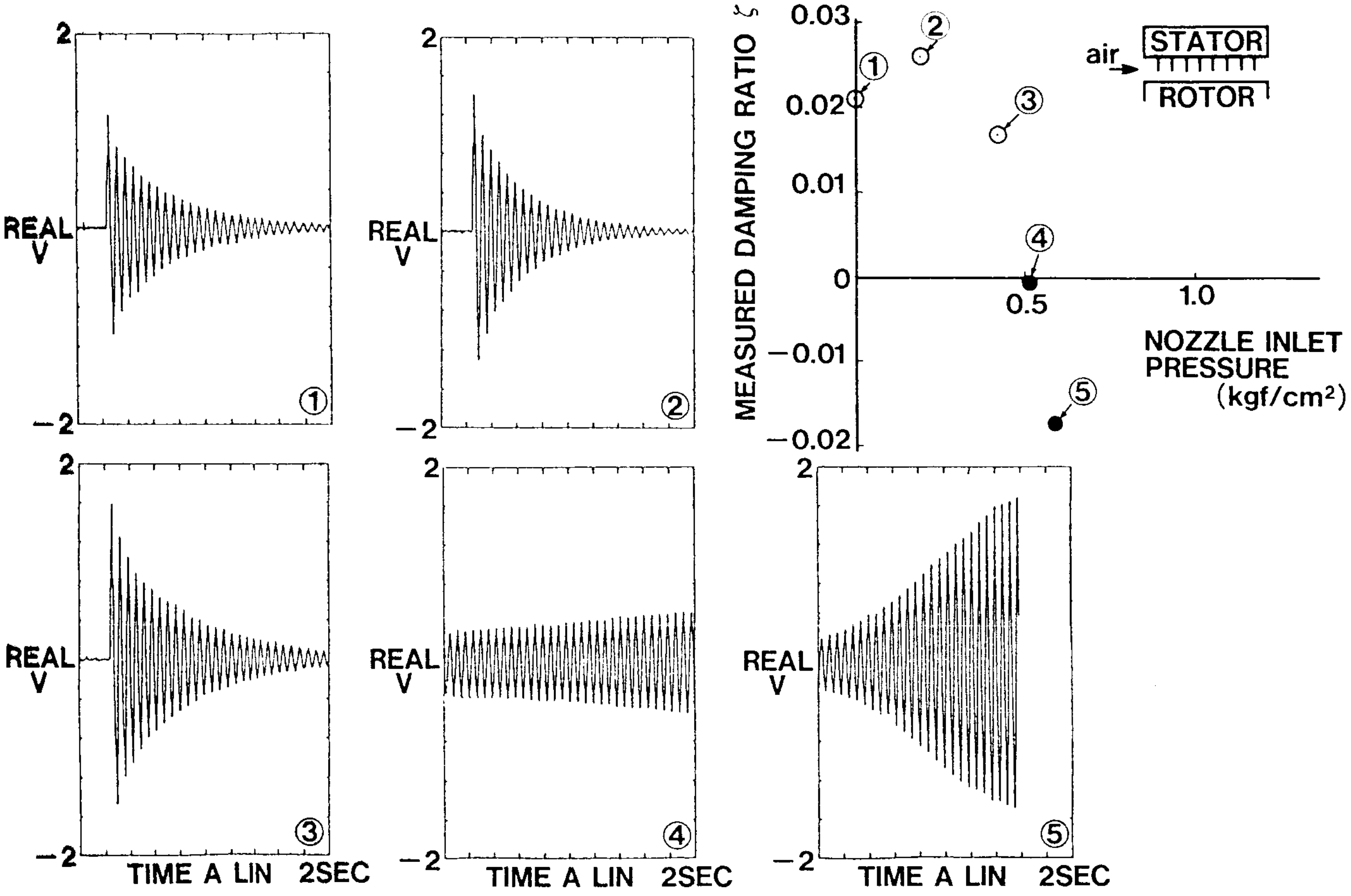

Figure 8. - Typical dynamic test results for straight seal.

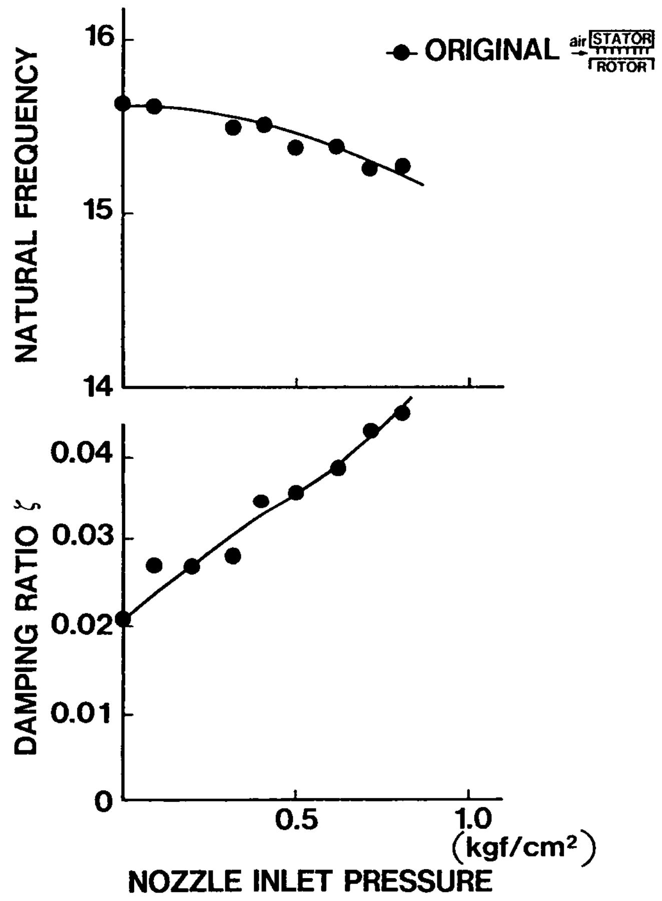

Figure 9. - Test results for nonswirl condition.

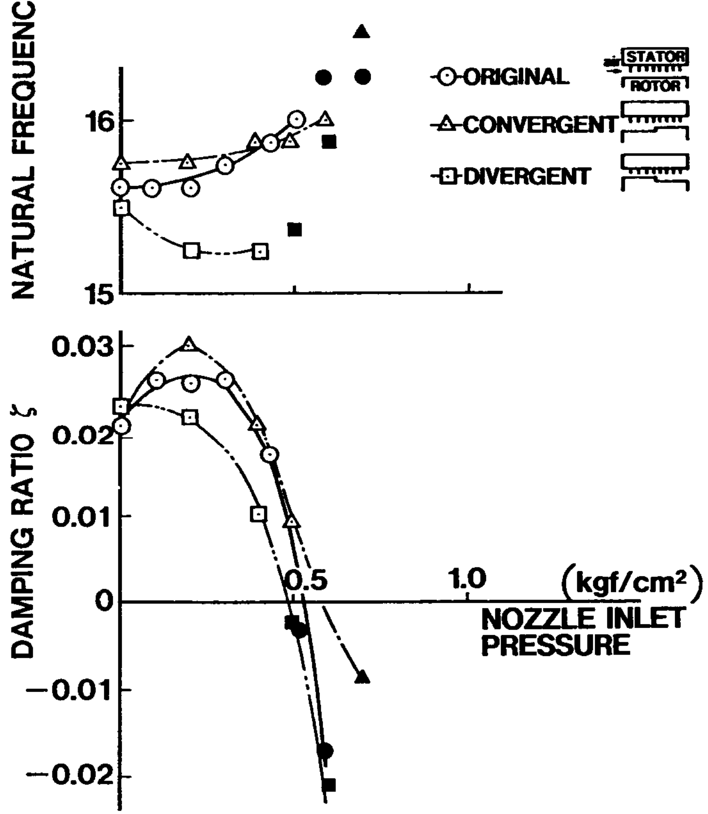

Figure 10. - Test results for swirl condition.

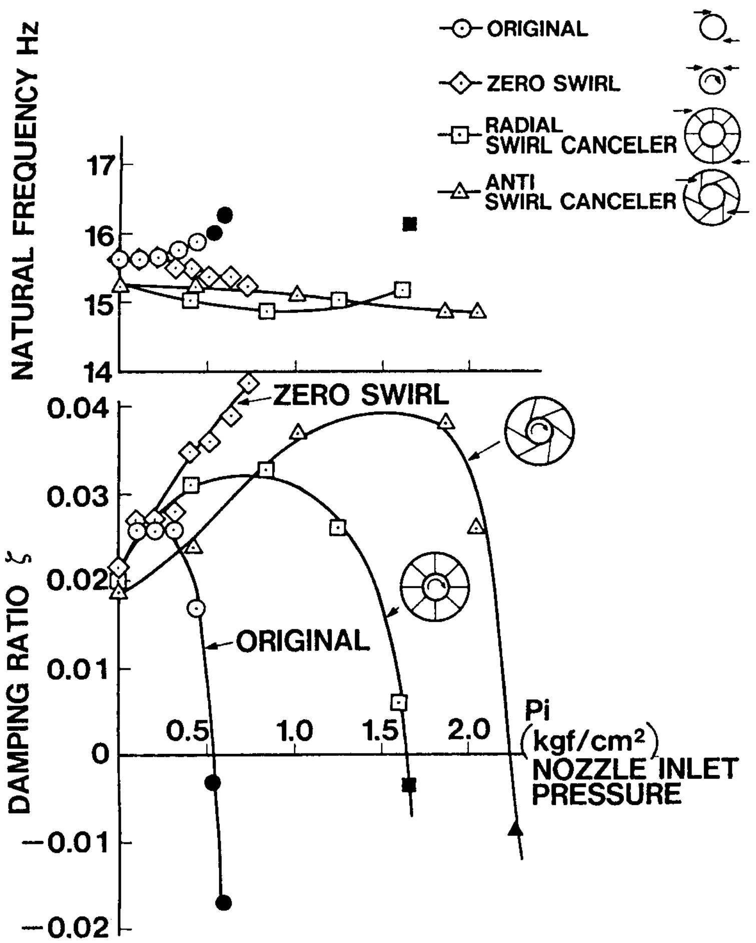

Figure 11. - Effect of swirl breaker.

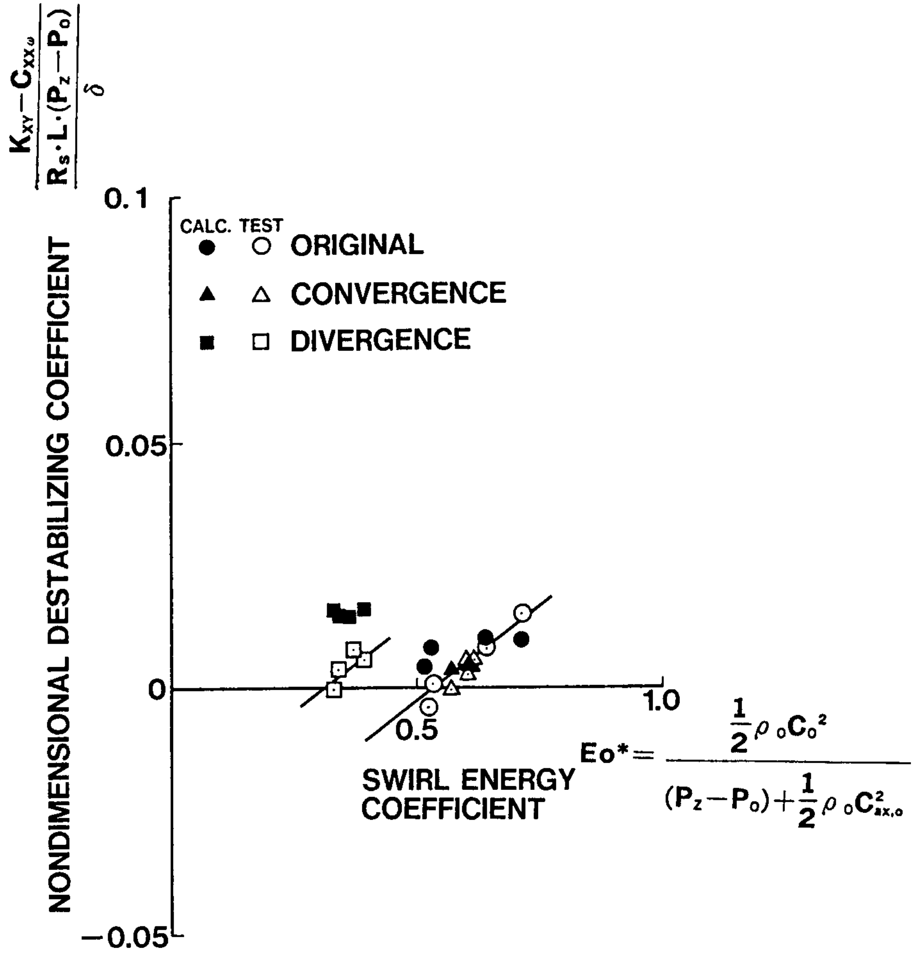

Figure 12. - Nondimensional comparison of test results and calculation.

ORIGINAL PAGE IS
OF POOR QUALITY

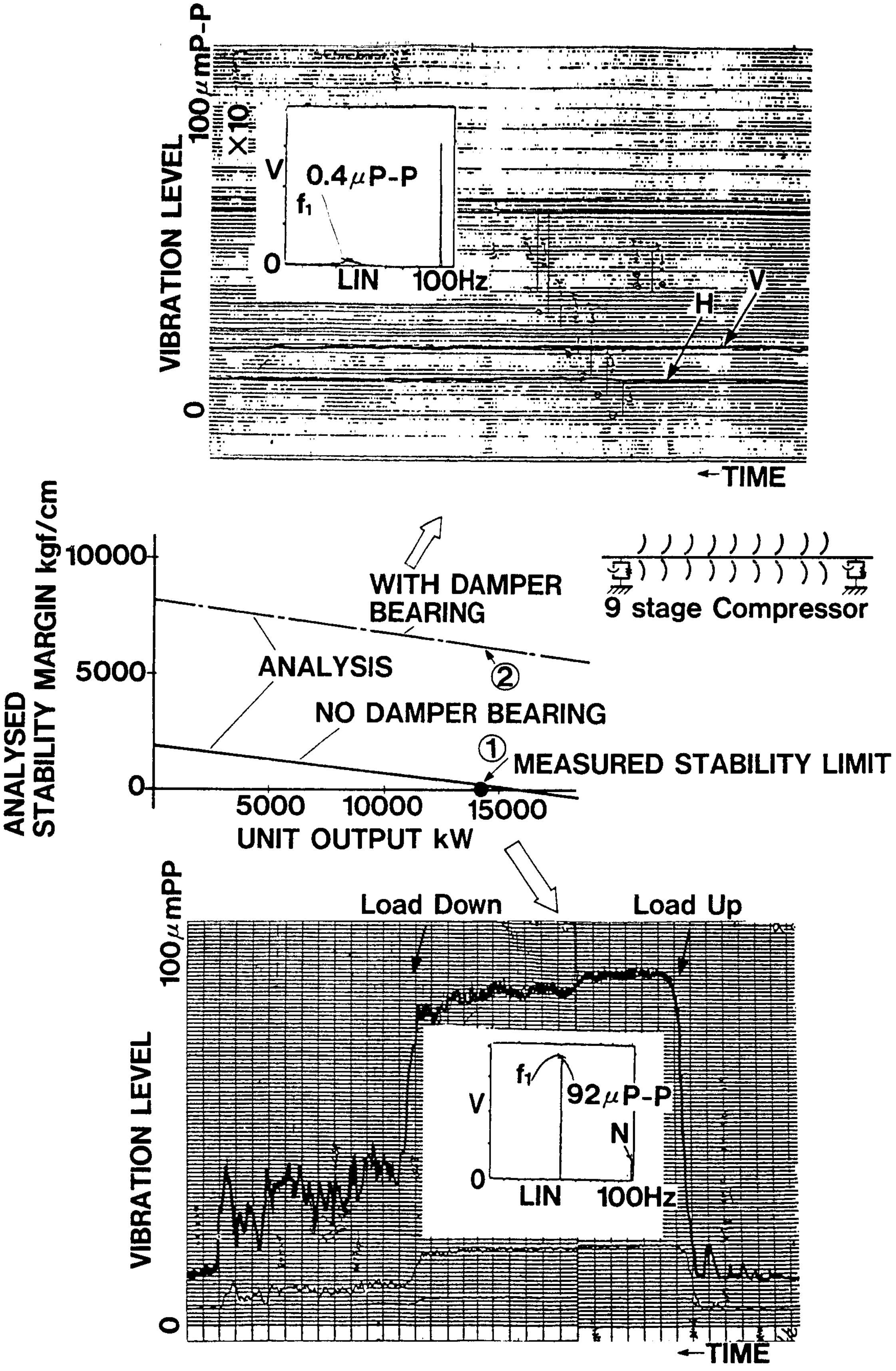

Figure 13. - Example of application of damper bearing to centrifugal compressor.

INFLUENCE OF DISK LEAKAGE PATH ON LABYRINTH SEAL INLET SWIRL RATIO

R. Gordon Kirk
Virginia Polytechnic Institute and State University
Blacksburg, Virginia 24061

The results of numerous investigators have shown the importance of labyrinth seal inlet swirl on the calculated dynamic stiffness of labyrinth seals. These results have not included any calculation of inlet leakage swirl as a function of geometry and sealing conditions of the given seal. This paper outlines a method of calculating the inlet swirl at a given seal by introducing a radial chamber to predict the gas swirl as it goes from the stage tip down to the seal location.

For a centrifugal compressor, this amounts to including the flow path from the impeller discharge, down the back of the disk or front of the cover, then into the shaft seal or eye packing, respectively. The solution includes the friction factors of both the disk and stationary wall with account for mass flow rate and calculation of radial pressure gradients by a free vortex solution.

The results of various configurations are discussed and comparisons made to other published results of disk swirl.

INTRODUCTION

Recent reports in the literature (1,2,3,4,5) have addressed the problem of calculating the rotordynamic coefficients for a labyrinth seal having a given inlet gas swirl, pressure drop, and resulting mass flow. The centrifugal design engineer has at his disposal from standard aerodynamic design codes the gas swirl and pressures at the impeller tip. The solution of the leakage gas path swirl and resulting pressure distribution is important not only for labyrinth seal coefficients but also for proper thrust balance calculations. This paper presents an approximate method of calculating these desired parameters using a modified version of the solution technique as proposed by Iwatsubo (1) and later extended by Childs and Scharrer (2). The extensions and modifications to the theory as outlined by (2) will be discussed in this paper.

The equations of the modified formulation have been incorporated into a single labyrinth seal analysis computer code to permit rapid evaluation of different design conditions. The accuracy of the reported solution technique will be compared to experimental and analytical solution results as reported in reference (6) and to the limit case condition of zero leakage (approximately zero for computer program results).

PRECEDING PAGE BLANK NOT FILMED

NOMENCLATURE

Values are given in both SI and U.S. Customary Units. The calculations were made in U.S. Customary Units.

b - tangential velocity ratio, $U/(r\omega)$

c_i - wall separation at i^{th} radial chamber and radial clearance for seal tooth, m (in)

H_i - height of ith seal element tooth, m (in)

L_i - axial length of ith seal chamber, m (in)

$\dot{m}$ - mass flow rate, Kg/sec (lbm/sec)

P - gas pressure, N/m^2 (lb_f/in^2)

r - radial position on disk, m (in)

R, R_o - outer radius of disk, m (in)

R - gas constant, ($lb_f \cdot ft/lbm/^oR$)

RM - mean chamber radius, m (in)

RR - average radius of rotor seal chamber surface area, m (in)

RS - average radius of stator seal chamber surface area, m (in)

R_e - disk Reynolds number, $= R_o^2\omega/\nu$

s - wall separation, m (in)

S - separation ratio, $= s/R_o$

SJ - leakage parameter, $= Vs/(R_o^2\omega)$

T - gas absolute temperature, ^oK (^oR)

U_t - tangential velocity, m/sec (in/sec)

V_r - radial velocity, m/sec (in/sec)

Z - gas compressibility

ρ - gas density, Kg/m^2 (lbm/in^2)

τ_{rw} - radial wall shear stress, N/m^2 (lbf/in^2)

τ_{rd} - radial disk shear stress, N/m^2 (lbf/in^2)

ν - gas kinematic viscosity, m^2/sec (in^2/sec)

χ - position factor, $= (R_o - r)/R_o$

ω - rotor (disk) angular spin velocity, sec^{-1}

ω_β - swirl velocity for free vortex, sec^{-1}

METHOD OF SOLUTION

The solution technique proposed was developed to permit the same basic theory and computer code to calculate both the circumferential swirl and pressure distribution down the disk and across the labyrinth as one coupled system. This technique was initially intended as a quick first pass method but the results have proven to be very close to the more exact theories such that the added complication of coupling different theories and matching boundary conditions of pressures, temperatures, flows, and swirls may not be justified for rotordynamic evaluations. A typical configuration is shown in Figure 1 for a centrifugal compressor stage disk cover leakage flow path.

For the radial direction down the disk leakage path the equilibrium equation is given by the following equation (6):

$$-V_r \frac{dV_r}{dr} - \frac{U_t^2}{r} = -\frac{1}{\rho}\frac{dP}{dr} + \frac{\tau_{rw}}{\rho s} \pm \frac{\tau_{rd}}{\rho s} \qquad [1]$$

For a free vortex flow neglecting the radial shear force which will be accounted for by the crossflow factor in the circumferential equations, the pressure distribution equation becomes

$$\frac{dP}{dr} = \frac{\rho (r\omega_\beta)^2}{r} \qquad [2]$$

or

$$\frac{dP}{dr} = \rho r \omega_\beta^2 \qquad [3]$$

where

ω_β = gas swirl angular velocity at the radius, r.

Therefore, the pressure at any radius r is given by

$$P(r) = P(R) - \rho \frac{\omega_\beta^2}{2}(R^2 - r^2) \qquad [4]$$

This equation predicts the pressure along the disk if the gas swirl is known. The gas swirl can be calculated from the circumferential momentum equation as outlined in (2) and further modified to the following equation to account for variation in rotor, stator and mean flow chamber radius. In addition, the crossflow turbulence correction factors may be included in the solution to account for the inward flow resistance.

$$\frac{\dot{m}}{2\pi R_M}(Vo_i - Vo_{i-1}) = \frac{1/2\, Po_i}{ZRT_i}(R\omega - Vo_i)^2 * YNR * \left(\frac{|R\omega - Vo_i|DHY}{\nu}\right)^{YMR} \qquad [5]$$

$$* ARL * \text{sign}(R\omega - Vo_i) * \frac{RR}{RM} * C3$$

$$-1/2\,\frac{Po_i}{ZRT_i} Vo_i^2 * YNS * \left(\frac{|Vo_i| * DHY}{\nu}\right)^{YMS} * ASL * SIGN(Vo_i) * \frac{RS}{RM} * C4$$

where

RM = mean chamber radius

RR = mean rotor surface radius

RS = mean stator surface radius

C3, C4 = crossflow turbulence factors

$Vo_i = RM_i \, \omega_{\beta i}$ = average chamber swirl velocity

DHY = hydraulic diameter of chamber

YNR, YNS, YMR, YMS = turbulence factors per reference (2)

ARL, ASL = shear area for rotor and stator

$\frac{P_{oi}}{ZRT_i}$ = pressure and temperature dependent gas density in i^{th} chamber

ν = gas kinematic viscosity

The leakage flow, $\dot{m}$, can be calculated as outlined in (2) or by other suitable calculations with the modification to radial chamber pressures given by equation (4).

The solution process requires that an initial swirl be selected to calculate the pressure field and leakage. A swirl of 50% is suggested for starting the solution. With this pressure field and flow, the momentum equation given by Eq. (5) is solved for the first pass swirl values. These swirl values are then used to recalculate the pressure drops down the disk and through the labyrinth and the resulting flow. Another pass through Eq. (5) solution yields the second pass swirl values. Typically, three passes give the desired convergence and the inlet swirl to the labyrinth is then taken from the chamber ahead of the first sealing tooth.

A general geometry input is used such that for the radial chambers a very small tooth height and length with a tooth clearance equal to the disk to wall spacing can be used to model the flow path. The radial surface area is calculated using the indicated radius of each tooth location.

RESULTS OF SWIRL PREDICTED IN GAS LEAK PATH

The evaluation of the proposed swirl calculation procedure has been based upon numerous similar conditions as reported by Jimbo (6). Initial comparisons of actual compressor swirl results from similar geometry is overplotted in Fig. 2. The parameter for leakage flow was noted to be similar to those given by Jimbo. The leakage flow parameter is defined as

$$SJ = \frac{V}{R_o \omega} * \frac{s}{R_o} \qquad [6]$$

where

V = radial gas velocity

R_o = disk outer radius

ω = rotor speed

s = wall separation

For SJ = 0.0002 it is obvious that the compressor disk swirl does not agree with the reported complete analytical solution. The swirl rates are greater from the labyrinth program approximate solution. However, the other parameter, the disk Reynolds number given by

$$Re = R_o^2\ \omega/\nu \qquad [7]$$

was calculated and found to be considerably different from the test results. The analysis results by Jimbo used air and a $R_e = 9.82 \times 10^5$ was quoted. These initial compressor test results had an $R_e = 1.1 \times 10^8$. To match the parameters for the two systems the gas, pressure drop, and rotor speed were changed as given in Table 1 under test rig conditions. This gave a disk Reynolds number of $R_e = 3 \times 10^6$, only off by a factor of 3 from Jimbo, compared to a factor of 112 for the compressor stage results.

The results for the labyrinth analysis overplot to the accuracy that the curves can be evaluated. The swirl results for the compressor stage and the test result condition are given in Tables 2 and 3, respectively. The swirl down the disk and through the labyrinth are given in the table with the radius χ-position factor indicated for comparison to the analysis results of Figure 2. The results are in excellent agreement for the case of near zero flow (i.e., swirl ~0.5) and for SJ = 0.0002 where the swirl at χ-position factor of 0.31 is now calculated as 0.563 as compared to 0.63 for the compressor gas. A comparison of the compressor swirl, test case calculation, Jimbo calculation, and test results reported by Jimbo are shown in Figure 3. The test results show a slowing of the swirl that is not predicted. The test rig was equiped with numerous flow and pressure measuring ports in the stator wall and it is very possible that the cause of the test rig result reduced swirl was the increased surface roughness resulting from the measuring instruments. Complex flow fields could also be the cause of the discrepancy and are beyond the scope of the present analysis. Results for reduced leakage, SJ = .000052, are given in Fig. 4 and labyrinth analysis compressor results for SJ = .0000372 overplotted. This case of reduced leakage compares closely even though the disk Reynolds numbers are not similar. The test rig results once again show a reduced swirl ratio with great restriction noted in the χ-position factor range of 0.4-0.5. The overall trend is similar as concluded by Jimbo.

One additional labyrinth program result is given in Table 4 for the condition of leakage from the final compressor stage through a balance piston full labyrinth. These results have a wall spacing that reduces as the radius reduces. A swirl of 0.82 is predicted for this geometry and gas properties, even though the flow SJ parameter is 0.00021 and a uniform spacing air test result would give a swirl rate closer to 0.6 (see Fig. 2 for χ-position ~0.4).

CONCLUSIONS

(1) The proposed approximate calculation procedure produces results that are acceptable for rotor dynamic evaluations of labyrinth seals.

(2) The flow parameter, SJ, and disk Reynolds number, Re, used by Jimbo to present results are very useful in comparing results for different designs and give great insight into disk swirl behavior.

(3) Non-uniform leak path geometry can be used to increase or decrease the swirl in the gas leak path.

(4) Increased stator surface roughness will suppress the swirl due to the increased shear drag on the swirling flow.

RECOMMENDATIONS

(1) Test evaluations using current technology flow measurement capability should be conducted on typical compressor and turbine disk design gas leak path configurations.

(2) The importance of gas properties and actual system configurations must be closely evaluated.

(3) The proposed calculation procedure can be used, with a high degree of confidence, for entry swirl evaluation of compressor labyrinth designs.

REFERENCES

(1) Iwatsubo, T., N. Matooka, and R. Kawai, "Spring and Damping Coefficients of the Labyrinth Seal," NASA CP 2250, 1982, pp. 205-222.

(2) Childs, D. W., and J. K. Scharrer, "An Iwatsubo-Based Solution for Labyrinth Seals - Comparison to Experimental Results," Rotordynamic Instability Problems in High Performance Turbomachinery - 1984, Texas A&M University, College Station, Texas, May 28-30, 1984.

(3) Benckert, H., and J. Wachter, "Flow Induced Spring Coefficients of Labyrinth Seals for Application in Rotordynamics," NASA CP 2133 Proceedings of a Workshop held at Texas A&M University May 12-14, 1980, Rotordynamic Instability Problems of High Performance Turbomachinery, pp. 189-212.

(4) Jenny, R., "Labyrinths as a Cause of Self-Excited Rotor Oscillations in Centrifugal Compressors," Sulzer Technical Review 4, 1980, pp. 149-156.

(5) Kirk, R. G., "Evaluation of Aerodynamic Instability Mechanisms for Centrifugal Compressors," ASME Paper 85-DET-147. Presented at Design Engineering Vibration Conference, Cincinnati, Ohio, September 10-13, 1985.

(6) Jimbo, H., "Investigation of the Interaction of Windage and Leakage Phenomena in a Centrifugal Compressor," ASME Paper 56-A-47, presented at ASME Annual Meeting, New York, NY, July 30, 1956.

TABLE 1 SYSTEM PARAMETERS FOR ACTUAL COMPRESSOR STAGE DESIGN CONDITIONS AND AN ASSUMED SYSTEM TO APPROXIMATE THE RESULTS OF TEST CONDITIONS FROM REFERENCE 6.

PARAMETER	COMPRESSOR STAGE	TEST RIG CONDITIONS (Ref. 6 assumed conditions)
MW	21.33	25.95
ν, m^2/s (in^2/sec)	2.79×10^{-7} (4.32×10^{-4})	4.64×10^{-6} (7.19×10^{-3})
Z	.89	.955
PS, N/m^2) (lb/in^2)	5.90×10^{6} (855)	3.43×10^{5} (49.7)
PE, N/m^2 (lb/in^2)	5.17×10^{6} (750)	1.01×10^{5} (14.7)
T, ^oK (^oR)	331.6 (602.9)	301.4 (548.5)
N, Hz (RPM)	207.4 (12566)	100.0 (6000)
R_o, m (in)	.154 (6.05)	.154 (6.05)
R_e	1.1×10^{8}	3×10^{6}

TABLE 2 RESULTS FOR COMPRESSOR STAGE GIVING PREDICTED CHAMBER FLOW SWIRL RATIO

CHAMBER	χ	SJ = 0.000023	0.00014	0.000236	0.00034
DISK TIP	0	.52	.52	.52	.52
2	.08	.5033	.534	.548	.557
3	.17	.5053	.5496	.571	.5867
4	.25	.5095	.5689	.600	.6225
5	.31	.5144	.5938	.632	.6603
RADIAL ↑ 6	.34	.5045	.5997	.6425	.6731
TURN 7	-	.452	.5605	.6111	.6472
SEAL 8	-	.384	.5121	.571	.6131
↓ 9	-	.359	.475	.5377	.5834
10	-	.350	.447	.5097	.5574
11	-	.346	.425	.4862	.5347
12	-	.345	.408	.4663	.5146

$$R_e = \frac{R_o^2 \omega}{\nu} = 1.1 \times 10^8$$

TABLE 3 RESULTS FOR TEST CASE GIVING PREDICTED CHAMBER SWIRL RATIO FOR ASSUMED SUPPLY PRESSURE CONDITIONS (SEE TABLE 1)

CHAMBER	χ	SJ = .000015	0.0001	0.00022	0.00034
Disk Tip	0	.52	.52	.52	.52
2	.08	.496	.509	.522	.534
3	.17	.496	.513	.532	.549
4	.25	.497	.519	.544	.567
5	.31	.492	.529	.563	.592
RADIAL ↑ 6	.34	.47	.524	.564	.597
TURN 7	-	.43	.473	.518	.558
SEAL 8	-	.3513	.4105	.465	.511
↓ 9	-	.3445	.3798	.431	.478
10	-	.3438	.364	.408	.453
11	-	.3438	.3558	.392	.434
12	-	.3438	.3512	.382	.421

$$R_e = \frac{R_o^2 \omega}{\nu} = 3 \times 10^6$$

TABLE 4 RESULTS OF LEAKAGE AND GAS SWIRL FOR FLOW FROM LAST STAGE TO A BALANCE PISTON LABYRINTH HAVING 15 TEETH

CHAMBER	χ (dim.)	SWIRL (dim.)	RADIUS (in.)	WALL SPACE (in.)
0	0	.637	9	-
1	.001	.641	8.94	.15
2	.07	.6756	8.34	.4
3	.15	.705	7.65	.36
4	.22	.732	7.02	.32
5	.293	.765	6.36	.3
RADIAL ↑ 6	.375	.81	5.62	.26
TURN 7	.42	.823	5.18	.22
SEAL ↓ 8	-	.781	5.14	-
9	-	.74	5.14	-
10	-	.71	5.14	-
11	-	.68	5.14	-
12	-	.66	5.14	-
13	-	.64	5.14	-
14	-	.62	5.14	-
15	-	.61	5.14	-
16	-	.598	5.14	-
17	-	.588	5.14	-
18	-	.580	5.14	-
19	-	.573	5.14	-
20	-	.567	5.14	-
21	-	.563	5.14	-

N = 11097. RPM
MW = 18.3
PS = 948 PSI
PE = 253 PSI
$\nu = 7.63 \times 10^{-4}$ in^2/sec
Z = 0.979
$\gamma = 1.255$
leakage = 1.09 lb$_m$/sec

SJ ≃ 0.00021

$$R_e = \frac{9^2(1162)}{7.63 \times 10^{-4}} = 1.23 \times 10^8$$

$C_p = 0.52$
c = 0.0115 in. radial clearance
type seal = interlocking

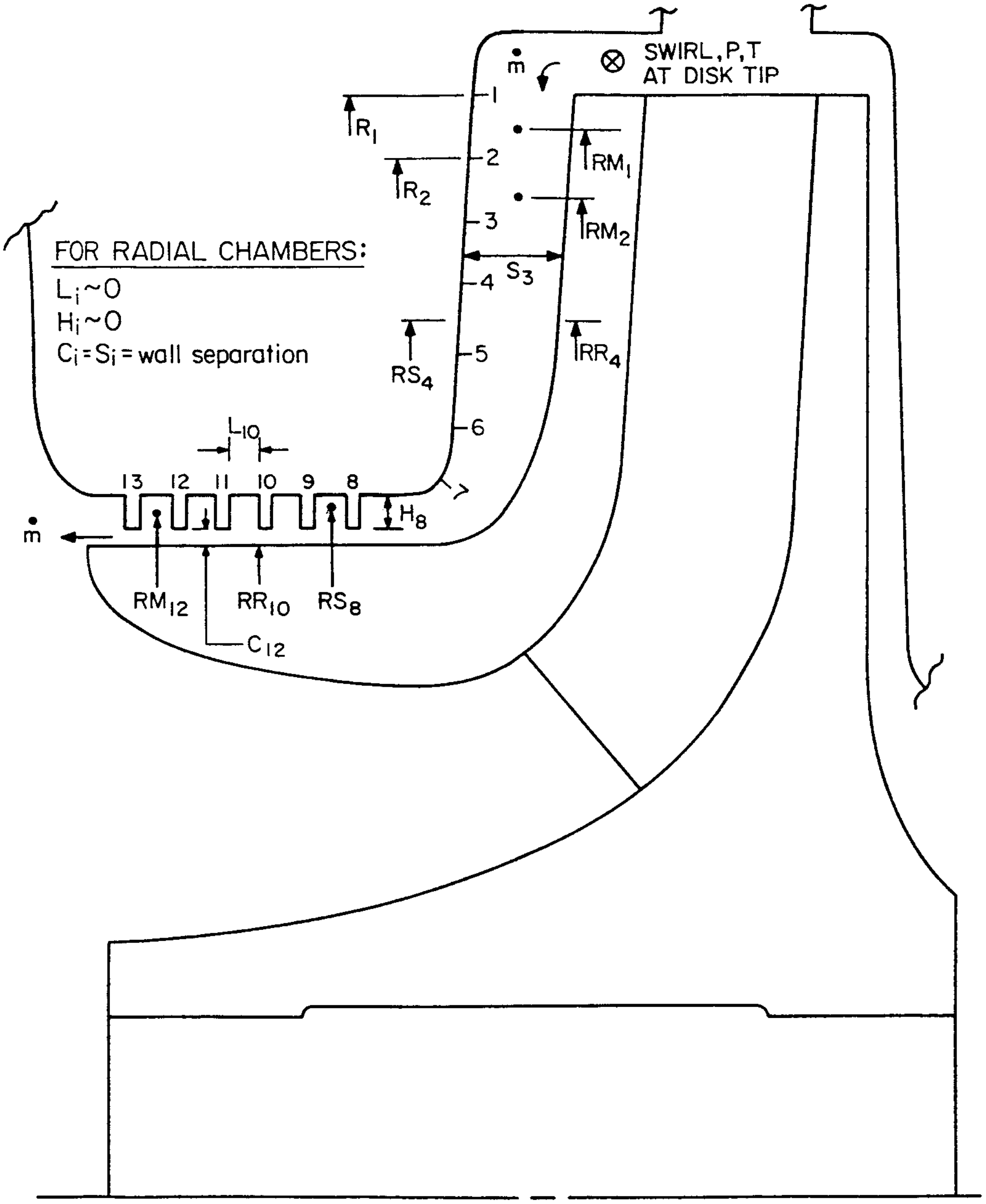

$\dot{m}$
SWIRL, P, T AT DISK TIP
1
2
3
4
5
6
7
R_1
R_2
RM_1
RM_2
S_3
RS_4
RR_4
FOR RADIAL CHAMBERS:
$L_i \sim 0$
$H_i \sim 0$
$C_i = S_i$ = wall separation
L_{10}
13
12
11
10
9
8
H_8
$\dot{m}$
RM_{12}
RR_{10}
RS_8
C_{12}

Figure 1. - Typical compressor stage showing disk cover gas leakage path with nomenclature for analysis.

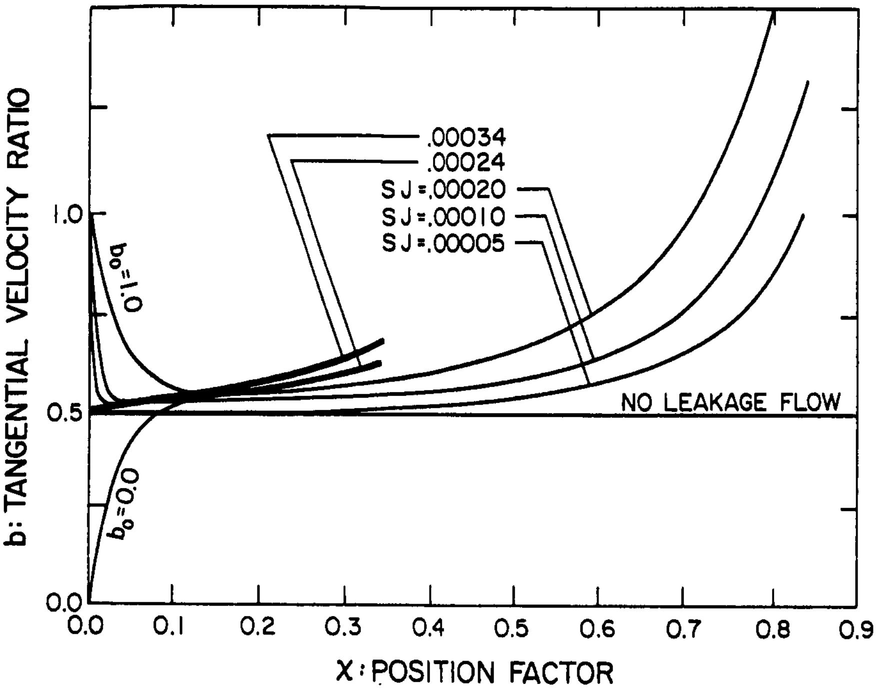

Figure 2. - Velocity profile along radius, $b = U/(r\omega)$ versus $\chi = (R_0-r)/R_0$ at $R_e = R_0^2\ \omega/\nu = 9.82 \times 10^5$. Overplot of typical compressor result with $R_e = 1.1 \times 10^8$ (From Jimbo - fig. 6 ref. (6)).

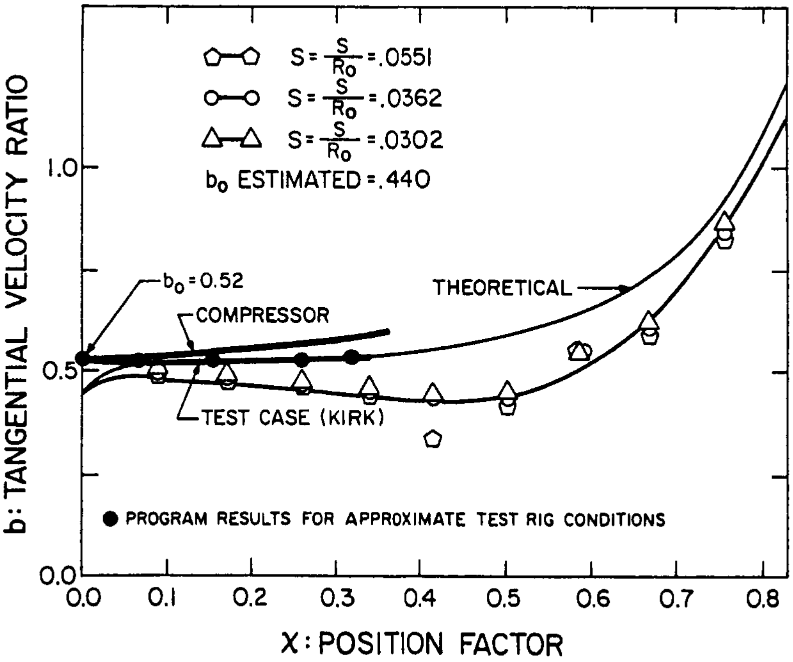

Figure 3. - Tangential velocity profile along radius $b = U/(r\omega)$ versus $\chi = R_0-r/R_0$ for constant leakage flow $SJ = (s/R_0)[V/R_0\omega)] = 0.000104$ at $R_e = 9.82 \times 10^5$. Overplot of a typical compressor result with $SJ = 0.00014$ and $R_e = 1.1 \times 10^8$; test case points for $SJ = 0.0001$ and $R_e = 3 \times 10^6$ (overplot on fig. 18 of ref. (6)).

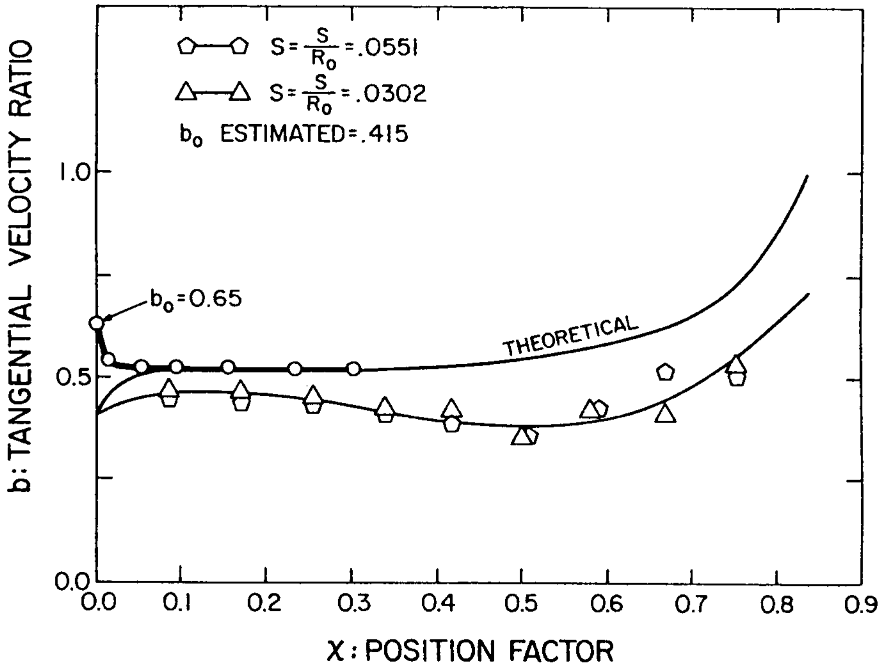

Figure 4. - Tangential velocity profile along radius $b = U/(r\omega)$ versus $\chi = R_0 - r/R_0$ for constant leakage flow $SJ = (s/R_0)[V/(R_0\omega)] = 0.000052$ at $R_e = 9.82 \times 10^5$. Overplot of compressor having $SJ = 0.0000372$ and $R_e = 1.3 \times 10^8$ (overplot on fig. 20 of ref. (6)).

N87-22211

THEORY AND MEASUREMENTS OF LABYRINTH SEAL COEFFICIENTS FOR ROTOR STABILITY OF TURBOCOMPRESSORS

H.R. Wyssmann
Sulzer-Escher Wyss Ltd
Zurich, Switzerland

The prediction of rotordynamic coefficients for gas seals is achieved with the aid of a two-volume bulk flow model based on turbulent rotationally symmetric 3D flow calculations including swirl flow. Comparison of cross-coupling and damping coefficients with measurements confirm this approach. In particular the theoretically predicted phenomenon that labyrinth damping is retained without inlet swirl is confirmed. This is important for the design of high pressure compressors, where labyrinth damping is a major contribution improving rotor stability. Discrepancies are found when comparing theory with measured direct stiffness and the cross-coupling damping coefficients. First measurements of labyrinth seals on a recently installed test rig operated with water are presented. Since forces are larger than on test stands operated with air and since individual chamber forces are obtained phenomena like inlet effects may be studied.

INTRODUCTION

For many years radial seal forces have been studied and investigated for stability of turbomachinery, especially for pumps and turbocompressors. Many papers on this subject have appeared, most of them either presenting measurements or a theoretical approach. Few authors have compared measurements with theory, mainly because a reasonably simple theory producing results in reasonable agreement with measurements was not available. The author in a former paper has presented a theory based on a two volume bulk flow approach, incorporating results from 3D finite difference calculation of the rotationally symmetric single cavity turbulent flow, based on time averaged Navier Stokes equations with a k-ε turbulence closure. Comparison of the results for cross-coupling coefficients of straight through labyrinths with measurements showed good agreement. However, test results where not available at the time for labyrinth damping, which the theory predicted to be substantial compared to bearing damping at high densities found in turbocompressors for the oil and gas industry. This paper attempts to present the latest findings both on the theoretical side and in measurements for the straight through seal with teeth on stator or on rotor. For the larger part the measurements have been carried out at the Turbomachinery Laboratories at Texas A&M University.

SYMBOLS

a	area of cross-section between 2 strips
A	area of cross-section of labyrinth channel
b_Q	cross-coupling damping
b_R	direct damping
c_f	friction coefficient
d	distance between two strips
e	eccentricity
h	labyrinth strip height
k_Q	cross-coupling stiffness
k_R	direct stiffness
l	mixing length
$\dot{m}$	leakage flow rate through labyrinth

$\dot{m}_r$	mass rate exchange between 2 control volumes
p	pressure
Q	cross-coupling force
R	direct force
r	labyrinth radius
Δr	radial clearance of concentric labyrinth
t	time
w	circumferential velocity
z	number of labyrinth strips
β	mixing factor
δ	radial clearance of eccentric labyrinth
μ	labyrinth flow coefficient
u	viscosity
ρ	density
τ	stress
φ	angle

Subscripts:

in	inlet
j	jet
r	rotor or radial
s	stator
out	outlet

THEORY

The theory gives the solution for the circumferential pressure distribution of straight through labyrinths for gas and (incompressible) hydraulic flow. With some modifications, the theory is also applicable for staggered and full labyrinths. Here only a summary of the theory is given. More detailed results may be found in [10]. The calculation is based on bulk flow assumptions, i.e. on a uniform flow profile in the region between the strips and (a different) uniform profile between strip tips and bushing (for rotor seal) or rotor (for stator seal). This is schematically depicted in Fig. 1. The validity of the assumed velocity profiles has been confirmed by extensive numeric flow calculations for the rotationally symmetric 3D turbulent flow in a single chamber. In these the velocity field v is decomposed into a time averaged part $\bar{v}$ and a turbulent fluctuation part v':

$$v = \bar{v} + v'. \qquad (1)$$

The continuity equation for v, assuming incompressibility within the chamber, reads after insertion of (1) and time averaging:

$$\nabla \cdot \bar{v} = 0.$$

where ∇ denotes the Nabla Operator.

The time averaged Navier Stokes equations become:

$$\partial \bar{v}/\partial t + (\bar{v} \cdot \nabla)\bar{v} = - \nabla p + \nabla \upsilon \times \nabla \times \bar{v} + \text{turbulent diffusion.}$$

The turbulent diffusion term is described by a two parameter model, based on $k = {}^1/_2\, v_i'\, v_i'$, the turbulent kinetic energy and $\varepsilon = \upsilon \partial v_l'/\partial x_i \cdot \partial v_l'/\partial x_i$, the dissipation rate of the kinetic fluctuation energy. For k and ε transport equations may be written down with a total of 5 empiric parameters. Correlation of the parameters to flow measurements has been given by Stoff [8].

As boundary conditions, the pressure difference across the chamber, the rotational speed and the inlet circumferential velocity are given. The numerical calculations yield the pressure and velocity distributions (time averaged) within the chamber. The analysis does not consider the flow contraction across the strip however. The results of this analysis has been used for the modelling of the eccentric quasi-stationary flow in the labyrinth chamber as given below. The following equations are valid for seals with strips on the rotor, similar equations hold for stator seals. The field equations for the two control volumes in Fig. 1 read:

Continuity:

$$a\partial w_i/\partial\varphi + \delta d\partial w_m/\partial\varphi - w_m d\partial\delta/\partial\varphi - r\partial A/\partial t = 0, \qquad (2)$$

$$a\partial w_i/\partial\varphi - m_r/\rho = 0. \qquad (3)$$

Momentum:

$$\begin{aligned} &-2\rho a w_i\partial w_i/\partial\varphi - 2\rho\delta d w_m\partial w_m/\partial\varphi - \rho w_m^2 d\partial\delta/\partial\varphi + \\ &+ \dot{m}(w_{in} - w_{out}) - a_r r\,\tau_r - \\ &- a_s r\,\tau_s - \rho r d\partial(\delta w_m)/\partial t - \rho r a\partial w_i/\partial t = A\partial p/\partial\varphi \qquad (4) \end{aligned}$$

$$\begin{aligned} &-2\rho a w_i\partial w_i/\partial\varphi + \dot{m}_r w_o - a_r r\,\tau_r - \\ &- d r\tau_j - \rho r a\partial w_i/\partial t = a\partial p/\partial\varphi. \qquad (5) \end{aligned}$$

Here, the w's denote the circumferential velocity components of the flow: w_i the velocity of the core flow between the strips, w_m of the free jet between strip tips and stator and w_o the circumferential velocity at the interface between the two flow regions.

The axial flow is described by the classical leakage equation for the compressible flow through a seal (see Neumann [6], for instance):

$$\dot{m} = 2\pi\mu r\delta\rho_o\sqrt{(p_o/\rho_o)}\sqrt{(1 - \pi_p^2)/z}. \qquad (6)$$

The flow coefficient μ follows the definition of Neumann [6] and takes into account the labyrinth strip geometry.

The turbulent wall shear stresses are given by

for the rotor, and

$$\tau_r = 1/2\, c_{fr}\,\rho\,|w_i - w_{rot}|(w_i - w_{rot}) \qquad (7)$$

$$\tau_s = 1/2\, c_{fs}\rho\sqrt{(c_{ax}^2 + w_m^2)}\,w_m \qquad (8)$$

for the stator, where the friction coefficients c_{fr} and c_{fs} are calculated with Prandtl's universal law for the tube flow.

The interaction of the two flow regions is described by a turbulent free shear stress τ_j modelled according to Prandtl's mixing length theory:

$$\tau_j = \rho l^2\,|\partial u/\partial y\,|\partial u/\partial y,$$

where u is the flow velocity in the shear flow zone. For free jets, an obvious chioce for the mixing length l is the mixing thickness b (Abramovich [1]). For the obstructed jet flow at hand, a proportionality factor β is introduced, such that $l = \beta b$, where β is a function of the labyrinth geometry. β has been determined by correlation of the (bulk flow) solution of the concentric labyrinth to the 3D finite difference calculations of the rotationally symmetric flow described above and to measurements.

In order to obtain the stiffnes and damping coefficients of the seal, a first order solution of the equations (2) through (8) in e and $\dot{e}$ is sufficient. Hence, the gap between strips and stator may be written as

$$\delta = \Delta r + e(t)\cos\varphi,$$

where $e/\Delta r \ll 1$. The flow quantities and the pressure in equations (2) through (8) may therefore be written as:

$$w_i = \bar{w}_i + \tilde{w}_i(\varphi,t), \quad m = \bar{\dot{m}} + \tilde{\dot{m}}(\varphi,t),$$
$$w_m = \bar{w}_m + \tilde{w}_m(\varphi,t), \quad p = \bar{p} + \tilde{p}(\varphi,t).$$

The zeroth order solution describes the concentric labyrinth and has been used to determine the mixing factor β by correlation to the 3D finite difference calculations of the rotationally symmetric flow described above.

The pressure $p(\varphi,t)$, linear in e and e is obtained upon integration of the linearization of equations (2) through (8). The force components acting on the rotor read:

$$Q = \int_0^{2\pi} \tilde{p} \sin\varphi r d d f, \quad R = \int_0^{2\pi} \tilde{p} \cos\varphi r d d\varphi, \qquad (9)$$

with Q orthogonal to and R in line (but opposite) with the rotor eccentricity e. In cartesian coordinates the force components may be written as:

$$\begin{bmatrix} K_x \\ K_y \end{bmatrix} = - \begin{bmatrix} k_R & k_Q \\ -k_Q & k_R \end{bmatrix} \begin{bmatrix} x \\ y \end{bmatrix} - \begin{bmatrix} b_R & b_Q \\ -b_Q & b_R \end{bmatrix} \begin{bmatrix} x \\ y \end{bmatrix} \qquad (10)$$

where k_R= stiffness, k_Q= cross-coupling stiffness, b_R= damping, and b_Q= cross-coupling damping of the seal.

For staggered and straight labyrinths, a similar theory may be applied. 3D calculations of the concentric labbyrinths have shown the circumferential velocity to be almost uniform across the whole chamber here, hence a single circumferential velocity may be assumed [10].

COMPARISON OF CROSS-COUPLING STIFFNESS WITH MEASUREMENTS

The cross-coupling coefficients obtained from the theory as presented above has been compared to measurements carried out by different authors. It agrees well with the laboratory measurements carried out by Benckert [2] for various types of labyrinths. The least agreement has been found for staggered and full labyrinths. For reference see [10]. Measurements on a real compressor at high pressures with Nitrogen have been carried out for the first time by the authors company. The circumferential pressure distribution of the first stage impeller shroud seal in a four stage natural gas compressor designed for a discharge pressure of 320 bar has been measured for different rotor eccentricities relative to the seal. Fig. 2 shows the test labyrinth in the lower half of the inner casing. The measurements have been carried out with and without a swirl brake (Fig. 3) to confirm the theoretically predicted influence of the inlet swirl velocity on cross-coupling stiffness. The circumferential velocity of the leakage flow was measured by pitot tubes in front of the first labyrinth strip and has been used as inlet condition for the calculation. Fig. 4 shows measured and calculated cross-coupling stiffness of the seal for different pressure levels and rotor speeds. The theory agrees well with measurements. With swirl brake installed, theory gives less negative cross-coupling than found by measurement. However, the absolute value of the cross-coupling stiffness compared to the case without swirl brake is very small (scale in Fig. 4 is blown up by factor 10 for case with swirl brake), hence for practical applications this discrepancy has no importance. All these tests could not produce damping coefficients, but they basically confirmed the theoretical approach presented above. They also confirmed the dominating influence of the inlet swirl velocity on the magnitude of the cross-coupling coefficients and hence were in line with the many cases where rotor stability problems have been solved by reducing the inlet swirl velocity of the labyrinth leakage flow. The theory however predicts damping coefficients of labyrinth seals of a magnitude to improve substantially the rotor damping for high pressure compressors. Hence, a confirmation by measurements is of great importance.

COMPARISON OF FULL SET OF LABYRINTH COEFFICIENTS WITH MEASUREMENTS

A test rig for air seals has been set up at the Turbomachinery Laboratories of Texas A&M University, capable to measure the full set of labyrinth coefficients as defined by (10). The rotor is moved by a hydraulic shaker performing translatory movements. By measuring the reaction forces the dynamic coefficients can be identified. This differs from the measurements described above, where forces were obtained by integration of pressures. Extensive measurements have been carried out with straight- through teeth on stator and teeth on rotor labyrinth seals with 16 chambers by Childs and Scharrer ([3], [7]). Rotor speed varied between 500 and 8000 RPM or 4 m/s to 63 m/s in circumferential velocity, inlet pressures between 3.08 and 8.25 bar (against ambient). Inlet circumferential velocity of the leakage flow could be varied by employing different inlet guide vanes. Further measurements have been carried out with higher rotor speeds and different labyrinth geometry, but no data has been available until now. Fig. 5 through 10 show some of the results taken from [7], together with the theoretical results obtained by the theory presented above. Agreement of both cross-coupling and damping coefficients with theory for both teeth on rotor and teeth on stator is more than satisfactory, keeping in mind that a stated experimental uncertainty of 7 kN/m for stiffness and 87.5 Ns/m for damping exists. Moreover inlet swirl velocity has not been measured directly but is calculated by knowing the guide outlet vane corrected by a factor obtained by guide vane cascade tests. No uncertainty is given here. Also the tested chamber geometry was not exactly modeled in the theory, theoretical results correspond to a tooth wall angle of 15° compared to 6° for the tested labyrinth. Nevertheless, the agreement is reasonably good, especially for the lower pressure ratios for non-choked flow conditions, which are the more realistic ones in practice. In the case of direct stiffness the theory gives a completely different dependence on inlet swirl as compared to the measurements. The measured coefficients change almost linearly with inlet swirl velocity, whereas theory gives a parabolic dependence and virtually zero stiffness without swirl. The experimental results are somewhat in contrast to other measurements, namely those by Benckert, where dependence on swirl is similar to that given by theory. This point has to be investigated further, since the influence of negative labyrinth stiffness on critical speeds and stability may be substantial, especially for back-to-back compressors with the piston labyrinth midspan. Most of the cross-coupled damping measurements are in the order of the given uncertainty. Theory here gives considerably larger values, at least for high inlet swirl. Moreover, the dependence on swirl as given by theory is linear whereas the measurements show little variation.

THE INTRINSIC IDENTITIES OF STATIC AND DYNAMIC COEFFICIENTS

The following simple kinematic reflections show that cross-coupling and direct damping forces are basically two different representations of the same physical phenomena. This is not further surprising, since they both have their origin in the fluid dissipation forces. We will further show that if the cross-coupling forces (as functions of inlet swirl velocity) are known, the damping forces can directly be determined from them. The same holds true for direct stiffness and cross-coupling damping. This implies then, that if the static forces (i.e. direct stiffness and cross-coupling) are known (for instance by measurements) for a sufficient range of inlet swirl velocities and with a sufficient accuracy, the dynamic forces (i.e. direct and cross- coupling damping) can be determined without further measurements. The above holds true if no centrifugal effects are present, which is generally tacitly assumed (otherwise, forces on the rotor would be different from those acting on the stator).

Let us consider a labyrinth with strips on the rotor (without loss of generality). The rotor has rotational speed Ω, eccentricity e and a velocity of the rotor center of Ωe, i.e. the rotor is rotating around the seal center. Let the inlet swirl velocity be w_{in} (see Fig. 11a). Then the lateral force F acting on the rotor is given by

$$F = (k_{Qrot} - b_{Rrot}\Omega)e,$$

where k_{Qrot} is the cross-coupling stiffness and b_{Rrot} the direct damping coefficient. Seen from the rotating reference frame (x',y'), the rotor is stationary, the stator rotates with $-\Omega$ and the inlet swirl velocity is $-(w_{rot}-w_{in})$, where w_{rot} is the circumferential rotor speed (see Fig. 11b). With the above assumption i.e no centrifugal effects, the forces have not changed by the change of coordinates and by the same token we can interchange rotor and stator without changing the forces (Fig. 11c), i.e. we have now a seal with teeth on stator, static eccentricity e, rotor speed $-\Omega$ and inlet swirl velocity $-(w_{rot}-w_{in})$. The force acting on the rotor is now simply a cross-coupling force $k_{Qstat}e$ in the opposite direction of F. Setting the two forces equal, we obtain the following equation:

$$k_{Qrot}(w_{in}) - b_{Rrot}(w_{in})\,\Omega = - k_{Qstat}(w_{rot}-w_{in}),$$

or

$$b_{Rrot}(w_{in}) = 1/\Omega\,[k_{Qrot}(w_{in}) + k_{Qstat}(w_{rot}-w_{in})]. \qquad (11)$$

Hence, the damping coefficient is completely determined by cross-coupling coefficients. For stiffness and cross-coupling damping the same reasoning leads to

$$b_{Qrot}(w_{in}) = 1/\Omega\,[k_{Rstat}(w_{rot}-w_{in}) - k_{Rrot}(w_{in})]. \qquad (12)$$

Since both expressions involve differences, the practical value for determining damping coefficients may be questionable. However, the identities may be used for either a check for measurement accuracy or for secondary effects not included in the theory. Also it follows from the identities that a theory which predicts well cross-coupling stiffness will also predict damping with the same accuracy and the same is true for the other two coefficients. Therefore, it is no coincidence that the presented theory performs equally well for cross-coupling and damping.

WATER OPERATED TEST STAND FOR ROTORDYNAMIC FORCE MEASUREMENTS

A test rig has been set up at the Institut für Flüssigkeitstechnik at the Federal Institute of Technology in Zurich, Switzerland. It is water operated and was initially designed for the measurements of rotordynamic coefficients of hydraulic seals for pumps and water turbines. Important features of this test rig are the high measuring accuracy, which allows precise measurements even at zero inlet swirl and low rotor speeds, the seperate measurement of the individual chambers and the hydraulically operated stator, allowing various orbit configurations, such as circular orbits. Rotor speed varies between 0 and 3570 RPM (i.e. 0 - 67 m/s), pressure up to 8 bar, stator frequency up to 30 Hz. Inlet swirl is either zero or close to rotor circumferential speed (produced by rotor blades). The pressure distribution is measured in the individual chambers by static and dynamic pressure probes, inlet swirl velocity by total pressure probes. Fig. 12 gives a cross section of the test stand and Fig.13 a schematic of the hydraulic stator drive. Fig. 14 shows the test stand after installation (Figures by courtesy of Institut für Flüssigkeitstechnik, Federal Institute of Technology, Zurich Switzerland). Up to now, only static measurements of direct stiffness and cross-coupling stiffness have been carried out with no inlet swirl. The first measurements have been carried out with a three chamber straight-through labyrinth seal with teeth on the stator. Fig. 15 shows the results of the measurements of the different chambers for different pressures and rotor speeds. An interesting fact is the positive stiffness in the first chamber. It may be explained by the circumferential variation of the axial friction losses in an eccentric seal (also called Lomakin effect [4], [5]). For a plain annular seal the centering stiffness coefficient is given by ([9]):

$$k \;=\; \Delta p \frac{r l^2}{2\Delta r^2(\lambda l/2\Delta r + 1)^2} \pi\lambda^4 e,$$

where Δp is the pressure drop along the seal, l the length, Δr the radial clearance and λ the pipe flow number. Considering the first labyrinth chamber as a plain annular seal with clearance equal to tip clearance, we obtain the values for k very close to the measured direct stiffness (see Fig. 16), at least for the lower rotor speeds. Hence it seems that for direct stiffness the first chamber acts rather like a plain annular seal. Even in the second and third chamber the direct stiffness shows anomalous behaviour for the lower rotor speeds, only for high rotor speed is the behaviour as predicted by theory, i.e. a reduction of the (negative) stiffness with increasing pressure difference. This reduction is a consequence of the smaller pick-up of circumferential speed in the chambers with the increase of axial flow with pressure difference. For gas seals, where the density increases with pressure, the (negative) stiffness increases also (see Fig. 7 and 8). Another interesting feature is the strong dependence of the stiffness on rotor speed as predicted by theory. This is in contrast to the measurements by Scharrer [7], where stiffness was virtually independent of rotor speed. Cross-coupling stiffness shows an expected negative sign, but it increases from first to second chamber as opposed to theory. Again, it sems that the first chamber is behaving differently compared to the following ones. As in the comparison for the short labyrinth in Fig. 4 for zero inlet swirl, the theory gives generally larger cross-coupling stiffness (in the algebraic sense) compared to measurement. Since the cross-coupling forces are very small at zero swirl compared to practical inlet swirl velocities found in reality (without swirl brakes), this does not impair seriously the theory for predicting rotor stability, as long as damping coefficients are predicted accurately. Further measurements will include damping coefficients with circular or elliptical orbits of the stator and measurements with inlet swirl velocity.

CONCLUSIONS

The theoretical prediction of cross-coupling and damping coefficients has been corroborated by several independent measurements for different rotor speeds and inlet swirl velocities of the leakage flow, the most important ones being the gas seal tests at the Turbomachinery Laboratories at Texas A&M University. In particular, it has been shown that the damping coefficients of the seals are behaving as predicted by theory, i.e. they are insensitive to a wide range of inlet swirl velocities. This has important consequences for the design of high pressure centrifugal compressors, where the seals may be considered as passive dampers for rotor vibrations. For the direct stiffness and the cross-coupling damping coefficients, the theory differs largely from measurements, at least for the gas seal measurements from Texas A&M University. Here, further work is necessary on the theoretical and also on the experimental side. The water operated test stand presented gives new insights into the behaviour of labyrinth seals due to its high measuring resolution and the possibility of measuring individual chambers. Further measurements may show the way how to resolve the discrepancy between theory and measurements for direct stiffness and cross-coupling damping.

REFERENCES

1. Abramovich, G. N., *The Theory of Turbulent Jets*, MIT Press, Cambridge, Mass., 1963.
2. Benckert, H., ""Spaltströmung." Forschungsberichte Forschungs- vereinigung Verbrennungskraftmaschinen," Frankfurt, Vol. 252, 1978.
3. Childs, D. W., and Scharrer, J. K., "Experimental Rotordynamic Coefficient Results for Teeth-on-Rotor and Teeth-on-Stator Labyrinth Gas Seals," Mechanical Engineering Department, Turbomachinery Laboratories, Texas A&M University, College Station, Texas 77843.
4. de Salis, J., "Lomakin-Effekt bei Durchblicklabyrinthen ?," Interner Bericht 635-9, Institut für Flüssigkeitstechnik, Eidg. Techn. Hochschule, Zürich, 1984.
5. Lomakin, A. A., "Die Berechnung der kritischen Drehzahl und der Bedingungen für dynamische Stabilität der Läufer von Hochdruckströmungs- maschinen unter Berücksichtigung der in der Dichtung auftretenden Kräfte (in Russian)," Energomasinostroenie, Vol. 4, 1958, pp. 1-5.
6. Neumann, K., "Zur Frage der Verwendung von Durchblickdichtungen im Dampfturbinenbau," Maschinentechnik, Vol. 13, 1964, Nr.4
7. Scharrer, J. K., "A Comparison of Experimental and Theoretical Results for Rotordynamic Coefficients for Labyrinth Gas Seals," Turbomachinery Laboratories Report No. SEAL-2-85, Texas A&M University, May 1985.
8. Stoff, H., "Calcul et mesure de la turbulence d'un écoulement incompressible dans le l labyrinthe entre une arbre en rotation et un cylindre stationnaire," Thesis No. 342 (1979) Swiss Federal Institute of Technology, Lausanne, Juris Verlag Zürich, 1979.
9. Trutnovsky, K., *Berührungsfreie Dichtungen*, VDI Verlag, 1973.
10. Wyssmann, H., Pham, T. C. and Jenny, R., "Prediction of Stiffness and Damping Coefficients for Centrifugal Compressor Labyrinth Seals," Journal of Engineering for Gas Turbines and Power, Vol. 106, 1984, pp. 920-926.

ORIGINAL PAGE IS
OF POOR QUALITY

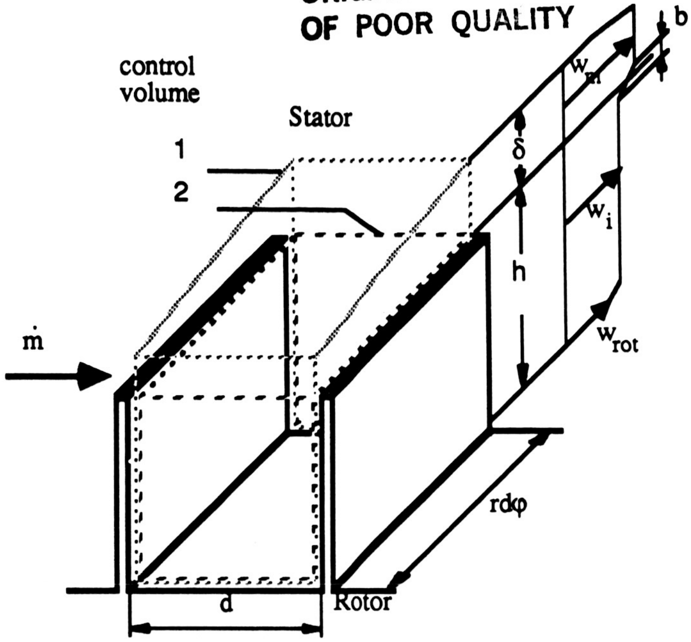
control volume
Stator
1
2
ṁ
b
w_m
δ
h
w_i
w_{rot}
rdφ
d
Rotor

Fig. 1 Control volumes and circumferential velocity of the straight labyrinth

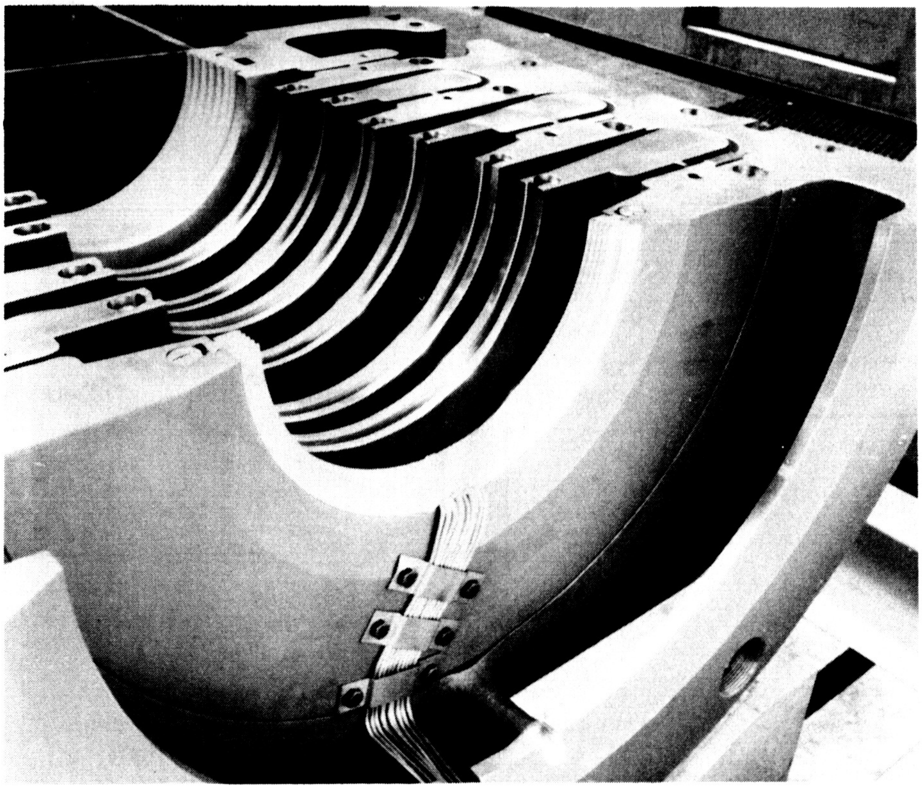

Fig. 2 Test labyrinth in the casing bottom half

ORIGINAL PAGE IS
OF POOR QUALITY

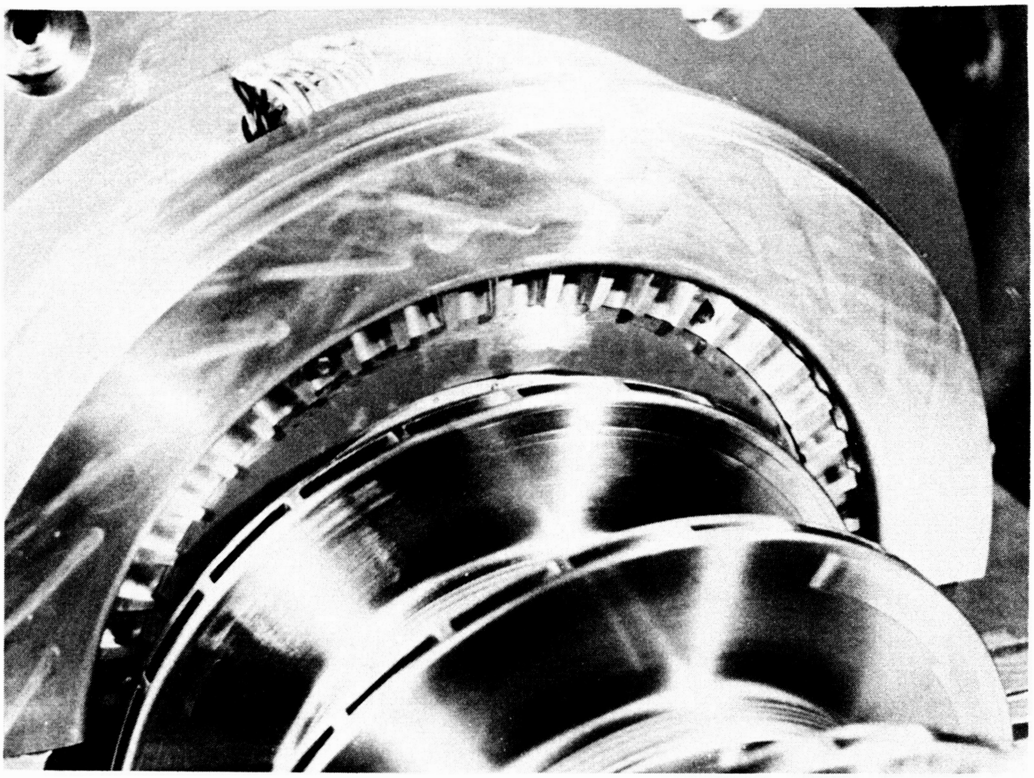

Fig. 3 Swirl brake installed in high pressure centrifugal compressor

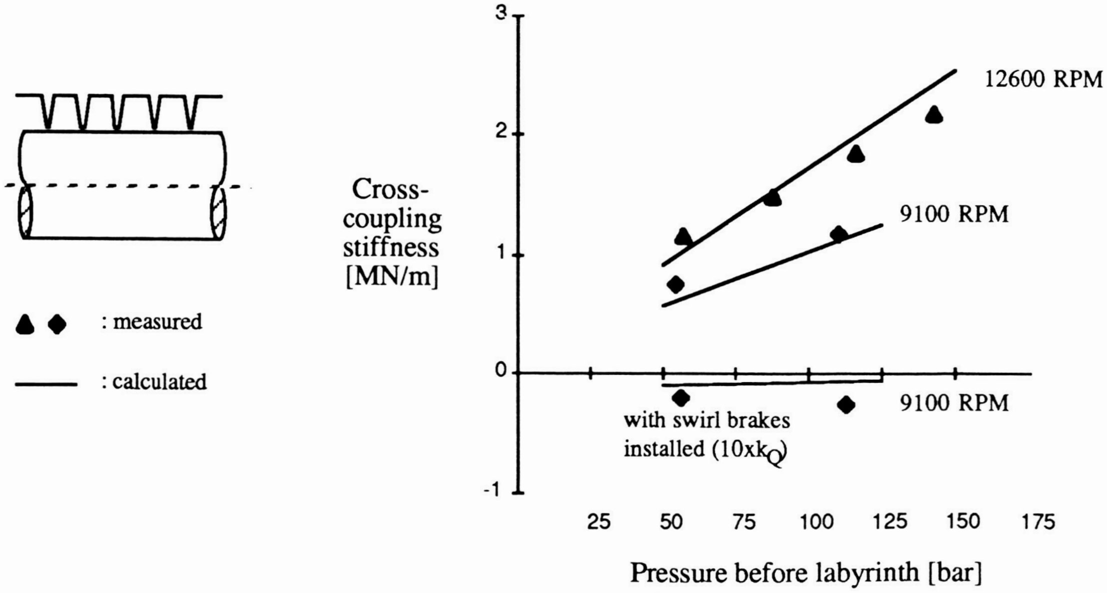

Fig. 4 Measurement vs. theory for cross-coupling coefficients of high pressure centrifugal compressor

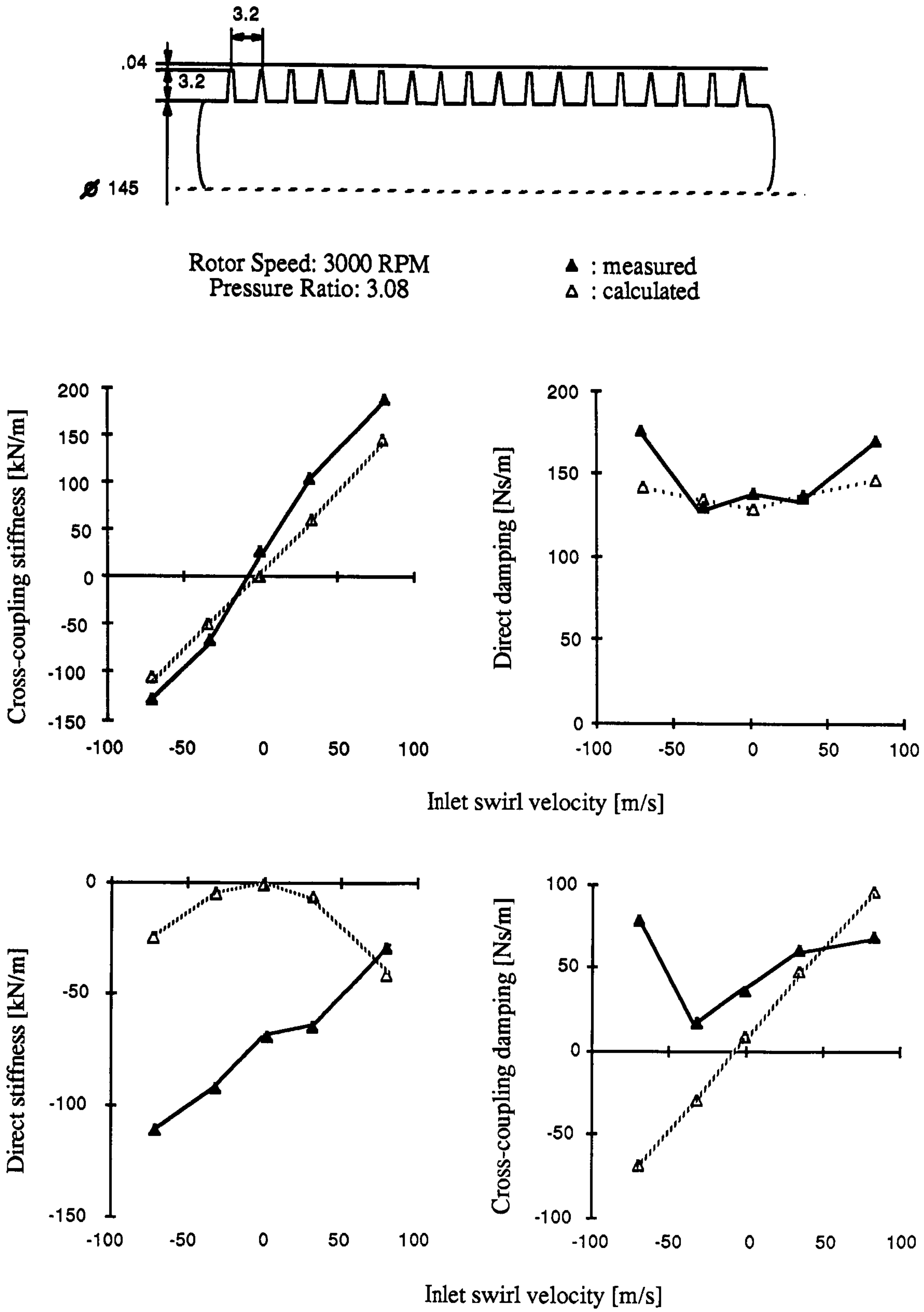

Fig. 5 Labyrinth coefficients vs. inlet swirl velocity for teeth on rotor labyrinth (measurements from [7])

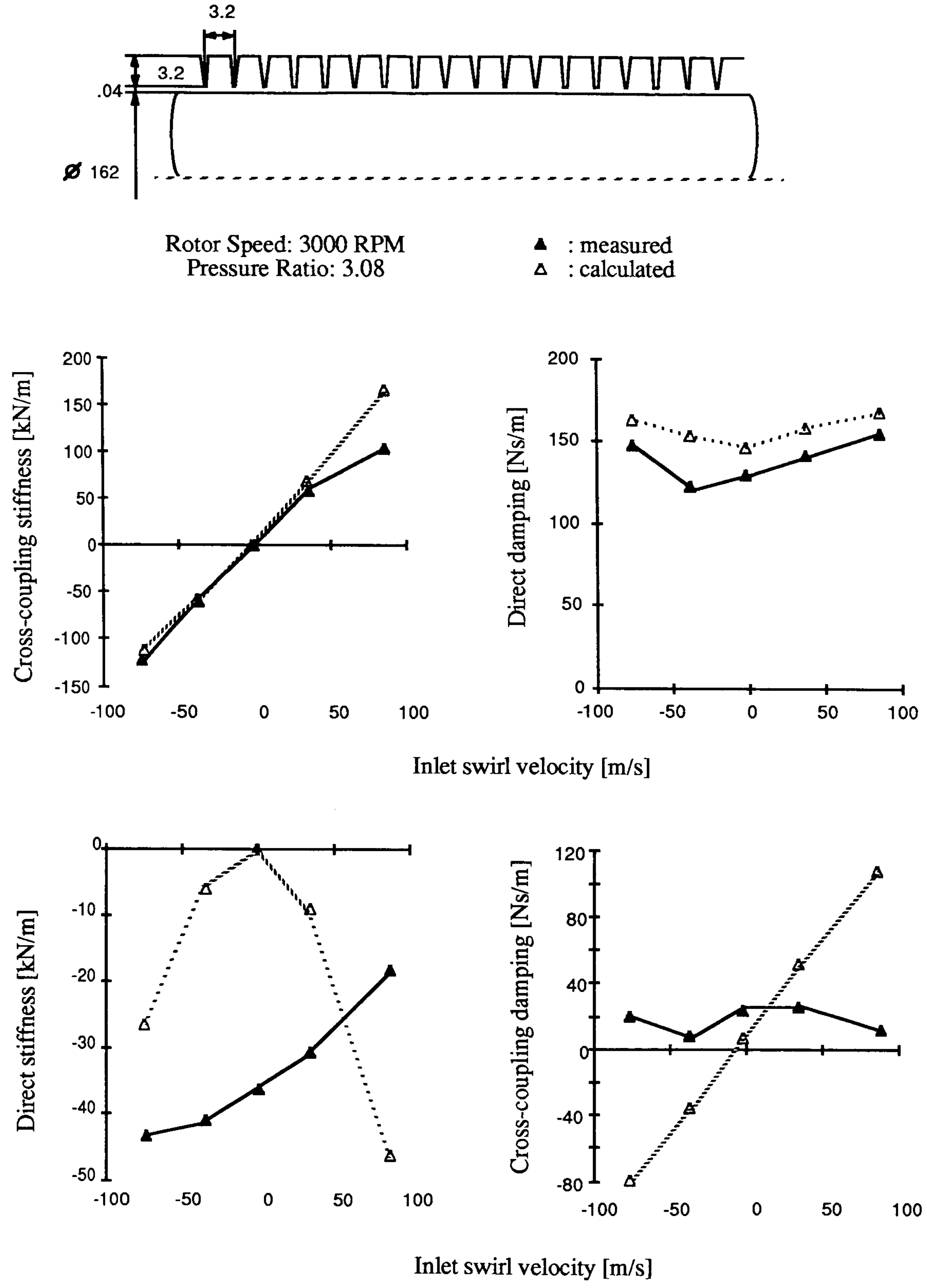

Fig. 6 Labyrinth coefficients vs. inlet swirl velocity for teeth on stator labyrinth (measurements from [7])

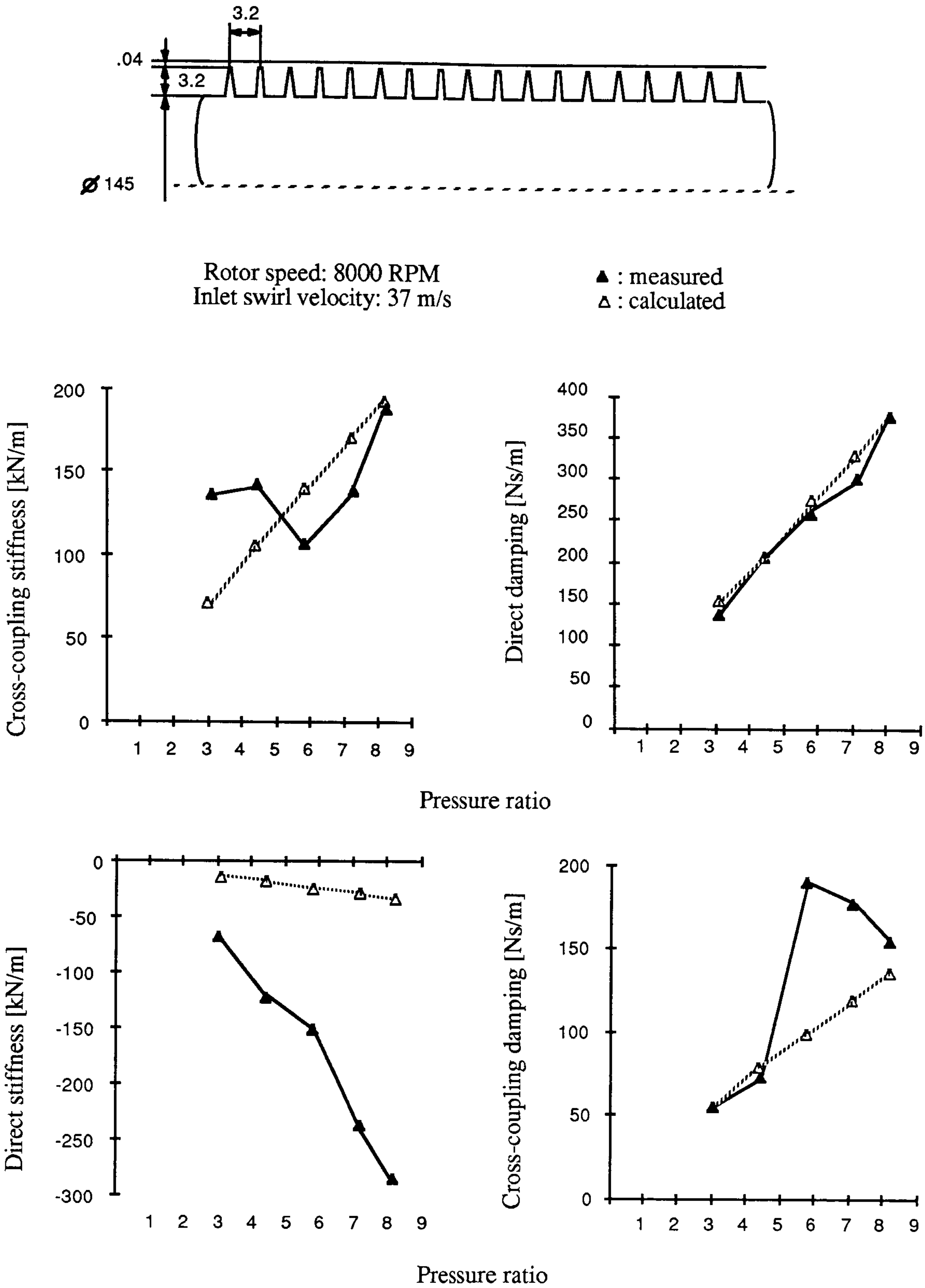

Fig. 7 Labyrinth coefficients vs. pressure ratio for teeth on rotor labyrinth (measurements from [7])

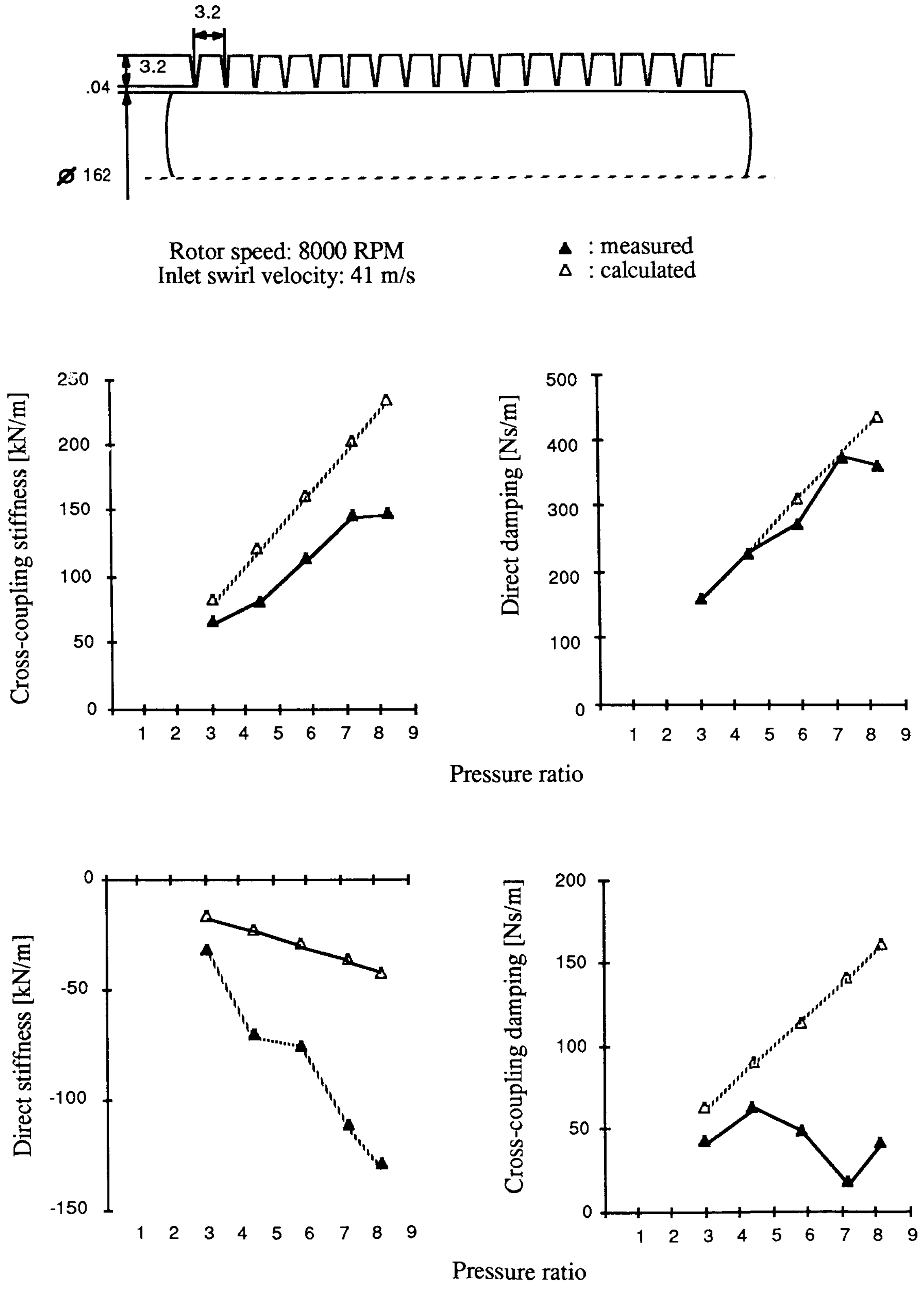

Fig. 8 Labyrinth coefficients vs. pressure ratio for teeth on stator labyrinth (measurements from [7])

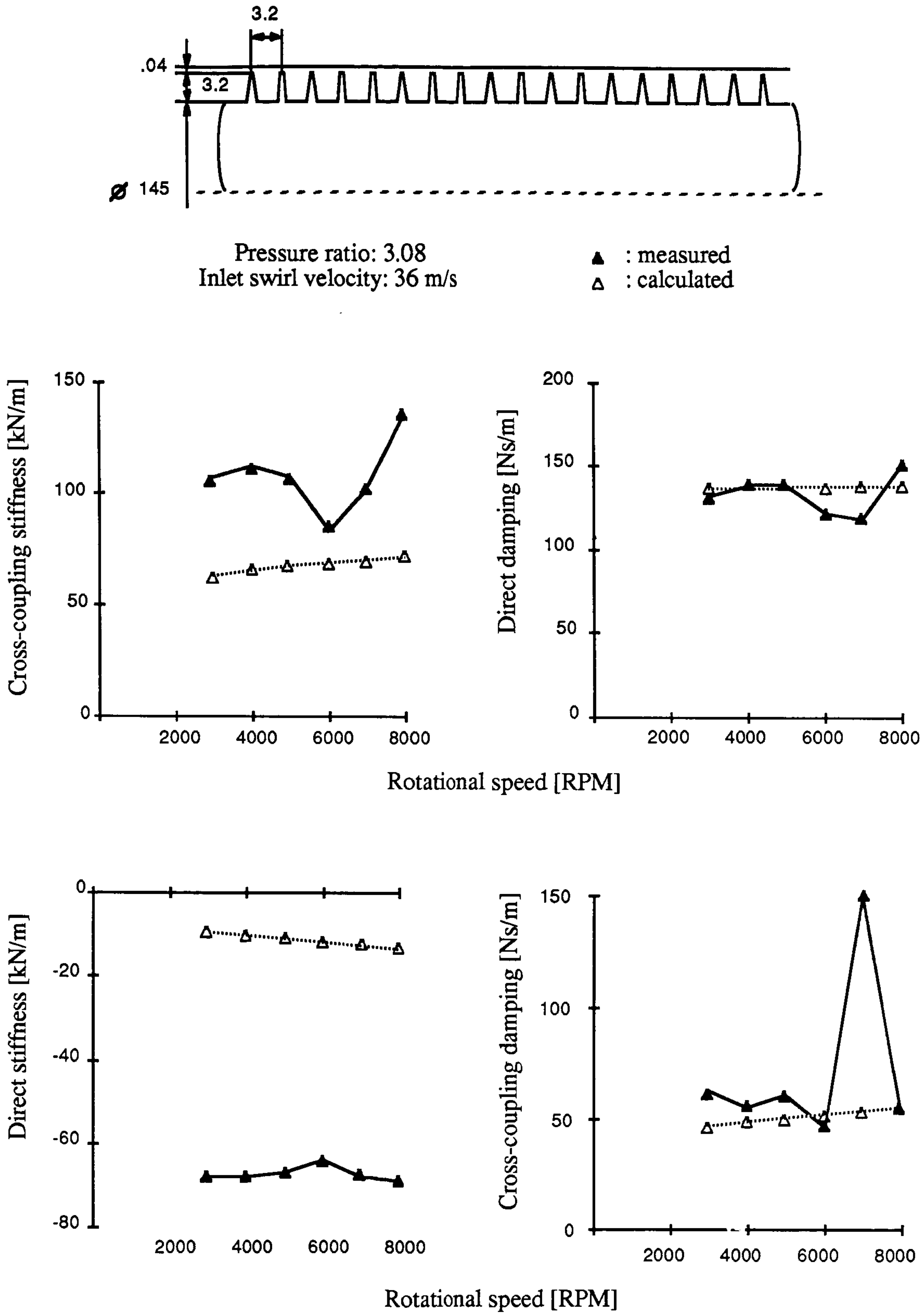

Pressure ratio: 3.08
Inlet swirl velocity: 36 m/s

Fig. 9 Labyrinth coefficients vs. rotor speed for teeth on rotor labyrinth (measurements from [7])

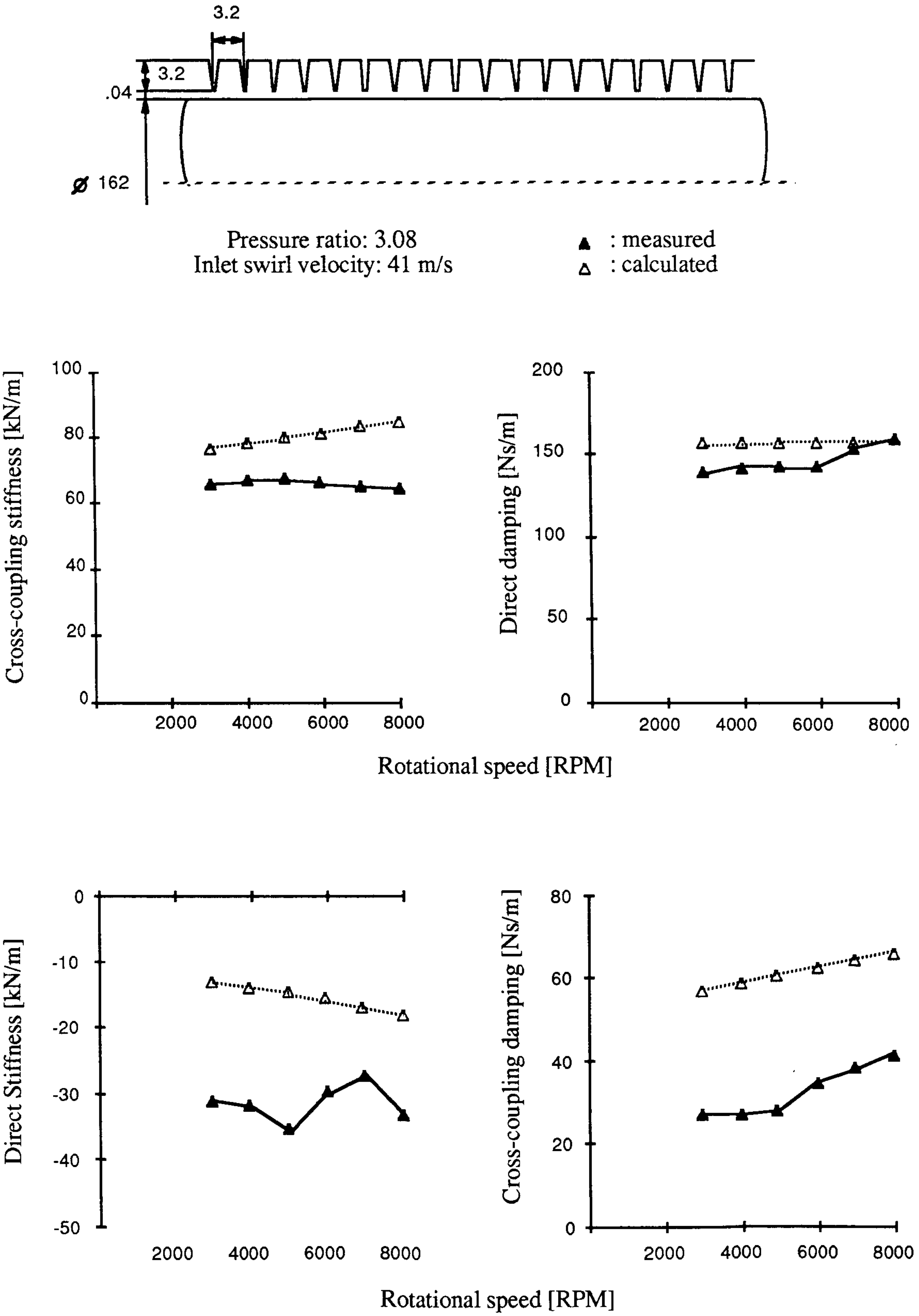

Fig. 10 Labyrinth coefficients vs. rotor speed for teeth on stator labyrinth (measurements from [7])

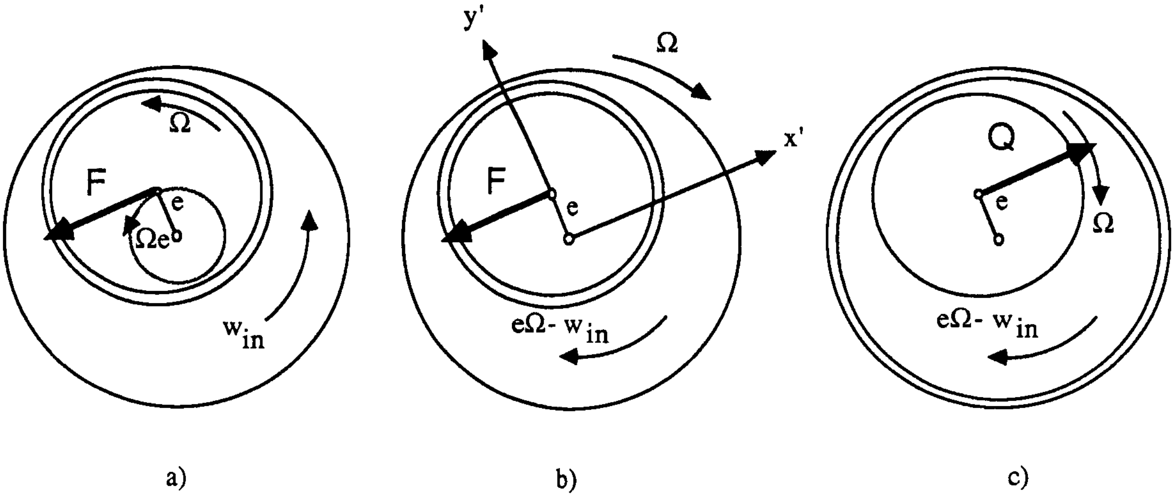
Ω
F
e
Ωe
w_in
y'
Ω
x'
F
e
eΩ- w_in
Q
e
Ω
eΩ- w_in
a)
b)
c)

Fig. 11 The basic identity of cross-coupling and damping forces

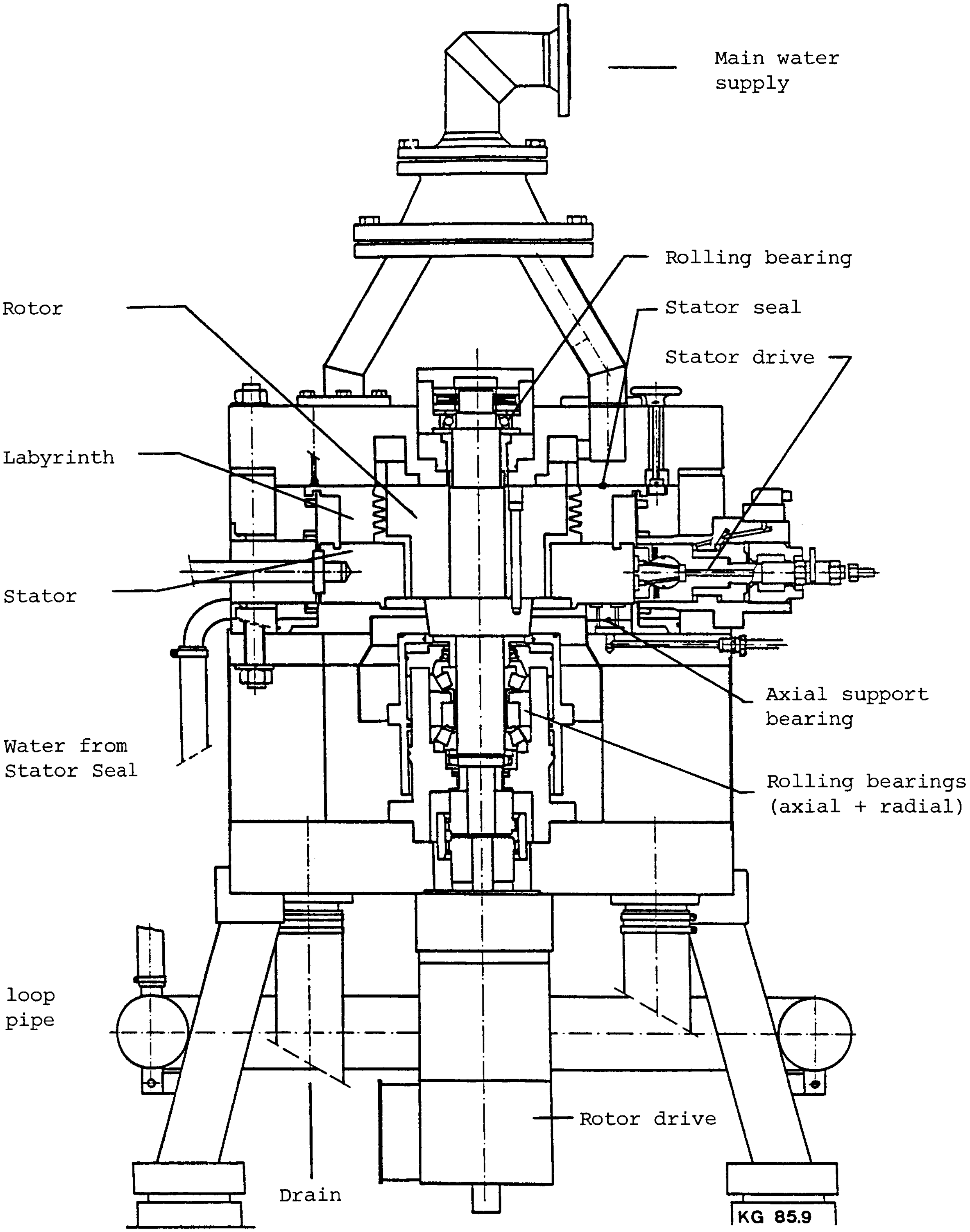
Main water supply
Rolling bearing
Stator seal
Stator drive
Rotor
Labyrinth
Stator
Water from Stator Seal
Axial support bearing
Rolling bearings (axial + radial)
loop pipe
Rotor drive
Drain
KG 85.9

Fig. 12 Cross-section of water operated labyrinth test stand

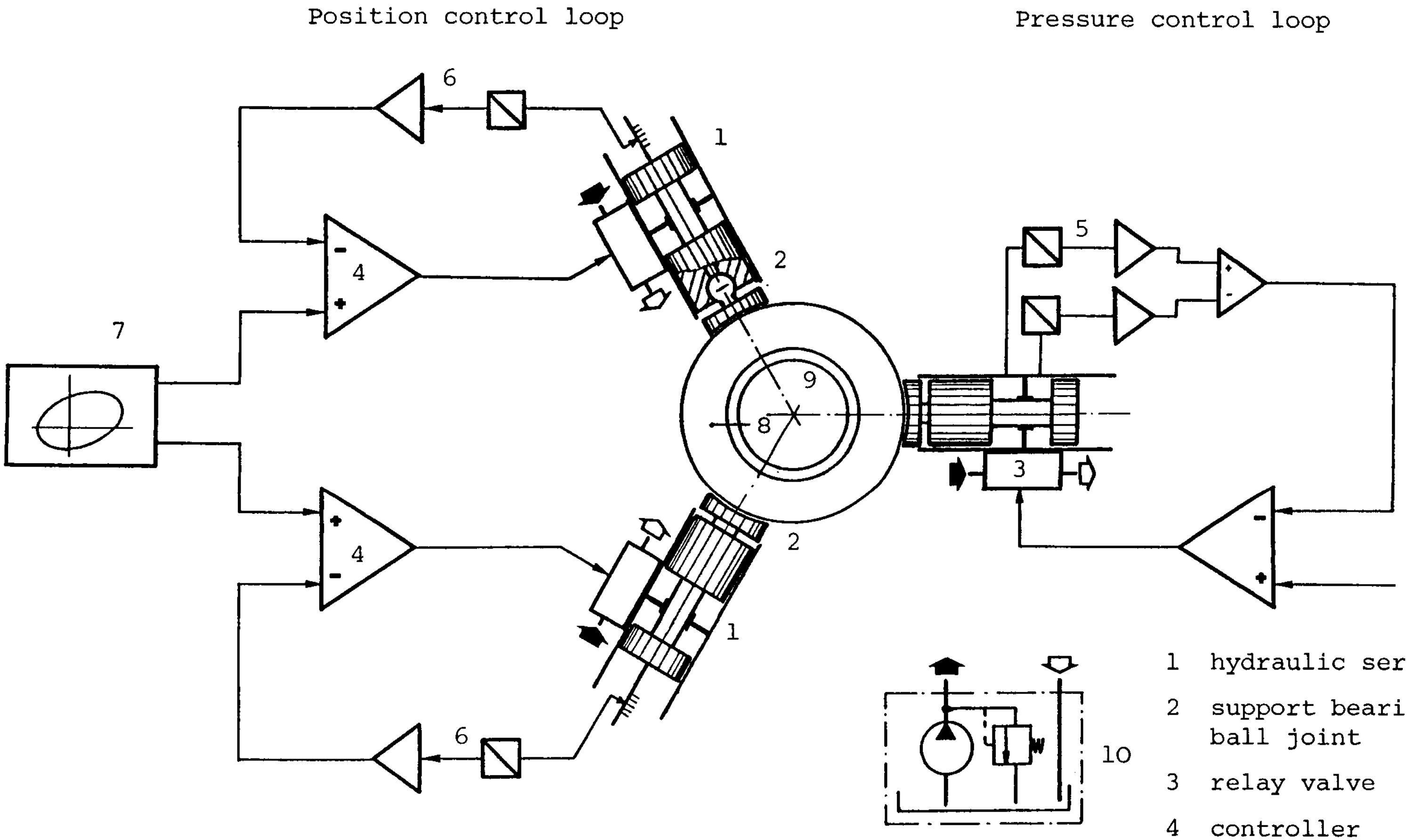
Position control loop
Pressure control loop
6
1
2
5
4
7
9
8
3
2
4
1
6
10

Fig. 13 Schematic of hydraulically operated stator

1	hydraulic servomotor
2	support bearing with ball joint
3	relay valve
4	controller
5	pressure transmitter
6	position transmitter
7	control unit
8	stator
9	rotor
10	oil supply unit

ORIGINAL PAGE IS
OF POOR QUALITY

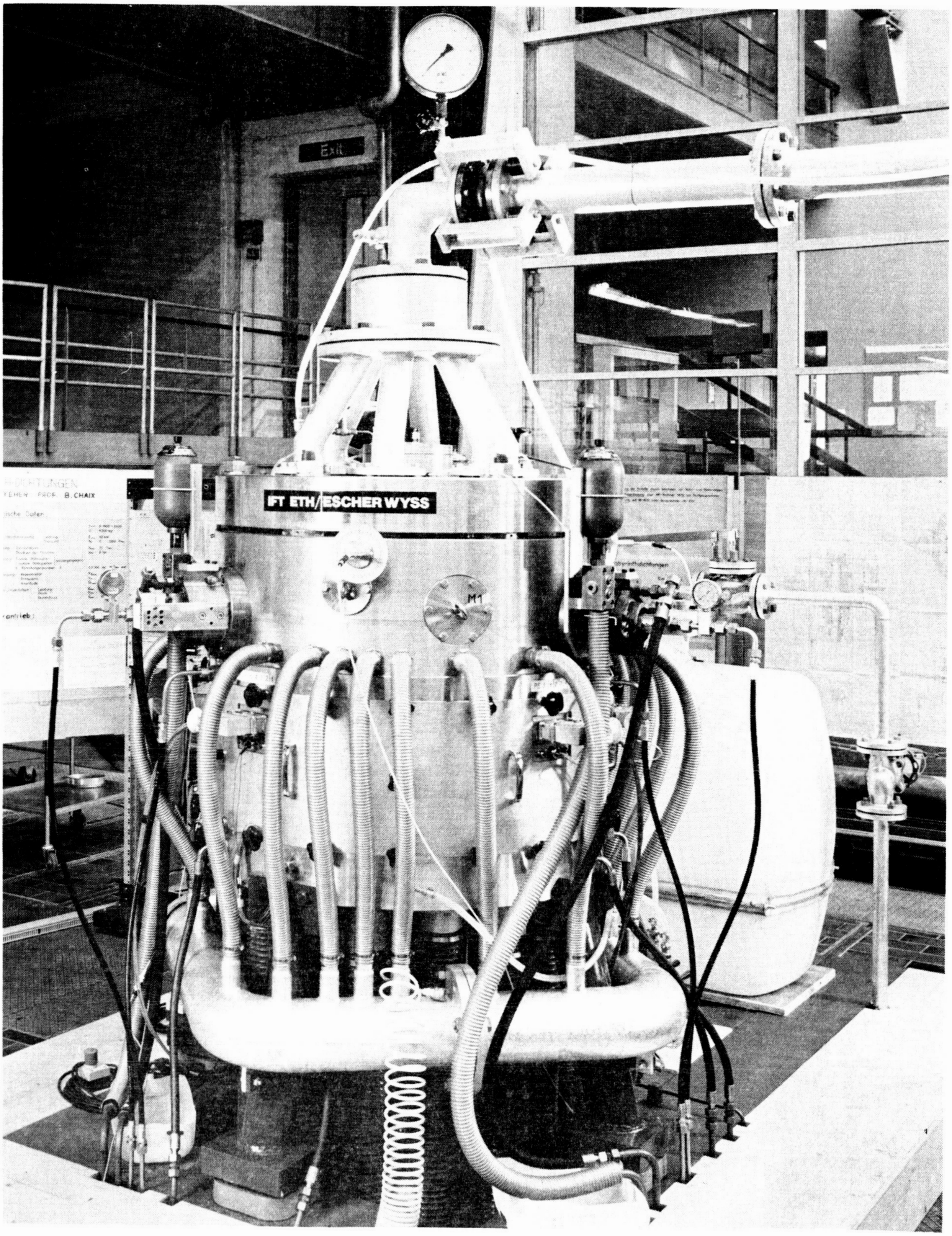
Exit
PROF. B. CHAIX
IFT ETH/ESCHER WYSS
M1

Fig. 14 Water operated labyrinth test stand

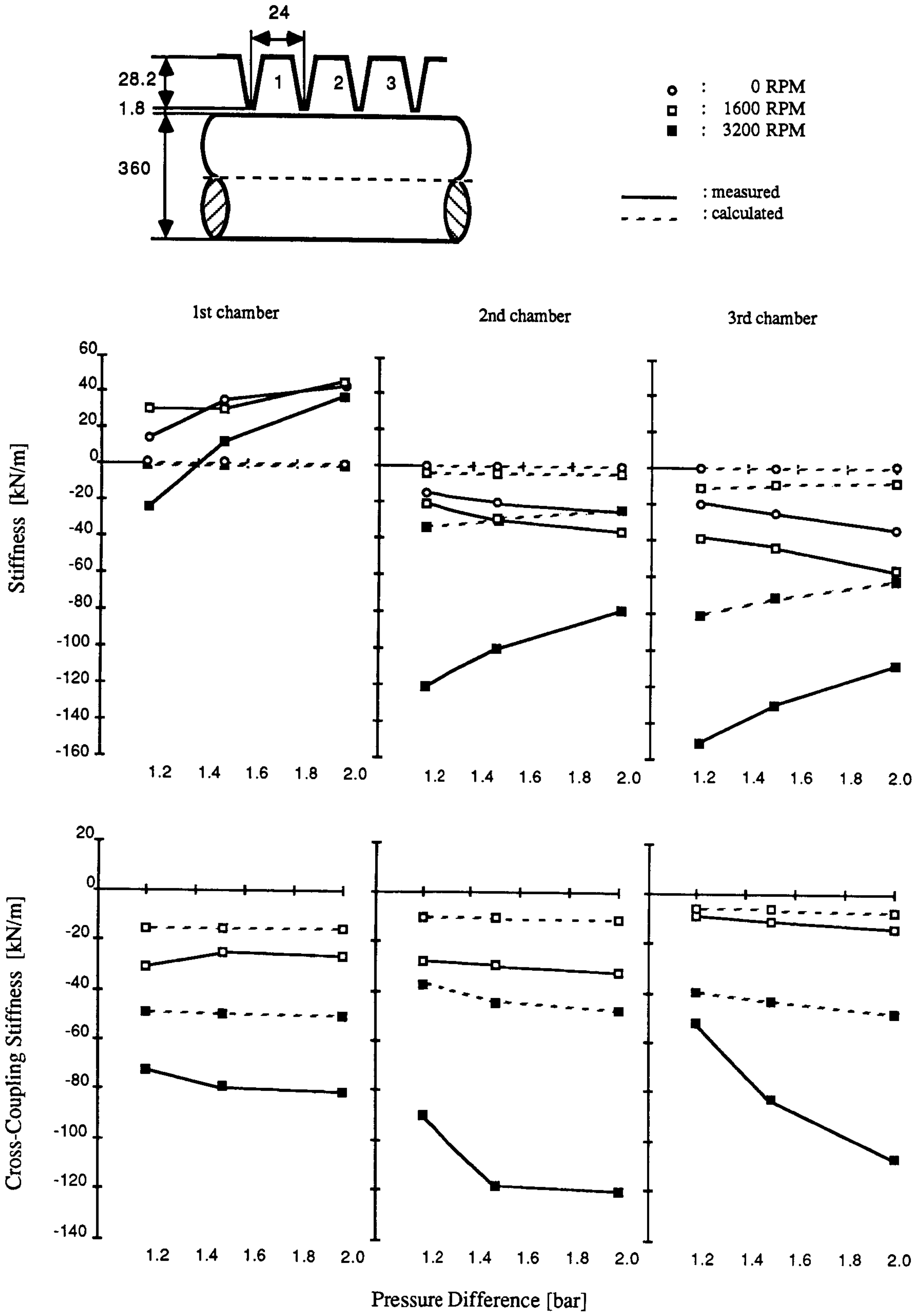

Fig. 15: Measurement of stiffness and cross-coupling stiffness without inlet swirl (water tests)

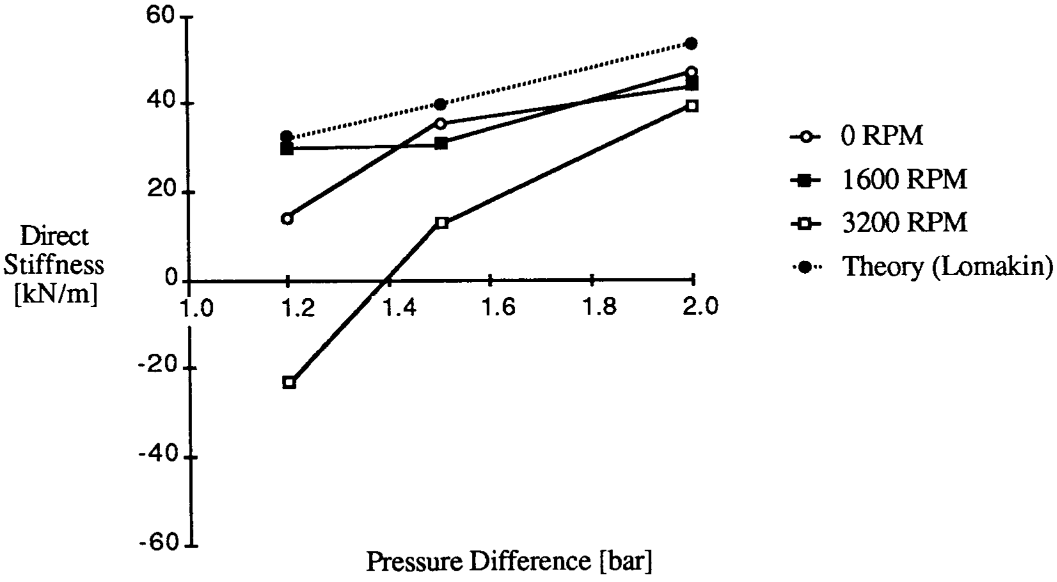

Fig. 16 Comparison with Lomakin formula

N87-22212

EXPERIMENTAL ROTORDYNAMIC COEFFICIENT RESULTS FOR TEETH-ON-ROTOR AND TEETH-ON-STATOR LABYRINTH GAS SEALS[1]

Dara W. Childs and Joseph K. Scharrer
Texas A&M University
College Station, Texas, 77843

An experimental test facility is used to measure the rotordynamic coefficients of teeth-on-rotor and teeth-on-stator labyrinth gas seals. Direct damping coefficients are presented for these seals for the first time. The results are presented for the two seal configurations at identical operating conditions, and show that, in a rotordynamic sense, the teeth-on-stator seal is more stable than the teeth-on-rotor seal, for inlet tangential velocity in the direction of rotation.

NOMENCLATURE

A	Seal orbit radius (L); illustrated in figure 9.
B	Tooth height (L); illustrated in figure 1.
C,c	Direct and cross-coupled damping coefficients (FT/L)
C_r	Radial clearance (L); illustrated in figure 1.
K,k	Direct and cross-coupled stiffness coefficients (F/L)
F	Seal reaction-force (F)
L	Tooth pitch (L); illustrated in figure 1.
Pr	Seal inlet pressure (F/L^2)
Rs	Seal radius (L); illustrated in figure 1.
X,Y	Rotor to stator relative displacement components (L)
Ω	Shaking frequency (1/T)
ω	Shaft angular velocity (1/T)

Subscripts

i	Value in i-th cavity
r	Radial component
t	Tangential component
x,y	Rectangular coordinate directions

---

[1] This work was supported in part by NASA Grant NAS3-181 from NASA Lewis Research Center (Technical Monitor, Robert Hendricks) and AFOSR Contract F49620-82-K-0033 (Technical Monitor, Tony Amos).

INTRODUCTION

The design, development, and operation of the test apparatus and facility which have been developed to measure the leakage and rotordynamic coefficients of annular gas seals has been described by Childs et al. [1]. This apparatus has been designed and used to measure rotordynamic coefficients of plain annular seals, plain seals with honeycomb stators, and labyrinth seals. Nelson et al. [2] presented the results for plain annular seals with constant-clearance and convergent-tapered geometries. This paper presents the results for "see-through" labyrinth seals, as shown in figure 1, with teeth on the rotor and teeth on the stator.

As described in [1], the rotordynamic coefficients for a gas seal are defined by the following linearized force-displacement model.

$$-\begin{Bmatrix} F_x \\ F_y \end{Bmatrix} = \begin{bmatrix} K_{xx} & K_{xy} \\ K_{yx} & K_{yy} \end{bmatrix} \begin{Bmatrix} X \\ Y \end{Bmatrix} + \begin{bmatrix} C_{xx} & C_{xy} \\ C_{yx} & C_{yy} \end{bmatrix} \begin{Bmatrix} \dot{X} \\ \dot{Y} \end{Bmatrix} \quad (1)$$

Where (X,Y) define the motion of the seal's rotor relative to its stator, (F_x,F_y) are the components of the reaction force acting on the rotor, and $(K_{xx},K_{yy},K_{xy},K_{yx})$ and $(C_{xx},C_{yy},C_{xy},C_{yx})$ are the stiffness and damping coefficients respectively. Equation (1) applies for small motion of the rotor about an arbitrary eccentric position. For small motion about a centered position, the following simpler model applies.

$$-\begin{Bmatrix} F_x \\ F_y \end{Bmatrix} = \begin{bmatrix} K & k \\ -k & K \end{bmatrix} \begin{Bmatrix} X \\ Y \end{Bmatrix} + \begin{bmatrix} C & c \\ -c & C \end{bmatrix} \begin{Bmatrix} \dot{X} \\ \dot{Y} \end{Bmatrix} \quad (2)$$

Although the test apparatus has the capability of separately identifying the eccentric-position rotordynamic coefficients of equation (1), the results presented here are for the centered-position case only.

A limited amount of experimental data have been published to date on the determination of the stiffness coefficients for labyrinth gas seals. However, no data have been published concerning the damping coefficients of labyrinth gas seals. The first published results for stiffness coefficients were those of Wachter and Benckert [3,4,5]. They investigated the following three types of seals: a) teeth-on-stator, b) interlocking teeth on the rotor and stator, and c) teeth on the stator and steps or grooves on the rotor. Seals were tested in the following two modes: a) No seal rotation, but fluid prerotation, and b) seal rotation but zero fluid prerotation. These results were limited in that the pressure drop was small, much of the data was for nonrotating seals, no data were presented for teeth-on-rotor seals. The next investigation was carried out by Wright [6], whose results were for single-cavity teeth-on-stator seals with convergent, divergent, or straight geometries. Although this was a very limited and special case, these results did give insight into the effects of pressure drop, convergence or divergence of the clearance, and forward or backward whirl of a seal. The most recent investigation was that of Brown and Leong [7], who investigated various teeth-on-stator seal configurations. Their results include variations of pressure, geometry, rotor speed, and inlet tangential velocity.

In reviewing previous experimental programs, there is a clear need for extensive testing of seals with teeth on the rotor and results for measured damping coefficients. This paper present some initial results for stiffness and damping coefficients for two, nominally-identical seals, differing only in that one is a tooth-on-rotor configuration and the other is a tooth-on-stator configuration. The test apparatus, facilities, and data-identification procedures used in this study are described in detail in references [1] and [2].

EXPERIMENTAL RESULTS

The rotor and results for measured damping coefficients. This paper present some initial results for stiffness and damping coefficients for two, nominally-identical seals, differing only in that one is a tooth-on-rotor configuration and the other is a tooth-on-stator configuration. The test apparatus, facilities, and data-identification procedures used in this study are described in detail in references [1] and [2].

The test results reported here were developed as a part of an extended, joint NASA-USAF funded research program for annular gas seal studies. Tests were of a smooth-rotor/labyrinth-stator seal and a labyrinth-rotor/smooth-stator seal. The test program had the initial objective of comparing the leakage and stability performance of a teeth-on-stator and a teeth-on-rotor labyrinth seal. Air is the test fluid.

Test Apparatus and Seal Configuration

The rotor shaft is suspended pendulum-fashion from an upper, rigidly mounted pivot shaft, as shown in supported in the test section housing by three configuration. Different seal stator designs are obtained by the use of inserts.

The dimensions and pertinent data for each seal configuration are given in table 1. The constants given in table 1 for Fanning friction factor determination (mr,nr,ms,ns) are the same as those determined for the constant-clearance seal case as discussed by Nelson et al. [2]. The smooth and labyrinth stator inserts used for these tests are shown in figure 4. The labyrinth rotor and the tooth detail for both rotor and stator are shown in figures 5 and 6.

Table 1. Dimensions and parameters of seals tested in this study

	Teeth on rotor	Teeth on stator
Radius (cm)	7.25	7.56
Length (cm)	5.08	5.08
Tooth pitch (cm)	0.3175	0.3175
Tooth height (cm)	0.3175	0.3175
Clearance (cm)	0.0406	0.0406
mr	-0.33	-0.33
nr	0.187	0.187
ms	-0.33	-0.33
ns	0.187	0.187
Avg. Inlet Temp. (K)	300.0	300.0

Test Variables

When shaking about the centered position, the Dynamic-Seal-Apparatus is capable of controlling the following three independent variables: pressure ratio, rotor speed and inlet tangential velocity. The actual test points for each of these three independent variables are shown in table 2. When reviewing the following figures, table 2 should be consulted for the definitions of all symbols used.

The pressure ratios achieved at the TAMU facility were up to 2.5 times larger than those published by Wachter and Benckert [3,4,5]. The reservoir pressures, as measured upstream of the flowmeter, are given in table 2. These values differ from the actual inlet pressure, as given in the pressure distribution plots, because of frictional losses and an acceleration of the fluid due to the inlet guide vanes. No tests could be run at zero pressure difference, since a small pressure difference is necessary to keep the rotor from shifting axially and rubbing the inlet guide vanes.

Table 2. Definition of symbols used in figures.

Supply Pressure	Rotor Speeds	Inlet Tangential Velocities
1-3.08 bar	1-500 cpm	1-High velocity against rotation
2-4.46 bar	2-1000 cpm	2-Low velocity against rotation
3-5.84 bar	3-2000 cpm	3-Zero tangential velocity
4-7.22 bar	4-3000 cpm	4-Low velocity with rotation
5-8.25 bar	5-4000 cpm	5-High velocity with rotation
	6-5000 cpm	
	7-6000 cpm	
	8-7000 cpm	

The rotor speeds tested to date at the TAMU facility were comparable to those published by Wachter and Benckert. The surface velocities reached here were about half of those reported by Wachter and Benckert. However, Wachter and Benckert published very little data which combines rotor rotation and inlet fluid prerotation. In this study, all possible combinations of independent variables are given. For discussion purposes, the 3000 cpm rotor speed will be highlighted. The results showed little sensitivity to rotor speed and the 3000 cpm point tended to yield the clearest and most descriptive data. No zero rotor speed tests were run, since rotor rotation was necessary to prevent damage to the thrust bearing during shaking.

The inlet tangential velocities attained were up to 2.0 times those published by Wachter and Benckert. The inlet tangential velocities are given in figures 7 and 8 as a function of pressure ratio for both teeth-on-rotor and teeth-on-stator seals. The figures show that inlet tangential velocity remains fairly constant over the pressure ratios tested. There were five test points for inlet tangential velocity; two positive, two negative, and one at zero. The zero inlet tangential velocity point corresponds to the x-axis in the figures 7 and 8. The negative numbers shown in the figures mean that the inlet tangential velocity was opposed to the direction of rotor rotation. The positive numbers mean that the inlet tangential velocity was in the same direction as rotor rotation. The two different magnitudes of inlet tangential velocity, for each direction, correspond to the different inlet guide vane geometries, as discussed in [9]. The ratio of inlet tangential velocity to rotor surface velocity, ranged from about -13 to about 16. Although the larger numbers are practically unrealistic, they do give insight into the effects of inlet tangential velocity that would have otherwise gone unnoticed. This is most evident in the plots of direct damping versus inlet tangential velocity.

The effects of the three independent variables; pressure ratio, inlet tangential velocity, and rotor speed on the dynamic (rotordynamic coefficients) results will be reviewed in order.

Dynamic Results

For a circular orbit of amplitude A, the resultant radial and tangential forces developed by the seal model of equation (2) are illustrated in figure 9 and are defined by:

$$-F_r/A = K + c\omega$$

$$F_t/A = k - C\omega$$

From a stability standpoint, the destabilizing tangential force, F_t, is of most interest. The destabilizing influence comes from the cross-coupled stiffness, k, and the stabilizing influence comes from the direct damping, C. The radial force usually has little influence on stability, except in rare cases involving multistage "back-to-back" centrifugal compressors with midspan seals where large negative direct stiffness values may reduce the natural frequencies. Since the focus of this study was on stability, the cross-coupled stiffness and direct damping results, which have the most influence, will be presented first. The direct stiffness will follow.

Relative Uncertainty

Before proceeding with the results, a statement must be made concerning the uncertainty present in the experimental results. Using the method described by Holman [8], the uncertainty in the dynamic coefficients can be determined. The uncertainty in the force, excitation frequency, and displacement measurements are 0.89 N (0.2 lb), 0.13 Hz , and 0.0013 mm (0.05 mils), respectively. The resulting calculated uncertainty in the stiffness coefficients is 7 N/mm (40 lb/in) and 0.0875 N-s/mm (0.5 lb-s/in) for the damping coefficients. Since the measured cross-coupled damping results were rarely greater than the uncertainty, test results are not provided here for this parameter; however data are available in [9].

Cross-coupled Stiffness Comparison

Figure 10 shows a comparison of the cross-coupled stiffness versus rotor speed for the inlet tangential velocity set of table 2. The figure shows that the teeth-on-rotor labyrinth develops a larger cross-coupled stiffness than the teeth-on-stator configuration. This figure also shows that cross-coupled stiffness results for the the two seals were insensitive to rotor speed over the range of speeds tested (500-8000 cpm). Figure 11 shows the results for cross-coupled stiffness versus inlet tangential velocity for the two seals for the inlet pressure set of table 2. This figure shows that the teeth-on-rotor seal develops consistently larger cross-coupled stiffness than the teeth-on-stator seal for all inlet tangential velocity values tested. Figure 12 shows a comparison of the cross-coupled stiffness of the two seals versus pressure ratio at 3000 cpm. This figure shows that the cross-coupled stiffness of both seals increase with pressure ratio. However, the cross-coupled stiffness for the teeth-on-stator seal levels off under choked conditions (Pr>5.84 bar).

Direct Damping Comparison

Figure 13 shows a comparison of the direct damping versus inlet tangential velocity for the inlet pressure set of table 2. The results show that the teeth-on-rotor case also develops larger direct-damping coefficients than the teeth-on-stator case. This figure also shows that the direct damping for both seals is very sensitive to inlet tangential velocity. Figure 14 shows a comparison of the direct damping versus pressure ratio at 3000 cpm. This figure shows that the direct damping for both seals increases with increasing inlet pressure. Figure 15 compares the direct damping versus rotor speed for the inlet pressure set of table 2, and shows that direct damping is relatively insensitive to rotor speed.

Direct Stiffness Comparison

Figure 16 shows the results for direct stiffness versus rotor speed with the inlet pressure set of table 2. The figure shows that the teeth-on-rotor case develops a substantially larger magnitude of direct stiffness than the teeth-on-stator case. Note that the direct stiffness is negative which would reduce the system natural frequency and reduce the stability. Figure 17 shows a comparison of the direct stiffness for the two seals versus pressure ratio at 3000 CPM. This figure shows that the magnitude of direct stiffness increases with increasing pressure ratio for both seals. The direct stiffness for the teeth-on-stator seal seems to level off for choked exit conditions (Pr>5.84 bar). Figure 18 shows a comparison of the direct stiffness versus inlet tangential velocity for the two seals for the inlet pressure set of table 2. The figure shows that the direct stiffness for the teeth-on-stator seal increases with increasing inlet tangential velocity, while the direct stiffness for the teeth-on-rotor seal decreases with increasing inlet tangential velocity.

Whirl Frequency Ratio Comparison

Since a direct comparison of the coefficients of the two seals does not show any clear stability advantage, another method of comparison must be used. One method in which the dynamic coefficients of the two seals can be directly compared is through their respective non-dimensional whirl frequency ratios. Whirl ratio is defined by

$$\text{Whirl ratio} = k/C\Omega$$

where Ω is the shaking frequency, and is the ratio of the destabilizing influence of the cross-coupled stiffness and the stabilizing influence of direct damping. From a stability viewpoint, a minimum whirl ratio is desirable. Figure 19 shows a comparison plot of the whirl frequency ratios for the two seals versus inlet tangential velocity with the inlet pressure set of table 2, and shows that the teeth-on-stator seal has a smaller whirl ratio than the teeth-on-rotor seal for positive inlet tangential velocities. This result is significant because most turbomachines have positive inlet tangential velocities for seals and teeth-on-stator seals are shown to be clearly superior to teeth-on-rotor seals from a stability viewpoint.

CONCLUSIONS

Test results have been presented for stiffness and damping coefficients of teeth-on-rotor and teeth-on-stator labyrinth seals which are geometrically similar. The seals were tested under identical operating conditions to investigate the influence of rotor speed, pressure ratio and inlet tangential velocity on the rotordynamic coefficients.

The experimental results of the previous section support the following conclusions:

(1) The stiffness and damping coefficients are insensitive to rotor speed for both seal configurations tested. This may be due to a lack of shear forces developed by the seals and may change as higher speeds are attained.

(2) The stiffness and damping coefficients are very sensitive to inlet tangential velocity.

(3) The stiffness and damping coefficients increase with increasing inlet pressure.

(4) From a rotordynamic standpoint, the teeth-on-stator seal is more stable than the teeth-on-rotor seal for positive inlet tangential velocity.

As a point of interest, the theory of reference [10] was in reasonable agreement with the cross-coupled stiffness results presented here. However predictions for direct stiffness and damping are unsatisfactory. Details of the comparison are provided in reference [9].

REFERENCES

1. Childs, D., Nelson, C., Nicks, C., Scharrer, J., Elrod, D., Hale,.K., "Theory Versus Experiment for the Rotordynamic Coefficients of Annular Gas Seals: Part 1, Test Facility and Apparatus," 85-Trib-1, ASME-ASLE Joint Lubrication Conference, Atlanta, GA, 8-10 October 1985; also recommended for ASME Trans. Journal of Tribology Technology.

2. Nelson, C., Childs, D., Nicks, C., Elrod, D., "Theory Versus Experiment for the Rotordynamic Coefficients of Annular Gas Seals: Part 2, Constant-Clearance and Convergent-Tapered Geometry", 85-Trib-2, ASME-ASLE Joint Lubrication Conference, Atlanta, GA, 8-10 October 1985; also recommended for ASME Trans. Journal of Tribology Technology.

3. Wachter, J., and Benckert, H.,"Querkrafte aus Spaltdichtungen-Eine mogliche Ursache fur die Laufunruhe von Turbomaschinen," Atomkernenergie Bd. 32, 1978, Lfg. 4, pp. 239-246.

4. Wachter, J., and Benckert, H., "Flow Induced Spring Coefficients of Labyrinth Seals for Applications in Rotordynamic," NASA CP 2133, Rotordynamic Instability Problems in High Performance Turbomachinery, proceedings of a workshop held at Texas A&M University 12-14 May 1980, pp 189-212.

5. Benckert, H., "Stromungsbedinte Federkennwerte in Labyrinthdichtungen," Doctoral dissertation at University of Stuttgart, 1980.

6. Wright, D.V.: Labyrinth Seal Forces on a Whirling Rotor. Rotor Dynamical Instability. Proceedings of the ASME Applied Mechanics, Bioengineering, and Fluids Engineering Conference, June 20-22, 1983, Houston, Texas. pp. 19-31.

7. Brown, R.D, and Leong, Y.M.M.S, "Experimental Investigation of Lateral Forces Induced by Flow Through Model Labyrinth Glands," NASA CP 2338, Rotordynamic Instability Problems in High Performance Turbomachinery, proceedings of a workshop held at Texas A&M University 28-30 May, 1984. pp. 187-210.

8. Holman, J.P., Experimental Methods for Engineers, McGraw Hill, 1978, pp. 45.

9. Scharrer, J., "A Comparison of Experimental and Theoretical Results for Rotordynamic Coefficients for Labyrinth Gas Seals," TRC Report No. SEAL-2-85, Texas A&M University, May 1985.

10. Childs, D., and Scharrer, J., "An Iwatsubo-Based Solution for Labyrinth Seals-Comparison to Experimental Results," ASME Paper 85-GT-136, ASME Gas Trubine Conference, March 1985, Houston, Texas, also accepted for publication, ASME Trans. Journal of Engineering for Gas Turbine and Power.

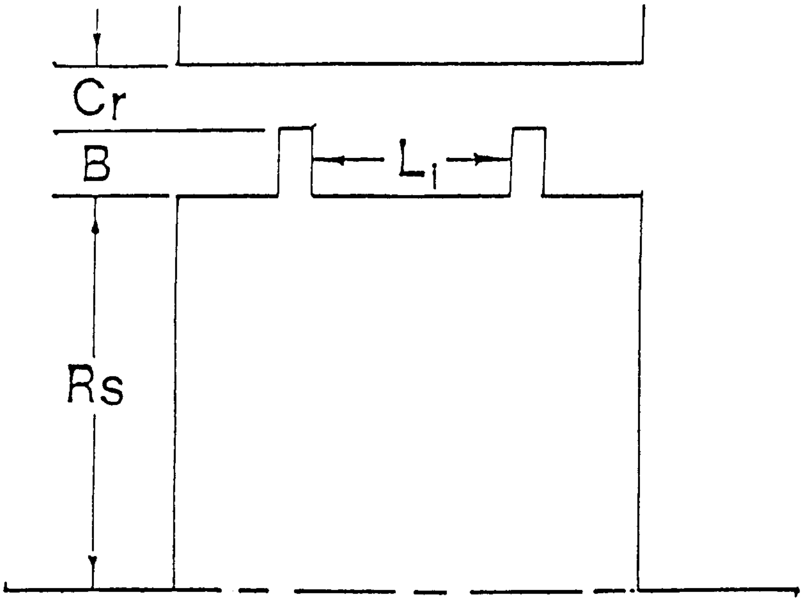

Fig. 1 A typical cavity.

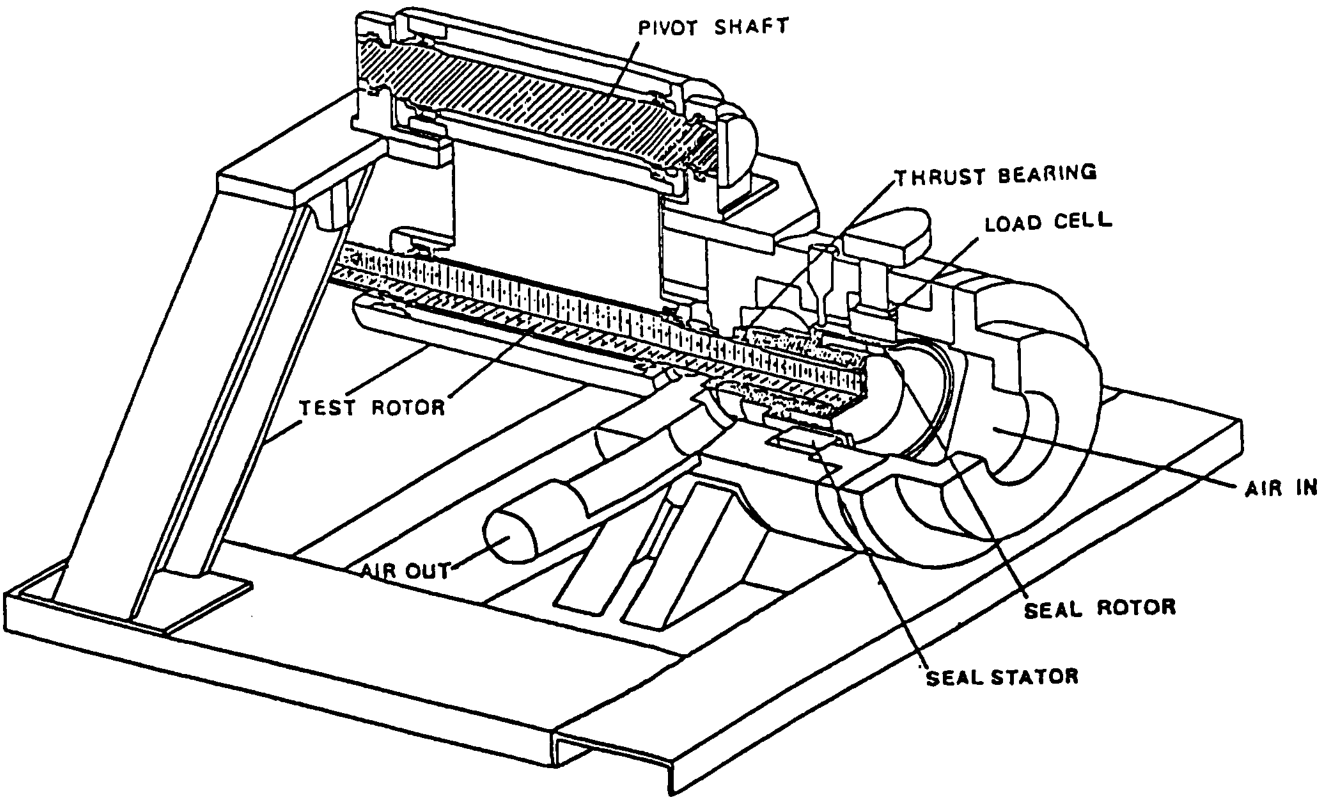
PIVOT SHAFT
THRUST BEARING
LOAD CELL
TEST ROTOR
AIR IN
AIR OUT
SEAL ROTOR
SEAL STATOR

Fig. 2 Test apparatus

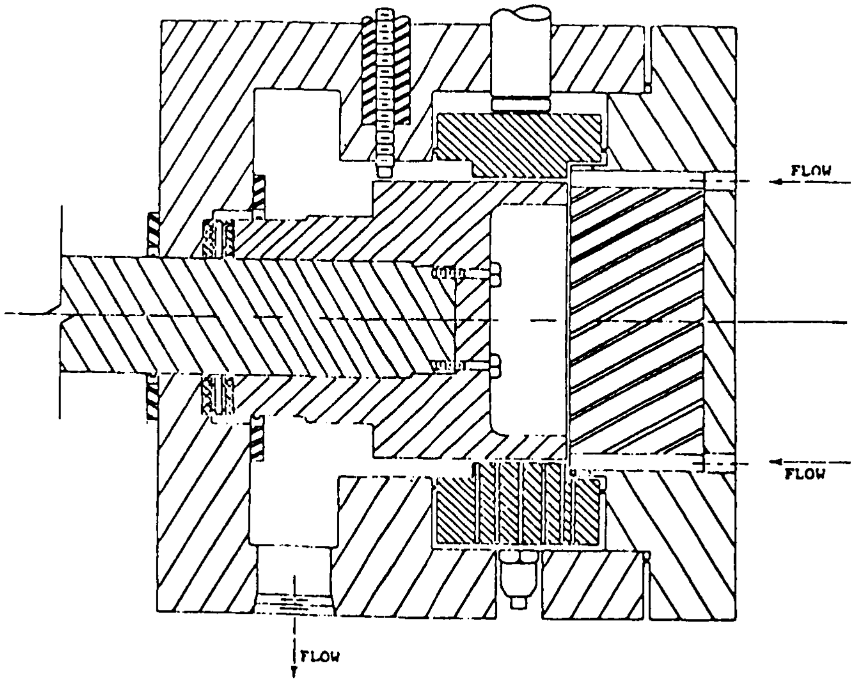
FLOW
FLOW
FLOW

Fig. 3 Cross-sectional view of test section showing smooth stator.

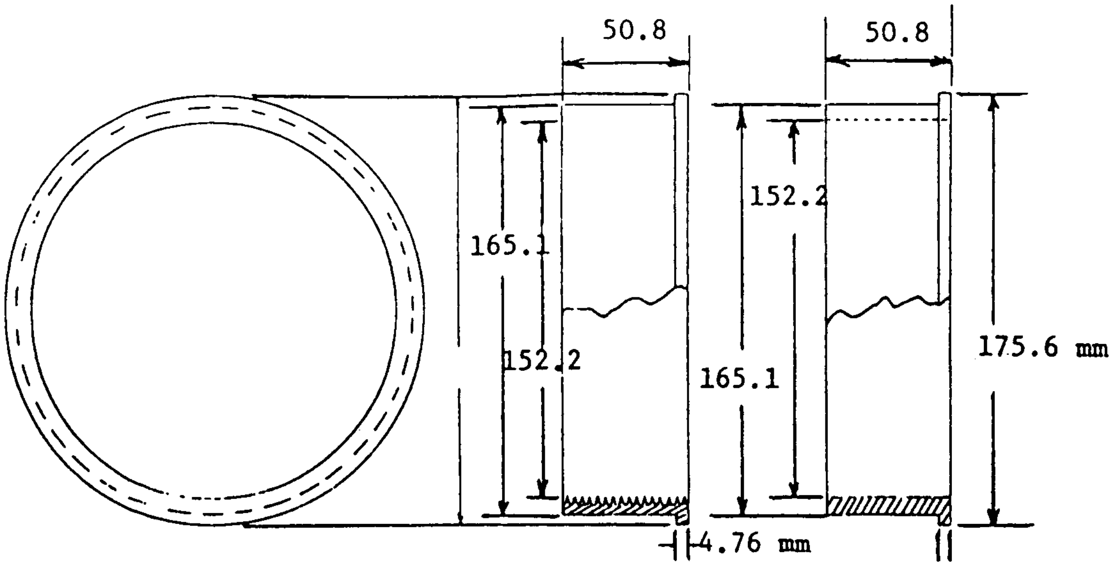
50.8
50.8
165.1
152.2
152.2
165.1
175.6 mm
4.76 mm

Fig. 4 Detail of smooth and labyrinth stator inserts.

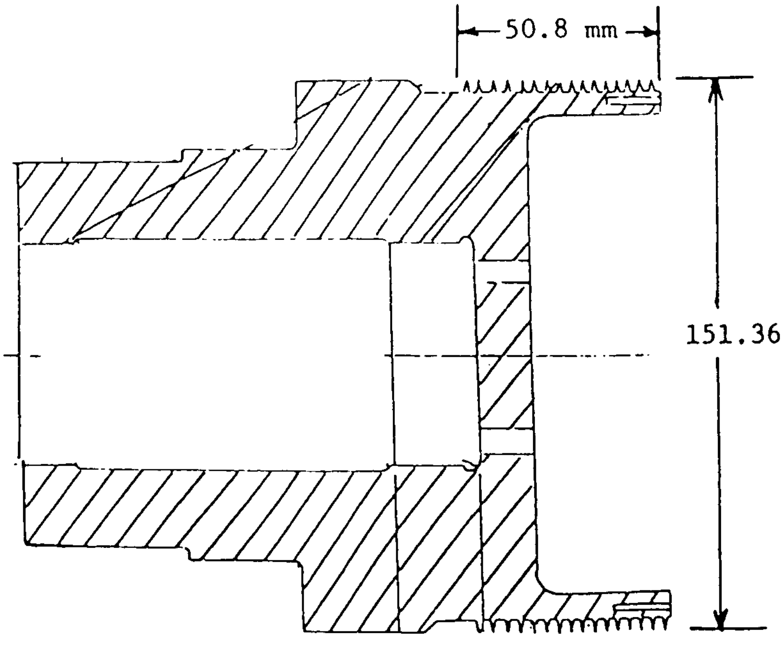
50.8 mm
151.36 mm

Fig. 5 Cross-section of labyrinth rotor.

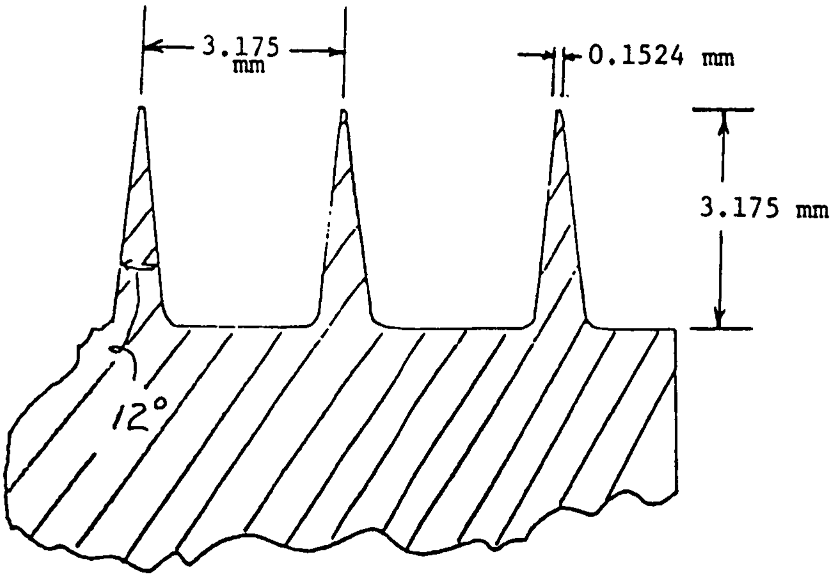
3.175 mm
0.1524 mm
3.175 mm
12°

Fig. 6 Detail of labyrinth teeth for seals tested.

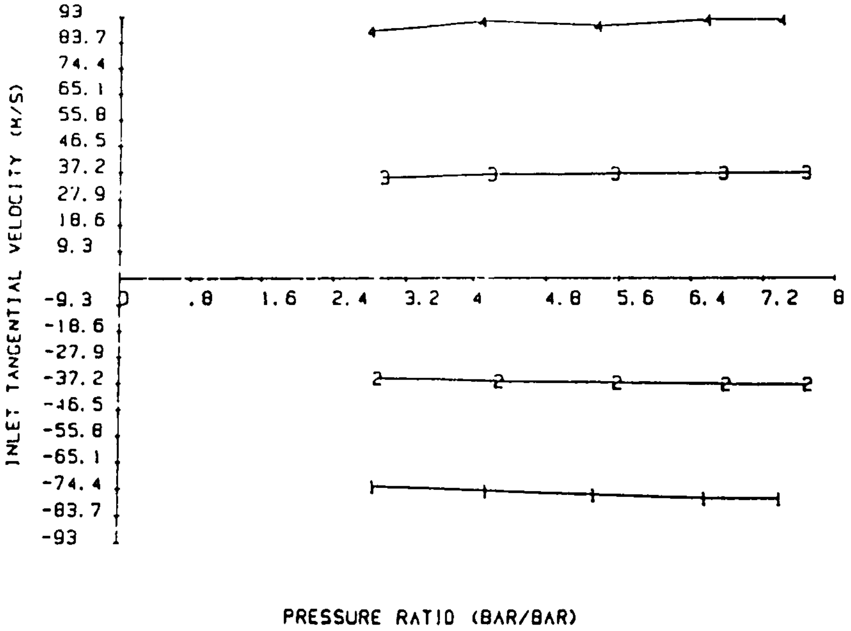

Fig. 7 Inlet tangential velocity vs. pressure ratio for teeth-on-rotor labyrinth seal.

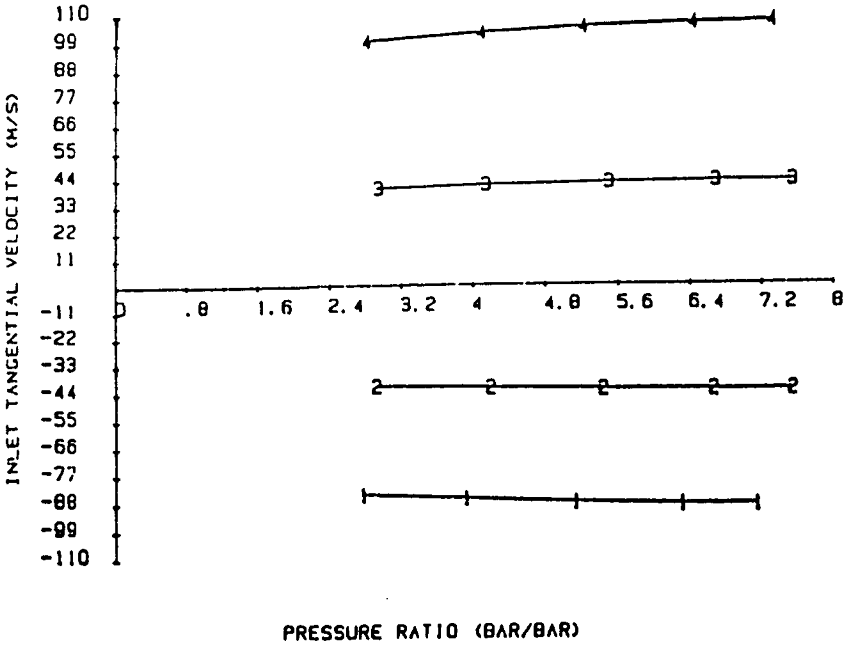

Fig. 8 Inlet tangential velocity vs. pressure ratio for teeth-on-stator labyrinth seal.

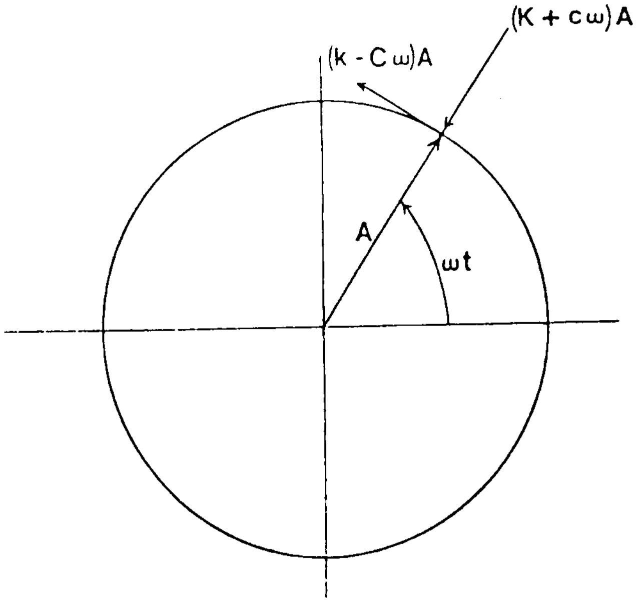
(K + cω)A
(k - Cω)A
A
ωt

Fig. 9 Forces on a rotor.

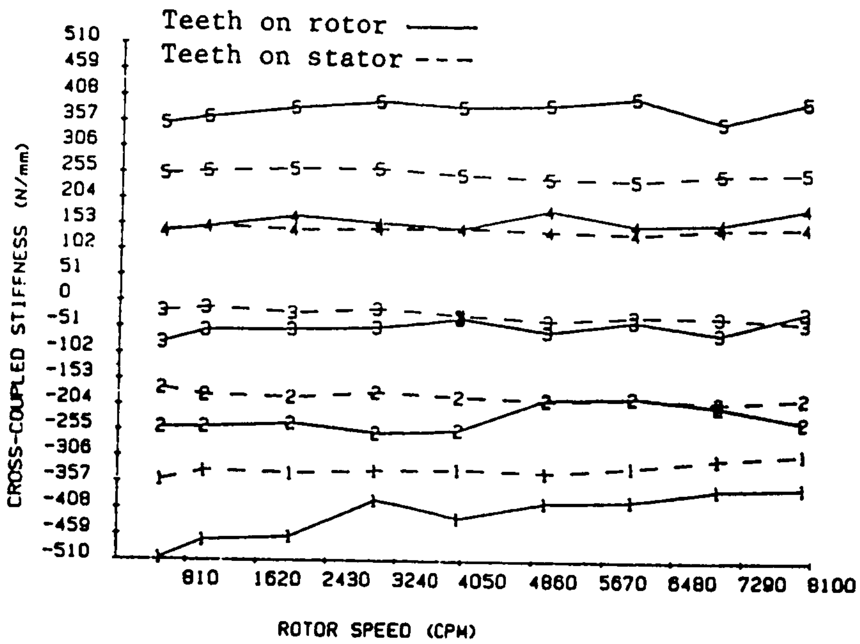

Fig. 10 Cross-coupled stiffness vs. rotor speed.

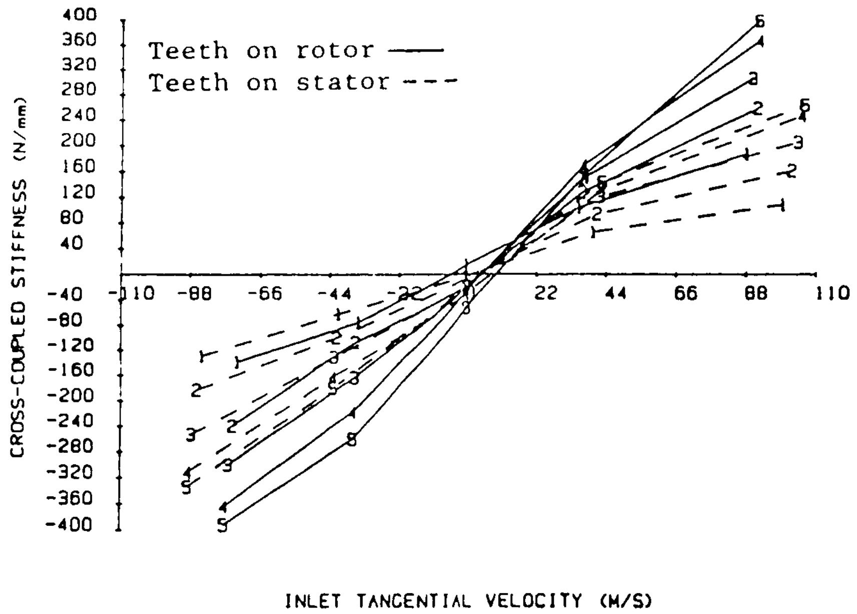

Fig. 11 Cross-coupled stiffness vs. inlet tangential velocity.

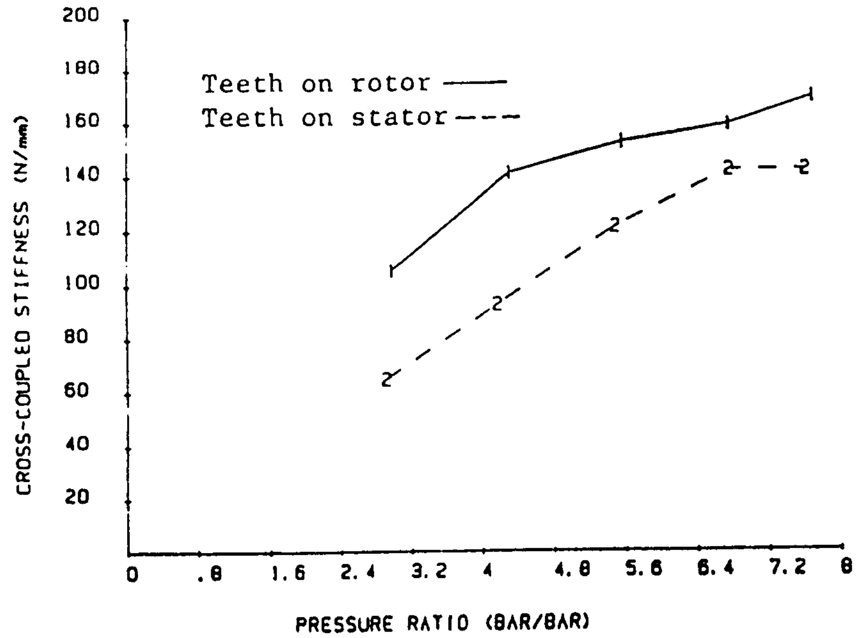

Fig. 12 Cross-coupled stiffness vs. pressure ratio.

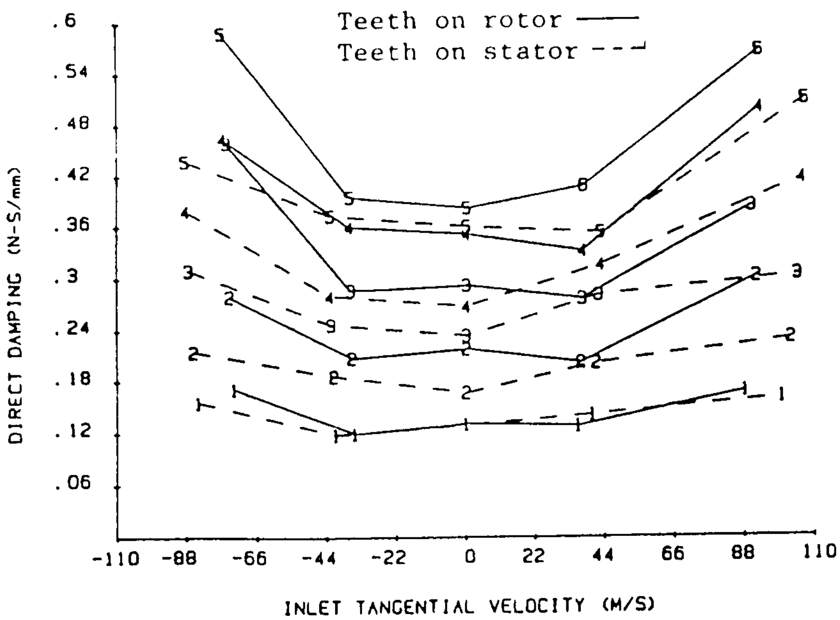

Fig. 13 Direct damping vs. inlet tangential velocity.

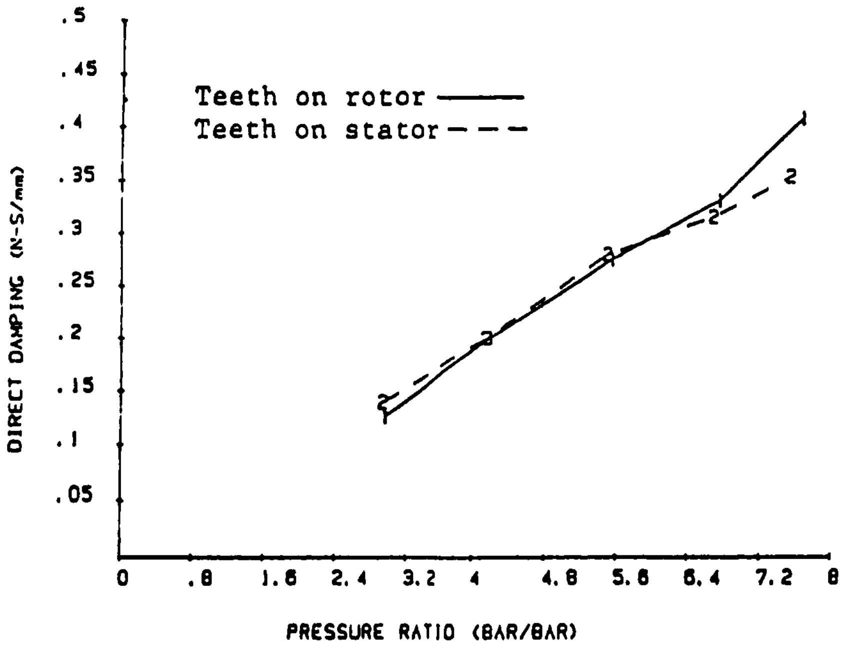

Fig. 14 Direct damping vs. pressure ratio.

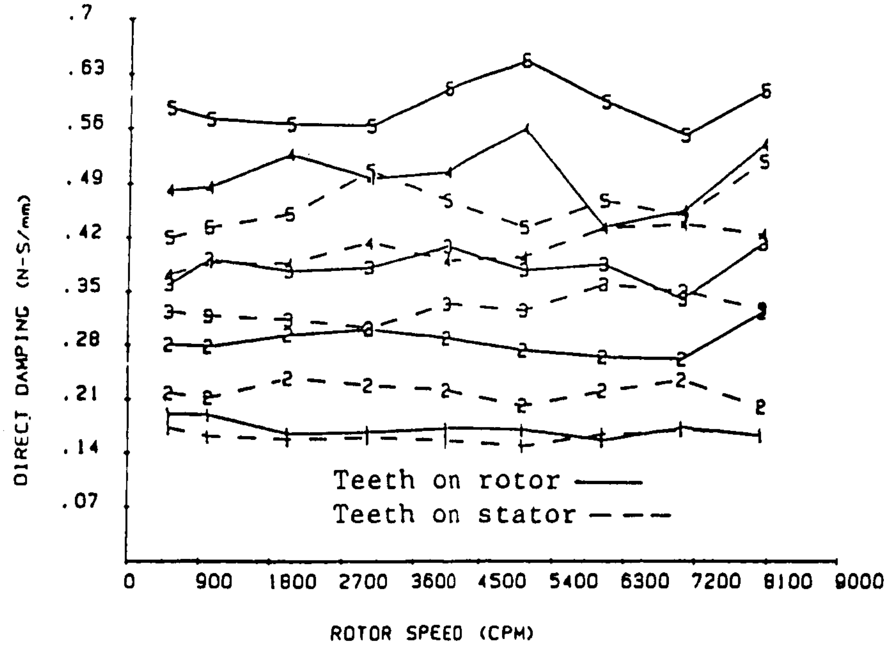

Fig. 15 Direct damping vs. rotor speed.

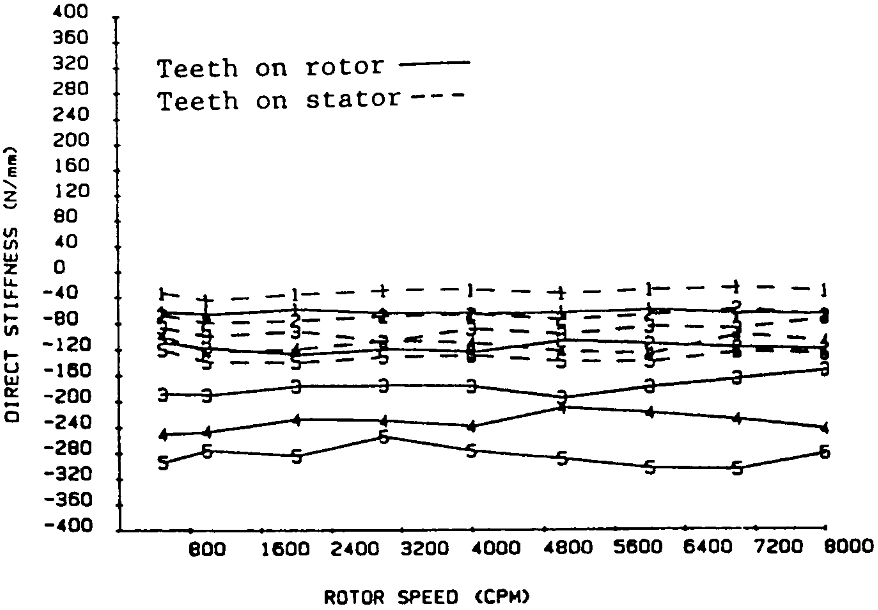

Fig. 16 Direct stiffness vs. pressure speed.

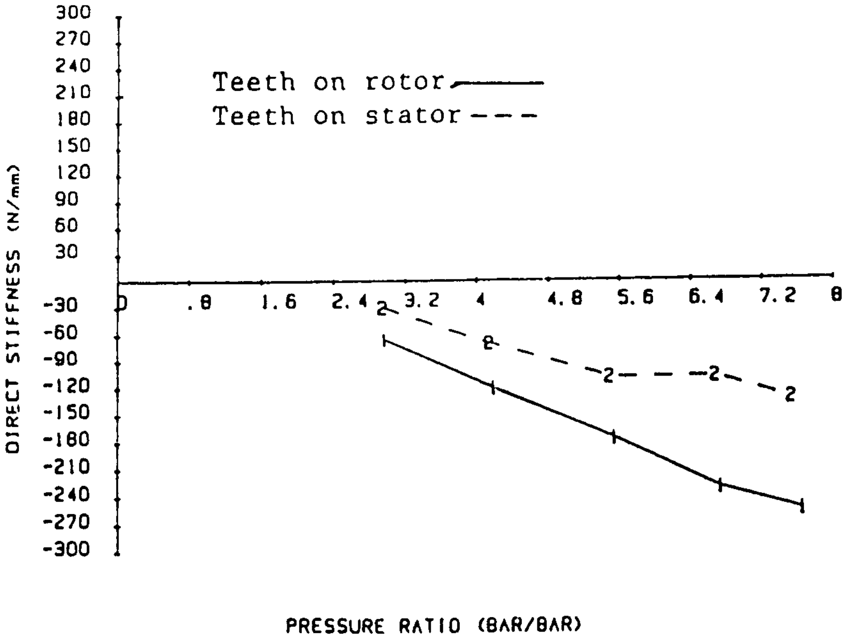

Fig. 17 Direct stiffness vs. pressure ratio.

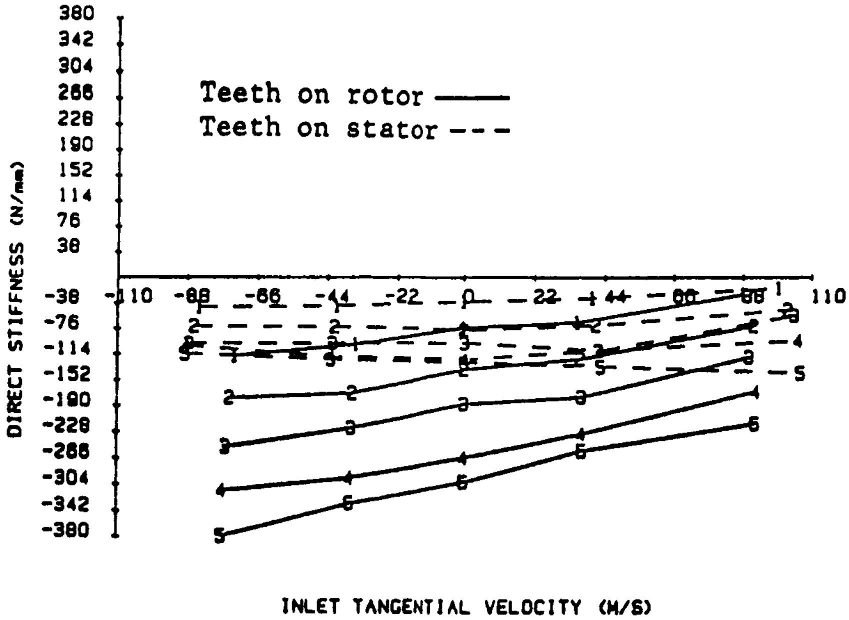

Fig. 18 Direct stiffness vs. inlet tangential velocity.

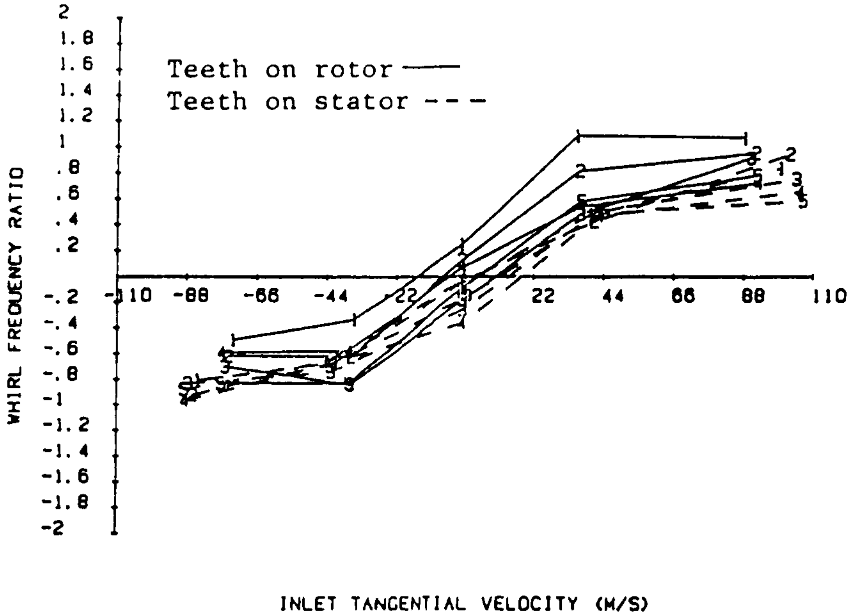

Fig. 19 Whirl frequency ratio vs. inlet tangential velocity.

N87-22213

NON-LINEAR IDENTIFICATION OF A SQUEEZE-FILM DAMPER

Roger Stanway, John Mottershead, and Riaz Firoozian
University of Liverpool
Merseyside, England

In this paper the authors describe an experimental study to identify the damping laws associated with a squeeze-film vibration damper. This is achieved by using a non-linear filtering algorithm to process displacement responses of the damper ring to synchronous excitation and thus to estimate the parameters in an nth-power velocity model. The experimental facility is described in detail and a representative selection of results is included. The identified models are validated through the prediction of damper-ring orbits and comparison with observed responses.

INTRODUCTION

A fundamental problem in rotor-bearing dynamics is the experimental determination of mathematical models to represent the dynamics of oil-film bearings, sometimes referred to as the problem of bearing identification. One category of oil-film bearing is the squeeze-film damper which often forms part of an isolation system for vibration control in turbomachinery. Damping is provided by lubricant supplied to an annulus between the bearing housing and damper-ring. The damper ring does not rotate but is free to whirl in response to applied excitation: thus the lubricant in the annulus is able to dissipate vibrational energy.

The simplest linear analysis of the squeeze-film dynamics indicates that a model involving two viscous damping coefficients can be used to characterise the behaviour of the film (ref. 1). It is generally accepted that such a model can account for the damper ring's response to small perturbations around the concentric position. However the comprehensive tests reported by Tonnesen (ref. 2) show that larger excursions about eccentric positions cannot be predicted using a linear model.

In the last five years considerable progress has been made in the development of techniques for bearing identification. Most attention has been given to frequency-domain methods which have been used to estimate direct- and cross-damping terms associated with a model squeeze-film isolator (ref. 3) and can readily be extended to identify models of multi-mode rotor-bearing systems (ref. 4). However, frequency-domain algorithms are based upon a prior assumption of linearity and thus significant non-linearities cannot readily be accommodated. At Liverpool the identification of linearised squeeze-film models has, in general, been approached using time-domain techniques. A series of numerical experiments indicated that a least-squares filtering algorithm is particularly suitable for estimating the four squeeze-film damping terms from displacement responses to synchronous excitation (ref. 5). A model squeeze-film isolator was constructed and a comprehensive survey of the linearised dynamics has now been completed (ref. 6). A well-known advantage

C-4

of the time-domain approach is that certain geometrical non-linearities can be accommodated and, following the success of the linear experiments, work began to identify non-linear models of the squeeze-film dynamics.

In this paper the authors describe the first series of non-linear experiments. The objective of these tests was to identify the damping law of the squeeze-film from records of large amplitude displacements to single-frequency excitation. This was achieved by estimating the parameters in n^{th}-power velocity models of the squeeze-film dynamics. The resulting models were validated by using them to predict the damper-ring's orbits and comparing these with directly observed responses. The significance of the results is discussed in some detail.

SYMBOLS

c_{xx}, etc.	squeeze-film damping coefficients (N.s/m)
c_{nxx}, etc.	coefficients in damping law
f_x, f_y	applied forces in x and y directions (N)
F_x, F_y	squeeze-film forces (N)
$\underline{f}(\underline{x},t)$	vector functions associated
$\underline{h}(\underline{x},t)$	with parameter estimation
$2k_s$	total stiffness of damper-ring retaining spring (N/m)
2m	total mass of damper ring (kg)
n_{xx}, etc.	exponents in damping law
$\underline{P}(T)$	error covariance matrix
$\underline{Q}$	weighting matrix
t	time (s)
T	interval of observations (s)
u_x, u_y	$= f_x/m,\ f_y/m$
$\underline{x}$	state vector
x_1-x_4	physical state variables
x_5-x_{10}	parameter state variables
x	vertical displacement of damper ring (m)
y	horizontal displacement of damper ring (m)
$\underline{z}(t)$	vector of observations

ω_n^2 $= k_s/m$

$(\ )^T$ denotes matrix transpose

$(\hat{\ })$ denotes estimate

IDENTIFICATION OF LINEARISED SQUEEZE-FILM DYNAMICS

Before describing the non-linear experiments, the more traditional linear problem will be defined and the results of some recent linear identification experiments will be summarised.

Equations of Motion

Consider a lumped parameter model of a squeeze-film vibration isolator such as that considered by Holmes (ref. 1). In fixed co-ordinates the equations of motion are written

$$
\begin{aligned}
m \frac{d^2 x}{dt^2} + F_x(x, \frac{dx}{dt}, y, \frac{dy}{dt}) + k_s x &= f_x \\
m \frac{d^2 y}{dt^2} + F_y(x, \frac{dx}{dt}, y, \frac{dy}{dt}) + k_s y &= f_y
\end{aligned}
\tag{1}
$$

where all terms are defined under "Symbols".

Equation (1) implies that the forces F_x and F_y developed within the squeeze-film are functions of both displacement and velocity in the x and y directions. The objective of bearing identification is to determine these functions experimentally. Experimental determination of the functions F_x and F_y usually involves two steps: the choice of a suitable model structure followed by the estimation of unknown parameters in this structure. At the simplest level it is usual to assume that the squeeze-film damping forces in the x and y directions are proportional to the component of (damper-ring) velocity in the respective direction. This leads to the expressions

$$F_x = c_{xx} \frac{dx}{dt}\ ,\ F_y = c_{yy} \frac{dy}{dt} \tag{2}$$

so that equations (1) are uncoupled and identification requires the determination of the two constants of proportionality, i.e. the viscous damping coefficients c_{xx} and c_{yy}. This type of model was used in the experimental parametric study described by Tonnesen (ref. 2). In any actual squeeze-film isolator, imperfections in the construction of the damper-ring and bearing housing will invariably produce cross-axis damping forces in the squeeze-film. If the cross-axis forces are signicant in relation to the direct-axis forces then the identification of coefficients in an uncoupled model (equation (2)) will lead to the misinterpretation of the results. Such misinterpretation can be avoided by assuming that coupling is present, i.e.

$$F_x = c_{xx} \frac{dx}{dt} + c_{xy} \frac{dy}{dt},\ F_y = c_{yx} \frac{dx}{dt} + c_{yy} \frac{dy}{dt} \tag{3}$$

and estimating the four unknown damping coefficients c_{xx}, c_{xy}, c_{yx} and c_{yy}. Some recent work by the authors has resulted in a promising new experimental technique for determining these four damping coefficients.

Numerical Experiments

In reference 5, one of the authors proposed a scheme of combined state and parameter estimation for identifying the four squeeze-film damping terms. Essentially, the four unknown coefficients were defined as state variables and an algorithm for non-linear state estimation was used to reconstruct the coefficients from time-series records of the displacement responses of the damper ring to synchronous excitation. A series of numerical experiments showed that such a scheme was feasible and moreover that the estimation algorithm was relatively insensitive to the effects of (zero-mean) measurement noise. Further numerical studies showed that the scheme could readily be extended to estimate the four damping coefficients associated with a journal bearing oil-film (ref. 7).

Experiments with a Model Squeeze-Film Isolator

Following the success of the numerical experiments a model squeeze-film isolator was constructed so that the technique in reference 5 could be applied to real data. The experimental facility will be described in detail in the sections which follow. A comprehensive survey of the dynamics of the squeeze-film damper (ref. 6) showed that the four squeeze-film damping terms could be readily identified using non-linear state estimator. As expected, there were considerable discrepancies between the identified coefficients and those predicted by short-bearing lubrication theory (ref. 1). However, by comparing the ability of both identified and theoretical coefficients to predict the amplitude and phase characteristics of the isolator's frequency response, it was shown that the identified coefficients were the more effective, especially for characterising the cross-axis dynamics.

The application of a non-linear technique to estimate linearised coefficients may appear to be a computationally inefficient way of solving an apparently simple problem. However the advantage of this approach is that it can, in principle, be extended to accommodate certain types of non-linearity. The motivation behind the body of work described in this paper is to determine if non-linear models of the squeeze-film dynamics could be identified without imposing unrealistic requirements on the experimental facility.

NON-LINEAR IDENTIFICATION

Introduction

The theory underlying the linear identification experiments described in the previous section is based upon the assumption that the damping forces in equations (2) and (3) arise from small perturbations of the damper ring. Even when this assumption seems justified there can be large discrepancies between theoretically- and experimentally-derived coefficients, especially at higher values of static eccentricity ratio (ref. 2). To investigate these discrepancies, and to be able to account for squeeze-film behaviour under large perturbations of the damper-ring, it was decided to attempt to identify the damping law of the squeeze-film. This implies the estimation of the parameters (coefficients and exponents) associated with an nth-power velocity model of the squeeze-film.

A Damping-Law Model

As part of a related study it has been established that the damping law associated with a single degree-of-freedom dissipative element can be identified from forced response measurements (ref. 8). Owing to the significant amount of cross-axis coupling it was not considered feasible to employ so simple a model of the squeeze-film. Consequently a tentative model to include cross-axis effects was proposed, i.e.

$$\begin{aligned} F_x &= c_{nxx}\left|\frac{dx}{dt}\right|^{n_{xx}}\mathrm{sgn}\left(\frac{dx}{dt}\right) + c_{nxy}\left|\frac{dy}{dt}\right|^{n_{xy}}\mathrm{sgn}\left(\frac{dy}{dt}\right) \\ F_y &= c_{nyx}\left|\frac{dx}{dt}\right|^{n_{yx}}\mathrm{sgn}\left(\frac{dy}{dt}\right) + c_{nyy}\left|\frac{dy}{dt}\right|^{n_{yy}}\mathrm{sgn}\left(\frac{dy}{dt}\right) \end{aligned} \tag{4}$$

which assumes that the damping forces are proportional to the nth-power of the appropriate components of damper-ring velocity. Identification of such a model requires the estimation of eight parameters, four coefficients c_{nxx}, etc and four exponents n_{xx}, etc. from records of the damper-ring's displacement response. To reduce the number of parameters to be estimated in these preliminary experiments it was decided to assume that the cross-damping terms were reciprocal, i.e. $c_{nxy} = c_{nyx}$, $n_{xy} = n_{yx}$. This had the effect of reducing the number of parameters to be estimated to six. The consequences of making this simplification will be discussed later.

Combined State and Parameter Estimation

To begin the development of the necessary estimation equations, consider the substitution of the functions F_x and F_y from the damping-law model, equation (4), into the equations of motion (1). The four "physical" state variables usually associated with a vibrating system with two degrees of freedom are $x_1 \triangleq x_1$, $x_2 \triangleq dx/dt$, $x_3 \triangleq y$ and $x_4 \triangleq dy/dt$. Substituting these expressions into equations (1) and (4) and noting the $dx_1/dt = x_2$ and $dx_3/dt = x_4$, results in a set of four non-linear differential equations. A further six "parameter" state variables, corresponding to the six unknowns in equation (4), are defined, i.e. $x_5 \triangleq c_{nxx}/m$, $x_6 \triangleq n_{xx}$, $x_7 \triangleq c_{nxy}/m$, $x_8 \triangleq n_{xy}$, $x_9 \triangleq c_{nyy}/m$ and $x_{10} \triangleq n_{yy}$. If it is assumed that the time-derivatives of these six extra states are zero (to characterise time-invariant parameters) then six further equations emerge to augment the four original state equations. The ten equations can be collected together and written in the form:

$$\frac{d\underline{x}}{dt} = \underline{f}(\underline{x},t) \tag{5}$$

where

and $$\underline{x} = [x_1 \quad x_2 \quad x_3 \quad x_4 \quad x_5 \quad x_6 \quad x_7 \quad x_8 \quad x_9 \quad x_{10}]^T$$

$$\underline{f}(\underline{x},t) = \begin{bmatrix} x_2 \\ -x_5|x_2|^{x_6}\operatorname{sgn}(x_2)-x_7|x_4|^{x_8}\operatorname{sgn}(x_4)-\omega_n^2 x_1+u_x \\ x_4 \\ -x_7|x_2|^{x_8}\operatorname{sgn}(x_2)-x_9|x_4|^{x_{10}}\operatorname{sgn}(x_4)-\omega_n^2 x_3+u_y \\ 0 \\ 0 \\ 0 \\ 0 \\ 0 \\ 0 \end{bmatrix}$$

To characterise the measurements on the physical system, a sensor equation is introduced:

$$\underline{z}(t) = \underline{h}(\underline{x},t) + \text{(observation noise)} \tag{6}$$

where $\underline{h}(\underline{x},t)$ is a vector function which, if necessary, can account for observations which are non-linear functions of the states. For the problem in hand, however, assume that the two displacement states x_1 and x_3 are available directly and thus $\underline{h}(\underline{x},t) = [x_1 \;\; x_3]^T$.

Given this formulation, the objective is to employ the information contained in the vector of observations $\underline{z}(t)$ over the time interval $0 \leq t \leq T$ to predict the behaviour of the state vector $\underline{x}$ over the same interval. Since $\underline{x}$ contains the six unknown parameters associated with the damping law of the squeeze-film, the estimation of $\underline{x}$ automatically produces estimates of the unknown parameters. A useful by-product of this parameter estimation scheme is that the estimates $\hat{x}_1$ and $\hat{x}_3$ of the displacement states provide instant prediction of the orbital motion of the damper-ring on the basis of the identified model and thus serve to validate the estimated parameters.

An Algorithm for Non-Linear State Estimation

To estimate the state vector $\underline{x}$ from the vector of observations $\underline{z}$ requires an algorithm for non-linear state estimation. The application of one suitable algorithm is described in detail in reference (ref. 5). For the sake of completeness, the relevant equations are summarised here. The algorithm (ref. 9) is based upon a predictor-corrector type equation:

$$\frac{d\hat{\underline{x}}}{dT} = \underline{f}(\hat{\underline{x}},t) + \underline{\Gamma}(T)\;\{\underline{z}(T) - h(\hat{\underline{x}},T)\} \tag{7}$$

the solution of which produces an estimate, denoted $\hat{\underline{x}}$, of the state vector. The driving term in equation (7) is the vector of residuals $\{\underline{z}(T) - \underline{h}(\hat{\underline{x}},T)\}$ which is weighted by the time-varying matrix $\underline{\Gamma}(T)$. The matrix $\underline{\Gamma}(T)$ is made up of three terms, i.e.

$$\underline{\Gamma}(T) = 2\,\underline{P}(T)\underline{H}(\hat{\underline{x}},T)\underline{Q} \tag{8}$$

The matrix $\underline{P}(T)$ is the error covariance array which evolves in time according to the equation

$$\begin{aligned}\frac{d\underline{P}}{dT} &= \frac{\partial \underline{f}(\hat{\underline{x}},T)}{\partial \hat{\underline{x}}} \cdot \underline{P} + \underline{P}\,\frac{\partial \underline{f}^{T}(\hat{\underline{x}},T)}{\partial \hat{\underline{x}}} \\ &\quad + 2\,\underline{P}\,\frac{\partial}{\partial \hat{\underline{x}}}\,[\underline{H}(\hat{\underline{x}},T)\underline{Q}\{\underline{z}(T) - \underline{h}(\hat{\underline{x}},T)\}]\underline{P}\end{aligned} \tag{9}$$

and must be computed in parallel with equation (7). The remaining two terms in equation (8) take account of the structure of the observations, i.e.

$$\underline{H}(\hat{\underline{x}},t) \triangleq \partial \underline{h}(\hat{\underline{x}},T)/\partial \hat{\underline{x}}$$

and $\underline{Q}$ is a matrix which allows constant weightings to be attached to each sequence of observations.

For the problem in hand the estimation of the state vector $\underline{x}$ from equation (7) involves the solution of ten non-linear differential equations. The matrix $\underline{P}$ is of dimension (10 x 10) and thus the estimation of $\underline{P}$ from equation (9) involves the solution of one hundred non-linear differential equations. Since $\underline{P}$ is symmetric (ref. 9) only 55 of these equations need to be solved. The only practical way of solving these equations is to employ a numerical method operating on the sequences of observations obtained from the experimental facility.

EXPERIMENTAL FACILITY

The model squeeze-film isolator used in the experiments is shown in the general arrangement drawing, figure 1. Essentially the isolator consists of two main components

(i) a non-rotating damper ring, symmetrically supported by a flexible shaft;
(ii) a bearing housing containing two plain lands, separated by a central circumferential groove.

The flexible shaft provides the static load capacity while a film of oil in the annulus between the damper ring and housing provides the damping forces. The oil is force-fed to the annulus by a pump through holes at the top and bottom of the circumferential groove. No end seals are fitted and so the lubricant is free to discharge into a reservoir prior to re-circulation. The critical bearing and suspension parameters are Bearing land length 12.0 mm; Damper-ring radius 60.0 mm; Radial clearance 0.254 mm; Damper ring mass (per land) 4.5 kg; Stiffness of supporting shaft (per land) 250 kN/m. There are no rotating components in the experimental facility and excitation of the squeeze-film is provided by two electromagnetic shakers, mounted at right angles to each other, as shown in figure 1. Using this arrangement any desired form of forcing can be provided. In particular, if each shaker is provided with a sinusoidal signal of identical frequency and amplitude, but displaced in phase by 90°, then synchronous unbalance forcing is readily simulated.

The static eccentricity ratio of the squeeze-film bearing is adjusted by moving the bearing housing in relation to the damper ring. The position of the housing is monitored using mechanical clock gauges. Other static measurements are the lubricant pressure at the inlet to the housing and the lubricant temperature as it discharges from the annulus. In the absence of rotation there is no significant temperature drop across the squeeze-film.

Instrumentation for the generation of dynamic forces and monitoring of the responses is shown schematically in figure 2. Forces applied to the damper ring are measured by quartz load cells connected to suitable charge amplifiers. The displacement responses of the damper ring are measured by two sets of non-contacting capacitance probes, two in the vertical plane and two in the horizontal plane. Suitable sequences of input/output data are gathered for subsequent parameter estimation by a data-acquisition system comprising a 12-bit analogue-to-digital converter controlled by a digital micro computer. Data are stored on floppy discs before being transferred for off-line processing to obtain estimates of the appropriate squeeze-film parameters.

EXPERIMENTAL PROCEDURE AND RESULTS

Immediately prior to each set of tests to identify the non-linear squeeze-film dynamics, the oil ("Shell" Tellus 27) was pumped through the bearing until a steady operating temperature was reached. A typical oil temperature was 28°C, corresponding to a viscosity of 0.06 N.s/m. During all the tests the lubricant inlet pressure was held constant at 7 kN/m^2. With the bearing housing locked firmly in the desired position, the damper ring was perturbed by forces supplied by the electromagnetic shakers. The signals supplying these shakers were sinusoidal and of the same frequency (20 hz) but displaced in phase by 90°. For the linear tests described in reference 6 the peak-to-peak amplitudes of the applied forces were limited to approximately 50 N. which produced displacement amplitudes of around 5-10 per cent of the radial clearance. For the non-linear tests described here, applied forces of approximately 250 N. were used to produce peak-to-peak displacement amplitudes of around 50 per cent of the radial clearance. Experiments involving greater amplitudes are currently in progress but were not possible originally owing to the limited range of the displacement probes.

Using the procedure described above, non-linear orbits were generated for nine equispaced values of static eccentricity ratio and for static attitude angles of 0°, 30° and 90°. At each static equilibrium position 1000 cycles of the steady-state displacement responses in the x and y direction were gathered. With the chosen sampling interval of 300 μs this produced some six cycles of vibration data - sufficient according to the results of numerical experiments. The digitized records of input forces and output displacements were processed according to equations (7), (8) and (9). Numerical solutions were obtained using a fourth-order Runge-Kutta-Merson routine.

The results in figure 3 show the evolution of the elements of the state vector $\underline{x}$ with time with the damper ring in the concentric position. Figure 4 shows the damper-ring orbits measured directly and those predicted from identified models for zero attitude angle and at static eccentricity ratios of 0.2, 0.4, 0.6 and 0.8. To illustrate results obtained from experiments where additional cross-axis coupling was induced in the squeeze-film, figure 5 shows the evolution of state estimates for an attitude angle of 30° and a static eccentricity ratio of 0.6. Again with an attitude angle of 30° the damper-ring orbits (direct observations and predictions) for eccentricity ratios of 0.2, 0.4, 0.6 and 0.8 are shown in figure 6.

DISCUSSION OF RESULTS

The results shown in figure 3 show that the identified model predicts the oscillatory responses of the damper-ring (states x_1-x_4) and produces steady estimates of the six damping law parameters (states x_5-x_{10}). All the three damping coefficients (c_{nxx}, c_{nxy} and c_{nyy}) assume positive values and the estimates of the three exponents (n_{xx}, n_{xy} and n_{yy}) are all close to unity - thus tending to confirm that for this operating condition the damping forces are viscous. Models of this form are fully capable of predicting the measured damper ring orbits, even without prior knowledge of the position of the orbit in the clearance circle, as shown in figure 4. Figure 4 illustrates how, owing to the amplitude of the excitation forces and the relatively soft retaining spring, the orbits are displaced away from the original equilibrium position and towards the centre of the clearance circle. Nevertheless, a good approximation to the observed orbit is generated by the identified model.

The results presented in figure 5 for an attitude angle of 30° and static eccentricity ratio of 0.6 show how, away from the concentric position, the estimates of the damping law exponents do not converge towards unity but toward approximately 0.7. The estimates of the direct damping terms are still positive (as in figure 3) but the cross-term is now negative. Figure 6 shows the measured and predicted orbits for various eccentricities with an attitude angle of 30°. Some significant departures from the elliptical shape are now evident but the identified model is still reasonably successful in reproducing the observed shapes. Taken overall, the performance of the parameter estimation algorithm appeared to improve as the orbits become more distorted. It is probably fair to speculate that this is due to the increasing presence of additional harmonics which improves the correspondence between the observed responses and the coefficients which are to be fitted. Work is currently in hand to examine this aspect of non-linear identification using numerical simulation techniques.

Discrepancies between measured and predicted responses still exist but these are probably due to the relatively simple non-linear damping model which has been used as the basis for the present study. Obviously the assumption of reciprocal cross-damping introduces errors and, as yet, no attempt has been made to include stiffness effects in the squeeze-film. The absence of stiffness effects must call into question the physical significance of the damping law parameters obtained from the experiments. The inclusion of squeeze-film stiffness effects is the subject of ongoing research.

CONCLUDING REMARKS

In this paper the authors have described an experimental study to identify non-linear models of a squeeze-film vibration damper. A non-linear filtering technique has been used to estimate coefficients and exponents associated with an nth-power velocity model of the forces developed in the squeeze-film. The results presented here have been obtained from processing the displacement responses of the damper ring to synchronous excitation and so it should be possible to apply the technique to examine the dynamics of industrial dampers and fluid seals.

The quality of the empirical fits between the observed and predicted orbits is an indicator of the success of these preliminary experiments. However there are various modifications to the present processing algorithm which should improve the accuracy of prediction and enable the physical significance of the results to be assessed - obvious modifications include the provision of non-reciprocal cross-damping terms and terms to account for squeeze-film stiffness.

REFERENCES

1. Holmes, R.: "Vibration and its control in rotating systems", Proc. IUTAM Symposium "Dynamics of Rotors", Denmark, 1974, pp. 156-181.

2. Tonnesen, J.: "Experimental parametric study of a squeeze-film bearing", Trans. ASME, J. Lub. Tech., 98, 1976, pp. 206-213.

3. Burrows, C. R. and Sahinkaya, M. N.: "Frequency-domain estimation of linearised oil-film coefficients", Trans. ASME-ASLE Joint Lub. Conf., 1981, 81-LUB-7.
4. Burrows, C. R. and Sahinkaya, M. N.: "Parameter estimation of multi-mode rotor-bearing systems", Proc. Royal Soc., 379(A), 1982, pp. 367-387.

5. Stanway, R.: "Identification of linearized squeeze-film dynamics using synchronous excitation", Proc. I. Mech. E., 197(C), 1983, pp. 199-204.

6. Stanway, R., Firoozian, R. and Mottershead, J. E.: "Identification of the linearised dynamics of a squeeze-film vibration isolator", submitted for publication to Proc. I. Mech. E.

7. Stanway, R.: "Journal bearing identification under operating conditions", Trans. ASME, J. Dyn. Syst. Meas. Control, 106, 1984, pp. 178-182.

8. Mottershead, J. E. and Stanway, R.: "Identification of nth-pwer velocity damping", J. Sound and Vibration, 105, 1986, pp. 309-319.

9. Detchmendy, D. M. and Sridhar, R.: "Sequential estimation of states and parameters in noisy, non-linear dynamical systems", Trans. ASME, J. Bas. Eng., 88, 1986, pp. 362-368.

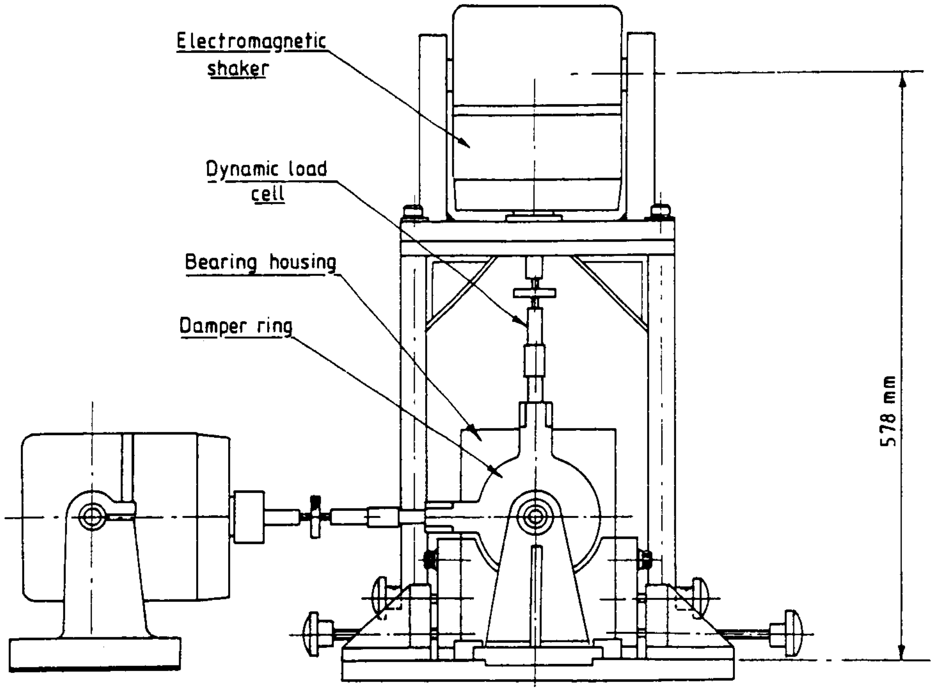
Electromagnetic shaker
Dynamic load cell
Bearing housing
Damper ring
578 mm

Fig. 1 Squeeze-film isolator: general arrangement of experimental facility.

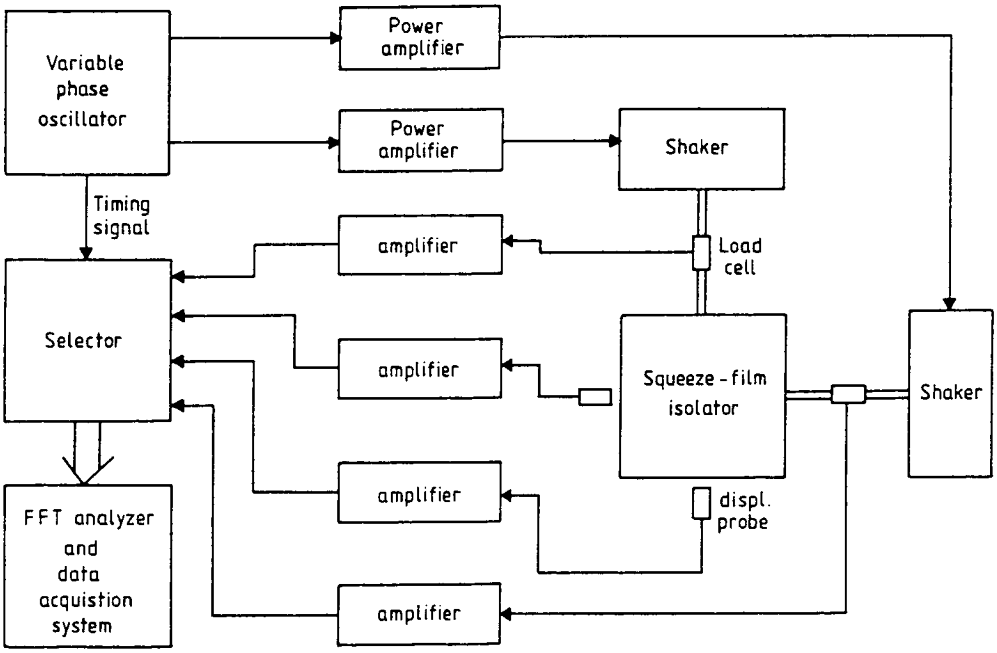
Variable phase oscillator
Power amplifier
Power amplifier
Shaker
Timing signal
amplifier
Load cell
Selector
amplifier
Squeeze-film isolator
Shaker
amplifier
displ. probe
FFT analyzer and data acquistion system
amplifier

Fig. 2 Schematic showing instrumentation used in identification experiments.

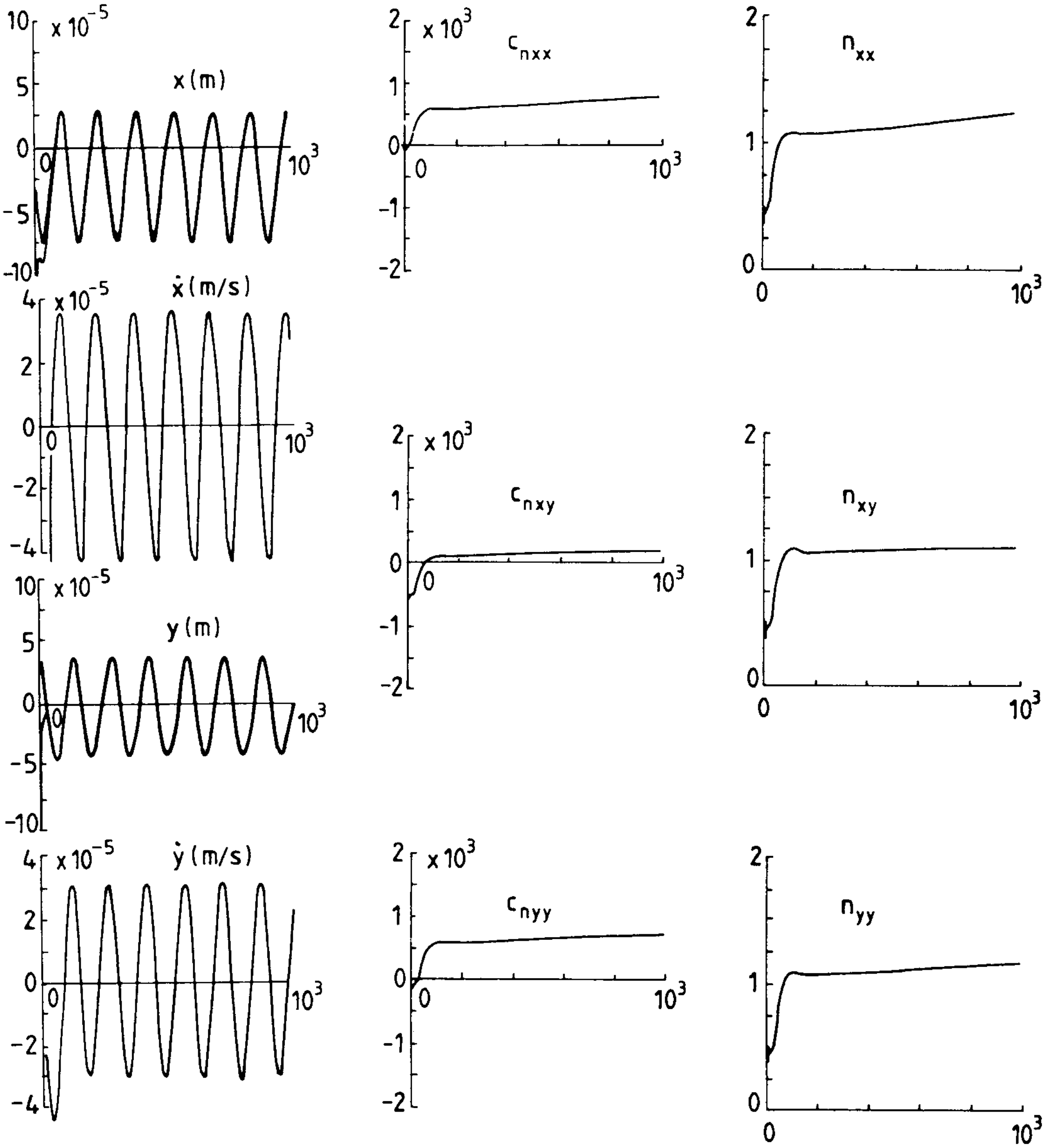

Fig. 3 Estimates of physical and parameter states versus number of iterations. Damper ring in concentric position.

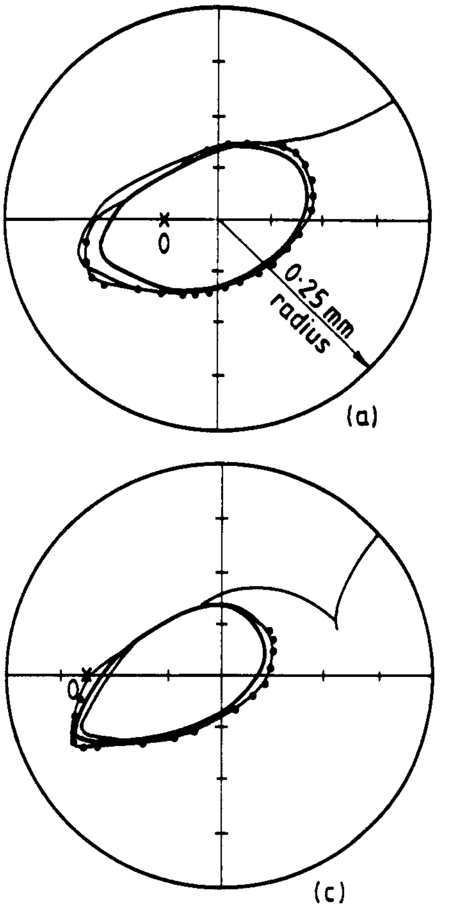

Fig. 4 Damper ring orbits with zero attitude angle and various values of static eccentricity ratio: (a) 0.2, (b) 0.4, (c) 0.6 and (d) 0.8.

—●—●—●—	directly observed
———	predicted by estimate
x	original static equilibrium position

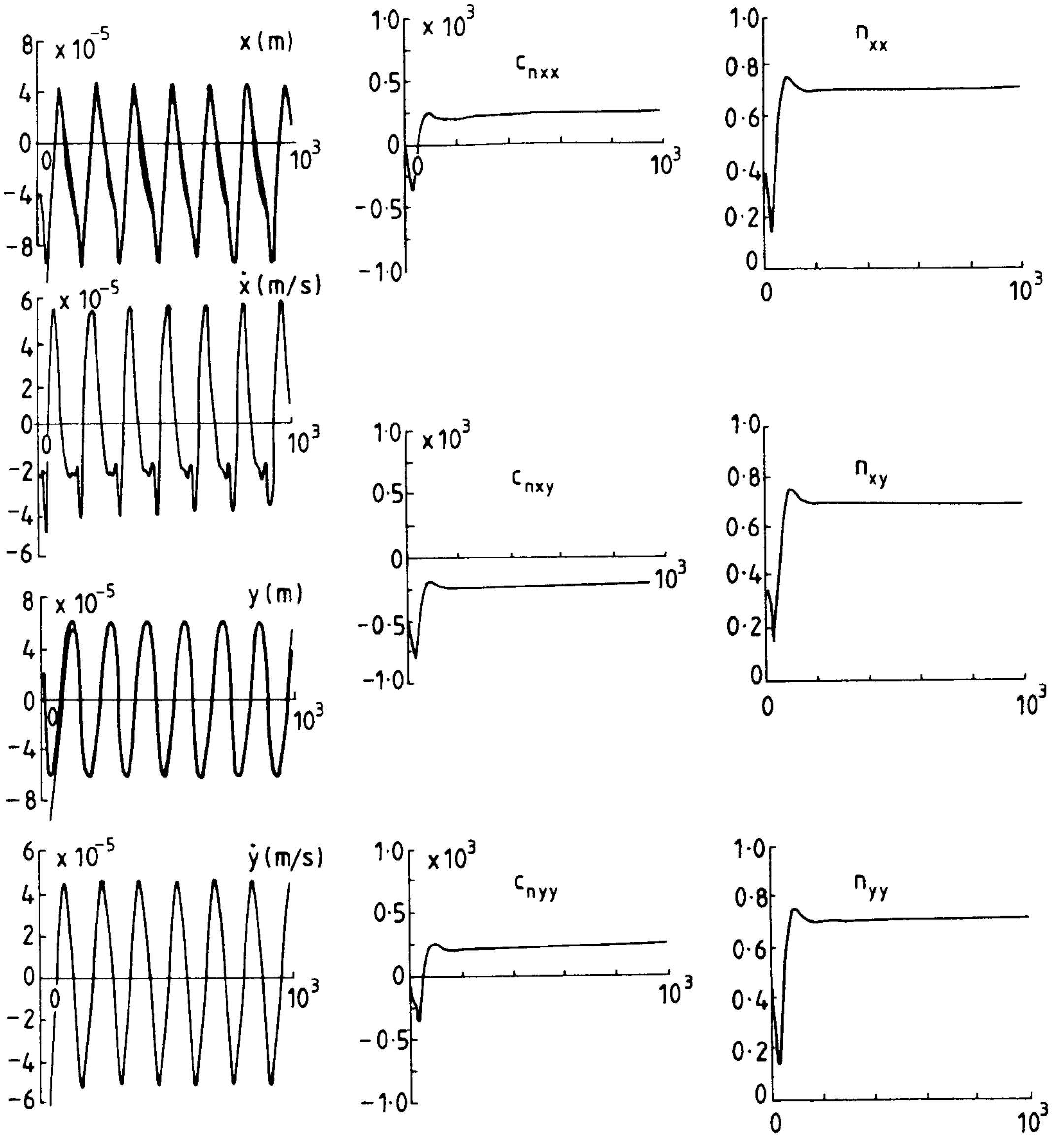

Fig. 5 Estimates of physical and parameter states versus number of iterations. Attitude angle 30°, static eccentricity ratio 0.6.

ORIGINAL PAGE IS
OF POOR QUALITY

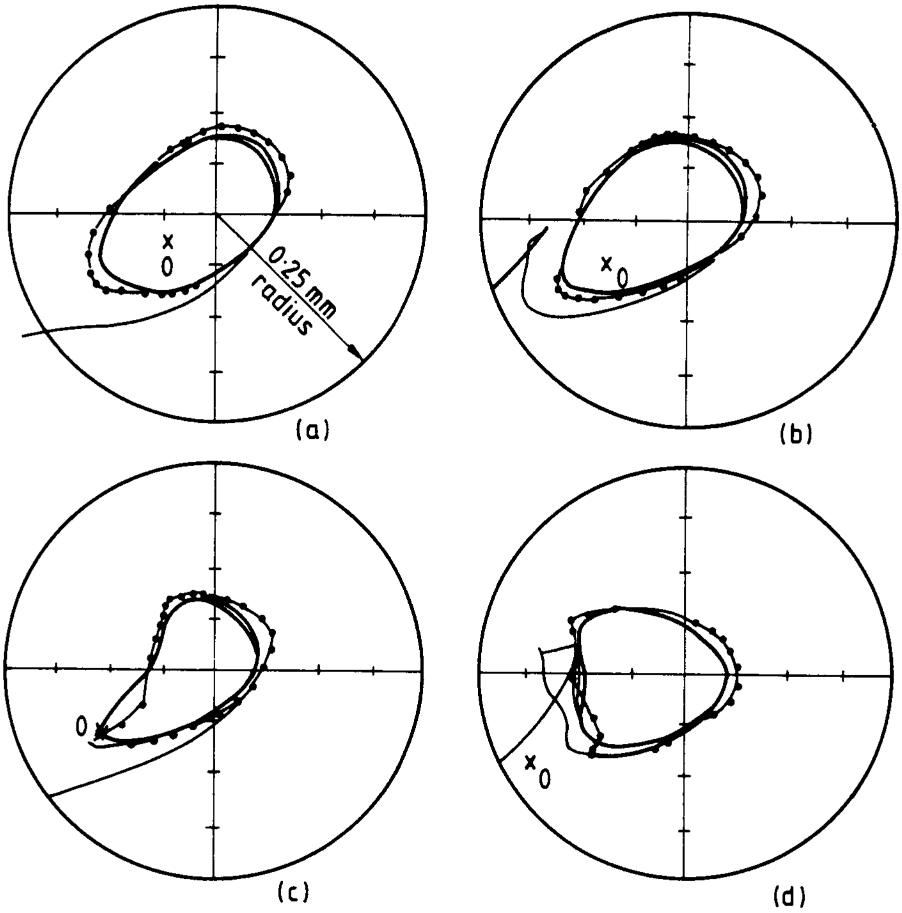

Fig. 6 Damper ring orbits with attitude angle of 30° and various values of static eccentricity ratio: (a) 0.2, (b) 0.4, (c) 0.6 and (d) 0.8.

—●—●—●— directly observed

——— predicted by estimator

x original static equilibrium position

N87-22214

ESTIMATION OF SQUEEZE-FILM DAMPING AND INERTIAL COEFFICIENTS FROM EXPERIMENTAL FREE-DECAY DATA

J.B. Roberts
University of Sussex
Brighton, England

R. Holmes
University of Southampton
Southampton, England

P.J. Mason
Chelsea College of Aeronautical and Automobile Engineering
Shoreham, Sussex, England

This paper describes the results obtained from an experimental programme concerned with a parametric identification of the damping and inertial coefficients of a cylindrical squeeze-film bearing, through an analysis of transient response data. The results enable the operating range for which a linear model of the squeeze-film is appropriate to be determined. Comparisons are made between the estimated coefficients and theoretical predictions. Presentation is by courtesy of the Council of the Institution of Mechanical Engineers, London.

INTRODUCTION

Accompanying the development of modern machinery has been an increasing demand for higher running speeds. As a result critical speeds have been encountered before the desired running speed of the machine has been reached. The consequences of this can result in failure of associated components or, in some cases, an inability to reach the desired operating speed. The present work is concerned with the squeeze-film damper, which is proving very successful in mitigating these problems. A manageable and realistic model for a squeeze-film damper can be derived by applying linearisation techniques to the oil-film forces, which are obtained by solving the Reynolds equation. This leads to a representation of the dynamic behaviour in terms of damping coefficients. The ability to provide damping is a feature of this device but there is no capacity to provide linear stiffness as the latter depends on journal rotation.

The conventional representation of a squeeze-film in terms of damping coefficients has the attraction that it is very simple to incorporate these coefficients into a discrete mathematical model of a rotor-bearing system. This approach implicitly assumes that inertial forces within the oil-film are negligible. However, theoretical investigations by a number of workers [1-11] suggest that inertial forces can be very significant in squeeze-films. Indeed, this is evident if one considers the "gap Reynolds number"

$$R_e = \frac{\rho\omega c^2}{\eta} = \frac{\text{fluid inertia force}}{\text{fluid viscous force}}$$

PRECEDING PAGE BLANK NOT FILMED

where ρ is the density of the lubricant, ω is the frequency of vibration, c is the radial clearance in the squeeze-film damper and η is the viscosity of the lubricant. In many practical applications R_e is of order one, or greater. For such values one cannot expect conventional lubrication theory, based on the Reynolds equation (ie. on the assumption that $R_e \ll 1$), to give an accurate representation.

In a linearised approach, inertial forces can be incorporated into the model through the introduction of "acceleration coefficients" in addition to the normal damping coefficients. However, experimental estimates of acceleration coefficients (or "hydrodynamic mass" effects), in geometries typical of many squeeze-films, do not appear in the literature; indeed, inertial effects have not been taken into account at all in many previous comparisons between theoretical and experimental dynamic behaviour. This may explain, at least partly, why it has proved so difficult to obtain satisfactory agreement between theoretical and experimental values of the damping coefficients.

In the present investigation a transient testing technique has been developed and used to obtain the dynamic characteristics of a "short" squeeze-film bearing, with a geometry typical of that currently adopted in engineering applications and with Reynolds numbers in the range $0.5 < R_e < 1.5$. The experimental results are processed using a parametric identification technique to yield estimates of the dynamic coefficients and these are compared with predictions from existing theory. Limitations of the theory are highlighted which indicate promising avenues for further research.

NOTATION

b_{rr}, b_{ss}	direct fluid damping coefficients, for the r and s directions, respectively.
b_r^o, b_s^o	structural damping coefficients, for the r and s directions, respectively.
B_{rr}, B_{ss}	non-dimensional, direct fluid film damping coefficients, for the r and s directions, respectively.
c	radial clearance between the journal and the bearing.
c_{rr}, c_{ss}	direct fluid film inertial coefficients, for the r and s directions, respectively.
d	initial displacement
d^*	non-dimensional initial displacement (see equation (27)).
h(u)	time domain response function (see equation 17).
k_r, k_s	shaft stiffnesses, in the r and s directions, respectively.
ℓ	land length of the bearing.
m	effective, first mode mechanical mass.
m_H	hydrodynamic mass (c_{rr} in the radial direction, c_{ss} in the transverse direction).

P	hydrodynamic film force.
r	journal displacement in the radial direction (i.e. in the direction of the attitude line).
R	radius of the journal.
Re	Reynolds number ($=\rho\omega c^2/\eta$)
s	journal displacement in the transverse direction (i.e. in a direction perpendicular to the attitude line).
t	time.
$x(t)$	displacement.
$X(t)$	non-dimensional displacement.
$y(t)$	measured, free-decay record.
$\alpha(\omega)$	frequency response function, defined by equation (23).
$\beta(\omega)$	frequency response function, defined by equation (23).
γ	damping parameter, defined in equations (3).
γ_0	value of γ, in the absence of a fluid film.
γ^*	non-dimensionalised γ (see equations (10)).
δ	stiffness parameter, defined by equations (3).
δ_0	value of δ, in the absence of a fluid film.
δ^*	non-dimensionalised δ (see equations (10).
ζ_r, ζ_s	critical damping factors, in the case of no fluid film, in the r and s direction, respectively.
ε	eccentricity ratio.
ε_0	static eccentricity ratio.
η	absolute viscosity of the squeeze-film fluid.
ρ	density of the squeeze-film fluid.
$\Delta\tau$	sampling interval.
ω	frequency of vibration.
ω_{ro}, ω_{so}	natural frequencies of undamped vibration, in the radial and transverse directions, respectively.
τ	non-dimensional time ($= \omega_0 t$).

THEORETICAL TREATMENT

The equations of motion

The system consists of a mass of finite size (the squeeze-film journal) attached to the centre of a beam, which is built-in to rigid supports at each end and which plays the rôle of a conventional retainer spring. If the central mass is given some initial,transverse displacement, achieved by a force applied at the centre of the journal, and then released, the first mode of vibration will be dominant in the subsequent motion. Thus to a close approximation, the motion can be described in terms of two second order equations of motion.

In the present investigation, the squeeze-film bearing was run under full-film conditions, that is with no cavitation. In these circumstances, it can be shown, theoretically, that no cross-damping terms appear.

We thus write, for radial r and transverse s, displacements

$$\begin{aligned}(m + c_{rr})\ddot{r} + (b^o{}_r + b_{rr})\dot{r} + k_r r = 0 \\ (m + c_{ss})\ddot{s} + (b^o{}_s + b_{ss})\dot{s} + k_s s = 0\end{aligned} \qquad \ldots (1)$$

Here c denotes inertial coefficients and b damping coefficients in the squeeze-film, b^o denotes structural damping and k structural stiffness emanating from the spring beam. m is the effective, first mode mechanical mass. Both equations can be written in the standard form

$$\ddot{x} + \gamma\dot{x} + \delta x = 0, \qquad \ldots (2)$$

where γ and δ are constants. For the radial direction:

$$\begin{aligned}\gamma &= \frac{b^o{}_r + b_{rr}}{m + c_{rr}} \\ \delta &= \frac{k_r}{m + c_{rr}}\end{aligned} \qquad \ldots (3)$$

and similarly for the transverse direction.

From a free decay test, one can determine γ and δ, by using a parametric identification technique. Suppose that a free decay test is carried out in the radial direction, in the absence of a fluid film in the squeeze-film bearing. Then $b_{rr} = c_{rr} = 0$, and we obtain the coefficients

$$\begin{aligned}\gamma_0 &= \frac{b^o{}_r}{m} = 2\zeta_r\omega_0 \\ \delta_0 &= \frac{k_r}{m} = \omega_{ro}{}^2\end{aligned} \qquad \ldots (4)$$

where ω_{ro} is the natural frequency of undamped vibration and ζ_r is the damping factor. On combining equations (3) and (4) one obtains

$$\begin{aligned}b_{rr} &= m\left[\gamma \frac{\delta_0}{\delta} - \gamma_0\right] \\ c_{rr} &= m(\frac{\delta_0}{\delta} - 1)\end{aligned} \qquad \ldots (5)$$

for the damping and inertial coefficients, where

$$m = \frac{k_r}{\delta_0} \qquad \ldots (6)$$

m can be determined from measurements of k_r and from a free decay test without fluid in the squeeze-film bearing (giving γ_0 and δ_0). By combining this information with estimates of γ and δ, from free decay with fluid in the squeeze-film bearing, one can estimate b_{rr} and c_{rr}, by using equation (5). Similarly, measurements of free decay in the transverse direction can be used to yield estimates of b_{ss} and c_{ss}.

In practice the structural damping is very small and one finds ω_{r0} and ω_{s0} by simply measuring the frequency of vibration, without fluid in the bearing.

Before processing the decay curves it is convenient to non-dimensionalise the equation of motion (equation (2)). If ω_0 is the frequency of undamped vibration, without fluid, then a convenient non-dimensional time is

$$\tau = \omega_0 t = \delta_0^{\frac{1}{2}} t \qquad \ldots (7)$$

Also, the displacement $x(t)$, can be non-dimensionalised by dividing by the initial displacement, $x(0)$. Thus,

$$X(t) = \frac{x(t)}{x(0)} \qquad \ldots (8)$$

Equation (2) can then be recast as

$$\ddot{X} + \gamma^* \dot{X} + \delta^* X = 0 \qquad \ldots (9)$$

where

$$\gamma^* = \frac{\gamma}{\omega_0} = \frac{\gamma}{\delta_0^{\frac{1}{2}}}$$

$$\delta^* = \frac{\delta}{\omega_0^2} = \frac{\delta}{\delta_0} \qquad \ldots (10)$$

are non-dimensional coefficients and differentiation is now with respect to τ. On substituting these equations into equation (5) we obtain

$$b_{rr} = m\omega_{r0} \, [\gamma^*/\delta^* - \gamma_0^*]$$

$$c_{rr} = m(\frac{1}{\delta^*} - 1) \qquad \ldots (11)$$

and similarly for b_{ss} and c_{ss}.

The damping coefficients

The conventional approach to evaluating the coefficients b_{rr} and b_{ss}, for a full squeeze-film is to use the Reynolds equation as the basis of the calculation. For the general case it is necessary to solve this equation numerically, but simple, asymptotic results can be derived for

(a) the short bearing: $\ell/R \to 0$
(b) the long bearing: $\ell/R \to \infty$.

The short bearing theory gives the following results[12]

$$b_{rr} = \left[\frac{\pi\eta R\ell^3}{c^3}\right] \frac{(1 + 2\,\varepsilon_0^2)}{(1 - \varepsilon_0^2)^{5/2}}$$

$$b_{ss} = \left[\frac{\pi\eta R\ell^3}{c^3}\right] \cdot \frac{1}{(1 - \varepsilon_0^2)^{3/2}} \qquad \ldots (12)$$

The corresponding long-bearing results are as follows[13]

$$b_{rr} = \left[\frac{12\pi\eta R^3\ell}{c^3}\right] \cdot \frac{1}{(1 - \varepsilon_0^2)^{\frac{1}{2}}\,(1 - \varepsilon_0^2)}$$

$$b_{ss} = \left[\frac{12\pi\eta R^3\ell}{c^3}\right] \cdot \frac{2}{(2 + \varepsilon_0)(1 - \varepsilon_0^2)^{\frac{1}{2}}} \qquad \ldots (13)$$

As pointed out earlier, the use of the Reynolds equation implicitly assumes that inertial forces within the fluid film are negligible. Theoretical studies of the influence of fluid inertia on the damping coefficients of a squeeze-film bearing have been undertaken by Tichy[3] and San Andrès and Vance[7]. Their results indicate that, for the particular geometry of bearing studied in this investigation, and for the range of frequencies of oscillation studied, the influence of fluid inertia on the damping coefficients is negligible.

The inertial coefficients

A linearised approach to the evaluation of squeeze-film fluid forces allows a separate evaluation of the inertial coefficients, which arise from the effect of journal acceleration.

Smith[1] has shown that for a very short full-film bearing ($\ell << R$) these coefficients are given by,

$$c_{rr} = \frac{\pi\rho R\ell^3}{12c} \left\{\frac{2}{\varepsilon_0^2} \left[\frac{1}{(1 - \varepsilon_0^2)^{\frac{1}{2}}} - 1\right]\right\}$$

$$c_{ss} = \frac{\pi\rho R\ell^3}{12c} \left\{\frac{2}{\varepsilon_0^2} \left[1 - (1 - \varepsilon_0^2)^{\frac{1}{2}}\right]\right\} \qquad \ldots (14)$$

and $c_{rs} = c_{sr} = 0$. In the special case of zero static eccentricity ($\varepsilon_0 = 0$), a limiting operation performed on equation (14) gives

$$c_{rr} = c_{ss} \quad \frac{\pi\rho R\ell^3}{12c} \quad (\varepsilon_0 = 0) \qquad \ldots (15)$$

This agrees with the result obtained by Fritz for very short bearings, in the concentric case[2].

For a long, full-film bearing (ℓ>>R) the appropriate expressions for the coefficients are as follows [1]:

$$c_{rr} = c_{ss} = \frac{\pi\rho R^3\ell}{c} \{\frac{2}{\varepsilon_0{}^2} [1 - (1 - \varepsilon_0{}^2)^{\frac{1}{2}}\} \qquad \ldots (16)$$

and $c_{rs} = c_{sr} = 0$. In the special case where $\varepsilon_0 = 0$ (concentric operation) equation (16) reduces to

$$c_{rr} = c_{ss} = \frac{\pi\rho R^3\ell}{c} \quad (\varepsilon_0 = 0) \qquad \ldots (17)$$

which is a result first derived by Stokes [14].

It is interesting to note that, for $\varepsilon_0 = 0$, the ratio of c_{rr} for the long bearing case to c_{rr} for the short bearing case, is from equations (15) and (17).

$$12(\frac{R}{\ell})^2$$

The damping coefficients from the long and short bearing theories, for the concentric case, are in exactly the same ratio (see equations (12) and (13)). It follows that, for short bearings (ℓ << R), the damping and inertial coefficients are, according to the short bearing theory, considerably less than those predicted from the long bearing theory.

Recently Szeri et al [9] have presented, graphically, numerical values for the inertial coefficients, c_{rr} and c_{ss}, for squeeze-films with finite values of ℓ/R, in the range $0.2 \leqslant \ell/R \leqslant 4.0$. They found it necessary to introduce an approximation, based on the assumption that ℓ/R is small, in their analysis but have indicated that their results should be more accurate than a full short-bearing approximation, provided that ℓ/R is small. Their numerical results are in virtually exact agreement with Smith's short-bearing results (equation (14)) for $\ell/R < 0.5$.

2.4 Parametric identification

It was shown in section 2.1 that the damping and inertial coefficients can be related to the non-dimensional parameters γ^* and δ^*, which occur in the second-order linear equation of motion given by equation (9). From the experiment to be described one can obtain a free-decay curve - i.e. X(t) versus time. The problem is then to find, the values of γ^* and δ^* for which the solution to equation (9) gives a "best fit" to the experimental observations.

This is a problem in parametric identification, on which considerable literature exists (for example see Ref. [15]). Of the various available techniques, we have here selected the sequential method of Detchmady and Stidhar[16], since this enables estimates to be obtained from a knowledge of a single measured state variable (here the displacement of the journal versus time - either r(t) or s(t). Details of the algorithm are given in the Appendix.

The algorithm operates on a discretely sampled record of the decay curve. Suppose the experimental values are of $y(i\Delta\tau)$ (i=0,1,2,...), where $\Delta\tau$ is the sampling interval and τ is given by equation (7). The data is conveniently scaled so that the start displacement y(0), is unity. By sequentially processing the data, the algorithm generates least-square estimates of the state vectors X(t) and $\dot{X}(t)$, and also least-square estimates of γ^* and δ^*, at the times $i\Delta\tau$. These estimates "track" the experimental data and should converge as time increases - i.e. the estimated state vector X(t) should approach the measured response, y(t), and the estimated values of γ^* and δ^* should approach constant values.

To obtain improved estimates of γ^* and δ^*, the algorithm can be applied in an iterative manner. In the first iteration, values of γ^* and δ^* are guessed and used to start the sequential estimation computation. The algorithm will give estimates of γ^* and δ^*, at the end of the data sequence; i.e. at time τ_m, where τ_m is the time of the last data sample. These estimates can now be used, in place of the initial guesses, as a start to the second iteration. By repeating the iteration a number of times, the estimates of γ^* and δ^*, at time τ_m, should converge to constant values.

Prior to using this procedure on real decay data it was tested thoroughly on simulated data, from which it could be concluded that the algorithm was an efficient and useful method, for the present application.

Memory effects

The use of damping and inertial coefficients is based on the assumption that the fluid film forces depend only on the instantaneous velocity and acceleration of the journal. Although the coefficient approach is simple to incorporate into a discrete mathematical model of a rotor-bearing system, there are two serious objections which can be raised, concerning its validity:

(i) Implicit in the method is the assumption that the velocity and acceleration are linearly independent variables, so far as the fluid film is concerned. This poses conceptual difficulties - e.g. how can the acceleration be varied whilst the velocity is held constant?

(ii) No allowance is made for "memory" effects, which can be expected when the bearing is running under cavitation conditions. Even in the case of a completely non-cavitated bearing, considered in the experimental work reported here, memory effects may be significant, for sufficiently high frequency motion, due to the visco-elastic properties of typical lubricants (e.g. see Ref.[3]).

Considering, for example, the case of radial motion only, a general linear form for the relationship between the hydrodynamic force P_r, and the motion, r(t), is as follows:

$$P_r(t) = \int_{-\infty}^{\infty} h(t - \tau)\, r(\tau)\, d\tau \qquad \ldots (18)$$

Where h( ) is a time domain impulse response function.

The use of equation (18) allows a generalisation of the coefficient representation discussed earlier. To demonstrate this, consider the simple case of harmonic motion

$$r(\tau) = Ae^{i\omega\tau} \qquad \ldots (19)$$

On substituting this motion into equation (18) one obtains

$$P_r(t) = Ae^{i\omega t}[\alpha(\omega) + i\beta(\omega)] \qquad \ldots (20)$$

where

$$\alpha(\omega) = -\int_{-\infty}^{\infty} h(u) \cos \omega u \, du$$
$$\beta(\omega) = \int_{-\infty}^{\infty} h(u) \sin \omega u \, du \qquad \ldots (21)$$

Equation (20) may be compared with the corresponding result obtained by the coefficient approach, which states that, for a squeeze-film bearing

$$P_r(t) = b_{rr} \dot{r} + c_{rr} \ddot{r} \qquad \ldots (22)$$

Combining equations (19) and (22) one has

$$P_r(t) = A^{i\omega t} [-\omega^2 c_{rr} + i\omega b_{rr}] \qquad \ldots (23)$$

Equations (20) and (23) are identical if

$$\alpha(\omega) = -c_{rr} \omega^2$$
$$\beta(\omega) = b_{rr}\omega \qquad \ldots (24)$$

However, the integral representation of equation (18) allows an arbitrary variation of the "coefficients" with frequency, whereas, according to the coefficient approach, the damping and inertial coefficients are necessarily independent of frequency.

It remains to be tested by experiment whether, over a frequency range of practical concern, the frequency independent coefficient approach gives a satisfactory approximation, or whether there is a significant "memory effect", with the result that the coefficients must be treated as frequency dependent parameters. In the latter case, an integral representation, such as that given by equation (18) is more appropriate than the coefficient representation.

DESIGN OF EXPERIMENT

An outline drawing of the general arrangement of the rig is shown in Fig. 1 and a photograph of the rig is shown in Fig. 2. A non-rotating journal is contained within the circular bearing and is supported by a beam of circular cross-section which provides a stiffness in parallel with the squeeze-film. A cross-sectional view of the journal and beam assembly is shown in Fig. 3. The journal is heat shrunk along its entire contact length with the beam, and the beam is rigidly clamped at both ends.In the experimental work, three different beams were used, of varying stiffness.

Adjustment of the static equilibrium position in the horizontal direction was achieved by providing a machined channel in which the bearing housing could slide. Care was taken to ensure that the journal was accurately aligned with respect to the bearing. The alignment could be adjusted by moving the position of the beam end supports, using shims. Angular misalignment could be effectively eliminated by ensuring that the distance through which the journal could be moved, within the bearing, was maximised.

The bearing consisted of two plain lands separated by a central circumferential groove. Lubricant was supplied from a pump, through top and bottom feed holes and distributed around the bearing by the groove. No end seals were fitted and the lubricant was free to discharge into a reservoir prior to recirculation. By applying an adequate supply pressure to the inlet oil, full lubricant film conditions were maintained with no cavitation.

The experimental technique consisted of pulling back the journal, across the clearance circle, to a known position by a length of wire looped over the core of a solenoid. The journal was released by actuating the solenoid. Capacitive probes then transmitted the transient decay to a microprocessor based data-acquisition system. This allowed the dynamic characteristics (i.e. the mass, stiffness and damping of the squeeze-film, support beam and journal mass) to be evaluated and compared with simple linear theory.

EXPERIMENTAL RESULTS

In all the tests reported here the line of centres of journal and bearing, ie the radial direction, was horizontal when the journal was in its static equilibrium position. In the radial tests the journal was pulled out radially a further initial displacement, d, and released. Processing of the results from these tests enabled estimates of the damping coefficient, b_{rr}, and the inertial coefficient c_{rr}, to be derived. In the transverse tests, the journal was given an initial transverse displacement, d, (perpendicular to the line of centres) and released. From these tests, estimates of the damping coefficient, b_{ss}, and the inertial coefficient, c_{ss}, could be derived.

It is convenient, henceforth, to refer to a non-dimensional initial displacement, d*, defined by

$$d^* = \frac{\text{initial displacement (d)}}{\text{radial clearance (c)}} \qquad \ldots (25)$$

Tests without fluid in the bearing

For each of the three beams available, tests were carried out, in both the radial and transverse directions, with no fluid in the squeeze-film bearing. Here the damping is very small, and is structural in origin; it follows that the measured natural frequency of oscillation is, in these circumstances, a very close approximation to the undamped natural frequency

By applying the parametric identification procedure to the results, estimates of the undamped natural frequencies, ω_0, and the structural damping factor, ζ, were obtained. For a given shaft these values were found to differ slightly, in the radial and transverse directions (the maximum difference was about 5%),and results from each direction were averaged. Table 1 summarises the results obtained from these tests.

Tests with fluid in the bearing

A series of tests was carried out, with Tellus R10 as a lubricant in the squeeze-film bearing, and with a sufficient supply pressure to ensure that full-film conditions were maintained throughout (i.e. no cavitation). Measured decay curves, in both radial and transverse directions, were obtained for static eccentricity ratios of 0, 0.1, 0.2, 0.3, 0.4 and 0.5 and for initial displacements, d*, of 0.2 and 0.4. The decay curves were normalised, in every case, to give an initial displacement of unity.

If the journal-bearing system behaves linearly, then the normalised decay curves should be independent of the initial displacement, d*, if other parameters are kept constant. Thus by performing a series of decay tests, with differing initial displacements,and comparing normalised decay curves, one can assess the range within the bearing clearance circle, for which linear conditions prevail.

At ε_0 = 0.0 and ε_0 = 0.3, the system behaved linearly (to a close approximation), in both directions, for start amplitudes up to d* = 0.4. At the highest static eccentricity ratio studied, ε_0 = 0.5, a good collapse of the normalised decay curves was still obtained in the transverse direction for d* = 0.2 and 0.4, whereas, in the radial direction there was distinct evidence of non-linearity, for d* = 0.4. It can be concluded that there is a fairly wide range of journal displacement position, within the clearance circle, for which a linear mathematical representation is reasonable.

Figs. 4 (a) to (f) show a set of experimental, normalised decay curves, obtained with the squeeze-film journal mounted on beam 1. The results cover the static eccentricity range ε_0 = 0.0 to 0.5, and relate to both radial and transverse tests. Similar series of results were obtained for beams 2 and 3. In general, for each beam, ε_0 value, and chosen direction, results were obtained for d* = 0.2 and 0.4; where these collapsed reasonably well they were averaged to produce curves such as those shown in Fig. 5. Where non-linearity was indicated by a lack of collapse (generally at ε_0 = 0.4 and ε_0 = 0.5, in the radial direction), the result for d* = 0.2 only was used.

A comparison between the results for ε_0 = 0.0 for beam 1, in the radial and transverse directions, (see Figs. 5(a) and (b)) indicates some degree of asymmetry in the journal bearing configuration. For example, the second, positive overshoot in the radial direction is appreciably less than that observed in the transverse direction. The reason for this asymmetry is not clear, but may be due to the geometry of the oil-feed arrangement (fluid was supplied at the top and bottom of the central circumferential groove). The corresponding results for beams 2 and 3 indicated that the asymmetry was much less marked at higher frequencies of oscillation.

Beam stiffness results

To enable estimates of the damping and inertial coefficients to be derived from the free decay data, it is necessary to know the value of the effective, first mode mass, m. This value will be related to the actual mass of the journal, together with the mass of the beam, and so will vary, depending upon which beam is used in the experiments.

In the face of various uncertainties regarding the precise end conditions of the beams, it was decided to evaluate m, for each beam, from a knowledge of the natural frequency of oscillation, ω_0. and the beam stiffness. Thus

$$m = \frac{k}{\omega_0^2}$$

will give an estimate of m, if k is the effective, first mode stiffness.

The beam stiffness, k, was determined experimentally, by pulling the journal, radially, with a known static force, and measuring the resulting radial journal displacement. Table 1 shows the results obtained for the effective masses of the journal and beams.

COMPARISON BETWEEN THEORY AND EXPERIMENT

Parameter estimation

As a first stage in the analysis of the decay data, the parameter estimation procedure described in section 2 was applied to each decay curve. This yielded estimates of the parameters γ^* and δ^*, in the linear, second order model given by equation (9).

Figs. 6 show typical results of applying the estimation method to a particular decay curve. Here the experimental decay curve of Fig 6(b) was obtained for beam 1, in the radial direction, and with the journal initially concentric ($\varepsilon_0 = 0$) (see also Fig. 5(a)). The iterative technique, described in section 2, was used to refine the estimates of γ^* and δ^*, denoted $\hat{\gamma}^*$ and $\hat{\delta}^*$, respectively. Fig. 6(a) shows the variation of $\hat{\gamma}^*$ and $\hat{\delta}^*$, with time (measured in units of $\tau = \omega_0 t$) during the fifth iteration; at this iteration stage convergence is achieved, as evidenced by the fact that the final estimates in the cycle are equal to the initial estimates ($\hat{\gamma}^* = 0.601$, $\hat{\delta}^* = 0.662$). Fig.6(b) shows a corresponding comparison (for the fifth iteration, again) between the estimated displacement state variable, $\hat{x}(t)$, and the experimental decay curve; this shows that the estimated state "tracks" the experimental curve extremely well. A better idea of the degree of fit achieved can be obtained by comparing the experimental curve with the theoretical curve, found by using the final parameter estimates; this comparison is shown in Fig. 6(c).

The excellent degree of fit obtained in Fig. 6(c) can only be obtained, of course, by allowing both the parameters γ^* and δ^* to "float". If one assumes that the squeeze-film produces only a damping effect then it is necessary to set $\delta^* = 1$ and to obtain a best fit by allowing only γ^* to vary. This can be achieved, using the same parametric identification procedure as before, but setting the initial, off-diagonal elements of the P matrix to zero (see Appendix); this has the effect of "locking" the δ^* parameter to its initially set value, with the result that optimisation is sought with respect to the γ^* parameter alone. Fig. 6(d) shows a comparison between the experimental decay curve and the best-fit theoretical curve, with $\delta^* = 1.0$ and γ^* optimised ($\gamma^* = 0.912$). A comparison between Figs. 6(c) and (d) reveals that the effect of deviations of δ^* from unity (due to inertial effects in the squeeze-film) is very significant and that a very poor fit to the data is achieved by assuming that only damping is present in the squeeze-film. Similar comparisons have been made with other decay curves and these lead to a similar conclusion.

Damping and inertial coefficients

Once γ^* and δ^* have been estimated from a particular decay curve, then the damping and inertial coefficients may be found.

To present the damping results it is convenient to introduce the non-dimensional coefficients per land.

$$B_{rr} = b_{rr} \frac{c^3}{2\pi\eta R \ell^3}$$

$$B_{ss} = b_{ss} \frac{c^3}{2\pi\eta R \ell^3} \qquad \ldots (26)$$

According to the short-bearing theory,(equation (12)),

$$B_{rr} = \frac{(1 + 2\varepsilon_0{}^2)}{(1 - \varepsilon_0{}^2)^{5/2}}$$

and

$$B_{ss} = \frac{1}{(1 - \varepsilon_0{}^2)^{3/2}} \qquad \ldots (27)$$

In the experimental rig the following values apply:

$R = 0.06$ m, $c = 2.54 \times 10^{-4}$m, $\ell = 0.012$ m, $\eta = 22 \times 10^{-3}$ Ns/m^2,

Using these values in equations (26), and equations (11) one obtains an equation for B_{rr} (and also B_{ss}) of the form

$$B_{rr} = k_i \frac{\gamma^*_{cor}}{\delta^*} \quad (i = 1,2,3) \qquad \ldots (28)$$

where

$$\gamma^*_{cor} = \gamma^* - \gamma_0{}^*\delta^* \qquad \ldots (29)$$

is the damping parameter, corrected for the effect of structural damping and k_i is a non-dimensional constant, dependent on the beam used. The appropriate k_i values are given in Table 1

The relationship between the present experimental values of B_{rr} and B_{ss}, and the corresponding theoretical values, according to both long and short-bearing theories, is shown in Figs. 7(a) and (b). It is evident that the experimental values lie much closer to the short-bearing theoretical curve. At zero eccentricity there is a factor of 300 between the two theoretical values, whereas the experimental values are only a factor of about 1.5 higher than the short-bearing theoretical result. There is little indication of any "memory effect", due to changes in the natural frequency of oscillation.

The inertial coefficients, c_{rr} and c_{ss}, defined in section 2, have the physical significance of hydrodynamic masses. Thus m_H, the hydrodynamic mass, is given by

$m_H = c_{rr}$ (radially)

$= c_{ss}$ (transversely)

Figs. 8(a) and (b) show the variations of m_H with static eccentricity ratio, ε_0, for the radial and transverse directions, respectively. Here the experimental estimates of m_H are compared with both long and short bearing theoretical values. The significant feature here is the magnitude of the inertial effect. In both directions, the hydrodynamic mass is an order of magnitude greater than the short bearing theoretical prediction. This is rather surprising in view of the small ℓ/R ratio pertaining in the experimental rig (0.2). For this value of ℓ/R the results of Szeri et al[9] lead one to expect that the short-bearing theory should give a reasonably accurate estimate of m_H.

CONCLUSIONS

Damping coefficients for both the radial and transverse directions, agreed reasonably well with the short-bearing theoretical results, although the experimental values were generally higher than the theoretical values. The variation of damping coefficients with static eccentricity ratio, ε_0, was very similar to the variation predicted by short-bearing theory. Thus, in the radial direction there was a marked increase in damping coefficient with ε_0, whereas in the transverse direction this effect was much less significant.

The experimentally-determined inertial coefficients (or hydrodynamic masses) were generally much higher than the theoretical values given by the short-bearing theory - typically an order of magnitude higher.

The experimentally determined damping and inertial coefficients, for the three shafts, were found to collapse fairly well, when plotted against static eccentricity ratio. This is a strong indication that, at least over the frequency range studied here, "memory effects" within the squeeze film are not significant.

APPENDIX

Parametric Identification of Free Decay Data

General theory

Consider a dynamic system defined by the following differential equation of motion:

$$\dot{\tilde{x}} = \tilde{g}(\tilde{x}) \qquad \ldots (A1)$$

Here x is an n-vector containing the states, $x_1, x_2, \ldots, x_n$, of the system and g(x) is an n-vector function. If the system is stable, and is released from some initial condition, $\tilde{x}(0)$, then a transient response will result, with the motion decaying to zero. Suppose that observations of the output, or response, of the system are made during the time interval $0 < t < T$. An observation vector, $\tilde{y}(t)$ will be defined by

$$\tilde{y}(t) = \tilde{h}(\tilde{x}) + (\text{observation error}) \qquad \ldots (A2)$$

where y is an m-vector output and h is an m-vector function. Here the (observation error) term accounts for the fact that the output observation is of limited precision, due to quantisation errors in A/D conversion, electrical noise, etc. The estimation problem is to estimate the state vector x(T) from the observation vector y(t), measured in the interval $0 < t < T$ - i.e. to find the vector $\hat{x}(T)$, say, which corresponds to a "best fit" to the observations, and is consistent with equation (A1).

A "best fit" is most conveniently achieved in a least-square sense. Suppose that the following residual errors are defined:

$$\tilde{\varepsilon}_1(t) = \tilde{y}(t) - \tilde{h}(\tilde{x}^*) \qquad \ldots (A3)$$

$$\tilde{\varepsilon}_2(t) = \dot{\tilde{x}}^* - \tilde{g}(\tilde{x}^*) \qquad \ldots (A4)$$

Here $\underset{\sim}{x}^*$ is a "nominal" trajectory - i.e. a possible time history of $\underset{\sim}{x}$. From the residual errors one can form the integral

$$I = \int_{0}^{T} [\,||\underset{\sim}{\varepsilon}_1(t)||_{Q^2} + ||\underset{\sim}{\varepsilon}_2(t)||_{W^2}]dt \qquad \ldots (A5)$$

where $||\cdot||_{Q^2}$ and $||\cdot||_{W^2}$ are suitably defined quasi-norms.
Suppose that I is minimised when $\underset{\sim}{x}^*(t) = \underset{\sim}{\hat{x}}(t)$; a least-squares estimate of $\underset{\sim}{x}(T)$ is then $\underset{\sim}{\hat{x}}(T)$.

In practice, $y(t)$ is usually measured at equi-spaced times, t_i x $i\Delta t$ (i = 0,1,2,...). It is then convenient to use a recursive algorithm, which will generate sequential estimates of $\hat{x}(t)$, at times t_i. It has been shown by Detchmendy and Stidhar[16], using the method of invariant imbedding, that $\hat{x}(t)$ can be generated sequentially by using the following equations:

$$\frac{d\underset{\sim}{\hat{x}}}{dt} = \underset{\sim}{g}(\hat{x}) + 2\underset{\sim}{P}(t)\,\underset{\sim}{H}(\underset{\sim}{\hat{x}})\,\underset{\sim}{Q}\{\underset{\sim}{y}(t) - \underset{\sim}{h}(\underset{\sim}{\hat{x}})\} \qquad \ldots (A6)$$

$$\frac{d\underset{\sim}{P}}{dt} = \frac{\partial \underset{\sim}{g}}{\partial \hat{x}}\underset{\sim}{P} + \underset{\sim}{P}\left[\frac{\partial \underset{\sim}{g}}{\partial \underset{\sim}{\hat{x}}}\right]^T + 2P\frac{\partial}{\partial \underset{\sim}{\hat{x}}}[\underset{\sim}{H}(\hat{x})\underset{\sim}{Q}\{y(t) - \underset{\sim}{h}(\underset{\sim}{\hat{x}})\}]P \qquad \ldots (A7)$$

where

$$\underset{\sim}{H}(\underset{\sim}{\hat{x}}) = \left|\frac{\partial}{\partial \underset{\sim}{\hat{x}}}\,h(\underset{\sim}{\hat{x}})\right|^T \qquad \ldots (A8)$$

Here P(t) is an n x n matrix and Q is an m x m matrix. The latter matrix allows weighting to be assigned to the elements in the observation vector. $\underset{\sim}{H}$ is an n x m matrix.

By integration of equations (A6) and (A7) one can generate estimates, $\hat{x}(t_i)$, at the observation times, t_i. An initial estimate, $\hat{x}(0)$ of the start condition, $\underset{\sim}{x}(o)$, is required, but the estimates $\underset{\sim}{\hat{x}}(T)$ will usually be insensitive to the choice of $\underset{\sim}{\hat{x}}(0)$, providing that T is sufficiently large.

REFERENCES

1. Smith, D.M. "Journal Bearing Dynamic Characteristics - Effect of Inertia of Lubricant", Proc. Inst. Mech.Engs., Vol.179, Part 3J, 1964-65, pp.37-44.

2. Fritz, R.J. "The Effects of an Annual Fluid on the Vibrations of a Cory Rotor. Part 2 - 1st", Trans. ASME, Journal of Basic Engineering, Vol. 20, 1970, pp.930-937.

3. Tichy, J.A. "Effects of Fluid Inertia and Visco-elasticity on Squeeze-Film Bearing Forces", ASLE Trans., Vol.25, Part 1, January 1982, pp.125-132.

4. Tichy, J.A. "Effects of Fluid Inertia and Viscoelasticity on Forces in the Infinite Squeeze-Film Bearing", ASLE Paper 83-AM-3E-1, 1983.

5. Tichy, J.A. "The Effect of Fluid Inertia in Squeeze-Film Damper Bearings : A Heuristic and Physical Description", ASME Paper No. 83-GT-177, 1983.

6. Tichy, J.A. "Measurement of Squeeze-Film Bearing Forces to Demonstrate the Effect of Fluid Inertia", ASME Paper No. 84-GT-11, 1984.

7. San Andrés, L. and Vance, J.M. "Effects of Fluid Inertia and Turbulence on Force Coefficients for Squeeze-Film Dampers", NASA publication CP 2338 (1984).

8. Reinhardt, E. and Lund, J.W. "The Influence of Fluid Inertia on the Dynamic Properties of Journal Bearings", Journal of Lubrication Technology, ASME, Vol. 97, 1975, pp.159-175.

9. Szeri, A.Z., Raimondi, A.A. and Giran-Duarte, A. "Linear Force Coefficients for Squeeze-Film Dampers", Journal of Lubrication Technology, ASME, Vol. 195, 1983, pp.326-334.

10. Lund, J.W. Smalley, A.J., Tecza, J.A. and Walton, J.F., "Squeeze Film Damper Technology : Part 1 - Prediction of Finite Length Damper Performance, ASME PAPER 83-GT-247, 1983.

11. Nelson, C. "The Effect of Turbulence and Fluid Inertia on a Squeeze-film Damper", AIAA/SAE/ASME 16th Joint Propulsion Conference, June 30-July 2, 1980.

12. Holmes, R. "The Vibration of a Rigid Shaft on Short Sleeve Bearings", J.Mech.Eng. Science, Vol. 2, 1960, pp 337-341.

13. Holmes, R. "Oil-Whirl Characteristics of a Rigid Rotor in 360° Journal Bearings", Proc. Inst. Mech. Engs., Vol.117, No. 11, 1963, pp.291-308.

14. Stokes, G.G. "On Some Cases of Fluid Motion", Proceedings of the Cambridge Philosophical Society, Vol. 8, May 1843, pp.105-137.

15. Astrom, K.J. and Eykhoff, P. "System Identification - a Survey", Automatica, Vol. 7, 1971, pp123-162.

16. Detchmendy, D.M. and Stridhar, R. "Sequential Estimation of States and Parameters in Noisy Non-linear Dynamical Systems", Trans. ASME, Journal of Basic Engineering, Vol.16, 1966, pp.363-368.

TABLE 1

Beam No.	Nat. freq. (Hz)	Damping factor $\zeta = \gamma_0{}^*/2$	Effective mass of journal & beam (kg)	k_i
1	33.8	0.010	7.73	1.88
2	58.8	0.010	8.35	3.53
3	94.3	0.015	9.60	6.50

ORIGINAL PAGE IS
OF POOR QUALITY

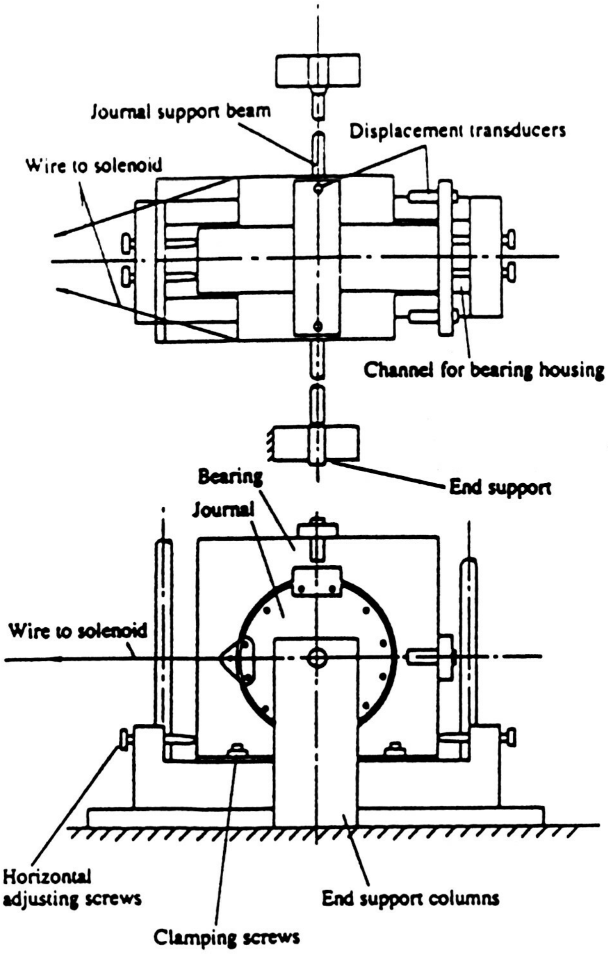
Journal support beam
Displacement transducers
Wire to solenoid
Channel for bearing housing
End support
Bearing
Journal
Wire to solenoid
Horizontal adjusting screws
End support columns
Clamping screws

Figure 1. - Squeeze-film bearing rig.

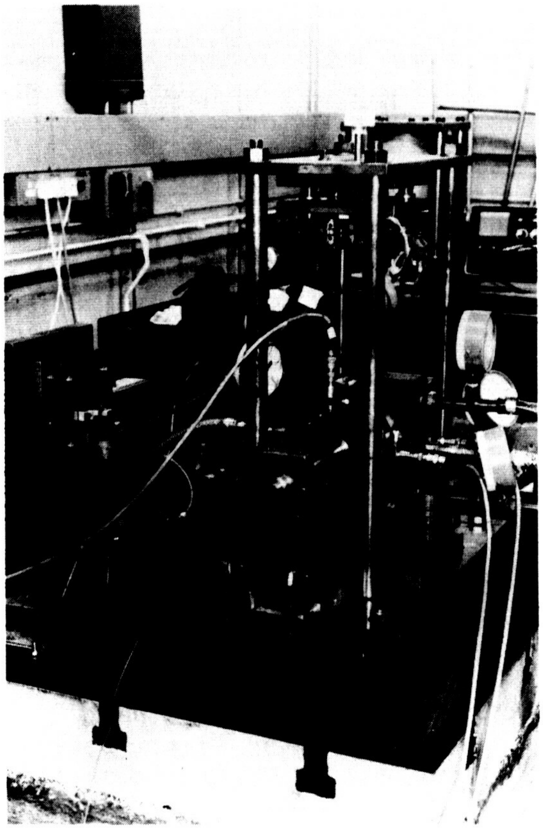

Figure 2. - Photograph of the experimental rig.

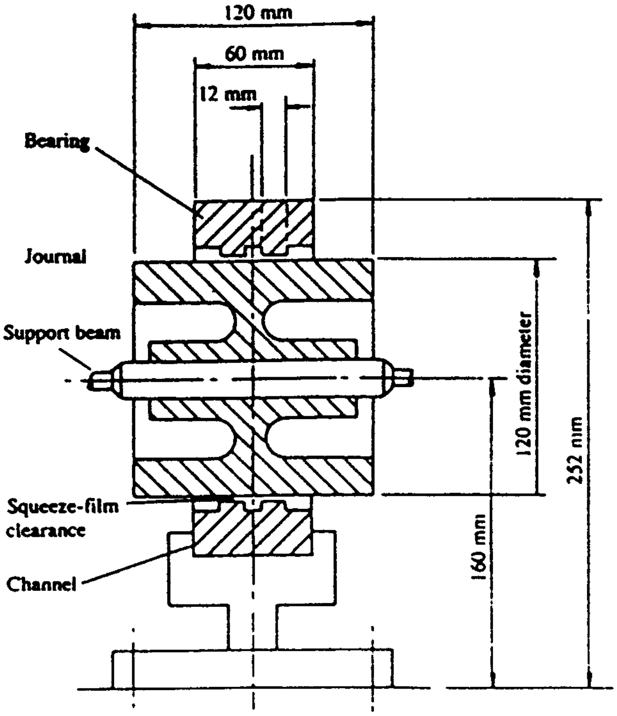
120 mm
60 mm
12 mm
Bearing
Journal
Support beam
Squeeze-film clearance
Channel
120 mm diameter
252 nim
160 mm

Figure 3. - Cross section of journal and beam assembly.

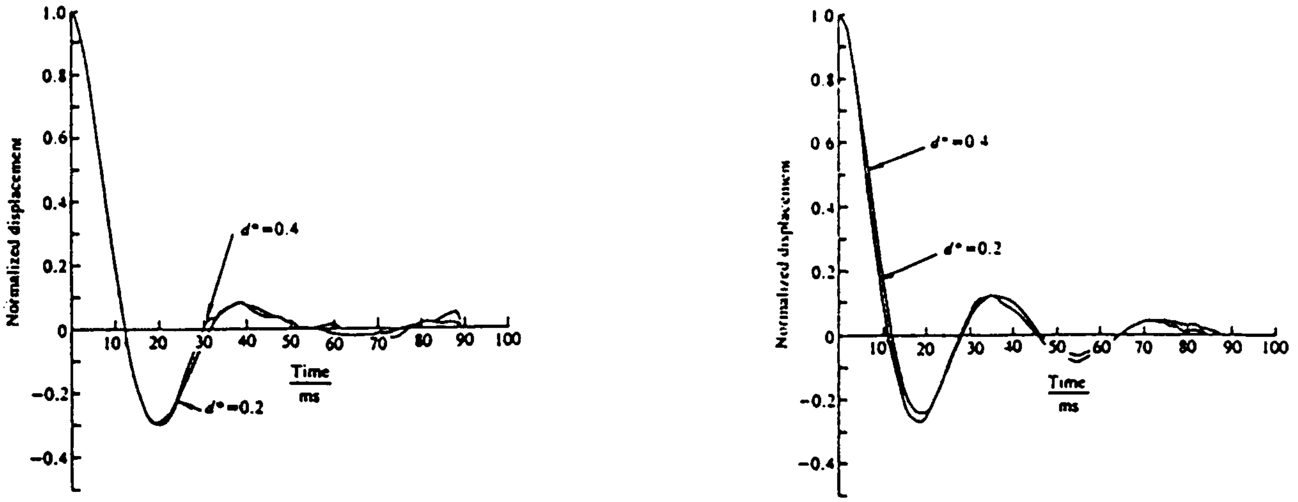

(a) ϵ_o = 0; radial displacement.

(d) ϵ_o = 0.3; transverse displacement.

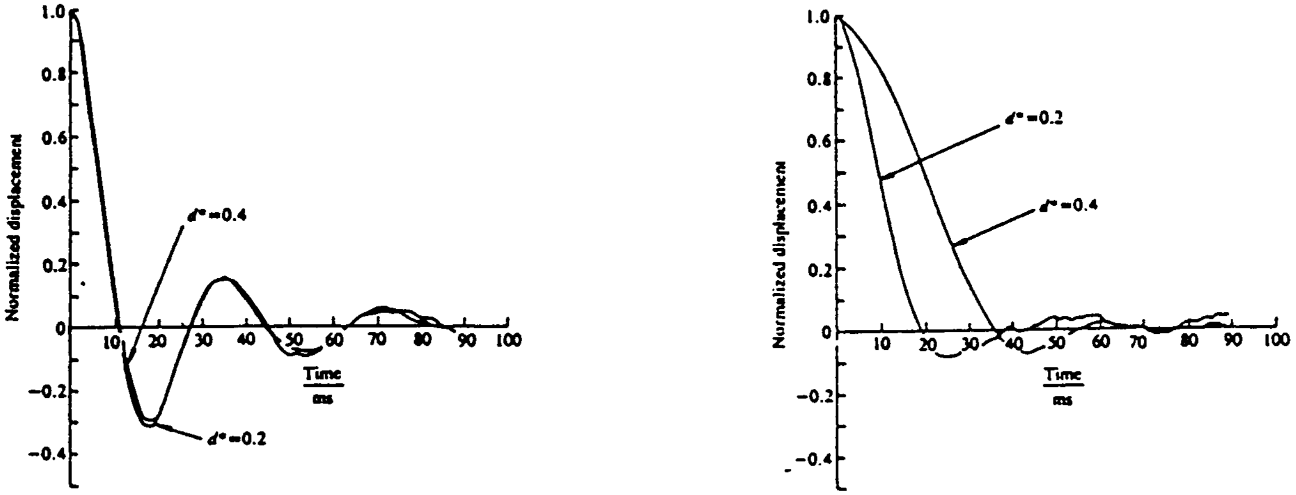

(b) ϵ_o = 0; transverse displacement.

(e) ϵ_o = 0.5; radial displacement.

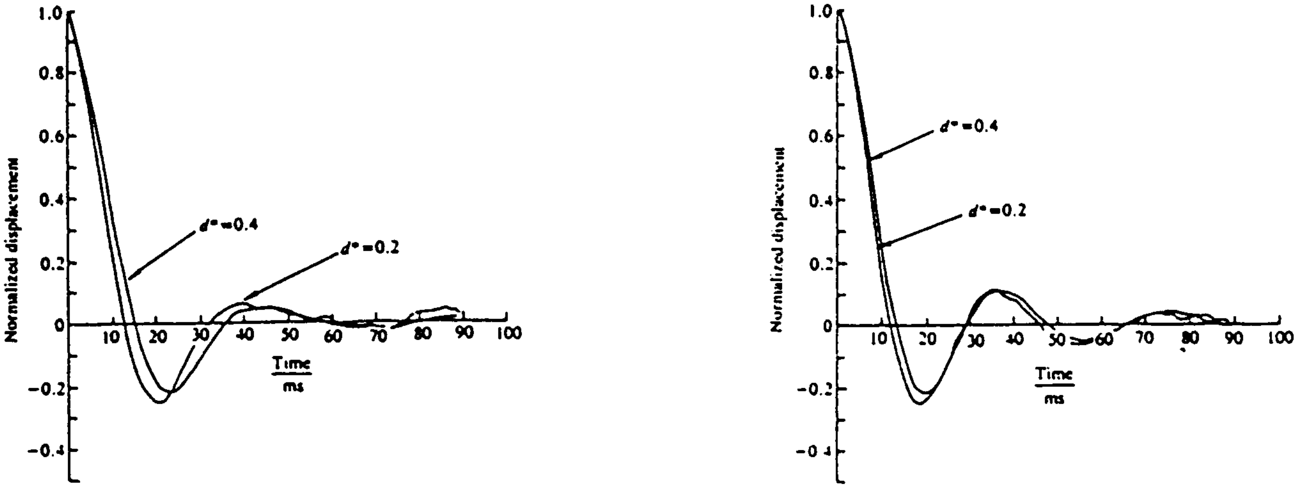

(c) ϵ_o = 0.3; radial displacement.

(f) ϵ_o = 0.5; transverse displacement.

Figure 4. - Experimental transient decay results; beam 1.

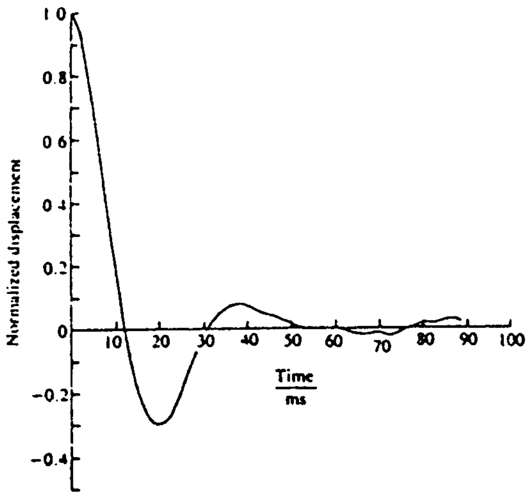

(a) $\epsilon_0 = 0$; radial displacement.

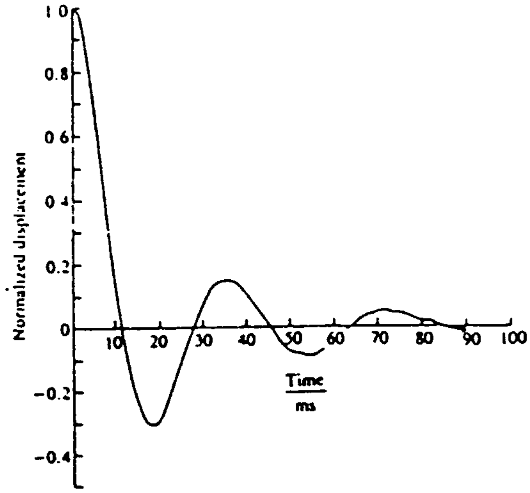

(b) $\epsilon_0 = 0$; transverse displacement.

Figure 5. - Averaged experimental transient decay results.

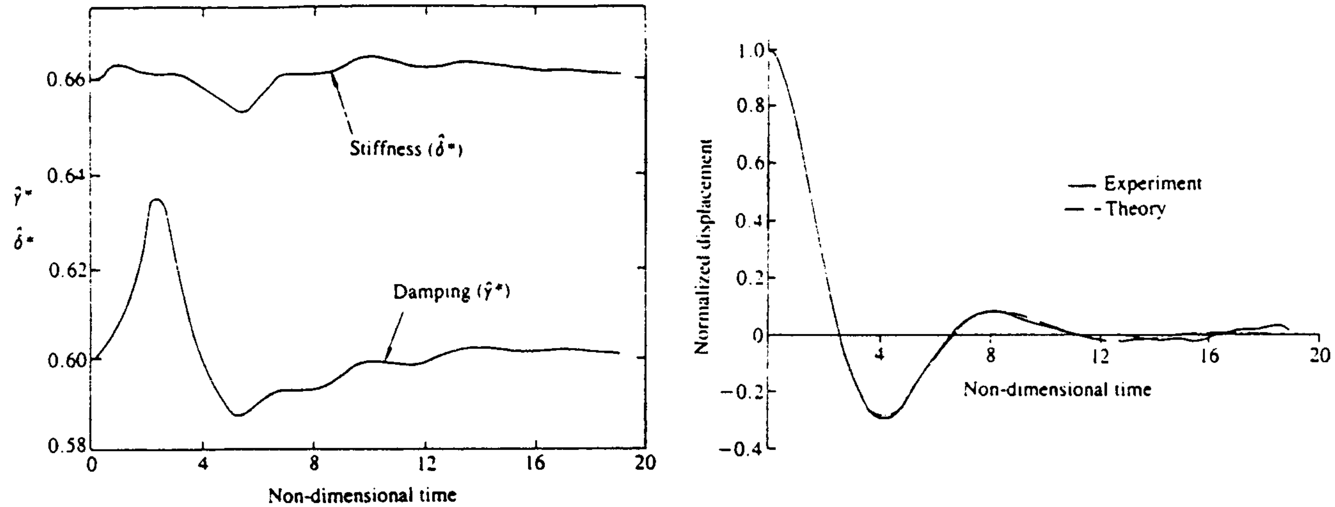

(a) Variation of $\hat{\delta}^*$ and $\hat{\gamma}^*$ with non-dimensional time.

(c) Comparison between the experimental decay curve and the theoretical curve, using final parameter estimates.

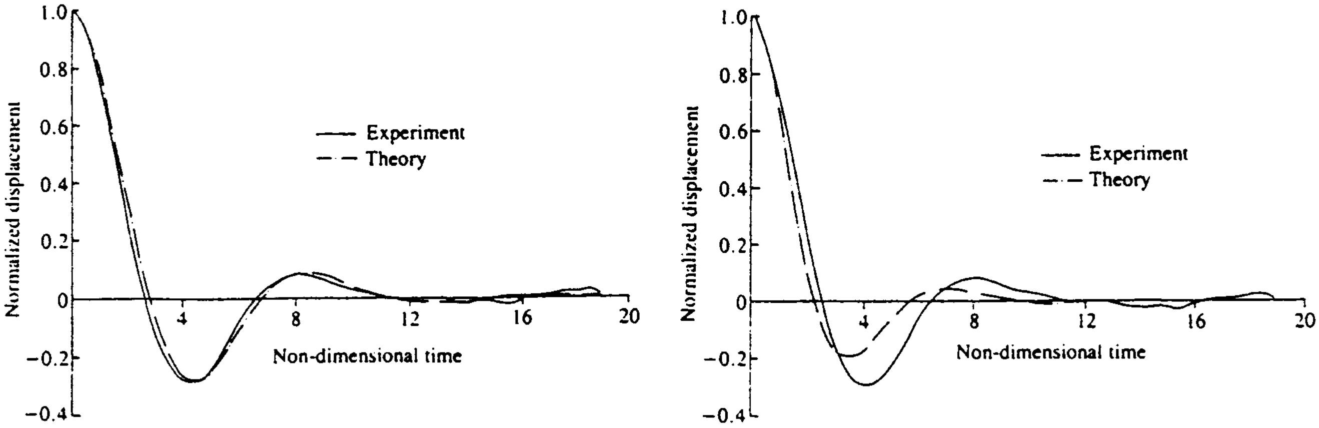

(b) Comparison between the experimental decay curve and the estimated displacement state variable, $\hat{X}(t)$.

(d) Comparison between the experimental decay curve and the theoretical curve, obtained by setting $\delta^* = 1$ and using the estimated value of γ^*.

Figure 6. - Results of applying parametric identification to an averaged experimental transient decay result for $\epsilon_0 = 0$; radial displacement.

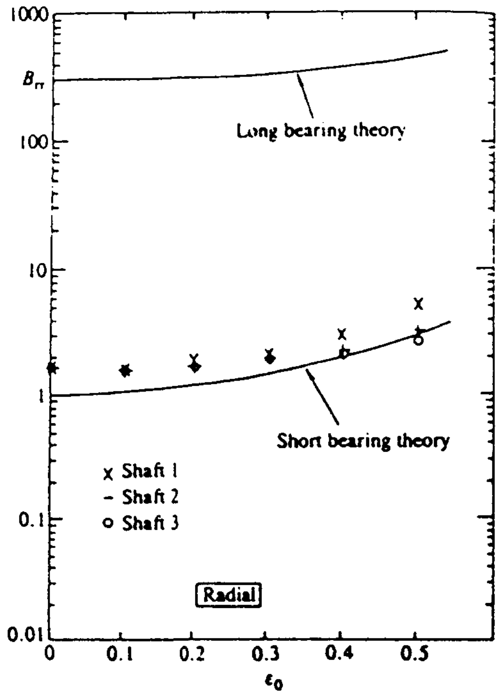

(a) B_{rr}; radial displacement.

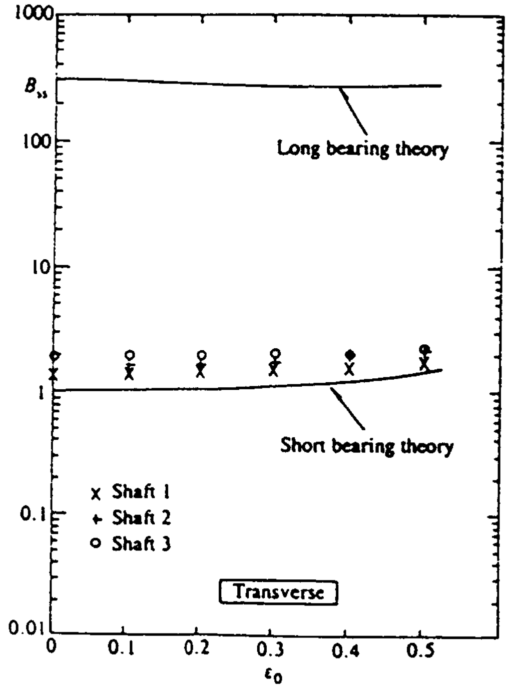

(b) B_{ss}; transverse displacement.

Figure 7. - Comparison between experimental results for B_{rr} and B_{ss} and the corresponding theoretical values, from short and long bearing theory.

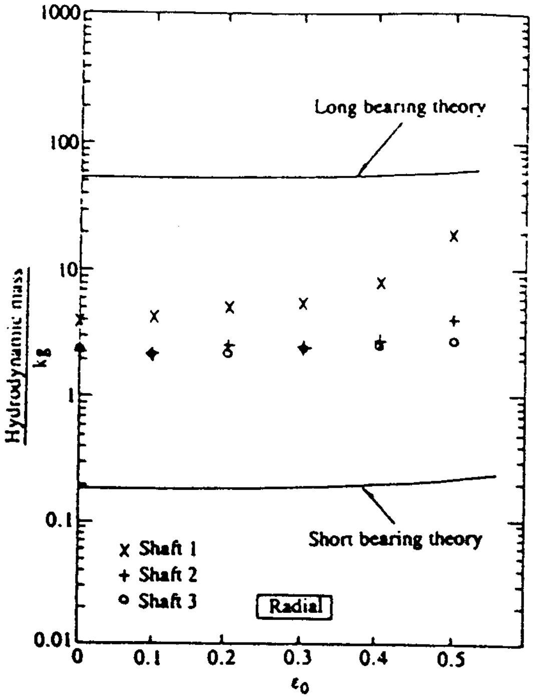

(a) c_{rr}; radial displacement.

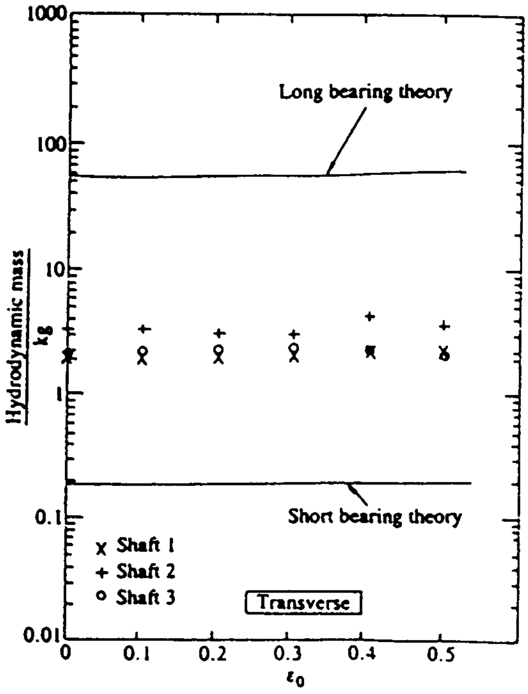

(b) c_{ss}; transverse displacement.

Figure 8. - Comparison between experimental results for m_H and the corresponding theoretical values from short and long bearing theory.

N87-22215

INSTABILITY OF AN INTERSHAFT SQUEEZE FILM DAMPER IN A TWO-SPOOL ROTOR DYNAMICS SIMULATOR

R.G. Alderson
Garrett Corporation
Phoenix, Arizona 86010

ABSTRACT

An instability associated with an intershaft squeeze film damper is described. The squeeze film is located between the intershaft bearing outer race and the low-speed shaft of a five-bearing, two-spool test rig. The instability is dominated by response of the third system mode to destabilizing excitation of the type described by Hibner, et al. Installing a spring cage in place of the intershaft damper removes the instability and produces satisfactory performance throughout the operating range.

INTRODUCTION

Trends in advanced technology engines are toward significantly higher turbine inlet temperatures, higher work stages, increased thrust-to-weight ratios, greater durability requirements, and reduced life-cycle costs. These trends are producing departures from traditional rotor systems that have significant effects on system rotor dynamics.

One Garrett design in this area is a two-spool engine that uses an intershaft roller bearing to support the turbine end of the high-pressure (HP) spool. This eliminates the high-temperature structure otherwise needed to support the HP turbine-end bearing. However, the intershaft bearing is a path for nonsynchronous excitation not found in traditional configurations.

Shaft diameters are kept to a minimum in order that disk bores and bearing diameters will be minimized. These measures for improving disk low-cycle fatigue lives and bearing lives are accomplished without requiring the low-pressure (LP) spool to operate supercritically. Although many of the modes encountered in the operating range display some flexure, the synchronous flexural critical speeds of the LP rotor are outside of the operating range. However, nonsynchronous excitation of these modes by the HP rotor via the intershaft bearing needs to be considered.

Shafting technology for advanced propulsion engines has not yet progressed to the extent that satisfactory operation can be guaranteed in this regime on the basis of analytical predictions alone. Commitment of an advanced engine design to a configuration incorporating these features requires a program of testing with a rotor dynamics simulator.

The dynamics rig designed to simulate the engine dynamics is a two-spool, corotating system driven by air impingement. Figure 1 depicts the dynamic system in schematic form. Individual spools are separately controlled and driven. The LP spool is supported by three bearings, two straddling the simulated fan, with the third bearing aft of the simulated LP turbine. The HP spool is supported by two bearings, including the intershaft bearing that has the inner race carried by the HP rotor.

The rotor system is installed in a rigid frame, with the spring cages used as bearing supports simulating engine structural stiffnesses. Each of the four structure-supported bearings is provided with an unsealed squeeze film damper. Centering springs are not used.

Originally, a squeeze film damper was also used with the intershaft bearing. This feature was employed in an effort to exploit fully the benefits of squeeze film dampers in controlling unbalance. The oil film was formed between the outer race and a housing rotating with the LP spool. The subsequent need to eliminate a subsynchronous instability led to removal of this damper in favor of a spring cage.

Initial rig testing revealed subsynchronous whirl that appeared at a part-speed condition and persisted throughout the operating range. The instability did not grow to destructive proportions, probably due to relatively well-balanced rotors. It was the dominant feature of the rotor response, however, and unacceptable for engine operation.

The intent of this paper is to describe the characteristics of the instability, and to discuss the influence of the intershaft squeeze film damper.

EARLY TEST EXPERIENCE

Figure 2 shows the speed schedule followed in early tests to approximate engine conditions. Acceleration through the speed range revealed some system modes synchronous with the LP rotor, while others were synchronous with the HP rotor. Initially, the LP-synchronous modes tended to be more severe. But trim balancing effectively reduced all synchronous response to relatively low levels. Subsynchronous response also was observed, beginning at a part-speed condition and persisting throughout the speed range. Trim balancing was not effective in reducing the amplitude of the subsynchronous response.

Figure 3 is an RPM spectrum map that typifies the system response. This data was obtained from a proximity probe sensing displacement of the simulated HP turbine wheel. This spectrum map is identical in character to maps for the simulated HP compressor and LP turbine wheels. These similarities emphasize the dynamic coupling provided by the intershaft bearing. Proximity probe data from the simulated fan showed less prominent subsynchronous response, probably due to the combined effects of fan mass and LP shaft flexibility.

Figure 3 shows the main subsynchronous response near 120 Hz, with a secondary subsynchronous response near 60Hz. The maximum amplitude of the 120 Hz component is in the range of 0.10 to 0.15 mm (4 to 6 mil) peak-to-peak for the HP turbine, and about twice that for the LP turbine. The 120 Hz component displays an increasing trend from its initiation through maximum operational speed for the rig. This response is regarded as an instability. Although these subsynchronous whirl amplitudes are not a threat to rig integrity, the presence of an instability would not be tolerable for engine operation.

CHARACTERIZATION OF RESPONSE

Figure 4 combines Figures 2 and 3 with the results of undamped whirl speed calculations. The solid lines define system whirl frequencies for various whirl ratios (LP spin speed/system whirl speed). The analysis was done in the whirl frame of reference, and extended from zero whirl ratio (nonrotating system) through unity whirl ratio (LP unbalance excitation). Whirl ratios corresponding to HP unbalance excitation vary according to the speed schedule. At 100 percent speed, the whirl ratio corresponding to HP unbalance is between 0.5 and 0.6.

Figure 4 also shows that the analytical model is in reasonable correlation with the test data. Particularly prominent is the agreement between response peaks and calculated whirl speeds for LP unbalance excitation (unity whirl ratio). The first three mode shapes corresponding to LP unbalance excitation are shown in Figure 5. Amplitude and phase data from the various displacement transducers are consistent with these mode shapes. All three modes display shaft flexure but are not dominated by it. Analysis shows that most of the strain energy in these modes results from support participation rather than shaft flexure.

Figure 4 suggests that the subsynchronous activity around 60 Hz and 120 Hz is associated with the first and third system modes, respectively. Figure 5 shows that these two modes (particularly mode 3) involve participation by the intershaft bearing and squeeze film damper.

INSTABILITY OF INTERSHAFT DAMPER

The intershaft bearing is installed with the inner race mounted on the HP rotor. The squeeze film is formed between the outer race and a housing that rotates with the LP rotor. The damper is of the open-end type. Following the approach of Hibner, Kirk, and Buono (Ref. 1), the intershaft damper was modeled by a solution of the Reynolds Equation:

$$\frac{1}{6}\left[\frac{1}{R^2}\frac{\partial}{\partial\theta}\left(\frac{h^3}{\mu}\frac{\partial P}{\partial\theta}\right)+\frac{\partial}{\partial Z}\left(\frac{h^3}{\mu}\frac{\partial P}{\partial Z}\right)\right] = (W_1 + W_2 - 2\phi)\frac{\partial h}{\partial\theta} + 2\frac{\partial h}{\partial t} \qquad (1)$$

Making the "short bearing" assumption permits the first term on the left to be neglected. For steady whirl in a circular orbit,

$$h = C\,(1+\varepsilon\cos\theta) \qquad (2)$$

as is shown in Figure 6.

Then (1) reduces to

$$\frac{\partial^2 P}{\partial Z^2} = -\frac{12\mu\varepsilon\sin\theta}{C^2\,(1+\varepsilon\cos\theta)^3}\,(W_L-\phi) \qquad (3)$$

Assuming that the pressure is symmetric across the width of the squeeze film, (3) can be integrated to obtain the pressure distribution:

$$P(Z,\theta) = -\frac{6\mu\left(Z^2-\frac{L^2}{4}\right)\,\varepsilon\sin\theta}{C^2\,(1+\varepsilon\cos\theta)^3}\,(W_L-\phi) \qquad (4)$$

For the open-end damper, the circumferential pressure distribution is approximated by the "π-film" in which pressure is positive over half of the annulus and zero elsewhere. Two cases need to be considered in the integration of the pressure to obtain the radial and tangential damper forces. In the first case, the damper spin speed is less than the journal whirl rate. The opposite situation constitutes the second case.

Case 1 - $\phi > W_L$, $P=0$ for $0 \leq \theta \leq \pi$

$$F_r = 2\int_{\pi}^{2\pi}\int_{0}^{\frac{L}{2}} P(Z,\theta)\cos\theta\, R\,d\theta\, dZ =$$

$$-\frac{2\mu RL^3}{C^2}\,\frac{\varepsilon}{(1-\varepsilon^2)^2}\,(\phi-W_L) \qquad (5)$$

which tends to center the journal.

$$F_t = 2\int_{\pi}^{2\pi}\int_{0}^{\frac{L}{2}} P(Z,\theta)\sin\theta\, R\,d\theta\, dZ =$$

$$-\frac{\pi\mu RL^3}{2C^2}\,\frac{\varepsilon}{(1-\varepsilon^2)^{3/2}}\,(\phi-W_L) \qquad (6)$$

which tends to oppose whirl (stabilizing).

Case 2 - $\phi < W_L$, $P=0$ for $\pi \leq \theta \leq 2\pi$

$$F_r = \int_{0}^{\pi}\int_{0}^{\frac{L}{2}} P(Z,\theta)\cos\theta\, R\,d\theta\, dZ =$$

$$-\frac{2\mu RL^3}{C^2}\,\frac{\varepsilon^2}{(1-\varepsilon^2)^2}\,(W_L-\phi) \qquad (7)$$

which tends to center the journal, as in Case 1.

$$F_t = \int_{0}^{\pi}\int_{0}^{\frac{L}{2}} P(Z,\theta)\sin\theta\, R\,d\theta\, dZ =$$

$$+\frac{\pi\mu RL^3}{2C^2}\,\frac{\varepsilon}{(1-\varepsilon^2)^{3/2}}\,(W_L-\phi) \qquad (8)$$

which tends to promote whirl (destabilizing). This is the opposite of the effect noted in Case 1.

This analysis, together with the mode shapes shown in Figure 5, offers an interpretation of the system response shown in Figure 4. As the LP rotor is accelerated, LP-synchronous response in each of the first three system modes can be seen at LP speeds around 3300, 5000, and 7200 rpm. According to the analysis, intershaft damper forces due to LP-synchronous whirl are small since $\phi \simeq W_L$. Simultaneously, HP-synchronous whirl is present due to excitation of the second and third system modes by the HP rotor. Excitation of the sixth mode probably occurs also. Stabilizing forces are developed in the intershaft damper due to HP-synchronous whirl since $\phi > W_L$. Evidently these stabilizing forces, together with damping furnished by the grounded squeeze film dampers, are the dominant influences on system response.

For LP speeds above 8000 rpm, the character of the response changes. Following the expected sharp drop in LP-synchronous response as the LP rotor passes through the third system mode, a subsynchronous response appears around 120 Hz. The amplitude of the subsynchronous response continues to increase throughout the operating range. The unique feature of the third system mode (in contrast with the first and second modes) is the degree of participation of the intershaft damper. This is illustrated in Figure 5.

A plausible explanation of the response derives from the abundance of transients in the system. Noncircular damper orbits and the nonlinearity of squeeze film damper forces are primary sources of transients which ordinarily are of little consequence. Even though system response to transients will tend to include response in the system modes, system damping usually suppresses the transients immediately. But because the intershaft damper participates strongly in the third system mode, destabilizing forces become significant since $\phi < W_L$ for this mode. It appears that the secondary subsynchronous response around 60 Hz that occurs in the same speed range as the 120 Hz instability is a similar but weaker phenomenon. Damper participation in the first system mode is significantly reduced compared with the third mode. Virtually no intershaft damper activity occurs in the second system mode, nor is there subsynchronous response associated with it.

REMOVAL OF INSTABILITY

A limited test program was undertaken in which various system parameters were modified in an attempt to remove the instability. These modifications included clearance changes in the intershaft damper, the HP compressor-end damper, and the LP turbine-end damper. Support stiffness at the LP turbine-end bearing also was varied. Significant reduction of subsynchronous response was not observed.

Removal of the instability was accomplished by refitting the test rig with a spring cage in place of the intershaft damper. The result of this modification is shown in Figure 7, an rpm spectrum map of the simulated HP turbine response after the refit. The subsynchronous responses that appeared previously above 8000 rpm are absent. Although a slightly different speed schedule was used in this test, many of the synchronous features identified previously can be seen. The speed schedule modification does not affect the validity of the test. The modified speed schedule was followed merely to give a better simulation of engine conditions than the schedule shown in Figure 2.

CONCLUSIONS

Use of a squeeze film damper in an intershaft application is responsible for the instability observed during testing of a two-spool rotor dynamics simulator. Replacing the intershaft damper with a spring cage removed the instability. A limited program of testing alternate damper clearances and support stiffnesses revealed no significant effects on the instability. The instability was driven by destabilizing hydrodynamic forces in the intershaft damper that develop when the system tends to whirl at a speed less than the damper spin speed. The instability appears to be associated with the third system mode, in which the intershaft damper is influential.

NOMENCLATURE

C	Damper Radial Clearance
e	Eccentricity
F_r	Damper Oil Film Radial Force
F_t	Damper Oil Film Tangential Force
h	Damper Oil Film Thickness
P	Damper Oil Film Pressure
R	Damper Radius
t	Time
Z	Damper Axial Coordinate
ε	Eccentricity Ratio
θ	Angle From Line of Centers, In Direction of Rotation
μ	Oil Kinematic Viscosity
$\dot{\phi}$	Journal Whirl Rate
W_1	Inner Journal Spin Speed
W_2	Outer Journal Spin Speed
W_L	LP Rotor Spin Speed

REFERENCES

1 Hibner, D.H., Kirk, R.H., and Buono, D.F., "Analytical and Experimental Investigation of Intershaft Squeeze Film Dampers, Part I-Demonstration of Instability," Journal of Engineering for Power, Trans. ASME, Vol. 99, Series A, No. 1, Jan. 1977, pp. 47-52.

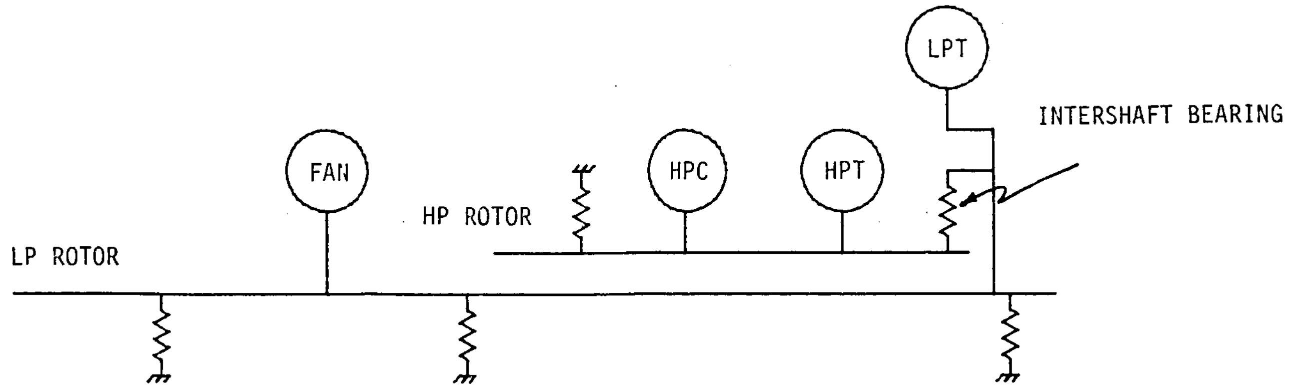

Figure 1. Rotor Dynamics Simulator Schematic.

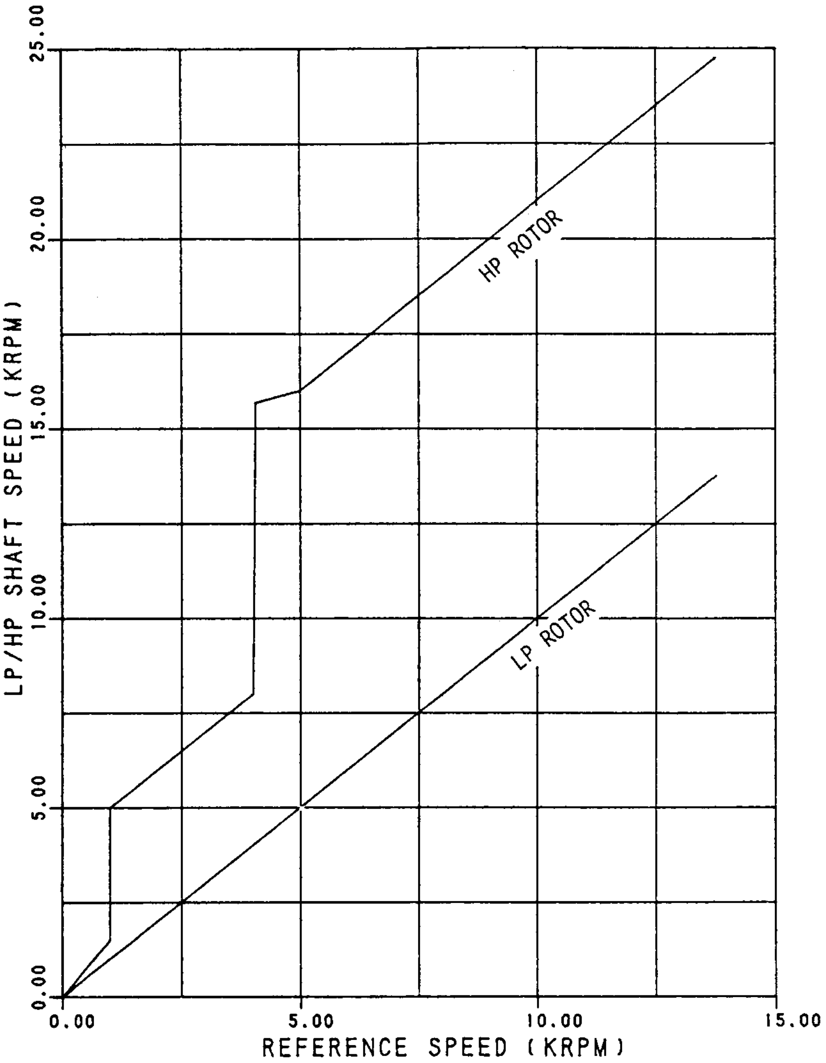

Figure 2. Rotor Dynamics Simulator Speed Schedule. System Includes Intershaft Squeeze Film Damper.

ORIGINAL PAGE IS
OF POOR QUALITY

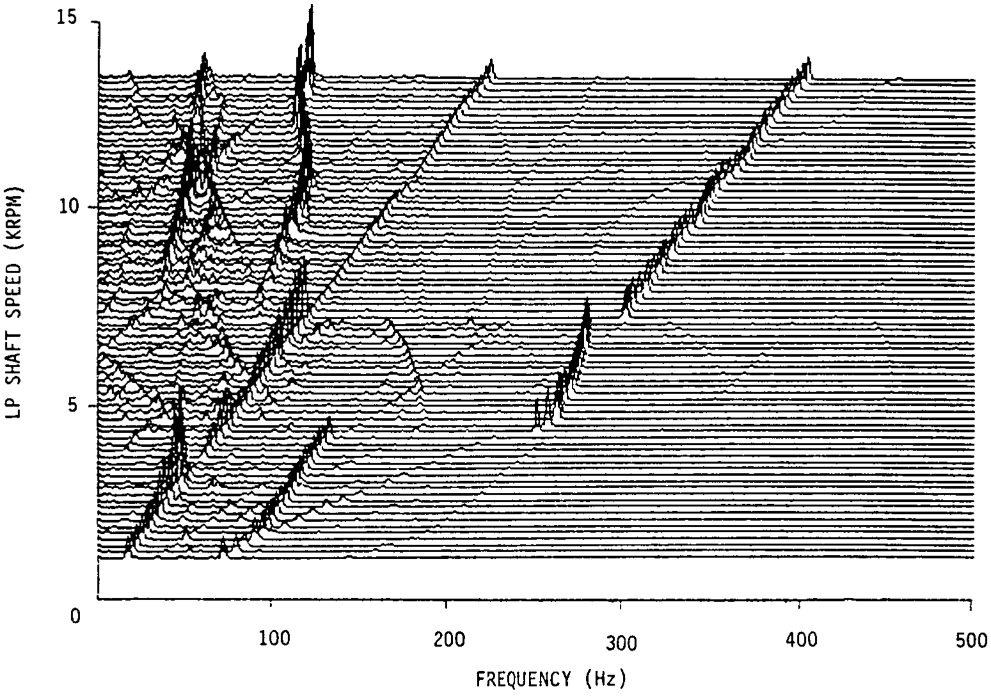

Figure 3. RPM Spectrum Map for Simulated HP Turbine.

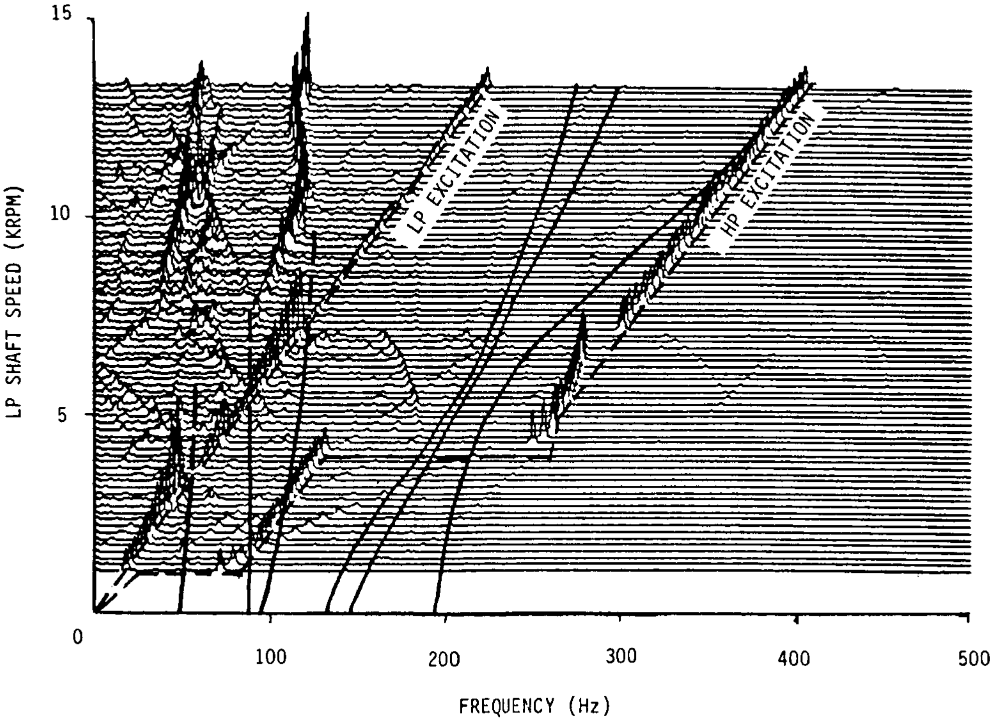

Figure 4. RPM Spectrum Map with Predicted Whirl Map Superimposed.

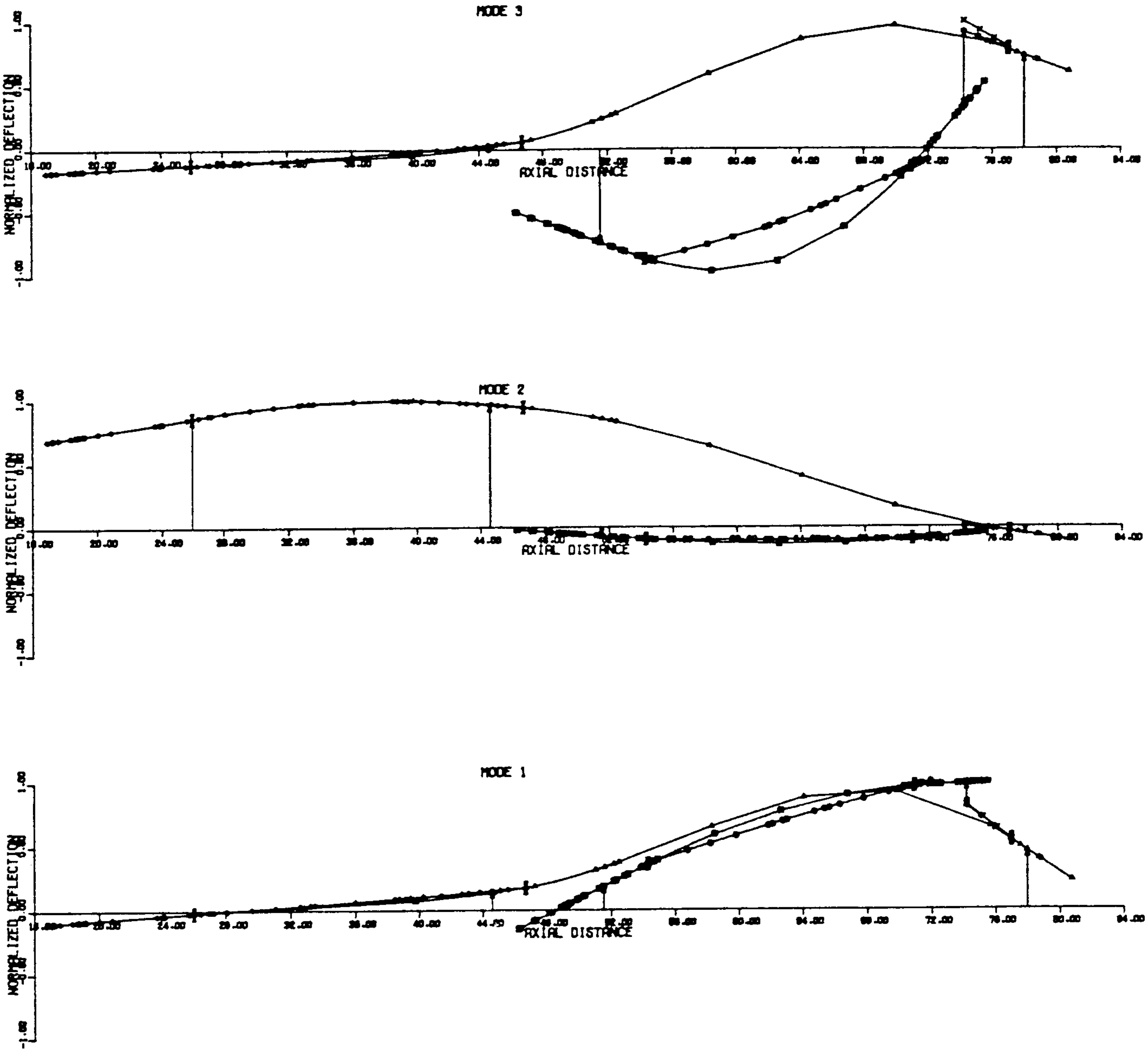

Figure 5. Deformed Shapes for System Modes 1 - 3.

ORIGINAL PAGE IS
OF POOR QUALITY

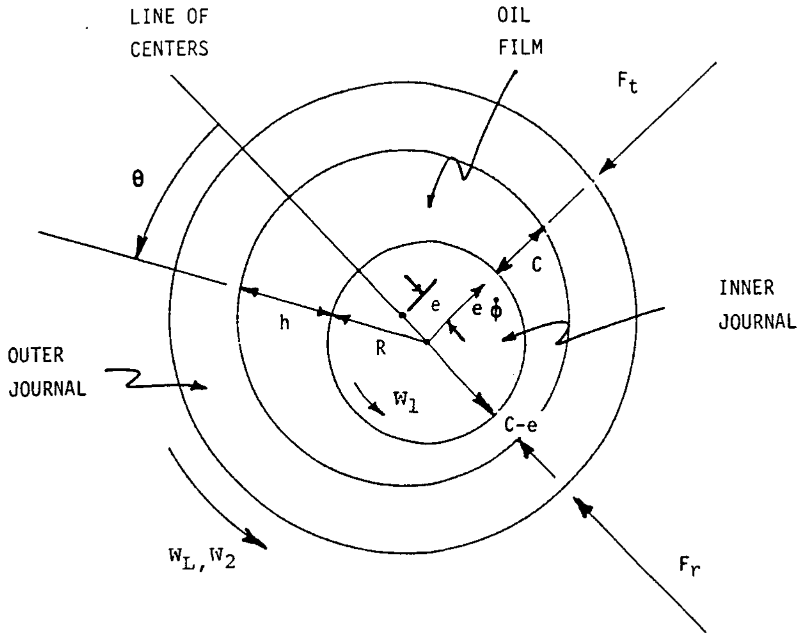
LINE OF CENTERS
OIL FILM
F_t
θ
C
e
e $\dot{\phi}$
h
R
INNER JOURNAL
OUTER JOURNAL
W_1
C-e
W_L, W_2
F_r

Figure 6. Intershaft Squeeze Film Damper Geometry.

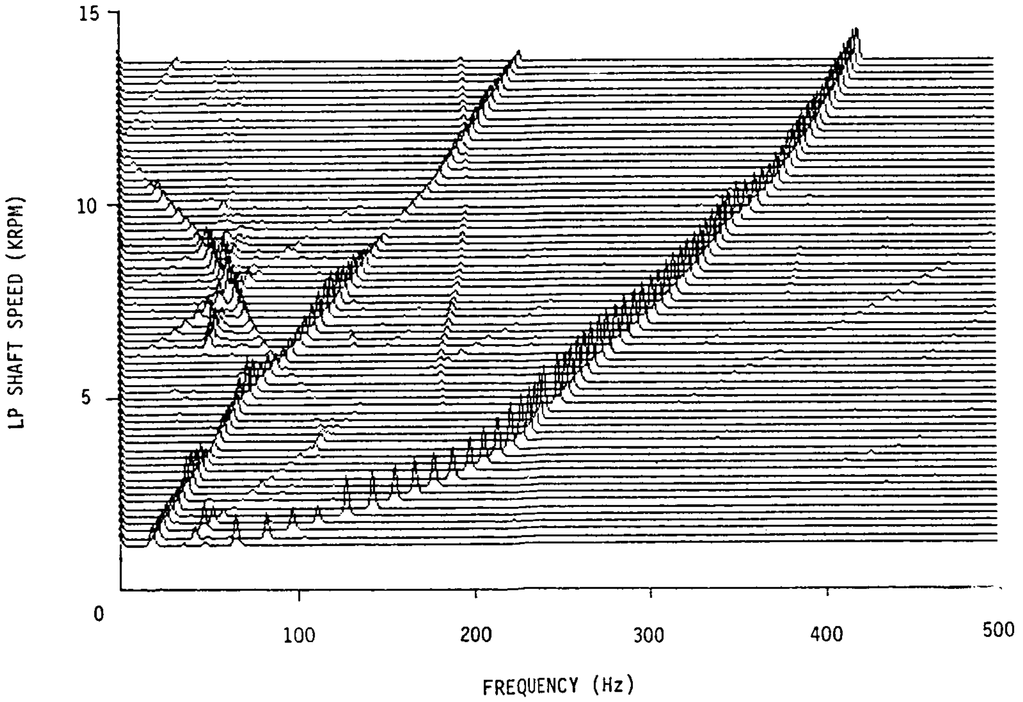

Figure 7. RPM Spectrum Map for Simulated HP Turbine.
Spring Cage Replaces Intershaft Squeeze Film Damper.

N87-22216

A NOVEL FORM OF DAMPER FOR TURBO-MACHINERY

R.D. Brown and J.A. Hart
Heriot-Watt University
Riccarton, Edinburgh EH14 4AS
Scotland

Anti-swirl vanes are used by some manufacturers to delay the full development of half speed circulation in annular clearance spaces. The objective is to reduce the aerodynamic cross-coupling in the forward direction. The novel feature of a jet damper is a number of tangential nozzles discharging against the rotor surface speed. Some preliminary results on a 33.9 Kg rotor demonstrate that significant reductions in amplitude are obtained at the synchronous critical speeds.

INTRODUCTION

The vibration of rotating machinery is due to a large number of forces which act on the surface of a rotating shaft. These forces include mechanical unbalance, bearing forces and fluid forces from impellers, seals, diffusers and labyrinths among others. If the response to the net action of all these forces is excessive the result is an unacceptable machine. An increase in damping of the rotor system can reduce the vibration response to acceptable levels.

Some experimental work on a small scale test rig has demonstrated that high speed tangential flow acting on the surface of a rotor can produce significant cross-coupling forces. If the direction of the flow is against the surface velocity then additional forces acting against rotor motion can be produced. These forces will considerably reduce response to synchronous unbalance and may also combat forward sub-synchronous whirl. A major advantage is that these forces act in the same direction as external damping but do not depend significantly on rotor motion.

An experimental test rig has been constructed to demonstrate the feasibility of the jet damper concept to reduce synchronous and sub-synchronous whirls in the forward direction. The rig has been designed to explore the effects of jet velocity and surface roughness on the magnitude of the force produced. The aim of the experimental work is to produce design data for a damper on a full size machine.

Among the potential advantages of a jet damper are the ease of fitting to existing machines, using a shaft extension if necessary. If such a damper is installed it can be left in an un-operational state until required. For example run-down or the detection of sub-synchronous vibration. Tangential flow on the rotor surface can then be initiated using a fast acting solenoid or fluidic valve. Damping forces can then be introduced as and when required.

PRECEDING PAGE BLANK NOT FILMED

NOMENCLATURE

C	radial clearance
H	total head
L	length
P	static pressure
R	radius
F_x, F_y	fluid forces
K_{xx}, K_{yy}	direct stiffness coefficients
K_{xy}, K_{yx}	cross stiffness coefficients
$\bar{K}_{xx}$, $\bar{K}_{yy}$	non-dimensional direct stiffness coefficient
$\bar{K}_{xy}$, $\bar{K}_{yx}$	non-dimensional cross stiffness coefficient
f	friction coefficient
h	local radial clearance
n	eccentrcity ratio
$\bar{u}$	mean fluid circumferential velocity
u	local fluid circumferential velocity
Re	Reynolds Number
θ	peripheral angle,measured from minimum gap
ρ	density
δ	rotor displacement
τ_o	wall shear stress
ω	angular velocity
ν	Kinematic viscosity

BACKGROUND

Significant vibration response in rotating machines is either forced response or instability. Both types of response can be reduced by external damping.

Forced Response

Response is largely a matter of unbalance distribution especially where flexible rotors are involved. In certain cases a rotor that was initially well balanced may have been running for a long time at a running speed considerably above a natural frequency. The original balance is often disturbed by a combination of blade erosion and deposits from the process fluid. For large machines not fitted with a braking mechanism the run down time is considerable thus allowing a significant time at speeds near resonance. This problem is recognised in the petro-chemical industry by specifying that vibration measurements are obtained during run-down tests. High response is due to the small damping of the natural frequencies of the rotor system. One well known method of reducing vibration response is to increase damping. However conventional methods of damping rely on using the motion of the vibrating body itself to provide the damping force e.g. an oil dash pot or shock absorber. As the motion is necessarily small, viscous fluids are normally used to provide sufficient damping forces. For rotating machinery squeeze film bearings are often used particularly in aero engines.

Instability

A common problem found in high speed turbo-machinery rotors is instability due to increases of speed and/or load beyond the stability boundary. The problem usually manifests itself as an increase in the vibration level at a non-synchronous frequency. In most cases this frequency is a natural frequency of the system which is insufficiently damped. As this frequency is often exceeded in the acceleration to running speed its reappearance as a result of instability is normally sub-synchronous i.e. at a frequency less than that corresponding to running speed. However unlike synchronous resonance it is usually impossible to pass through successfully without either reduced load or speed.

Instabilities of this sort are generally referred to as aerodynamic cross-coupling. A simple form of cross-coupling can be modelled by a lateral motion of the shaft causing a force perpendicular to that displacement. When the force vector is aligned with the translational velocity of the precessing shaft it behaves as a negative damping force. Experimental measurements of cross-coupling forces of this general nature are well established in bearings, impellers, blade rings and seal passages. In small annular clearances, typical of labyrinth seals the inlet flow, mainly axial, develops a strong circumferential component as a result of friction from the rotating shaft. Eventually the mean tangential component is equivalent to half the surface velocity of the shaft. Following a suggestion in reference 1 some manufactuers fit anti-swirl vanes at the entrance to labyrith seals to impose a backward swirl to the inlet flow. This delays the full development of the mean circumferential half-speed swirl and so reduces any cross-coupling that may be present in the labyrinth. A combination of a roughened stator with a smooth rotor has been shown in reference 2 to reduce the mean tangential velocity. However neither of these approaches essentially alters the basic nature of the circumferential flow.

Principle of Damper

The damper uses high velocity backward facing jets impinging tangentially on a roughened rotor surface which can produce significant increases in damping forces and substantially improve stability characteristics of turbo-machines. The essential feature of the jet damper is to use a number of high speed jets of fluid to give a relative motion in the appropriate direction to provide a damping force. As the relative velocity is largely independent of shaft orbital motion, high velocities can be used and therefore low viscosity fluids e.g. air are practical to generate forces of considerable magnitude.

PRELIMINARY RESULTS OBTAINED USING A PROPRIETARY ROTOR KIT

A proprietary rotor kit was adapted by the manufacture of a chamber and nozzle assembly to provide an annular space around which fluid could be circulated at high velocity. The rotor consisted of a 280 mm. long shaft of 9.5 mm. diameter, with an 0.846 Kg. steel disc of diameter 76.2 mm. mounted at midspan. This disc was supplied with its surface ground to give a smooth finish. Supporting the shaft at either end were brass bushes mounted in housings with a single rubber 'O' ring between the bush and housing. The rotor was driven by a 380 W reversible d.c. electric motor connected to the shaft through a flexible coupling. On running the rotor it was found that the first critical speed was at 3150 r.p.m. (52.5 Hz.), thus the maximum motor speed of 7000 r.p.m. meant that rotor speeds above twice the first critical could be achieved. More details are discussed in reference 3.

Plenum Chamber and Nozzle Assembly

An exploded view of the chamber and nozzle assembly is shown in figure 1. This was constructed from three aluminium plates arranged in a sandwich assembly, forming a chamber into which a compressed air supply could be fed. Mounted on one plate were four nozzles of 10 degrees included angle and 0.50 mm. by 9.50 mm. exit area. These nozzles directed high velocity air tangentially onto the surface of the central mass. Radial clearance between the stator and the rotor was 0.46 mm.

A pair of non-contact proximity probes, placed 90 degrees apart, measured the shaft vibration at a location approximately midway between the central mass and a bearing. The output from these probes was fed into an X-Y oscilloscope and a real-time spectrum analyser which derived the frequency components of the vibration.

Test Procedure and Results

The tests conducted can be classified into two main groups

(a) Effect of Fluid Flow on Rotor Stability

While running the rotor at constant speed, the plenum pressure was carefully increased and both the resultant orbit and response spectrum noted. Any instability could then be observed from the orbital pattern and the plenum pressure at the onset of this instability recorded. This test was repeated for flow in the same (forward) and opposite (reverse) direction to shaft rotation, and for a number of rotor speeds.

It was found that an instability could be induced by the circumferential flow of air in the annulus. The pressure ratio (plenum presure/atmospheric pressure) at the onset of this instability is plotted against the speed ratio (rotor speed/first critical speed) on figure 2. It can be seen that the stability boundary appears to be unaffected by the direction of rotor rotation. However it should be noted that the nozzle exit velocity is of the order of 100 - 250 m/s compared with a maximum rotor surface speed of only 25 m/s. The destablising forces generated are therefore of similar magnitude regardless of the direction of rotation. This test was found to be highly repeatable, the variation in the required pressure ratio being about 3%.

(b) Effect of Fluid Flow on Rotor Response

The averaging facilities of the spectrum analyser were used to obtain smoothed spectral densities of the rotor response for constant speed tests at various values of plenum pressure. This was repeated for a number of rotor speeds in both the forward and reverse direction.

A typical set of frequency spectra for the rotor response are shown on figure 3. Similar data was first shown in reference 4. These show the response for various running speeds at a steady plenum gauge pressure of 41.37 kN/m^2 (6.0 psig). This pressure corresponds to a nozzle exit velocity of about 230 m/s. As a threshold speed is reached sub-synchronous vibration suddenly appears the frequency of which was found to be about 50.4 Hz. This frequency is slightly less than the system resonant frequency of 52.5 Hz. A typical orbit is also shown once sub-synchronous behaviour is initiated for both forward and reverse flow.

While performing the experimental work it was observed that if rotation was in the opposite direction to the high velocity fluid flow, then any value of plenum pressure tended to reduce the amplitude of the synchronous vibration. This reduction was pronounced at speeds near the first critical speed.

As a result of this preliminary experimental work it was concluded that the use of reverse flow as a means of reducing synchronous vibration amplitudes in the speed range around the first critical was an effect worthy of further investigation. It should be noted that these results were obtained using nominal values of radial clearance and a smooth rotor surface. Variation in these parameters could lead to experimental data for the optimal design of an industrial device.

EXPERIMENTAL TEST RIG

The main objective of the more elaborate test rig was to isolate the circumferential velocity induced effects from other rotordynamic phenomena. As this work is concerned with the damping of supercritical rotors, the maximum rotor speed must lie well above its first critical. Further requirements of the rig were a realistic rotor velocity and ease of disassembly and modification.

The experimental approach being undertaken is to measure the effect of the fluid flow on the vibration response of the rotor for a number different values of annular chamber geometry and rotor surface roughness. Measurements are planned under various fluid supply pressures.

Overall Layout

The test rig consists of a vertical flexible shaft onto which a central disc is mounted, surrounded by a nozzle chamber. Into this chamber, pressurised fluid is fed before being injected tangentially onto the disc surface by virtue of the nozzle arrangement.

Consistent with the need to isolate other rotordynamic phenomena, the rotor is mounted vertically in self aligning ball bearings thus eliminating gravitational and oil-film effects respectively. These grease lubricated bearings allow for the angular misalignment caused by vibration of the flexible shaft.

Component Design

The rotor was constructed from a machined steel shaft of about 45 mm. diameter onto which three discs were shrunk. A central steel mass 152 mm. long and 149 mm. in diameter, provided a rotor surface velocity of up to 80 m/s at the maximum rotor speed. In order to avoid any problems due to an internal friction mechanism at the shrink fit interface, the shaft was undercut so that the contact was only over two 38 mm. lengths. Two brass discs 38 mm. wide and 123 mm. in diameter were similarily attached to the shaft at about one quarter and three-quarters span. These discs performed two basic functions. They provided a surface, free from residual magnetic inpurities, from which the rotor deflection could be measured using a pair of non-contact proximity probes. Secondly, these discs acted as a safety device such that if excessive rotor deflection occurred then the disc would come into contact with a PVC guard ring before damage was done to the nozzle assembly by the central rotor mass. Following fabrication, the complete rotor assembly, of mass 33.9 kg, was finished ground to obtain the required surface finish and concentricity tolerances between the discs and bearing journals. Tapped holes were machined in the end faces of the central disc into which grubscrews could be inserted in order to partially balance the rotor. A known amount of unbalance could then be supplied in order to investigate the unbalance response of the rotor.

At the design stage the rotor was modelled using a computer program available within the department. This program calculates the critical speeds, mode shapes and forced response using a transfer matrix/Rayleigh-Ritz method. This software is described in more detail in reference 5. Utilising this program the rotor was designed to have a first critical speed of about 4200 r.p.m.

Drive was by means of a horizontally mounted 8.5 kW variable speed reversible DC motor with the motor output shaft being connected to a right angle gearbox of ratio 1.1 through a flexible coupling. Using a timing belt and toothed pulleys of ratio 1:3.33, a maximum rotor speed of 8000 r.p.m. could be achieved.

The rotor was mounted in a casing consisting of three main sections - the upper and lower body and a central chamber which housed the nozzle assembly. These components were fabricated from steel tube onto which flanges were welded. To ensure concentricity throughout the assembly, each body had spigots machined thus ensuring a total eccentricity of not greater than 0.025 mm. The upper and lower bodies were press fitted with steel rings which acted as mounts for the PVC guard rings. The upper bearing housing was bolted to the upper body and the lower housing to a plate which was mounted between the lower body and the base. A sectioned assembly of the main body of the test rig is shown on figure 4.

Compressed air was chosen as the working fluid being supplied to the test rig from the departmental compressors via a receiver, filter and regulating valve. Four delivery pipes supplied the fluid to the plenum chamber which allowed a settled pressure to be achieved before entry to the nozzle assembly. Machined aluminium blocks were arranged to create eight convergent nozzles of about 10 degrees included angle. The nozzle block geometry and a section through the assembly are shown in figure 5. These blocks were assembled in six layers of eight blocks each block being located by a spring dowel pin into its neighbour. Steel rings top and bottom of the stack allowed eight through bolts to fasten the assembly. The exit dimensions of each nozzle formed by the build up of six blocks was 0.51 mm. by 127 mm. with the geometry being such that the flow was tangential to the rotor surface. The flow discharged through four ports in the wall of the upper and lower bodies. Figure 6 shows the built up nozzle assembly.

Experimental Parameters, Procedure and Instrumentation

The experimental parameters are:

(i) Rotor speed
(ii) Plenum pressure and mass flowrate
(iii) Radial clearance between nozzles and rotor
(iv) Rotor surface roughness
(v) Unbalance

For each setting of these parameters the rotor response is measured at the upper and lower brass discs.

Rotor speed was measured by a proximity probe mounted in the upper bearing cover plate. A small slot cut in a disc mounted on the shaft end provided a once per revolution signal for an electronic counter. Plenum pressure was measured at eight locations equi-spaced around the chamber using diaphragm type pressure transducers. These tappings provided information regarding any assymetry in the plenum circumferential pressure field. The fluid mass flowrate through the rig was measured by a commercially available flow sensor. Mounted on the main supply line to the rig downstream of the regulating valve, this consisted of a device which measures the difference between the mean dynamic and static pressure in the line. Measurement of this difference and the flow temperature allowed the flowrate to be calculated by reference to the flow instrument manual. Further experimental values recorded included the plenum temperature and the rig outlet pressure and temperature. A pressure tapping was also made through the nozzle assembly and into the annular space such that the pressure at the exit from a nozzle could be recorded. A close up of the main body of the test rig is shown in figure 7.

Whereas the tests regarding the effect of fluid flow parameters on the rotor response can be carried out without any modification of the test rig, the variation in the radial clearance and the rotor surface roughness require stripdown and reassembly. These two parameters can be altered by means of steel sleeves which are machined to fit over the central rotor mass, secured with setscrews. The external diameter and machining of these sleeves dictates the radial clearance and surface roughness employed.

During a typical test run, analysis of the signals generated by the four proximity probes is carried out using a real-time spectrum analyser. Averaging and decomposition of the time histories into frequency spectra can then be carried out while a test is proceeding. On completion of a test, averaged time histories and frequency spectra are transferred to a disc file via an IEEE interface unit controlled by a microcomputer. Supplementary data such as the plenum pressure field, temperatures and flowrate data can be added to this file via the computer keyboard. Data analysis, hardcopy output and graphical presentation can then be carried out as required. A schematic diagram of the complete test rig and instrumentation is shown on figure 8 while figure 9 illustrates the complete experimental set up and data logging equipment.

On running the rotor a casing resonance which lay within the speed range was observed, thus necessitating the fabrication of four angled struts which stiffened the rotor casing. With this modification in place the first critical speed was raised to about 5000 r.p.m. due to the increased support stiffness. Two critical speed close to one another were observed due to a slight anisotropy of the casing and supporting frame stiffness. The structural resonance was not completely eliminated however the vibration amplitudes produced were considerably reduced.

EXPERIMENTAL RESULTS

All experimental measurements of response presented in figures 10 - 12 are obtained by ensemble averaging of 256 time records from which time averaged orbits can be plotted.

Figure 10 and figure 11 show the response at the upper brass disc for a combination of reverse flow, a smooth rotor surface and a radial clearance of 0.508 mm. The two plots shown represent the orbits of significant magnitude in the speed range thus corresponding to the two critical speeds. The outer orbits are obtained with no flow present whereas the smaller time averaged orbits are obtained as a result of reverse flow being present. Each successive orbit represents a pressure increase of 6.98 kN/m^2 (1.0 psi.) in the plenum chamber.

It is obvious that a distinct reduction in the response at these two speeds is obtained by the introduction of reverse flow in the annular space around the rotor. A plenum gauge pressure of 34.5 kN/m^2 (5.0 psig.) can be seen to reduce the response by over 50%. This pressure corresponds to a mean air velocity at nozzle exit of around 70 m/s compared with a rotor surface speed of about 40 m/s. This velocity is calculated from the plenum pressure and temperature and a single static pressure measurement near a nozzle exit.

The orientation of the ellipical orbit can be seen to change as the pressure increases as would be expected by the introduction of a tranverse force acting on the rotor. These orbits result from residual unbalance only and thus this change in orientation cannot be directly compared to conventional phase angle.

The effect of reverse flow on rotor response was measured for a number of rotor speeds in the region of resonance and some results are shown on figure 12. Each point on this graph represents a stable orbit with no significant non-synchronous components visible on the frequency spectra.

Not only are the magnitude of the two peaks corresponding to the critical speeds reduced, but a considerable reduction is evident across the speed range. As the vibrational amplitudes in the region of resonance are controlled by the amount of damping present, it would appear that reverse flow has dramatically increased the system damping. Both synchronous peaks appear to be shifted to a higher frequency as would be predicted by a single degree of freedom model with increased damping. A reduction in the system natural frequency might be expected due to the negative stiffening of the Bernoulli Effect (See Appendix A). However the experimental results would suggest that the increased damping dominates this movement of the peaks.

The above results show that a reverse flow of relatively low velocity considerably reduces the synchronous response of the rotor. The effect of surface roughness and radial clearance may lead to even greater reductions being possible. Results to date illustrate that reverse flow may be a feasible and reliable basis for the development of a damper to be used on industrial turbomachinery.

JET DAMPER DESIGN

The concept of a jet damper has been shown to work on a laboratory scale. However it is necessary to demonstrate that it is practical for a full size machine. If we consider a compressor of about 90 Kg. mass and a natural frequency of 80 Hz. then the shaft stiffness is around 23×10^6 N/m.

Assuming the following data for a jet damper:

R = 70mm
L = 50 mm
ρ = 1.22 Kg/m
$\bar{u}$ = 150 m/sec
C = 0.5 mm

then: $\frac{RL\,\rho\bar{u}^2}{2C} = 96000$ N/m

Therefore the direct stiffness coefficient (see Appendix A) is about 600,000 N/m which is 2.5% of the shaft stiffness.

The magnitude of the cross-stiffness depends on the value of the friction coefficient f. For the assumed conditions the Reynolds number based on mean flow $\bar{u}$ is 5100.

In this region the friction depends on the roughness and the majority of the data available is only concerned with smooth or moderately rough surfaces. If the surface is deliberately roughened then f could lie between 0.01 and 0.1. In this case the cross stiffness could be as large as 60,000 N/m. This is a significant fraction of the cross-stiffness magnitude associated with impeller and diffuser instability. Hence two or three dampers of these dimensions suitably located could act against forward whirl and so increase the stability margin.

If the friction force is too large (a combination of a number of damper jets with high velocity) there is a danger of promoting a backward whirl as discussed above. An arrangement which incorporates a degree of semi-active control would be necessary. A prime requirement would be fast acting valves controlling the nozzle flow. However this would be alleviated if the essential repetitive nature of the rotor motion was taken into account.

APPENDIX A

STIFFNESS COEFFICIENTS

The basic purpose of a number of tangential jets is to obtain a high circumferential flow acting against the forward rotation of the rotor. A simplified analysis assumes a constant circumferential flow in an annular channel at the periphery of a spinning rotor, figure 13. When the rotor is concentric with the stator the fluid friction is a pure torque due the mean flow u in the radial clearance C. However when the rotor is moved laterally the overall effect of the friction force acts at right angles to the displacement. When the direction of the jets is against the forward rotor motion the friction force acts against forward precession thus giving extra damping.

Direct Stiffness

With regard to Figure 13 a displacement δ in the positive x direction produces a normal pressure distrituion on the rotor surface which can be obtained using Bernoulli.

$$P + \tfrac{1}{2}\,\rho u^2 = H$$

Resolving pressures:

$$F_x = -RL\int_0^{2\pi} (H - \tfrac{1}{2}\,\rho u^2)\cos\theta\, d\theta \;,\quad F_y = -RL\int_0^{2\pi} (H - \tfrac{1}{2}\,\rho u^2)\sin\theta\, d\theta$$

Since $h = C\,(1 - n\cos\theta)$, $n = \delta/c$ and letting $u = \bar{u}\,C/h$

then by substitution and neglecting n^2 and higher powers:

$$F_x = RL\,\rho u^2\,\pi n \quad \text{and} \quad F_y = 0$$

Therefore direct stiffness coefficient $K_{xx} = F_x/\delta = RL\pi\, u^2\,\rho/C$

Defining non-dimensional stiffness $\bar{K}_{xx} = \dfrac{CK_{xx}}{\tfrac{1}{2}\,\rho u^2 RL}$

then $\bar{K}_{xx} = -2\pi$

Cross Stiffness

Referring to figure 13 for a displacement δ in the positive x direction the friction forces F_x and F_y are obtained by integrating the shear stress components round the rotor surface.

$$F_x = RL \int_0^{2\pi} \tau_0 \sin\theta \, d\theta \qquad F_y = -RL \int_0^{2\pi} \tau_0 \cos\theta \, d\theta$$

Now $\tau_0 = \frac{1}{2}\rho u^2 f$ where $f = 0.079R_e^{-0.25}$ assuming fully developed turbulent flow .

Reynolds Number $R_e = \bar{u}C/\nu$ or uh/ν locally

Now this particular friction coefficient is appropriate for smooth pipes in well developed turbulence. Friction relationships for rough sections of shaft in annular clearances will obviously need to be determined experimentally.

As before by substitution and neglecting n^2 and higher powers

$$F_x = 0 \quad , \quad F_y = -RL\rho\bar{u}^2 f \pi n$$

Since $K_{yx} = -F_y/\delta$ then $K_{yx} = RL\rho\bar{u}^2 \pi/C$

Defining non-dimensional stiffness $\bar{K}_{yx} = \dfrac{CK_{yx}}{\frac{1}{2}\rho\bar{u}^2RL}$

then $\bar{K}_{yx} = 2\pi f$

Following a similar analysis for a rotor displacement in the y direction the fluid forces can be summarised as

$$\begin{bmatrix} F_x \\ F_y \end{bmatrix} = \frac{\rho\bar{u}^2RL\pi}{C} \begin{bmatrix} 1 & f \\ -f & 1 \end{bmatrix} \begin{bmatrix} x \\ y \end{bmatrix}$$

APPENDIX B

ADDITIONAL MATERIAL PRESENTED AT WORKSHOP

The effect of reverse flow on response was further investigated by conducting run-down tests on the rotor. Figure 14 presents waterfall diagrams of a typical run-down for the cases of no flow and reverse flow caused by a plenum pressure of 41.4kN/m^2. It can be seen that a large reduction in the synchronous amplitude is obtained as a result of the reverse flow. These waterfall diagrams also show that no significant non-synchronous vibration components are present. The magnitudes of the synchronous components are plotted on figure 15 for each orthogonal direction.

The results generated by these run-down tests again illustrate that a damper based on reverse flow may indeed be a feasible means of reducing synchronous vibration amplitudes. The use of such a device during run-up or run-down through critical speeds is also clearly shown.

As a matter of interest, tests were conducted to investigate the effect of flow in the same direction as rotation on the response. Figure 16 displays the effect of a plenum pressure of 34.5kN/m^2 on the synchronous amplitude at a number of steady rotor speeds. It can be seen that while the response is slightly suppressed at the first peak, it is magnified at the second peak. There is also a shift to a higher frequency of both peaks. Figures 17 and 18 show the frequency response and synchronous amplitude during run-down. A small sub-synchronous component of unknown origin can be seen in the response. The overall effect of forward flow is obviously detrimental to the response of the rotor.

REFERENCES

1. Black, H.F.; Allaire, P.E. and Barrett, L.E.: Inlet Flow Swirl in Short Turbulent Annular Seal Dynamics. 9th International Conference in Fluid Sealing, BHRA Fluids Engineering, Leeuwenhorst, The Netherlands, April 1981.

2. Von Pragenau, G.L.: Damping Seals for Turbomachinery. NASA Technical Paper 1987, 1982

3. Hart, J.A. and Brown, R.D.: Laboratory Demonstration of Sub-Synchronous Rotor Vibration Induced by Fluid Friction. Paper accepted for publication International Journal of Mechanical Engineering Education.

4. Leong, Y.M.M.S. and Brown, R.D.: Experimental Investigations of Lateral Forces Induced by Flow through Model Labyrinth Glands. Proceedings 3rd Workshop on "Rotordynamic Instability Problems in High-Performance Turbomachinery". NASA CP 2338, May 1984.

5. Black, H.F.: Calculation of Forced Whirling and Stability of Centrifugal Pump Rotor Systems. Journal of Engineering for Industry, Trans. of the ASME. Paper No. 73-DET-131.

6. Brown, R.D.: Improvements in or relating to Dampening the Radial Vibration of Rotors. U.K. Patent Application, Patent Application No. 8421142, August 1984.

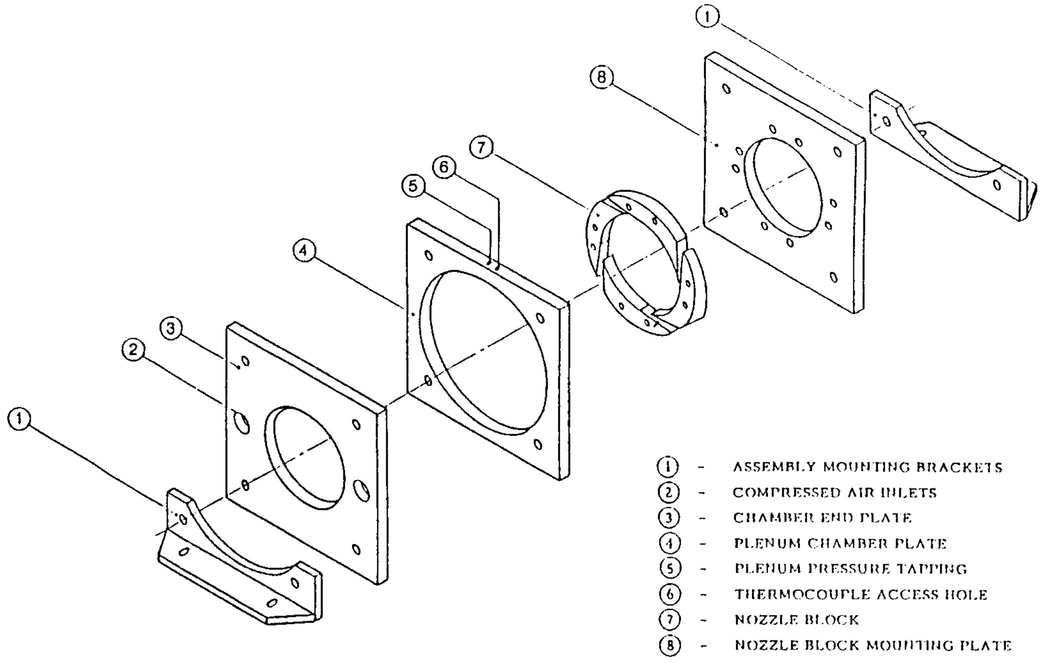
① - ASSEMBLY MOUNTING BRACKETS
② - COMPRESSED AIR INLETS
③ - CHAMBER END PLATE
④ - PLENUM CHAMBER PLATE
⑤ - PLENUM PRESSURE TAPPING
⑥ - THERMOCOUPLE ACCESS HOLE
⑦ - NOZZLE BLOCK
⑧ - NOZZLE BLOCK MOUNTING PLATE

Figure 1 Chamber and nozzle assembly

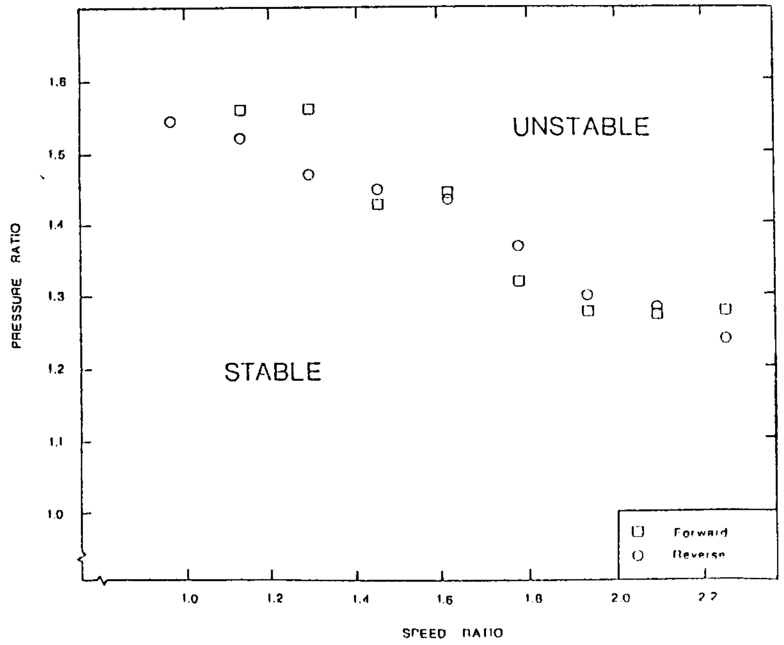

Figure 2 Rotor stability boundary

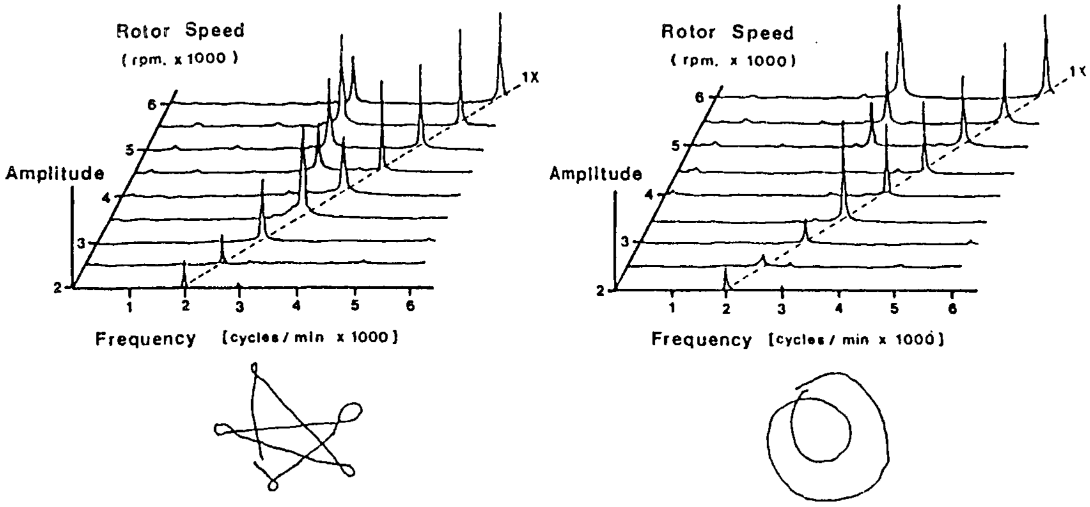

Typical Orbit at 5000 rpm.

Typical Orbit at 5000 rpm.

Figure 3 Response and orbit plots

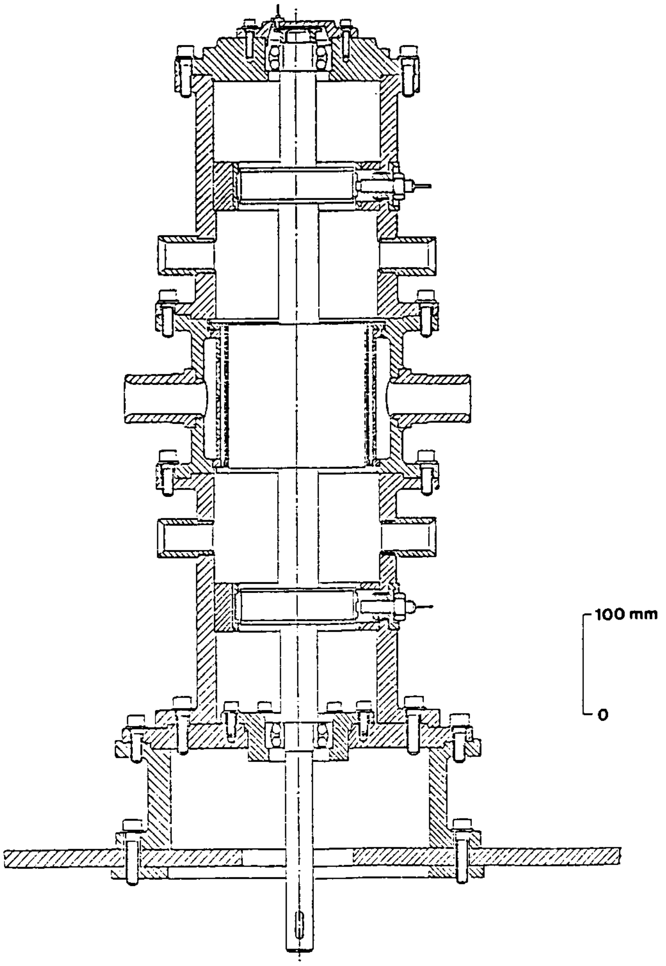

Figure 4 Sectioned assembly of test rig (main body)

ORIGINAL PAGE IS
OF POOR QUALITY

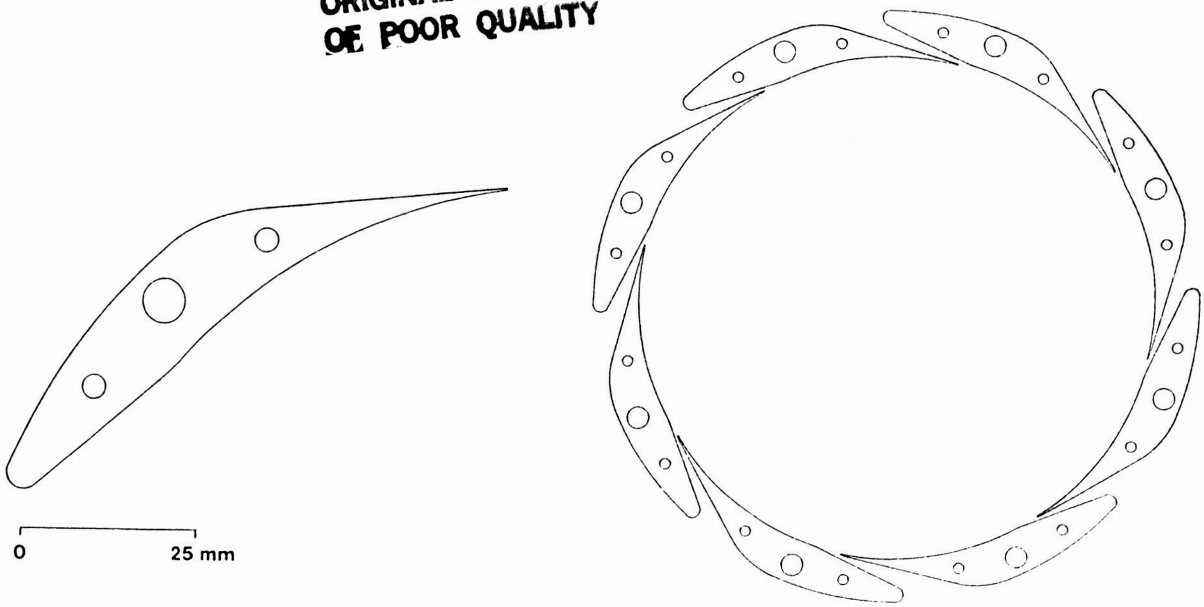

Figure 5 Nozzle block geometry and section through assembly

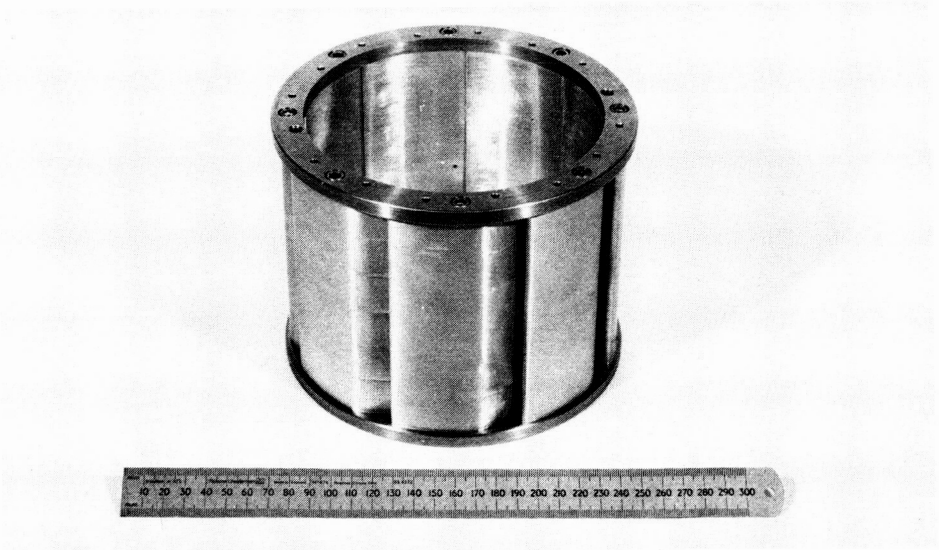

Figure 6 Built up nozzle assembly

ORIGINAL PAGE IS
OF POOR QUALITY

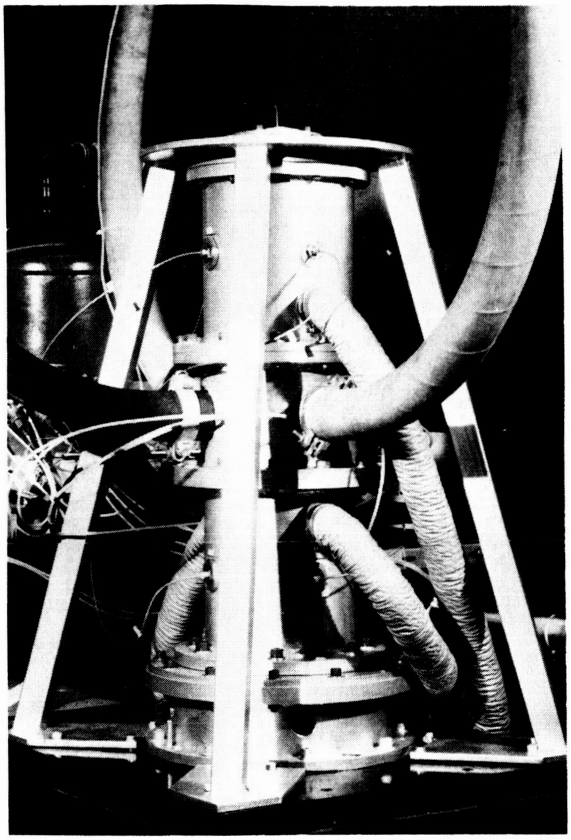

Figure 7 Main body of test rig

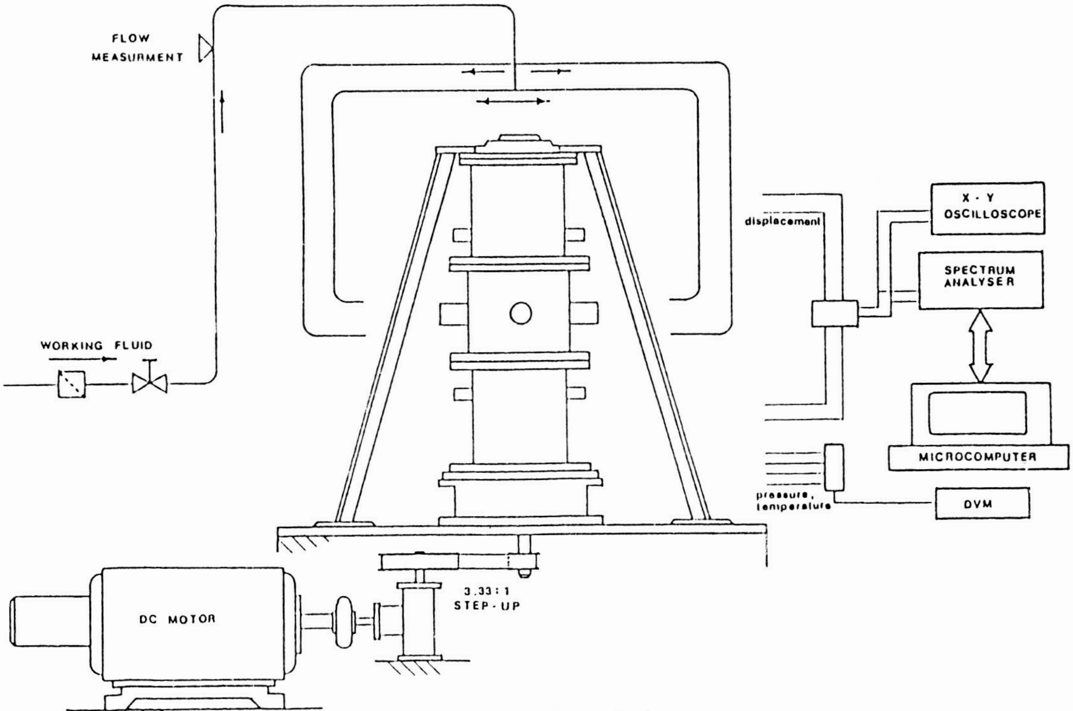
FLOW
MEASURMENT
WORKING FLUID
displacement
X - Y
OSCILLOSCOPE
SPECTRUM
ANALYSER
MICROCOMPUTER
pressure,
temperature
DVM
DC MOTOR
3.33:1
STEP-UP

Figure 8 Schematic layout of test rig and instrumentation

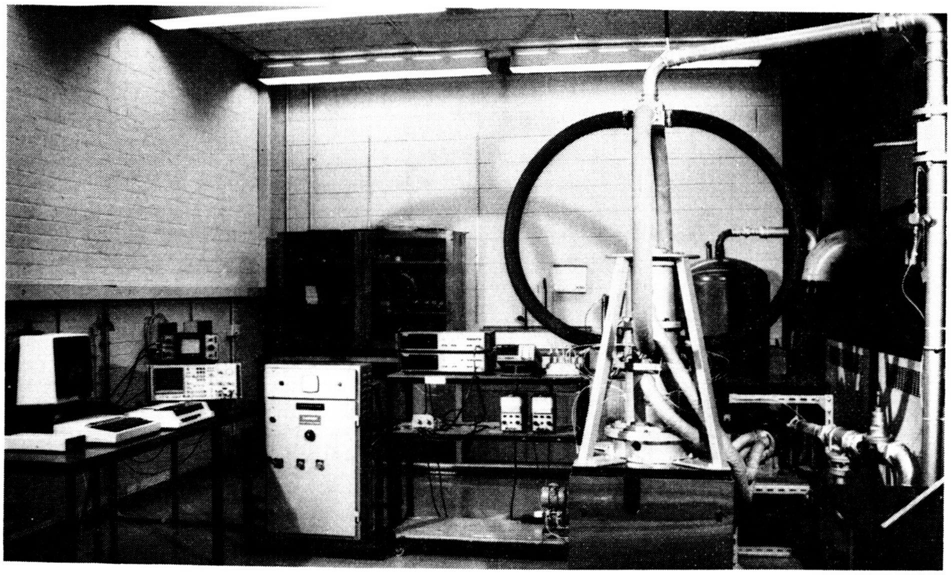

Figure 9 Experimental set-up

ORIGINAL PAGE IS OF POOR QUALITY

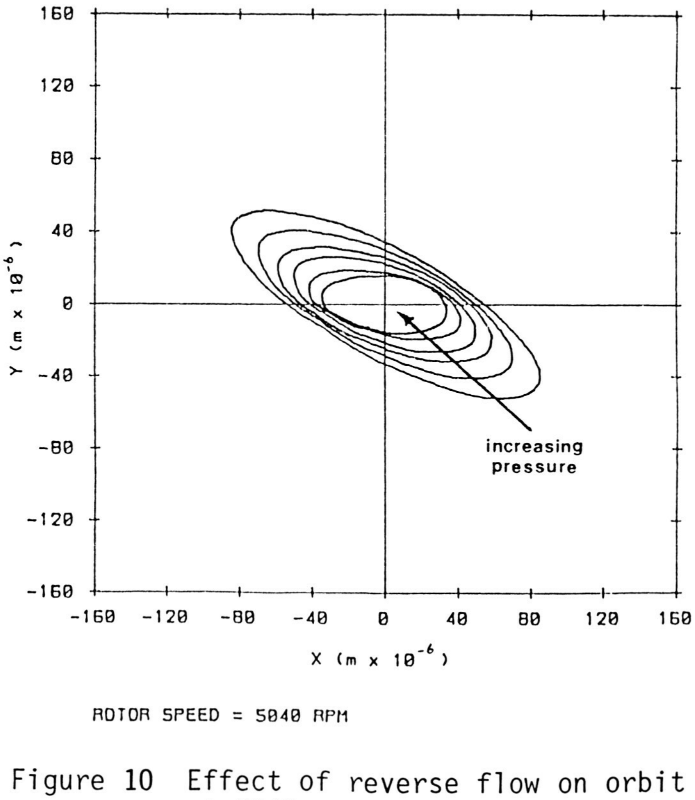

Figure 10 Effect of reverse flow on orbit at 5040 r.p.m.

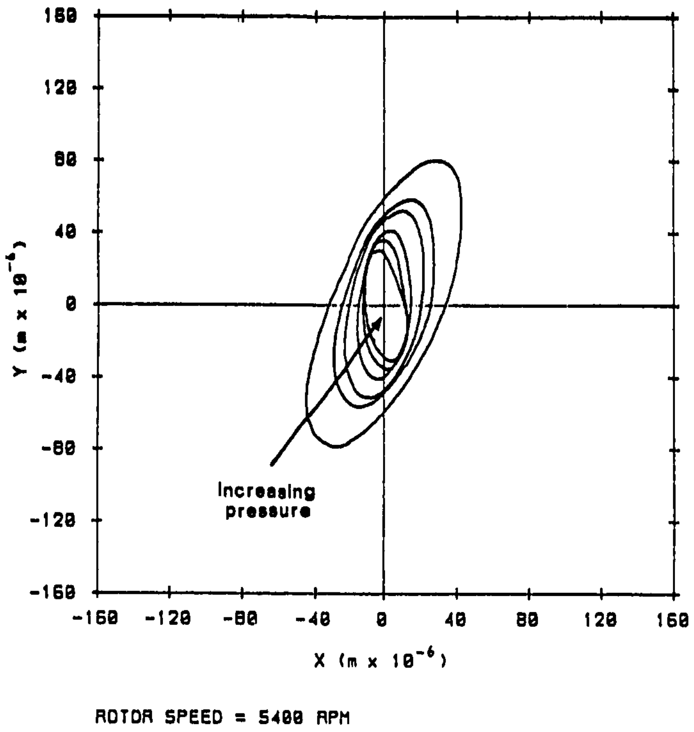

Figure 11 Effect of reverse flow on orbit at 5400 r.p.m.

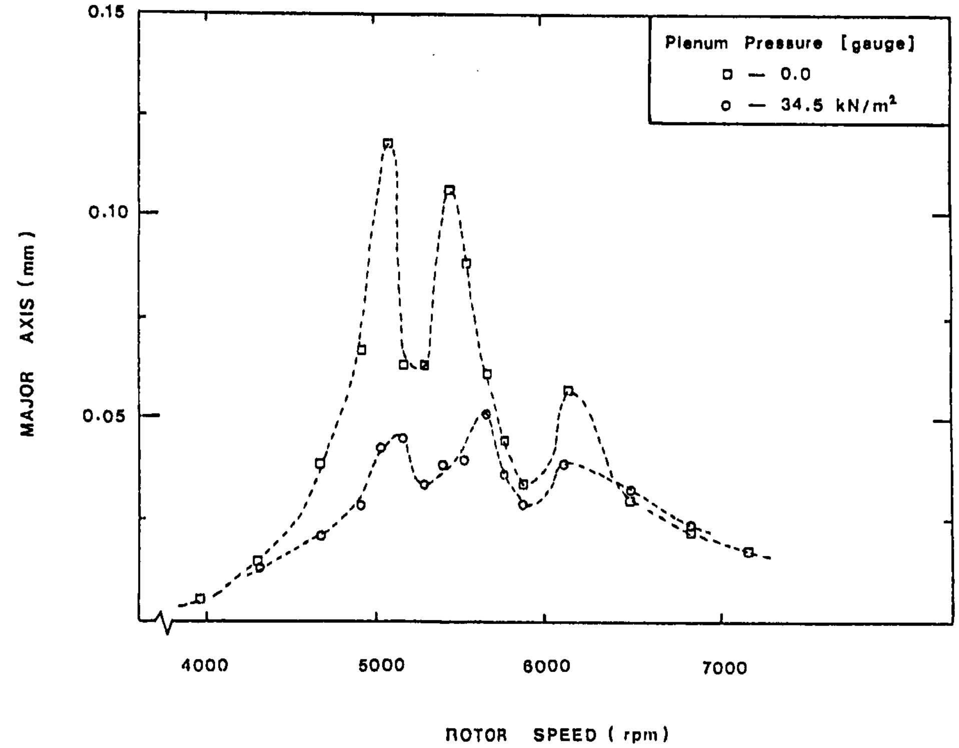

Figure 12 Rotor unbalance response, effect of reverse flow

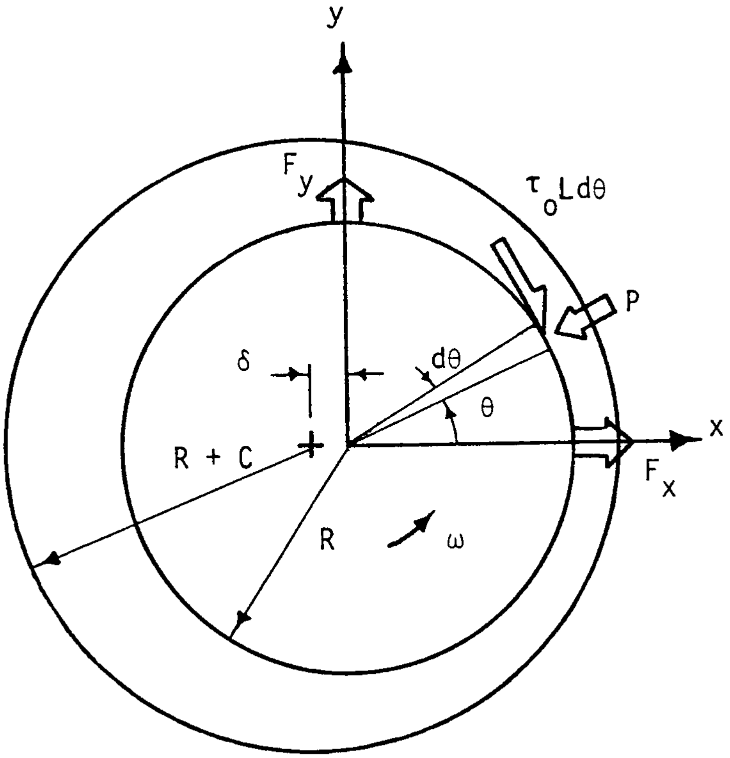
y
F_y
$\tau_o L d\theta$
P
δ
$d\theta$
θ
x
R + C
F_x
R
ω

Figure 13 Annular gap geometry

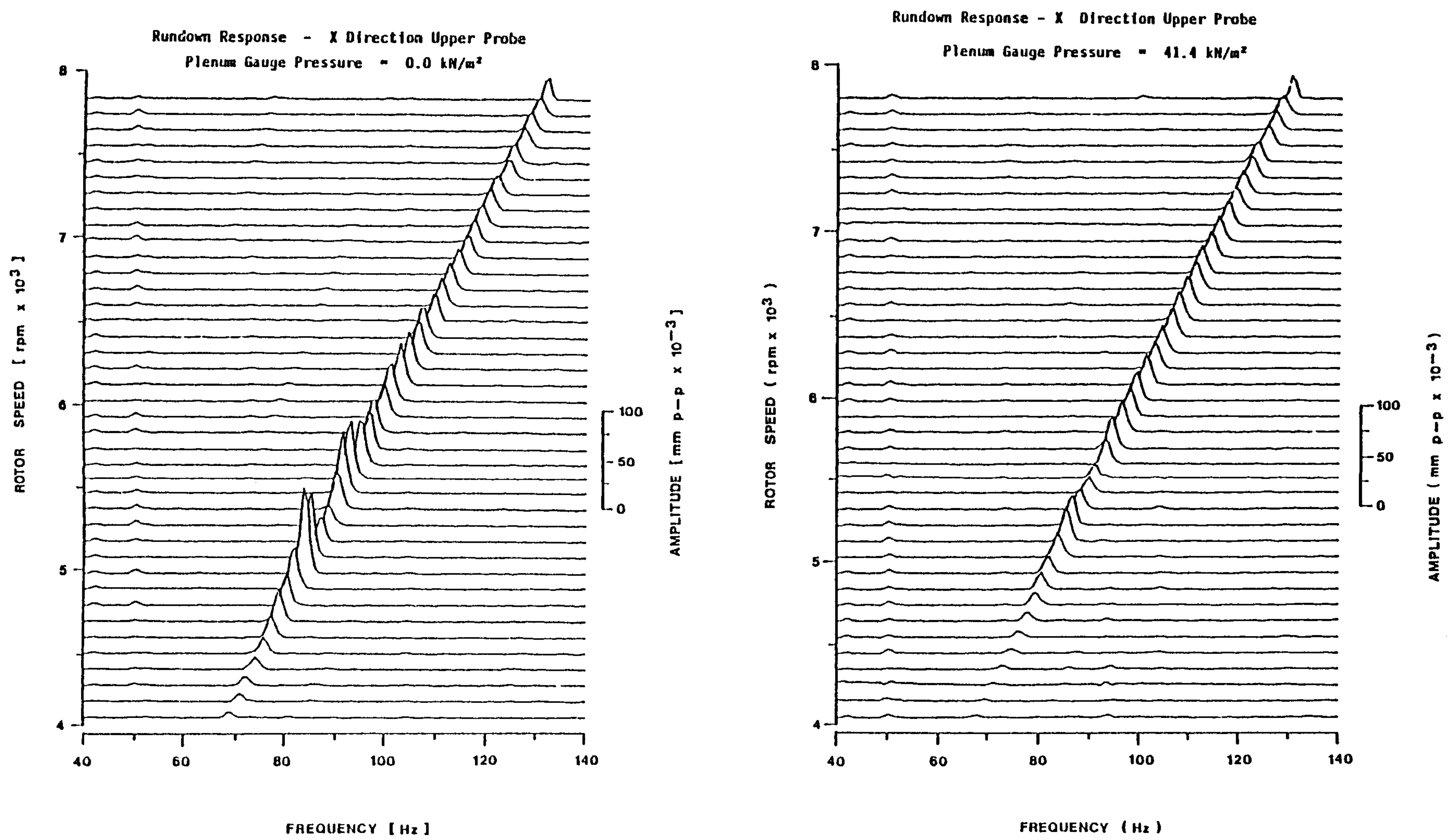

Figure 14 Rundown Response, effect of reverse flow

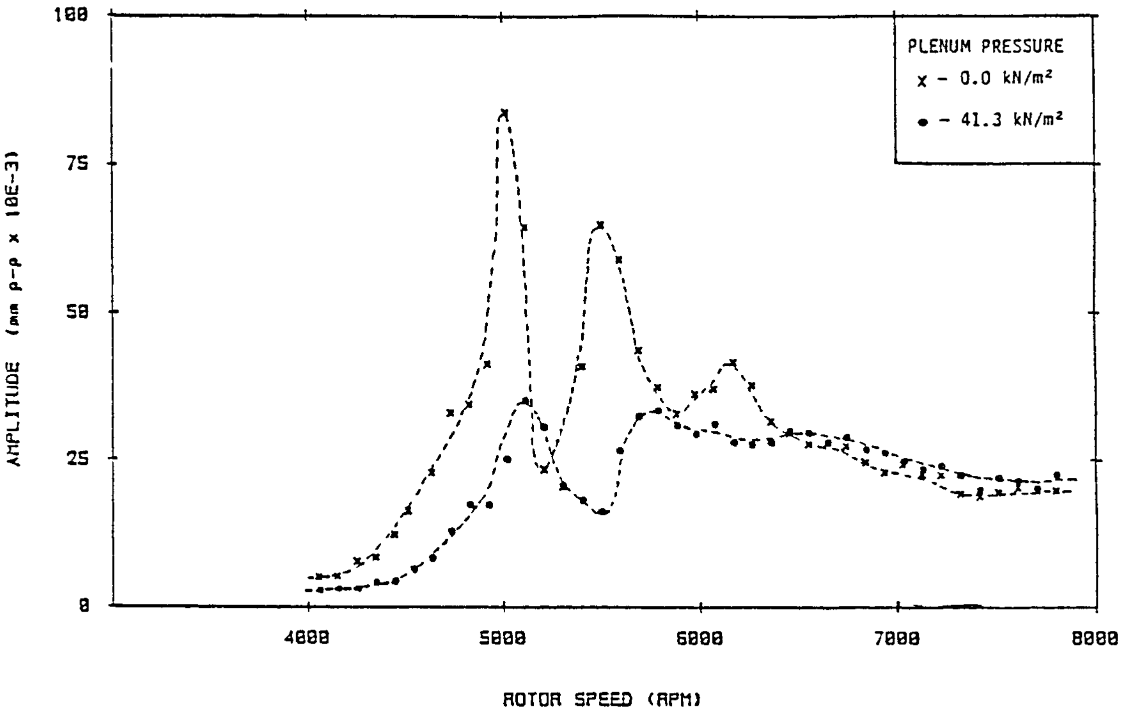
RUNDOWN RESPONSE - X DIRECTION (Upper Probe)

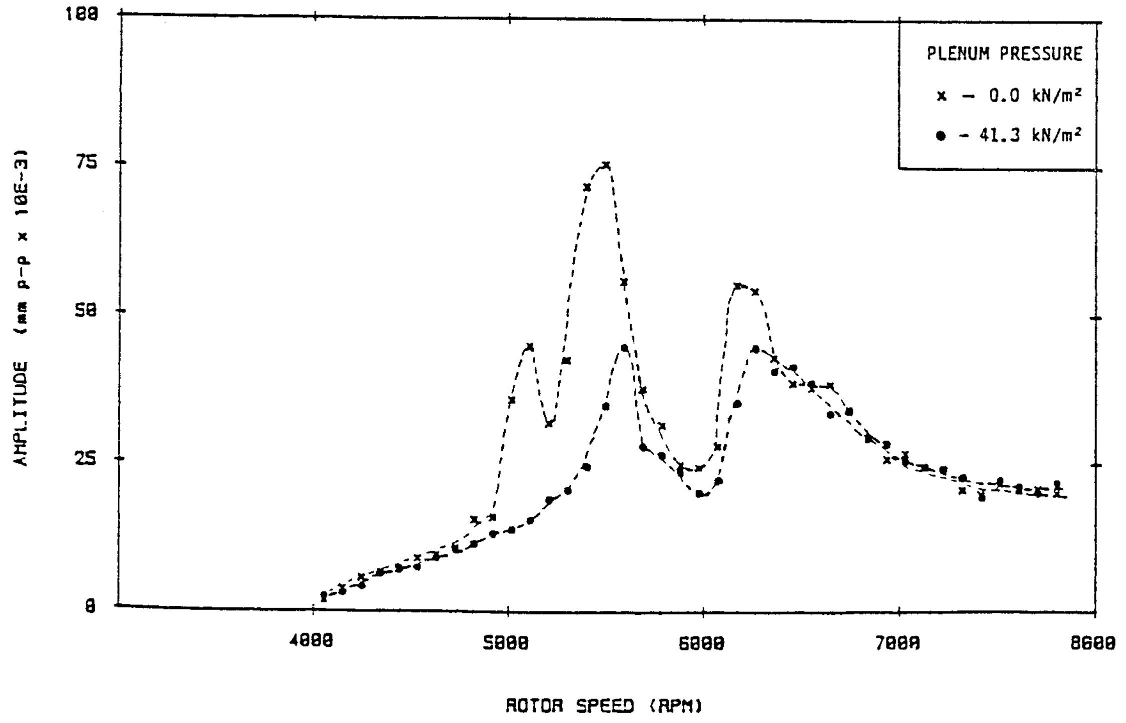
RUNDOWN RESPONSE - Y DIRECTION (Upper Probe)

Figure 15 Rundown Response, effect of reverse flow on Synchronous component

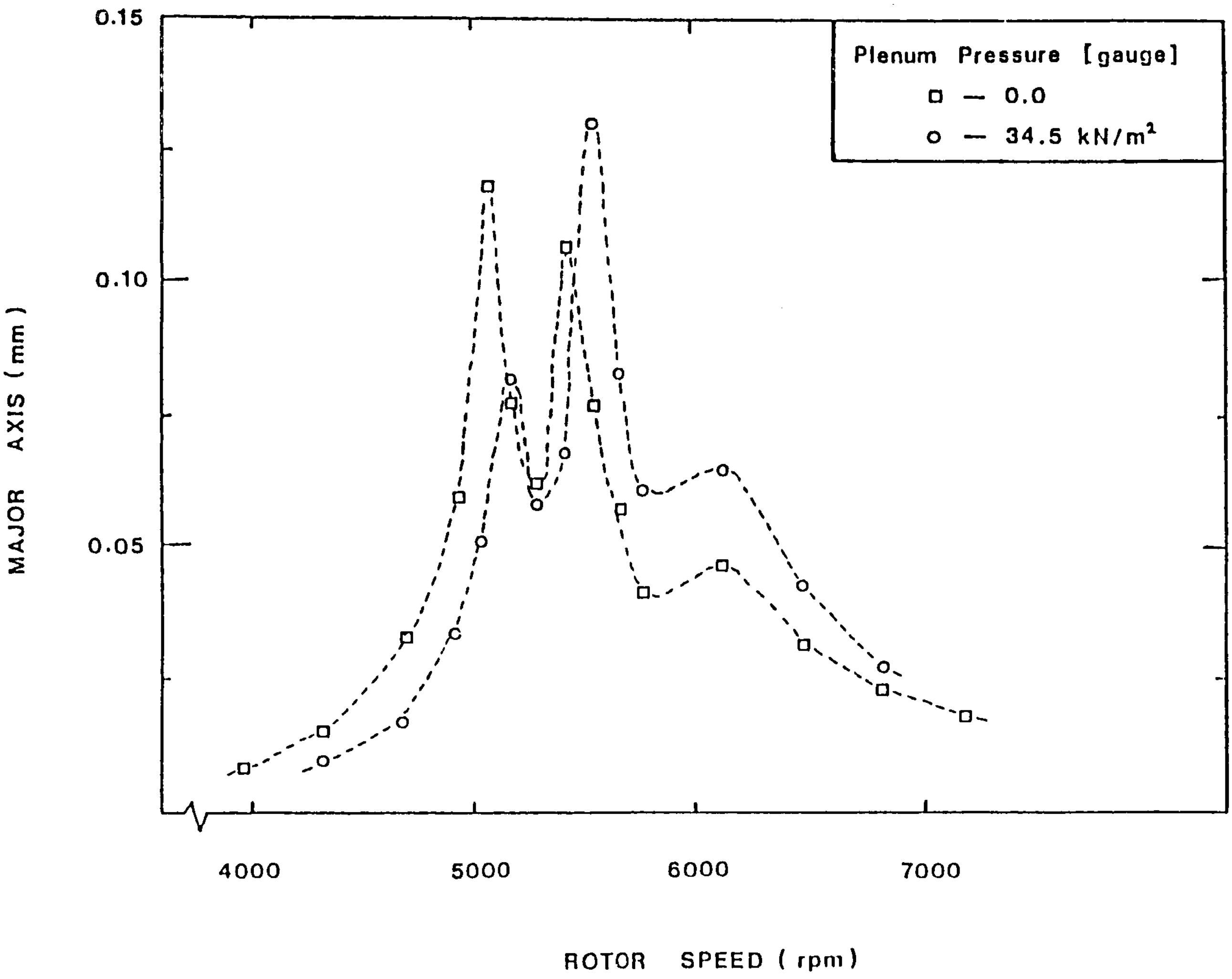

Figure 16 Rotor unbalance response, effect of forward flow

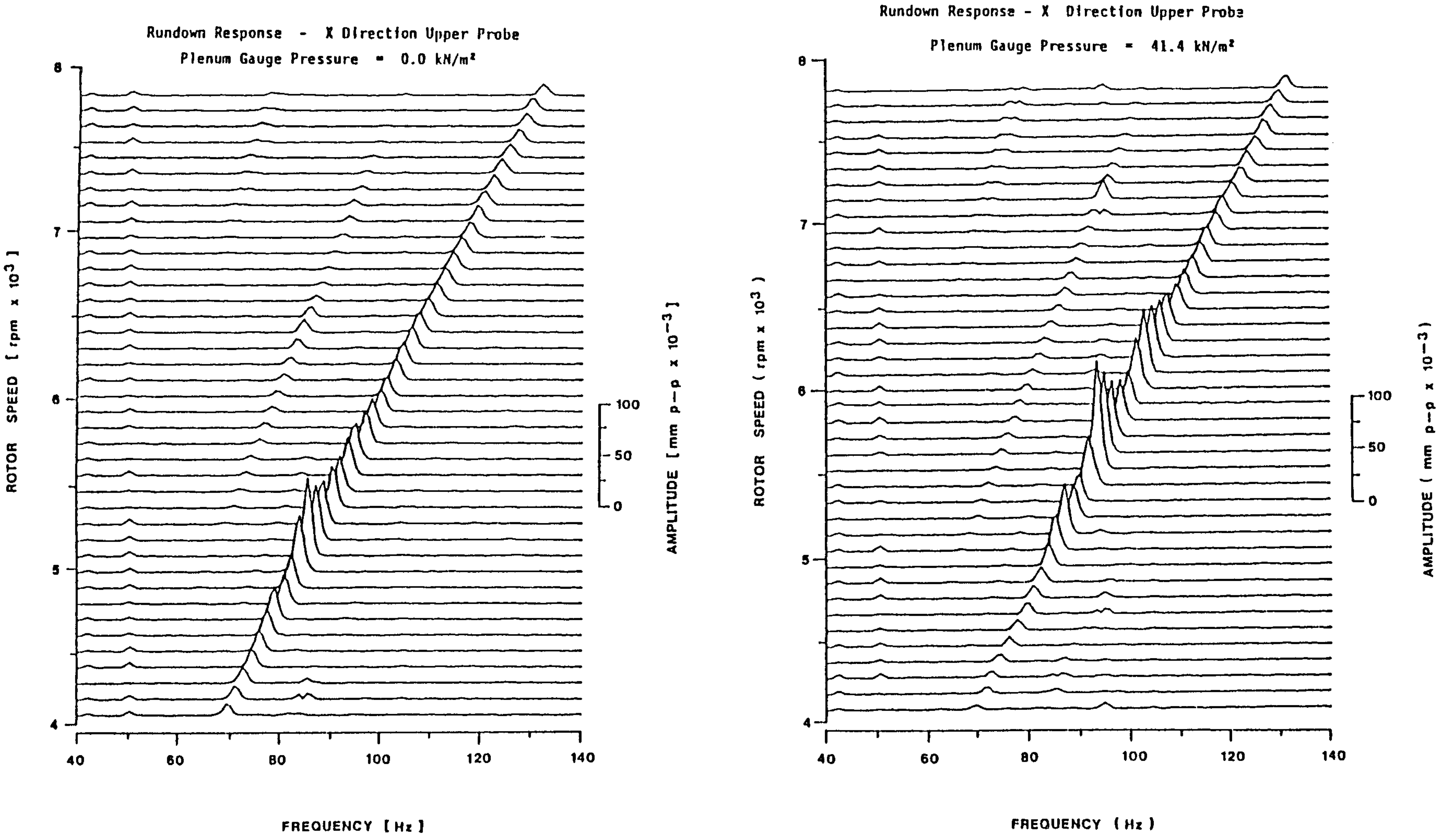

Figure 17 **Rundown Response, effect of forward flow**

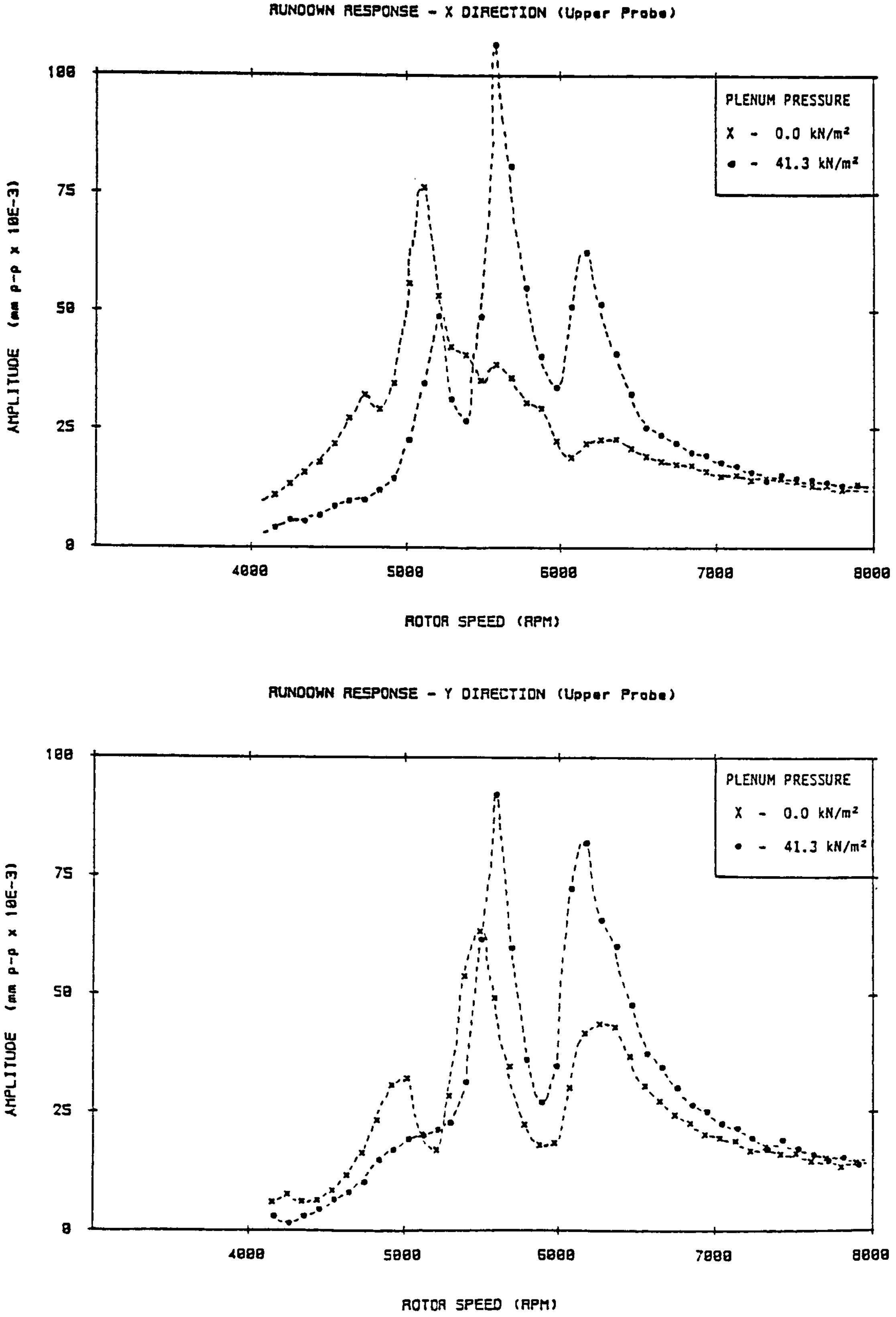

Figure 18 Rundown Response, effect of forward flow on Synchronous component

N87-22217

NON-LINEAR PERFORMANCE OF A THREE-BEARING ROTOR INCORPORATING A SQUEEZE-FILM DAMPER

R. Holmes and M. Dede
University of Southampton
Southampton, England

This paper is concerned with the non-linear vibration performance of a rigid rotor supported on three bearings, one being surrounded by a squeeze-film damper. This damper relies on the pressure built up in the squeeze film to help counteract external forces arising from unbalance and other effects. As a result a vibration orbit of a certain magnitude results.

Such vibration orbits illustrate features found in other non-linear systems, in particular sub-harmonic resonances and jump phenomena. Comparisons between theoretical predictions and experimental observations of these phenomena are made.

INTRODUCTION

The rotors of aero-engine gas turbines are often supported on three rolling-element bearings, the intermediate bearing usually providing a thrust capacity. The reason for this is that axial expansions take place from the thrust face and, being proportional to distances along the shaft to the ends of the rotor, these expansions do not impose such stringent demands on axial clearance at these ends as they would if the thrust bearing were at one extreme end of the rotor.

However, many aero-engine rotors are stiff, (running well below any flexural critical speed), and this means that problems of misalignment almost inevitably exist. The presence of a squeeze-film damper around one of the bearings helps considerably to alleviate these problems. However, since such dampers carry very little radial load under these circumstances, non-linear response to unbalance and sub-harmonic resonance with the casing flexibility are likely to occur.

Non-linear response manifests itself as persistence of synchronous vibration well beyond the undamped natural frequency of the assembly with a sudden jump-down to a lower vibration level at some higher speed. During engine run-down the lower vibration level persists until a speed lower than the original jump-down speed is reached, when a sudden jump-up will occur in the vibration amplitude. On occasion a jump-up with run-up has also been observed.

Sub-harmonic resonances occur due to the weak non-linearity offered by the squeeze-film damper, usually at rotational speeds equal to some integer multiple of the natural frequency of either of the bounce modes of the rigid rotor in its casing. These resonances can be just as damaging in their own way as the resonances which occur at speeds equal to these natural frequencies (that is when the integer is unity).

PRECEDING PAGE BLANK NOT FILMED

NOTATION

A	$\pi\eta R(\ell/c)^3/\sqrt{km}$
c	radial clearance of squeeze film
C_J	dynamic journal (or rotor) centre
C_{JS}	equilibrium position of journal centre
C_B	centre of oil container (bearing)
e	eccentricity of journal in bearing
F	dynamic force transmitted to engine frame
k	stiffness of parallel spring per land
$\bar{K}$	$k/m\omega^2$
ℓ	squeeze-film land length
m	journal mass per land
P_1, P_2	squeeze-film forces
P_c	rotating force vector per land
Q_c	$P_c/mc\omega^2 = u/c$
R	journal radius
T	transmissibility
t	time
u	displacement of rotor centre of mass from geometric centre due to addition of unbalance mass or loss of mass.
β	$\eta R\ell^3/mc^3\omega$
ε	dynamic eccentricity ratio (= e/c)
η	oil viscosity
ψ	dynamic attitude angle
ω	frequency of dynamic load
ω_n	$\sqrt{k/m}$
λ	$\eta\ell R^3/mc^2$
w_j	journal angular velocity
f, F, $h_{1,2}$	functions of

FEATURES OF THE PRESENT INVESTIGATION

To elucidate these problems, consider a stiff rotor in its flexible casing (Fig. 1a), in which the intermediate bearing is surrounded by a squeeze-film damper. To formulate ideas let the stiffnesses of bearing pedestals 1 and 2 be high compared with that of bearing 3. Further, assume that bearing 2 is held fairly centrally within its squeeze-film damper. Under these circumstances the equivalent system can be drawn as in Fig. 1b, in which m, k and b are equivalent properties decided by the dimensions of the original assembly. In particular, b will describe a non-linear damper.

During running any vibration is likely to produce a concentric orbit and the squeeze-film damper is not called upon to provide a static load-carrying capacity. Consequently, if the oil-supply pressure is of reasonable magnitude, the damper annulus remains full. The damper is often supplied with oil to a central circumferential oil groove which effectively separates the squeeze film axially into two parts or lands. Governing parameters are usually assumed to be appropriate to one land.

If the oil supply to the damper is sufficient for the squeeze-film to remain full and uncavitated a rotor vibration response curve such as (a) in Fig. 2 may be expected [1], [2]. If however cavitation occurs, this has the effect of introducing a stiffness term in the radial restoring force provided by the squeeze film and curves such as (b) are predicted [1]. The latter curve reveals a hardening-stiffness non-linearity and a deleterious influence on rotor response. At moderate frequencies three amplitude ratios are possible, the intermediate ratio being unstable, resulting in a jump-down with engine run-up and a jump-up with engine run-down. Such jumps have been reported in practical systems, as has the occasional jump-up with increase in engine speed. Fig. 2c shows the result of accelerating a rotor up to a speed of 3500 rev/min. and back over a period of 8.3 minutes. The degree of blackness depicts the strength of each harmonic from 1 x rotor speed to 3 x rotor speed, the other harmonics being practically non-existent. A predominant feature is the disappearance of the 2 x and 3 x harmonics after the jump-down on run-up and a reappearance of them after the jump-up on run-down. This suggests that the jumps form a demarcation between effectively linear and non-linear vibration and have been noted in test engines. Numerical investigations have also been carried out to test the possibility of sub-harmonic resonance arising [1]. Fig. 3 shows predicted sub-harmonic transients for a rotor-bearing assembly incorporating a squeeze-film offering fairly light damping. Subharmonic vibration occurs at speeds in the regions of two, three and four times the lower bounce mode critical speed. Such effects have also been reported in practical systems [3].

Very few experimental programs have been conducted to investigate problems of non-linear jumps and subharmonic resonances in rotor-bearing assemblies. The experiments of Nikolajsen et al [3] and Simandiri et al [4] are limited respectively to flexible transmission shafts with squeeze-film isolators and to a highly idealised test facility, showing little resemblance to an engine assembly.

RESPONSE CALCULATIONS

Fig. 4 shows in diagrammatic form the outer race of a rolling-element bearing within the oil container (the bearing pedestal), under the action of a restoring force $kc\varepsilon$ arising from the equivalent stiffness k of a parallel spring as in Fig. 1b. Vibration results from a dynamic force P_c due to some cause, such as unbalance. The amplitude of orbital motion depends upon $kc\varepsilon$, P_c, P_1 and P_2, the last two forces arising hydrodynamically from the squeeze-film. Any gravity load on the squeeze-film is assumed to be effectively neutralised by the parallel spring.

The equations governing the concentric motion of the shaft centre are then,

$$P_c \cos(\omega t - \psi) - P_1 - kc\varepsilon = -mc\varepsilon\omega^2$$

and ... (1)

$$P_c \sin(\omega t - \psi) - P_2 = 0$$

where ε is the dynamic eccentricity ratio resulting from unbalance. In equations (1) the squeeze-film forces, P_1 and P_2, can be shown from hydrodynamic considerations, to be given, for concentric motion, by

$$P_1 = 0$$

and

$$P_2 = \frac{\pi\eta R\ell^3}{c^2(1-\varepsilon^2)^{3/2}} \cdot \varepsilon\omega \qquad \ldots (2)$$

Equations (1) may be made non-dimensional by dividing by $mc\omega^2$ to give

$$Q_c \cos(\omega t - \psi) = -\varepsilon(1 - \bar{K})$$

and ... (3)

$$Q_c \sin(\omega t - \psi) = \frac{\pi\eta R}{m\omega} \left(\frac{\ell}{c}\right)^3 \cdot \frac{\varepsilon}{(1-\varepsilon^2)^{3/2}}$$

where $\bar{K} = k/m\omega^2 = (\omega/\omega_n)^{-2}$, and $Q_c = P_c/mc\omega^2$.

If P_c arises due to mass unbalance mu, then $P_c = mu\omega^2$ and $Q_c = u/c$.

Putting $\beta = \dfrac{\eta R(\ell/c)^3}{m\omega}$, equations (3) may be re-written to give

$$\frac{u}{c} \cos(\omega t - \psi) = (\bar{K} - 1)\varepsilon$$

and ... (4)

$$\frac{u}{c} \sin(\omega t - \psi) = \pi\beta\varepsilon/(1-\varepsilon^2)^{3/2}$$

Hence, after some manipulation, we obtain

$$\cdot \left[\frac{u}{c}\right]^2 \frac{(1-\varepsilon^2)^3}{\varepsilon^2} \cdot \left[\frac{\omega}{\omega_n}\right]^4 = A^2 \left[\frac{\omega}{\omega_n}\right]^2 + \left[1 - \left[\frac{\omega}{\omega_n}\right]^2\right]^2 (1-\varepsilon^2)^3 \qquad \ldots (5)$$

where

$$A = \frac{\pi\eta R}{\sqrt{km}} \left(\frac{\ell}{c}\right)^3$$

and

$$\omega_n = \sqrt{k/m}$$

Assuming a fairly typical value of $A = 0.0^7$, say, a family of response curves of $\dfrac{\varepsilon}{u/c}$ versus ω/ω_n may be constructed for different values of u/c (Fig.5a).

From these curves an indication can be obtained of the amount of vibration ε, suffered by the rotor in the symmetric bounce mode, a common mode of vibration in many rotating assemblies. Of equal importance is the dynamic force F transmitted to the engine frame. Bearing in mind that P_1 is zero, the force F is given by

$$F = [P_2^2 + (kc\varepsilon)^2]^{1/2} \qquad \ldots (6)$$

and is best expressed as a ratio (the transmissibility) of the unbalance force P_c. This transmissibility T is given by

$$T = F/P_c = \frac{F/mc\omega^2}{u/c} \qquad \ldots (7)$$

From equations (2), (6) and (7) we obtain

$$T^2 = \left[\frac{\pi^2\beta^2\varepsilon^2}{(1-\varepsilon^2)^3} + \bar{k}^2\varepsilon^2 \right] /(u/c)^2$$

Now from equation (4),

$$\frac{\pi^2\beta^2\varepsilon^2}{(1-\varepsilon^2)^3} = (u/c)^2 - \varepsilon^2\, [\bar{k} - 1]^2$$

and so finally

$$T^2 = 1 + \left(\frac{\varepsilon}{u/c}\right)^2 \left[\frac{2}{(\omega/\omega_n)^2} - 1\right]$$

Again, assuming a value of A of 0.07, a family of curves showing the dependence of T on ω/ω_n for different values of u/c is shown in Fig. 5b.

An inspection of Figs. 5a and 5b shows that both $\varepsilon/(u/c)$ and the transmissibility T depend upon u/c. This is expected since the system is essentially non-linear. Also, only for ω/ω_n above $\sqrt{2}$, is T less than unity. This speed ratio should thus be made to correspond to the lower limit of normal operation of the engine, when it can readily be seen from Figs 3a and 3b that a low value of u/c is desirable on three counts - low vibration amplitude, low transmissibility and low transmitted force.

Now suppose that the supply pressure is insufficient to maintain a positive pressure in areas of the squeeze film where the boundary surfaces are instantaneously separating. For the sake of simplicity assume that as a result the squeeze film becomes half cavitated. It may then be shown that P_2 is halved and that P_1 is no longer zero, being given by

$$P_1 = \frac{2\eta R l^3\omega}{c^2} \cdot \frac{\varepsilon^2}{(1-\varepsilon^2)^2}$$

Hence, for circular concentric whirl, we have the following equations which correspond to equations (4) for the uncavitated case

$$\frac{u}{c}\cos(\omega t - \psi) = (\bar{k} - 1)\varepsilon + \frac{2\beta\varepsilon^2}{(1-\varepsilon^2)^2}$$

$$\frac{u}{c}\sin(\omega t - \psi) = \frac{\pi\beta}{2} \cdot \frac{\varepsilon}{(1-\varepsilon^2)^{3/2}} \qquad \ldots (8)$$

in which $\beta = A(\bar{k})^{\frac{1}{2}}/\pi$.

Hence $$\left(\frac{u}{c}\right)^2 = \beta^2 \left[\frac{\pi^2\varepsilon^2}{4(1-\varepsilon^2)^3} + \frac{4\varepsilon^4}{(1-\varepsilon^2)^4} \right] + \varepsilon^2(\bar{k} - 1)^2 + \frac{4\varepsilon^3}{(1-\varepsilon^2)^2}\,\beta(\bar{k} - 1) \qquad \ldots (9)$$

In this case

$$T^2 = \frac{\varepsilon^2}{(u/c)^2} \left[\beta^2\left(\frac{\pi^2}{4(1-\varepsilon^2)^3} + \frac{4\varepsilon^2}{(1-\varepsilon^2)^4} \right) + \bar{k}^2 + \frac{4\beta\varepsilon\bar{k}}{(1-\varepsilon^2)^2} \right]$$

Using equation (9) this may be rewritten as

$$T^2 = 1 + \left(\frac{\varepsilon}{u/c}\right)^2 \left[\frac{4\varepsilon\beta}{(1-\varepsilon^2)^2} + 2\bar{K} - 1\right]$$

in which $\bar{K} = k/m\omega^2 = \left(\frac{\omega}{\omega_n}\right)^{-2}$

The effect of cavitation is shown in Figs. 5c, d, which reveal a deleterious influence on vibration and on transmissibility. The distortions in the response curves of Fig. 5c compared with what one would expect from a linear system are responsible for the so-called jump phenomenon. At high frequencies three amplitude ratios are possible, the intermediate one being unstable.

STABILITY CONSIDERATIONS

In most applications of a journal bearing we are concerned with the stability of a static equilibrium position e.g. [6]. In the present work it is necessary to consider the stability of a circular concentric equilibrium orbit. The two cases can be compared as shown in Fig. 6a, b. It may be shown [6] that for perturbations from a static equilibrium position the hydrodynamic forces P_1' and P_2' of a journal bearing oil film are given by

$$P_{1,2}' = \lambda\omega_j(1 - 2\dot{\alpha}/\omega_j)f_{1,2}\left(\varepsilon, \frac{\dot{\varepsilon}/\omega_j}{1 - 2\dot{\alpha}/\omega_j}\right)$$

With little loss of accuracy [7] we may write them as

$$P_1' = \dot{\varepsilon}F_1(\varepsilon) \pm \left(\frac{\omega_j}{2} - \dot{\alpha}\right) h_1(\varepsilon)$$

$$P_2' = \dot{\varepsilon}F_2(\varepsilon) \pm \left(\frac{\omega_j}{2} - \dot{\alpha}\right) h_2(\varepsilon)$$

in which the positive sign relates to the squeeze damper and its force directions (Fig. 6b) and the negative sign to the journal bearing and its force directions (Fig. 6a). Now in the case of the squeeze damper, if the journal centre is moving on a circular concentric orbit at angular velocity $\dot{\alpha}_s$, then $\omega_j = 0$ and $\dot{\alpha} = \omega + \dot{\alpha}_s$.

Hence we finally have for the journal bearing

$$P_1' = \dot{\varepsilon}F_1(\varepsilon) - \left(\frac{\omega_j}{2} - \dot{\alpha}\right) h_1(\varepsilon)$$

$$P_2' = \dot{\varepsilon}F_2(\varepsilon) - \left(\frac{\omega_j}{2} - \dot{\alpha}\right) h_2(\varepsilon)$$

while for the squeeze-film damper

$$P_1' = \dot{\varepsilon}F_1(\varepsilon) - (\dot{\alpha}_s + \omega)\, h_1(\varepsilon)$$

$$P_2' = \dot{\varepsilon}F_2(\varepsilon) - (\dot{\alpha}_s + \omega) h_2(\varepsilon)$$

Now for a journal bearing, for $\dot{\alpha} \ll \omega_j$ and neglecting second order terms

$$dP_r = dP_1' - P_2' d\alpha = F_1 d\dot{\varepsilon} - \frac{\omega_j}{2}\frac{\partial h_1}{\partial \varepsilon} d\varepsilon + h_1 d\dot{\alpha} + \frac{\omega_j}{2} h_2 d\alpha$$

and

$$dP_s = dP_2' + P_1' d\alpha = F_2 d\dot{\varepsilon} - \frac{\omega_j}{2}\frac{\partial h_2}{\partial \varepsilon} d\varepsilon + h_2 d\dot{\alpha} - \frac{\omega_j}{2} h_1\, d\alpha$$

while for a squeeze damper, for $\dot{\alpha}_s \ll \omega$

$$
\begin{aligned}
dP_r &= dP_1' + P_2' d\alpha_s = F_1 d\dot{\varepsilon} - \omega \frac{\partial h_1}{\partial \varepsilon} d\varepsilon - h_1 d\dot{\alpha}_s - \omega h_2 \, d\alpha_s \\
dP_s &= -dP_2' + P_1' \, d\alpha_s = -F_2 d\dot{\varepsilon} + \omega \frac{\partial h_2}{\partial \varepsilon} d\varepsilon + h_2 \, d\dot{\alpha}_s - \omega h_1 \, d\alpha_s
\end{aligned}
\qquad \ldots (10)
$$

Now r, s correspond to the ε and α directions, respectively. Thus for the squeeze damper the direct damping terms are equal and of the same sign as for the journal bearing; the cross damping terms are equal but of opposite sign; the direct stiffness terms are twice the values and of the same sign, and the cross stiffness terms are twice the values and of opposite sign.

The effect of adding an extra radial force $kc\varepsilon$ due to the retainer spring is to increase dP_r and dP_s respectively in equations (10) by $kcd\varepsilon$ and $kc \, \varepsilon d\alpha_s$. This in turn has the effect of adding the stiffness k to each of the direct stiffness terms in equations (10). Applying these new equations to perturbations of a rotor from a concentric circular orbit indicates that part of the response curve is indeed unstable.

SUBHARMONIC RESONANCE

Figure 3 shows subharmonic transients, which could persist if some negative damping were present to counteract the positive damping from the squeeze film damper. Such negative damping could emanate from any journal bearings present [3] or from internal shaft friction, say.

TEST RESULTS

To create a realistic engine configuration, a two-bearing test facility used in a previous research programme [5] has been adapted to form a three-bearing rigid rotor incorporating the essential features of a medium-sized aero-engine assembly.It is not uncommon in gas turbine rotor vibration for an antisymmetric rigid-rotor mode to exhibit a node near one of the rolling-element bearings. With such an application in mind, the test rig shown in Fig. 7 was used for the investigation of the squeeze-film damper, 1, at one of its three rolling-elements, 2. The self-aligning bearing, 3, constituted a pivot about which an antisymmetric (i.e. conical) mode of vibration would occur, when the rotor, 4, was acted upon by a force arising from rotation of the unbalance mass, 5. Flexible bars, 6, simulated the pedestal flexibility of an actual engine. The flexible bars were screwed into a heavy foundation block, 8, which represented ground. The squeeze-film dimensions sere set by the outer diameter of the rolling bearing (136 mm), and damper land (9 mm) and its radial clearance (0.216 mm). Oil of 6 cp viscosity was supplied to the damper via three supply holes, 9, and a central circumferential groove. End plates were attached at the ends of the outer element of the damper to afford some sealing. Proximity vibration pick-ups were used to measure the vibration of the shaft relative to the pedestal and relative to ground, and strain gauges were provided on the flexible bars from which transmitted forces were recorded.

Tests indicated the existence of jump phenomena during run-up and run-down, when the squeeze-film damper ran at low supply pressure (Fig. 8a), but no such jumps when it can with a higher supply pressure (Fig. 8b). These results agree with the trends predicted by Figs. 2b and 2a and by Fig 5c, d.

Figs. 9a, b show further comparisons, this time between the predicted and the measured horizontal components of force transmitted to ground, as measured by strain gauges fixed to the flexible bars 6 of the rig (Fig. 7). The same trends can be seen in both, the one exception being the continuous fairly steep rise in transmitted force with speed for the largest unbalance (1.9 gr-m) in Fig 9b. Fig.10a shows a predicted waterfall diagram which illustrates vibration occurring at engine-orders half, one and two. These engine orders are encouraged by such factors as transients or slight eccentricity from the centre of the squeeze-film damper. The rig's natural frequency component at 33Hz is however present at all rotor speeds, and, in particular, is excited by the half-order when the rotor speed is 66 rev/min. The jump-down in the 1EO is clearly discernible and coincides with the disappearance of the 2EO. As such it agrees with the experimental observations illustrated in Fig. 2c.

Finally, Fig. 10b shows an experimental waterfall diagram, for comparison with Fig.10a. Common features can be clearly seen, such as the strong first engine order, the ½EO exciting the natural frequency of 33 Hz at a rotor speed of 66 Hz and the 2EO, with its disappearance after the jump in the 1EO. Owing to the scale adopted to bring out the ½EO and 2EO, the 1EO was everywhere extremely large, but the jump certainly occurred at about 48 Hz as can be verified from Fig. 9b. The response at 84 Hz illustrates another natural frequency of the experimental rig which was not catered for in the theoretical model .

CONCLUSIONS

This paper has considered the case of a flexibly supported three-bearing rigid rotor utilising a squeeze-film damper at one of its bearings. It has shown that the assembly can be regarded for analysis as a parallel combination of spring and non-linear damper supporting the rotor mass. As a result, subharmonic resonances and jump phenomena are predicted.

A test facility has been described, which displays such phenomena and these have been presented in the form of response curves and a waterfall diagram. The frequency content in these shows close resemblance to theoretical predictions presented in the same form.

Finally, a relationship has been established between the linear stiffness and damping coefficients of a rotating-journal bearing for perturbation from an equilibrium position and the corresponding coefficients of a non-rotating squeeze-film damper for perturbation from an equilibrium orbit.

REFERENCES

[1] HOLMES, R. "The control of engine vibration using squeeze-film dampers". Trans ASME Journal of Engineering for Power July 1983 Vol 105 pp 525-529.

[2] MOHAN, S and HAHN, E.J. "Design of Squeeze film damper supports for rigid rotors" Trans. ASME Journal of Engineering for Industry Aug. 1974 pp 976-982.

[3] NIKOLAJSEN, J.L. and HOLMES, R. "Investigation of squeeze-film isolators for the vibration control of a flexible rotor" Jnl.Mech.Eng.Sci. Vol.21 No.4 1979 pp 247-252.

[4] SIMANDIRI, S. and HAHN, E.J. "Experimental evaluation of the predicted behaviour of squeeze-film bearing supported rigid rotors". Jnl. Mech. Eng.Sci. Vol.21 No. 6 1979 pp 439-457,

[5] HOLMES, R. and DOGAN,M. "Investigation of a rotor-bearing assembly incorporating a squeeze-film damper bearing" Jnl. Mech. Eng.Sci. Vol.24 No. 3 1982 pp 129-137.

[6] PINKUS, O and STERNLIGHT, B. "Theory of hydrodynamic lubrication 1961, 267 (McGraw-Hill, New York).

[7] HOLMES, R. "Instability phenomena due to circular bearing oil-films". Jnl.Mech.Eng.Sci. Vol.8, No. 4, 1966, pp419-425.

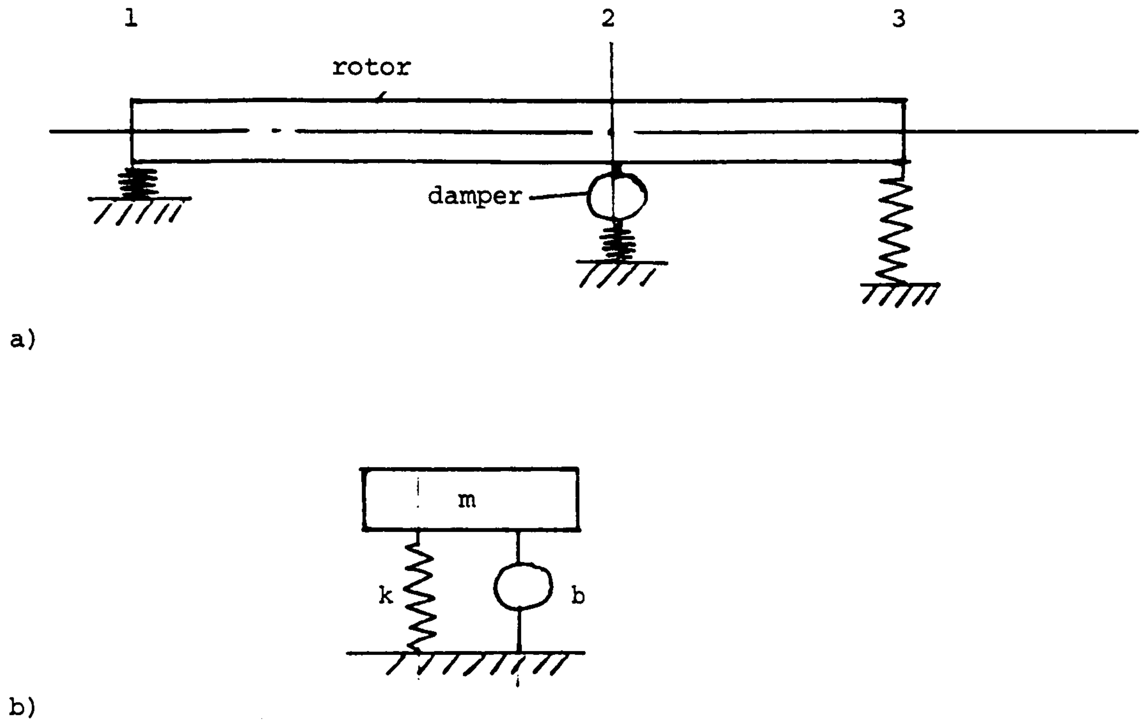

Figure 1. - Rotor and equivalent system.

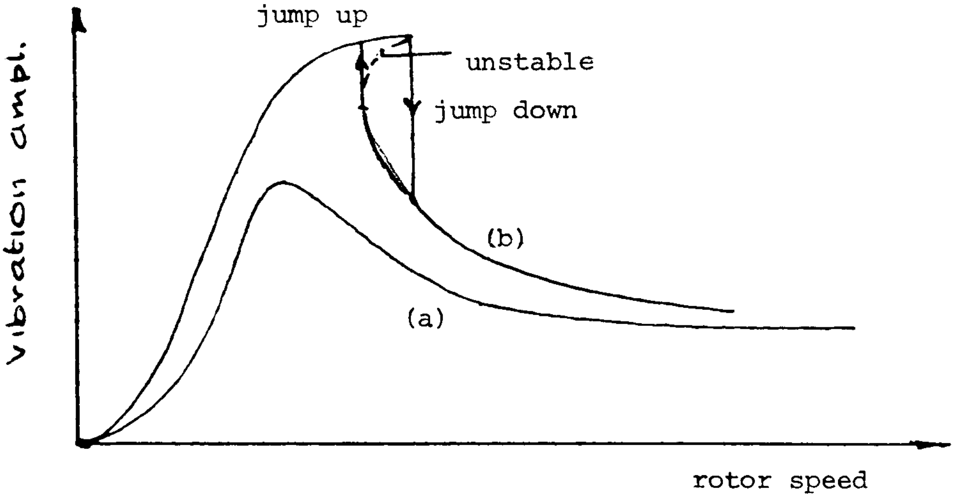

(a) Uncavitated rotor vibration response curve.
(b) Cavitated rotor vibration response curve.

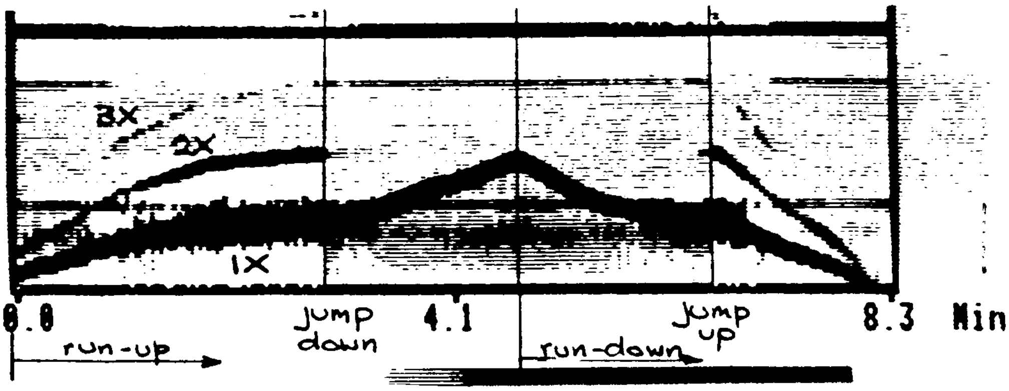

(c) Frequency diagram.

Figure 2. - Response curves and frequency diagram.

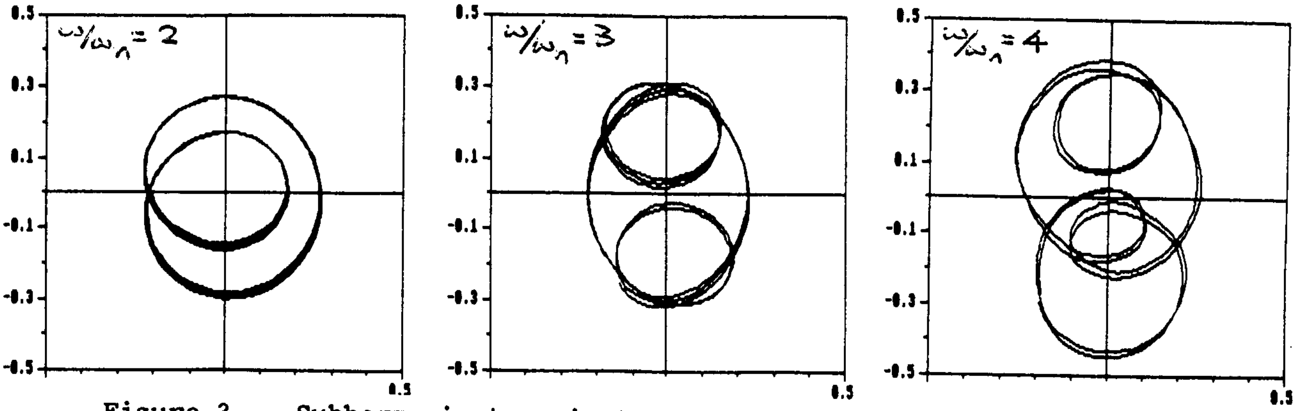

Figure 3. - Subharmonic transients; A = 0.014, u/c = 0.091; π film.

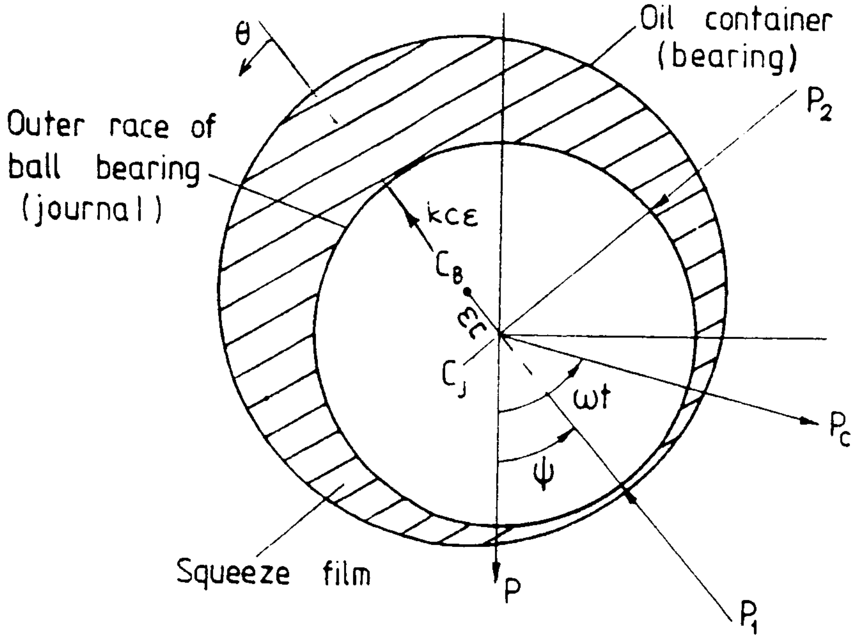
θ
Oil container
(bearing)
P_2
Outer race of
ball bearing
(journal)
kcε
C_B
εc
C_J
ωt
ψ
P_c
Squeeze film
P
P_1

Figure 4. - Damper assembly.

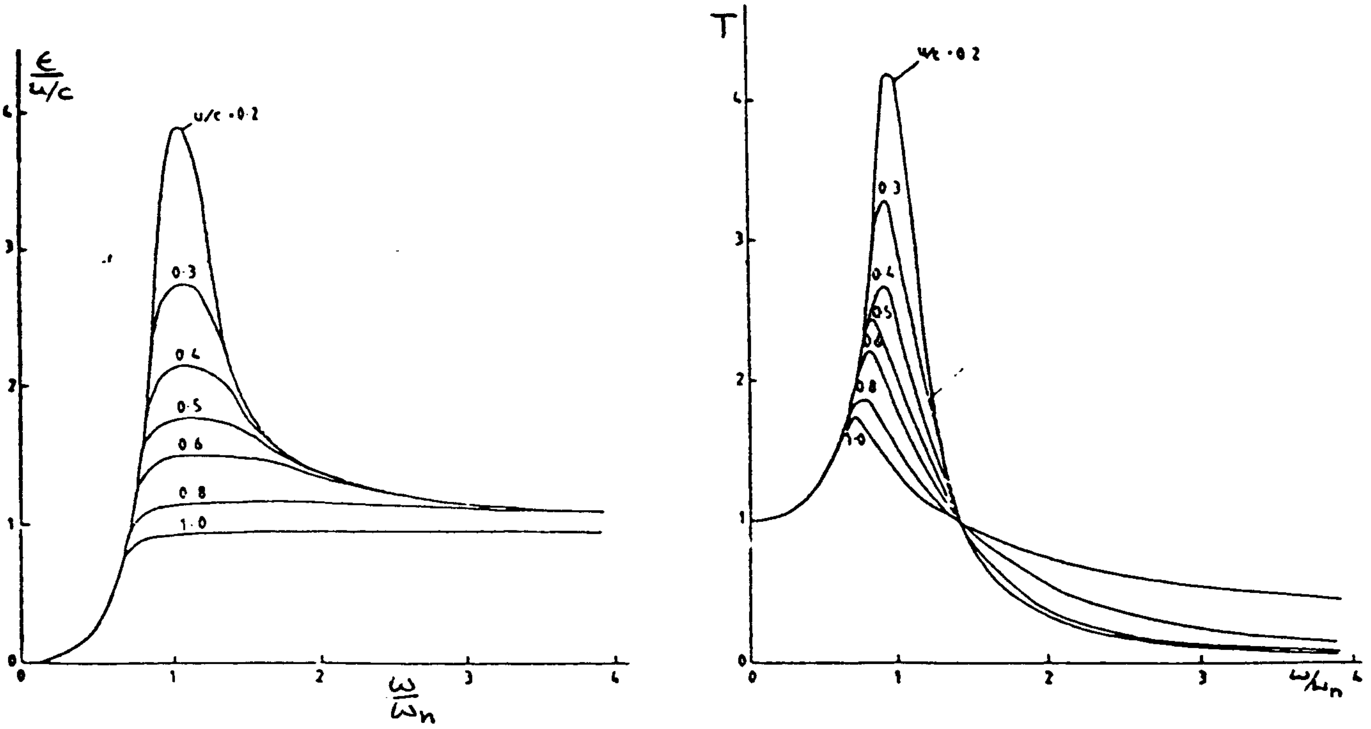

(a) Full-film frequency response.

(b) Full-film transmissibility.

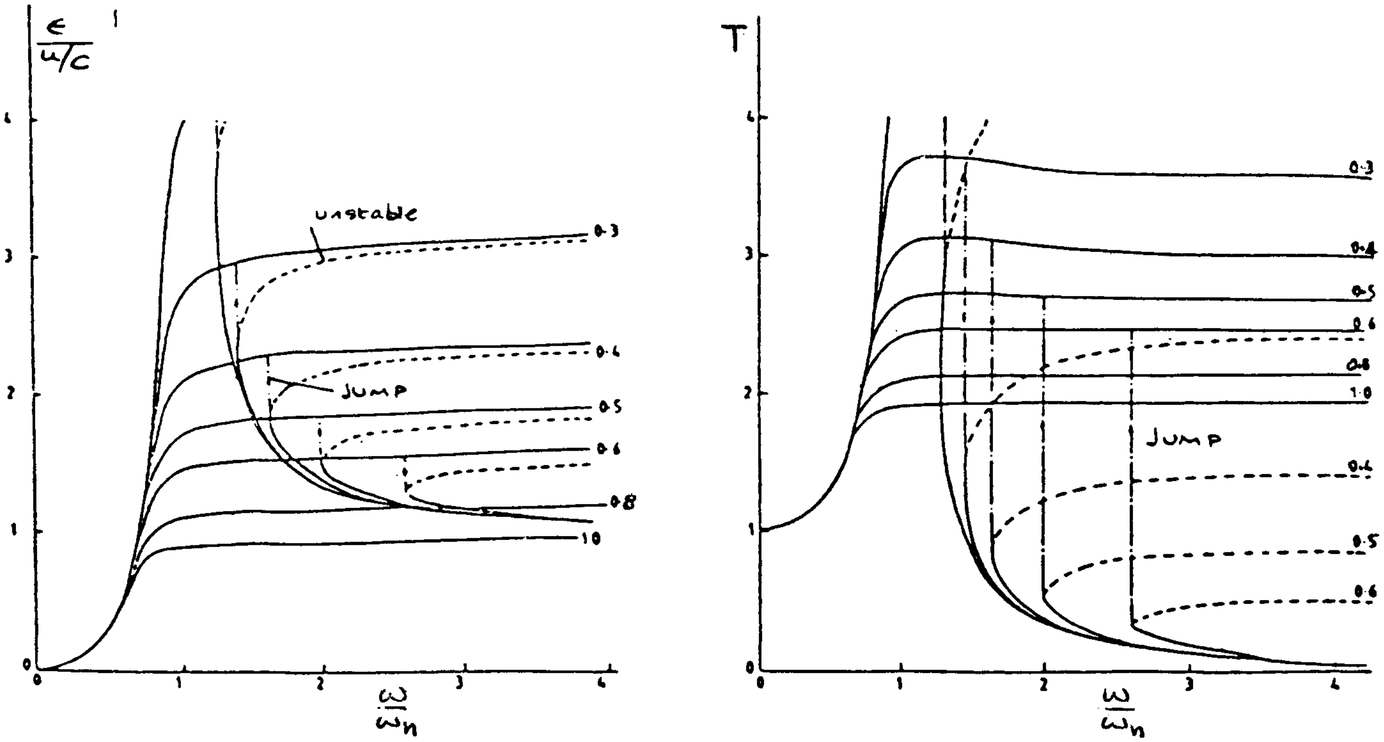

(c) Half-film frequency response.

(d) Half-film transmissibility.

Figure 5. - Response curves.

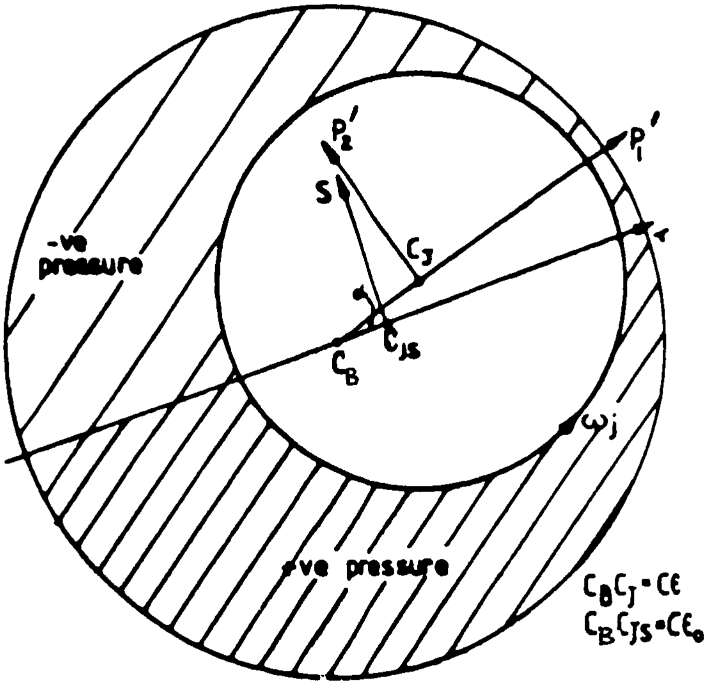
P_2'
S
P_1'
r
-ve pressure
C_J
α
C_{JS}
C_B
ω_j
+ve pressure
$C_BC_J = C\varepsilon$
$C_BC_{JS} = C\varepsilon_0$

(a) Journal bearing; r and s are stationary coordinates.

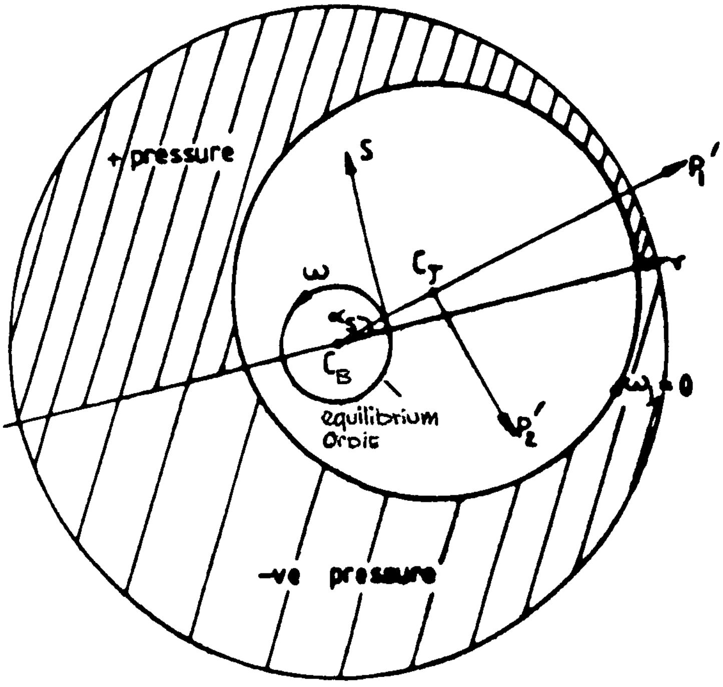
+ pressure
S
R_1'
ω
C_J
r
α_s
C_B
equilibrium orbit
P_2'
$\omega_J = 0$
-ve pressure

(b) Squeeze-film damper; r and s are rotating coordinates.

Figure 6. - Comparison of journal bearing with squeeze-film damper.

ORIGINAL PAGE IS
OF POOR QUALITY

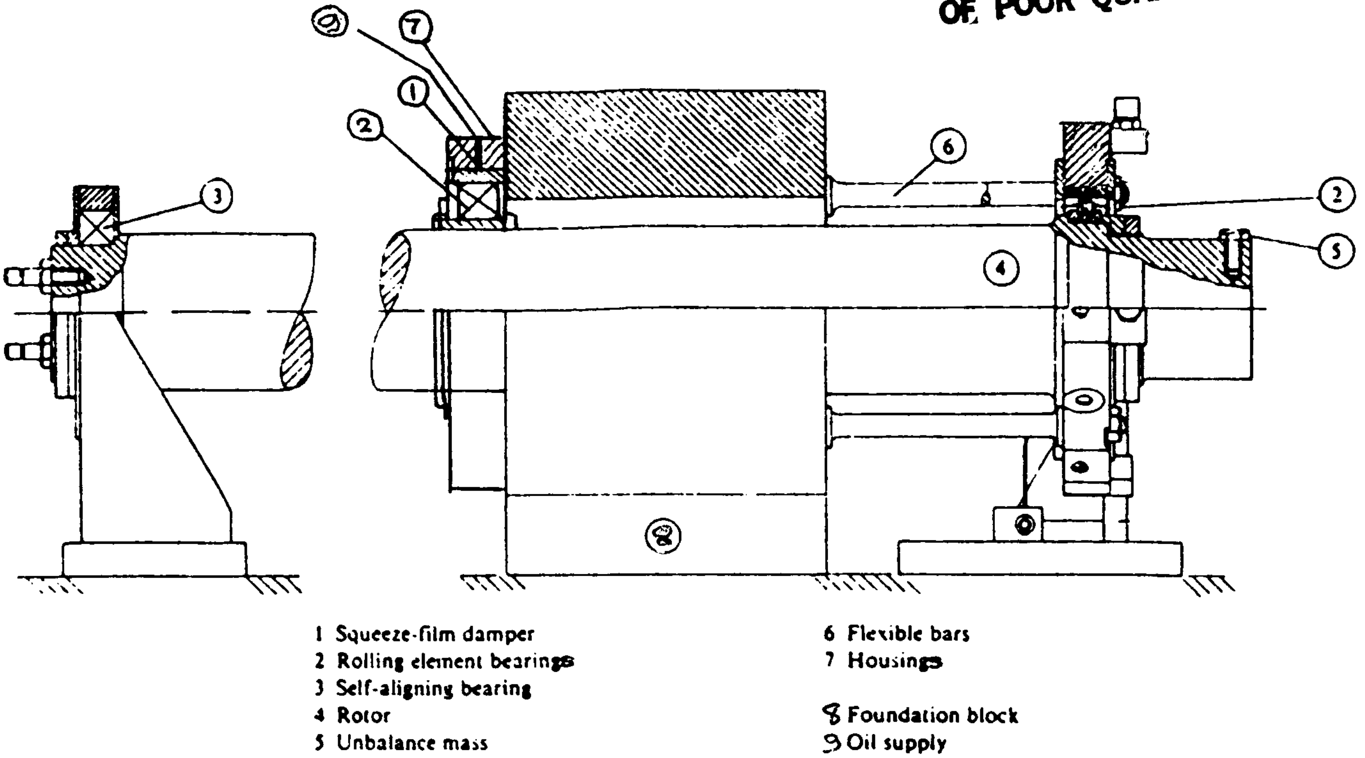
⑨
⑦
①
②
③
⑥
②
⑤
④
⑧
1 Squeeze-film damper
2 Rolling element bearings
3 Self-aligning bearing
4 Rotor
5 Unbalance mass
6 Flexible bars
7 Housings
8 Foundation block
9 Oil supply

Figure 7. - Experimental rig.

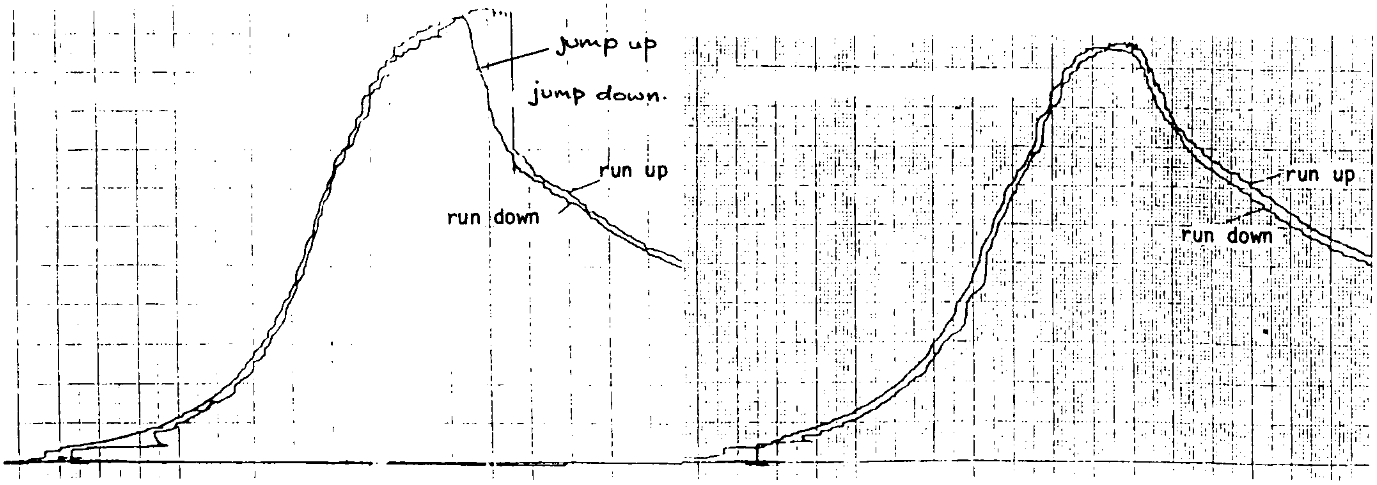

(a) Supply pressure, 2 lbf/in^2.

(b) Supply pressure, 10 lbf/in^2.

Figure 8. - Responses.

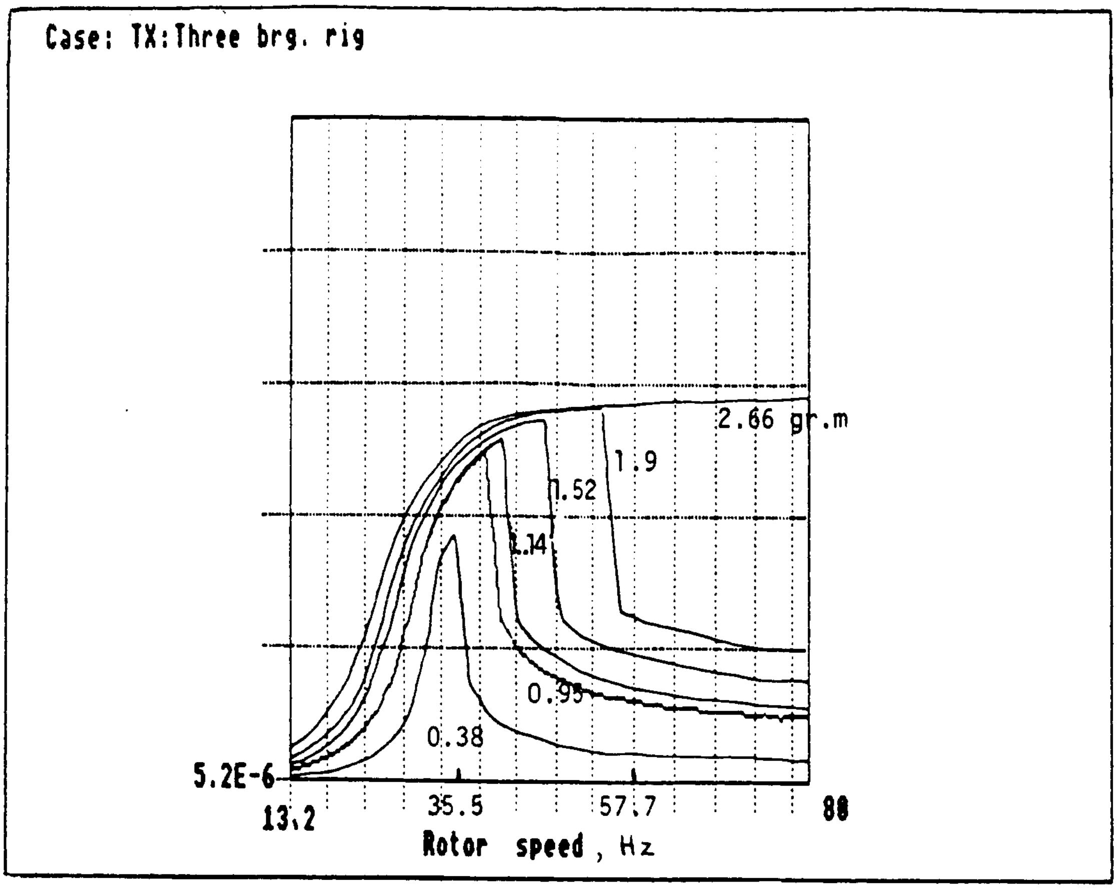

(a) Predicted responses.

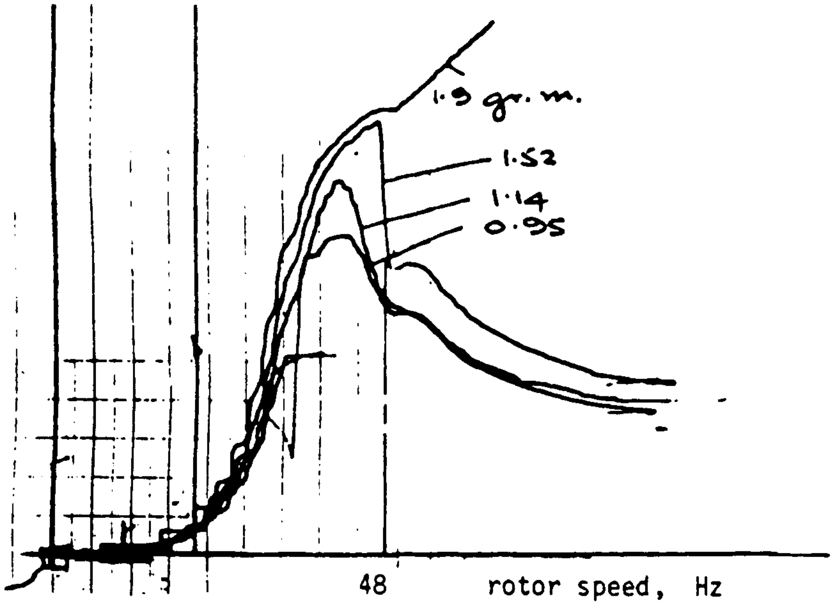

(b) Measured responses.

Figure 9. - Horizontal components of force transmitted to ground.

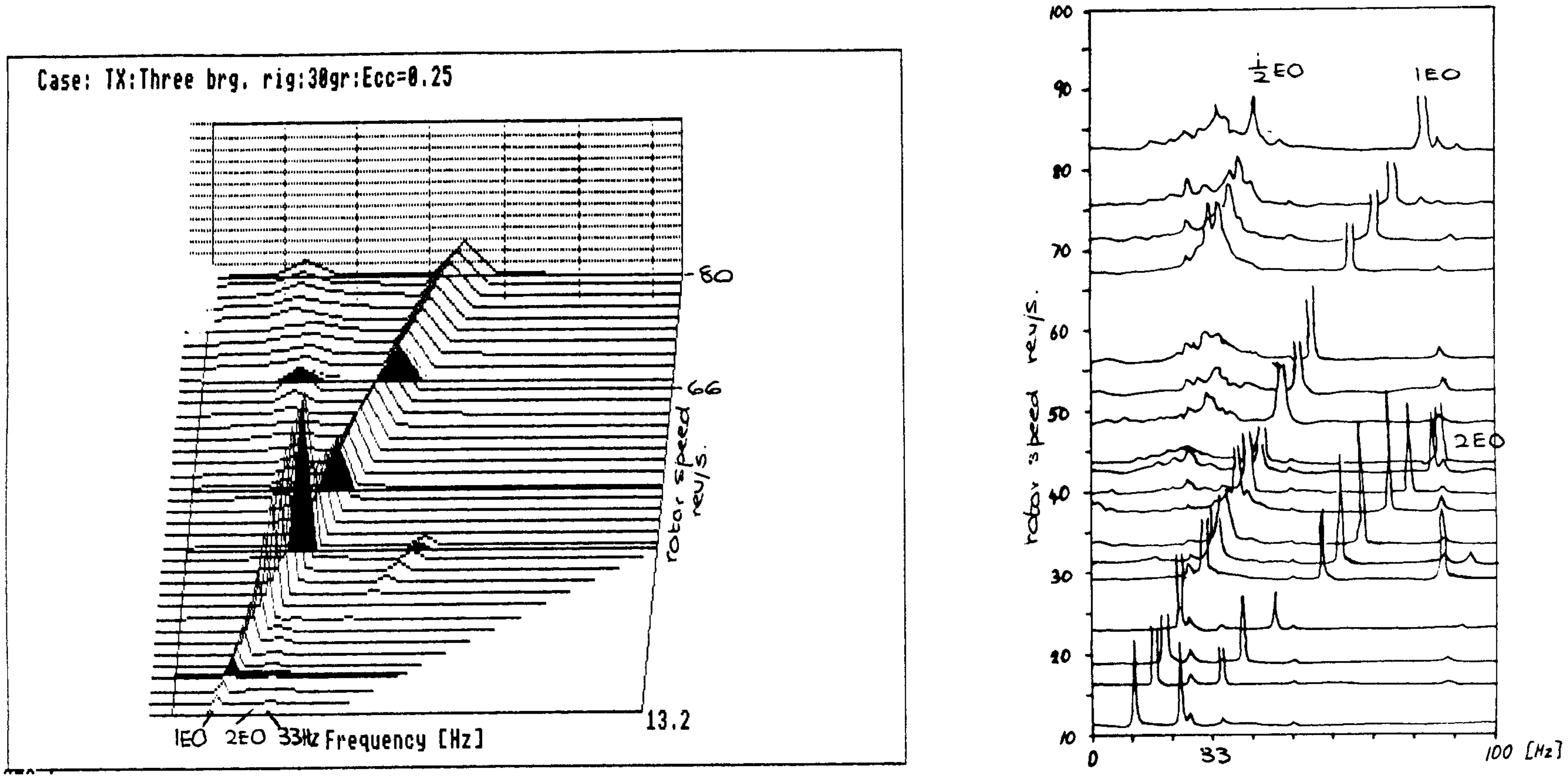

(a) Predicted. (b) Experimental.

Figure 10. - Waterfall diagram.

N87-22218

DYNAMIC PERFORMANCE OF SQUEEZE-FILM BEARINGS

C.R. Burrows, M.N. Sahinkaya, and N.C. Kucuk
University of Strathclyde
Glasgow, Scotland

D. Taylor
Cornell University
Ithaca, New York 14853

1. INTRODUCTION

Squeeze-film elements are widely used for vibration control and force isolation. The dynamic characteristics of these components are of great importance in the design and analysis of rotor-bearing systems.

It is generally assumed that Reynolds equation can be used to provide an adequate model for a bearing oil-film. Various simplifying assumptions are used, e.g. the short bearing approximation, to enable the equation to be solved and thus yield an expression for the pressure distribution in the oil-film (1). The oil-film force is obtained by integrating the pressure distribution circumferentially and along the axis of the bearing, and this gives both positive and negative pressure regions. It is frequently assumed for simplicity that negative pressures cannot be sustained in a cavitated oil-film, hence the oil-film force is obtained by performing the integration only in the positive pressure region. It follows that the limits of integration are of great importance (2,3).

It is often assumed that squeeze-film bearing coefficients can be deduced from those obtained from a journal bearing simply by suppressing the angular rotation. This leads to the conclusion that the stiffness coefficients are zero whereas in practice a squeeze-film bearing can support a dynamic load without the use of centering springs. The limitation of this assumption was noted by Holmes (3) in relation to the velocity coefficients. He suggested that the only case in which the damping coefficients for a squeeze-film bearing and a journal bearing would be equal is a full film of oil because the limits of integration for both bearing films are then identical. This limitation has been frequently overlooked. Thus in general the linearized coefficients used to model a squeeze-film bearing cannot be deduced from journal bearing coefficients. The problem determining squeeze-film coefficients has been tackled by various authors using several different approaches e.g. (4,5).

In this paper the squeeze-film force equations, with the correct integration limits, are used to show that the classical linearization process cannot be adopted to derive oil-film coefficients for a squeeze-film bearing. This leads to a discussion of the physical meaning and usefulness of linearized models to represent squeeze-film bearings.

1.2 Nomenclature

$c_{e\phi}$ ... etc.	oil-film damping coefficients
c	radial clearance
d	mass unbalance eccentricity of the shaft
e	shaft displacement from bearing centre line
$F_e, F_\phi, F_{ej}, F_{\phi j}$	oil-film forces in n_e, n_ϕ directions for squeeze-film bearing and journal bearing respectively
g_1, g_{1j} .... etc.	particular integral solutions for squeeze-film bearing and journal bearing respectively
h	oil-film thickness
l	bearing length
$\vec{n}_e, \vec{n}_\phi$	direction vectors defined in Fig. 1
p	oil-film pressure in the clearance
R	bearing radius
$\underline{V}$	velocity vector in Fig. 1
z	axis along the bearing length
$\underline{Z}$	state vector
ε	eccentricity ratio e/c
ε_o	static value of ε
ϕ	attitude angle
ϕ_o	static value of ϕ
θ_1, θ_2	oil-film limits
ψ	angle defined in Fig. 1
η	small change in ε
ξ	small change in ϕ
ω	angular velocity of journal
μ	fluid viscosity
$(\dot{\ })$	differential with respect to time
$(\ )^T$	transpose

2. OIL FILM FORCES

The pressure distribution p in a short bearing of length l is given by Reynolds' equation as

$$\frac{\partial}{\partial z}\left(h^3 \frac{\partial p}{\partial z}\right) = 12 \frac{\mu}{c^3} \left(\dot{e} \cos \theta + e (\dot{\phi} - \omega/2) \sin \theta\right) \tag{1}$$

where z is the distance along the longitudinal bearing axis, c is the clearance and μ is the oil viscosity. Variables θ, ϕ and e are defined in Fig. 1, and ω is the angular velocity of the journal (zero for a squeeze-film bearing). Integration of equation (1) twice with respect to z and insertion of the boundary conditions $p = 0$, $z = \pm l/2$ gives the pressure distribution

$$p(\theta) = -\frac{\mu l^2 V}{c^3 h^3} \left(\dot{e} \cos \theta + e (\dot{\phi} - \omega/2) \sin \theta\right) \tag{2}$$

Thus the oil-film forces along the orthogonal axes, defined in Fig. 1 are

$$F_e = Rl \int_{\theta_1}^{\theta_2} p \cos\theta \, d\theta$$

$$F_\phi = Rl \int_{\theta_1}^{\theta_2} p \sin\theta \, d\theta \qquad (3)$$

For an uncavitated film the limits are 0 to 2π. For a ruptured film the force is computed by using only the positive region and assuming zero pressure elsewhere. A positive pressure occurs in the arc θ_1 to $\theta_1 + \pi$ defined from equation (1) by

$$\dot{e} \cos\theta + e(\dot{\phi} - \omega/2) \sin\theta < 0$$

That is

$$\tan\theta_1 = - \frac{\dot{e}}{e(\dot{\phi} - \omega/2)} \qquad (4)$$

Equation (4) is central in explaining the different characteristics of journal and squeeze-film bearings.

2.1 Journal Bearing

For small changes in the attitude angle ϕ, as occurs in a journal bearing $\dot{\phi} << \omega/2.$,

$$\tan\theta_1 = 2\dot{e}/e\omega \qquad (5)$$

Since ω is positive θ_1 is always positive, thus the positive pressure arc oscillates with a small amplitude around $\theta_1 = 0$. Hence the limits of integration can be taken as 0 and π and the oil-film forces are

$$F_{ej} = - \frac{\mu R l^3}{c^2} (\varepsilon g_{1j} (\dot{\phi} - \omega/2) + \dot{\varepsilon} g_{2j})$$

$$F_{\phi j} = - \frac{\mu R l^3}{c^2} (\varepsilon g_{3j} (\dot{\phi} - \omega/2) + \dot{\varepsilon} g_{1j}) \qquad (6)$$

where $g_{1j} = - 2 \varepsilon (1 - \varepsilon^2)^{-2}$

$g_{2j} = \frac{\pi}{2} (1 + 2 \varepsilon^2)(1 - \varepsilon^2)^{-5/2}$

$g_{3j} = \frac{\pi}{2} (1 - \varepsilon^2)^{-3/2}$

If ω is set to zero in equation (5) then $\theta_1 = \pi/2$ whereas in practice it is known that in a squeeze film the positive pressure region rotates around the bearing.

2.2. Squeeze-film Bearing

For a ruptured squeeze-film, equation (4) becomes

$$\tan\theta_1 = -\dot{e}/e\dot{\phi} \qquad (7)$$

Angle ϕ can be positive or negative depending upon the position of the journal in the clearance circle (see Fig. 1), thus θ_1 is finite, and can take positive or negative values. It was at this stage in his analysis that White (2) incorrectly set $\theta_1 \simeq 0$ for small values of $\dot{e}$. This is equivalent to suppressing angular motion of the journal, that is to derive the squeeze-film bearing coefficients from those for a journal bearing by setting ω to zero.

If equation (7) is used, to define the limits of the positive pressure arc, then as the journal describes an orbit in the clearance circle the cavitation region rotates. This region is determined by the squeeze velocity and makes a complete rotation for each rotation of the journal. The maximum pressure occurs in the direction of the velocity vector $\underline{V}$ shown in Fig. 1. Thus the oil-film behaves in a totally different manner to that in a journal bearing where there are only small oscillations of the cavitation region.

With the correct variable limits inserted the oil-film forces for a π squeeze-film bearing become (6)

$$F_e = -\frac{\mu R l^3}{c^2}\,(\dot{\phi}\,\varepsilon\, g_1 + \dot{\varepsilon}\, g_2)$$

$$F_\phi = -\frac{\mu R l^3}{c^2}\,(\dot{\phi}\,\varepsilon\, g_3 + \dot{\varepsilon}\, g_1) \tag{8}$$

where $g_1 = -2\varepsilon\cos^3\theta_1\,(1 - \varepsilon^2\cos^2\theta_1)^{-2}$

$$g_2 = \varepsilon\sin\theta_1\,[3 + (2 - 5\varepsilon^2)\cos^2\theta_1]\,(1 - \varepsilon^2)^{-2}\,(1 - \varepsilon^2\cos^2\theta_1)^{-2}$$
$$+ \alpha\,(1 + 2\varepsilon^2)\,(1 - \varepsilon^2)^{-5/2}$$

$$g_3 = \varepsilon\sin\theta_1\,[1 - 2\cos^2\theta_1 + \varepsilon^2\cos^2\theta_1]\,(1 - \varepsilon^2)^{-1}\,(1 - \varepsilon^2\cos^2\theta_1)^{-2}$$
$$+ \alpha\,(1 - \varepsilon^2)^{-3/2}$$

$$\tan\theta_1 = -\varepsilon/\varepsilon\dot{\phi}$$

$$\alpha = \frac{\pi}{2} + \tan^{-1}[\varepsilon\sin\theta_1\,(1 - \varepsilon^2)^{-\frac{1}{2}}]$$

since $\theta_1 \neq 0$, $g_{ij} \neq g_1$ etc. and the squeeze-film forces F_e, F_ϕ cannot be derived from F_{ej} and $F_{\phi j}$.

It can be seen from equations (6) and (8) that the oil-film forces are non-linear functions of the states $(\varepsilon, \dot{\varepsilon}, \phi, \dot{\phi})$

3. LINEARITY

There are many analytical benefits to be gained if linear models can be derived which adequately represent these non-linear forces. If we define a state vector as $\underline{Z}$, one possibility is to seek to linearize the system about the equilibrium position $\underline{Z}_o$ defined by $\underline{Z}_o^T = (\varepsilon_o, 0, \phi_o, 0)$. We then assume small perturbations η, ξ about $\underline{Z}_o$, that is

$$\underline{Z}^T = (\varepsilon_o + \eta \, , \, \dot{\eta} \, , \, \phi_o + \xi \, , \, \dot{\xi}) \tag{9}$$

The procedure defined in equation (9) is used in most of the literature which is concerned with deriving linearized oil-film coefficients. When this approach is applied to a π-film journal bearing it yields expressions for four stiffness and four damping coefficients (7). As noted earlier some workers have incorrectly suggested that by setting $\omega = 0$ in these expressions the resulting stiffness and damping coefficients are obtained for a squeeze-film bearing. To linearize about $\underline{Z}_o$ for a squeeze-film we must use equation (8). Consider one coefficient

$$c_{e\phi} = - \left. \frac{\partial F_e}{\partial \dot{\phi}} \right|_{\underline{Z}_o}$$

$$- \left. \frac{\partial F_e}{\partial \dot{\phi}} \right|_{\underline{Z}_o} = \frac{\mu R l^3}{c^2} \left. \left(\varepsilon \, g_1 + \varepsilon \, \dot{\phi} \frac{\partial g_1}{\partial \dot{\phi}} + \dot{\varepsilon} \frac{\partial g_2}{\partial \dot{\phi}} \right) \right|_{\underline{Z}_o}$$

$$\left. \frac{\partial g_1}{\partial \dot{\phi}} \right|_{\underline{Z}_o} = [6 \, \varepsilon \cos^2 \theta_1 \sin \theta_1 (1 - \varepsilon^2 \cos^2 \theta_1)$$

$$\left. + \, 8 \, \varepsilon \cos^3 \theta_1 (1 - \varepsilon^2 \cos^2 \theta_1)(\varepsilon^2 \cos^2 \theta_1 \sin \theta_1)] \frac{\partial \theta_1}{\partial \dot{\phi}} \right|_{\underline{Z}_o}$$

An expression can be derived for $\partial g_2 / \partial \dot{\phi}$, but this tedious operation need not be performed. Now $\theta_1 = \tan^{-1} - \frac{\dot{\varepsilon}}{\varepsilon \dot{\phi}}$, but at the equilibrium point θ_1 is undefined, thus $c_{e\phi}$ cannot be evaluated. Hence the classical approach to obtaining linearized oil-film coefficients cannot be applied to a cavitated squeeze-film bearing. The question arises: do linear oil-film coefficients have any meaning for a cavitated squeeze-film bearing? To answer the question it is necessary to appreciate the physics of the situation.

The linearization described above is performed about a point which is usually defined as the centre of the orbit. In practice state $\underline{Z}_o$ is not achieved, that is there is no point on the orbit that both velocities are simultaneously zero. Thus we must reject the concept of linearized coefficients for a ruptured squeeze-film bearing, or adopt an alternative approach to obtaining equivalent linearized coefficients (4,5) or seek a new analytical approach to the problem.

4. FURTHER CONSIDERATIONS

Consider a perturbation $\dot{\eta}$ in $\dot{\varepsilon}$ with $\dot{\xi} = 0$.

If $\dot{\eta}$ is positive the shaft moves against the thin part of the oil-film and a large negative radial force is produced. If $\dot{\eta}$ is negative the shaft squeezes a thicker film and the magnitude of the radial force is lower, as shown in Fig. 2. The force is linear in velocity and the slope depends upon ε_o. However the force also depends upon the sign of $\dot{\varepsilon}$ (or $\dot{\eta}$) and

$$F_e\ (\dot{\eta}) \neq -F_e\ (-\dot{\eta})$$

This essentially non-linear behaviour is not reproduced by setting $\omega = 0$ in the journal bearing expressions as shown in Fig. 2.

Now consider perturbations in $\dot{\phi}$ with $\dot{\varepsilon} = 0$. If $\dot{\xi}$ is positive a radial force is produced which seeks to centralise the journal. The magnitude of the force depends upon $\dot{\phi}$ and ε_o. As shown in Fig. 3 if $\dot{\xi}$ is negative the same centralising force is produced, that is

$$F_e\ (\dot{\xi}) = F_e\ (-\dot{\xi})$$

Once again this highly non-linear behaviour disappears when we compute the bearing forces from the journal bearing expressions with $\omega = 0$ (Fig. 3).

Figures 2 and 3 demonstrate why the classical approach to linearization breaks down, namely that the principle of superposition is violated.

CONCLUSIONS

Earlier work by the authors (5) has shown that oil-film forces can be modelled by linear coefficients. In that work they used identification techniques to generate numerical values for these coefficients. This paper has shown the invalidity of applying the perturbation techniques normally used in bearing studies to derive expressions for linearized coefficients to represent a cavitated oil-film.

Hahn (14) has developed an alternative approach based upon energy techniques to obtain estimates for linearized coefficients. Some current work being undertaken by the authors suggests that an alternative analytical approach is possible. These results will be reported in due course.

REFERENCES

1) Mohan, S., Hahn, E.J. "Design of Squeeze Film Damper Supports for Rigid Rotors", ASME, Journal of Eng. for Industry, Vol. 96, 1974, p976.

2) White, D.C. "The Dynamics of a Rigid Rotor Supported on Squeeze Film Bearings", Conference on Vibrations in Rotating Systems, London, Feb. 14-15, 1972, p213.

3) Holmes, R. "Vibration and its Control in Rotating Systems". IUTAM Symposium on Dynamics of Rotors, Lyngby, Denmark, August 12-16, 1974, p.156.

4) Hahn, E.J. "Equivalent Stiffness and Damping Coefficients for Squeeze Film Dampers", I. Mech.E. Conf., Vibrations in Rotating Machinery, York 1984, Paper C325/84, p507.

) Burrows, C.R, Sahinkaya, M.N. and Kucuk, N.C. "Modelling of Oil-Film Forces in Squeeze-Film Bearings". ASME/ASLE 1985 Tribology Conference, October 8-10, 1985, Paper 85-Trib. 19. To be published in Journal of Lubrication Technology.

) Capriz, Q. "Sulle Vibrazioni Delle Aste Roberti", Ann. Scuola Normale Superiore, Vol. 17, 1963, p31.

7) Holmes, R. "The Vibration of a Rigid Shaft on Short Sleeve Bearings", Journal of Mech. Eng. Science, Vol. 2, 1960, p337.

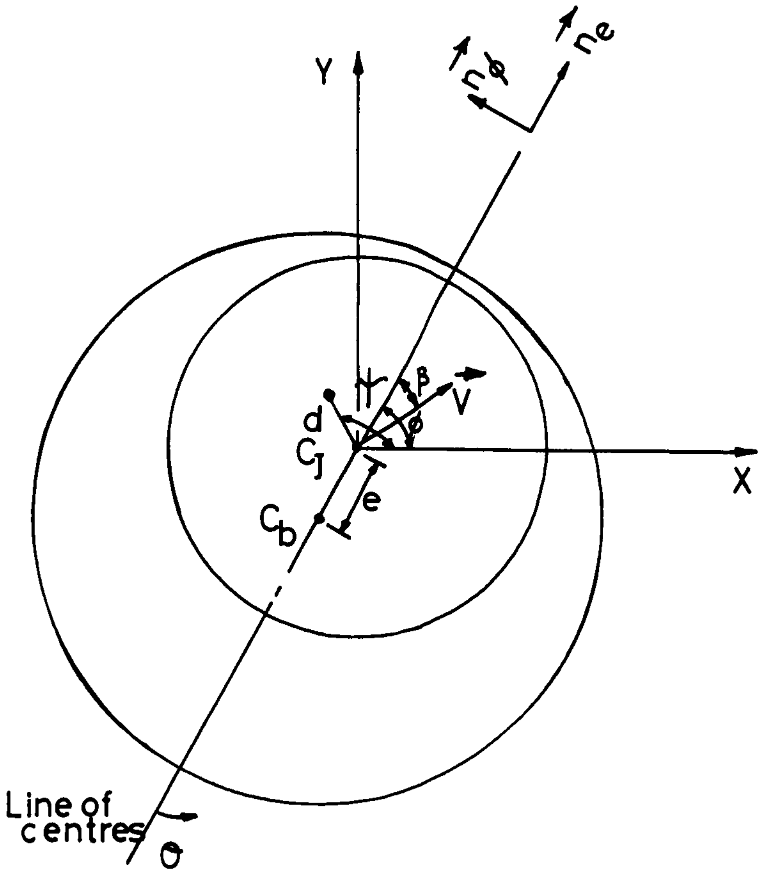

C_b - Centre of the bearing

C_J - Centre of the journal

Fig. 1 Bearing coordinate axes

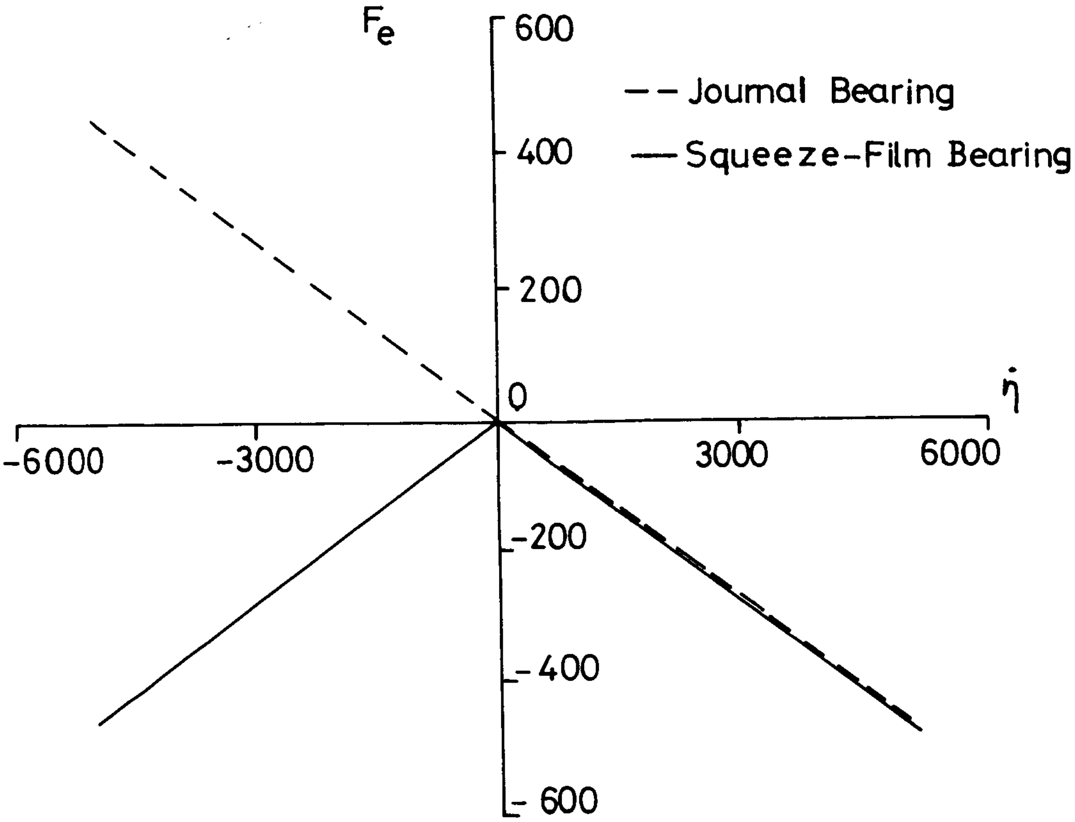

Fig. 2 Oil-film force in n_e direction plotted against $\dot{\eta}$

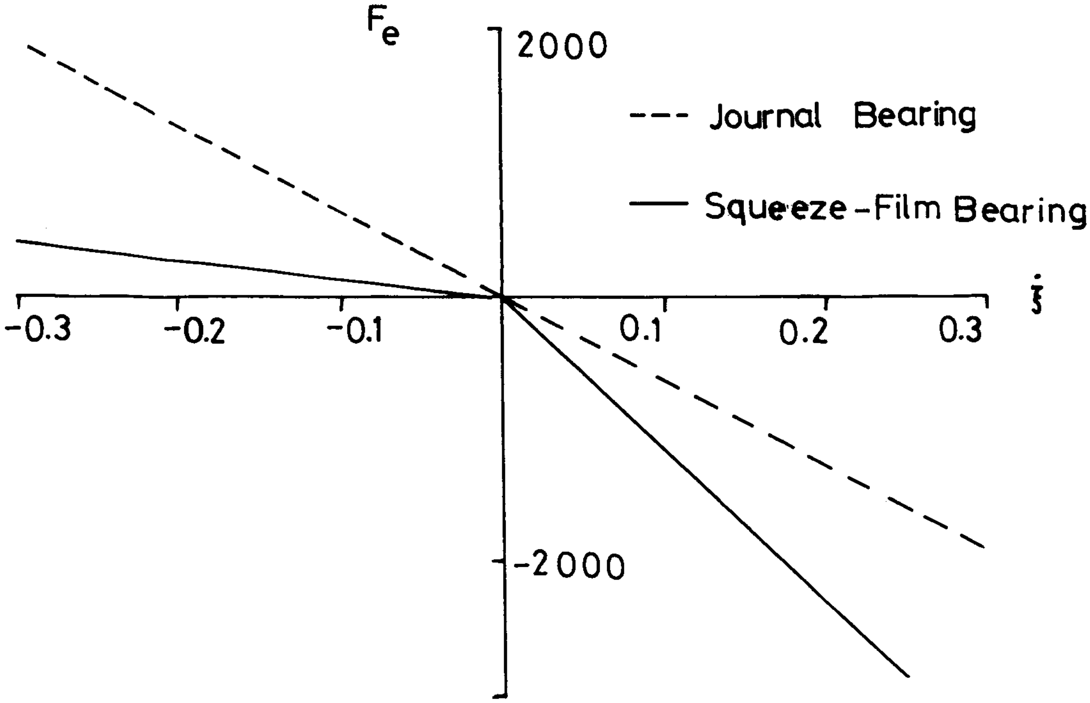

Fig. 3 Oil-film force in n_e direction plotted against $\dot{\xi}$

C - 5

N87-22219

EXPERIMENTAL MEASUREMENT OF THE DYNAMIC PRESSURE DISTRIBUTION IN A SQUEEZE FILM BEARING DAMPER EXECUTING CIRCULAR CENTERED ORBITS

L.A. San Andres and J.M. Vance
Texas A&M University
College Station, Texas 77843

A review of previous experimental measurements of squeeze film damper (SFD) forces is given. Measurements by the authors of SFD pressure fields and force coefficients, for circular centered orbits with $\varepsilon = 0.5$, are described and compared with computer predictions. For Reynolds numbers over the range 2-6, the effect of fluid inertia on the pressure fields and forces is found to be significant.

Introduction

Squeeze Film Dampers (SFD) have been the subject of numerous experimental investigations since their development in the early 1960's to attenuate turborotor vibration in aircraft engines. A number of investigators have compared measured pressure fields and/or transmitted forces with predictions based on approximate or limiting geometry solutions to the Reynolds equation for incompressible inertialess flows. Correlation between test and experiments has ranged from good to excellent in some cases to poor in other instances. Among the most important considerations that have been shown to be of considerable influence on the measured pressure profiles and forces are: oil feed mechanisms, use of end seals to prevent axial leakage, level of inlet pressure supply and cavitation pressure of the lubricant, coupling of the damping device to the rotordynamics of the system and, in some circumstances, fluid inertia effects. The review of past experimental work on SFDs treats only the reported investigations for circular centered orbits (CCO). Other types of investigations, although important but less relevant to the subject of the present study, are mainly oriented to determine the overall behavior of rotor systems supported in SFD's.

Thomsen and Anderson [1] studied the range of damping available from the squeeze film by varying the radial clearance and oil viscosity in a test rig. For a centralized preloaded SFD, the damping coefficient was obtained by measuring the deflection in the radial supports of the bearing housing. Comparison with a linearized theory, valid for small amplitude CCO, showed good agreement and independence of the damping coefficient from rotor speed and amplitude of vibration. A significant contribution (although no measured data is presented) is the statement that the measured radial stiffness is much lower than the measured static stiffness, showing the substantial effect of the added mass effect on the oil film forces.

Vance and Kirton [2] carried out an experimental study of the hydrodynamic force response of a damper with end seals. A controlled orbit test rig, independent of the interactions with the rotor bearing systems, was developed. The pressure field was measured around a journal performing circular centered orbits, and then integrated to determine the force components of the squeeze film. Comparisons show fair agreement with the long bearing theory. Paradoxically, larger-than-predicted dimensionless pressures and forces were measured for a light viscocity oil and smaller-than-predicted pressures and forces were measured with high viscosity oil. An attempt to explain the first case was made by suggesting that the damper could be operating in the Taylor Vortex regime. However, the Taylor Vortex regime arises in rotational Couette type flows, and is considered to be a natural convection process resulting from centrifugal forces. The phenomenon would not be expected at all in a SFD. The discrepancy from Reynolds (long bearing) Theory should be attributed to other phenomena, such as oil inlet conditions, which may have caused distortion in the pressure field, or it is possible that the large radial clearance used could have induced significant fluid inertia effects.

Tonnesen [3] obtained damping coefficients by measuring the force impedance of the squeeze film in a test rig for small amplitude centered motions. The measured force coefficients were constant over a considerable speed range provided the transmitted force was below a certain level. As the oil supply was increased, agreement with the full film short SFD theory was found excellent for low frequency motions. With zero supply pressure, the damping capacity of the SFD disappeared and large forces were transmitted to the supports. For offset motions, the correlation was generally poor and misguiding.

Feder, Bansal, and Blanco [4] made an experimental study of a damper with a low L/D ratio (0.3), end seals with negligible leakage, and with oil supplied through small holes in an annular groove at the ends of the damper. A smaller clearance ratio than in reference [2] was used, In this way, the effects of fluid inertia and the lubricant inlet on the squeeze film pressure distribution were minimized. Excellent agreement of measured values with the long bearing theory was reported. Measured pressure profiles and forces were found strongly dependent on the inlet and lubricant cavitation pressures.

Miyachi et. al. [5] conducted measurements of the viscous damping coefficient for a damper with L/D=0.2 and several types of inlet and outlet conditions. The results were compared with numerical predictions from a FEM code. Using simple end plate seals and small inlet holes, as well as a central groove, the measured damping coefficients were much higher than predicted, even in the case of an open ended SFD. For small amplitude motions, and using O-ring and piston ring seals at the ends of the SFD, the measured damping values were consistently higher than predicted, perhaps due to the inherent damping capacity of the end seals. Certainly the end conditions, at the boundaries of the damper are more complicated than the models incorporated in current theories.

Fluid Inertia Studies

The effect of fluid inertia on squeeze film forces has been largely overlooked by rotordynamicists and lubrication engineers, even though theoretical analyses which account for fluid inertia at moderate Reynolds numbers have predicted large discrepancies from classical lubrication theory. These analyses have raised controversial issues that must be resolved by experimental evidence.

To date, several different measurements of fluid inertial forces in squeeze film configurations have been reported in the literature, but these investigations have mainly been concerned with small amplitude motions of journal about the centered position.

Fritz [6] performed analyses and tests to investigate the added mass and damping forces of a fluid in a thin annulus surrounding a rotor vibrating due to unbalanced forces. Comparison of test and theory gave measured added mass values 25% lower than predicted. The discrepancy was attributed to the axial leakage through the end seals of the test rig. Results also showed the extreme importance of the fluid forces in determining the critical speeds of the rotor.

Chen et. al. [7], and Yang [8] measured the added mass and damping forces for vibrating rods in confined viscous fluids. Results from the damped free oscillations of the rod were compared with numerically predicted results. Correlation of experiment with theory is excellent although the clearance ratios tested were higher than those usually found in lubrication applications.

Mulcahy [9] derived finite length corrections for the fluid forces acting on a central rigid rotor translating periodically in a finite length annular region of confined fluid. Predictions for the added mass are quite satisfactory and within 2.3% of the measured data. Damping showed a variation of 10%, a deviation considered acceptable given the usual scatter encountered in measuring damping values.

There have been some recent efforts directed toward the experimental determination of fluid inertia forces for large amplitude CCOs. In this case the analytical problem becomes more complicated since the full nonlinear Navier-Stokes equations are to be considered. If cavitation is present, a clear isolation of damping and fluid inertia forces is no longer possible. Since damping forces increase rapidly with the orbit radius and are likely to dominate added mass forces, at least for the Reynolds numbers currently found in practice, experimental measurements of fluid inertia forces is more difficult in these operating regions. Tecza et. al. [10] reported experimental results which strongly support the existence of large inertia forces, although inferences must be drawn from the dynamic behavior of the rotor system rather than a direct measurement of damper forces.

Tichy [11] presented measured results which show a substantial effect of fluid inertia in the damping force at quite moderate Reynolds numbers. A tightly sealed damper with an L/D ratio of .15 was used in the experimental work. The journal was constrained to describe CCOs of about 20% and 50% of the radial clearance. Cavitation of the fluid was not allowed. For small Reynolds numbers (<1), the measured film forces were 30% lower than the values from the inertialess solution of the infinitely long bearing theory. These results are opposite to those of Feder [5] referred above. Tichy argues that end leakage is playing an important role in damper behavior.

In Tichy's experiments with Reynolds numbers over the range 2-9, the measured fluid film forces were substantially higher than the values predicted by the theories which account for fluid inertia effects in the flow. These measured results would be in the right direction if the phase shift between the purely viscous damping and added mass forces increased as the inertial parameter Re increased. However, virtually no change is detected in the phase angle. This striking result means that the total fluid force is always opposite to the journal motion. The added mass effect would thus be almost null.

This paper reports experimental pressure measurements made by the authors to determine the influence of fluid inertia in squeeze film dampers. The test rig employed is a modification of the one used by Vance and Kirton [2]. The modifications were made to improve the accuracy of the measurements and to understand better the test results. The basic concept of the test apparatus is to provide a journal with a known constrained motion within an annular clearance filled with oil, so the characteristics of the squeeze film can be studied independently of the dynamics of the rotor system.

Test Apparatus and Instrumentation

A schematic view of the SFD Test rig is shown in Figure 1. The relevant parameters and basic geometric characteristics of the test rig are given in Appendix 1. The relatively large radial clearance of the squeeze film in the test apparatus is designed to produce significant fluid inertia effects on the film forces at low whirling frequencies.

The journal is mounted on the eccentric lobe of a stiff shaft running on ball bearings with solid steel supports. The shaft is driven through a flexible coupling by an electric motor at a fixed rotational speed of 1770 rpm.

The outer damper bearing housing is supported by bearing index plates using locational fits in order to allow it to rotate through 360 degrees. The journal is prevented from rotation by 4 axial pins, equally spaced, which enter from the end of the journal into a loose fit in the bearing index plates. The ends of the journal are sealed against these plates using O-rings. The axial flow, or amount of leakage, passing the seals is practically zero (none was ever observed).

Oil is supplied to the SFD through a circumferential groove located in the central plane of the bearing housing. The lubricant supply can be varied by using pressurized air and a pressure regulator connected to the supply tank. For the experimental tests reported here, the inlet supply pressure was adjusted to 830 KPa (120 psig) so as to maintain a positive pressure throughout the squeeze film. Cavitation was thereby prevented and a full 360 degree film was developed as shown by the measured pressure waves.

Measurement of the dynamic pressure distribution in the oil film was chosen here over a direct measure of the transmitted forces since the former provides a more direct check of the SFD theories and does not introduce external effects, such as inertia of the housing or forces generated by the end seals. In the axial direction, 3 holes equally spaced 11.11mm(7/16 in) were machined on one side of the central groove. The pressure transducers installed in these holes are designated from end to middle as PT1 to PT3 and correspond, respectively, to the axial distances Z1 to Z3 measured from the closest edge of the groove.

In order to detect if significant changes in the pressure field can be observed at the same axial location but different circumferential position, three holes separated by 120° were tapped at axial location Z2. The measured differences were negligible in preliminary tests with CCO. Thus, as theory indicates, the pressure field around the journal is the same as the dynamic pressure measured at a fixed point for a complete revolution of the shaft and only one pressure transducer is necessary to make the measurement.

Two proximity probes, 90 degrees apart and installed midway between the ends of the bearing, are used to measure the journal center motion and accurately determine the orbit shape and radius. In all the tests performed, it was determined that the orbital motion was circular and centered (CCO) within small tolerances (see Appendix 2).

The pressure transducers are of quartz type and the gap probes are of the eddy-current type. The characteristics of these transducers are given in Appendix 2.

The fluid temperature is measured at the axial location Z2 with a type T thermocouple which is in contact with the lubricant. Oil viscosity is determined from prior measured viscometer data for a range of temperatures, and algebraic expressions are obtained for the fluid viscosity in terms of its temperature using ASTM D-341 formulae.

Two different kinds of oils have been used to date in the experimental procedures: SAE 30 oil (ISO 100) and a silicone fluid (ISO 32). The viscosity versus temperature formula obtained are given in Appendix 2.

Figure 2 shows the instrumentation arrangement. The output voltage of the proximity probe (PP) and the pressure transducers (PT) pass through a signal conditioner calibrated to give a voltage output in the range between +-5 volts. After this operation, the dynamic signals go to an 8 bit analog/digital converter to finally be processed in a desktop computer. At the same time, the oil temperature is read, and the orbit shape and the voltage signal from one of the pressure transducers are displayed and stored in oscilloscopes.

With CCOs and provided the effect of inlet/outlet mechanisms is minimal, the film pressure wave is synchronous with rotor speed and fixed relative to the rotating shaft. Therefore, the measured pressure vs. time waveform could be transformed to a pressure vs. angle relationship. Thus, at the axial location of measurement Zi, experimental fluid film radial and tangential forces and force coefficients are determined by numerical integration of the measured pressure profile for one rotor revolution. Appendix 3 contains the parameters employed to define the dimensionless pressure, p, and film forces and force coefficients at the axial location Zi of measurement.

In the experimental procedure, typically 60 pressure data points were taken for a rotor revolution at the location of measurement, and which corresponds to a data point for every 6° of rotor rotation. This number is considered to describe with detail the film pressure wave and provide calculated film forces with exactitude.

Results and Discussion

Parallel to this experimental investigation, a finite element code was developed to calculate the pressure field, film forces and dynamic force coefficients for finite length SFDs describing circular centered orbits [12]. The analysis, strictly valid for small Reynolds numbers, includes the effect of fluid inertia. Both temporal and convection terms are retained in the nonlinear flow equations which are solved iteratively. Different kinds of inlet and end boundary conditions such as local or global type end seals are included.

The SFD test rig has a length to diameter ratio, L/D, equal to 0.84, a central groove and O-rings at the journal end. Due to these characteristics, neither the long SFD nor short SFD models can be used for comparison with the experimental results.

The following observations, which are relevant to understand the nature of the measured results, were made along the experimentation:

a) Pressure field variations at the same axial location but different circumferential positions were found to be insignificant. This result is a direct consequence of the smallness of the inlet orfice which allowed the pressure waves to be independent of the circumferential location.

b) No oil leakage occured at the damper ends due to the effective sealing action of the O-rings: hence, any through or global axial flow was prevented. Therefore, as measurements confirmed, the region of largest pressures was closer to the damper end walls (at Z1) and decreased as the central groove location was approached.

c) It is a well known practice to assume the pressure is uniform and equal to the supply pressure in a grooved region. However, throughout the experimentation it was found the pressure at the central groove differed considerably from the simple assumption used in practice. Furthermore, the measured pressure gradient in the squeeze film lands was much less than the linear relation expected for a SFD model with uniform pressure at the groove.

By simple geometric similarity and assuming no axial flow and curvature effects, the ratio of pressures in the groove to those in the film lands should be approximately equal to 1/25. However, the observed pressure values at the groove were considerably larger and approximately equal to 1/3 of the film pressure at axial location Z1. These unexpected results can be attributed to the effect of fluid inertia, since at the groove region the Reynolds number is 25 times larger than in the film lands. A Bernoulli type effect and steep pressure gradients are inferred to occur at the interface between the groove and the squeeze film lands.

Thus, the condition of uniform pressure at the inlet of the squeeze film lands was thought to be too simple to be used in the theoretical treatment. The groove acts as a second squeeze film damper and its interface with the squeeze film lands should be provided in terms of flow continuity rather than in pressures due to the Bernoulli type effect most likely to occur in this region. Hence, the groove-squeeze film interface was modelled assuming a local flow constraint was present at the groove edges [13]. This boundary condition relates the local balance of the axial flow with the pressure drop across the film discontinuity through an End coefficient, $\overline{CL}$, which is a parameter in the flow solution. A value of end coefficient, $\overline{CL}=0$, represents a uniform axial film geometry; while as $\overline{CL}$ approaches ∞, a uniform pressure at the groove is obtained.

This type of ad-hoc procedure has also been used in the experimental work reported in [10]. In it, a damper with inlet and drain grooves was modelled as if it was locally sealed so as to obtain closer agreement between measured and predicted forces.

From a parametric study performed, values of the end coefficient, $\overline{CL}$, in the range from 0.2 to 0.3 were found to predict film pressures which closely matched those at Z1. Then, a value of $\overline{CL}=0.25$ was subsequently selected to predict film forces and compare with the experimental results at axial locations Z1 and Z2.

At this point, a brief explanation of the effect of fluid inertia on the film pressures for the full film solution is thought to be necessary. Consider, as in Figure 3a, a journal contrained to perform circular centered orbits of dimensionless radius e/c and frequency ω. If fluid inertia is neglected in the analysis, Figure 3b shows the predicted dynamic pressure wave p observed at circumferential position A and Z2 as the journal center describes a complete orbit. The purely viscous dynamic pressure is in phase with the film thickness velocity, i.e. is zero when the gap time rate of change is zero (at $\omega t=0,\pi,2\pi$, etc.) The pressure is antisymmetric with respect to the line $\omega t=\pi$ and the same level of peak positive and negative pressures are obtained.

The inclusion of fluid inertia gives rise to an additional pressure field which is in phase with the acceleration of the film thickness H. Figure 3b shows the pressure wave solely due to fluid inertia for increasing values of the squeeze film Reynolds number. Minimum and maximum pressures are given at $\omega t=0$ and π where the gap acceleration has its extreme values. The purely inertial pressure field is symmetric with respect to the line $\omega t=\pi$.

Figure 4 shows the addition of the purely viscous and inertial pressure waves for increasing values of the Reynolds number. The significant effect that fluid inertia has on the film pressures is clearly seen; at the minimum film locations ($\omega t=0,2\pi,4\pi$) the dynamic pressure has a negative value, while at the maximum gap locations the pressure gets above the zero pressure line. For increasing Reynolds numbers, the peak negative pressures p increase in an absolute sense, while the maximum peak positive pressure p stays relatively constant.

Figures 5, 6 and 7 show a comparison between the measured and predicted pressure waves at Z2 for Reynolds numbers equal to 2.54, 4, and 5.137, respectively. The experimental pressure waves show clearly the effect of fluid inertia as outlined above, and the good comparison with the finite element predictions is typical of most measurements. Measured pressures at locations Z1 and Z3 are similar in form to those at Z2, and are not reproduced here for brevity.

Figure 8 shows the peak experimental dynamic pressures p at the axial locations of measurement as the Reynolds number, Re, increases. The predictions for the SFD model with a $\overline{CL}$=0.25 are also included in the figure, and it is seen the predicted axial pressure drop follows approximately the measured pressure drop.

Fluid film forces and force coefficients at the axial locations of measurement, Zi, are determined by integration of the measured pressure profile for one rotor revolution. Figures 9 and 10 show, as the Reynolds number increases, the direct damping and inertia force coefficients, $\overline{Ctt}$ and $\overline{Drr}$ calculated from the experimental pressure data. The damping coefficients range between 65% to 85% of the damping value for the long SFD model. Comparison with the predictions is regarded as satisfactory considering the limitations of the model employed. The inertia coefficients show a better agreement with the predictions, although discrepancies exist for the largest Reynolds number tested. Figure 10 also includes predicted values of $\overline{Drr}$ for a SFD model which only accounts for temporal inertia terms in the flow model [14]; comparison with the experimental results emphasizes that a large error in inertia force predictions are made if a linearized model is used in damper design.

Figures 11 and 12 show the total dimensionless film force f and the force phase angle obtained from the force coefficients given in Figures 10 and 11. is the angle of the resultant force f and measured from the maximum film thickness. The predictions from the SFD model with $\overline{CL}$=0.25 are in an average sense close to the values calculated from the measured pressures. The effect of fluid inertia in the experimental results is seen to be significant specially in regard to the force phase angle which shows a 20° shift, at the highest Re, when compared to the 90° value derived from lubrication inertialess theories.

Conclusions

The effect of fluid inertia on the pressure field and film forces in a squeeze film damper test rig with circular centered orbits has been measured experimentally for one value of the dimensionless orbit radius (e/c=0.5).

Large levels of pressures were observed at the damper central groove and its influence on the measured pressures in the squeeze film lands is of paramont importance in the damper performance. The groove-squeeze film interface was modelled by assuming a balance between the local axial flow and pressure drop across the interface. An end coefficient, $\overline{CL}$=0.25, was determined to reproduce satisfactorily the measured pressure field.

Comparison of the experimental results with predictions from a non linear finite element SFD model are regarded good considering that fluid inertia renders the problem close to untractable even by numerical means. Major discrepancies are attributed to the limitation of the fluid flow model employed and which is strictly valid for low values of the squeeze film Reynolds number.

Previous analyses of fluid inertia effects on SFDs, which take into account only temporal terms [14], are shown to be in error for prediction of fluid inertia SFD forces.

The experimental measurements have shown that there is an urgent need to develop better theoretical boundary conditions which will account for the local detailed effects of fluid inertia and film geometry.

APPENDIX 1

Components of squeeze film damper test rig. Nominal dimensions and general characteristics.

Angular speed of eccentric shaft: 185.35 rad/sec (1770 rpm)

	Dimension	Z/R
Journal Diameter:	127.000 mm(5.000 in)	
Length :	119.702 mm(4.712 in)	
Bearing Diameter:	130.175 mm(5.125 in)	
Radial clearance:	1.587 mm(1/16 in)	
Orbit radius :	0.794 mm(1/32 in)	
Central groove depth :	6.350 mm(1/4 in)	
width :	12.700 mm(1/2 in)	
Inlet orifice : Diameter:	0.400 mm(1/64 in)	
Axial distance from edge of central groove to pressure transducers		
to PT1 (Z1):	42.773 mm(1.684 in)	0.657
to PT2 (Z2):	31.554 mm(1.242 in)	0.485
to PT3 (Z3):	20.570 mm(0.810 in)	0.3157

Dimensionless orbit radius: $\varepsilon = e/c = 0.50$
Dimensionless clearance ratio: $\delta = c/R = 0.025$
Damper test rig L/D ratio: 0.8425

Note: For parameter L/D, groove width has not been considered in calculation.

APPENDIX 2

1. Characteristics of quartz pressure transducers:

Average sensitivity: 0.7251 mv/KPa (4.99 mv/psi)
Linearity: 0.2% of full scale
Range: 0 - 6895 KPa (0 - 1000 psi)

2. Characteristics of proximity system:

Scale factor: 7.865 V/mm (200 mv/mil) + 0.4%
Linearity: 0.15% of full scale
Range: 1.143 - 3.81 mm (45 - 150 mils)

3. Oil viscosity formulae and range of viscosities and squeeze film Reynolds numbers tested:

viscosity ν in centistokes:

$$\log[\log(\nu+0.7)] = a + b \log[1.8\, T(^{\circ}C) + 492]$$

Factor	SAE 30 oil	Silicone fluid
a	10.052320	3.87822
b	-3.542052	-1.31010
r*	0.997500	0.99530
Specific gravity at 21°C(70°F)	0.8710	0.960
Range of tested oil temperatures	25 - 44 °C	25 - 37 °C
Range of measured oil viscosities	226 - 85 cst	100 - 79 cst
Range of tested Reynolds numbers	2 - 5.50	4.7 - 5.9

r*: denotes the correlation of linear regression analysis of experimental data.

4. Dimensional tolerances of the test rig and its orbital motion for circular centered orbits.

Radial clearance (c): 1.618 mm(0.0637 in) maximum
1.584 mm(0.0624 in) minimum

Dimensiolness orbit radius (e/c): 0.51072 maximum
0.48972 minimum

Dimensionless journal center offsets: $\delta x/c = 1.223 \times 10^{-5}$
$\delta y/c = 615.521 \times 10^{-5}$

APPENDIX 3

Definition of dimensionless pressure and force coefficients at axial locations of measurement

Squeeze film Reynolds number: $Re = \omega \cdot c / \nu$

Dimensionless pressure: $\bar{p}(\theta, z) = p/Cp$; $Cp = \mu\, w\, R^2/c^2$

Radial and tangential dimensionless fluid film forces:

$$fr = Fr/Cf = \int_0^1 \oint \bar{p} \cdot \cos\theta \, d\theta \, d\beta = \sum_{i=1}^{N} fr_i \, \Delta\beta$$

$$ft = Ft/Cf = \int \oint \bar{p} \cdot \sin\theta \, d\theta \, d\beta = \sum_{i=1}^{N} ft_i \, \Delta\beta$$

$\beta = z/L$, $Cf = \mu\, \omega\, L\, R^3/c^2$, N: N°of axial locations of measurement

fr_i and ft_i are local dimensionless film forces at Z_i, the axial location of measurement, and given by:

$$fr_i = 0\, \bar{p}(\theta, \beta_i) \cdot \cos\theta \, d\theta; \quad ft_i = 0\, \bar{p}(\theta, \beta_i) \cdot \sin\theta \, d\theta$$

Total film force: $f_i = [(fr_i)^2 + (ft_i)]^{2\ 1/2}$

Force phase angle: $\phi_i + 90^\circ + tg^{-1}(fr_i/ft_i)$
measured from maximum gap location

Local damping, $\overline{Ctt}_i$, and inertia, $\overline{Drr}_1$, force coefficients at the axial location Z_i of measurement are defined as:

$$\overline{Ctt}_i = -ft_i/\varepsilon \quad ; \quad \overline{Drr}_i = fr_i/\varepsilon$$

Global dimensional values of the force coefficients are given approximately by:

$$Ctt = -Ft/(\omega e) = \mu\, L\, R^3/C^3 \sum_{i=1}^{N} \overline{Ctt}_i \, \Delta\beta_i$$

$$Drr = -Fr/(-\omega^2 e) = \mu\, \omega\, L\, R^3/c^3 \sum_{i=1}^{N} \overline{Drr}_i \, \Delta\beta_i$$

References

1. Thomesen K.K., and H. Andersen, "Experimental Investigation of a Simple Squeeze Film Damper," Journal of Engineering for Industry, May 1974, pp. 427-430.

2. Vance J.M., and A.J. Kirton, "Experimental Measurement of the Dynamic Force Response of a Squeeze-Film Bearing Damper," Journal of Engineering for Industry, November 1975, pp 1282-1290.

3. Tonnesen J., "Experimental Parametric Study of a Squeeze Film Bearing," Journal of Lubrication Technology, April 1976, pp. 206-212.

4. Feder E., P.N. Bansal, and A. Blanco, "Investigation of Squeeze Film Damper Forces Produced by Circular Centered Orbits," Journal of Engineering for Power, Jan. 1978, v.100, pp. 15-21.

5. Miyachi T., S. Hoshiya, Y. Matsuki, and T. Torisaki, "Oil Squeeze Film Dampers For Reducing Vibration of Aircraft Gas Turbine Engines," ASME paper 79-GT-133, 1979.

6. Fritz, R.J., "The effects of an Annular Fluid on the Vibrations of a Long Rotor, Part 2 - Test," Journal of Basic Engineering, December 1970, pp. 930-937.

7. Chen S.S., M.W. Wambsganss, and J.A. Jendrezejczyk, "Added Mass and Damping of a Vibrating Rod in Confined Viscous Fluids," Journal of Applied Mechanics, June 1976, pp. 325-329.

8. Yang, C.I., and T.J. Moran, "Finite Element Solution of Added Mass and Damping of Oscillation Rods in Viscous Fluids," Journal of Applied Mechanics, September 1979, v. 46, pp. 519-522.

9. Mulcahy T.M., "Fluid Forces on Rods Vibrating in Finite Length Annular Regions," Journal of Applied Mechanics, June 1980, v. 47, pp. 234-240.

10. Tecza, J.A., J.C. Giordano, E.S. Zorzi, and S.K. Drake, "Squeeze-Film Damper Technology: Part 2 - Experimental Verification Using a Controlled-Orbit Test Rig," ASME paper 83-GT-248, 1983.

11. Tichy, J.A., "Measurements of Squeeze Film Bearing Forces to Demonstrate the Effect of Fluid Inertia," ASME paper 84-GT-11, 1984.

12. San Andre's, L.A., "Effect of Fluid Inertia on Squeeze Film Damper Force Response," Ph. D. Dissertation in Mechanical

13. Marmel, R.A., and J.M. Vance, "Squeeze Film Damper Characteristics for Gas Turbine Engines," Journal of Mechanical Design, ASME Trans., Vol. 100, 1978, pp. 139-146.

14. Lund, J.W., A.J. Smalley, J.A. Tecza, and J.F. Walton, "Squeeze Film Damper Technology. Part 1: Prediction of Finite Length Damper Performance," ASME Trans., Paper No. 83-9T-247, 1983.

ORIGINAL PAGE IS
OF POOR QUALITY

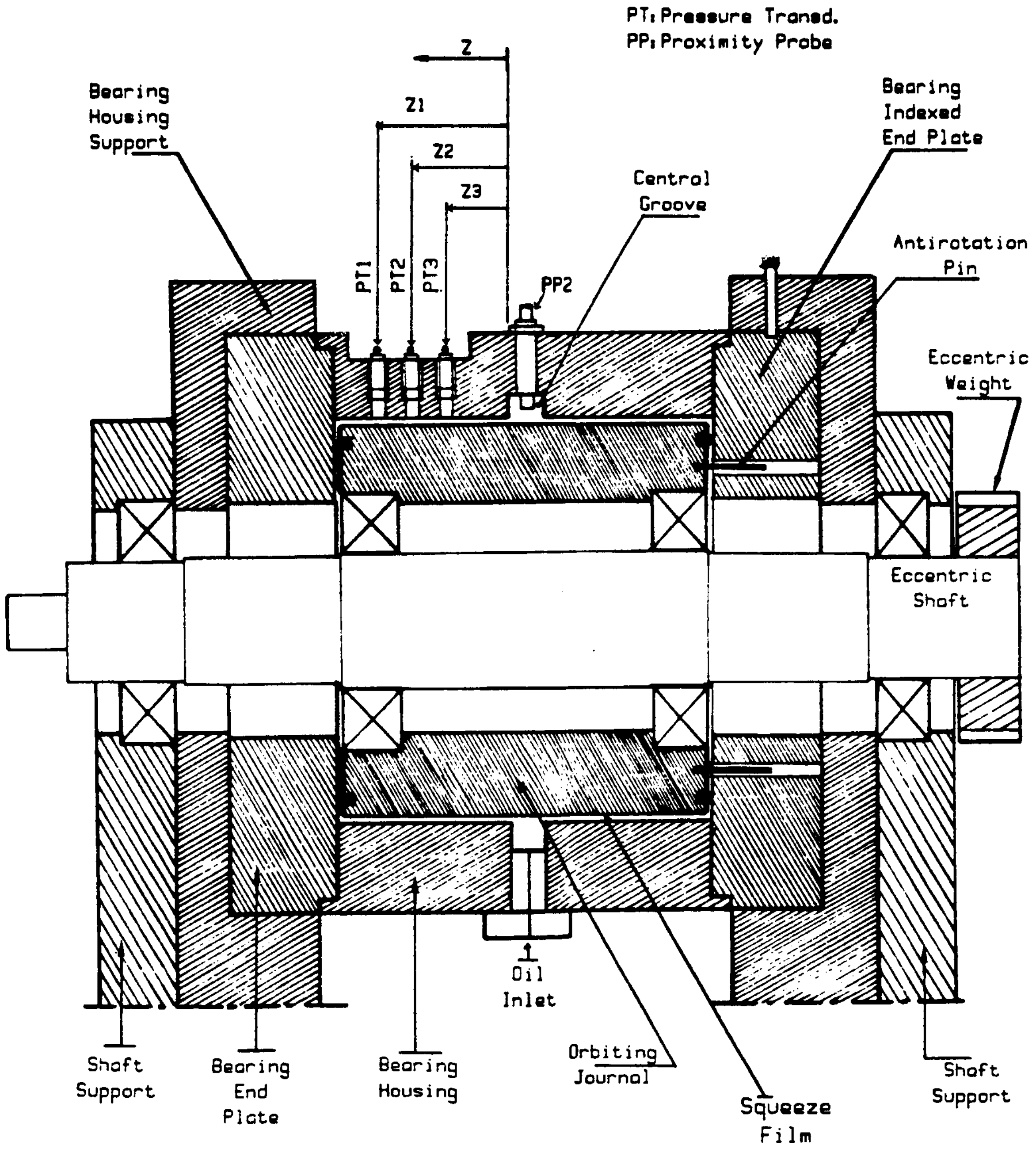
PT: Pressure Transd.
PP: Proximity Probe
Z
Z1
Z2
Z3
PT1
PT2
PT3
PP2
Bearing Housing Support
Central Groove
Bearing Indexed End Plate
Antirotation Pin
Eccentric Weight
Eccentric Shaft
Oil Inlet
Shaft Support
Bearing End Plate
Bearing Housing
Orbiting Journal
Squeeze Film
Shaft Support

Figure 1. Squeeze Film Damper Test Rig. Axial cross section.

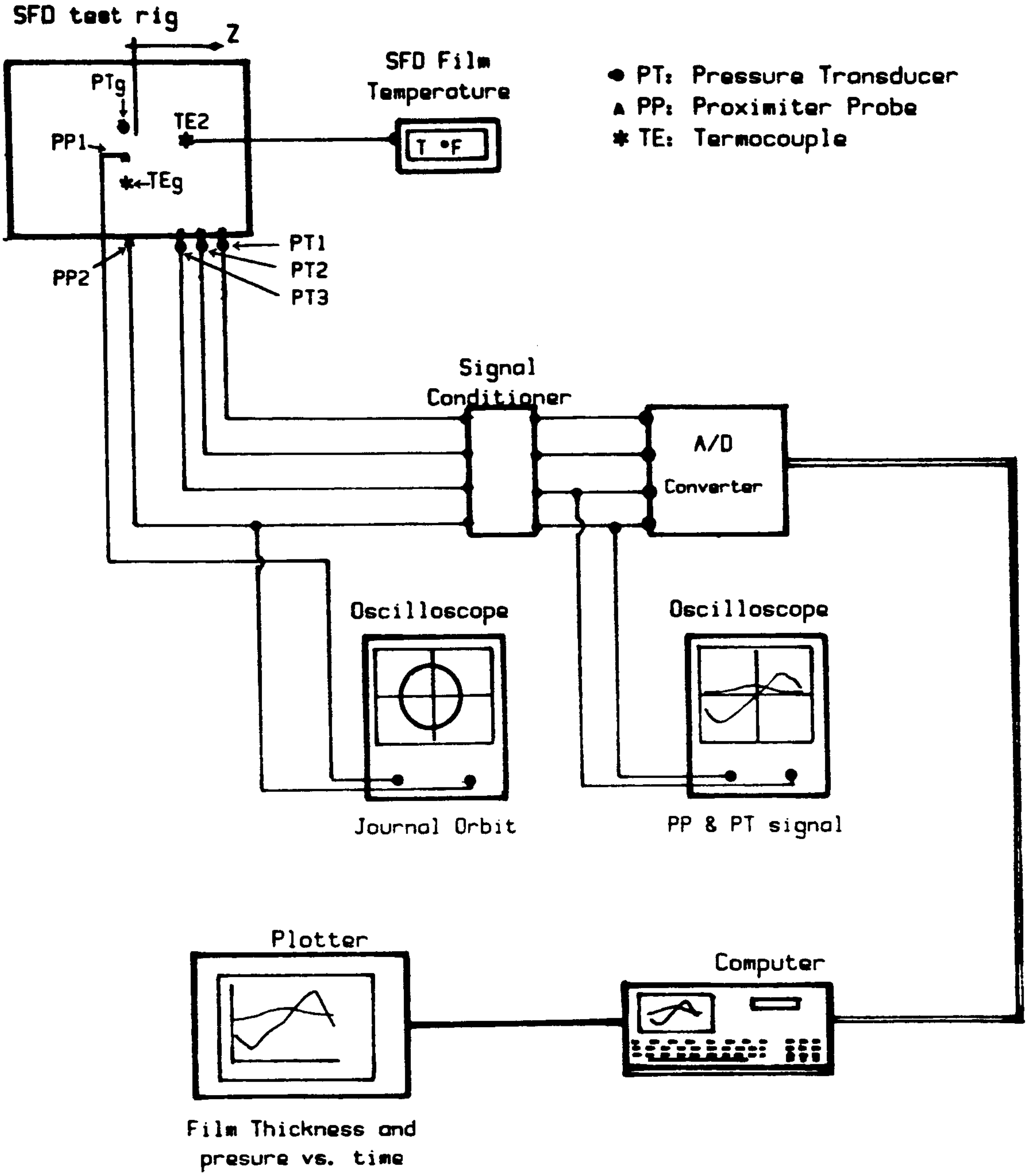
SFD test rig
Z
PTg
TE2
PP1
TEg
PP2
PT1
PT2
PT3
SFD Film Temperature
T °F
● PT: Pressure Transducer
▲ PP: Proximiter Probe
✱ TE: Termocouple
Signal Conditioner
A/D Converter
Oscilloscope
Journal Orbit
Oscilloscope
PP & PT signal
Plotter
Film Thickness and presure vs. time
Computer

Figure 2. Schematic drawing of Instrumentation for SFD test rig.

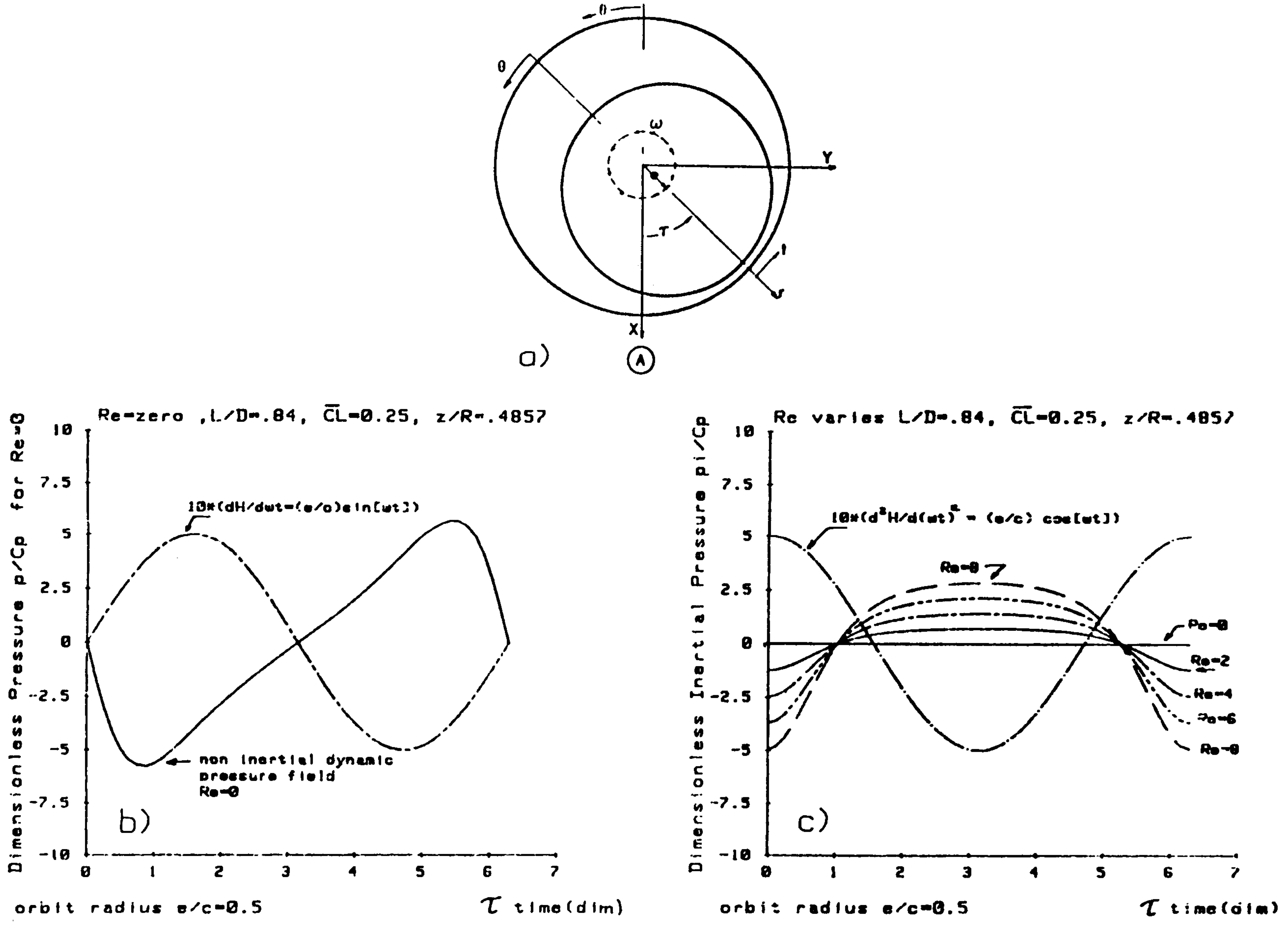

Figure 3. Film thickness H and predicted purely viscous and inertial dimensionless pressures for SFD model: L/D=0.84 and end coefficient $\overline{CL}$=0.25, at axial location Z2.

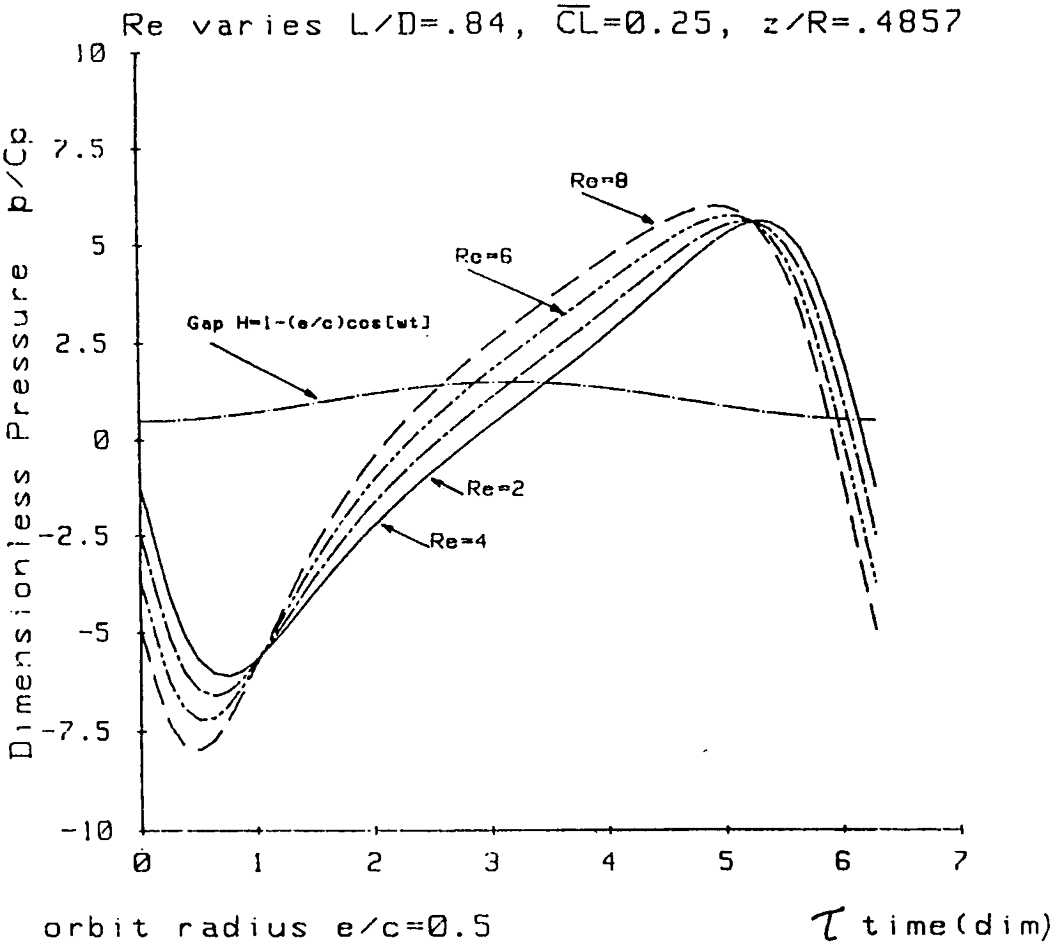

Figure 4. Predicted total dimensionless pressure vs. time for SFD model: L/D=0.84, $\overline{CL}$=0.25, at axial location Z2.

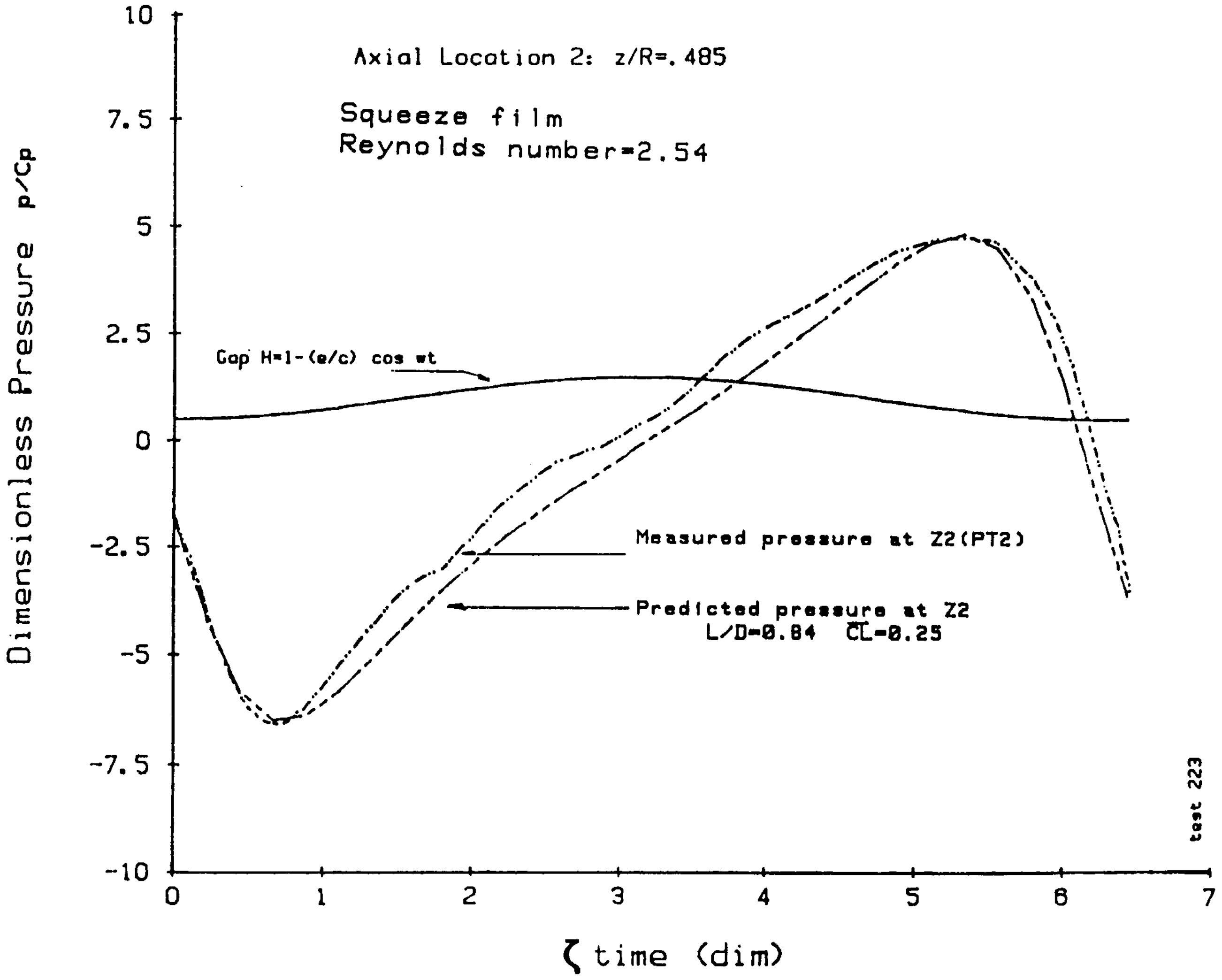

Figure 5. Dimensionless pressure wave $\bar{p}$ vs. wt at axial location Z2. Re=2.54. Experimental and predicted results.

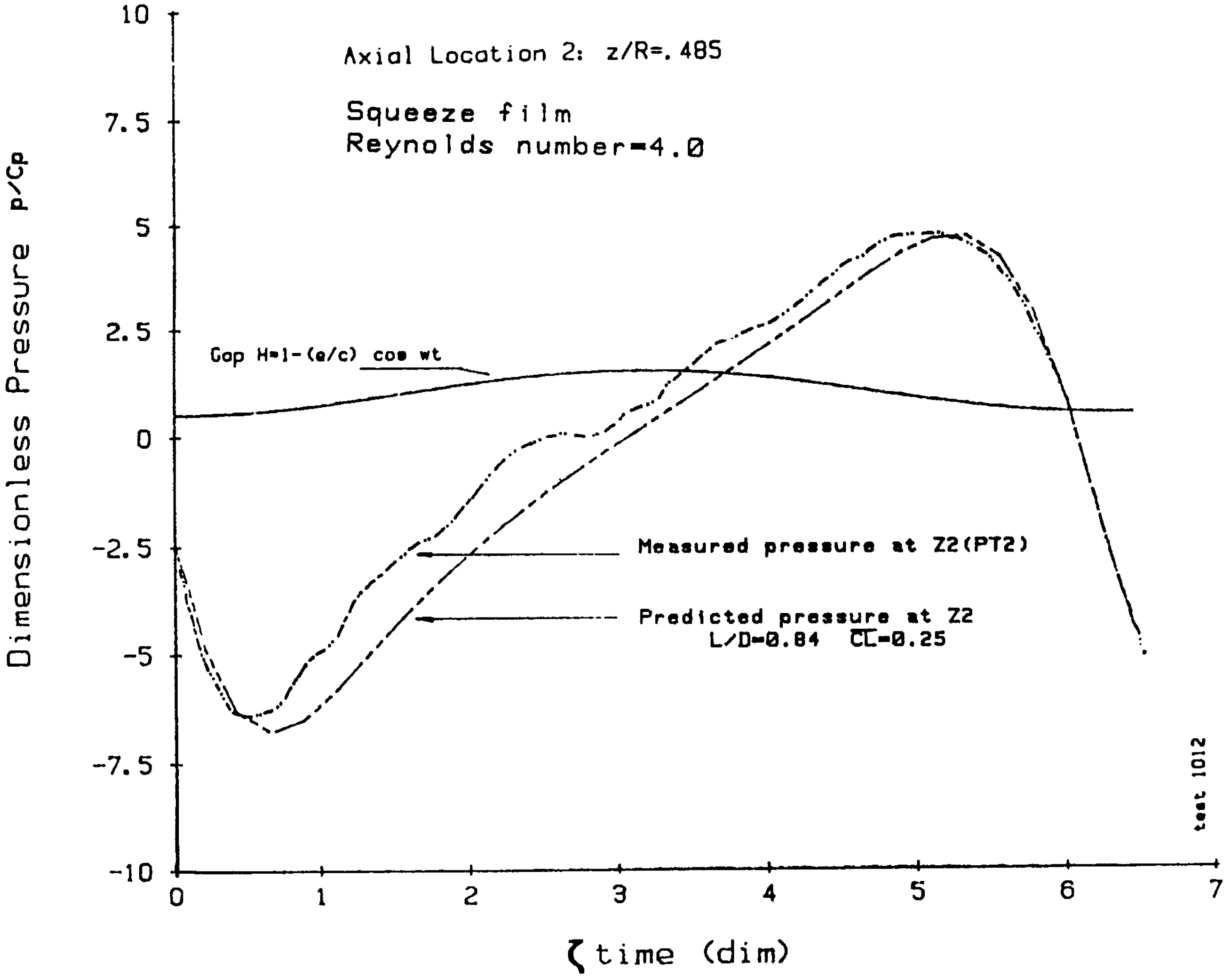

Figure 6. Dimensionless pressure wave $\overline{p}$ vs. wt at axial location Z2. Re=4.00. Experimental and predicted results.

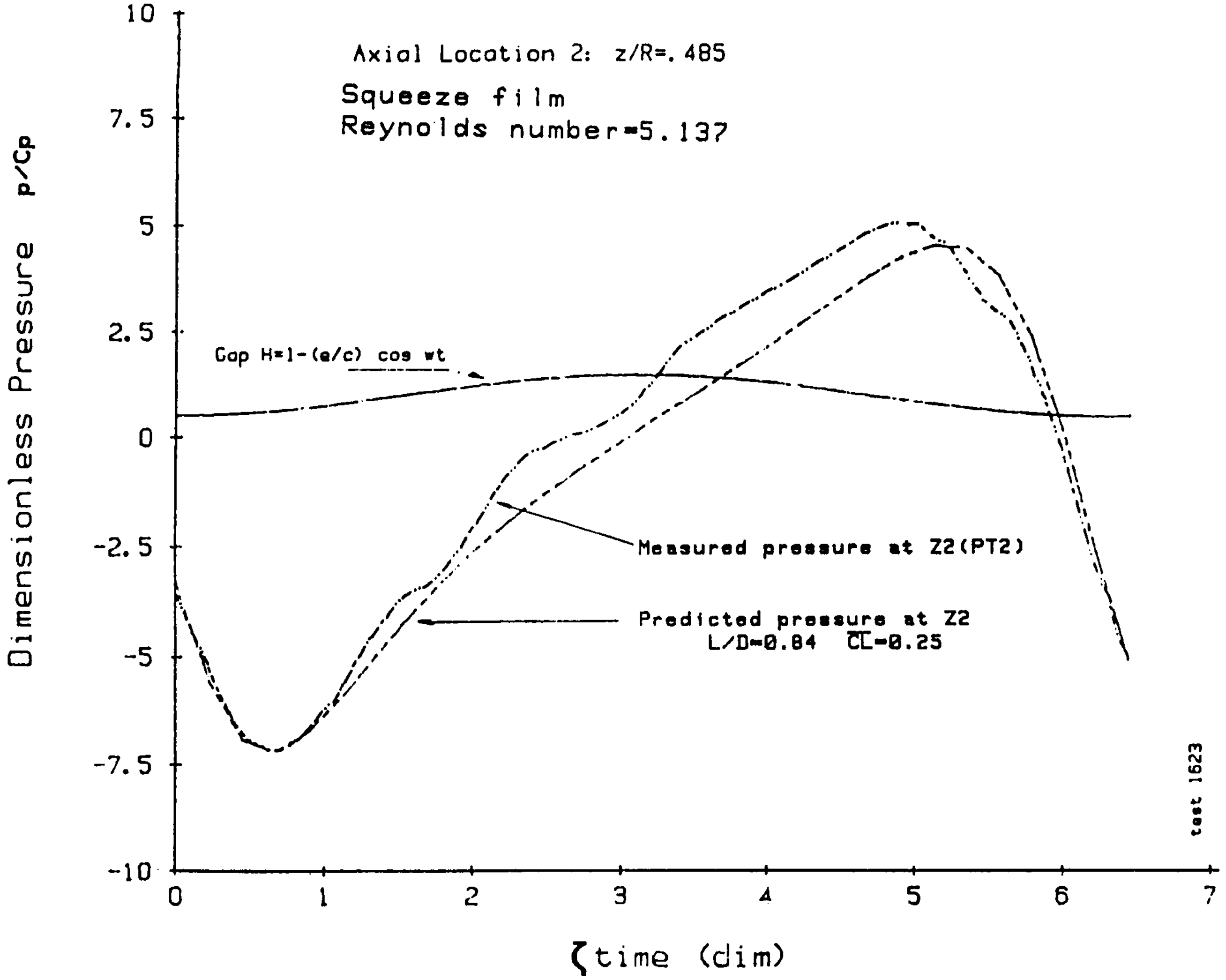

Figure 7. Dimensionless pressure wave $\overline{p}$ vs. wt at axial location Z2. Re=5.137. Experimental and predicted results.

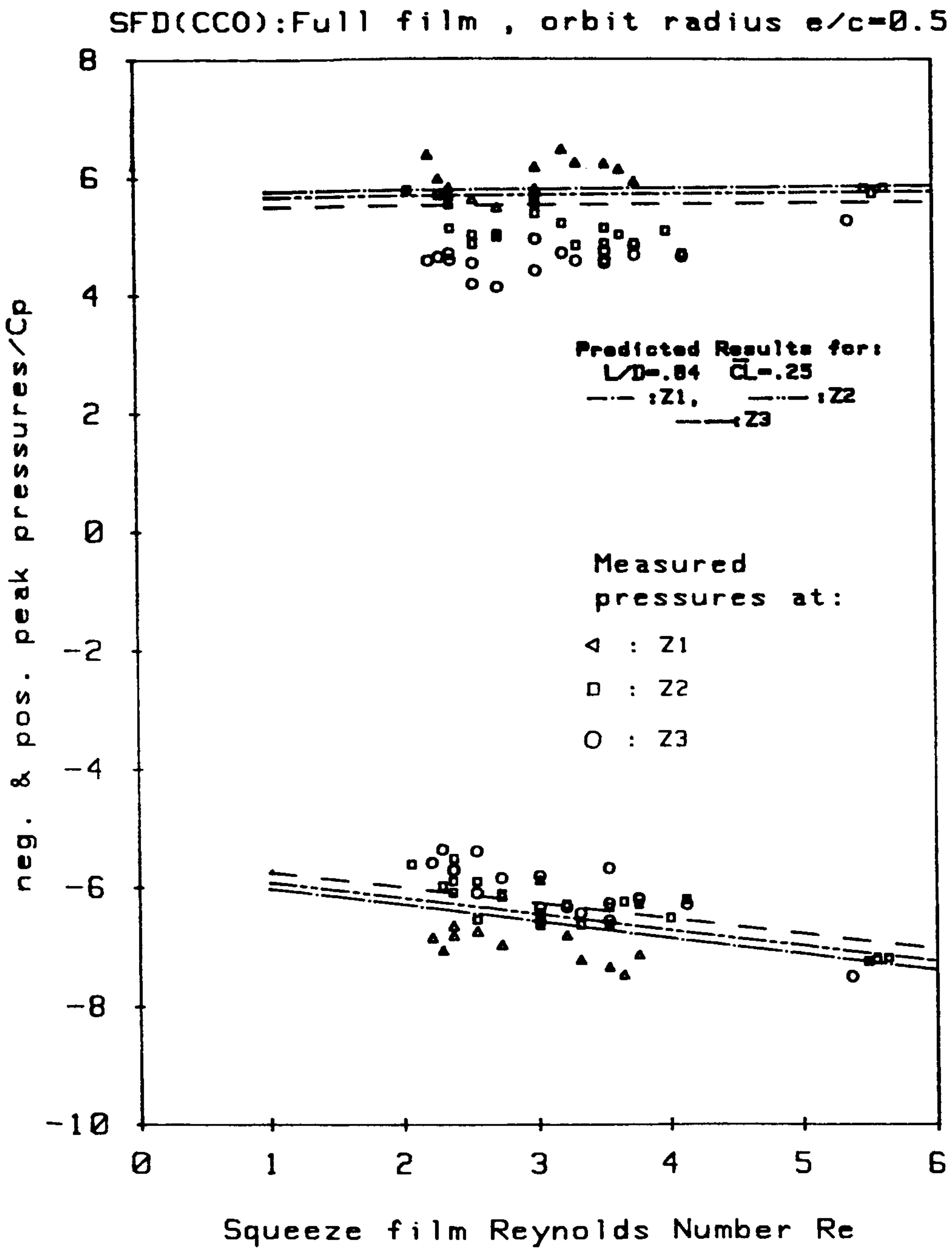

Figure 8. Dimensionless peak pressures $\overline{p}$ vs. squeeze film Reynolds. Experimenta and predicted results.

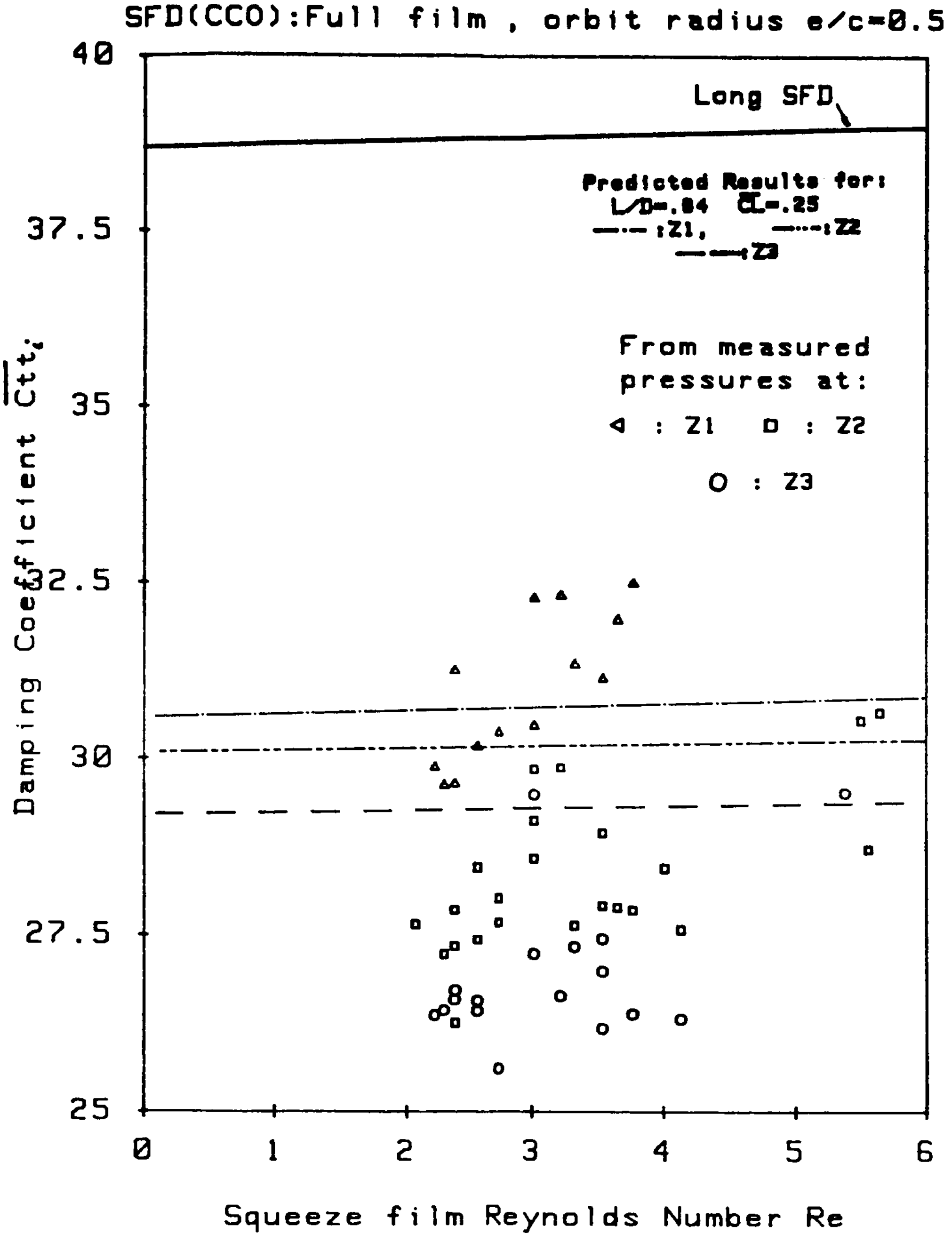

Figure 9. Dimensionless damping coefficient $\overline{Ctt}$ vs. Reynolds number calculated from measured pressures. Experimental and predicted results.

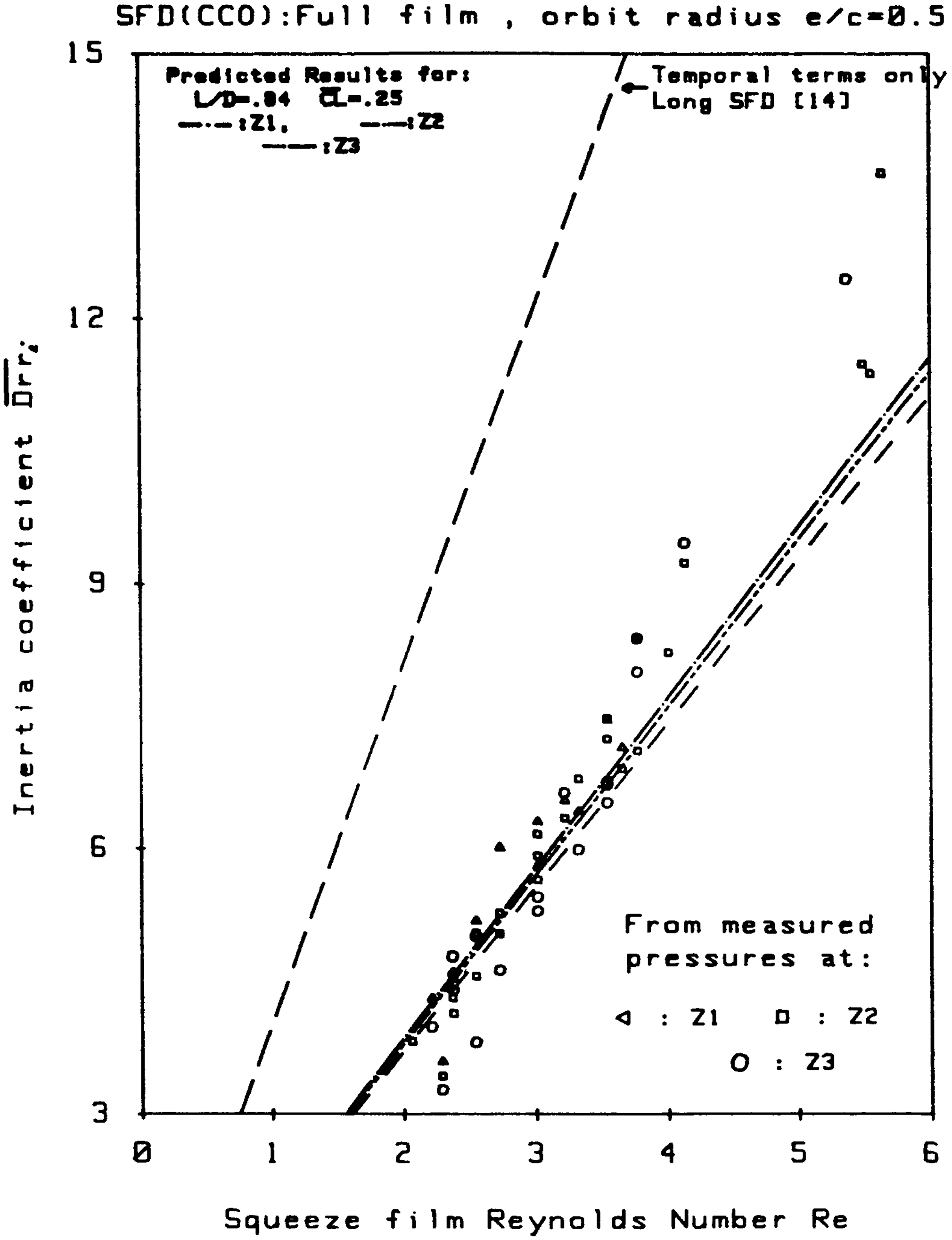

Figure 10. Dimensionless inertia coefficient $\overline{Drr}$/Re vs. Reynolds number calculated from measured pressures. Experimental and predicted results.

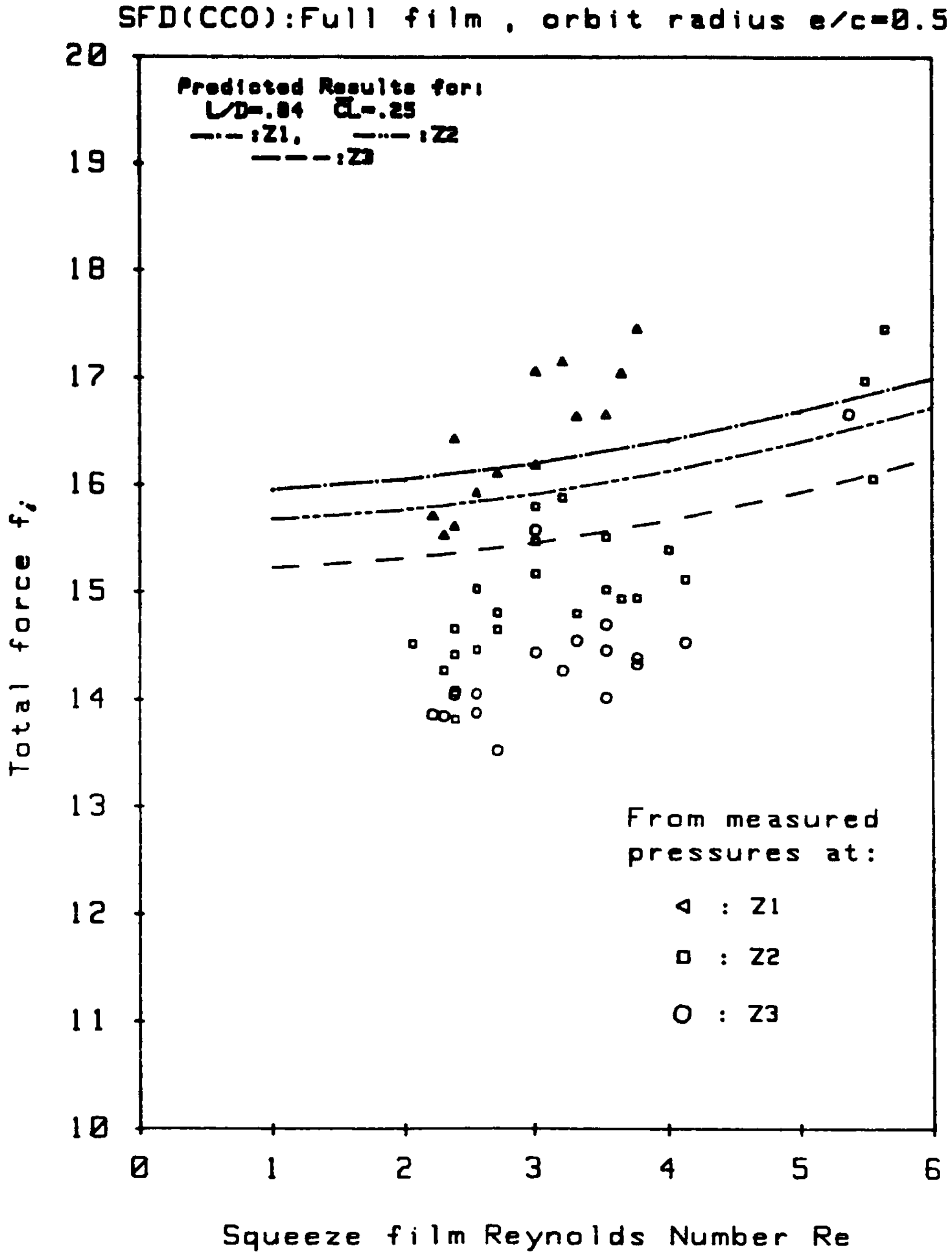

Figure 11. Dimensionless fluid film forces f vs. Reynolds number. Experimental and predicted results.

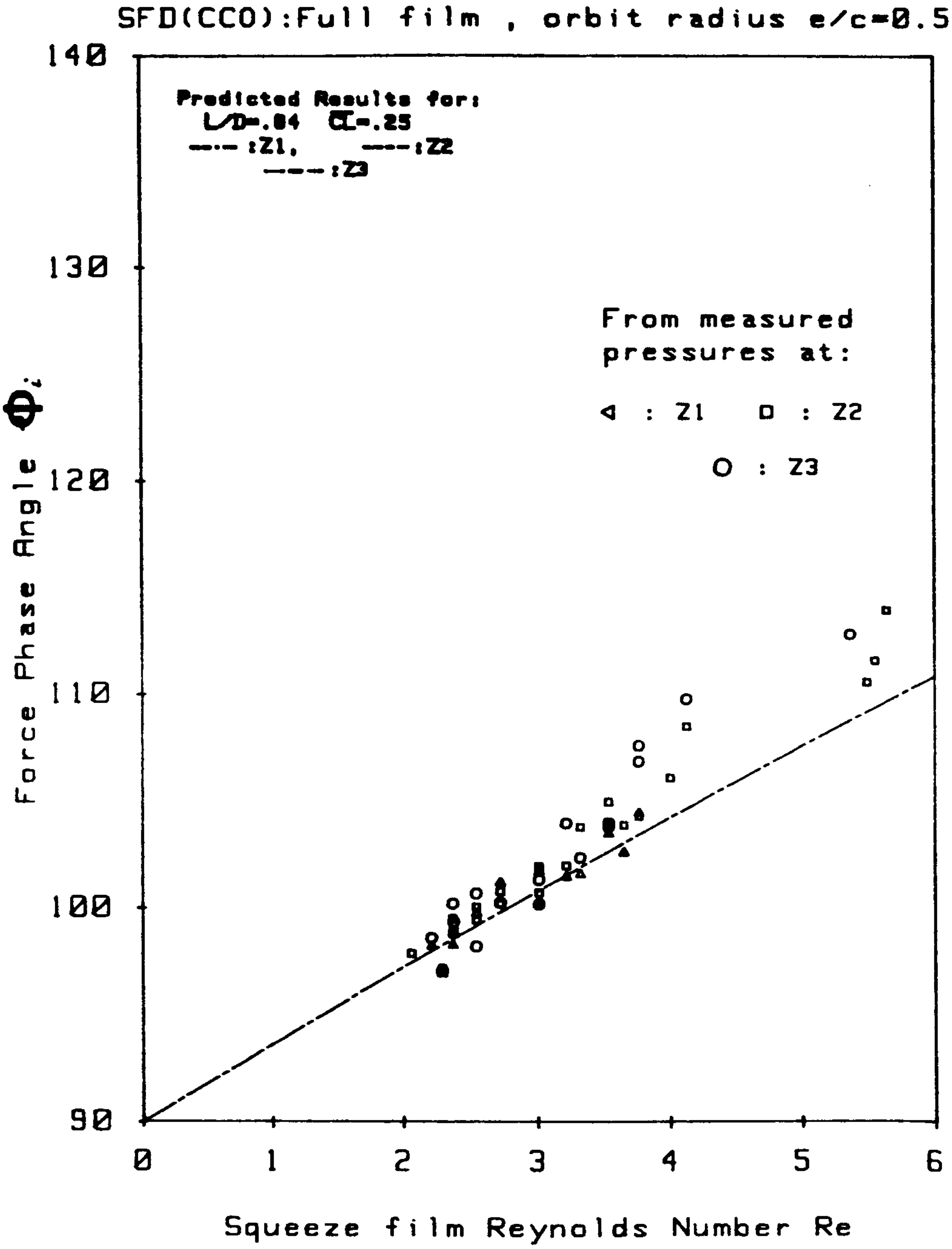

Figure 12. Force phase angle ϕ vs. squeeze film Reynolds number. Experimental and predicted results.

N87-22220

NONLINEAR DYNAMICS OF ATTRACTIVE MAGNETIC BEARINGS[1]

K.V. Hebbale[2] and D.L. Taylor
Cornell University
Ithaca, New York 14853

The nonlinear dynamics of a ferromagnetic shaft suspended by the force of attraction of 1, 2, or 4 independent electromagnets is presented. Each model includes a state variable feedback controller which has been designed using the pole placement method. The constitutive relationships for the magnets are derived analytically from magnetic circuit theory, and the effects of induced eddy currents due to the rotation of the journal are included using Maxwell's field relations.

A rotor suspended by four electro-magnets with closed loop feedback is shown to have nine equilibrium points within the bearing clearance space. As the rotor spin speed increases, the system is shown to pass through a Hopf bifurcation (a flutter instability). Using center manifold theory, this bifurcation can be shown to be of the subcritical type, indicating an unstable limit cycle below the critical speed. The bearing is very sensitive to initial conditions, and the equilibrium position is easily upset by transient excitation. The results are confirmed by numerical simulation.

INTRODUCTION

The suspension of a rotating shaft in a magnetic field without mechanical contact or lubrication is an old idea. Many studies concerning the feasibility of electromagnetic levitation in various applications like magnetic bearings, high speed ground transportation, electromagnetic dampers for vibration control, etc. can be found in the literature [refs. 1,2,3]. Now, with advanced electronic control, high speed magnetic bearings are a commercial reality, being used in grinding and polishing machinery, vacuum pumps, compressors, turbines, generators, and centrifuges [refs. 4,5]. Electromagnetic dampers have been shown to be capable of effectively eliminating vibration at the critical speed associated with the first bending mode of shafts [refs. 3,6]. In addition, the dampers have been seen to suppress the system instability associated with the fluid film bearings.

This paper only considers attraction systems under active control. Passive systems using permanent magnets in repulsion are usually incapable of generating sufficient load carrying capacities. However, the constitutive model presented here is applicable to electromagnets operating at sufficient speed that the dead weight is carried by eddy currents generating lift from the lower magnet.

The control system studied varies the voltage to each magnet in response to the motion of the mass. Such a suspension system with multiple magnets is a multiple input - multiple output system. A state variable feedback controller, designed on the basis of pole placement technique, is used to stabilize the system and meet the design specifications. Unlike in a single input - single output system, the multivariable problem has a much richer structure and has many gain matrices yielding the same pole placement [ref. 7]. The direct method of choosing an arbitrary vector and reducing the multi-input - multi - output system into a single input - single output system is used to obtain the gain matrix.

Research and development activity on passive, active, and combination magnetic bearing systems spans over

---

[1] This work was supported in part by the Office of Naval Research under contract no. N0014-80-C-0618.

[2] Presently at General Motors Research Laboratories.

150 years. Earnshaw in 1839 demonstrated [ref. 8] mathematically that it is impossible for a pole placed in a static field of force to have a stable equilibrium position when an inverse square law relates force and distance. Braunbek in 1939 carried out [ref. 8] a similar mathematical analysis specifically for suspensions in unvarying magnetic fields and deduced that levitation is impossible in such fields when all the materials have relative permeabilities (μ_r) greater than or equal to 1, but possible if materials with $\mu_r < 1$ can be introduced. It follows that it is impossible to achieve levitation in static magnetic fields, that is, using permanent magnets or fixed current dc electromagnets, unless part of the system consists of either diamagnetic material ($\mu_r < 1$) or a superconductor ($\mu = 0$).

Examples of hybrid passive and active systems appeared as early as 1950 in which photoelectric positional feedback was used. Stiffness and damping were minimal because of the lack of sophisticated control components. Early experiments with fully active systems (1957) were largely thwarted by the then high cost and size of control system components. In time, it became clear that hybrid systems with simple electronics capable of carrying industrial loads depended heavily on complex mechanical dampers. Meanwhile the cost and size of sophisticated electronics for purely active systems continued to come down as performance rose. Since active magnetic bearings provide both damping and support, the choice became clear. Subsequent efforts have concentrated on active magnetic bearings.

Several reviews of electromagnetic levitation are available in the literature [ref. 8,9]. Two electromagnetic levitation methods have met with success: direct, position feedback control techniques; and ac modulated or indirect feedback methods. In the latter, the magnet inductance is part of a tuned circuit whose natural frequency depends on the gap between the suspended mass and magnet. This method has been used to suspend gyroscopic devices for inertial sensors. It suffers from high eddy current losses and a small range of stable air gaps. Analysis of ac tuned circuit methods may be found in Kaplan [ref. 10].

For heavily loaded bearings, direct feedback methods have to be used. However, dynamics has not seen as much attention as it has in journal bearings. Most of the available literature deals with empirical ideas and concentrates on reliability of the bearing, reducing the size, weight and complexity of the devices [ref. 11].

Insight can be gained by studying a ferromagnetic suspension (suspended mass is not moving). Moon [ref. 12] and Woodson and Melcher [ref. 13] are good starting points.

When the suspended rotor is spinning under the magnets and if the rotor is not laminated, eddy currents will be induced in the material. The induced eddy currents create two kinds of force on the rotor: drag force which leads to additional power dissipation and coupling of motions of the rotor in two perpendicular directions, and repulsive force which tends to counter balance the attractive force. Expressions for the drag and repulsive forces can be derived by studying the effect of material motion on the diffusion of magnetic fields [ref. 13], starting from Maxwell's field relations. Moon [ref. 12] has shown that in certain magnetic levitation configurations eddy currents can produce a positive or negative damping force depending on the speed.

Although a good analytical model is not available for eddy currents due to shaft rotation, a number of authors calculate the eddy current effects in other geometrical configurations using a hypothetical simplified model and finite element methods [refs. 14,15]. Several studies on linear induction motors are available [refs. 1,16] which can be extended to magnetic bearings by making several assumptions and manipulations. In the above studies, the authors calculate the induced forces by cross multiplying the current density vector, which does not take care of the attractive force when the moving material is ferromagnetic. In this paper , the forces are calculated using the Maxwell's stress tensor approach which in one calculation gives all the forces involved.

Matsumara [ref. 17] has derived the fundamental equations for a horizontal shaft magnetic bearing taking into account the rolling, pitching, and yawing of the rotor. In deriving the equations of motion, he assumes that the rotor consists of a laminated core and consequently no eddy currents are generated in the material. He has proposed an integral type control system which stabilizes the system without steady state shaft position error.

Hebbale [ref. 18] has studied the nonlinear dynamics in terms of equilibrium points, transient response, on-set of instability, limit cycle size, and forced response. The material which follows was taken from [ref. 18].

NOMENCLATURE

a	Distance of magnet pole corner (near) from center line
A	Area of magnet pole face, Linearized state matrix
b	Distance of magnet pole corner (far) from center line
B	Control input matrix, a Magnetic Flux density
B_0	Magnetic flux density under the magnet pole
C_i	Feedback gains of controller
D	Diameter of rotor

$\vec{e}$	Unit vectors
$E(t)$	Control voltage
E_i	Total voltage to magnet
E_{0i}	Initial voltage to magnet
f, F	Nonlinear functions
F_{mag}	Magnetic force
g	Acceleration due to gravity
H	Magnetic field intensity
I_i	Current in coil
j	$\sqrt{-1}$
k	Wave number
K	Feedback gain matrix
L	Inductance of circuit
L_i	Flux path length
M	Mass of rotor
n_1, n_2	Real and imaginary parts of γ
N	Number of turns in coil
q	Complex wave number
R	Resistance of coil
s_i	Nondimensional velocity
t	Time
$\vec{V}$	Velocity vector
V	Velocity (magnitude)
W_d	Field energy density
W_f	Field energy stored
x	shaft displacement
X	State vector
y	shaft displacement
Z	Linearized state vector
α	System constant $= \mu_0 N^2 A$
β	System constant $= L_1/\mu_{r1} + L_2/\mu_{r2}$
γ	Complex number $= \cosh k\Delta + \mu_0 q/\mu k \sinh k\Delta$
Γ	Magnetomotive force
δ	variation from equilibrium
Δ	Equilibrium gap length
θ	Magnet pole angle with respect to vertical
λ	Flux linkage
μ, μ_r	Permeability
σ	Electrical conductivity of rotor material
Σ	Closed surface, Summation sign
Φ	Magnetic flux
Ω	Spin speed of rotor

FOUR MAGNET BEARING

The shaft is suspended within four magnets, as shown in Fig. 1. The shaft has high permeability and high conductivity and is not laminated. (Lamination would serve to inhibit eddy currents.) All of the four electromagnets are identical, modelled as a coil of N turns on a laminated core of high permeability. The coil has resistance R and an initial voltage E_0 applied. The dead weight is suspended by the difference in forces exerted by top and bottom magnets. All magnets carry a steady state voltage, adjusted so that at zero speed, the gap lengths under the magnets are equal.

This fully energized configuration was chosen so that the magnets could generate the effect of repulsion by decreasing the attraction. The horizontal magnets generate equal force when the shaft is centered and the control system is commanding equal voltages. The shaft displacement is measured by two coordinates (x, y) as shown in

Fig. 1, measured from the center of the clearance space in the horizontal and vertical directions respectively. When the rotor is not spinning, the center of the rotor is at the origin and the gap lengths are all equal to Δ.

If the shaft is not laminated, motion of the conducting shaft through the supporting magnetic fields will generate induced eddy currents. Eddy current effects cause both loss of lift and a drag force in the perpendicular direction. It is assumed that the rotor is spinning in the clockwise direction so that the drag force due to the top magnet acts in the negative x direction, that due to the right magnet acts in the y direction, and so on.

Several geometrical assumptions are made. The rotor always remains perfectly aligned within the bearing (no tilting). Under small displacements the surfaces of the rotor and the magnet pole faces are assumed to remain parallel. Since the individual poles are located at angles $\pm\theta$ relative to the vertical axis in the case of vertical magnets or relative to the horizontal axis in the case of horizontal magnets, it is assumed that when the rotor moves vertically a distance y, the change in gap length for the vertical magnets is $y\cos\theta$. Similarly, when the rotor moves horizontally by a distance x, the change in gap length for the horizontal magnets is $x\cos\theta$. Any other translational motion of the rotor can be written as a superposition of the motions in x and y directions. The effect of unequal gap lengths under a vertical magnet caused by a rotor motion in the horizontal direction or vice versa is neglected because the total gap length under that magnet remains constant.

The control system studied varies the voltage to each magnet in response to the motion of the mass. Such a suspension system with multiple magnets is a multiple input - multiple output system. A state variable feedback controller, designed on the basis of pole placement technique, is used to stabilize the system and meet the design specifications. Unlike in a single input - single output system, the multivariable problem has a much richer structure and has many gain matrices yielding the same pole placement [10]. The direct method of choosing an arbitrary vector and reducing the multi-input - multi - output system into a single input - single output system is used to obtain the gain matrix.

EQUATIONS OF MOTION

The differential equations of motion describing the response of the rotor are given by

$$\begin{aligned} M\ddot{y} &= \sum \vec{F}_{mag}\cdot\vec{n}_y - Mg \\ M\ddot{x} &= \sum \vec{F}_{mag}\cdot\vec{n}_x \end{aligned} \tag{1}$$

where $\sum \vec{F}_{mag}$ are the vectorially combined magnetic forces from all the magnets. Expressions for resolutes of $\vec{F}_{mag}$ have been derived in Appendix B for a single magnet. The reader is cautioned that the x, y coordinates in Appendix B are local tangential and normal directions for each individual magnet and do not correspond the the x, y coordinates for motion of the shaft. $\vec{F}_{mag}$ includes the steady state attraction forces and eddy current forces (both repulsion and drag). Only spin velocity is assumed to generate eddy currents. Motion of the shaft $(\dot{x}, \dot{y})$ doesn't generate eddy currents.

The remaining differential equations are obtained from a voltage balance in each of the four electromagnetic circuits:

$$E_i = I_i R_i + N_i \dot{\phi}_i \qquad i = 1,2,3,4 \tag{2}$$

where subscripts refer to the top, right, bottom, and left magnets respectively. An expression for the magnetic flux ϕ has been derived in Appendix B.

Expressions for the magnetic forces are given in Appendices A and B. If eddy currents are neglected, then there are no terms in the differential equations which depend on speed. In general

$$\vec{F}_{mag} = f(x, y, I_1, I_2, I_3, I_4, \Omega) \tag{3}$$

and

$$\phi_i = f(x, \dot{x}, y, \dot{y}, \dot{I}_1, \dot{I}_2, \dot{I}_3, \dot{I}_4, \Omega) \tag{4}$$

The general procedure is to

(a) Determine E_{0i} such that the equilibrium location at zero speed is centered.

(b) Design a state variable controller by pole placement.

(c) Determine all steady state equilibrium locations as a function of speed.

(d) Linearize about equilibrium locations to determine stability as a function of speed.

Choosing eight state variables $\dot{y}, y, \dot{x}, x, I_1, I_2, I_3$, and I_4, Eqs. (1) and (2) can be put into a standard first order form

$$\dot{\mathbf{X}} = f(\mathbf{X}, \mathbf{E}, \Omega) \tag{5}$$

$$\mathbf{E} = \mathbf{E}_0 + \delta\mathbf{E} \tag{6}$$

$$\delta\mathbf{E} = K\mathbf{X} \tag{7}$$

$$\delta\mathbf{E} = (\delta E_1 \quad \delta E_2 \quad \delta E_3 \quad \delta E_4)^T \tag{8}$$

$$\mathbf{X} = (\dot{y} \quad y \quad \dot{x} \quad x \quad I_1 \quad I_2 \quad I_3 \quad I_4)^T \tag{9}$$

where $\mathbf{X}$ is a 8-vector containing the state variables.

SINGLE MAGNET CASE

The single magnet suspension serves as a paradigm for the more complicated models which follow. Consider only the top magnet, with x constrained to be zero, and with no rotation ($\Omega = 0.0$). The approximation for $\vec{F}_{mag}$ from Appendix A can be used, giving $\vec{F}_{mag} \propto (I^2, \frac{1}{h^2})$. Furthermore, $\vec{F}_{mag}$ is always positive.

This system is well known to be unstable without feedback. A complete state variable feedback would be

$$\delta\mathbf{E} = [C_1 \quad C_2 \quad C_3] \begin{Bmatrix} x - x_0 \\ \dot{x} \\ I - I_0 \end{Bmatrix} \tag{10}$$

Fig. 2 shows how the static magnetic force is affected by the choice of C_1. Obviously, there is some minimum value of C_1 to produce a positive slope at $x_0 = 0.001$. High values of C_1 produce a stiffer system but with a penalty. A second (unstable) equilibrium point exists. Increasing C_1 moves this point closer to the stable operating location. The safe operating domain in the state space is therefore decreased.

In addition, Fig. 2.5 shows the extreme nonlinearity of the system. The complete equations of motion can be written as a variation about the equilibrium point $(x_0, 0, I_0)$

$$\begin{aligned} u &= x - x_0 \\ v &= \dot{x} \\ w &= I - I_0 \end{aligned} \tag{11}$$

$$\frac{d}{dt}\begin{pmatrix} u \\ v \\ w \end{pmatrix} = \begin{bmatrix} A \end{bmatrix} \begin{pmatrix} u \\ v \\ w \end{pmatrix} + \begin{bmatrix} B \end{bmatrix} \delta\mathbf{E} \tag{12}$$

where

$$A = \begin{bmatrix} 0 & 1 & 0 \\ \frac{4gR}{E_0}\sqrt{\frac{Mg}{\alpha}} & 0 & -\frac{2gR}{E_0} \\ 0 & 2\sqrt{\frac{Mg}{\alpha}} & -\frac{E_0}{\alpha}\sqrt{\frac{\alpha}{Mg}} \end{bmatrix} \quad \text{and} \quad B = \begin{pmatrix} 0 \\ 0 \\ \frac{E_0}{\alpha R}\sqrt{\frac{\alpha}{Mg}} \end{pmatrix} \tag{13}$$

$$\delta\mathbf{E} = \begin{bmatrix} C_1 & C_2 & C_3 \end{bmatrix} \begin{pmatrix} u \\ v \\ w \end{pmatrix} \tag{14}$$

where

$$\alpha = \mu_0 N^2 A \tag{15}$$

Note, the equilibrium values (x_0, I_0, E_0) are related and consistent values must be used so that the position is actually a fixed point.

$$x_0 = \frac{1}{2}\left[\frac{E_0}{R}\sqrt{\frac{\alpha}{\mu g}} - \beta\right] \tag{16}$$

$$I_0 = \frac{E_0}{R} \tag{17}$$

The various terms in Eq (13) can be identified as representing the magnetic force, the voltage drop due to back emf and the voltage drop due to inductance.

The controllability of this system can be determined from the rank of the controllability matrix Q.

$$Q = [B \quad AB \quad A^2B\,] \tag{18}$$

Substituting from Eq. (13) results in a matrix that has full rank. The total dynamic matrix turns out to be

$$\frac{d}{dt}\begin{pmatrix} u \\ v \\ w \end{pmatrix} = \begin{bmatrix} 0 & 1 & 0 \\ \frac{4gR}{E_0}\sqrt{\frac{Mg}{\alpha}} & 0 & -\frac{2gR}{E_0} \\ \frac{E_0}{\alpha R}\sqrt{\frac{\alpha}{Mg}}C_1 & 2\sqrt{\frac{Mg}{\alpha}} + \frac{E_0}{\alpha R}\sqrt{\frac{\alpha}{Mg}}C_2 & -\frac{E_0}{\alpha}\sqrt{\frac{\alpha}{Mg}} + \frac{E_0}{\alpha R}\sqrt{\frac{\alpha}{Mg}}C_3 \end{bmatrix}\begin{pmatrix} u \\ v \\ w \end{pmatrix} \tag{19}$$

The system is stable if

$$\begin{aligned} &C_3 < R \\ &C_1 > 2R\sqrt{\frac{Mg}{\alpha}}\left(1 - \frac{C_3}{R}\right) \\ &C_1 < 2R\sqrt{\frac{Mg}{\alpha}}\left(1 - \frac{C_3}{R}\right) + \frac{E_0}{\alpha}\sqrt{\frac{\alpha}{Mg}}\left(1 - \frac{C_3}{R}\right)C_2 \end{aligned}$$

The first constraint can be interpreted as requiring the coil to behave with positive resistance. The minimum value of C_1 is that required to overcome the effective negative stiffness of the magnetic force. The third condition enforces an upper bound on C_1 which is dependent on C_2. This implies that the system cannot be stable without some velocity feedback. Apparently, the damping induced by the back emf is cancelled by the inductive lag of the coil, leaving an unstable system unless velocity feedback is used to add dissipation.

Given values of C_1, C_2, C_3, the system may be linearized about the other equilibrium point (the one at lower gap). This point is found still to be unstable. Fig. 3 shows a sketch of the response in 3-D state space. The stabilized equilibirium point is a focus in two dimensions and has a stable subspace in the other dimension. The unstable equilibrium point is a saddle point in two dimensions and has a stable subspace in the third dimension. The presence of the unstable equilibrium point close to the stable one significantly affects the domain of convergence.

Rather than developing this problem further (including for example, the effect of eddy currents) discussion will be shifted to a two magnet configuration.

TWO MAGNET VERTICAL CASE

Consider a bearing consisting of only the top and bottom magnets in Fig. 1, with x constrained to be zero. This problem will study how the eddy currents affect the system, and so Appendix B will be used to represent the magnetic forces. The rotor is suspended by the difference in magnetic forces due to the top and bottom magnets. The stationary steady state voltages are such that the gaps are equal top and bottom, and the magnetic flux density is well below the saturation value of 1.5 - 2.0 webers/m^2.

The 8 state vector reduces to $(\dot{y}, y, I_1, I_3)$. $\Sigma \vec{F}_{mag}$ becomes $F_{mag1} - F_{mag3}$. Since the system is constrained in x, the drag force due to eddy currents and the resulting coupling is neglected. The governing differential equations are

$$\begin{aligned} \frac{d}{dt}y &= \dot{y} \\ \frac{d}{dt}\dot{y} &= \frac{F_{mag1} - F_{mag3}}{M} - g \\ \frac{d}{dt}I_1 &= \frac{2(\Delta - y\cos\theta_1) + \beta_1}{\alpha_1}\left(E_{01} + \delta E_1 - R_1 I_1\right) - \frac{2\dot{y}I_1\cos\theta_1}{2(\Delta - y\cos\theta_1) + \beta_1} \\ \frac{d}{dt}I_3 &= \frac{2(\Delta - y\cos\theta_3) + \beta_3}{\alpha_3}\left(E_{03} + \delta E_3 - R_3 I_3\right) - \frac{2\dot{y}I_3\cos\theta_3}{2(\Delta - y\cos\theta_3) + \beta_3} \end{aligned} \tag{21}$$

The voltages E_{01}, E_{02} have been adjusted so that the equilibirium point is $y = 0$ with no spin speed. It then follows that

$$I_{01} = \frac{E_{01}}{R_1}$$
$$I_{03} = \frac{E_{03}}{R_3} \tag{22}$$
$$M g = F_{mag1} - F_{mag3}$$

A state variable feedback controller is designed for this case using the linearized set of equations at zero speed ($\Omega = 0.0$). Because eddy currents are not a factor at zero speed , the formulae in Appendix A can be used (giving a significant simplification over Appendix B) . The linearized system can be written as

$$\dot{\mathbf{Z}} = A\mathbf{Z} + B\begin{pmatrix} \delta E_1 \\ \delta E_3 \end{pmatrix} \tag{23}$$

A is the Jacobian, B is the control matrix containing the inverse of the inductances of the two circuits at equilibrium and $(\delta E_1 \ \delta E_3)^T$ is the control vector for the perturbation voltges to the magnets.

This is a two input - single output system and unlike the previous single magnet case, there are many gain matrices K yielding the same eigenvalues. The solution to this control problem is discussed in [18]. However, the result is a gain matrix K such that the poles of the closed loop system (at zero speed) are placed at −1000, −1000, $-100 \pm j100$.

$$\begin{pmatrix} \delta E_1 \\ \delta E_3 \end{pmatrix} = K \begin{pmatrix} \dot{y} \\ y \\ \delta I_1 \\ \delta I_3 \end{pmatrix} \tag{24}$$

The complete closed loop system can now be considered with speed as a parameter. The equilibrium points are found by the numerical solution of the right hand side of Eq. (21) with ($\dot{y} = 0$). It turns out that there are 3 equilibrium points. This can be understood from a graph of the net magnetic fource versus y as in Fig. 4. The point at $y = 0$ is a stable equilibrium point. However, points at $y \sim 4.4\ 10^{-4}$ and $y \sim -8.4\ 10^{-4}$ are also equilibrium points.

Furthermore, as speed increases, the force curve changes. The central equilibrium point drifts downwards, and the slope there decreases. Eventually, at sufficiently high speed, the central and lower equilibrium points coalesc and disappear. This is shown in Fig. 5.

The catastrophe occurs at $\Omega = 47000$rpm for the values of parameters in this paper.

However, before that occurs, a more interesting dynamic phenomenon is observed. The dynamic equations can be linearized at each (shifting) equilibrium point. Since the equilibrium points must be found numerically, the linearization was also performed numerically using a central difference scheme in each state variable. The eigenvalues of the resulting dynamic matrix are shown in Fig. 6 as a function of the shaft speed Ω.

At zero speed, the eigenvalues are very near the design points −1000, −1000, $-100 \pm j100$. The difference is because magnetic circuit theory (Appendix A) is used in the zero speed controller design, but the full eddy current field theory solution (Appendix B) is used when linearizing and calculating eigenvalues. The system is stable (in a small neighborhood of the central equilibrium point) up to a value of $\Omega = 40406$rpm, at which time a Hopf bifurcation (flutter instability) occurs.

The system loses stability through a single pair of eigenvalues crossing the imaginary asis at $\Omega = 40406$rpm. In such a case, a limit cycle must grow from the bifurcation point. This can be either a stable limit cycle which increases in amplitude for $\Omega \geq 40406$rpm or an unstable limit cycle which closes down around the focus as $\Omega \rightarrow 40406$rpm. A standard bifurcation analysis was performed using the program BIFOR2 [19]. A stable supercritical limit cycle is predicted. The amplitude is shown in Fig. 7 along with the limit cycle actually found by simulation. It should be noted that the actual phase space is four dimensional and only a 2-D subspace is shown.

The reader is cautioned that the study was not extended to determine what (if anything) happens to the limit cycle when the two equilibrium points coalesc and disappear at 47000 rpm.

FOUR MAGNET CASE

Each coil is excited by initial constant voltages denoted by E_{oi}, i = 1,2,3,4, and the steady state magnetic forces (at $\Omega = 0$) are such that

$$\sum \vec{F}_{mag} = -mg\hat{n}_y. \tag{25}$$

The equilibrium points for this system at any spinning speed can be determined by equating the right hand side of Eqs. (5) to zero. That is,

$$0 = f(\mathbf{X}_{eq}, \Omega) \tag{26}$$

give the equilibrium points of the system. Eq. (26) represents a set of coupled nonlinear algebraic equations which has to be solved by a numerical technique. But, at zero speed, the equations decouple in x and y giving two separate problems, one of which has been discussed briefly. Without feedback control, this system has a single equilibrium point. It is possible to track the movement of this equilibirium point as speed increases [18].

To find the nature of the equilibrium point at any speed Ω, the differential equations are linearized and studied for their behavior in the neighborhood of the equilibrium point. As expected, the eigenvalues of the linearized system show that the four magnet bearing without active controls is inherently unstable.

A state variable feedback controller is added to the system to stabilize the bearing and provide it with suitable damping and dynamic characteristics. The effect of a gain matrix which is speed dependent is beyond the scope of this paper, and the control system is designed using the system characteristics at $\Omega = 0.0$. At zero speed, the equations of motion are uncoupled, and two 4th order control problems can be solved rather than one 8th order problem. State variable feedback controllers were designed for each subsystem to place the closed loop poles at -1000, -1000, -100± j100. This placement provides dominantly second order response over a frequency range of 0 to 5000 rpm.

Note that because the system decouples, all states are not fed back to the control inputs for each magnet. For example, the variations of the gap length, velocity, and currents of the horizontal magnets are not being fed back to the vertical magnets and vice versa. Another advantage is that designing a state variable feedback controller for a four-input two-output system is more involved in terms of computation that two versions of a two-input single-output system. The feedback gain matrix K for this four magnet bearing is given in Table 3.

where

$$\begin{bmatrix} \delta E_1 \\ \delta E_2 \\ \delta E_3 \\ \delta E_4 \end{bmatrix} = [K]\mathbf{X} \tag{27}$$

It is not possible to derive analytical expressions for the equilibrium points of the system. However, the pattern of 3 equilibrium points for a pair of magnets in one dimension is extrapolated to an expectation of 3^2 equilibrium points in 2 dimensions. This has been confirmed by numerically solving the equations. As in the simpler cases, in designing the control system, the choice of pole assignments for the central equilibrium point (and resulting feedback gains and stiffness) affects the location of the surrounding equilibrium points. A faster, stiffer system (poles further into the left half of the s-plane) pulls the outlying equilibrium points closer together, as shown in Fig. (8).

As the spin speed increases, the equilibrium points shift due to changes in the magnetic forces, and in this case including the coupling due to eddy current drag forces. Furthermore, because the dynamics are affected by the gap lengths, the dynamic coefficients have changed, and the stability of the system is affected. Fig. 9 shows how all 9 points move within the clearance space. At low speeds not much happens but above 10,000 rpm the points begin to shift. At about 15,000 rpm points 3 and 9 coalesce and disappear.

At any running speed, the system can be linearized about any of the equilibrium points. Since the equations are rather unmanagable, the linearization was performed using a central difference method to find the derivatives of each function with respect to each state variable. The result is

$$\dot{\mathbf{Z}} = A\mathbf{Z}. \tag{28}$$

where the **Z** column vector contains perturbations about the speed dependent steady-state vector **X**. Eigenvalues of A give stability information about each point. Points 2-9 (the outlying points) were always unstable.

The eigenvalues corresponding to the central equilibrium point (1) as a function of the spinning speed are plotted in Fig. 10. The system is stable in a small neighborhood around the equilibrium point up to about 9306 rpm. As the spinning speed is further increased, a pair of complex conjugate eigenvalues crosses the imaginary axis with all the other eigenvalues still in the left half of the complex eigenvalue plane. This means that the system undergoes a classical Hopf bifurcation to flutter instability at the critical speed of 9306 rpm.

Because of the existance of the outlying unstable equilibrium points, a supercritical limit cycle was expected. However, a conventional Hopf bifurcation analysis on the full set of nonlinear equations, using BIFOR2, indicated that an unstable limit cycle will enclose the central equilibirum point for speeds less that Ω_{cr}. Fig. 11 shows three transient responses at Ω = 2500 rpm, calculated by numerical integration of the complete set of nonlinear equations. Two converge to the equilibrium point and one diverges. The domain of convergence was approximated by slowly incrementing $x(0)$ and $y(0)$ and noting convergence or divergence. The domain of convergence is marked in Figs. 11,12. This is an overly simple approach because changes in the initial conditions of the remaining 6 state variables are not explored. However, it does lend credence to the prediction of an enclosing unstable limit cycle.

Forced response of this system is discussed in detail in [18]. The global resopnse is quite different from what might be expected from a linear analysis. The linear eigenvalues at Ω = 2500 rpm indicates a damping ratio of 0.7. However, the orbit resulting from a periodic excitation of 25N only converges quite slowly (damping ratio $\leq$ 0.05). Further discussion is beyond the scope of this paper. The topic is opened here only to point out the pitfalls in extrapolating a linearized analysis.

CONCLUSION

Without considering eddy current effect, there is no speed dependent term in the constitutive model for a magnetic bearing. Eddy current cause a loss of effective lift which, viewed as as external load, causes a classical sag for a proportional controller. More importantly, eddy current drag causes coupling between (x,y). Any change in the x gap affects the drag force in the y direction. Straightforward proportional control produces extra equilibrium points as the applied voltage is driven negative but the force remains attractive. These points are unstable but affect the global response of the system. In fact, designing a stiff system draws these points quite close to the equilibrium point. The equilibrium point is surrounded by an unstable limit cycle. Furthermore, as speed increases, the unstable limit cycle shrinks until the central point loses stability in a classical Hopf bifurcation. Above critical velocity, there is no equilibrium response.

The loss of lift is about 30% at 12500 rpm, which agrees approximately with experimental results of Yamamura [20]. The expression for the drag force under a single sinusoidal field density wave is the same as that obtained by Meisenholder [1].

The system may also lose stability by a simple catastrophe, the coalescing and joint annihilation of two equilibrium points. For the parameters used in this paper, this happens after the Hopf bifurcation. However, further parameter studies are needed to determine if this might occure before the Hopf bifurcation.

Further study is needed in designing state variable controllers. The zero speed design point is useful because it decouples the system, reducing the order. However, many other types of control can be envisioned.

The size of the enclosing unstable orbit is quite small, as shown in Fig. 12. A transient excitation could rather easily throw the shaft outside this into an unstable response. Also, a periodic excitation such as rotating unbalance, produces an orbit about the central equilibrium point. Simulation has indicated that if this orbit is large enough to touch or exceed the enclosing unstable limit cycle, the system becomes unstable. The loss of stabiliity is quite complicated, with bifurcations of the periodic orbit and possibly bifurcation to chaos. Discussion of this is beyond the scope of this paper.

Further problems which should be investigated are the effects of flux saturation in the magnetic material. Also, the model developed in Appendix B is applicable to repulsion type electromagnets, which would run at high speed and likely require superconductivity to implement. Stability of these bearings has not yet been addressed.

A final comment is the topic of bearing coefficients (equivalent stiffness and damping matrices). The situation is different from that of journal bearings, it is not possible to determine the 8 classical coefficients just by differentiating the force expressions with respect to $x, y, \dot{x}, \dot{y}$. The dynamics of the electrical components must also be incorporated. However, in all cases, the response in one 'mode' was very fast(Fig. 3) indicating that some subspace reduction might be possible.

APPENDIX A
ESTIMATION OF MAGNETIC LIFT FORCE

Magnetic circuit theory can be used to approximate the magnetic lift force of a single magnet, but eddy currents must be neglected. The following assumptions are made in deriving the expressions for the magnetic lift force:

1. Field fringing is neglected.
2. Magnetization curve is linear ($B = \mu H$).
3. Magnetic flux density B and field intensity H are uniform over cross-sections of the core, gap, or mass.

An electromagnetic circuit is considered whose elements are gap, core, and suspended mass, as shown in Fig. A.1. Each element has constant crossection A_i and length L_i. The magnetic flux ϕ is assumed constant throughout the circuit, and Γ is the total magnetomotive force within the circuit elements.

The density relationship $\phi = BA$ and the constitutive law $B = \mu H$ can be used to express field intensity in the ferromagnetic material in terms of the field intensity within the air gap.

By definition $\Gamma = \int H dl$ Integrating around the circuit and equating Γ to the current linked (NI) results in an equation for field intensity within the air gap. The field energy is determined within each element $w = \frac{1}{2}\mu H$ and the total field energy is obtained by a volumn integral over all the elements.

By definition, the force is the rate of change of stored field energy with respect to the mechanical displacement.

$$F_{mag} = \frac{\mu_0 N^2 A I^2}{(2x + \frac{L_1}{\mu_{r1}} + \frac{L_2}{\mu_{r2}})^2} \tag{A.1}$$

In addition, the total flux ϕ, the magnetic field density B, the magnetic flux linkage λ, and the inductance L can be expressed in terms of the gap length x and current I as:

$$\phi = \frac{\mu_0 N I A}{(2x + \frac{L_1}{\mu_{r1}} + \frac{L_2}{\mu_{r2}})} \tag{A.2}$$

$$B = \frac{\mu_0 N I}{(2x + \frac{L_1}{\mu_{r1}} + \frac{L_2}{\mu_{r2}})} \tag{A.3}$$

$$\lambda = \frac{\mu_0 N^2 I A}{(2x + \frac{L_1}{\mu_{r1}} + \frac{L_2}{\mu_{r2}})} \tag{A.4}$$

$$L = \frac{\mu_0 N^2 A}{(2x + \frac{L_1}{\mu_{r1}} + \frac{L_2}{\mu_{r2}})} \tag{A.5}$$

APPENDIX B
ESTIMATION OF MAGNETIC FORCES INCLUDING EDDY CURRENT EFFECTS

Motion of a conducting material through a magnetic field will cause eddy currents to be generated within the material. These eddy currents will produce an additional magnetic field and change the net force acting across the air gap. The complete eddy current analysis for 4 magnets as shown in Fig. 1 is analytically intractable. (It is probably amenable to finite element techniques.) An approximate solution is developed in Ref [18], and only the assumptions, general method, and results will be presented here.

As the shaft starts spinning, the eddy currents tend to repel the applied magnetic field and the skin depth of penetration becomes very small. This motivates a semi infinite assumption in the radial direction.

First, the problem will be unwrapped and considered as periodic on a half-space. However, before net forces are calculated, the surface tractions predicted by Maxwell's stress tensor will be wrapped around a circular shaft.

Second, each magnet will be considered separately, and the magnetic field for each magnet can be determined individually. The net force of each magnet is then determined, leading to 4 vector forces which are then summed vectorially. An alternative (more complex) solution is developed in Ref. [18] to find net magnetic field for all four magnets as a single system (simultaneously). The net magnetic field of all 4 magnets may be determined, and a single force predicted. However, this approach requires the assumption that all the gaps are equal. At low spinning speeds there is no difference between the two methods. Only at very high speeds do the two differ. (For parameters in this paper, 4% at 10^5 rpm). The simpler technique has been used here.

The square wave applied flux density is expanded as a Fourier series

$$B(x) = \sum_i \frac{2B_o}{\pi i}\left[cos\left(\frac{2bi}{D}\right) - cos\left(\frac{2ai}{D}\right)\right] sin\left(\frac{2ix}{D}\right) \tag{B.1}$$

or

$$B(x) = \sum_i B_i sin(k_i x) \tag{B.2}$$

The field density and current density distributions within the moving material solve a linear problem, and hence the principle of superposition can be invoked and each harmonic handled separately. After finding the field density inside the whole region, the forces acting on the rotor can be determined by calculating the Maxwell's stress tensor and integrating it over the surface area.

The following assumptions are made to simplify the analysis:

1. The conductive plate is infinite in x,z and positive y directions.
2. The conductivity σ and permeability μ are constants.
3. The field problem is two dimensional.

The equation that describes the distribution of the magnetic field in the conducting medium is derived from Maxwell's field equations [7].

$$-\frac{1}{\mu\sigma}\nabla^2\vec{B} + \frac{\partial\vec{B}}{\partial t} = \nabla \times (\vec{V} \times \vec{B}) \tag{B.3}$$

where $\vec{B} = B_x\vec{e}_1 + B_y\vec{e}_2$($\vec{e}_1$ and $\vec{e}_2$ being unit vectors in x and y directions respectively). The y component B_y is determined from the y component of (B.3) The remaining component B_x can be determined from the relation $\nabla \cdot B = 0$. The magnetic field is driven by the applied magnetic field density, and so solutions with the same traveling wave dependence on (x,t) are assumed. That is, it is assumed that the flux density takes the form

$$\vec{B} = [B_x(y)\vec{e}_1 + B_y(y)\vec{e}_2]e^{j(kx-\omega t)} \tag{B.4}$$

The solution form in the y-direction is $e^{\pm qy}$ where

$$q_i = k_i\sqrt{1+js} = k_i\sqrt{1+j\frac{\mu\sigma V}{k_i^2}} \tag{B.5}$$

Eqn (B.5) can be used to predict the skin depth.

The solution domain is divided into two regions, denoted by subscripts 1 and 2 respectively:

Region (1), the air gap where $\sigma = 0 (0 \le y \le \Delta)$; and
Region (2), the moving conducting medium $(\Delta \le y \le \infty)$.

The solutions within each region have two constants of integration, determined from the following 4 boundary conditions:

(1) one is set to zero because the solution cannot grow as $y \to \infty$.
(2) the applied flux density at $y = 0$
(3) At the interface $y = \Delta$, the condition of conservation of flux $\nabla \cdot B = 0$ is invoked. Using the divergence theorem, this leads to $B_{y1} = B_{y2}$.
(4) at the interface, $\nabla \times H = 0$. Using Stokes theorem, this leads to $H_{x1} = H_{x2}$.

Hence, the flux density distribution throughout both regions can be determined.

The forces acting on the conducting medium are calculated by Maxwell's stress tensor [8]. For magnetic problems with currents and no charges, the forces acting on a body are given by

$$F = \int_{\Sigma} \frac{1}{\mu}[\vec{B}\vec{B} \cdot \hat{n} - \frac{1}{2}\vec{B}^2\hat{n}]dA \tag{B.6}$$

where Σ is any closed surface surrounding the body and not containing any other body and B is the value of the field on the closed surface., Choosing a closed surface Σ such that it extends from $-\infty$ to ∞ and includes only the conducting medium, the integration is carried out with $\hat{n} = -\hat{e}_2$.

The complete flux density distribution in the whole region of Fig. B.1 due to all the applied sinusoidal waves is determined by superposing the individual fields. Each component of the field (B_x, B_y) is an infinite series in sine or cosine terms. The value of the $\vec{B}$ field at the interface, which is required for calculating the forces, is calculated by substituting $y = \Delta$ and letting $B_x = B_{x1}$ and $B_y = B_{y1}$. Substituting for $\vec{B}$ and evaluating the integrals, the forces per unit area acting on the material turn out to be

$$F_x = -\frac{1}{4\mu_0}\frac{\mu_0}{\mu}\sum\frac{B_i^2}{(n_{1i}^2 + n_{2i}^2)}\frac{s_i}{Re\sqrt{1+js_i}} \tag{B.7}$$

$$F_y = -\frac{1}{4\mu_0}\sum \frac{B_i^2}{(n_{1i}^2 + n_{2i}^2)}[1 - (\frac{\mu_0}{\mu})^2\sqrt{1 + s_i^2}] \tag{B.8}$$

where

$$s_i = \frac{\mu\sigma V}{k_i} \tag{B.9}$$

and where n_1 and n_2 are the real and imaginary parts of γ_i.

$$\gamma_i = [cosh(k_i\Delta) + \frac{\mu_0}{\mu}\frac{q_i}{k_i}sinh(k_i\Delta)] \tag{B.10}$$

Eqs. (B.7) and (B.8) are the expressions for the drag and lift force per unit area acting on the moving conducting medium. As expected, when the currents are not induced in the slab (V=0) (S=0), there is no drag force (F_x) and F_y is the magnetic attractive force. There is an optimum value of V at which the maximum force per unit area F_x is produced. The lift force decreases as V is increased, and at some value of V the force becomes zero, and at high values acts in the opposite direction (repulsion). At very high values of V, there is no drag because all the flux is excluded from the material and the repulsion force reaches an asymptotic value irrespective of the permeability of the material.

It is interesting to note that the integral and the summation are interchangable in order. That is, the force for one component of the fourier series can be determined and then summed or, as in the preceding, the fields summed and the force determined. This is perhaps surprising because the problem is nonlinear, but the infinite series for B_x and B_y are made up of sine and cosine terms which are orthogonal to one another and all the cross terms drop out during integration over one period.

The total flux can also be calculated and compared with that predicted by magnetic circuit theory (Appendix A). The more detailed solution is about 8% lower, showing the effects of magnetic circuit assumptions (uniform field density and no leakage in air gap).

For the magnetic bearing, the forces acting on a rotating shaft are calculated by wrapping one period of the B field distribution back onto the circular shaft. Choosing a closed surface $\sum$ on the circumference of the rotor and simplifying the integral in Eq. (B.6) give the forces acting on the rotor per unit width as

$$F_x = -\frac{1}{\mu_0}\int_{-\frac{\pi D}{2}}^{\frac{\pi D}{2}} B_x B_y cos(\frac{2x}{D})dx - \frac{1}{2\mu_0}\int_{-\frac{\pi D}{2}}^{\frac{\pi D}{2}} (B_y^2 - B_x^2)sin(\frac{2x}{D})dx \tag{B.11}$$

$$F_y 1 = -\frac{1}{\mu_0}\int_{-\frac{\pi D}{2}}^{\frac{\pi D}{2}} B_x B_y sin(\frac{2x}{D})dx - \frac{1}{2\mu_0}\int_{-\frac{\pi D}{2}}^{\frac{\pi D}{2}} (B_y^2 - B_x^2)cos(\frac{2x}{D})dx \tag{B.12}$$

where

$$B_x = B_{x1}(y)\Big|_{y=\Delta} = \sum -\frac{1}{\gamma_i}\frac{\mu_0}{\mu}\frac{q_i}{k_i}B_i e^{jk_ix} \tag{B.13}$$

$$B_y = B_{y1}(y)\Big|_{y=\Delta} = \sum \frac{1}{\gamma_i}\frac{q_i}{k_i}B_i e^{jk_ix} \tag{B.14}$$

The effect on the values of the forces of the number of terms used in the fourier series was investigated. The magnetic forces were calculated at different spinning speeds using 10, 25, 50, 100, and 500 terms in the series. There is very little change in the results when the number of terms used in the series is 50 or more. There is approximately 3% change in the lift force when the number of terms is increased from 10 to 25 or from 25 to 50. The change is much less in the case of drag force calculations. Striking a compromise between these two, and to save computer time, 25 terms were used in all the calculations in this paper.

REFERENCES

1. Meisenholder, S.G.; Wang, T.C.: *Dynamic Analysis of an Electromagnetic Suspension System for a Suspended Vehicle System* , TRW Systems Group, Prepared for Federal Railroad Administration, 1972.
2. Wormley, D.N.; et al.: *Noncontacting Suspension and Propulsion for Ground Transportation* , University Research for U.S. Department of Transportation, December 1979.
3. Nikolajsen, J.L.; et al.: Investigation of an Electromagnetic Damper for Vibration Control of a Transmission Shaft, *Proc Inst Mech Engrs*, Vol 193, I Mech E, 1979.
4. Habermann, H.; Liard, G.L.: Practical Magnetic Bearings, *IEEE Spectrum*, pp 26-30, September 1979.
5. Habermann, H.; Liard, G.L.: An Active Magnetic Bearing System,*Tribology International*, pp 85-89, April 1980.
6. Bartlett, R.A.: *Active Vibration Control of Flexible Rotors using Magnetic Bearings*, M.S. Thesis, Cornell University, January 1984.
7. Kailath, T.: *Linear Systems* , Prentice Hall, Inc., 1980.
8. Geary, P.J.: Magnetic and Electric Suspension, *British Scientific Instrument Research Association Report R314.*
9. Frazier, R.H.; et. al.: *Magnetic and Electric Suspensions*, The MIT Press, 1974.
10. Kaplan, B.Z.: A New Analysis of Tuned Circuit Levitators *International Journal of Nonlinear Mechanics*, Vol 9, pp 75-87, Pergamon Press, 1974.
11. Studer, P.A.: A Practical Magnetic Bearing, *IEEE Transactions on Magnetics*, Vol MAG-13, n5, September 1977.
12. Moon, F.C.: *Magneto-solid Mechanics* , Cornell University, to be Published.
13. Woodson, H.H.; Melcher, J.R.: *Electromechanical Dynamics Part I, Part II*, John Wiley and Sons, Inc., New York, 1968.
14. Chari, M.V.K.; Silvester, P.P.: *Finite Elements in Electrical and Magnetic Field Problems*, John Wiley and Sons, Inc., New York, 1980.
15. Yoshimoto, T.: Eddy Current Effect in a Magnetic Bearing Model *IEEE Transactions on Magnetics*, Vol MAG-19, n5, September, 1983.
16. Wang, T.C.; et. al.: Single-Sided Linear Induction Motor, Sixth Annual IEEE-IGA Meeting, October, 1971.
17. Matsumara, F.; et. al.: Fundamental Equation for Horizontal Shaft Bearing and its Control System Design *Electrical Engineering in Japan*, Vol 101, n3, pp 123, May-June 1981.
18. K.V. Hebbale: *A Theoretical Model for the Study of Nonlinear Dynamics of Magnetic Bearings*, Ph.D. Dissertation, Cornell University, Jan., 1985.
19. Hassard, B.D.; et. al.: *Theory and Applications of Hopf Bifurcations*, London Mathematical Society Lecture and Notes 41, Cambridge University Press, 1981.
20. Yamamura, S.; Ito, T.: Analysis of Speed Characteristics of Attractive Magnet for Magnetic Levitation of Vehicles,*IEEE Transactions on Magnetics*, Vol MAG-11,n5, September, 1975.

TABLE 1

Single Magnet Suspension Parameters

Mass M = 8.91 kg
Acceleration due to gravity g = 9.80665 m/sec^2
Area of cross section A = 0.00025 m^2
Initial voltage E_0 = 5.0 volts
Resistance of coil R = 3.0 ohms
Path length in core L_1 = 0.28 m
Path length in Mass L_2 = 0.05 m
Permeability of free space μ_0 = $4\pi E - 07H/m$
Relative permeability of core material μ_{r1} = 10000.0
Relative permeability of mass material μ_{r2} = 100.0
Number of turns N = 800

FEEDBACK GAIN MATRIX: Poles at -1000 , -100 ± j100

K = [261013.13 1486.86 -92.44]

TABLE 2

Two Magnet Bearing Parameters

ROTOR

Diameter of rotor D = 0.15 m
Mass of rotor M = 15.6 kg
Path length in rotor L_2 = 0.05 m
Relative permeability of mass material μ_{r2} = 100.0
Electrical conductivity of mass material σ = 1.0 E+07 mho/m

MAGNET

Pole angle = 15 degrees
Path length in core L_1 = 0.28 m
Relative permeability of core material μ_{r1} = 10000.0
Area of pole face A = 0.00025 m^2
Width of pole face W = 0.008333 m
Number of turns N = 800.0
Distance of pole corner a = 0.0075 m
Distance of pole corner b = 0.0375 m
Initial voltage (top) E_{01} = 7.5 volts
Initial voltage (right) E_{02} = 2.5 volts
Initial voltage (bottom) E_{03} = 2.5 volts
Initial voltage (left) E_{04} = 2.5 volts
Resistance of coil R = 3.0 ohms

TWO MAGNET FEEDBACK GAIN MATRIX

Poles at -1000, -1000, -100 ± j100

$$K = \begin{bmatrix} 4570751.1 & 11052.9 & -565.5 & -2200.5 \\ 1523583.7 & 3684.3 & -188.5 & -733.5 \end{bmatrix}$$

TABLE 3

Feedback Gain Matrix for Four Magnet Bearing

$$K^T = \begin{bmatrix} 4570751.1 & 0.0 & 1523583.7 & 0.0 \\ 11052.9 & 0.0 & 3684.3 & 0.0 \\ 0.0 & 7185390.6 & 0.0 & 7185390.6 \\ 0.0 & 18021.2 & 0.0 & 18021.2 \\ -5675.5 & 0.0 & -188.5 & 0.0 \\ 0.0 & -3500.0 & 0.0 & -3500.0 \\ -2200.5 & 0.0 & -733.5 & 0.0 \\ 0.0 & -3677.7 & 0.0 & -3677.7 \end{bmatrix}$$

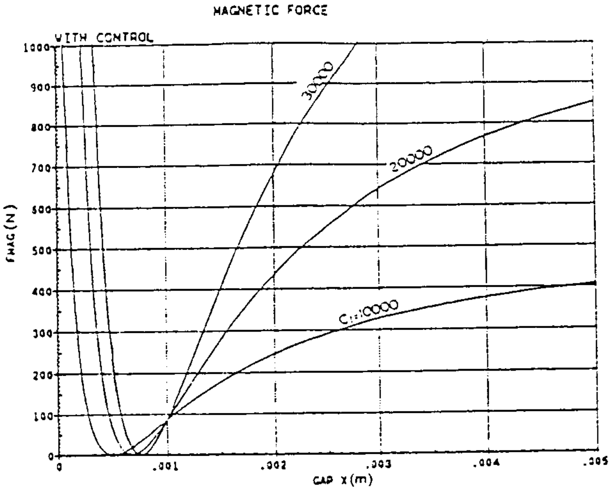

Figure 1: Four Magnet Bearing

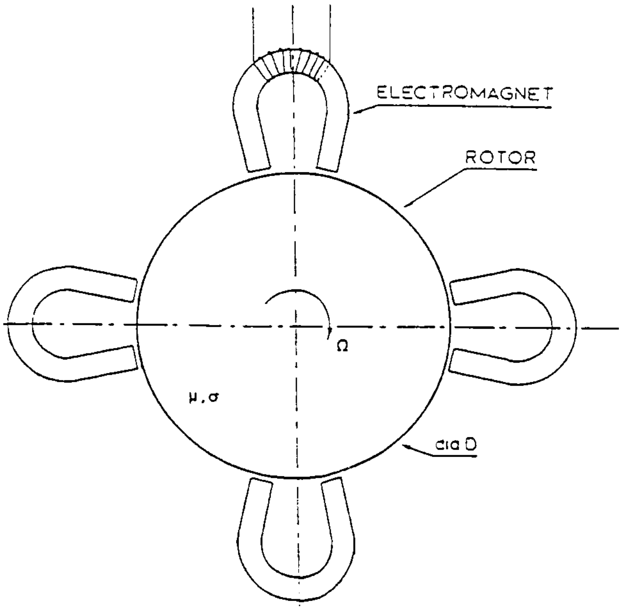
ELECTROMAGNET
ROTOR
Ω
μ, σ
dia D

Figure 2: Effect of Feedback Gain on Stiffness of Single Magnet Suspension

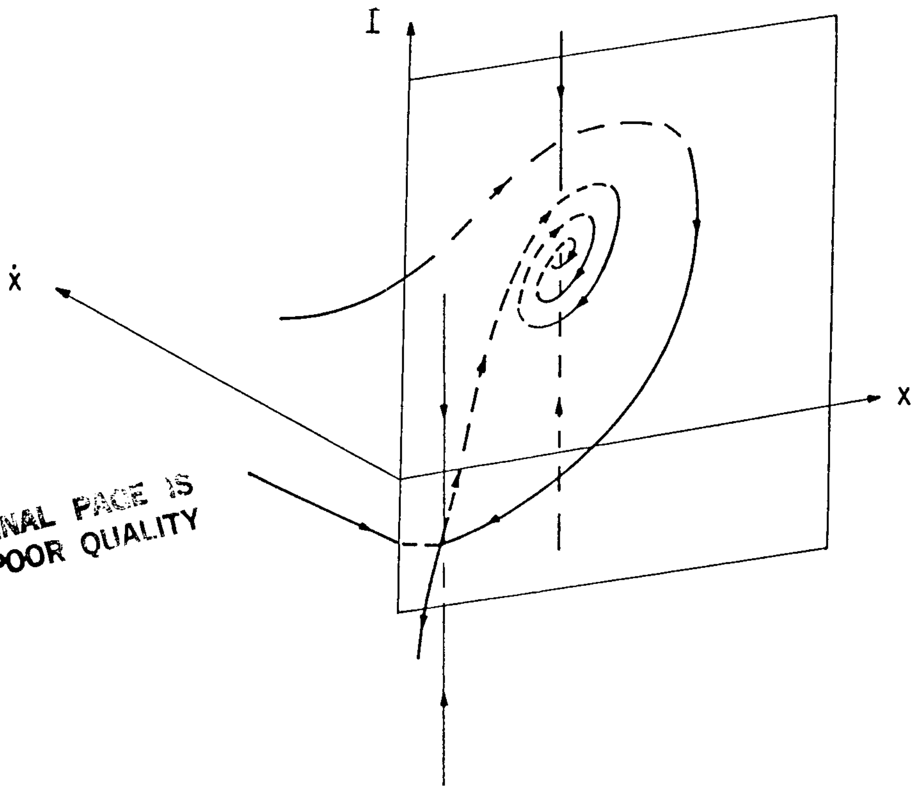

ORIGINAL PAGE IS
OF POOR QUALITY

Figure 3: Global Stability of Single Magnet Syspension

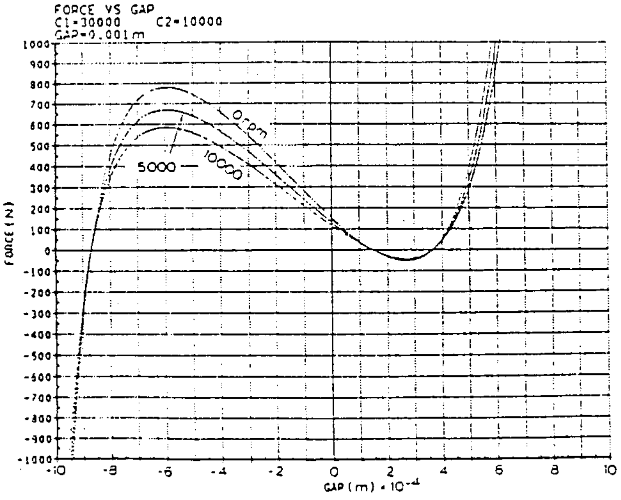

Figure 4: Net Magnetic Force vs Shaft Displacement, with Feedback

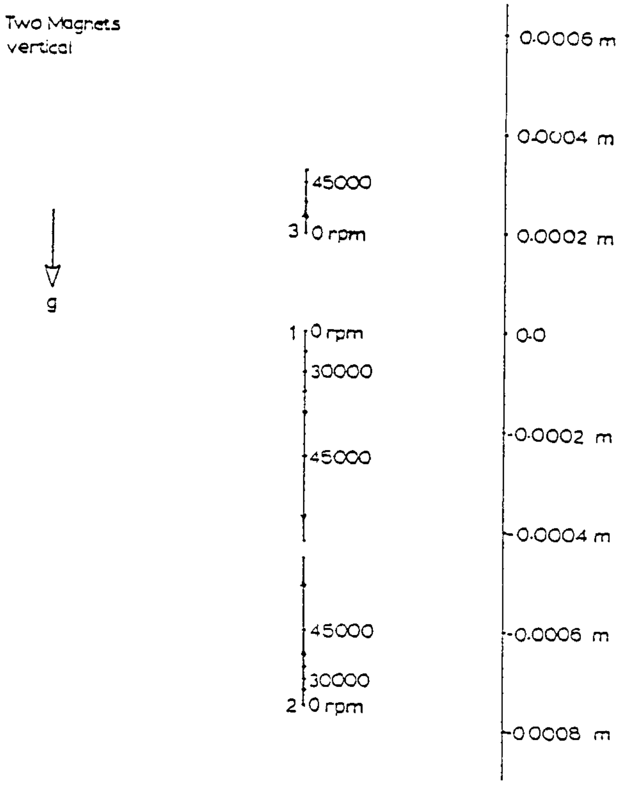

Figure 5: Locus of Equilibrium Points, with Feedback, as Speed Varies

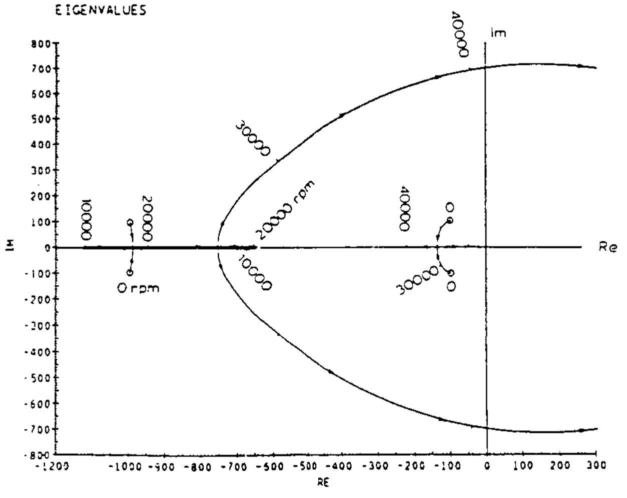

Figure 6: Root Locus for Two Magnet Bearing, as Speed Varies

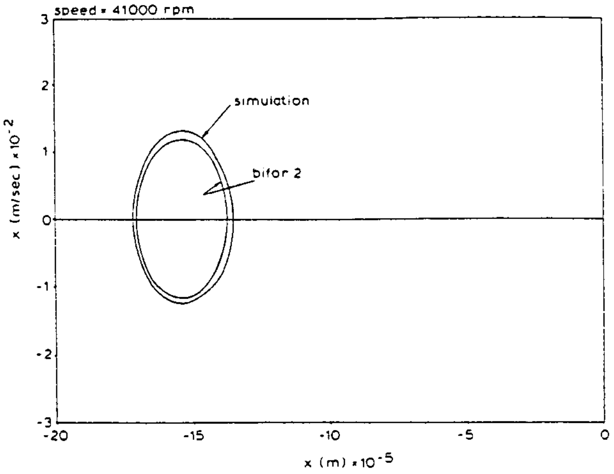

Figure 7: Limit Cycle Comparison for Two Magnet Bearing

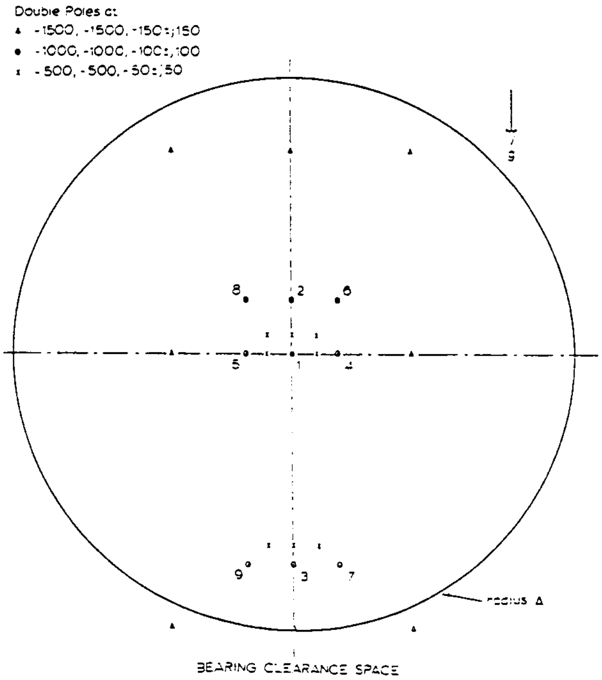

Double Poles at
▲ -1500, -1500, -150±j150
● -1000, -1000, -100±j100
x -500, -500, -50±j50
1
2
3
4
5
6
7
8
9
g
radius Δ
BEARING CLEARANCE SPACE

Figure 8: Equilibrium Points at $\Omega = 0$ for Three Different Pole Assignments

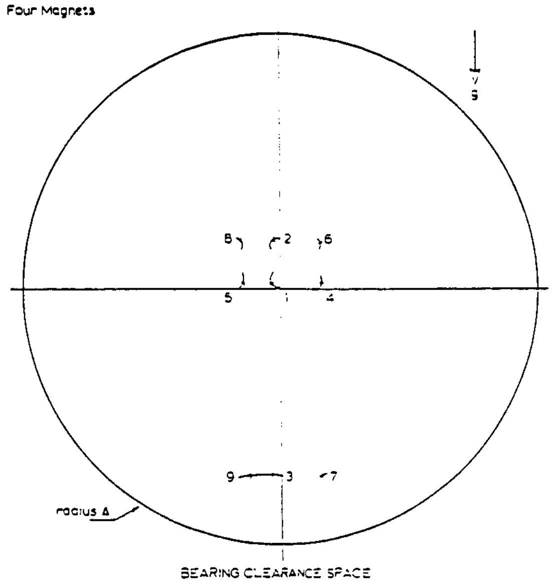
Four Magnets
V
S
8
2
6
5
1
4
9
3
7
radius Δ
BEARING CLEARANCE SPACE

Figure 9: Locus of Equilibrium Points as a function of Speed

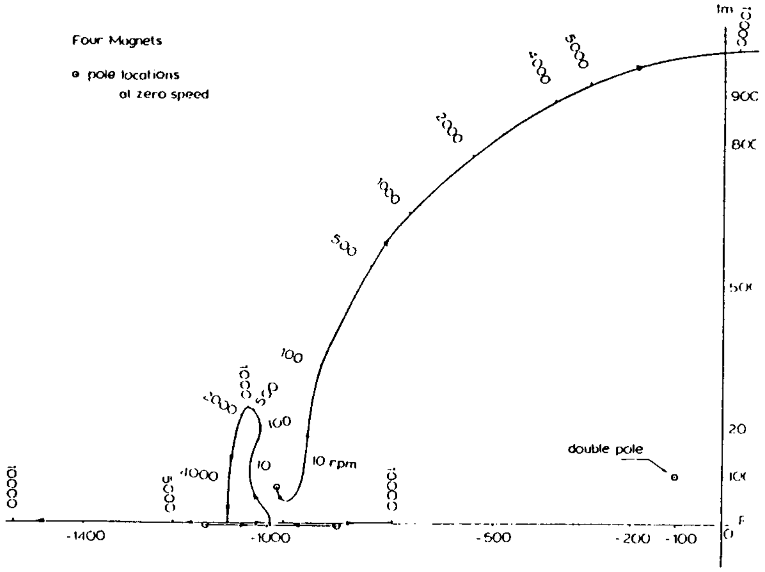

Figure 10: Root Locus as Speed Varies

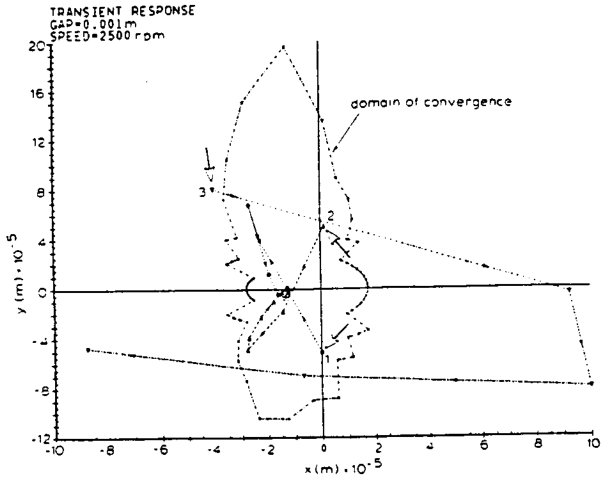

Figure 11: Transient Response at 2500 rpm

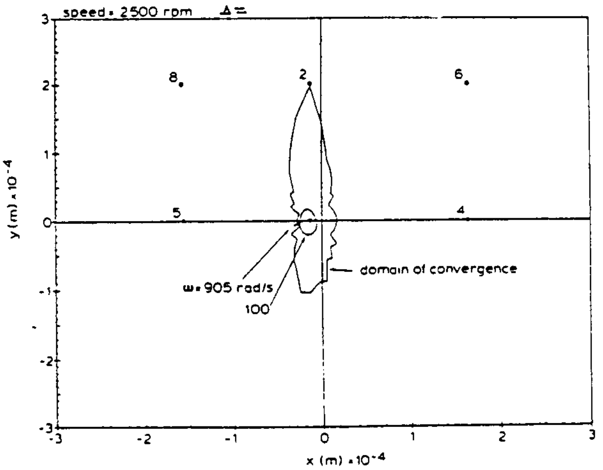

Figure 12: Equilibrium Points, Domain of Convergence, Δ =?

ORIGINAL PAGE IS
OF POOR QUALITY

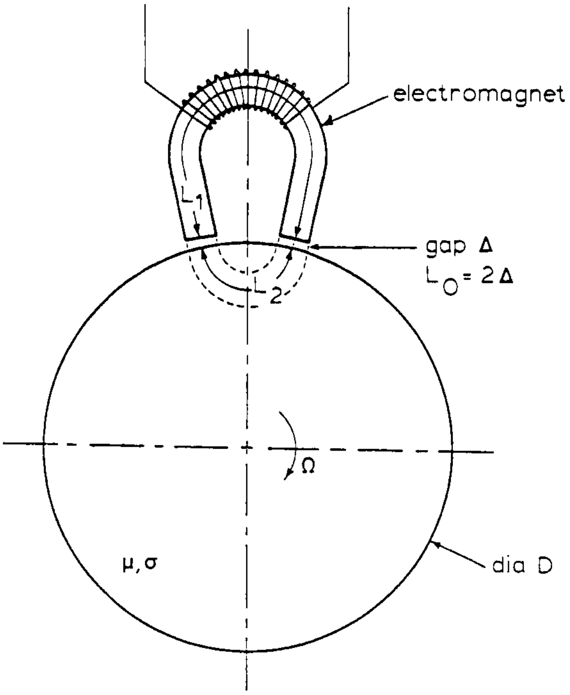
electromagnet
L_1
gap Δ
$L_O = 2Δ$
L_2
Ω
μ,σ
dia D

Figure A.1: Ferromagnetic Rotor under a Single Electromagnet

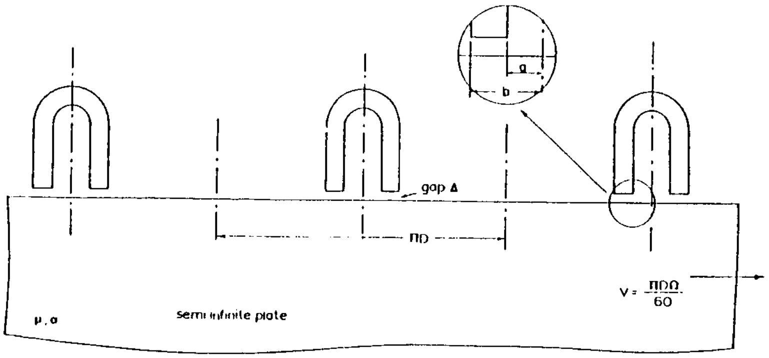
a
b
gap Δ
πD
$V = \frac{\pi D \Omega}{60}$
μ,σ
semi infinite plate

Figure B.1: Semi-Infinite Plane under a Series of Electromagnets

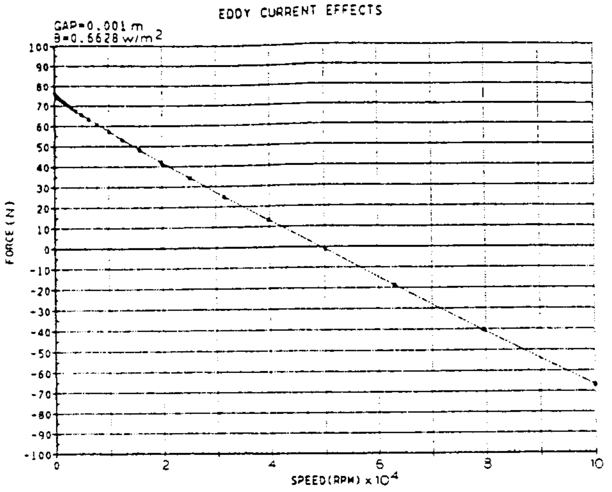

Figure B.2: Lift Force as a function of Spin Speed

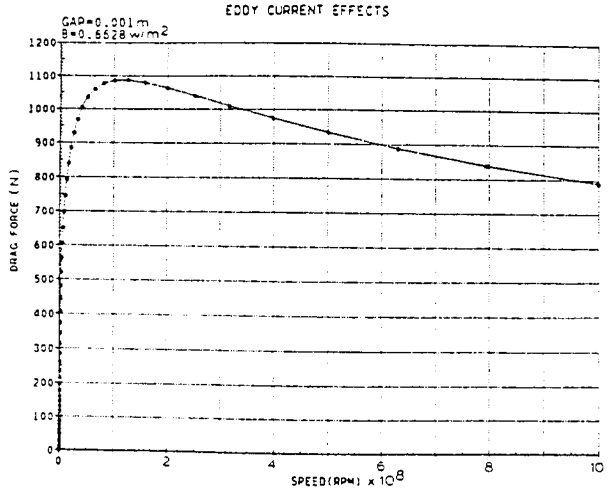

Figure B.3: Drag Force as a function of Spin Speed

N87-22221

DYNAMICS OF A FLEXIBLE ROTOR IN MAGNETIC BEARINGS*

P.E. Allaire and R.R. Humphris
University of Virginia
Charlottesville, Virginia 22901

R.D. Kelm
Dow Chemical USA
Houston, Texas 77253

Currently, speeds in rotating machines are limited because of bearing problems, internal fluid flow forces and machine unbalances which produce large vibrations. A recent high technology development is that of magnetic bearings, which replace the usual rolling element or fluid film bearings. The new magnetic bearings can largely eliminate the wear and lubrication problems of oil lubricated bearings because the rotating component is totally supported in air by magnetic forces. Another application is as a vibration controller which is used in conjunction with existing bearings. In this case, the shaft may be made longer so that additional stages may be added or seal clearances reduced because of lower vibration levels. Thus, machine performance may be increased.

This paper discusses a magnetic bearing which was designed and tested in a flexible rotor both as support bearings and as a vibration controller. The design of the bearing is described and the effect of control circuit bandwidth determined. Both stiffness and damping coefficients were measured and calculated for the bearing with good agreement. The bearings were then placed in a single mass rotor as support bearings and the machine run through two critical speeds. Measurements were made of the vibration response in plain bushings and magnetic bearings. Comparisons were also made of the theoretical calculations with the measured peak unbalance response speeds. Finally, runs were made with the magnetic bearing used as a vibration controller.

INTRODUCTION

Magnetic bearings are beginning to be used in a wide range of flexible shaft rotating machinery. Compressors for pipeline service have recently had magnetic bearings installed to reduce vibrations and reduce the possibility of fires related to oil lubrication. They have also been tried in large pumps, turbines and other rotating machines.

A magnetic bearing consists of four or eight electromagnets arranged radially around a shaft. The dynamic properties of the bearing are controlled electronically and stiffness and damping coefficients can be chosen, within certain ranges, to minimize the rotor vibrations. Such flexibility is not possible with conventional fluid film and rolling element bearings. Other advantages include removal of oil seals,

---

*The authors would like to thank the Institute for Computer Aided Engineering of the Center for Innovative Technology of the Commonwealth of Virginia for partial support of this project.

ability to operate in high temperature or hostile chemical environments, reduced operational costs, and significantly lower friction losses than other bearing types.

The first fully active magnetic suspension system was patented in 1957 [1]. Neiman, et. al [2], reported on the investigation of magnetic and electric forces for rotating shaft systems. Their work showed limited success with fully supporting a rotor due to axial instabilities.

The dynamics of a single mass rotor on rigid supports with control forces applied at the mass are reported in [3]. This work was then extended to include flexible supports [4]. Moore et. al [5] investigated the feasibility of active feedback control for a multimass flexible rotor with force actuators at bearing locations rather than at the shaft center. It was demonstrated that various levels of damping applied at the bearings would be a practical method of reducing vibrations.

Stanway and O´Reilly [6] presented a state space formulation for a flexible rotor with flexible supports. The method was further developed with a numerical example [7]. Forces were applied to the bearing housing to help stabilize plain oil film bearings.

Nikolajsen and Holmes [8] investigated an electromagnetic damper as applied to a transmission shaft. A test rig was built and tested, showing very good agreement with predicted amplitude through a critical speed. Gondhalekar and Holmes [9] designed and built a hybrid passive-active magnetic bearing system applied to a flexible transmission system through two critical speeds. Kaya and Roberts [10] further demonstrated the usefulness of active control flexible transmission shafts. They also developed an optimization method which would lend itself to use with a digital control approach with speed dependent characteristics.

Schweitzer and Ulbrich [11] reported on a vertical centrifuge controlled by using active magnetic bearings. Traxler and Schweitzer [12] also presented results for a rigid rotor. The emphasis was on the force and current measurements with the rotor stationary and rotating. The same authors [13] described a three level approach to designing magnetic bearings. Salm and Schweitzer [14] presented a model for a flexible rotor controlled by an active magnetic bearing at the center of a single mass rotor. Ulbrich and Anton [15] investigated the integration of displacement and velocity sensors within the magnetic bearing.

Bartlett and Taylor [16] developed a model of a solenoidal suspension and applied it to a flexible rotor. Hebbale [17] did a dissertation on the nonlinear dynamics of magnetic bearings. Yamamura [18] developed an analysis of active suspension for high speed vehicles.

Several articles have been published about the commercial possiblities of magnetic bearings [19,20]. The benefits claimed are operating speeds up to 80,000 rpm, rotor diameters of 15.2 mm to 610 mm (0.6 to 24 inches), load per bearing from 0.31 N to 2.0 E5 N (0.07 lb to 45,000 lb), ambient temperatures from -251^{0} C to 449^{0} C (-420 F to 840 F), and operating environments of vacuum, air, helium, hydrocarbons, steam, uranium hexaflouride, sea water, liquid oxygen, and liquid hydrogen.

Two previous works related to the magnetic bearing or its controls have already been published or accepted for publication. Allaire et. al [21] described the basic control scheme as applied to one pole magnetic support system. Humphris et. al [22] presented a theoretical description of the magnetic circuit and experimental measurements of the stiffness and damping coefficients. Several parameters in the controls were varied with agreement to within about 20 to 30%.

The purpose of this paper is to discuss magnetic bearings which were reported in [22] and tested in a multimass flexible rotor both as support bearings and as a vibration controller. First, a single mass rotor was supported in conventional bushings and the magnetic bearing used as a conroller near the center mass. Second, two disks for the magnetic bearings were added to the single mass rotor and the magnetic bearings used in a support mode.

MAGNETIC BEARING

The magnetic bearing [22] used in this study has four electromagnets distributed radially around a 12.7mm (0.5 inch) shaft as shown in Fig. 1. A soft iron disk 58.4 mm (2.3 inches) in diameter and 25.4 mm (1.0 inches) long was placed over the shaft to increase the area and provide a good magnetic circuit. The disks were placed either at the desired controller location or at the normal bearing support locations. Each magnet consisted of a solid soft iron core forming a horseshoe, with two pole faces cut to a diameter of 60.5 mm (2.38 inches). This gives a nominal clearance of 1.0 mm (0.040 inches). Each leg of the magnet was wound with 920 turns of wire. All magnets were the same. A rigid aluminum housing, shown in Fig. 1, provided the support for the magnets.

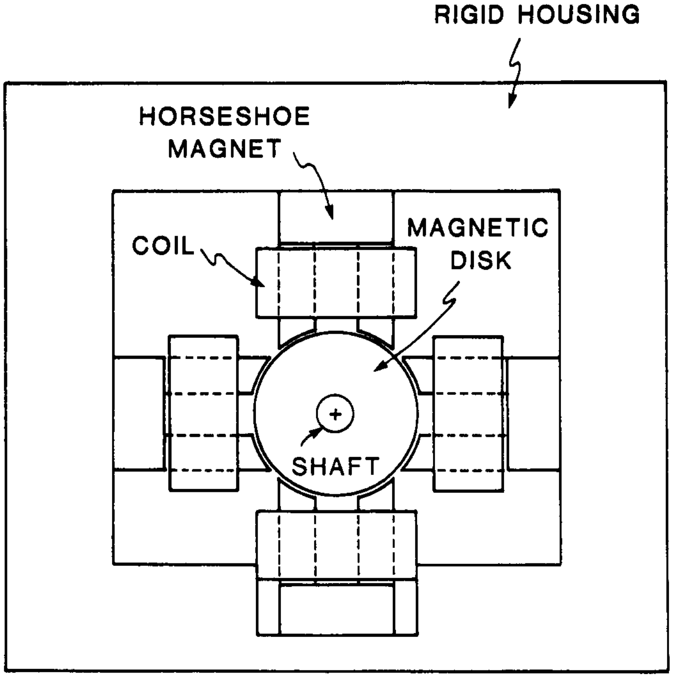

Figure 1. Magnetic Bearing Geometry

The shaft weight was supported by having a larger steady state current in the top magnet when the support mode was employed. The other three electromagnets had a steady state current in them to provide a value about which a set of linearized properties were determined.

Position sensors were located vertically and horizontally on the shaft a short axial distance from the bearing. These were standard eddy-current probes of the type normally used to monitor rotating equipment in the field. Tests showed that the magnetic fields from the bearing did not affect the probe measurements at a 25 mm (1 inch) distance.

The magnetic bearing control system is described in the Appendix. Components of the system are presented and the algorithms used to model them. Typical bearing linearized stiffness and damping coefficients are presented.

MAGNETIC CONTROLLER

In the controller mode, no rotor weight was supported. All load was carried by the conventional bearings at each end. Thus all steady state current levels were the same in all four electromagnets. Also, the required steady state currents in the control mode were much less than the current required in the support case since no load was carried. Similarly the controller dynamic coefficients (stiffness and damping) could have lower values because they were applied at the rotor center. Overall the power required for the controller mode was much less than for the support case.

The rotor was first assembled with the magnetic bearing as a controller, with the configuration illustrated in Fig. 2. The shaft had two masses on it, a center disk of weight 8.0 N (1.8 lb) and dimensions 73.15 mm (2.88 inches) in diameter by 25.4 mm (1.0 inch) thick, and the magnetic bearing disk as described in the previous section. The bearing disk weighed 4.9 N (1.1 lb). The shaft was 12.7 mm (0.5 inches) in diameter and 660 mm (26.0 inches) long. The bearing span was 508 mm (20 inches) with the center disk at midspam and the bearing disk at the one-third span. The total rotor weight for shaft plus both disks was 24.9 N (5.6 lb). As shown in Fig. 2, the rotor extended to a flexible coupling, which connected the shaft to a small electric motor drive.

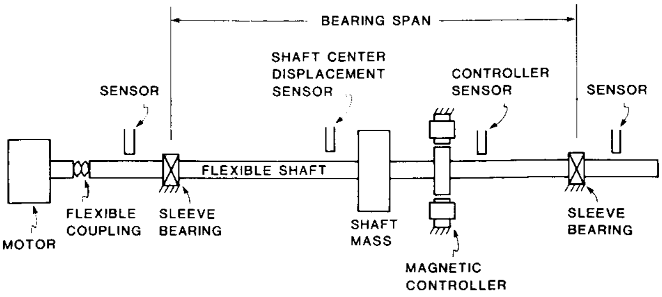

Figure 2. Diagram of Flexible Rotor Supported in Conventional Bearings With Magnetic Controller

At each end of the rotor were conventional sleeve bearings. They are of oil impregnated bronze construction backed by a rubber O ring. This type of bearing is common in many small laboratory rotor kits and is considered sufficient to demonstrate the principles of vibration reduction by magnetic controllers. The stiffness of the sleeve bearing and associated housing is approximately 3.5 E5 N/m (2000 lb/in). Also, the effective stiffness of the coupling is estimated to be about 8.8 E4 N/m (500 lb/in).

The rotor was run up in speed through one critical speed with the controller turned off. Figure 3 shows the horizontal peak to peak response. The peak response occurs at approximately 2845 rpm at 0.52 mm (20.5 mils). With the controller on, the critical speed increases to approximately 3610 rpm and the amplitude reduces to about 0.063 mm (2.5 mils). For this case, the magnetic controller gains were set to have a calculated stiffness of 1.2 E5 N/m (700 lb/in).

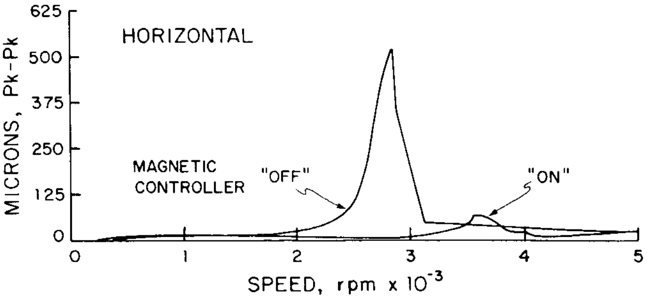

Figure 3. Flexible Rotor Response at Quarter Span, with and without Magnetic Controller

The critical speed increased 28% and the vibration level dropped to 12% of the original value. In this particular experiment, no efforts were made to optimize the vibration reduction by modifying the magnetic bearing control settings. In general, it would be expected that the introduction of stiffness and damping at the center of the rotor should greatly reduce the vibration levels. The point being made here is that the magnetic damper works and the measured results can be compared to predicted rotor behavior.

Figure 4 shows the rotor calculated first critical speed and mode shape, without the magnetic controller, determined by a standard transfer matrix method. The calculated value is 2766 rpm or only about 3% below the measured value. This indicates that the rotor model is a good one. Figure 5 gives the calculated critical speed and mode shape with the controller turned on. Again the calculated value of 3556 rpm is very close to the measured value of 3610 rpm.

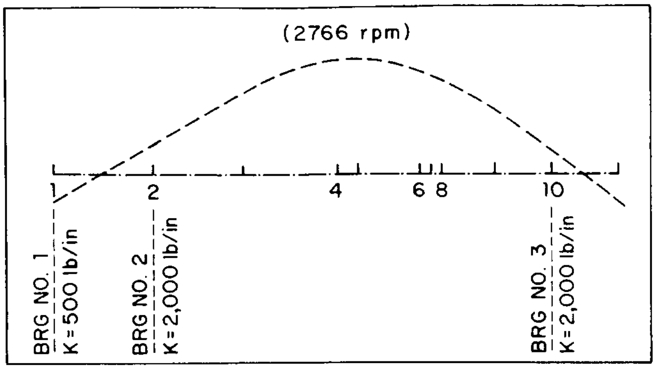

Figure 4. Computed Critical Speed and Mode Shape Without Magnetic Controller

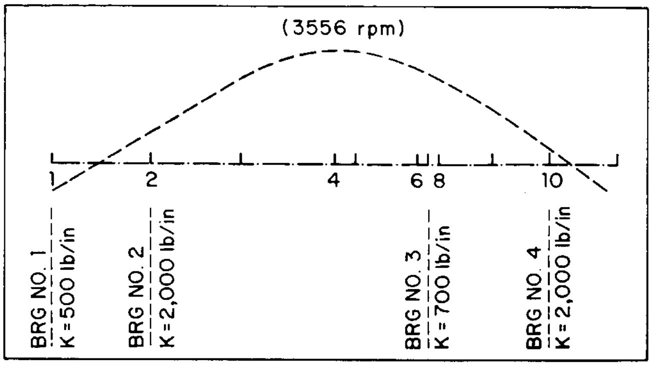

Figure 5. Computed Critical Speed and Mode Shape With Magnetic Controller

A series of spectrum analysis plots versus time, illustrating the effect of the magnetic controller, is shown in Fig. 6. The rotor was run at a constant speed of 2600 rpm or just below the first critical speed. Initially the controller was "off", with no current in any of the magnets. The vibration amplitude is large and constant over time. After approximately 32 seconds, the current was turned "on" in all four magnets. The amplitude of vibration immediately dropped to a very low level and remained at that level with no observable transient response.

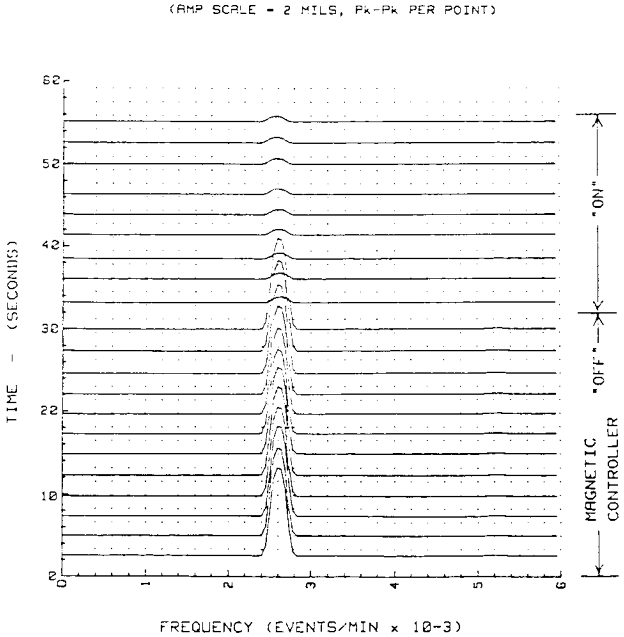

Figure 6. Spectrum Analysis Plots showing the effect of Magnetic Controller "off" and "on"

MAGNETIC SUPPORT BEARING

The rotor-bearing configuration was changed so that two identical magnetic bearings were used to replace the conventional bearings. Figure 7 illustrates the geometry. It had three masses on it - a center disk of weight 8.0 N (1.8 lb) and two magnetic bearing disks weighing 4.9 N (1.1 lb) each. Disk and shaft geometries were identical to those used in the controller mode. The total rotor weight was 24.9 N (5.6 lb). Again the bearing span was 508 mm (20 inches).

Backup bearings were placed inboard of each magnetic bearing. Each was a conventional sleeve bearing of the type described in the previous section except that they were bored out to a clearance of 0.51 mm (0.020 mils) radial. The magnetic bearing radial clearance was much larger at 0.76 mm (0.030 inches). The rotor amplitude of vibration near the bearings was always well below this value. Thus

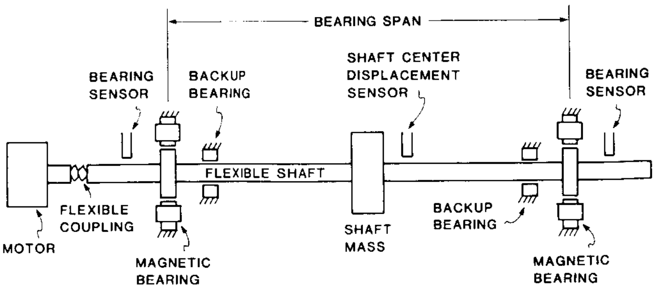

Figure 7. Diagram of Flexible Rotor Rig Supported in Magnetic Bearings

these bearings were never in contact when the magnetic bearings were activated. This included start-up conditions (no shaft rotation) or running through critical speeds.

The same type of noncontact induction probes were employed for the rotor. Two sets were used at the magnetic bearing disks for both feedback control and monitoring. A third was placed adjacent to the center mounted disk for monitoring.

Supporting the rotor weight required the use of higher currents in the top magnets than in the sides and bottom magnets. Typical values are reported in [22]. Both bearings had essentially the same operating conditions.

A preliminary run was made with the rotor in conventional bearings (without the magnetic controller). Then, the conventional bearings were immediately replaced by the magnetic bearings in exactly the same locations. Thus the shaft had the same unbalance level in the center disk. The state of unbalance of the added bearing disks was unknown.

Figure 8 gives the results plotted on the same axes. In the vertical direction, the peak amplitude was 0.72 mm (30 mils) at about 2,400 rpm with sleeve bearings. When the magnetic bearings were used, the vibration level dropped to about 0.14 mm (5.5 mils) at approximately 2,000 rpm. Thus the vertical vibration level was reduced by a factor of greater than 5. It had gain values of K_g = 1.75 and K_r = 20. In the horizontal direction, the vibration level was reduced from 0.56 mm (22 mils) with the sleeve bearing to about 0.13 mm (5 mils) with the magnetic bearing. The vibration level was reduced by factor of 4. Also, K_g = 1.0 and K_r = 20 were the gain settings for the horizontal direction. For this preliminary run, no attempt was made to "optimize" the magnetic bearing settings to reduce vibrations.

Two additional cases of runs were made with the magnetic bearings in the support mode. The cases are

	Vertical Gain		Horizontal Gain	
Case	K_g	K_r	K_g	K_r
1	1	2	4	10
2	4	8	4	10

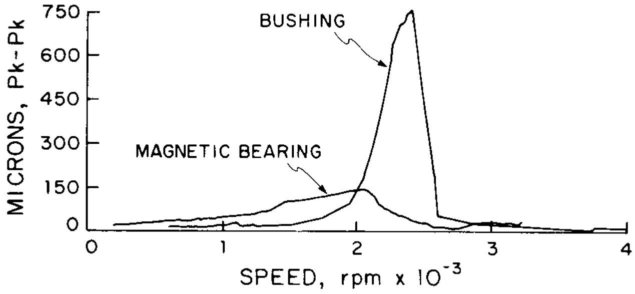

a) vibration level in vert. direction

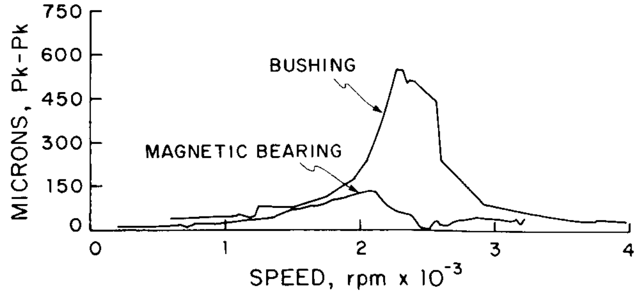

b) vibration level in horiz. direction

Figure 8. Comparison of Flexible Rotor Vibrations at Shaft Center For Conventional Bearings vs. Magnetic Bearings

Again the primary objective is to compare the measured first critical speeds to the calculated values based upon the magnetic bearing stiffness as evaluated by the theory in [22].

Figure 9 shows the vibration amplitude and phase angle vs. speed at the rotor midplane (near the center mass) for Case 1. Results from probes near the bearings are similar but with lower amplitudes. Figure 10 gives the frequency spectrum for the vertical direction at the midspan. The vibrations are nearly all synchronous.

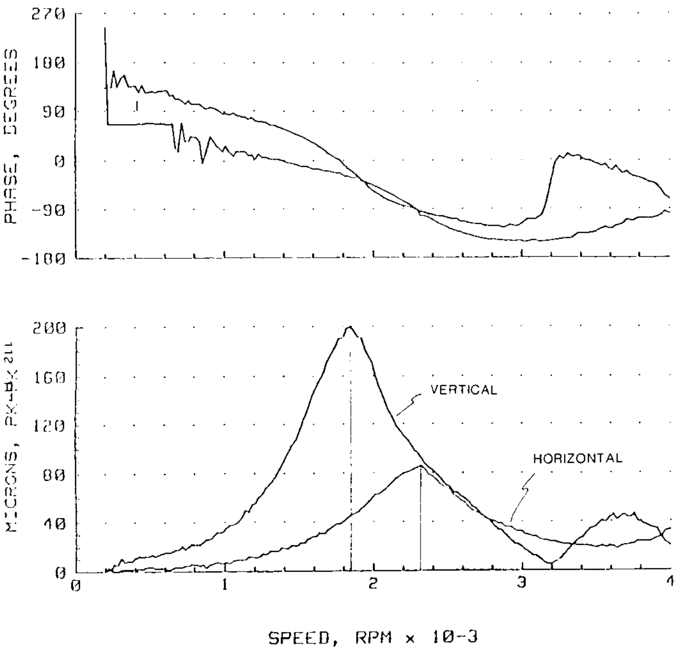

Figure 9. Horizontal and Vertical Midspan Vibration Plots for Rotor in Magnetic Support Bearing - Case 1

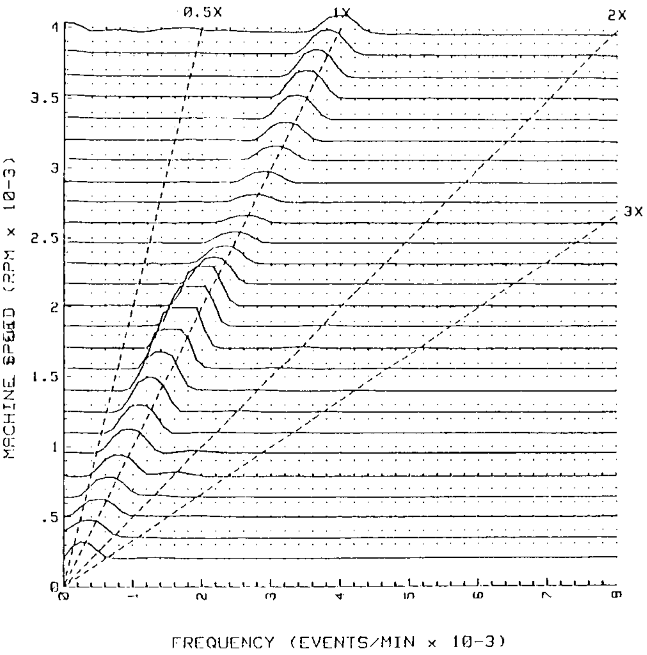

Figure 10. Frequency Spectrum for Vertical Direction at Midspan--Case 1

For Case 1, peak vibrations occur at 1860 rpm in the vertical direction and 2320 rpm in the horizontal direction. Again using the theory from [22] the calculated bearing stiffnesses are

Case 1

Direction	Stiffness N/mm (lb/in) Inboard	Outboard
Vertical	33 (187)	65 (370)
Horizontal	411 (2335)	333 (1890)

Figure 11 shows calculated critical speeds and the mode shapes for the above stiffnesses. In the vertical direction, the calculated value is 1803 rpm. This is only 3% below the actual value. The horizontal calculated critical is 2650 rpm which is 14% above the measured value.

For Case 2, the vertical gains were increased. Figure 12 gives the resulting vibration plot. The vertical critical speed increased to 2720 rpm (1860 rpm for Case 1) due to the higher bearing stiffness. Calculated bearing stiffnesses are shown on the following page. The calculated vertical critical speed is 2672 rpm. This is below the measured value by 3%. In the horizontal direction, the measured peak was 2260 rpm while the calculated value is 2625 rpm. The mode shapes for Case 2 were similar to those for Case 1.

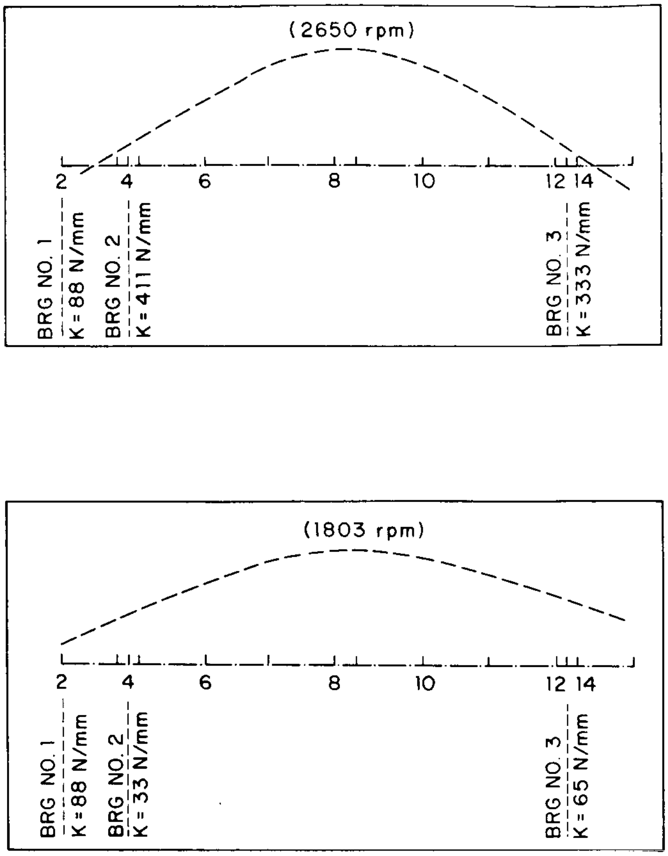

Figure 11. Calculated Mode Shapes and Critical Speeds for Case 1

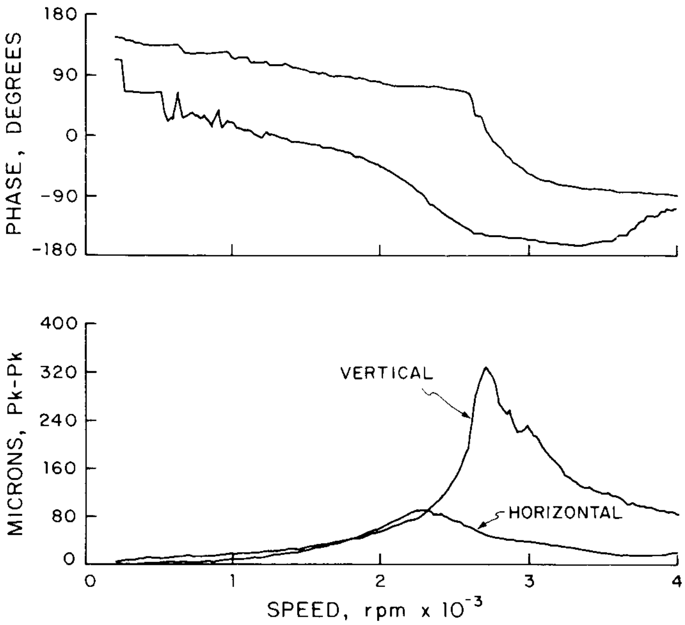

Figure 12. Horizontal and Vertical Midspan Vibration Plots For Rotor In Magnetic Support Bearing Case 2 (Vertical $K_g=4$, $K_r=8$ Horizontal $K_g=4$, $K_r=10$)

Case 2

Direction	Stiffness N/mm (lb/in) Inboard	Outboard
Vertical	372 (2125)	543 (3100)
Horizontal	420 (2400)	337 (1925)

CONCLUSIONS

This paper reports the effect of a magnetic bearing used in both controller and support modes. Generally the conclusion is that the magnetic bearing strongly affects the vibration levels in the rotor. Using the magnetic controller reduced the vibration level to 12% of the original value in the vertical direction. In the support mode, the vibration level decreased by about the same factor in the vertical direction as compared to the rotor in conventional support bearings. This reduction of vibration levels was achieved without optimizing the settings of the control parameters.

Another result of this work is a comparison of the measured and calculated critical speeds. Table 1 gives the summary for the cases considered in this work. In each case the stiffness values were evaluated using the method in [22]. The largest error for the calculated critical speeds is 16%. Overall, this indicates that machine undamped critical speeds can probably be accurately determined theoretically before magnetic bearings are installed in a machine.

APPENDIX - MAGNETIC BEARING PROPERTIES

A block diagram of the control circuit for each magnet in each bearing is shown in Fig. A.1. It operates as follows. The eddy-current induction probe senses the position of the shaft. The signal goes to the sensor amplifier which has a fixed gain, low pass filter and reference adjustment. A compensator has an adjustable position gain K_g and rate gain K_r. These are used to vary the bearing stiffness and damping. The next components are the summer and lead network. Finally the signal passes through the position amplifier which determines the steady state current provided to the electromagnet and hence the operating position of the shaft in the bearing.

Specific numerical values for the magnetic bearings are given in [22]. They are omitted here due to length considerations. Also the theoretical model of the bearing properties is developed and presented in [22] with comparisons to measured results.

One of the important characteristics of any bearing is the stiffness. An advantage of the magnetic bearing is that the stiffness can be varied simply by changing the gain in the control circuit. Figure A.2 shows the theoretical and measured static stiffness of one magnet of the bearing used in a support mode for two control circuits, A and B, with different bandwidths as a function of proportional control circuit gain. The agreement is within about 20%, with the theoretical values being higher than the measured stiffnesses.

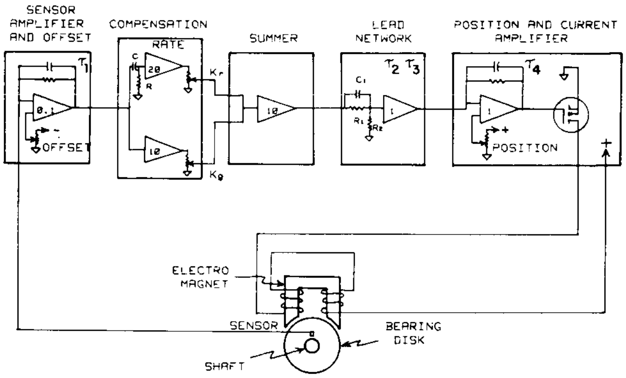

Figure A.1. Block Diagram of Magnetic Support System

Another important characteristic of a bearing is the damping coefficient. Often the primary vibration reduction in rotating machines comes from the oil lubricated bearings. Magnetic bearings should be at least as effective as conventional fluid film or rolling element bearings with squeeze film dampers. Figure A.3 gives a comparison between the theoretically calculated damping coefficient and measured values obtained from system responses to step inputs. There is some scatter in the experimental data but the agreement is within about 30% for both of the proportional gain cases considered. Note that for the damping, the coefficient is a function of both the proportional and rate gains due to the control circuit used. It may also be noted that both the stiffness and damping coefficients are reasonably linear over the ranges measured.

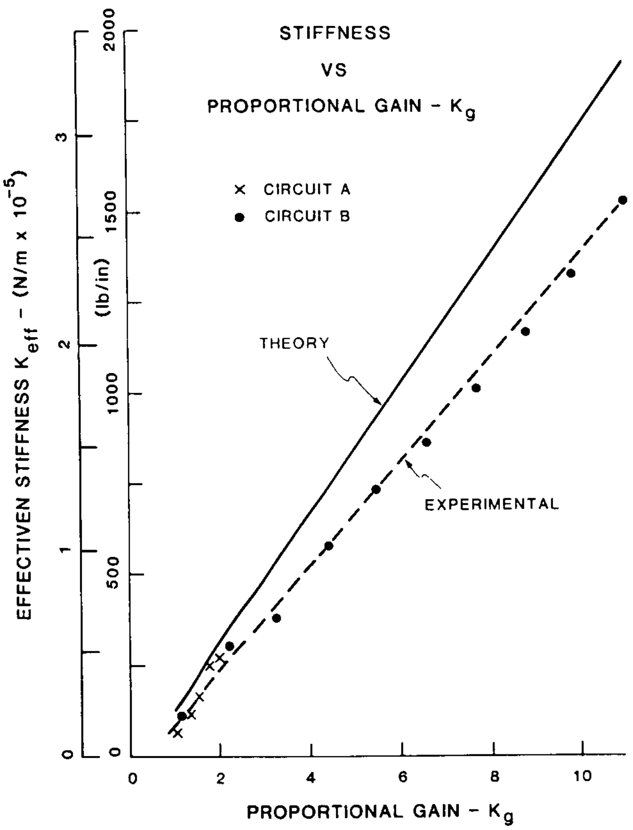

Figure A.2. Theoretical and Measured Stiffness for Magnetic Bearing

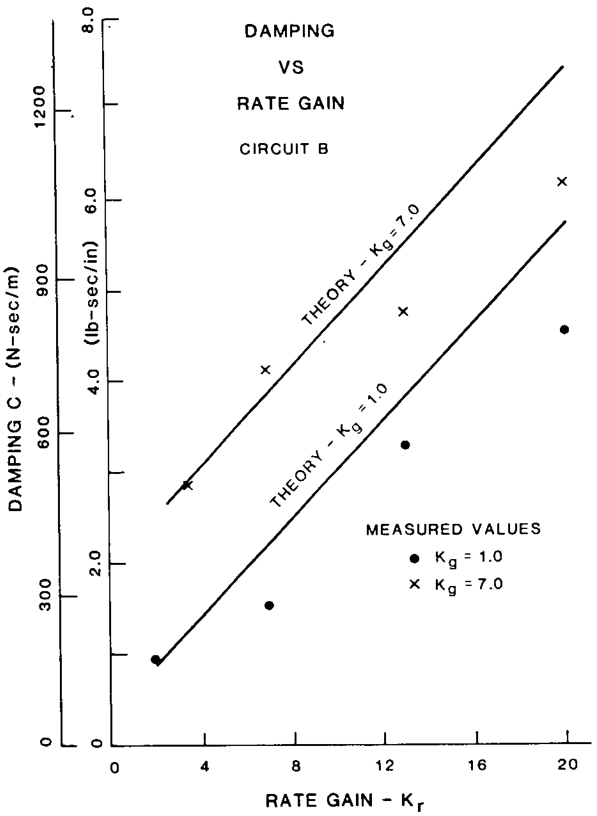

Figure A.3. Theoretical and Measured Damping for Magnetic Bearing

REFERENCES

1. Totally Active Magnetic Suspension System, French Patent 1186527, November 1957, issued to Societe D'Exploitation Des Materiels Hispano-Suiza.

2. Nieman, D., et. al, "Investigation of Magnetic and Electric Forces for Rotating Shaft Suspension," Technical Documentary Report ASD-TDR-62-441, May 1962.

3. Allaire, P., et. al, "Feedback Control of a Single Mass Rotor on Rigid Supports," Journal of the Franklin Institute, Vol. 312, No. 1, 1981, pp. 1-11.

4. Allaire, P., et. al, "Active Vibration Control of a Single Mass Rotor on Flexible Supports," Journal of the Franklin Institute, Vol. 315, No. 3, 1983, pp. 211-22.

5. Moore, J., Lewis, D., and Heinzmann, J., "Feasibility of Active Feedback Control of Rotordynamic Instability," NASA Workshop, Texas A & M University, May 12-14, 1980, NASA #2113, pp. 467-476.

6. Stanway, R. and O'Reilly, J., "State-Variable Feedback Control of Rotor-Bearing Suspension Systems," IMechE, 1984, pp. 515-24.

7. Stanway, R. and Burrows, C., "Active Vibration Control of a Flexible Rotor on Flexibly-Mounted Journal Bearings," Journal of Dynamic Systems, Measurement, and Control, Vol. 103, Dec. 1981, pp. 383-8.

8. Kaya, F. and Roberts, J., "Optimum Vibration Control of Flexible Transmission Shafts," IMechE, 1984, pp. 525-34.

9. Nikolajsen, J., Holmes, R., and Gondhalekar, V., "Investigation of an Electromagnetic Damper for Vibration Control of a Transmission Shaft," University of Sussex, March 1979.

10. Gondhalekar, V. and Holmes, R., "Design of an Electromagnetic Bearing for the Vibration Control of a Flexible Transmission Shaft," Rotordynamic Workshop at Texas A&M University, May 1984.

11. Schweitzer, G. and Ulbrich, H., "Magnetic Bearings - A Novel Type of Suspension," ImechE, 1980, pp. 151-6.

12. Traxler, A. and Schweitzer, G., "Measurement of the Force Characteristics of a Contactless Electromagnetic Rotor Bearing," Symposium on Measurement and Estimation, May 1984.

13. Schweitzer, G. and Traxler, A., "Design of Magnetic Bearings," International Symposium on Design and Synthesis, July 1984.

14. Salm, J. and Schweitzer G., "Modelling and Control of a Flexible Rotor with Magnetic Bearings," IMechE, 1984, pp. 553-61.

15. Ulbrich, H. and Anton, E., "Theory and Application of Magnetic Bearings with Integrated Displacement and Velocity Sensors," IMechE, 1984, pp. 543-51.

16. Bartlett, R., "Active Vibration Control of Flexible Rotors Using Magnetic Bearings," Cornell University Thesis, January 1984.

17. Hebbale, K., "A Theoretical Model for the Study of Nonlinear Dynamics of Magnetic Bearings," Cornell University Thesis, January 1985.

18. Yamamura, S. and Ito, T., "Analysis of Speed Characteristics of Attracting Magnet for Magnetic Levitation of Vehicles," IEEE, Vol. Mag.-11, No. 5, September 1975, pp. 1504-7.

19. Habermann, H. and Liard, G., "Practical Magnetic Bearings," IEEE Spectrum, September 1979, pp. 26-30.

20. Habermann, H. and Liard, G., "An Active Magnetic Bearing System," Tribology International, April 1980, pp. 85-9.

21. Allaire, P. E., Humphris, R. R., and Kelm, R. D., "Magnetic Bearings For Vibration Reduction and Failure Prevention," Proceedings of Mechanical Failures Prevention Group, National Bureau of Standards, April 1985.

22. Humphris, R. R., Kelm, R. D., Lewis, D. W., and Allaire, P. E., "The Effect of Control Algorithms on Magnetic Journal Bearing Properties," Accepted for presentation at ASME International Gas Turbine Conference, Dusseldorf, FRG, June 1986. Also accepted for publication in ASME Journal of Engineering for Power.

Table 1
Critical Speeds

Mode	Case	Measured (rpm)	Calculated (rpm)	Error (%)
Controller Mode	No Controller	2845	2766	-3%
	With Controller	3610	3556	-1%
Magnetic Bearing Support Mode	Case 1/Vertical	1860	1803	-3%
	Case 1/Horizontal	2320	2650	+14%
	Case 2/Vertical	2720	2672	-2%
	Case 2/Horizontal	2260	2625	+16%

N87-22222

PERFORMANCE OF AN ELECTROMAGNETIC BEARING FOR THE VIBRATION CONTROL OF A SUPERCRITICAL SHAFT*

C.D. Bradfield, J.B. Roberts, and R. Karunendiran
University of Sussex
Falmer, Brighton, England

The flexural vibrations of a rotating shaft, running through one or more critical speeds, can be reduced to an acceptably low level by applying suitable control forces at an intermediate span position. If electromagnets are used to produce the control forces then it is possible to implement a wide variety of control strategies.

A test rig is described which includes a microprocessor-based controller, in which such strategies can be realised in terms of software-based algorithms. The electromagnet configuration and the method of stabilising the electromagnet force-gap characteristic are discussed. The bounds on the performance of the system are defined. A simple control algorithm is outlined, where the control forces are proportional to the measured displacement and velocity at a single point on the shaft span; in this case the electromagnet behaves in a similar manner to that of a parallel combination of a linear spring and damper. Experimental and predicted performance of the system are compared, for this type of control, where various programmable rates of damping are applied.

INTRODUCTION

In many engineering applications it is desirable to control the amplitude of transverse vibrations of flexible transmission shafts, especially if the design speed range encompasses one or more critical speeds. It can be demonstrated theoretically (e.g. see Refs.1 to 3) that it is possible to satisfactorily control the flexural vibrations of a rotating shaft by applying control forces at a single intermediate span position. If the position of the control force application is suitably chosen then satisfactory reductions in the amplitude of vibration may be achieved over a speed range covering several critical speeds.

Two control devices, which are appropriate for this application, have been investigated in recent years - the squeeze-film bearing (e.g. see Refs. 4 and 5) and the electromagnetic bearing. The former has proved a relatively robust and reliable means of achieving vibration control. However, despite considerable efforts, it has proved difficult to predict its dynamic performance quantitatively, with any degree of accuracy.

---

* This work was supported by the Science and Engineering Research Council. The authors gratefully acknowledge this source of funding.

Electromagnetic bearings offer an attractive alternative approach and interest in such devices, as a means of active vibration control, has grown rapidly during the last few years [6-11]. The considerable advantage of such bearings is that it is possible to implement a wide variety of control strategies, particularly if they are operated under computer control. Moreover, it is possible, at least in principle, to predict their dynamic characteristics fairly accurately. This implies that it should be possible to design an electromagnetic control device which has a quantitatively predictable performance when applied to any particular rotor-bearing system.

Various types of electromagnetic control device have been described in the literature [6-11]. One of the simplest, and most promising, of such devices comprises six pole pieces surrounding the shaft, with three alternate energised poles. With this arrangement, combined with microprocessor control, it has been demonstrated experimentally that it is possible to control a rotating shaft satisfactorily, when it passes through critical speeds [11]. However, a quantitative comparison between experimental and predicted performance of the combined rotor-electromagnet system was not attempted in this earlier work.

In the present paper the rationale behind the adoption of this particular electromagnet configuration is initially discussed. This is followed by a description of the power electronics, and microprocessor-based control system used to drive the electromagnets, with emphasis on the factors which limit the performance of the system. The implementation of a simple control strategy, in which the electromagnet behaves approximately as a linear spring-plus-damper, is outlined and it demonstrated theoretically that, with this form of control, the complete rotor-electromagnet system can become unstable, under certain circumstances. A qualitative prediction of the influence of various factors on stability is obtained from this theory, which is fully in accord with experimental observations.

The paper concludes with some experimental results obtained from a test rig, in which the rotor is a simple shaft, of uniform cross-section, and the only source of excitation, when rotating, is the initial bend. For pure damping control, the results of free-decay tests are shown, which clearly demonstrate the effect of increasing the programmable rate of damping. A parametric identification technique, applied to the free-decay data, results in a direct calibration of the relevant damping coefficient. Results obtained from the test rig, when the shaft is rotating under damping control, are then presented and compared with corresponding theoretical predictions, for a speed range covering the first critical speed of the shaft.

EQUIPMENT

Rotor-Bearing System

The experimental rotor configuration is shown in Fig.1 and comprises a 25 mm diameter shaft of austenitic stainless steel, mounted in self-aligning ball races, giving a length between bearings of 1500 mm. The shaft is driven through a light flexible coupling, and can be driven at up to 6000 r.p.m. from a variable speed drive.

In this configuration, the first two critical speeds are 1260 and 5480 r.p.m. Additional masses may be added to bring the third critical speed within the design maximum speed. The active element used to control shaft motions, the electromagnet assembly, is located at the one-sixth span point, and can thus apply forces which are effective in controlling motions in at least the first three modes.

The shaft position is measured using capacitative transducers, which operate reliably in the magnetic fields encountered. These transducers operate satisfactorily as they are not subjected to oil contamination. Commercial equipment is used to energise the transducers and to demodulate their outputs. Transducers are mounted horizontally and vertically, and measure these components of shaft motion at two points, located between the magnet and the centre of the rotor.

Electromagnet Configuration

The active control element is shown in Fig.2 and comprises six pole pieces surrounding the shaft, with three alternate poles wound, and the three interleaved poles unenergised. The flux paths pass through the poles and their backing ring, through the small airgaps, and through a cylindrical core 50.8 mm diameter mounted on the shaft. This configuration gives radial fluxpaths in the central core and simplifies its construction, thin laminations being used to limit eddy current losses.

Design of the electromagnets is dominated by the need to linearise forces as the airgaps change. The attractive force F across an airgap is related to flux density B by the square-law relation $F = B^2 a/2\mu_0$, where a is the poleface area and μ_0 the permeability of free space ($= 4\pi \times 10^{-7}$ H/m). The flux density is proportional to current I, but inversely proportional to the total air-gap g. Neglecting leakage flux and working below saturation, $B = \mu_0 NI/g$ where N is the number of turns. An electromagnet thus produces forces which vary as $1/g^2$. At small gaps the rotor plus electromagnet will be unstable. To stabilise and linearise this behaviour, Salm and Schweitzer [9] have described an electromagnetic actuator in which each electromagnet coil contains two windings, carrying a bias current I_0, and a control current I. A pair of electromagnets on opposite sides of the core are connected such that flux on one electro-magnet is proportional to $I_0 + I$, while the opposite electromagnet produces flux proportional to $I_0 - I$. This system can be shown to linearise first order response only, with respect to both I and g. The system has a high steady power dissipation due to the bias currents I_0, and requires a unidirectional power amplifier (for bias current) and one bidirectional power amplifier per pair of electromagnets.

We have chosen instead to follow previous work on electromagnetic suspensions at Sussex [12], and control flux densities directly. Hall-effect plates are installed in the airgap at the centre of each energised pole to measure flux densities here. The electromagnets and their power amplifiers lie within an inner feedback loop, where the measured flux is compared with the drive signal, which is thus a flux demand. The non-linearity with respect to electromagnet gap is thereby removed. The Hall plates are 0.35 mm thick. They, and their mechanical protection, require a small increase in airgap.

The control system has been implemented under microprocessor control in order to develop sophisticated control strategies. At this point it is only necessary to note that complex drive waveforms can be readily generated. It is no longer necessary to obtain the linear characteristic which differential driving of a pair of opposed electromagnets can give. The minimum provision of electromagnets and their drive amplifiers can be re-examined.

The requirement is to control two degrees of freedom of shaft motion of the electromagnet location, using devices which can apply attractive forces only. For any n degrees of freedom considered together, the minimum number of electromagnets will be n+1, if a suitable geometry is chosen. The one additional electromagnet arises from the restriction to attractive forces. It can be best visualised by considering the suspension to require one indeterminacy, allowing (though not requiring) all magnets to be preloaded, with a set of self-equilibrating forces. Having provided this system any direction of resultant force can be generated by suitable matched changes in the magnet forces. Operation is, however, not restricted to this fully biased mode, and minimum power dissipation is obtained if bias is reduced until the first magnet drops to zero force.

It may be noted that this principle differs slightly from electromagnetic suspensions, in which the weight of an object may often be used to preload the system of electromagnets, which can then be reduced in number by one. Without this modification it is indeed possible to identify a system of 7 electromagnets which can apply all 6 independent force components to a platform.

If the two translational degrees of freedom of the shaft at the electromagnet location are considered separately, then two attractive forces are required to control each. The total requirement is four electromagnets and drive amplifiers, and there is little economy over previous systems. However, taking the two degrees of freedom together, three electromagnets, each with its drive amplifer, are sufficient. This offers considerable economies in power amplifiers, and simplifications in the packing of coils and poles in the electromagnet assembly. This configuration, shown in Fig.2, is used in the present work. Unwound poles are placed between each of the wound poles with a single backing ring. The layout ensures that only unidirectional current drive to each coil is required; this considerably simplifies the power amplifier design.

Power Electronics and Control

Each electromagnet coil is energised by a power amplifier of the pulse-width modulation (p.w.m.) type. The connections of the coil to the d.c. power supply of voltage V_S are switched to alternately drive increases and decreases in the coil current.

The switching frequency is high compared with the coil time constant L/R, and is normally above the audible frequency range. The input voltage to the amplifier sets the mark/space ratio of the switching signal. The on-time t_1 as a fraction of the total period τ is related to the current I, averaged over the switching cycle by:

$$t_1/\tau = \frac{1}{2} + (1/2V_s)((LdI/dt) + 2E + IR) \quad (1)$$

where E is the back-emf generated by the core velocity.

The block diagram of the control system is shown in Fig.3. The outputs of the equipment energising the displacement transducers are used directly as the displacement signals. They are also bandwidth limited and passed through analogue differentiators to give the velocity signals. The signals pass through sample and hold gates, and can be switched onto two 12-bit successive approximation analogue-to-digital converters. These are interfaced to the Z8002 microprocessor over the Z-bus. Outputs from the microprocessor are provided through 12-bit digital-to-analogue converters which drive the flux error amplifiers. Timing and shaft-speed measurement are driven through counter-timers.

As a prototype system, the Z8002 is mounted in a development module containing the monitor and a large area of random-access memory (RAM). The system is commanded from a terminal, and program editing, storage and assembly is carried out on a host system running under CP/M. Machine code programs are downloaded into the development module's RAM in order to operate the system. A production version would omit terminal and host system, and store the fixed program in ROM on the microprocessor system, with automatic initialisation and execution on reset as power is first applied.

The Z8000 series processor was selected for the project, as the only 16 bit processor available in the U.K. at the time the project started.

Software

The microprocessor software was developed using the Z8000 assembly language, and is required to operate at two levels. At the low level, for a high computation speed, a loop is executed, initiated by a timer which sets the 550 μs sampling rate. The sample-and-hold gates, multiplexors and ADC's are controlled to measure the shaft position and velocity in x- and y-directions, and these values are stored. The control forces are computed, and resolved onto the magnet directions. As the outputs are used as a flux demand, it is necessary to perform a square root extraction: this is performed as a direct look-up in a 4K word table. Finally the control signals are output through the DAC's.

At a higher, and slower, level the constants in the control law may be altered, in response to measurements of shaft speed or to observed performance. This level is performed in the processor's normal mode, and the low level tasks described above, and speed measurement, are initiated by vectored interrupts, which enter the processor's system mode and initiate these tasks as the appropriate interrupt service routines.

The results described below were obtained using an earlier development version of the software in which the higher software level is not implemented.

CHARACTERISTICS OF THE ELECTROMAGNET SYSTEM

Force Resolution

The electromagnet system is normally required to generated rotating forces which are synchronous with the rotor. In this mode, the required forces in x- and y-directions are computed as F_x and F_y, and the required forces in the three electromagnets are obtained as shown in Fig.4. For any direction of the resultant of F_x and F_y, one magnet can generate forces opposing the resultant, and it is reduced to the set minimum force F_o. The axes of the two magnets which are driven include the direction of the resultant.

The resolution is simple to program, and a pseudo-code for this is given in Appendix A. This gives the derivation of the required magnet forces F_1, F_2, F_3 in terms of the computed forces F_x,F_y. Addition of a minimum force F_o is included within the table look-up, which will be performed after execution of this code, to obtain the drive voltages to the power amplifiers.

Low Frequency Performance

At low frequencies, the capacity of the electromagnet system is limited by core saturation, and by coil dissipation. The shaft speeds are high compared with the coil thermal time constants. Mean power dissipation, rather than maximum instantaneous dissipation, will produce this limit. At constant air-gap, this mean dissipation is proportional to the area under the force waveform, but in general the currents are modulated by airgap variations.

High Frequency Performance

The p.w.m. amplifier open loop conductance was shown to vary with the signal frequency. The e.m.f. E is generally small, and the gain shows a first-order response

$$\frac{I}{t_1/\tau} = \frac{2V_s/R}{1 + j\omega/\omega_o} \qquad (2)$$

where the corner frequency ω_o is the inverse of the coil time constant L/R. This is the longest and dominant time constant in the system, and imposes severe performance limitations. The flux feedback loop operates to reduce gain but also increases the corner frequency, multiplying it by the loop gain. At the closed-loop corner frequency, substantial phase errors occur, as the amplifier contributes a 45° phase lag. Small contributions may be introduced elsewhere in the loop, as substantial filtering must be introduced at the p.w.m. switching frequency.

A further limitation arises when slew-rate limiting occurs. At low currents dI/dt cannot exceed ± V_s/L. This imposes a limiting linear rise or fall of current with time, and hence a parabolic limiting force-time curve. The force-time waveform for one magnet is shown in Fig.5.

A limiting slew-rate condition is shown by the broken line which at zero force is horizontal. For a zero bias level, i.e. $F_o = 0$, it will be seen that the initial rise in the force waveform can never be attained, and distortion will occur. A small bias level is of great benefit in allowing a useful rate-of-rise of current to be attained at point B. This also avoids operation conditions for the p.w.m. amplifiers at which commutation times become significant.

In operation, the choice lies between accepting a small distortion when a small bias level is used, and eliminating distortion but substantially increasing dissipation by adopting a high bias level. The former option is preferred at present.

The operating area of the power amplifier-electromagnet combination is shown in Fig.6. Further investigation shows that only the dissipation limit alters as the core moves within the magnet poles.

The magnet used in the present work is designed to produce 400 N at up to 100 Hz, using a 320 volt supply, within acceptable distortion limits.

CONTROL STRATEGY

In the present work the control strategy is to provide control forces which depend on the measured motion of the shaft, at one span position only. Since the shaft-bearing system under consideration is symmetrical, one need only describe the strategy for a single plane of vibration.

Suppose that the transverse displacement of the shaft is measured at a distance, x_m, from one end, and that the control force is applied at a distance, x_c, from the same end. Let $F_c(t)$ denote the time varying control force, and y_m be the measured displacement.

One of the simplest approaches, and that adopted here, is to generate a control force which is a linear combination of a displacement-proportional component and a velocity-proportional component, i.e.

$$F_c = -ky_m - c\dot{y}_m \qquad (3)$$

where k is a "spring" constant and c is a "damping" constant. When x_m and x_c are equal the constants k and c have their usual meaning. In the present application the shaft vibrates synchronously - i.e. y_m (and $\dot{y}_m$) fluctuate harmonically, with a frequency equal to the shaft's rotational speed, ω. It follows, from equation (3) that $F_c(t)$ is also harmonic.

If k and c are allowed to vary with ω than one can achieve "optimum" control, over any required speed range [3]. However, in the present investigation attention is focussed on the situation where both k and c are constant, independent of speed. As theoretical work has demonstrated, if k and c are chosen carefully, this type of control can successfully limit vibration amplitudes over a speed range covering several critical speeds [2].

THEORETICAL TREATMENT

Modelling the Shaft-Bearing System

To obtain theoretical predictions of the shaft vibrational behaviour, when controlled by a force, as given by equation (3), a computer program was written, based on the stiffness method. The shaft was discretised into a number of lumped masses, with the elastic segments between these masses being taken to be massless. The bearings were modelled as simple, pinned supports. The program could cater for any form of excitation, arising from the initial bend of the shaft, and the distribution of mass unbalance.

The equations of motion were formulated in the standard form

$$\underset{\sim}{m}\,\ddot{\underset{\sim}{y}} + \underset{\sim}{c}\,\dot{\underset{\sim}{y}} + \underset{\sim}{K}\,\underset{\sim}{y} = \underset{\sim}{Q}(t) \qquad (4)$$

where $\underset{\sim}{m}$, $\underset{\sim}{c}$ and $\underset{\sim}{K}$ are the mass, damping and stifness matrices, respectively, $\underset{\sim}{y}$ is a column of displacements and $\underset{\sim}{Q}(t)$ is a column of excitation components. A numerical solution of equation (4) enabled the vibration amplitudes of the discrete masses, at any rotational speed, to be calculated. Moreover, the stability of the system could be assessed, through an eigenvalue analysis of the homogeneous form of equation (4) ($Q(t) = 0$).

Approximate Analysis for Damping Control

If attention is focussed on a speed range covering the first critical speed only, and damping control alone is considered, then it is possible to obtain a simple analytical expression for the vibration response. This expression is likely to be fairly accurate in the case of the present shaft, since its natural frequencies are well separated.

Considering initially, for simplicity, the case of free vibration (i.e. no rotation) one can approximate vibration in the first mode by assuming that it is of the same form as undamped vibration - i.e.,

$$y(x,t) = Y(t)\sin\left(\frac{\pi x}{\ell}\right) \qquad (5)$$

where y, as before denotes transverse displacement, Y(t) is a function of time only and ℓ is the total shaft length. A single degree of freedom equation of motion can then be formulated using the energy relationship

Rate of change of total energy = - Rate of energy dissipation
(potential + kinetic) due to damping (6)

This leads (see Appendix B) to the equation

$$y'' + \beta y' + y = 0 \tag{7}$$

where here differentiation is with respect to the non-dimensional time

$$\tau = \omega_1 t \tag{8}$$

and ω_1 is the first natural frequency of the shaft. β, a non-dimensional damping coefficient is related to c (see equation (3)) through the equation

$$\beta = \frac{2c}{M\omega_1} \sin\left(\frac{\pi x_m}{\ell}\right) \sin\left(\frac{\pi x_c}{\ell}\right) \tag{9}$$

where M is the total mass of the shaft. In the experiments to be discussed later $x_m/\ell = 1/3$ and $x_c/\ell = 1/6$; hence, in this particular case,

$$\beta = \frac{\sqrt{3}c}{2M\omega_1} \tag{10}$$

For the case of a rotating shaft, with initial bend excitation only, equation (7) can be generalised by incorporating a non-zero right-hand side. If the initial bend is assumed to approximate to the shape of a half-sine wave then, at any shaft location, x, one finds, approximately, that

$$y'' + \beta y' + y = b \cos \omega t \tag{11}$$

where b is the initial bend at that location. Solving equation (11) for synchronous vibration shows that the amplitude of vibration, A, at location x, is given by

$$\frac{A}{b} = \left[\frac{1}{(1-\Omega^2)^2 + \beta^2\Omega^2}\right]^{½} \tag{12}$$

where

$$\Omega = \omega/\omega_1 \tag{13}$$

is a non-dimensional frequency.

Comparisons between predictions from equation (12), and the more accurate numerical approach described earlier, generally showed good agreement. Fig.7 shows a typical comparison for the case where c = 272

Ns/m. Here the amplitude of vibration, in one plane, at the damper position is plotted against rotational speed.

Stability Considerations

The ideal control law expressed by equation (3) can only be realised approximately, in practice. Due to the hardware limitations described earlier, the bandwidth of the electromagnetic system (EMS) is of order 100 Hz; at frequencies in excess of this the phase shifts and gain variations associated with the EMS become very significant and must be taken into account in any assessment of the overall stability of the total shaft-plus-EMS.

The total system may be regarded as two sub-systems - the shaft-bearing system (SBS) and the electromagnetic system (EMS). These sub-systems are coupled through the following two variables:

(i) the force $F_c(t)$, at position x_c
(ii) the shaft displacement, $y_m(t)$ at position x_m.

The appropriate block diagram representation of the total system is shown in Fig.8. For a stability assessment it is sufficient to consider the case of no rotation - i.e., no excitation, and motion in one plane only.

For the SBS, the Laplace transform of $y_m(t)$, denoted $Y_m(s)$, is related to the Laplace transform of $F_c(t)$, denoted $F_c(s)$, though the linear relationship

$$F_c(s) = M(s)Y_m(s) \tag{14}$$

Here M(s) is the "mechanical" transfer function for the shaft-bearing system. Similarly, for the EMS one can write (assuming that this sub-system behaves, at least approximately, in a linear fashion)

$$F_c(s) = E(s)Y_m(s) \tag{15}$$

where E(s) is the "electrical" transfer function. Eliminating $F_c(s)$ between equations (14) and (15) one finds that

$$D(s)Y_m(s) = 0 \tag{16}$$

where

$$D(s) = M(s) + \bar{E}(s) \tag{17}$$

and

$$\bar{E}(s) = -E(s) \tag{18}$$

The total systems characteristic equation is thus

$$D(s) = 0 \tag{19}$$

For stability all the roots of equation (18) must lie on the left hand side of the complex s-plane. The position of these roots can be determined numerically if both M(s) and E(s) can be expressed in algebraic form. Alternatively, a graphical procedure can be used.

In the present paper the graphical technique known as the Leonhard Locus (e.g. see Ref.13) will be used to examine the factors which influence total system stability. This involves a consideration of the mapping between the s-plane and the complex D-plane, where D is defined by equation (17). Firstly, it may be observed that the roots of the characteristic equation all map to the origin of the D-plane. Now if a point travels along the imaginary axis of the s-plane - i.e., $s = j\omega$, with ω increasing from $\omega = 0$ - it will map to a curved locus, $D(j\omega)$, in the D plane, known as the Leonhard Locus. In the case of a stable system all the roots in the s-plane lie to the left-hand side of the locus $s = j\omega$; this implies that the mapped, Leonhard locus, in the D-plane will be such that the origin will always lie on the left hand side, to an "observer" travelling along the locus in the direction of increasing frequency, ω. For a system at the threshold of stability the Leonhard locus should pass exactly through the origin of the D-plane.

In the present case the Leonhard locii, $M(j\omega)$ and $E(j\omega)$, may be evaluated separately and then combined, through a simple addition. According to equation (17) the combined Leonhard locus is given by

$$D(j\omega) = M(j\omega) + \bar{E}(j\omega) \tag{20}$$

Now $M(j\omega)$ and $\bar{E}(j\omega)$ are directly related to the frequency response functions for the mechanical and electrical sub-systems, respectively. Thus the stability of the total system can be deduced directly from the characteristics (amplitude and phase variation with frequency) of these two functions.

For a pinned-pinned uniform shaft the appropriate frequency response function, $M(j\omega)$, can be found by standard methods. If it is assumed that the introduction of structural damping does not lead to coupling between the modes then a modal expansion for the inverse of $M(j\omega)$ is as follows:

$$\frac{1}{M(j\omega)} = \sum_{n=1}^{\infty} \frac{\alpha_n}{[\omega_n^2 + (j\omega)^2 + 2(j\omega)\zeta_n\omega_n]} \tag{21}$$

where

$$\omega_n = n^2\pi^2 \frac{EI}{\ell^4} \tag{22}$$

is the nth natural frequency, E is Young's modulus for the shaft material, $I = \pi d^4/64$, where d is the shaft diameter, and m is the mass per unit length of the shaft. ζ_n ($n = 1,2...$) are the modal damping factors and the coefficients α_n are given by

$$\alpha_n = \frac{2}{m\ell} \sin\left(\frac{n\pi x_m}{\ell}\right) \sin\left(\frac{n\pi x_c}{\ell}\right) \tag{23}$$

Fig. 9 indicates the general behaviour of the Leonhard locus, M(jω), for the first three modes. The arrows indicate the direction of increasing frequency. It is noted that there is one "branch" of the locus, corresponding to each mode; the nth branch intersects the imaginary axis of the M(jω) plane at $\omega \sim \omega_n$. The height of such an intersection is, to a good approximation, directly proportional to the structural damping of the corresponding mode. In general the structural damping will become more effective as the mode number, n, increases; this is one reason why the branches of M(jω) become progressively higher, as Fig.9(a) indicates. For an imaginary observer moving along any particular branch the origin always appears to the left hand side - it follows that the mechanical sub-system, considered in isolation, is always stable.

For the "ideal" control law given by equation (3) the corresponding Leonhard locus $\bar{E}(j\omega)$ is easily found to be

$$\bar{E}(j\omega) = k + (j\omega)c \qquad (24)$$

This locus is sketched in Fig. 9(b). It is evident that a combination of M(jω) and $\bar{E}(j\omega)$ will lead to a total system locus, D(jω) which also satisfies the graphical stability criterion.

The main interest here concerns the effect of the electromagnet system's non-ideal characteristic on the total system stability. Figs. 10(a) and (b) show, qualitatively, the difference between the ideal pure spring, and the ideal pure damper, $\bar{E}(j\omega)$ loci, respectively, and the corresponding loci of the kind obtained in practice. As ω increases, the phase shifts, and gain reduction, becomes progressively more significant, resulting in curved loci.

A combination of M(jω) with the actual E(jω) can lead to a Leonhard locus which indicates instability. This is illustrated in Fig.11. If a particular branch of the M(jω) is "pulled" below the origin, through the addition of $\bar{E}(j\omega)$, then total system instability is indicated. The threshold of instability occurs, for a particular mode, when the relevant branch of the combined locus just passes through the origin.

Let s denote distance travelled along a Leonhard locus. Then it may be observed that ds/dω for M(jω), in the vicinity of a natural frequency, is normally much greater than the corresponding rate of change for $\bar{E}(j\omega)$. Also, for $\omega = \omega_n$, $M(j\omega_n)$ is, to a close approximation, entirely imaginary, with a value given by (from equation (21))

$$M(j\omega_n) = j.\,\frac{2\zeta_n\omega_n^2}{\alpha_n} \qquad (25)$$

This result follows from the fact that the contribution to $\underline{M}(j\omega_n)$ from the nth mode is dominant. If the combination of M(jω) and $\bar{E}(j\omega)$ is to result in a locus which passes above the origin then one requires, approximately, that

$$\frac{2\zeta_n\omega_n^2}{\alpha_n} + \mathrm{Im}(\bar{E}(j\omega_n)) > 0 \qquad (26)$$

This condition gives a criterion for "stability in the nth node". Total stability obviously requires that inequality (26) be satisfied for all n.

Several conclusions can be drawn from this stability criterion. Firstly, considering the case of pure stifness control, it is evident that, since ζ_n are generally very small quantities ($\zeta_n \ll 1$), very small phase shifts can result in instability (see Fig.10(b)). Thus this method of control is very prone to instability problems.

In considering the other extreme case of pure damping control it is convenient to represent $\bar{E}(j\omega)$ as

$$\bar{E}(j\omega) = j\omega c\, E_A e^{-j\Phi} \qquad (27)$$

Evidently, for ideal damping $E_A = 1$, $\Phi = 0$ and, from inequality (26), stability is assumed, for all n. However, if $90^o < \Phi < 270^o$, at a particular natural frequency, ω_n, then the corresponding mode can become unstable. The critical value of damping coefficient, c^*, at which the nth mode is marginally stable is given by (for $90^o < \Phi < 270^o$)

$$c^* = \frac{2\zeta_n\omega_n}{E_A\alpha_n|\cos\,\Phi|} \qquad (28)$$

Again, since ζ_n are usually very small compared with unity, c^* can be very low. It follows from equation (28) that improvements in the stable range of damping coefficient can be achieved by

(i) reducing the absolute value of $\cos\,\Phi$

(ii) reducing the non-dimensional gain, E_A

(iii) reducing the value of α_n, by repositioning the measuring location, x_m.

It is noted that, if only one mode of vibration is unstable, this instability can be removed, theoretically, by locating the measuring point at a node of that particular mode. This has the effect of making $\alpha_n = 0$, since the nth mode has the mode shape $\sin\,(n\pi x/\ell)$ (see equation (23)).

COMPARISON BETWEEN THEORY AND EXPERIMENT

Results will now be presented which relate to the case of nominally pure damping (i.e. $k = 0$ in equation (3)).

Stability Observations

With $x_c = \ell/6$, and x_m close to x_c, experiments revealed that the shaft became unstable when the damping coefficient exceeded a small, non-zero level. The self-excitation was in the form of vibration in the third mode.

Referring to equation (28) one can conclude that, for the third mode, the value of c^* is very low. This is mainly due to the value of Φ at $\omega 3$ (~ 180 Hz), which is in excess of 90°. It was found experimentally that c^* could be increased by moving the measurement position closer to a node position of the third mode ($x_m = \ell/3$). This observation is in qualitative agreement with equation (28). It was also found experimentally that c^* could be increased by reducing the value of Φ at ω_3, through modifications to the electronics and software. This again is in accord with equation (28).

To enable results to be obtained over a wide range of damping coefficient (c) values, the measuring point was located at a third mode node - i.e. at $x_m = \ell/3$. The total system was then found to be stable for c values up to about 700 Ns/m.

Free Decay Tests

Experimental estimates of the damping coefficient β, in equation (7), were obtained by performing free-decay tests on the non-rotating shaft. The shaft was pulled at its centre, through a small displacement, and then released. The subsequent transient decay was then recorded digitally, at equi-spaced time intervals, for various levels of damping coefficient.

Figs. 12(a) and (b) show typical free-decay experimental results, including the case where the electromagnetic damping is zero (i.e. structural damping only is present). The results were obtained for various programmable rates of damping by varying the rate constants (in arbitrary units) in the control program. To reduce the effects of noise, each of the free-decay results was obtained by averaging ten separate, individual results, obtained under identical conditions.

Each averaged free-decay result was processed by a parametric identification procedure, which fitted the experimental data to the solution of the following equation of motion, in a least-square sense [14,15];

$$y'' + \beta y' + \gamma y = 0 \qquad (29)$$

Figs.12 show comparisons between the solutions to equation (29) and the experimental data, where the theory is computed from the best fit values of β and γ. In every case a very good degree of fit is achieved. Table 1 summarises the results obtained for β and γ.

It is noted that γ is close to unity, as one would expect, for pure damping. Moreover, β is, to a very close approximation, proportional to the programmable damping rate, as Fig.13 shows. The results also show that the contribution of structural damping can be neglected.

Table 1

Programmable damping rate (arbitrary units)	estimated parameters	
	β	γ
0	0.013	1.00
199	0.123	0.08
272	0.178	1.01
397	0.279	1.02
496	0.357	1.08
595	0.407	1.12
744	0.501	1.08

It can be concluded, from the analysis of these tests, that the electromagnetic control system performs as expected, at least for frequencies in the vicinity of the shafts first natural frequency (~ 21 Hz).

Rotating Shaft Results

For rotational speeds in the range 200 to 2500 r.p.m., the shaft's amplitude of vibration, in a single plane, was measured and plotted against shaft speed. The measurement location was at $x \sim \ell/6$; close to the magnet position. Figs. 14 show some typical comparisons between the experimental variations of vibration amplitude with rotational speed, and corresponding theoretical predictions, for two levels of damping. The theoretical predictions were obtained from the lumped-mass computer program, with damping values deduced from the β values found in the free-decay tests, using equation (10) to convert β to the damping coefficient c. The initial bend of the shaft was measured experimentally and used as input data for the program. Generally the degree of agreement between theory and experiment is very satisfactory, and it is evident that the vibration amplitude at the first critical speed can be controlled very satisfactorily by the electromagnet system. It is interesting to note that there is some variation in the experimental results, at each level of damping. Thus, the variation of amplitude with speed as the speed increased from zero to its maximum value (labelled 'before'), was found to differ somewhat from the corresponding variation as the speed decreased to zero (labelled 'after'). Further traverses in speed were found to produce further variations. This phenomenon is attributed to variations in the initial bend of the shaft, as the results of stress cycling. This effect has been observed in earlier investigations (e.g. see Ref.2). Measurements of the initial bend confirmed that it changed, as the results of a sequence of rotational tests. The initial bend was found to return to its original shape over a time period of order one day.

A direct estimate of the non-dimensional damping parameter β, produced by the electromagnet system, can be found by using the simple approximate result given by equation (12). In particular, at $\Omega = 1$ one has, from this equation,

$$A/b = 1/\beta \qquad (30)$$

Thus, taking the average of the experimental results, at each damping level, and dividing the amplitude of vibration at $\omega = 0(b)$ by the amplitude of vibration at $\omega = \omega_1$, one obtains a simple estimate of β. In Fig.15 the estimates of β, obtained in this way, are plotted against the corresponding estimates obtained from the analysis of the transient data. Each point here relates to one programmable rate of damping. The points lie very close to a straight line, at 45° to the horizontal, showing a good degree of correlation. There is a small offset, which indicates that, in the case of rotation, there is a small additional contribution to the total damping. This contribution probably originates in the bearings. When allowance is made for this effect one can conclude, from Fig.15, that the test results obtained with the rotating shaft are in complete accord with the transient test results.

CONCLUSIONS

A microprocessor based electromagnet system for controlling the vibration of rotating flexible shafts has been described, and bounds on the performance of the system have been defined. Theoretical arguments have shown that, as a result of limitations to the performance of the electromagnet system, the complete shaft-plus-electromagnet system can become unstable under certain conditions. A simple stability criterion has been established which reveals the influence of various factors on stability. For the case where the electromagnet is programmed to behave as a simple damper, good agreement between experimental observations and theoretical predictions has been achieved, over a rotational speed range encompassing the shaft's first critical speed.

APPENDIX A

ALGORITHM FOR FORCE COMPONENT EVALUATION

```
  fx :=      (required forces)
  fy :=      (               )
  fx':= fx/√3

  if fx'>0 then
     if fx'>fy then
        call m3off
     else
       call m1off
 else
     if -fx'>fy then
     call m2off
    else
        call m1off
  endif

 procedure m1off
  f2 := fx' + fy
  f3 :=-fx' + fy
  f1 := 0
endproc
```

```
 procedure m2off
  f1 := -fx' - fy
  f2 :=  0
  f3 := -2*fx'
endproc

 procedure m3off
  f1 := fx' - fy
  f2 := 2*fx'
  f3 := 0
endproc
```

APPENDIX B
APPROXIMATE EQUATION FOR FIRST MODE FREE VIBRATION WITH DAMPING

For a uniform shaft with pinned supports, free undamped vibration takes the form

$$y(x,t) = Y(t)\sin(\pi x/\ell) \tag{A1}$$

where Y(t) is a function of time only. A good approximation, when damping is applied through the electromagnets, is to assume that this basic form of vibration is still applicable. This approximation clearly will be most accurate when the damping is light.

The total kinetic energy of the vibrating shaft is then given by

$$KE = \frac{1}{2}\int_0^\ell m y^2 dx \tag{A2}$$

where m is the mass per unit length. Combining equations (A1) and (A2) one finds that

$$KE = \frac{1}{4} M Y^2 \tag{A3}$$

where $M = m\ell$. The total potential energy, in the form of elastic strain energy in the shaft, can also be easily calculated; thus

$$PE = \frac{EI}{2}\int_0^\ell \left(\frac{d^2y}{dx^2}\right)^2 dx \tag{A4}$$

and, from equations (A1) and (A4),

$$PE = \frac{EI\,\pi^4 Y^2}{4\ell^3} \tag{A5}$$

Finally, the rate of energy dissipation, R, is given simply by

$$\begin{aligned} R &= \text{Damper force x velocity at damper} \\ &= c y_m y_c \end{aligned} \tag{A6}$$

where y_c is the velocity at the electromagnet position and y_m is the velocity at the measuring point. From equations (A1) and (A6) one has

$$R = cY^2 \sin\left(\frac{\pi x_m}{\ell}\right) \sin\left(\frac{\pi x_c}{\ell}\right) \qquad \text{(A7)}$$

Now, following the energy relationship expressed by equation (6), one has

$$\frac{d}{dt}(PE + KE) = -R \qquad \text{(A8)}$$

Hence, from equations (A3), (A5) and (A7), one obtains a single degree of freedom equation of motion, as follows:

$$\frac{1}{2} M \ddot{Y} + \frac{cY}{2} \sin\left(\frac{\pi x_m}{\ell}\right) \sin\left(\frac{\pi x_c}{\ell}\right) + \frac{EI\,\pi^4}{2\ell^3} Y = 0 \qquad \text{(A9)}$$

On introducing thge non-dimensional time, τ, defined by equation (8), and using the fact that y, at any value of x, is simply proportional to Y, one obtains equations (7) and (9). One also finds that

$$\omega_1^2 = \frac{\pi^4}{\ell^3} \frac{EI}{M} \qquad \text{(A10)}$$

This is, of course, the "exact" result for the undamped natural frequency of a pinned-pinned shaft, since equation (1) is the corresponding exact mode shape for this case.

REFERENCES

1. Dostal, M., Roberts, J.B. and Holmes, R., "Stability Control of Flexible Shafts Supported on Oil-Film Bearings", Journal of Sound and Vibration, Vol.35, No.3, 1974, pp.361-377.

2. Dostal, M., Roberts, J.B. and Holmes, R., "The Effect of External Damping on the Vibration of Flexible Shafts Supported on Oil-Film Bearings", Journal of Sound and Vibration, Vol.51, No.1, 1977, pp.69-87.

3. Kaya, F. and Roberts, J.B., "Optimum Vibration Control of Flexible Transmission Shafts", Proceedings of the Third International Conference on Vibrations in Rotating Machinery, York, U.K. September 1984. Published by the Institution of Mechanical Engineers, London, 1984, pp.525-534.

4. Nikolajsen, J.L. and Holmes, R., "Investigation of Squeeze-Film Isolators for the Vibration Control of a Flexible Rotor", Journal of Mechanical Engineering Sciences, Vol.21, No.4, 1979, pp.247-252.

5. Roberts, J.B. and Kaya F., "Vibration Control of a Flexible Transmission Shaft by Means of a Squeeze-Film Damper: An

Experimental Investigation", to be published in the Journal of Sound and Vibration, 1986.

6. Nikolajsen, J.N., Holmes, R. and Gondhalekar, V., "Investigation of an Electromagnetic Damper for Vibration Control of a Transmission Shaft", Proceedings of the Institution of Mechanical Engineers, Vol.193, No.31, 1979, pp.331-336.

7. Haberman, H., "Le Palier Magnetique Actif 'ACTIDYNE'", AGARD Conference Proceedings, No.323, "Problems in Bearings and Lubrication", Ottawa, Canada, May 1982.

8. Ulbrich, H. and Anton,E., "Theory and Application of Magnetic Bearings with Integrated Displacement and Velocity Sensors", Proceedings of the Third International Conference on Vibrations in Rotating Machinery, York, U.K., September 1984. Published by the Institution of Mechanical Engineers, London, 1984, pp.543-552.

9. Salm, J. and Schweitzer, G., "Modelling and Control of a Flexible Rotor with Magnetic Bearings", Proceedings of the Third International Conference on Vibrations in Rotating Machinery, York, U.K., September 1984. Published by the Institution of Mechanical Engineers, London, 1984, pp.553-561.

10. Anton, E. and Ulbrich, H., "Active Control of Vibrations in the Case of Asymmetrical High-Speed Rotors by using Magnetic Bearings", Journal of Vibration, Acoustics, Stress and Reliability in Design, ASME, Vol.107, October 1985, pp.410-415.

11. Gondhalekar, V. and Holmes, R., "Design of a Radial Electromagnetic Bearing for the Vibration Control of a Supercritical Shaft", Proceedings of the Institution of Mechanical Engineers, Vol.198C,1984.

12. Jayawant, B.V., Sinha, P.K. and Aylwin, D.G., "Feedback Control Systems for d.c. Electromagnets in Passenger Carrying Vehicles", International Journal of Control, Vol. 24, No.5, 1976, pp.627-639.

13. Naslin, P., "The Dynamics of Linear and Non-linear Systems", Blackie, Edinburgh, 1965. p.244.

14. Roberts, J.B., Holmes, R. and Mason, P.J., "Estimation of Squeeze-Film Damping and Inertial Coefficients from Experimental Free-Decay Data", to be published in the Proceedings of the Institution of Mechanical Engineers, Engineering Sciences Division, U.K., 1986.

15. Ramli, M.D., Roberts, J.B. and Ellis, J., "Determination of Squeeze-Film Dynamic Coefficients from Experimental Transient Data" (to be published).

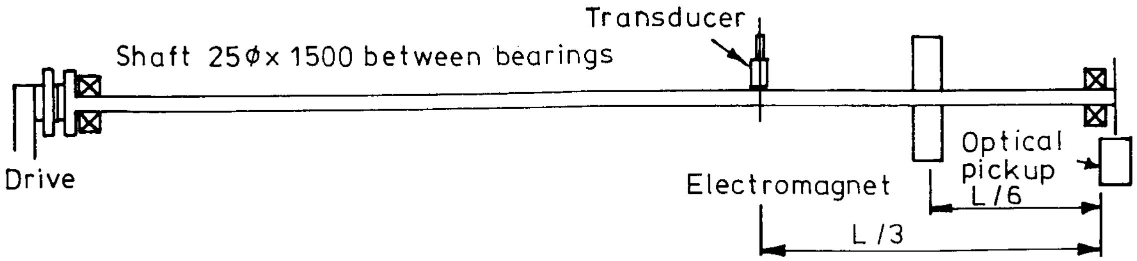
Transducer
Shaft 25ϕ x 1500 between bearings
Drive
Electromagnet
Optical pickup
L/6
L/3

Fig 1: Layout of test rotor

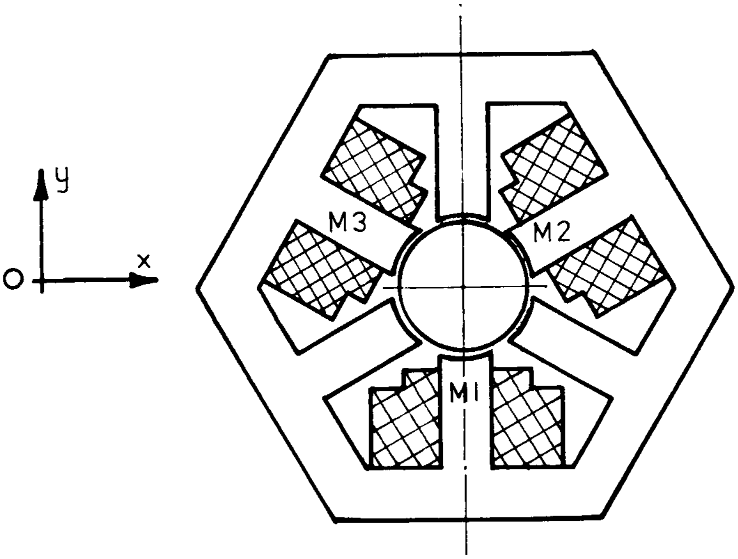

Fig 2: Configuration of electromagnet assembly

ORIGINAL PAGE IS
OF POOR QUALITY

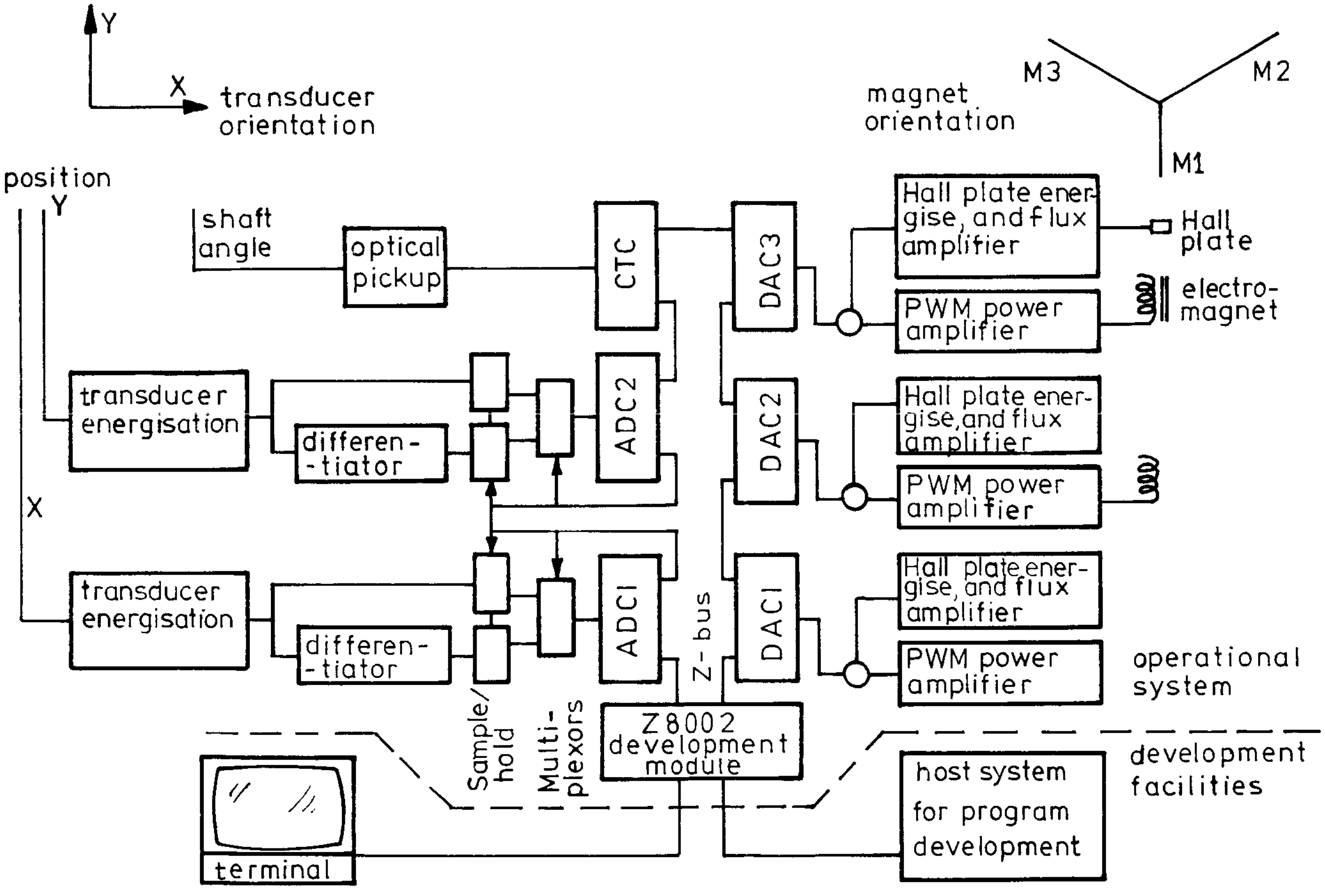
Y
X
transducer orientation
magnet orientation
M3
M2
M1
position
Y
X
shaft angle
optical pickup
CTC
DAC3
Hall plate energise, and flux amplifier
Hall plate
PWM power amplifier
electro-magnet
transducer energisation
differen-tiator
ADC2
DAC2
Hall plate energise, and flux amplifier
PWM power amplifier
transducer energisation
differen-tiator
ADC1
Z-bus
DAC1
Hall plate energise, and flux amplifier
PWM power amplifier
operational system
Sample/hold
Multi-plexors
Z8002 development module
terminal
host system for program development
development facilities

Fig 3: Schematic of electromagnet controller

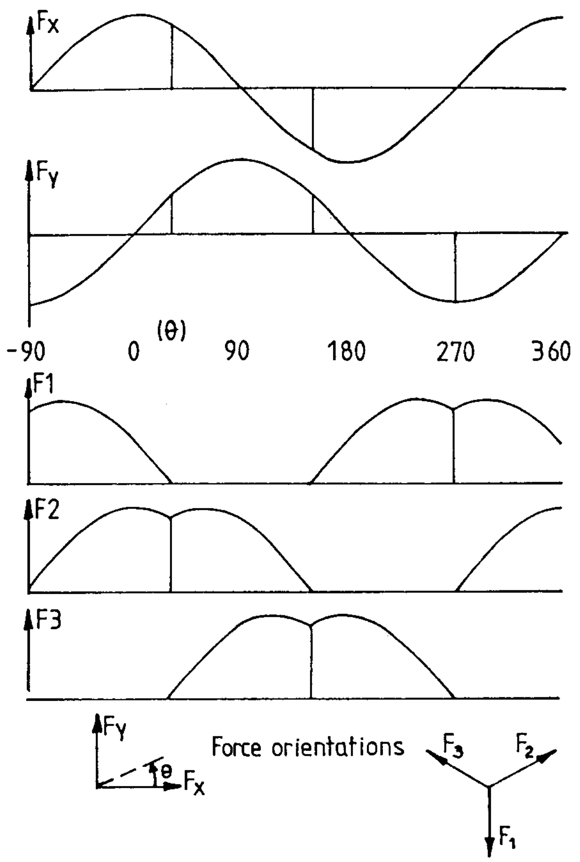

Fig 4: Waveforms of required forces along orthogonal and magnet axes.

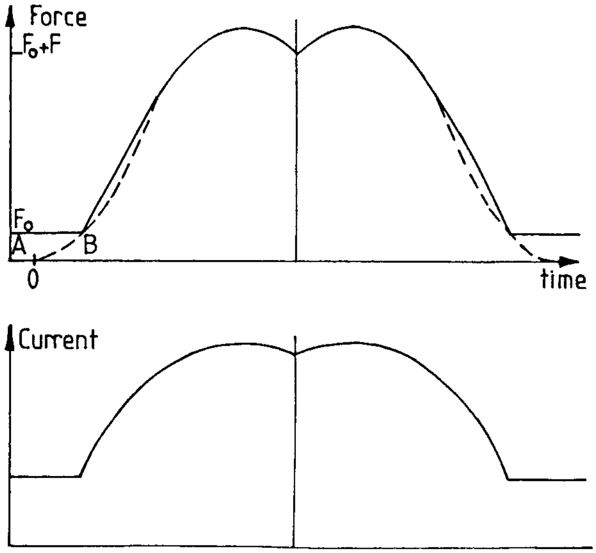

Fig 5: Effect of slew-rate limiting on current and force waveforms.

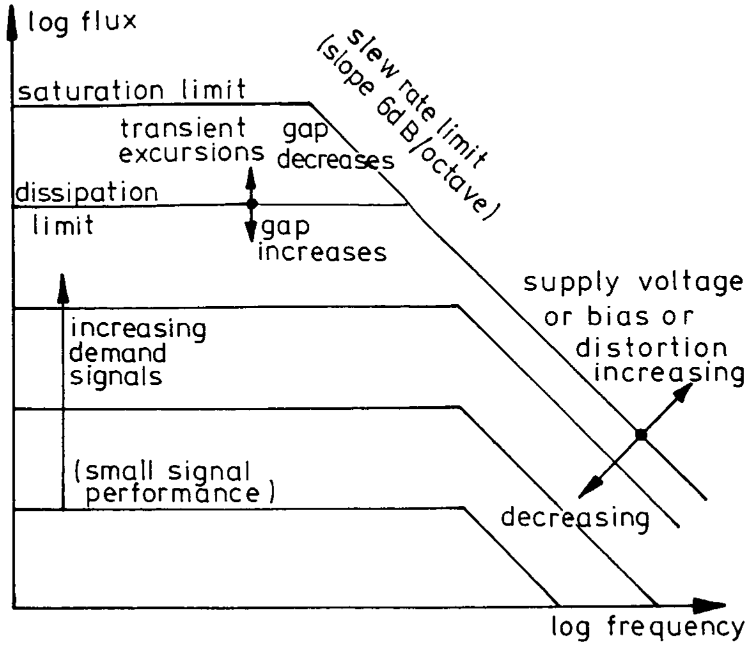
log flux
slew rate limit
(slope 6dB/octave)
saturation limit
transient excursions
gap decreases
dissipation limit
gap increases
supply voltage or bias or distortion increasing
increasing demand signals
(small signal performance)
decreasing
log frequency

Fig 6: Performance envelope for electromagnet-power amplifier combination

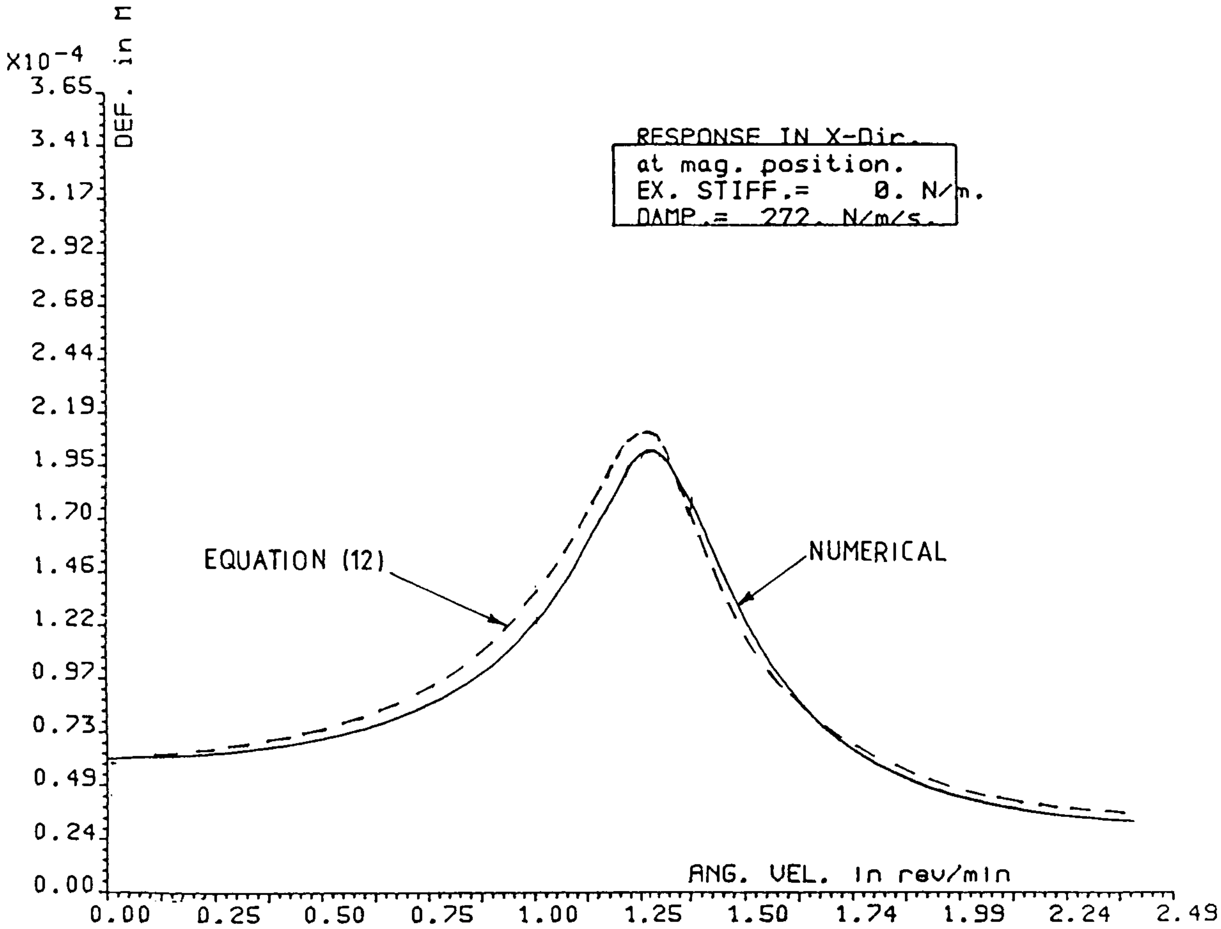

Fig 7: Predicted shaft responses

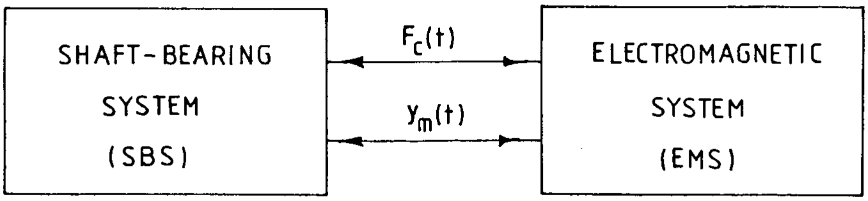
SHAFT-BEARING SYSTEM (SBS)
$F_c(t)$
$y_m(t)$
ELECTROMAGNETIC SYSTEM (EMS)

Fig 8: Mechanical and control block diagram

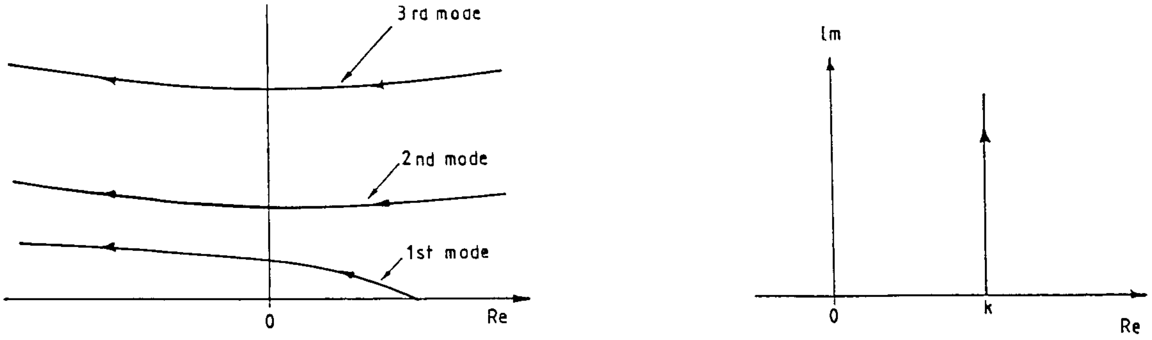
3rd mode
2nd mode
1st mode
0
Re
Im
0
k
Re

(a) SBS

(b) ideal controller

Fig 9: Leonhard locus

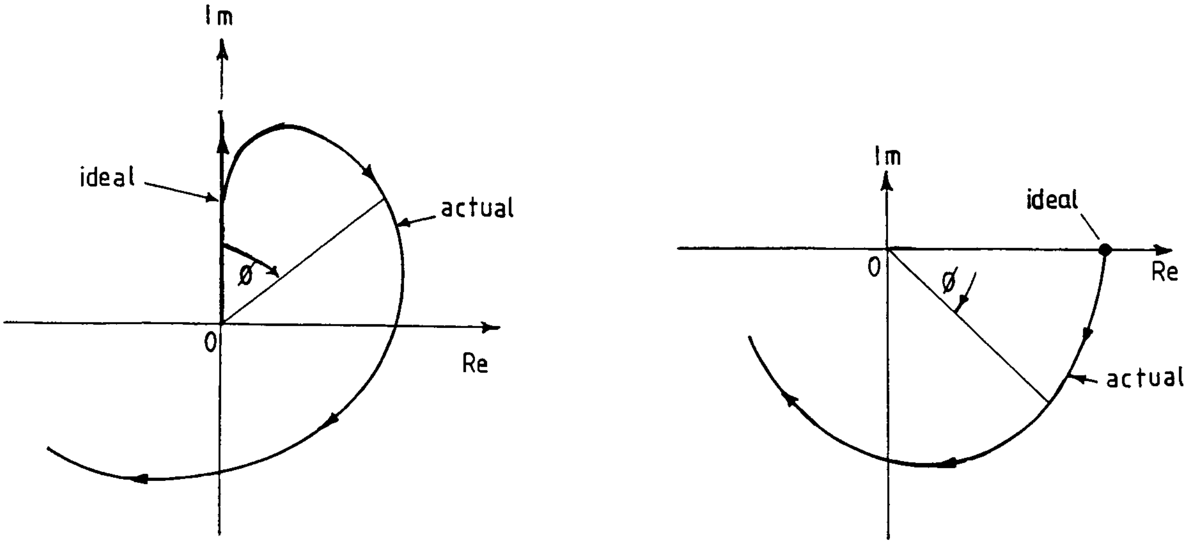
Im
ideal
actual
ø
0
Re
Im
ideal
0
ø
Re
actual

(a) damping mode

(b) stiffness mode

Fig 10: Leonhard loci for EMS

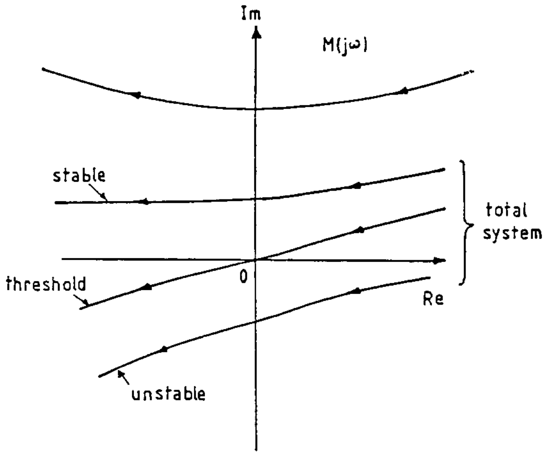
Im
M(jω)
stable
total system
threshold
0
Re
unstable

Fig 11: (right) Leonhard loci showing criteria for stability of complete system in stiffness mode

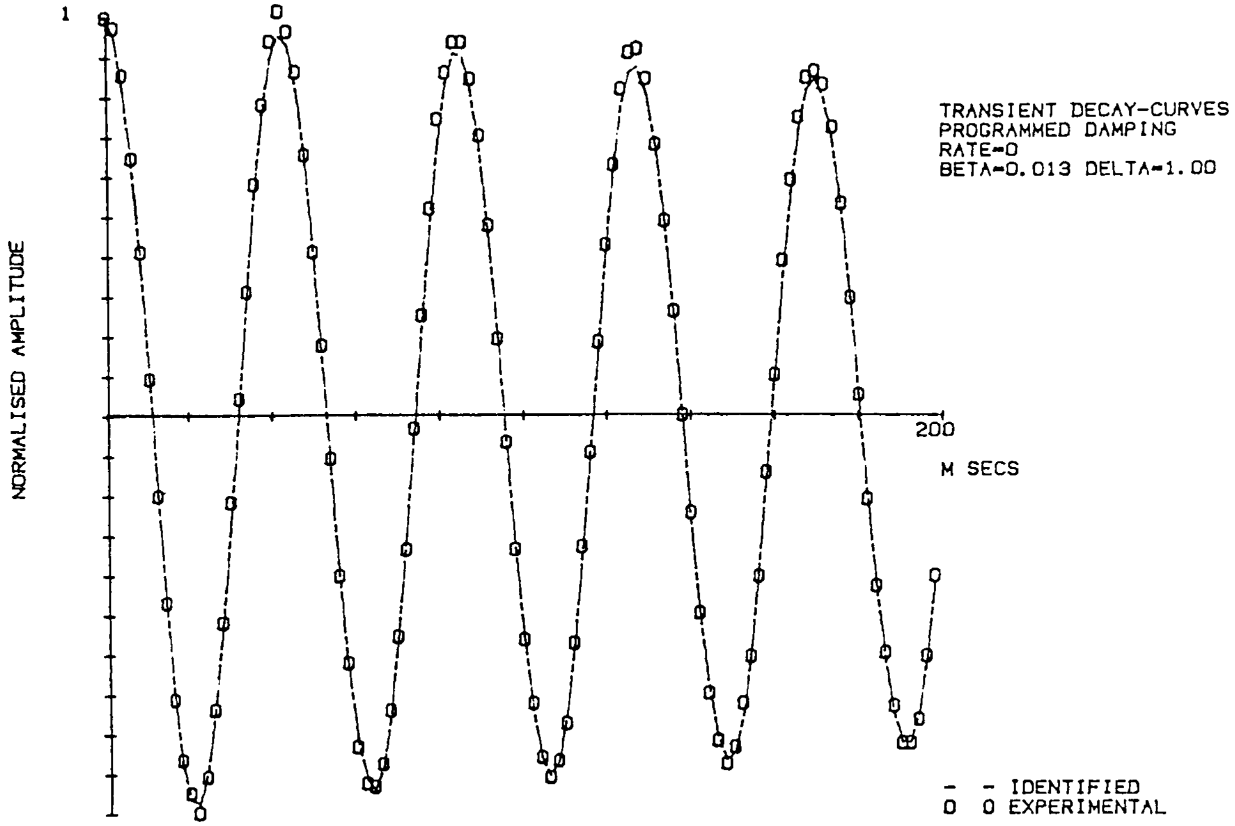

(a) controller inoperative

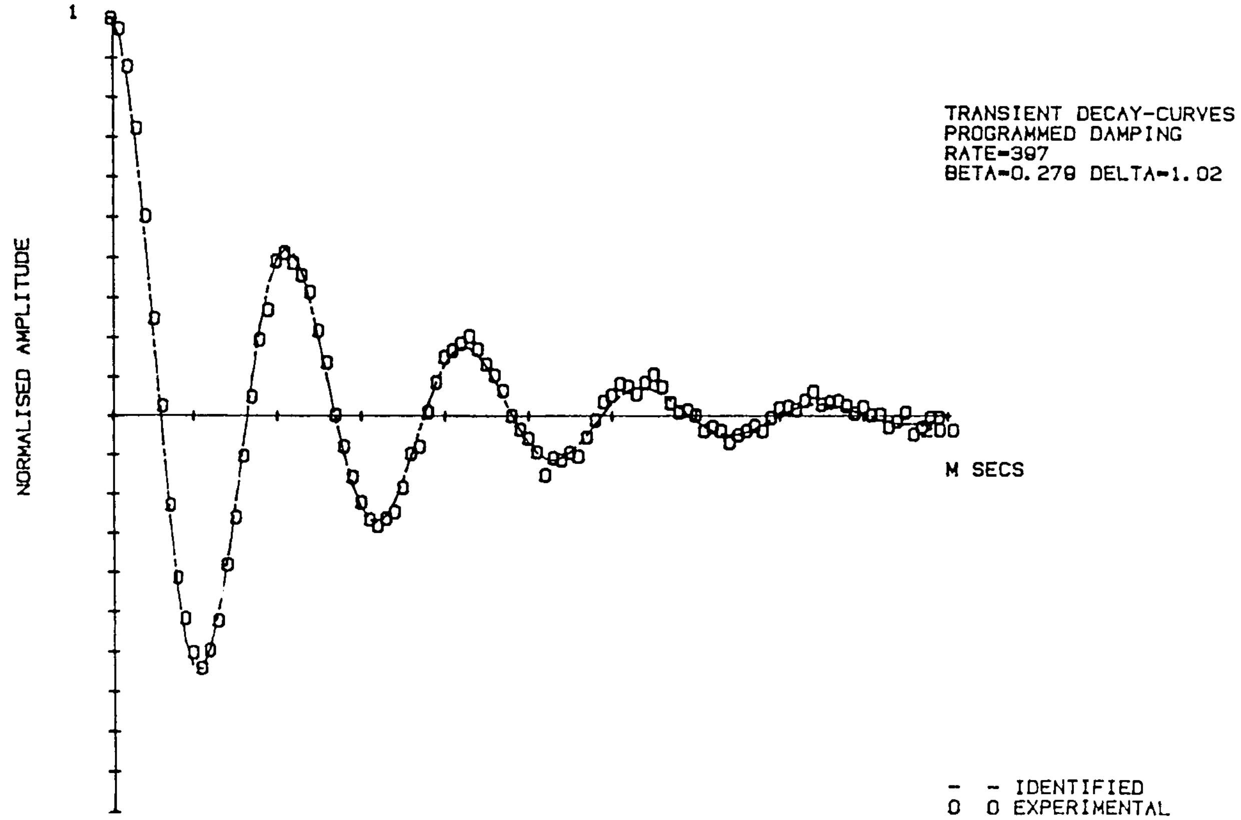

(b) with damping rate

Fig 12: Measured behaviour in free-decay tests

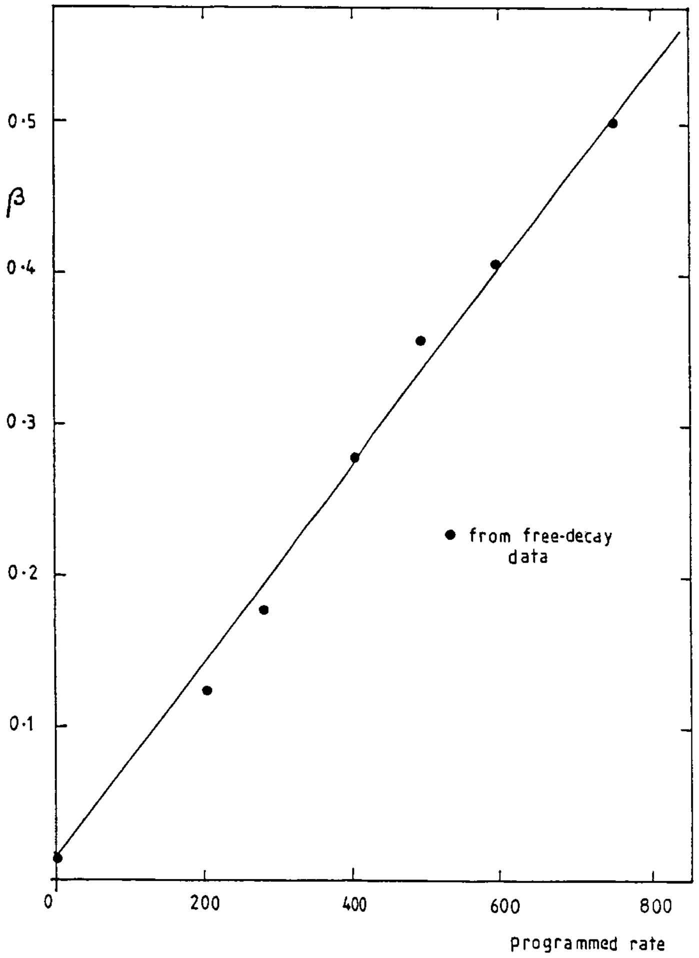

Fig 13: calibration of damping rate

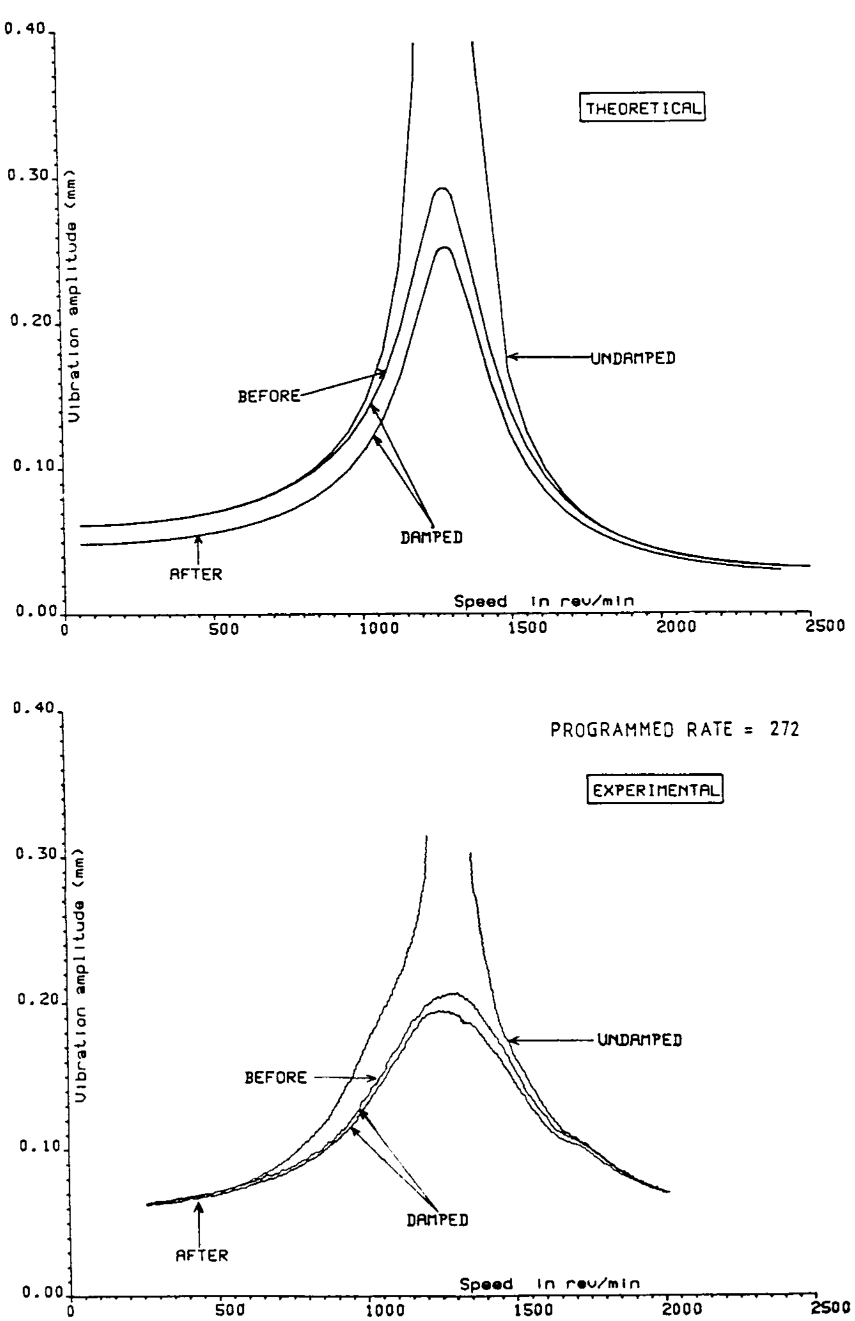

Fig 14: (a) measured and predicted responses lightly damped shaft

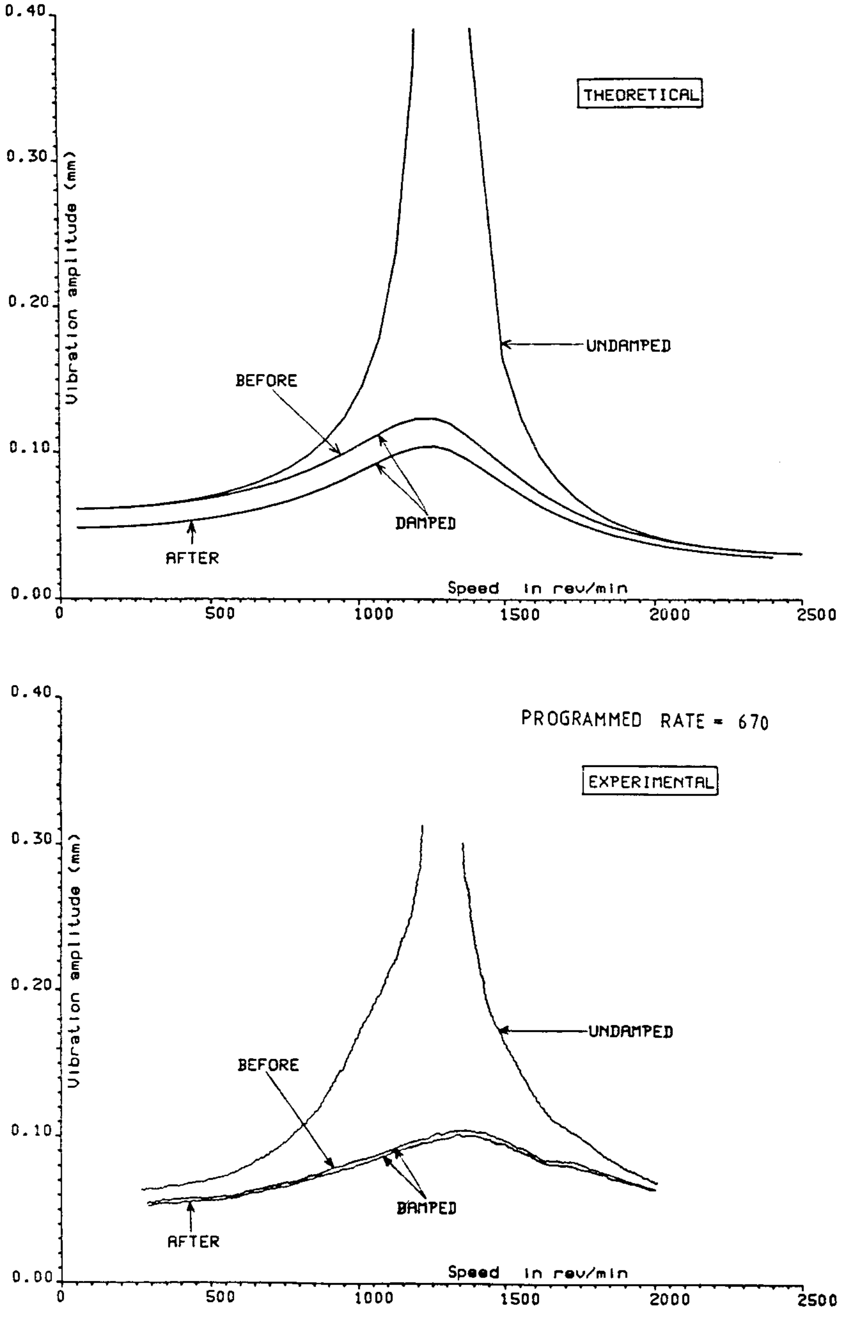

Fig 14: (b) measured and predicted responses of heavily damped shaft

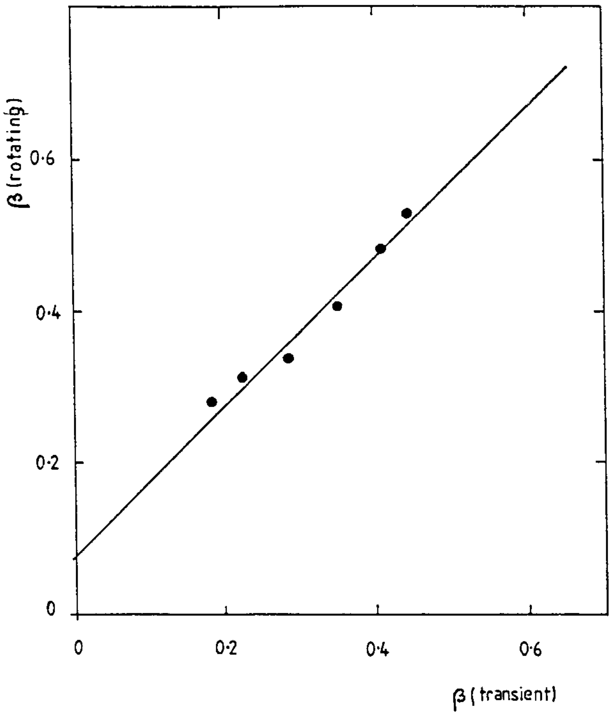

Fig 15: Comparison of damping rates from rotating and transient tests

N87-22223

A MAGNETIC BEARING BASED ON EDDY-CURRENT REPULSION

J.L. Nikolajsen
Texas A&M University
College Station, Texas 77843

This paper describes a new type of electromagnetic bearing, called the 'Eddy-Current Bearing,' which works by repulsion between fixed AC-electromagnets and a conducting rotor. The following advantages are expected: inherent stability, higher load carrying capacity than DC-electromagnetic bearings, simultaneous radial, angular and thrust support, motoring and generating capability, and backup mode of operation in case of primary power failure. A prototype is under construction.

INTRODUCTION

Levitation of conducting material by AC-electromagnets, as shown in figure 1, is a well-known phenomenon. The AC-current in the magnet sets up a constantly changing magnetic field which induces eddy-currents in the conducting plate. The direction of rotation of the eddy-currents is such that the resulting secondary magnetic field will oppose the primary field. E.g., whenever a north pole is being generated in the primary field, a north pole will also be generated in the secondary field and steady repulsion will take place between the magnet and the plate. This is the basic operating principle of the Eddy-Current bearing outlined in this paper.

BACKGROUND

AC-electromagnetic levitation of conducting material has inspired many inventions throughout this century. Some early outstanding examples are: the Foucault Railroad of 1912 (ref. 1), Anschutz-Kaempfe's gyro of 1923 (ref. 2), and Orkress' levitation of molten metal without a crucible in 1952 (ref. 3).

In the 1960's, the principle was applied in contactless suspension of high-speed ground transportation vehicles (ref. 4). Development took place in competition primarily with controlled DC-electromagnetic suspensions and cryogenic type suspensions using superconducting magnets. An excellent survey of these and other types of magnetic suspensions can be found in references 5 and 6.

The potential of the AC-electromagnetic type suspension was fully realized in 1974 when Eastham and Laithwaite presented their so-called 'Magnetic River' suspension (ref. 7). It consists of a single linear induction motor which has been adapted to provide not only stable levitation but also propulsion and guidance of itself along a conducting rail without any feedback control (fig. 2). There is even a technique available by which the 'Magnetic River' can be made to stop safely on the rail in case of power failure (ref. 8).

By their very nature, the competing suspensions have no capability for propulsion or emergency stopping. However, they remain strong contenders due to some problems with the Magnetic River which are still unresolved. The primary problem is a low power factor which appears to necessitate forced cooling of the magnets and use of heavy power-factor-correcting capacitors in order to achieve large levitation gaps (ref. 9). Also, the inherent damping in the system is apparently very light and some form of feedback control may be needed to improve it (ref. 10). Finally, analytical predictions of the performance are exceedingly difficult to make due to the complex three-dimensional interactions which take place between the primary and secondary electromagnetic fields. Thus, improvements have had to be made largely by trial-and-error experimentation based on the intuition of a few specialized engineers (ref. 7). This work has been made even more difficult by the fact that apparently minor changes in geometry have been found to produce large unexpected changes in performance. Relief finally appears to be in sight with recent developments of finite element methods intended specifically for design studies of the Magnetic River (refs. 10, 11 and 12).

THE EDDY-CURRENT BEARING

The Eddy-Current bearing, as shown in figure 3, is made simply by bending the Magnetic River of figure 2 into a circular shape. An extensive literature survey has indicated that this has not previously been done although the possibility of doing so has previously been mentioned in reference 13 during the discussion of another electromagnetic bearing.

The many advantages of the Magnetic River suspension, as mentioned previously, are expected to translate into similar advantages of the Eddy-Current Bearing as discussed in the following sections. Also, the problem with the low power-factor in the Magnetic River is expected to diminish in the Eddy-Current bearing because the airgap is much smaller. The inherent system damping will probably remain low in the Eddy-Current bearing, but this could be compensated by use of a passive eddy-current damper (ref. 14). Finally, the recent finite element methods for the Magnetic River are expected to be applicable to design studies of the Eddy-Current bearing also. A brief discussion of each of the expected advantages of the Eddy-Current bearing is given in the following sections.

Support and Motoring Capabilities

The Eddy-Current Bearing is expected to provide stable support in both the radial, angular, and axial directions simultaneously without any feedback control. This follows from the capability of the Magnetic River to fully support and guide itself along a rail without feedback control. Also, since the Magnetic River is essentially a linear induction motor, it has both motoring, braking and electricity generating capabilities (refs. 7, 8). The Eddy-Current Bearing is also basically an induction motor which can be expected to have those same capabilities.

Load Capacity

The load carrying capacity per unit weight of both DC-electromagnetic and AC-electromagnetic suspensions depend on size. DC-suspensions are more efficient the smaller they are while AC-suspensions are more efficient the larger they are (ref. 15). For vehicle size suspensions, levitation gaps of over 10 inches are possible with the Magnetic River whereas controlled DC-magnet suspensions are limited to less than 1 inch airgap (ref. 16). The effect on bearing derivatives of these suspensions is not known. However, the large difference in levitation gaps indicates a potential for improved load capacity of the Eddy-Current bearing which warrants further investigation.

Emergency Shutdown

The operating principle of the Eddy-Current bearing is such that it may be possible to continue operation after a power failure long enough to ensure safe shutdown without the need for catcher bearings. In principle, this can be done by switching to battery operated DC-power direct to the magnets. The operating principle would then change to so-called electrodynamic levitation with the eddy-currents induced by the motion of the rotor surface past a row of DC-electromagnets. This principle is used in eddy-current brakes (ref. 17) and in high-speed vehicles with superconducting magnet suspensions (ref. 18). Inherent stability is retained and the airgap is so small that a good possibility exists for generating sufficient lift with acceptable coil currents for a short time interval. The eddy-current drag will automatically decelerate the rotor and, eventually, metal contact will occur at low speed.

It is emphasized that no Eddy-Current Bearing yet exists and the capabilities suggested here remain speculation. A prototype of the bearing is currently under construction and a preliminary test program is scheduled for the summer of 1986 to determine whether further investigation is justified. A patent disclosure has been submitted and a patent search is underway.

CONCLUDING REMARKS

A new type of magnetic bearing, called the Eddy-Current Bearing, has been introduced. It derives from a magnetic vehicle-suspension called the Magnetic River. An extensive literature survey on the Magnetic River has suggested that the Eddy-Current bearing will have a number of important advantages over existing magnetic bearings. A research program is underway to determine the extent of these advantages.

REFERENCES

1. "Foucault and Eddy Currents put to Service," The Engineer, Vol. 114, Oct. 18, 1912, pp. 414 and 420-421.

2. Anschutz-Kaempfe, H., "On Gyroscopic Apparatus," U.S. Patent 1589039, 1923.

3. Orkress, E. C., et al., "Electromagnetic Levitation of Solids and Molten Metals," J. Phys., Vol. 23, No. 12, 1952, p. 1413.

4. Hochhausler, P., "The Magnetic Railroad," ETZ-B, Vol. 23, No. 13, 1971, pp. 311-313. (In German)

5. Jayawant, B. V., "Electromagnetic Levitation and Suspension Techniques," Edward Arnold, London, 1981.

6. Jayawant, B. V., "Electromagnetic Suspension and Levitation," IEE Proc., Vol. 129, Pt. A, No. 8, 1982, pp. 549-581.

7. Eastham, J. F., and Laithwaite, E. R., "Linear Induction Motors as Electromagnetic Rivers," Proc. IEE, Vol. 121, No. 10, 1974, pp. 1099-1108.

8. Laithwaite, E. R., "Three-Dimensional Engineering," Laithwaite, E. R. (Editor): "Transport Without Wheels," Elek Books, London, 1977, pp. 279-303.

9. Eastham, J. F., "The Magnetic River," SRC Advanced Ground Transportation Panel Meeting, London, U.K., Feb. 1978.

10. Rodger, D., and Eastham, J. F., "Dynamic Behavior of Linear Induction Machines in the Heave Mode," IEEE Trans. Vehic. Tech., Vol. VT-31, No. 2, May 1982, pp. 100-106.

11. Rajanathan, C. B., "Study of Xi-Core Transverse-Flux Plate Levitator," IEE Proc., Vol. 127, Pt. B, No. 3, May 1980, pp. 183-189.

12. Rajanathan, C. B., et al., "Finite Element Analysis of the Xi-Core Levitator," IEE Proc., Vol. 131, Pt. A, No. 1, Jan. 1984, pp. 62-66.

13. Bolton, H., "An Electromagnetic Bearing," IEE Conf. Publ. No. 120, Conf. on Linear Electric Machines, London, Oct. 1974, pp. 45-50.

14. Robinson, A. A., "Magnetically Suspended Momentum Wheel for Satellite Stabilization," IEE Conf. Publ. No. 142, 2nd Conf. Adv. Mag. Mater. & Appl., London, Sept. 1976, pp. 131-134.

15. Laithwaite, E. R., "Magnetic or Electromagnetic? The Great Divide," Electronics & Power, Vol. 19, No. 14, Aug. 1973, pp. 310-312.

16. Laithwaite, E. R., "Four Legs are Better than Two," Electrical Review, Vol. 202, No. 18, May 1978, pp. 30-31.

17. Singh, A., "Theory of Eddy-Current Brakes with Thick Rotating Disc," Proc. IEE, Vol. 124, No. 4, Apr. 1977, pp. 373-376.

18. Rhodes, R. G., and Mulhall, B. E., "Magnetic Levitation for Rail Transport," Oxford University Press, New York, 1981.

C-6

ORIGINAL PAGE IS OF POOR QUALITY

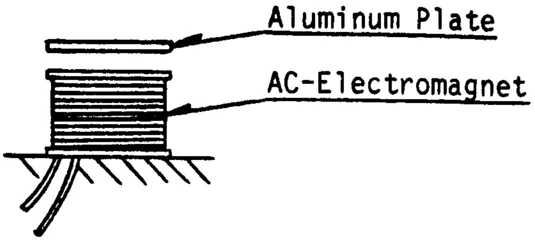
Aluminum Plate
AC-Electromagnet

Figure 1. Electromagnetic Levitation

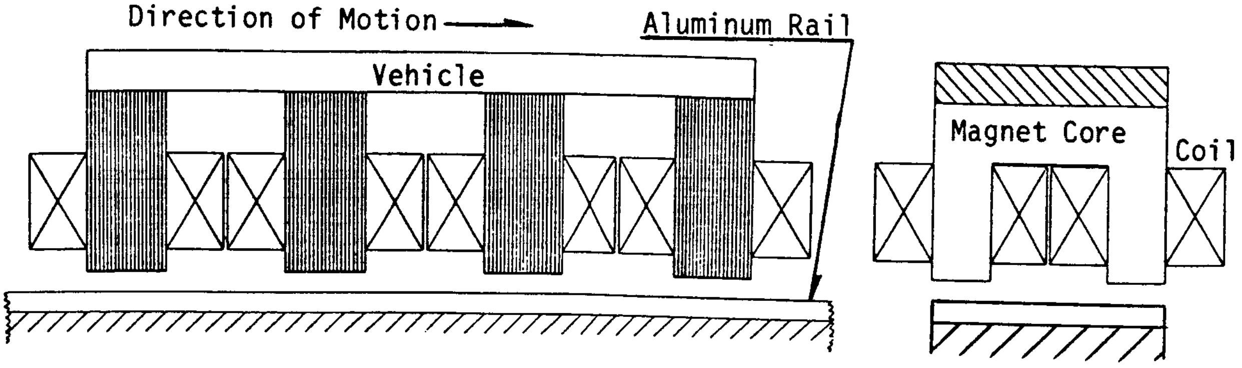
Direction of Motion
Aluminum Rail
Vehicle
Magnet Core
Coil

Figure 2. The Magnetic River Suspension (Schematic)

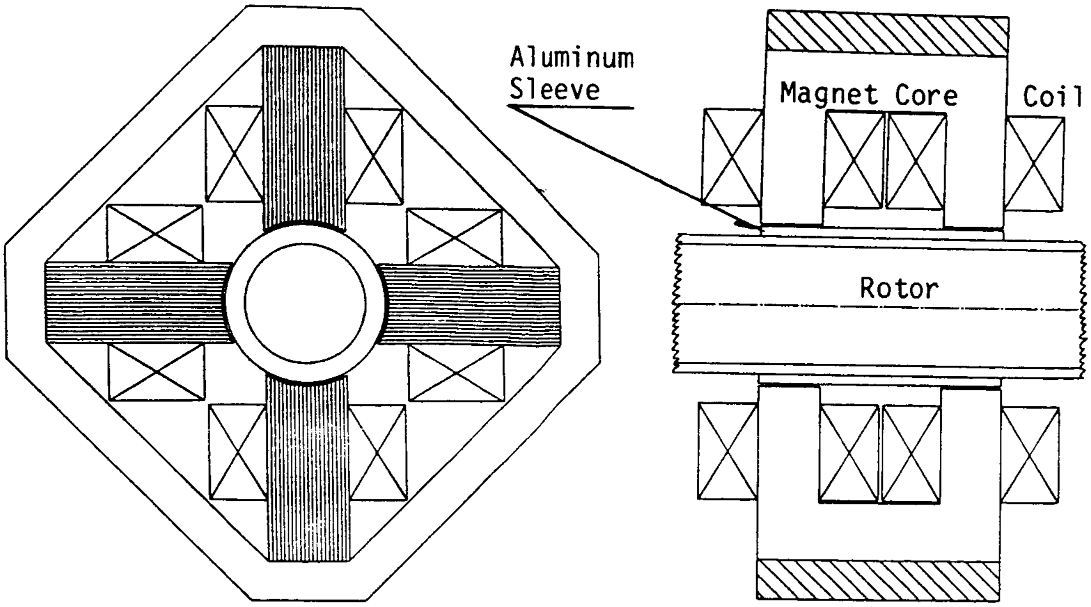
Aluminum Sleeve
Magnet Core
Coil
Rotor

Figure 3. The Eddy-Current Bearing (Schematic)

ADDITIONAL BIBLIOGRAPHY FOR MAGNETIC BEARINGS

1. Eisenhaure, D.B.; and Kingsbury, E.P.: Final Report on the Development of an Advanced Flywheel Bearing Performance Model. Sandia Laboratories. SAND79-7003, 1979.

2. Eusepi, M.; Martin, L.; and Ray, A.: Application of Magnetic Suspensions and Fluid Film Bearings to Energy Storage Flywheels. Sandia Laboratories. SAND79-7007, 1979.

3. Groom, Nelson J.; Woolley, Charles T.; and Joshi, Suresh M.: Analysis and Simulation of a Magnetic Bearing Suspension System for a Laboratory Model Annular Momentum Control Device. NASA TP-1799, 1981.

4. Henrikson, Carl H.; Lyman, Joseph; and Studer, Philip A.: Magnetically Suspended Momentum Wheels for Spacecraft Stabilization. Aerospace Sciences Conference, AIAA, 1974.

5. Kirk, James A.; Studer, Philip A.; and Evans, Harold E.: Mechanical Capacitor. NASA TN-D-8185, 1976.

6. Studer, Philip A.: Magnetic Bearings for Instruments in the Space Environment. NASA TM-78048, 1978.

7. Studer, Philip A.; and Gasser, Max G.: A Bi-directional Linear Motor/Generator With Integral Magnetic Bearings for Long Lifetime Stirling Cycle Refrigerators. First Biannual Conference on Refrigeration for Cryogenic Sensors, National Bureau of Standards (NBS) (Boulder, Colorado), Oct. 1980.

8. Wilson, Meredith; and Studer, Philip A.: Linear Magnetic Bearings. Proceedings of the Fifth International Workshop on Rare Earth-Cobalt Permanent Magnets and Their Applications (Roanoke, Virginia), Paper No. V-4, June 1981.

N87-22224

ORIGINS OF HYDRODYNAMIC FORCES ON CENTRIFUGAL PUMP IMPELLERS

Douglas R. Adkins* and Christopher E. Brennen
California Institute of Technology
Pasadena, California 91125

Hydrodynamic interactions that occur between a centrifugal pump impeller and a volute are experimentally and theoretically investigated. The theoretical analysis considers the inability of the blades to perfectly guide the flow through the impeller, and also includes a quasi-one dimensional treatment of the flow in the volute. The disturbance at the impeller discharge and the resulting forces are determined by the theoretical model. The model is then extended to obtain the hydrodynamic force perturbations that are caused by the impeller whirling eccentrically in the volute. Under many operating conditions, these force perturbations were found to be destablizing. Comparisons are made between the theoretical model and the experimental measurements of pressure distributions and radial forces on the impeller. The theoretical model yields fairly accurate predictions of the radial forces caused by the flow through the impeller. However, it was found that the pressure acting on the front shroud of the impeller has a substantial effect on the destablizing hydrodynamic forces.

NOMENCLATURE

b	width of impeller discharge
h	total head $(h^* = 2h/\rho\Omega^2 R_2^2)$
j	$\sqrt{-1}$
$\underset{\sim}{k}$	impeller phase coefficient = $\cos(\tan\gamma \ln(R)) + j\sin(\tan\gamma \ln(R))$
r,θ	polar coordinate system
s	length in tangential direction
t	time
v	relative velocity in impeller
w	width in volute
x,y,z	rectangular coordinate system

---

* Now at Sandia National Laboratories, Albuquerque, NM 87185

$\overline{A},\overline{rA},\overline{rrA}$	moments of volute cross-sectional area (defined in Equations 14a-e)
$\overline{\ln rA},\overline{r\ln rA}$	
A_{ij}	$(i = x,y\ ,\ j = x,y)$ components of generalized hydrodynamic force matrix [A] $(A^*_{ij} = A_{ij}/\rho\pi b\Omega^2 R_2^3)$
C_{ij}	$(i = x,y\ ,\ j = x,y)$ components of damping force matrix [C] $(C^*_{ij} = C_{ij}/\rho\pi b\Omega R_2^2)$
D_p	pressure coefficient at volute inlet = $2(P_v(R_2',\theta') - h_1)/\rho\Omega^2 R_2^2$
F	force acting on impeller $(F^* = F/\rho\pi b\Omega^2 R_2^3)$
F(t)	integration constant in Bernoulli's equation
J_{ij}	$(i = x,y\ ,\ j = x,y)$ coefficients of the jerk force matrix [J] $(J^*_{ij} = J_{ij}/\rho\pi b R_2^2/\Omega)$
K_{ij}	$(i = x,y\ ,\ j = x,y)$ components of stiffness force matrix [K] $(K^*_{ij} = K_{ij}/\rho\pi b\Omega^2 R_2^2)$
M_{ij}	$(i = x,y\ ,\ j = x,y)$ components of inertia force matrix [M] $(M^*_{ij} = M_{ij}/\rho\pi b R_2^2)$
P_i	pressure in impeller $(P_i^* = 2P_i/\rho\Omega^2 R_2^2)$
P_v	pressure in volute $(P_v^* = 2P_v/\rho\Omega^2 R_2^2)$
R	impeller radius (with no subscript, $R = R_2/R_1$)
R_t	radius of pressure tap ring
V	velocity in volute (with no subscript, $V^* = V_{\theta},/\Omega R_2$)
W_i	width of impeller at R_2 $(W_i^* = W_i/b)$
β	perturbation function for impeller flow
ζ	angular location of the impeller center $(= \omega t = \text{constant})$
γ	angle of flow path through impeller
ε	distance between impeller and volute centers $(\varepsilon^* = \varepsilon/R_2)$
ρ	fluid density
ϕ	flow coefficient = flowrate through pump/$2\pi b\Omega R_2^2$
ψ	total head rise coefficient = $(h\alpha - h_1)/\rho\,\Omega^2 R_2^2$
ω	orbit speed of impeller center (whirl speed)

Ω	rotational speed of impeller (shaft speed)

Subscripts:

c,s	cos ωt and sin ωt components (non-dimensionalized)
d	downstream of pump
exp	experimental result
m	force component due to momentum exchange
p	force component due to pressure
r,θ	radial or angular component
x,y	components in rectangular directions (real = x and imaginary = y)
1,2	impeller inlet and discharge

Superscripts:

$'$	measurement made in volute reference frame
$''$	measurement made from frame fixed to rotating impeller
$*$	non-dimensionalized quantity

Special Notation:

$\underset{\sim}{V}$	underbar denotes vector quantity
$\overline{V}$	overbar denotes centered impeller value (non-dimensionalized)
[A]	square brackets denote a matrix quantity
$\dot{x}$	dot represents a time derivative

INTRODUCTION

Several sources, both dynamic and hydrodynamic have been identified as contributing to the forces on centrifugal pump impellers. Figure 1 shows a typical configuration for a centrifugal pump with a few of the key components identified. The primary emphasis of this study was to investigate the forces that result from the hydrodynamic interaction between the impeller and the volute. The usual design criterion for a volute is that it should provide minimum interference to the symmetric impeller discharge flow that would occur if no volute was present. However, the discharge flow pattern will depend upon the overall flowrate through the impeller. Once the flowrate changes, the discharge conditions around the impeller become asymmetric for any given volute. Even at the volute design flowrate, the discharge conditions could still become asymmetric if the impeller is displaced from the "design" center of the volute by shaft deflection, bearing wear, etc.. In either case, the end result of the asymmetric discharge conditions is that there will be a net radial force on the impeller (see Figure 1).

It is customary in rotordynamic analyses to linearize the radial forces acting on the rotor in terms of a steady portion acting on the centered impeller, and a time dependent part due to the impeller whirling in a small circular orbit. Referring to Figure 1, these terms may be expressed as

$$\begin{Bmatrix} F_x^* \\ F_y^* \end{Bmatrix} = \begin{Bmatrix} \bar{F}_x \\ \bar{F}_y \end{Bmatrix} + \begin{bmatrix} A_{xx}^* & A_{xy}^* \\ A_{yx}^* & A_{yy}^* \end{bmatrix} \begin{Bmatrix} \varepsilon^* \cos \omega t \\ \varepsilon^* \sin \omega t \end{Bmatrix} \tag{1}$$

where $\bar{F}_x$ and $\bar{F}_y$ result from the interaction of the centered impeller with the volute, and the matrix [A] relates the perturbed force to the eccentric position of the impeller. The [A] matrix will be a function of the whirl speed, ω, and is often expressed as a quadratic in ω so that the system resembles a simple stiffness, damping, and mass model.

The steady or mean forces, $\bar{F}_x$ and $\bar{F}_y$, have been examined in several studies and an understanding of them has been greatly enhanced through papers by Iversen et al. [9], Csanady [7], and Agostinelli et al. [2] to name a few. All of these authors have shown that there is a particular flowrate where forces on the impeller will be minimized for a given volute. Previous experimental [5,10] and theoretical [6] investigations have also shown that the components of [A] are such that a whirling motion of the impeller would be encouraged rather than dissipated by the hydrodynamic effects. This has created concern that the rotor assembly may whirl at one of its critical speeds even though the shaft may be rotating well above this speed. There also exists the problem of the alternating flexural stress that would be developed if the impeller whirls at a subsynchronous speed (see Ehrich and Childs [8]).

In the current study, a theoretical model of the volute and impeller flows will be developed and compared to experimental results. Previously, a potential flow model for the steady forces on a centered impeller was given by [7] and this work was later extended by [6] to include the effects of the impeller whirling within the volute. Although the potential flow model presents a more classical approach of solving for the forces, problems arise in relating the two dimensional theoretical volute profile to the three dimensional geometry of a real volute. For this reason, a bulk flow description of the flow through the volute is chosen for the current work. A similiar treatment of the volute flow was presented by [9], but the influence of this flow on the impeller discharge conditions was largely ignored and only the non-whirling impeller was considered. The impeller/volute interaction will be included along with the effects of impeller whirl in the present analysis.

THEORETICAL ANALYSIS

In developing the theoretical model, the problem is broken into its two natural parts; models are constructed for the flow through the impeller and in the volute. The equations that are generated in these two parts are then combined by matching the pressures and velocities at the impeller discharge to those at the volute inlet. A full development of this model can be found in reference [1] and only brief summary will be presented here.

Governing Equations for the Impeller

Figure 2 illustrates the geometries used in developing the impeller model. To relate the pressure between the inlet and discharge of the impeller, a simplified unsteady form of Bernoulli's Equation is written as

$$\frac{P_i}{\rho} + \frac{v^2}{2} - \frac{\Omega^2 r''^2}{2} + \int_{s''} \frac{\partial v}{\partial t}\, ds'' - \omega^2 \varepsilon \int_{s''} \cos(\omega t - \Omega t - \theta'')\, dr'' - \omega^2 \varepsilon \int_{s''} \sin(\omega t - \Omega t - \theta'')\, r'' d\,\theta'' = F(t) \qquad (2)$$

Here the flow is assumed to be two dimensional and the impeller whirl speed constant.

To simplify the model, certain assumptions must be made about the velocity field within the impeller. Specifically, the flow in the impeller is assumed to follow a spiral path with inclination angle, γ, which is fixed relative to the impeller for a given flowrate and head rise so that

$$\theta_2'' = \theta'' + \tan\gamma \ln(r''/R_2) \qquad (3)$$

Here (r'',θ'') and (R_2,θ_2'') are the coordinates of a general point on a streamline within the impeller and at the position of discharge respectively. The flow path angle, γ, of the streamlines is permitted to deviate from the impeller blade angle. It is determined in a manner described in Section 2(c) so that the theoretical and experimental head/flowrate characteristics coincide. To account for the asymmetry caused by the volute, a circumferential perturbation is superimposed on this impeller flow. This flow perturbation is assumed to be stationary in the volute reference frame. Together, these observations require that

$$v = (v_{r''}^2 + v_{\theta''}^2)^{1/2} = \phi\, \Omega\, R_2^2\, \beta(\theta'', r'', \Omega t, \omega t, \varepsilon) \sec\gamma / r'' \qquad (4)$$

The perturbation function β, must from continuity considerations be constant along a streamline. For whirl motions with small eccentric orbits, β may be linearized as

$$\beta(\theta'', r'', \Omega t, \omega t, \varepsilon) = \bar{\beta}(\theta_2) + \varepsilon^* \{\beta_c(\theta_2)\cos\omega t + \beta_s(\theta_2)\sin\omega t\} \qquad (5)$$

Equations (4) and (5) can now be substituted into Equation (2). The pressure at the impeller discharge is then given as a function of β and the inlet pressure. The pressure is not known at the inlet of the impeller, but it can be written in terms of the inlet total head which is assumed to be circumferentially constant. If there is no pre-swirl at the inlet, this will give the inlet pressure as

$$\begin{aligned} P_i^*(R_1,\theta_1) \cong h_1^* &- \phi R \bar{\beta}(\theta_2)\{\phi R \bar{\beta}(\theta_2) + 2\varepsilon^* \frac{\omega}{\Omega}\sin(\theta_1 - \omega t)\} \\ &- 2\varepsilon^* \phi^2 R^2 \bar{\beta}(\theta_2)\{\beta_c(\theta_2)\cos\omega t + \beta_s(\theta_2)\sin\omega t\} \end{aligned} \tag{6}$$

for small eccentric displacements. By utilizing Equations (4) through (6) and neglecting terms of order ε^2 and higher, Bernoulli's Equation can now be separated into harmonics with steady, $\varepsilon\cos\omega t$, and $\varepsilon\sin\omega t$ dependence as

$$\phi\sec^2\gamma[2\ln(R)\frac{d\bar{\beta}}{d\theta_2} + \phi\bar{\beta}^2] + \bar{D}_p - 1 = 0 \tag{7a}$$

$$\begin{aligned} &2\phi\sec^2\gamma[\ln(R)\frac{d\beta_c}{d\theta_2} + \phi\bar{\beta}\beta_c + \frac{\omega}{\Omega}\ln(R)\beta_s] + D_{pc} - \sin\theta_2\frac{d\bar{D}_p}{d\theta_2} \\ &+ 2\frac{\omega}{\Omega}[\phi R\bar{\beta}\sin(\theta_2 + \tan\gamma\ln(R)) - \cos(\theta_2 + \tan\gamma\ln(R))/R] \\ &- 2\frac{\omega^2}{\Omega^2}[\cos\theta_2 - \cos(\theta_2 + \tan\gamma\ln(R))/R]/\tan^2\gamma = 0 \end{aligned} \tag{7b}$$

$$\begin{aligned} &2\phi\sec^2\gamma[\ln(R)\frac{d\beta_s}{d\theta_2} + \phi\bar{\beta}\beta_s - \frac{\omega}{\Omega}\ln(R)\beta_c] + D_{ps} + \cos\theta_2\frac{d\bar{D}_p}{d\theta_2} \\ &- 2\frac{\omega}{\Omega}[\phi R\bar{\beta}\cos(\theta_2 + \tan\gamma\ln(R)) + \sin(\theta_2 + \tan\gamma\ln(R))/R] \\ &- 2\frac{\omega^2}{\Omega^2}[\sin\theta_2 - \sin(\theta_2 + \tan\gamma\ln(R))/R]/\tan^2\gamma = 0 \end{aligned} \tag{7c}$$

where

$$D_p(\theta') = \bar{D}_p(\theta') + \varepsilon^*[D_{pc}(\theta')\cos\omega t + D_{ps}(\theta')\sin\omega t] \tag{8}$$

In Equations (7a-c) the impeller discharge pressure coefficient, $D_p(\theta')$, has been transformed into the impeller reference frame by the approximation, $\theta_2 = \theta' + \varepsilon^*\sin(\theta' - \omega t)$. This will prove convenient in the future, because the pressure at the impeller discharge is assumed to be equal to that at the volute inlet.

Governing Equations for the Volute

The geometries used in developing the volute model are shown in Figure 3. The volute flow will be described by a continuity equation, a moment of momentum equation, and an equation of motion in the radial direction. Each of these three equations can be written respectively as

$$\frac{\partial (wV_{\theta'})}{\partial \theta'} + \frac{\partial (wr'V_{r'})}{\partial r'} = 0 \tag{9}$$

$$\frac{\partial (wr'V_{\theta'}V_{\theta'})}{\partial \theta'} + \frac{\partial (wr'r'V_{\theta'}V_{r'})}{\partial r'} + wr'r' \frac{\partial V_{\theta'}}{\partial t} = -\frac{wr'}{\rho}\frac{\partial P_v}{\partial \theta'} \tag{10}$$

and

$$\frac{\partial P_v}{\partial r'} = \frac{\rho V_{\theta'}V_{\theta'}}{r'} \tag{11}$$

Here it has been estimated that $V_{r'}$ and $V_{z'}$ (and their gradients) are much less than $V_{\theta'}$, except at the inlet of the volute.

Within the volute, the flow is considered to be primarily in the θ' direction and to have a flat velocity profile. This will allow Equations (9), (10), and (11) to be integrated over the volute cross-section. When these equations are combined with Equations (4) and (5), the pressure and velocity distributions in the volute will be given in terms of moments of the volute cross-sectional area and the perturbation function, β. Both Equations (9) and (10) can then be separated into three parts (steady, $\varepsilon \cos \omega t$, and $\varepsilon \sin \omega t$) as follows:

Continuity:

$$\frac{d(\bar{V}\bar{A})}{d\theta'} = \phi\bar{\beta} \tag{12a}$$

$$\frac{d(V_c\bar{A})}{d\theta'} = W_i^* \frac{d(\bar{V}\cos\theta')}{d\theta'} + \frac{\omega}{\Omega}\sin\theta' + \phi[\beta_c + \frac{d(\bar{\beta}\sin\theta')}{d\theta'}] \tag{12b}$$

$$\frac{d(V_s\bar{A})}{d\theta'} = W_i^* \frac{d(\bar{V}\sin\theta')}{d\theta'} - \frac{\omega}{\Omega}\cos\theta' + \phi[\beta_s - \frac{d(\bar{\beta}\cos\theta')}{d\theta'}] \tag{12c}$$

Moment of momentum:

$$\frac{\overline{rA}}{2}\frac{d\overline{D_p}}{d\theta'} = -\frac{d(\overline{rA}\,\bar{V}^2)}{d\theta'} - \overline{r\ln rA}\,\frac{d(\bar{V}^2)}{d\theta'} + \phi(1 - \phi\tan\gamma\,\bar{\beta})\bar{\beta} \tag{13a}$$

$$\frac{\overline{rA}}{2}\frac{dD_{pc}}{d\theta'} = -2\frac{d(\overline{rA}\,\overline{V}\,V_c)}{d\theta'} + \frac{\omega}{\Omega}(W_i^*\sin\theta'\overline{V} - \overline{rrA}\,V_s)$$

$$+ (W_i^* + \overline{rA})\frac{d(\overline{V}^2\cos\theta')}{d\theta'} - 2\overline{rlnrA}\frac{d(\overline{V}\,V_c)}{d\theta'}$$

$$+ \phi^2\sin\theta'\overline{\beta}^2 + \phi\cos\theta'(\frac{\omega}{\Omega} + 2 - 2\phi\tan\gamma\,\overline{\beta})\overline{\beta}$$

$$+ \phi(1 - 2\phi\tan\gamma\,\overline{\beta})(\beta_c + \sin\theta'\frac{d\overline{\beta}}{d\theta'}) + \frac{W_i^*}{2}\cos\theta'\frac{d\overline{D_p}}{d\theta'} \qquad (13b)$$

$$\frac{\overline{rA}}{2}\frac{dD_{ps}}{d\theta'} = -2\frac{d(\overline{rA}\,\overline{V}\,V_s)}{d\theta'} - \frac{\omega}{\Omega}(W_i^*\cos\theta'\overline{V} - \overline{rrA}\,V_c)$$

$$+ (W_i^* + \overline{rA})\frac{d(\overline{V}^2\sin\theta')}{d\theta'} - 2\overline{rlnrA}\frac{d(\overline{V}\,V_s)}{d\theta'}$$

$$- \phi^2\cos\theta'\overline{\beta}^2 + \phi\sin\theta'(\frac{\omega}{\Omega} + 2 - 2\phi\tan\gamma\,\overline{\beta})\overline{\beta}$$

$$+ \phi(1 - 2\phi\tan\gamma\,\overline{\beta})(\beta_s - \cos\theta'\frac{d\overline{\beta}}{d\theta'}) + \frac{W_i^*}{2}\sin\theta'\frac{d\overline{D_p}}{d\theta'} \qquad (13c)$$

where

$$\overline{A}(\theta') = \int_{R_2}^{R_3'} wdr'/bR_2\ ,\ \overline{lnrA}(\theta') = \int_{R_2}^{R_3'} \ln(r'/R_2)wdr'/bR_2$$

$$\overline{rA}(\theta') = \int_{R_2}^{R_3'} r'wdr'/bR_2^2\ ,\ \overline{rrA}(\theta') = \int_{R_2}^{R_3'} r'r'wdr'/bR_2^3\ .$$

$$\overline{rlnrA}(\theta') = \int_{R_2}^{R_3'} r'\ln(r'/R_2)wdr'/bR_2^2 \qquad (14a\text{-}e)$$

and

$$V^*(\theta') = \overline{V}(\theta') + \varepsilon^*[V_c(\theta')\cos\omega t + V_s(\theta')\sin\omega t] \cong \frac{V_\theta'}{\Omega R_2} \qquad (15)$$

In Equations (12a-c) and (13a-c) the perturbation function, β, has been transformed into the volute reference frame for convenience in obtaining a solution.

To complete the basic equations for the volute problem, Equation (11) may be integrated to give the radial pressure variation in the volute as

$$P_v^* = \overline{D_p} + 2\overline{V}^2[\ln(r'/R_2) - \varepsilon^*\cos(\theta' - \omega t)] + \varepsilon^*[D_{pc} + 4\overline{V}V_c \ln(r'/R_2)]\cos\omega t$$
$$+ \varepsilon^*[D_{ps} + 4\overline{V}V_s \ln(r'/R_2)]\sin\omega t \qquad (16)$$

Closure Conditions

Equations (7), (12), (13), and (16) will describe the flow in the impeller and the volute after certain boundary conditions are satisfied. Even though β is referred to as the perturbation function, it was never assumed to be small. However, from the definition of the flow coefficient, β is required to have an average of one. The flow perturbation is further assumed to possess at least zeroth order continuity around the periphery of the impeller. This restriction on β can be met by satisfying the condition,

$$\beta(R_2,0) = \beta(R_2,2\pi) \qquad (17)$$

To account for what happens to the volute flow at the tongue, it is assumed that the average total head of the recirculated flow will be constant across the tongue, that is,

$$\int_{R_2'(0)}^{R_3'(0)} (P_v + \rho V_{\theta'}^2/2)\Big|_{\theta'=2\pi} w\,dr' = \int_{R_2'(0)}^{R_3'(0)} (P_v + \rho V_{\theta'}^2/2)\Big|_{\theta'=0} w\,dr' \qquad (18)$$

From the remaining flow that is discharged, the flow path angle, γ, will be determined. Previously it was stated that this angle will vary with flowrate and total head. Using this stipulation, γ can be found by equating the predicted and experimental total head rises across the pump. This requires that

$$\psi_{exp} = \overline{\psi} = [\overline{D_p}(2\pi) + C_v\overline{V}^2(2\pi)]/2 \qquad (19)$$

where

$$C_v = 1 + 2[\overline{\ln rA}(2\pi) - \overline{\ln rA}(0)]/[\overline{A}(2\pi) - \overline{A}(0)]$$

Admittedly, using an experimental result does limit the preliminary design applications of this model. However, the "H/Q" curve (in dimensionless form the function $\psi_{exp}(\phi)$) is normally available for any pump and it is important that this fundamental characteristic is properly represented in the model.

This completes the development of the equations necessary to obtain β, D_p, and V. The nine ordinary differential equations of (7), (12), and (13) were solved using centered differencing. The initial conditions of β, D_p, and V were chosen in an iterative manner to satisfy the closure conditions stated above.

Hydrodynamic Forces on the Impeller

Basically, there are two sources that contribute to the radial hydrodynamic forces on the impeller. One part is due to asymmetric pressure distribution around the impeller. The other is caused by the asymmetric momentum fluxes at the impeller inlet and discharge. The first contribution is evaluated by integrating the pressure around the inlet and discharge of the impeller:

$$\underset{\sim}{F}_p = (F_x + jF_y)_p = b\int_0^{2\pi} P_i(R_1,\theta_1)R_1 e^{j\theta_1} d\theta_1 - W_i\int_0^{2\pi} P_i(R_2,\theta_2)R_2 e^{j\theta_2} d\theta_2 \qquad (20)$$

where j denotes the imaginary part that corresponds to the y direction (see Figure 2). The second contribution is found by applying the momentum equation to obtain

$$\begin{aligned} \frac{\underset{\sim}{F}_m}{\rho b} = \frac{(F_x + jF_y)_m}{\rho b} &= - e^{j\Omega t}\frac{\partial}{\partial t} \int_0^{2\pi}\int_{R_1}^{R_2}(v_r'' + jv_\theta'')e^{j\theta''} r'' dr'' d\theta'' \\ &- e^{j\Omega t}\left[\int_0^{2\pi}(v_r'' + jv_\theta'')v_r'' e^{j\theta''} r'' d\theta''\right]\Big|_{R_1}^{R_2} \\ &- e^{j\Omega t}2\Omega\int_0^{2\pi}\int_{R_1}^{R_2}(jv_r'' - v_\theta'')e^{j\theta''} r'' dr'' d\theta'' \\ &+ \omega^2\varepsilon\pi(R_2^2 - R_1^2)e^{j\omega t} \end{aligned} \qquad (21)$$

When the pressure distributions of Equations (6) and (7) and the velocity profiles described by the no inlet pre-swirl condition and Equations (3)-(5) are applied to Equations (20) and (21), the resulting force on the impeller is

$$\underset{\sim}{F}^* = \underset{\sim}{F}_p^* + \underset{\sim}{F}_m^* = \overline{\underset{\sim}{F}} + \varepsilon^*(\underset{\sim}{F}_c \cos\omega t + \underset{\sim}{F}_s \sin\omega t) \qquad (22)$$

where

$$\begin{aligned} \overline{\underset{\sim}{F}} = \phi^2[W_i^*\sec^2\gamma + \underset{\sim}{k} R - 2 + 2j\tan\gamma]&\int_0^{2\pi}\overline{\beta}^2(\theta_2)e^{j\theta_2} d\theta/2\pi \\ - j\phi[W_i^*\sec^2\gamma \ln(R) + 1]&\int_0^{2\pi}\overline{\beta}(\theta_2)e^{j\theta_2} d\theta_2/\pi \end{aligned} \qquad (23a)$$

$$\begin{aligned} \underset{\sim}{F}_c = \phi^2[W_i^*\sec^2\gamma + \underset{\sim}{k} R - 2 + 2j\tan\gamma]&\int_0^{2\pi}\overline{\beta}(\theta_2)\beta_c(\theta_2)e^{j\theta_2} d\theta_2/\pi \\ - j\phi[W_i^*\sec^2\gamma \ln(R) + 1]&\int_0^{2\pi}\beta_c(\theta_2)e^{j\theta_2} d\theta_2/\pi \\ + \frac{\omega}{\Omega}\phi[W_i^*\sec^2\gamma \ln(R) + \underset{\sim}{k}/R - 1]&\int_0^{2\pi}\beta_s(\theta_2)e^{j\theta_2} d\theta_2/\pi \\ + \frac{\omega}{\Omega}[\phi R W_i^*&\int_0^{2\pi}\overline{\beta}(\theta_2)\sin(\theta_2 + \tan\gamma \ln(R))e^{j\theta_2} d\theta_2/\pi] \end{aligned}$$

$$- \frac{\omega}{\Omega}[2j\phi + W_i^*/(\underset{\sim}{k}\, R)] - \frac{\omega^2}{\Omega^2}\{W_i^*[1 - 1/(\underset{\sim}{k}\, R)]/\tan^2\gamma - 1 + 1/R^2\} \qquad (23b)$$

$$\begin{aligned} \underset{\sim}{F}_s = {} & \phi^2 [W_i^* \sec^2\gamma + \underset{\sim}{k}\, R - 2 + 2j \tan\gamma] \int_0^{2\pi} \bar{\beta}(\theta_2)\beta_s(\theta_2) e^{j\theta_2} d\theta_2/\pi \\ & - j\phi [W_i^* \sec^2\gamma \ln(R) + 1] \int_0^{2\pi} \beta_s(\theta_2) e^{j\theta_2} d\theta_2/\pi \\ & - \frac{\omega}{\Omega}\, \phi [W_i^* \sec^2\gamma \ln(R) + \underset{\sim}{k}/R - 1] \int_0^{2\pi} \beta_c(\theta_2) e^{j\theta_2} d\theta_2/\pi \\ & - \frac{\omega}{\Omega}\, [\phi\, R\, W_i^* \int_0^{2\pi} \bar{\beta}(\theta_2) \cos(\theta_2 + \tan\gamma \ln(R)) e^{j\theta_2} d\theta_2/\pi] \\ & - \frac{\omega}{\Omega}\, j[2j\phi + W_i^*/(\underset{\sim}{k}\, R)] - \frac{\omega^2}{\Omega^2} j\, \{W_i^*[1 - 1/(\underset{\sim}{k}\, R)]/\tan^2\gamma - 1 + 1/R^2\} \qquad (23c) \end{aligned}$$

and, $\underset{\sim}{k} = \cos(\tan\gamma \ln(R)) + j \sin(\tan\gamma \ln(R))$. Expressed in the terms used in Equation (1), these components are

$$\bar{\underset{\sim}{F}} = \bar{F}_x + j\bar{F}_y\ , \quad \underset{\sim}{F}_c = A_{xx}^* + jA_{yx}^*\ , \quad \text{and} \quad \underset{\sim}{F}_s = A_{xy}^* + jA_{yy}^* \qquad (24a\text{-}c)$$

Presentation of the calculated results will be postponed so that the experimental and theoretical results can be discussed together.

TEST FACILITY

The experimental results presented in this paper were obtained using the Rotor Force Test Facility at the California Institute of Technology, Pasadena. Details of the equipment have been given in previous papers [3,4,10], so only a brief description will be presented here. Figure 4 shows the test section where the centrifugal pump being examined is located. The impeller is mounted on the internal balance and the entire assembly is turned by the main shaft. The main shaft passes through an eccentrically drilled cylinder, which when rotated, causes the impeller to whirl in a 0.0990 inch diameter circular orbit. Forces on the impeller are sensed through strain gauges on four posts located in the internal balance. The relationships between the strains and forces were found by static calibration tests.

Descriptions of the impeller and one of the volutes that were tested are given in Figures 5 and 6. The impeller (referred to as Impeller X) is a five bladed cast bronze impeller with a specific speed of 0.57 and blade angle of 65°. The 86° spiral volute (Volute A) is constructed of fiberglass and designed to be "well matched" with Impeller X at a flow coefficient of 0.092. The dimensions of the volute cross-sections, shown in Figure 6, were used in evaluating the integrals of Equations (14a-e).

Two modifications have been made on the test facility for the benefit of this research. They were considered necessary in order isolate the interaction between the impeller and the volute from external influences. The modifications are illustrated in Figure 7. To separate the flow in the volute from the annular gap region, rings were installed 0.005 inch from the edge of the impeller. In addition, the flange of the test section was removed so that the front shroud of the impeller was exposed to the "reservoir-like" conditions of the test chamber (see Figure 4).

The removal of the front flange of the test section was judged to be essential after pressure measurements were made in the annual gap region with the flange in place and the rings removed. The measurements indicated that the fluid trapped in this region was responsible for a hydrodynamic stiffness (see Equation (26)) given approximately by

$$\begin{bmatrix} K_{xx} & K_{xy} \\ K_{yx} & K_{yy} \end{bmatrix} = \begin{bmatrix} -1.6 & 0.3 \\ -0.3 & -1.6 \end{bmatrix}$$

When compared with Chamieh's [5] direct measurements of the total hydrodynamic stiffness on the impeller (annular gap plus volute) given approximately by

$$\begin{bmatrix} K_{xx} & K_{xy} \\ K_{yx} & k_{yy} \end{bmatrix} = \begin{bmatrix} -2.0 & 0.9 \\ -0.9 & -2.0 \end{bmatrix}$$

it is seen that the contribution from the annular gap is significant. With the flange removed, it was anticipated that the fluid forces on the front shroud of the impeller would be largely eliminated.

COMPARISONS BETWEEN EXPERIMENTAL AND THEORETICAL RESULTS

A preliminary step in the theoretical calculations must be the estimation of the impeller flow path angle, γ (see Section 2(a)). In practice, information on the actual total head rise as a function of flowrate is almost always available; an example for Impeller X and Volute A is presented in Fig.8. By setting $\overline{\psi}=\psi_{exp}$, the flow path angle, γ, shown in Fig.9 was obtained. Note that the typical magnitude of γ is about 80° while the blade angle of Impeller X is 65°.

Measurements of the static pressure of the discharge from the impeller were made using holes drilled at the inlet to the volute (see Figures 6 and 7). The circumferential pressure distributions are compared with the theoretical results in Figures 10 and 11. The pressure taps were alternately placed in the front and back of the volute, resulting in the slight oscillation of the data. The results were obtained for a range of shaft speeds from $\Omega = 800$ to 1200 RPM, but the non-dimensionalized pressures were found to be independent of the speed. Figure 10 shows that the theory gives a good approximation of the the pressure distributions over a moderate range of flow coefficients. For flow coefficients larger than this range, the correlation begins to falter as shown in Figure 11. It was concluded that the deviation was caused by the inadequacy of a one dimensional treatment of the flow near the tongue of the volute. At the higher flowrates, it has been suggested [11] that there is a reversal of the direction of flow in the region just inside the tongue. The effect on the pressure distribution of displacing the impeller is also demonstrated in Figure 11. The model appears to follow the changes that occur, even when the absolute pressure predictions are rather poor.

A comparison between the experimental and theoretical steady forces on the impeller is given in Figure 12. One set of experimental results was obtained by placing the impeller in four equally spaced orbit positions and then averaging the internal balance force measurements. The second set (for $\phi = 0.06$ and 0.10) was obtained by integration of the discharge pressure measurements. The theoretical model tends to overpredict the steady or average radial forces somewhat, but it does give reasonable results considering the crudeness of the model. Colding-Jorgensen's [6] steady force calculations for a 67.5° blade angle impeller in an 86° spiral volute are also shown in Figure 12. The present model appears to give a more accurate assessment of the steady forces when compared with the experimental results. The agreement between the two sets of experimental data indicates that the primary cause of the radial force is the asymmetric pressure distribution at the discharge of the impeller. Moreover, the theoretical model predicted that the discharge pressure was responsible for 99% of the total force on the impeller while the net momentum flux contribution was essentially negligible. It might also be of interest to note that over the entire range of flowrates for which theoretical results are presented, the predicted perturbation in the impeller discharge flow never exceeded 6% of the mean flow.

Figure 13 presents the components of the generalized hydrodynamic force matrix, [A], that result when the impeller whirls in an eccentric orbit at the pump design flowrate ($\phi = 0.092$). From the experimental data, it is seen that the cross-coupled terms (i.e. A_{xy}, A_{yx}) imply that forces act in the direction of the whirl orbit up to $\omega/\Omega = 0.10$. This destabilizing influence is predicted by the theoretical model to occur up to $\omega/\Omega = 0.14$. Due to the coupled nature of Equations (7b) and (7c), it was not possible to calculate [A] beyond the range of whirl ratios shown in Figure 13. This problem is believed to be the result of the current limitations of the iterative technique used in obtaining the solution.

As was mentioned in the introduction, it is a standard practice to express the matrix elements of [A] in powers of ω. By examining the A_{yx} term in Figure 13, it is apparent that a quadratic in ω will not adequately describe the features of the matrix element. A cubic, however, can approximate all of the [A] matrix element variations with ω giving the coefficients of such an expansion as

$$\begin{bmatrix} A_{xx} & A_{xy} \\ A_{yx} & A_{yy} \end{bmatrix} = \begin{bmatrix} -K_{xx} - \omega C_{xy} + \omega^2 M_{xx} + \omega^3 J_{xy} & -K_{xy} + \omega C_{xx} + \omega^2 M_{xy} - \omega^3 J_{xx} \\ -K_{yx} - \omega C_{yy} + \omega^2 M_{yx} + \omega^3 J_{yy} & -K_{yy} + \omega C_{yx} + \omega^2 M_{yy} - \omega^3 J_{yx} \end{bmatrix} \tag{25}$$

or alternatively as

$$[A(\omega/\Omega)] \begin{Bmatrix} x \\ y \end{Bmatrix} = -[K] \begin{Bmatrix} x \\ y \end{Bmatrix} - [C] \begin{Bmatrix} \dot{x} \\ \dot{y} \end{Bmatrix} - [M] \begin{Bmatrix} \ddot{x} \\ \ddot{y} \end{Bmatrix} - [J] \begin{Bmatrix} \dddot{x} \\ \dddot{y} \end{Bmatrix} \tag{26}$$

where

$$x = \varepsilon \cos \omega t \text{ and } y = \varepsilon \sin \omega t$$

The [K], [C], and [M] matrices correspond to the stiffness, damping, and inertial components that are commonly employed in rotordynamics. Since the [J] matrix is related to the third order time derivative of the impeller displacement (which is conventionally known as the jerk), it will be referred to as the "jerk" matrix.

The resulting [K] matrix elements of the cubic expansion are given in Figure 14, and the [C], [M], and [J] matrix elements are presented in Figure 15. Included in Figure 14 are the stiffnesses that were calculated using the force measurements (from the internal balance and the pressure distributions) taken at four impeller positions. Also shown in Figure 14 are the stiffnesses predicted by Colding-Jorgensen [6] for an 86° spiral volute. With the exception of the K_{yx} term, the current model does a fair job of describing the variation of stiffness with flowrate. The magnitudes, however, tend to be underpredicted by the theory. Over most of the range of flow coefficients, the stiffness is such that it would encourage the whirling motion of the impeller. The same is also true of the damping when the flowrate drops below $\phi = 0.07$ as shown in Figure 15. The magnitude of the damping components computed by [6] (not shown here) were less than 10% of those predicted by the present model. In general, the inertial force would discourage an orbital motion of the impeller, but it will tend to drive the impeller in the direction of the displacement. The jerk force attains significant values only at the lower flow coefficients.

CLOSING COMMENTS

A theoretical model has been developed to describe the flow in the impeller and the volute, along with the interactions that occur between them. This investigation was undertaken to provide a better understanding of the destabilizing hydrodynamic forces that have been observed [5,10] on a whirling centrifugal pump impeller. To implement the model requires only a knowledge of the dimensions of the volute and impeller, and the total head rise across the entire pump. Comparisons between the predicted and experimental results are encouraging. Experimentation with different volute geometries and over a wider range of operating conditions (flow coefficient and whirl ratio) would provide a more crucial test of the theoretical model. It might also prove insightfull to incorporate the effects of inducers and diffuser vanes into the theoretical model. These devices are now commonly employed on many high performance centrifugal pumps.

Previous experimental results [5,10] have tended to over-estimate the contribution of the volute/impeller interaction to the total stiffness force acting on the impeller. The over-estimation came about because of an asymmetric pressure distribution in the fluid trapped on the front shroud of the impeller. Since real pumps do have fluid in this region, it will be important in the future to perform a detailed study of this area.

ACKNOWLEDGEMENTS

This research was funded by NASA George Marshal Space Flight Center, Huntsville, Alabama under contract NAS 8-33108. Both of the authors would like to express their gratitude to A.J. Acosta and T.K. Caughey for their helpful advice, and R. Franz and N. Ardnt for their assistance with the experiments. One of the authors (D.R. Adkins) would also like to thank the Shell Companies Foundation for a fellowship that supported his graduate studies and Susan Berkley for her invaluable help in preparing this paper.

REFERENCES

1. Adkins, D.R., "Analyses of Hydrodynamic Forces on Centrifugal Pump Impellers", Ph.D. Thesis, Division of Engineering and Applied Sciences, California Institute of Technology, 1985.

2. Agostinelli, A., Nobles, D., and Mockridge, C.R., "An Experimental Investigation of Radial Thrust in Centrifugal Pumps", Trans. ASME, J. of Engr. for Power, Vol. 82, pp. 120-126, April 1960.

3. Brennen, C.E., Acosta, A.J., and Caughey, T.K., "A Test Program to Measure Fluid Mechanical Whirl-Excitation Forces in Centrifugal Pumps", First Workshop on Rotordynamic Instability Problems in High Performance Turbomachinery, Texas A&M University, NASA Conf. Pub. 2133, pp. 229-235, 1980.

4. Chamieh, D.S., "Forces On A Whirling Centrifugal Pump-Impeller", Ph.D. Thesis, Division of Engineering and Applied Sciences, California Institute of Technology, 1983.

5. Chamieh, D.S., Acosta, A.J., Brennen, C.E., Caughey, T.K., and Franz, R., "Experimental Measurements of Hydrodynamic Stiffness Matrices for a Centrifugal Pump Impeller", 2nd Workshop on Rotordynamic Instability Problems in High Performance Turbomachinery, Texas A&M University, NASA Conf. Pub. 2250, pp. 382-398, May 10-12, 1982.

6. Colding-Jorgensen, J., "The Effect of Fluid Forces on Rotor Stability of Centrifugal Compressors and Pumps", First Workshop on Rotordynamic Instability Problems in High Performance Turbomachinery, Texas A&M University, NASA Conf. Pub. 2133, pp. 249- 266, May 12-14, 1980.

7. Csanady, G.T., "Radial Forces in a Pump Caused by Volute Casing", Trans. ASME, J. of Engr. for Power, Vol. 84, pp. 337-340, October 1962.

8. Ehrich, F., and Childs, D., "Self-Excited Vibration in High Performance Turbomachinery", Mech. Engr., Vol. 106, No. 5, pp. 66-79, May 1984.

9. Iversen, H.W., Rolling, R.E., and Carlson, J.J., "Volute Pressure Distribution, Radial Force on the Impeller and Volute Mixing Losses of a Radial Flow Centrifugal Pump", Trans. ASME, J. of Engr. for Power, Vol. 82, pp. 136-144, April 1960.

10. Jery, B., Acosta, A.J., Brennen, C.E., and Caughey, T.K., "Hydrodynamic Impeller Stiffness, Damping and Inertia in the Rotordynamics of Centrifugal Flow Pumps", Rotordynamic Instability Problems in High Performance Turbomachinery, Texas A&M University, NASA Conf. Pub. 2338, pp. 137-160, May 28-30, 1984.

11. Lazarkiewicz, S., and Troskolanski, A.T., "Impeller Pumps", Pergamon Press, Translated by D.K. Rutter (Polish Ed. Title: Pompy Wirowe), 1965.

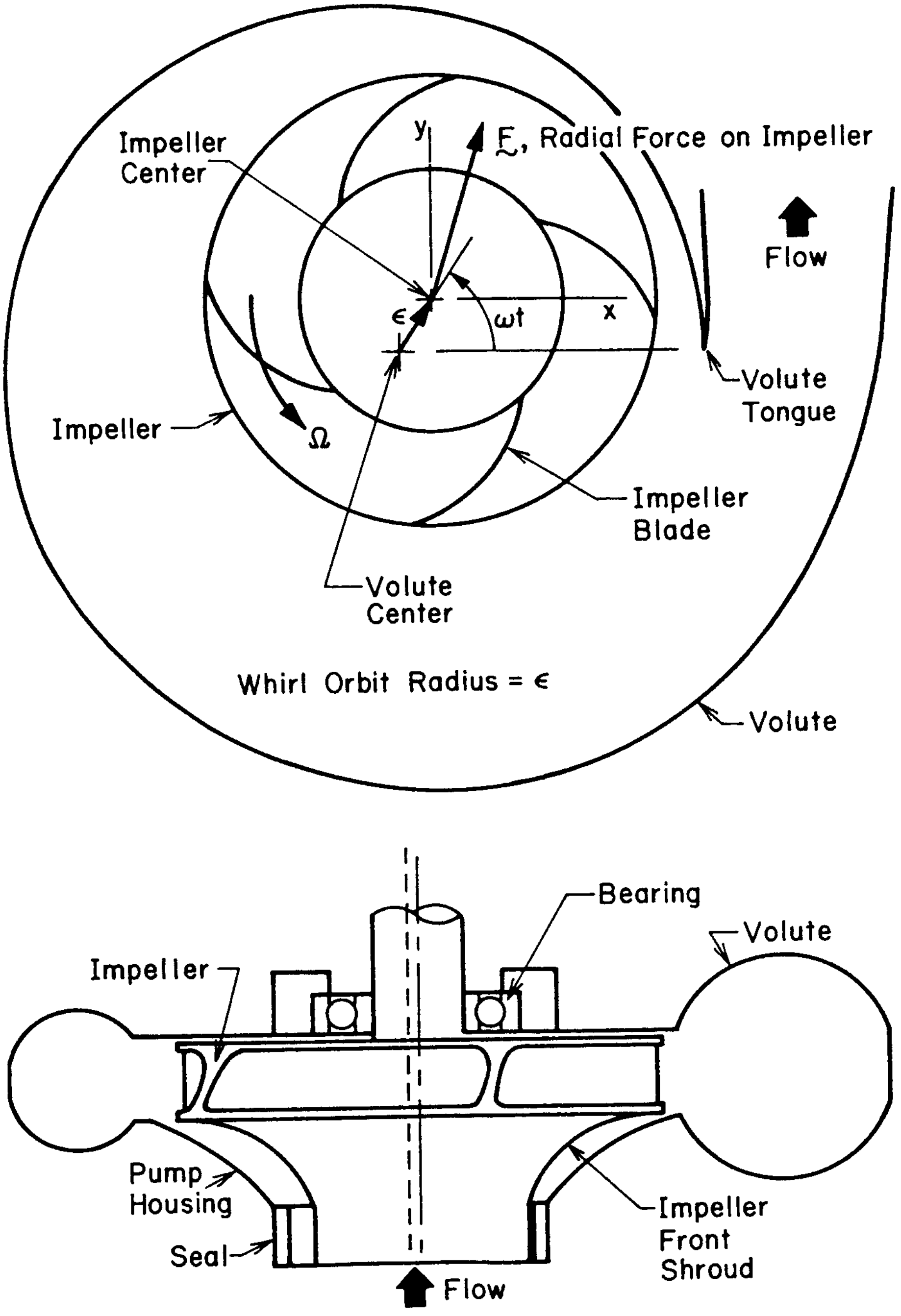
Impeller
Center
y
F, Radial Force on Impeller
Flow
ε
ωt
x
Volute
Tongue
Impeller
Ω
Impeller
Blade
Volute
Center
Whirl Orbit Radius = ε
Volute
Bearing
Volute
Impeller
Pump
Housing
Seal
Flow
Impeller
Front
Shroud

Figure 1. Description of a centrifugal pump.

ORIGINAL PAGE IS
OF POOR QUALITY

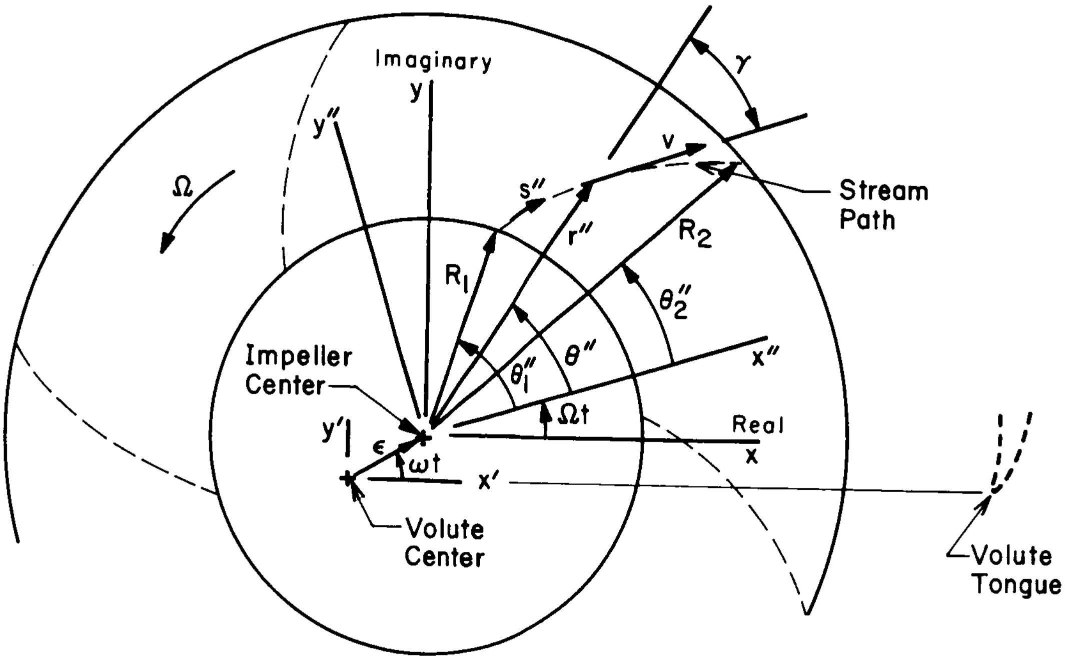
Imaginary
y
y″
Ω
γ
v
s″
Stream
Path
r″
R₂
R₁
θ₂″
Impeller
Center
θ₁″
θ″
x″
Ωt
Real
x
y′
ϵ
ωt
x′
Volute
Center
Volute
Tongue

Figure 2. Geometry of a centrifugal pump impeller.

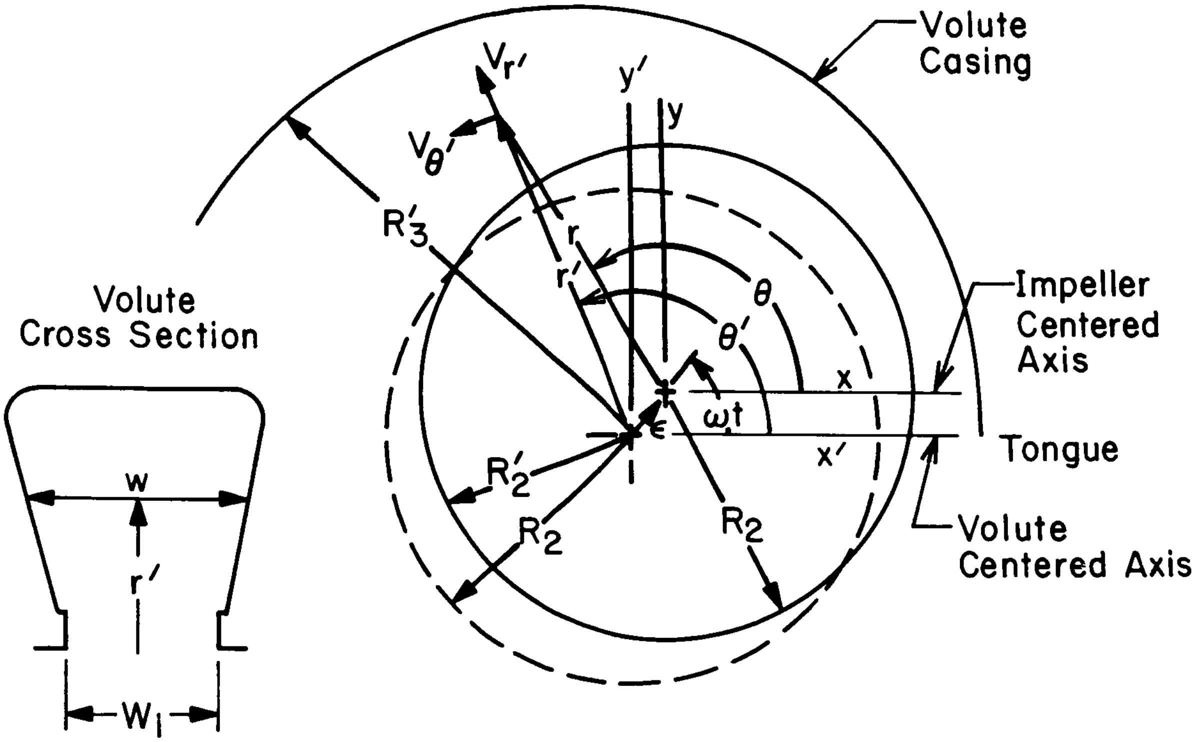
Volute
Casing
V_r′
y′
y
V_θ′
R₃′
r
r′
θ
θ′
Impeller
Centered
Axis
x
ωt
ϵ
x′
Tongue
R₂′
R₂
R₂
Volute
Centered Axis
Volute
Cross Section
w
r′
W₁

Figure 3. Geometry of a volute.

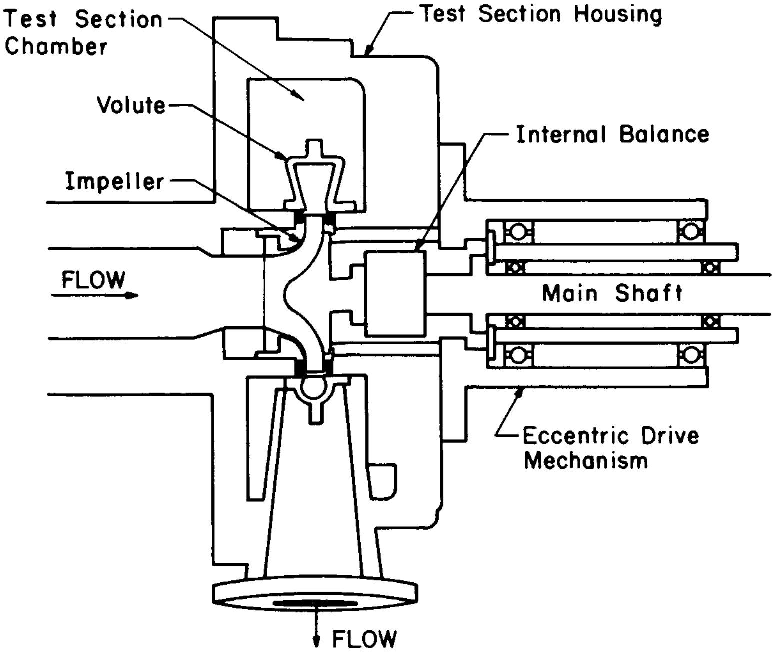
Test Section Chamber
Test Section Housing
Volute
Internal Balance
Impeller
FLOW
Main Shaft
Eccentric Drive Mechanism
FLOW

Figure 4. Schematic of the test section.

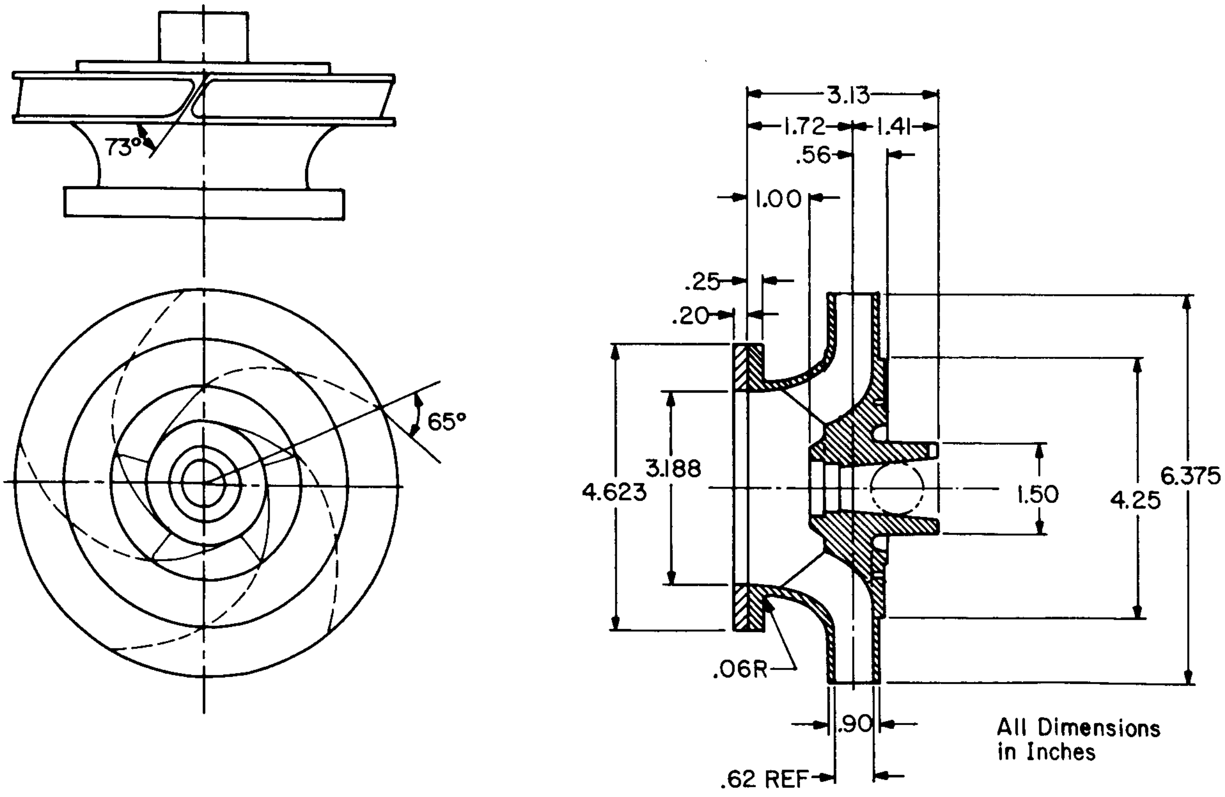
73°
65°
3.13
1.72
1.41
.56
1.00
.25
.20
4.623
3.188
1.50
4.25
6.375
.06R
.90
.62 REF
All Dimensions in Inches

Figure 5. Dimensions of Impeller X.

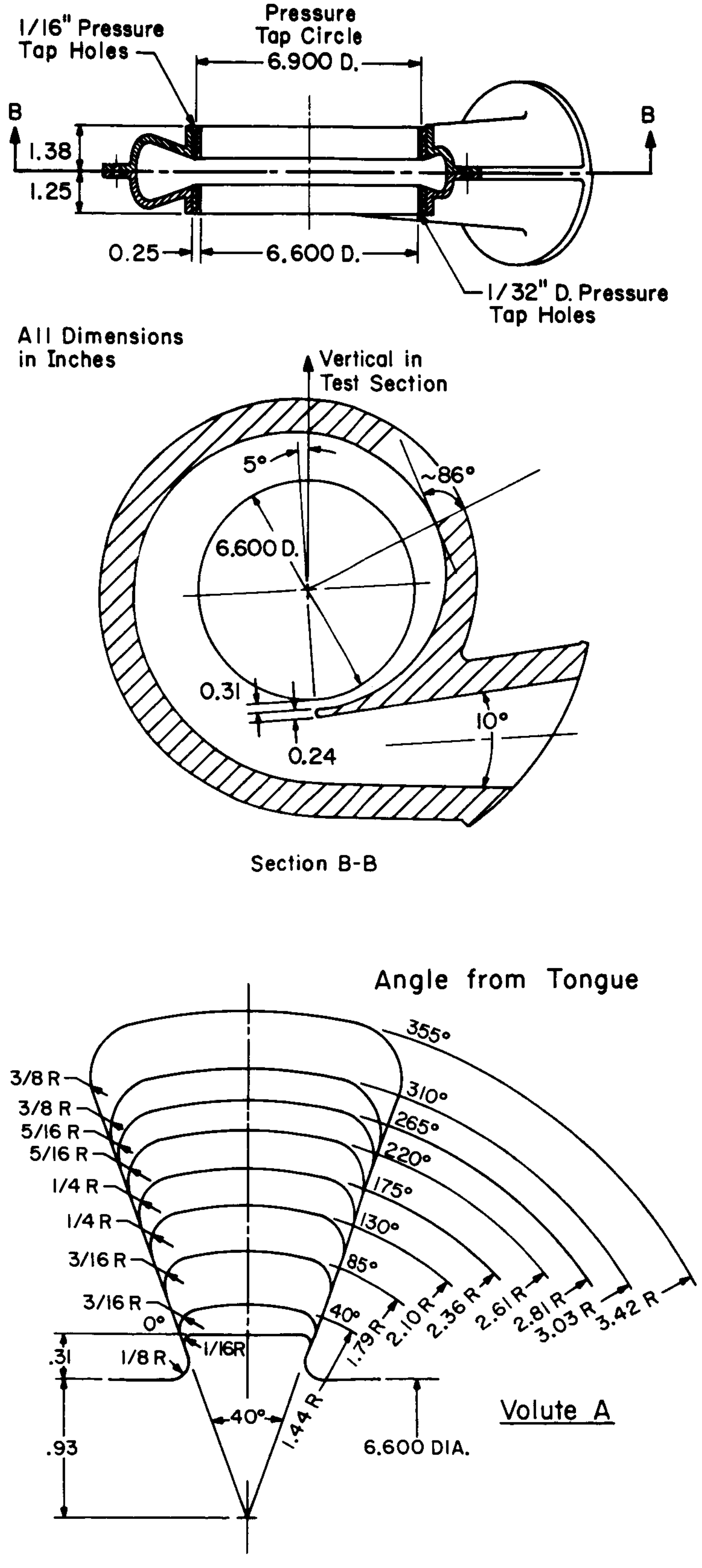
1/16" Pressure Tap Holes
Pressure Tap Circle
6.900 D.
B
B
1.38
1.25
0.25
6.600 D.
1/32" D. Pressure Tap Holes
All Dimensions in Inches
Vertical in Test Section
5°
~86°
6.600 D.
0.31
0.24
10°
Section B-B
Angle from Tongue
355°
310°
265°
220°
175°
130°
85°
40°
0°
3/8 R
3/8 R
5/16 R
5/16 R
1/4 R
1/4 R
3/16 R
3/16 R
1/16R
1/8 R
.31
.93
40°
1.44 R
1.79 R
2.10 R
2.36 R
2.61 R
2.81 R
3.03 R
3.42 R
6.600 DIA.
Volute A

Figure 6. Dimensions of Volute A.

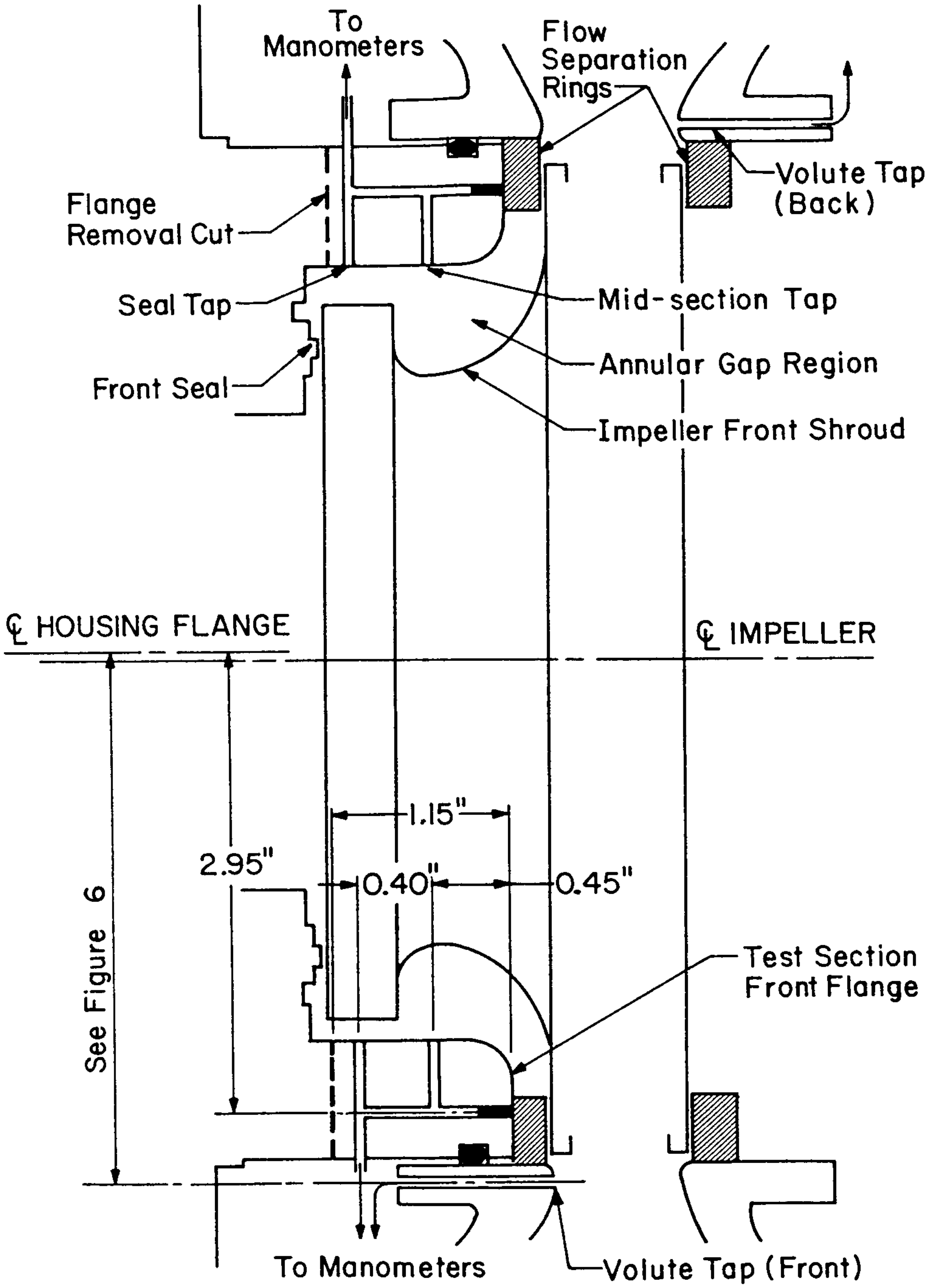
To Manometers
Flow Separation Rings
Volute Tap (Back)
Flange Removal Cut
Seal Tap
Mid-section Tap
Annular Gap Region
Front Seal
Impeller Front Shroud
℄ HOUSING FLANGE
℄ IMPELLER
1.15"
2.95"
0.40"
0.45"
See Figure 6
Test Section Front Flange
To Manometers
Volute Tap (Front)

Figure 7. Modifications of the test facility.

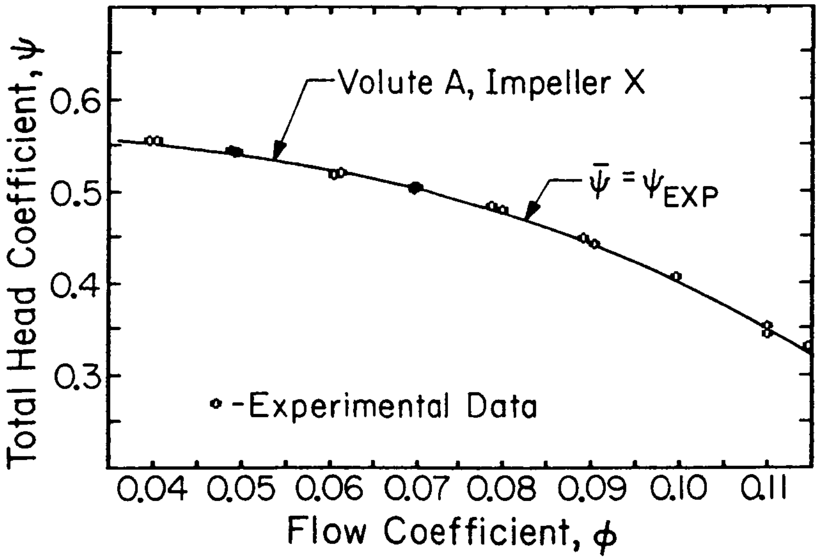

Figure 8. Total head coefficient vs. the flow coefficient for the Impeller X and Volute A pump. The solid line represents the average value of the experimental data.

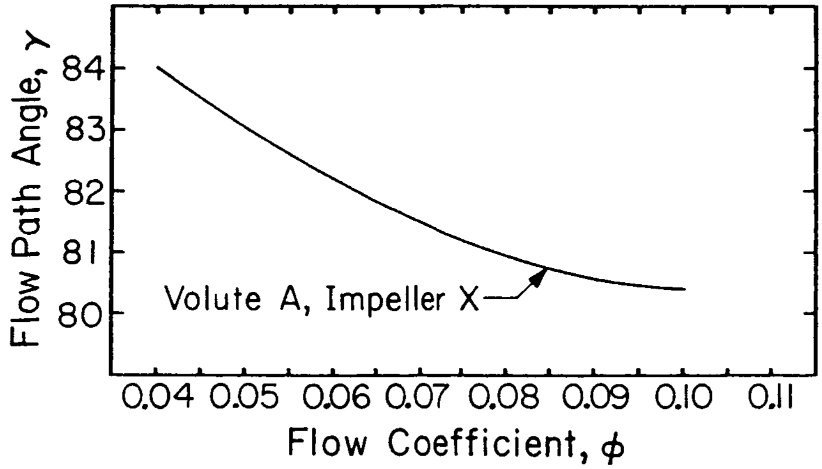

Figure 9. The average angle the flow follows through the pump (measured with respect to the radial line) as a function of flowrate.

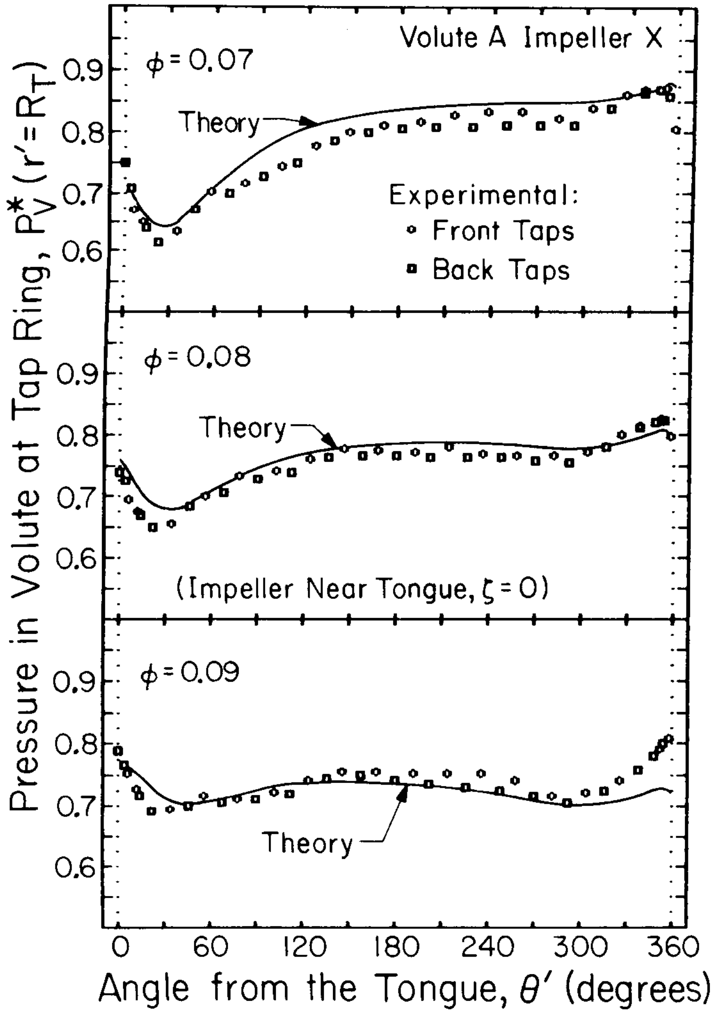

Figure 10. Experimental and theoretical pressure distributions at the inlet of the volute for three different flowrates with the impeller placed near the tongue. Measurements were taken with $\Omega = 1000$ RPM.

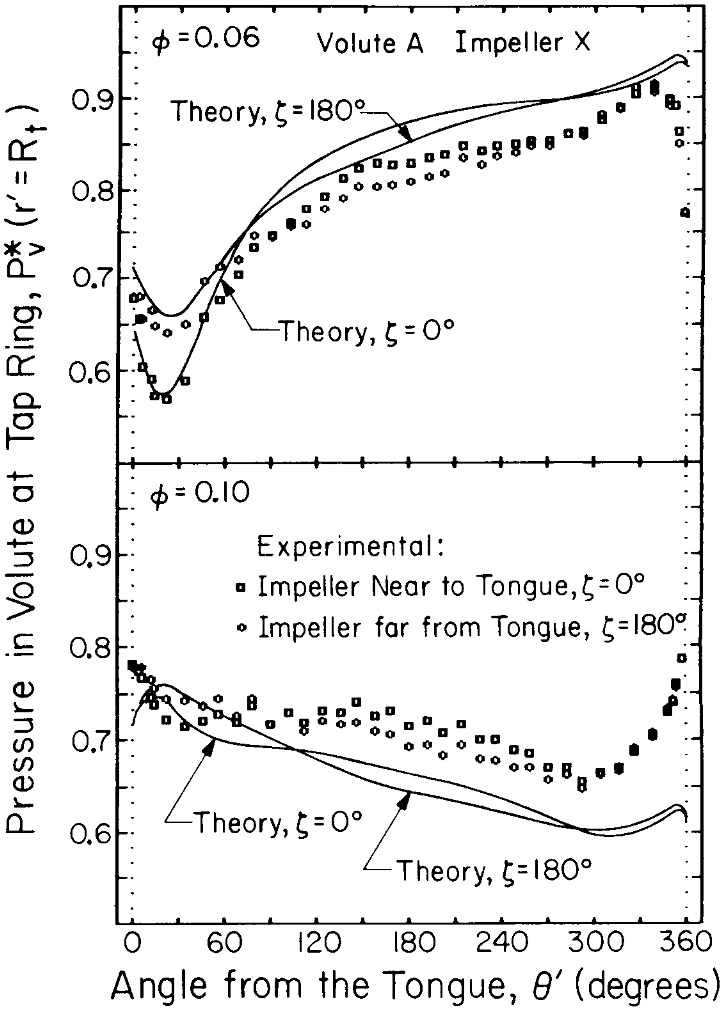

Figure 11. Experimental and theoretical pressure distributions at the inlet of the volute for two different flowrates with the impeller placed near to and far from the volute tongue.

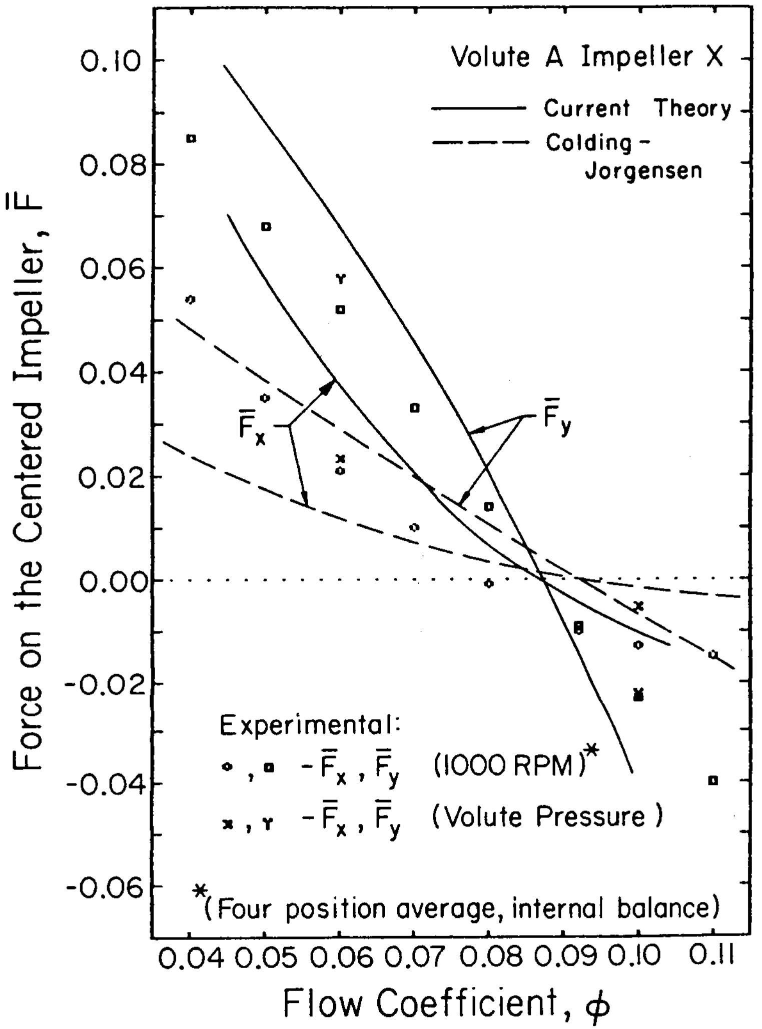

Figure 12. Steady hydrodynamic forces acting upon Impeller X as function of flowrate. Experimental forces were obtained by both internal balance and discharge pressure measurements. Colding-Jorgensen's [6] results are for an 86° spiral volute with a 67.5° blade angle impeller.

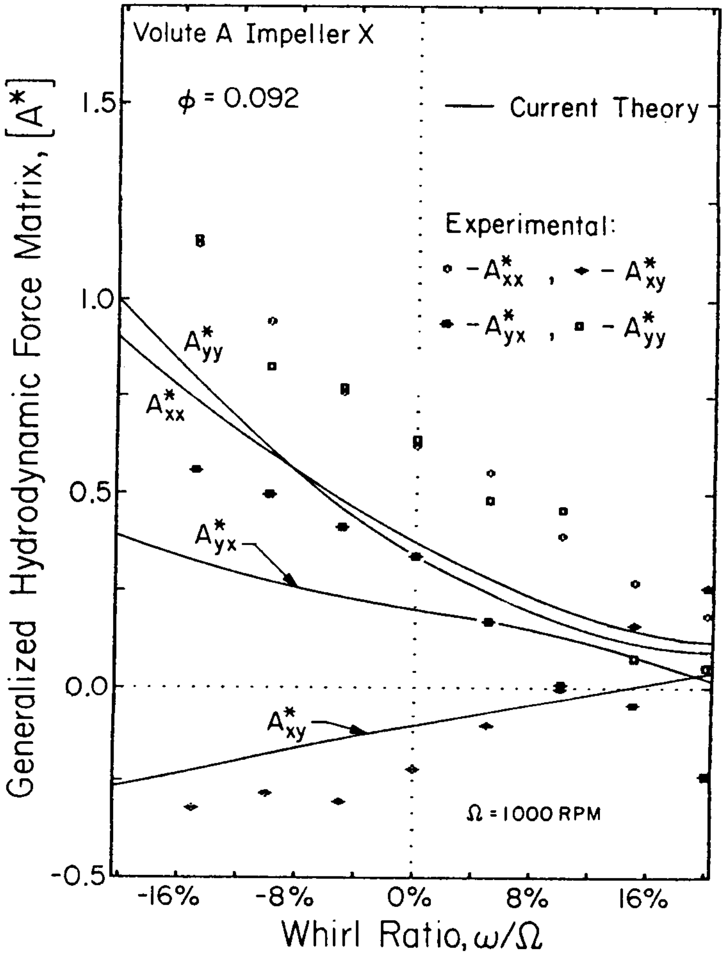

Figure 13. The Generalized Hydrodynamic Force coefficients as functions of whirl speed at the volute design flow coefficient ($\phi = 0.092$). The experimental results were obtained from the direct force measurements of the internal balance. The radius of the whirl orbit for Impeller X was $\epsilon = 0.0495$ inches.

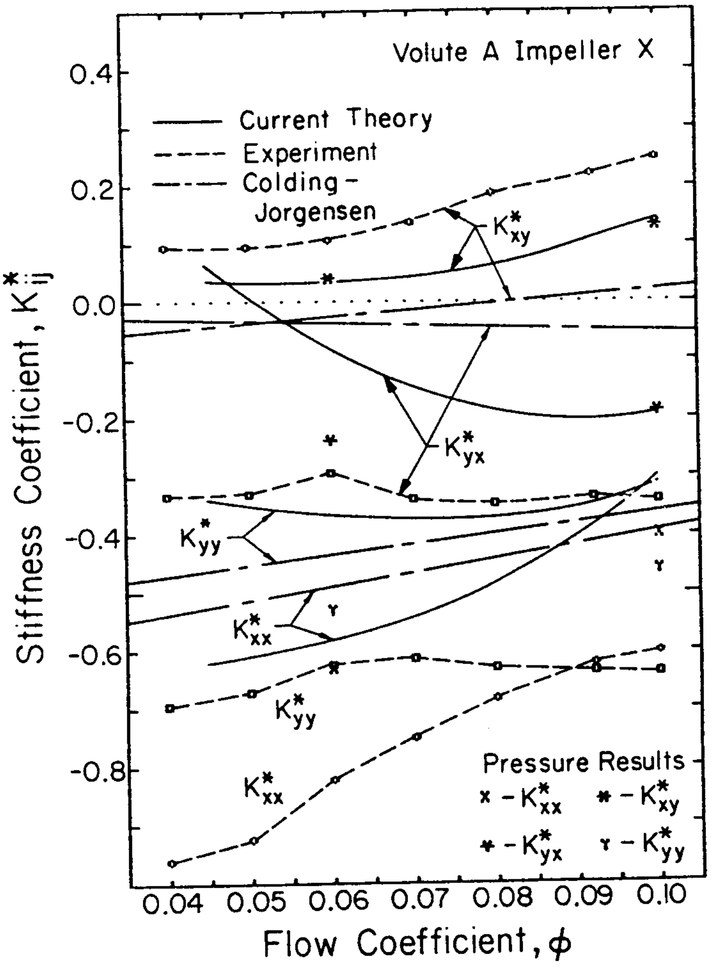

Figure 14. Hydrodynamic stiffnesses as functions of the flowrate. Experimental results are from internal balance and pressure measurements. Colding-Jorgensen's [6] results are for an 86° spiral volute with a 67.5° blade angle impeller.

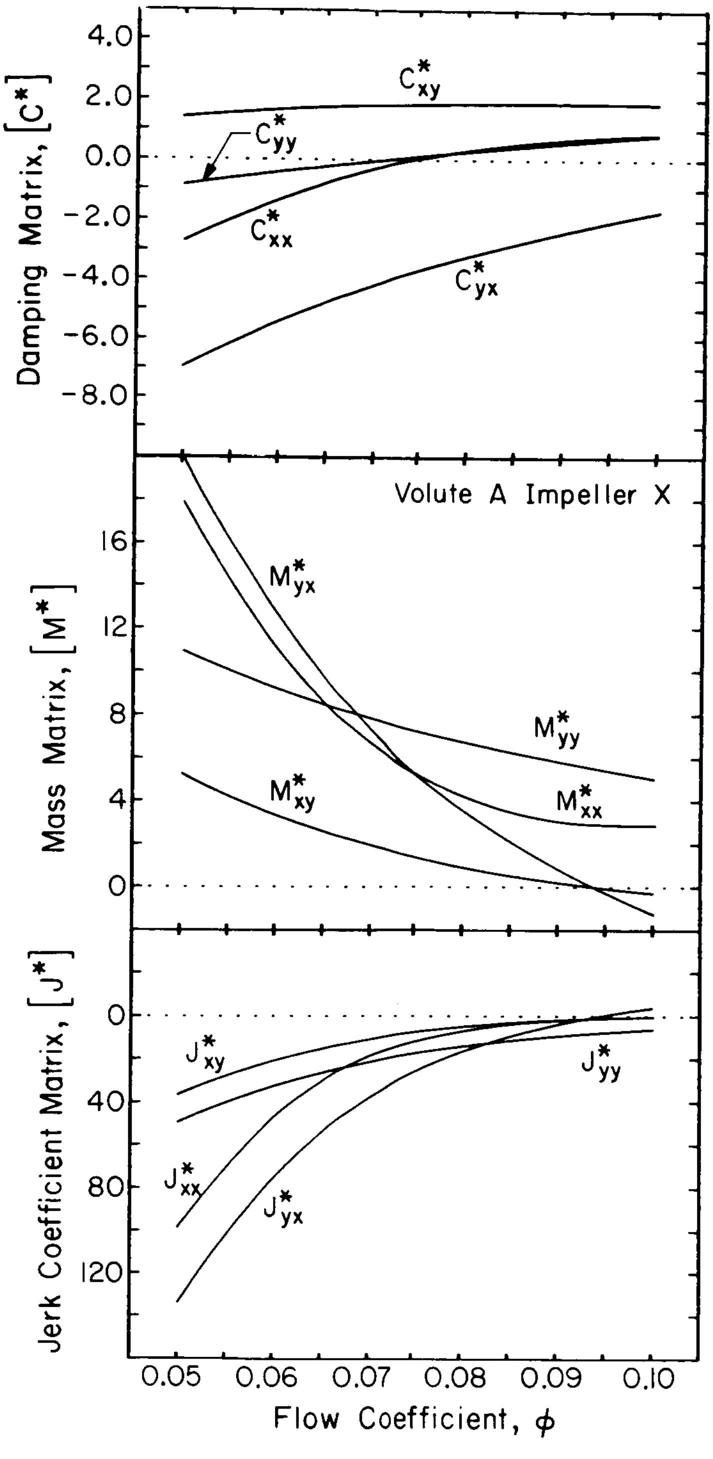

Figure 15. Damping, mass, and jerk force coefficients as functions of the flowrate as predicted by the current theoretical model.

N87-22225

ON THE EFFECT OF CAVITATION ON THE RADIAL FORCES AND HYDRODYNAMIC STIFFNESS OF A CENTRIFUGAL PUMP*

R.J. Franz, C.E. Brennen, A.J. Acosta, and T.K. Caughey
California Institute of Technology
Pasadena, California 91125

The asymmetric flow within a volute exerts a radial force on a centrifugal impeller. The present paper presents experimental measurements of the radial forces on the impeller in the presence of cavitation.

NOMENCLATURE

[A]	hydrodynamic force matrix, non-dimensionalized by $\rho\pi\omega^2 r_2^2 b_2$
A_1, A_2	impeller inlet area (πr_1^2), outlet area $(2\pi r_2 b_2)$
b_2	impeller discharge width (0.62 in)
{F}	6-component generalized force vector
F_1, F_2	components of the instantaneous lateral force on the impeller in the rotating dynamometer reference frame
F_x, F_y	components of the instantaneous lateral force on the impeller in the fixed laboratory reference frame (X,Y), non-dimensionalized by $\rho\pi\omega^2 r_2^3 b_2$
F_{ox}, F_{oy}	values of F_x and F_y if the impeller was located at the the origin of the (X,Y) coordinate system (volute center), non-dimensionalized by $\rho\pi\omega^2 r_2^3 b_2$

---

* The authors are indebted to the NASA George Marshall Space Flight Center, Alabama for continued sponsorship of this research under contract NAS8-33108. We are also grateful for the help given by D. Brennen.

PRECEDING PAGE BLANK NOT FILMED

F_N, F_T	components of the lateral force on the impeller normal to and tangential to the whirl orbit, averaged over the orbit, non-dimensionalized by $\rho\pi\omega^2 r_2^2 b_2 \varepsilon$ $F_N = (A_{xx} + A_{yy})/2 \quad F_T = (-A_{xy} + A_{yx})/2$
p_1, p_{t1}	upstream static, total pressure
p_2, p_{t2}	downstream static, total pressure
p_I	static pressure at impeller inlet, $p_{t1} - \rho(\frac{Q}{A_1})^2/2$
p_v	vapor pressure of water
Q	flow rate
r_1, r_2	impeller inlet, discharge radius (1.594 in., 3.188 in.)
t	time
(X,Y)	fixed laboratory reference frame
x,y	instantaneous coordinates of the impeller center in the fixed laboratory reference frame (X,Y), non-dimensionalized by r_2
ε	radius of the circular whirl orbit
θ	angle of the impeller on the eccentric circle, measured from the volute tongue in the direction of impeller rotation
ρ	density of water
σ	cavitation number, $\frac{p_I - p_v}{\rho\omega^2 r_1^2/2}$

ϕ	flow coefficient based on the impeller discharge area and tip speed, $\frac{Q}{\omega r_2 A_2}$
ψ	total head coefficient, $\frac{p_{t2}-p_{t1}}{\rho\omega^2 r_2^2}$
ω	radian frequency of the impeller (shaft) rotation

INTRODUCTION

Earlier papers (refs.1-8) have described measurements of the radial forces and hydrodynamically induced rotordynamic coefficients of centrifugal pumps with various impellers and volutes. All of these earlier measurements were made in the absence of any cavitation within the pump. Yet there is some evidence that the presence of cavitation may have a significant effect on these forces and coefficients. Indeed some tests of the high speed pumps in the Space Shuttle Main Engine have suggested a change in the rotordynamics when cavitation occurs (ref. 9). The present paper is a supplement to our earlier measurements of forces and coefficients and constitutes an exploration of the influence of cavitation.

The references 6-8 provide a complete description of the facility. Briefly, the dynamometer, composed of two parallel plates connected by four strain gaged posts, is mounted between the impeller and the drive shaft. It measures the six components of a generalized hydrodynamic force vector {F} acting on the impeller. The impeller can be subject to whirling motion in an orbit eccentric to the volute center, in addition to the normal impeller rotation. Since the eccentric motion is in the lateral plane, perpendicular to the impeller centerline, only the two components of the force vector {F} in this lateral plane will be discussed.

These forces can be represented by

$$\begin{Bmatrix} F_x \\ F_y \end{Bmatrix} = \begin{Bmatrix} F_{ox} \\ F_{oy} \end{Bmatrix} + [\ A\ ] \begin{Bmatrix} x \\ y \end{Bmatrix} \tag{1}$$

Refering to figure 1, F_x and F_y are in the volute frame of reference, and x and y represent the coordinates of the impeller center measured from the volute center. Dimensionless quantities are used throughout (see Nomenclature for definitions). The present results are only for the case of no whirl: x and y are fixed in time. When the impeller is located at an angular position, θ, on the circular whirl orbit of radius ε, equation (1) is written as

$$\begin{Bmatrix} F_x \\ F_y \end{Bmatrix} = \begin{Bmatrix} F_{ox} \\ F_{oy} \end{Bmatrix} + [\ A\ ] \begin{Bmatrix} \varepsilon/r_2 \cos\theta \\ \varepsilon/r_2 \sin\theta \end{Bmatrix} \tag{2}$$

The steady lateral forces, represented by F_x and F_y, can be considered as the sum of two forces: a fixed force, represented by F_{ox} and F_{oy}, which the impeller would experience if located at the volute center, and a force due to the eccentric displacement of the impeller, represented by a "stiffness" matrix [A]. By taking data at four fixed eccentric positions of the impeller, 90 degrees apart, the matrix [A] and the vector $\{F_o\}$ can be extracted. The gravitational and buoyancy forces on the rotor are subtracted out.

EXPERIMENTS

In references 6-8 results were presented for a typical impeller (impeller X), a five bladed Byron-Jackson centrifugal impeller with a specific speed of 0.57, operating in a spiral volute (volute A) at various impeller speeds ($\lesssim$ 2000 rpm) and flow rates. In order to test under cavitating conditions, the impeller speed was increased to 3000 rpm and the water was substantially de-aerated.

In the following pages the results for three different flow rates are presented: the flow rates chosen are below design (ϕ=0.060), design (ϕ=0.092) and above design (ϕ=0.104). Cavitation performance curves for each of these flow rates are presented in figure 2. We observe that the breakdown cavitation numbers for the three flow rates tested are 0.17, 0.26 and 0.30 respectively.

RESULTS

Results for the radial forces, F_{ox} and F_{oy}, and for the stiffness coefficients are presented in figures 3 through 8. A quick glance will show that large changes occur in both characteristics as the pump approaches and passes through breakdown. Notice that the steady force shown in figures 3 and 4 changes in both magnitude and direction.

Figures 3 and 4 show that for ϕ=0.060 the magnitude of $\{F_o\}$ decreases with performance loss with a small change in direction. For both ϕ=0.092 and ϕ=0.104, the magnitude of $\{F_o\}$ has a minimum with decreasing head coefficent. For each flow coefficient, the direction of $\{F_o\}$ rotates away from the tongue. For ϕ=0.092, $\{F_o\}$ rotates through more than 180° as the pump progresses through breakdown.

Figures 5-8 show the hydrodynamic force matrix [A] from equation (2). These no-whirl results corrrespond to -[K] of the quadratic fit of reference 2 to whirl data for mass, damping and stiffness matrices. The three flow coefficients exhibit the same trends. The diagonal elements decrease with performance loss. The off-diagonal elements first decrease slightly in magnitude with lower cavitation number then increase with performance loss. Figure 8 indicates that the off-diagonal elements do not change monotonically with head coefficient.

In summary, cavitation affects the steady forces, both the impeller-centered force $\{F_o\}$ and the hydrodynamic force matrix [A], exerted upon an eccentric impeller. It is useful to interprete the matrix [A] in terms of the average normal force, F_N, and the tangential force, F_T, acting on a whirling impeller in the limit as the whirl speed approaches zero. With cavitation breakdown, the normal force is reduced while the tangential force is increased. Further tests are planned to examine the unsteady flow effects which occur at non-zero whirl speed. More specifically, the frequency dependence in the matrix [A] (the damping and added mass components) will shortly be examined as a function of cavitation number.

REFERENCES

1. Agostinelli, A., Nobles, D., and Mockridge, C. R., "An Experimental Investigation of Radial Thrust in Centrifugal Pumps", ASME Journal of Engineering for Power, Vol. 82, pp. 120-126, April 1960.

2. Domm, H., and Hergt, P., "Radial Forces on Impeller of Volute Casing Pumps", Flow Research on Blading (L. S. Dzung, ed.), Elsevier Pub. Co., The Netherlands, pp 305-321, 1970.

3. Ohashi, H. and Shoji, H., "Lateral Fluid Forces Acting on a Whirling Centrifugal Impeller in Vaneless and Vaned Diffuser," Third Workshop on Rotordynamic Instability Problems in High-Performance Turbomachinery, Texas A&M University, May 28-30, 1984.

4. Chamieh, D. S., "Forces on a Whirling Centrifugal Pump-Impeller", Ph. D. Thesis, Division of Engineering and Applied Science, California Institute of Technology, February 1983.

5. Chamieh, D. S., Acosta, A. J., Brennen, C. E. and Caughey, T. K., "Experimental Measurements of Hydrodynamic Radial Forces and Stiffness Matrices for a Centrifugal Pump-Impeller," ASME Journal of Fluids Engineering, Vol. 107, Sept. 1985, pp. 307-315.

6. Jery, B., Acosta, A.J., Brennen, C.E., and Caughey, T.K., "Hydrodynamic Impeller Stiffness, Damping and Inertia in the Rotordynamics of Centrifugal Pumps," "Third Workshop on Rotordynamic Instability Problems in High Performance Turbomachinery", Texas A&M University, May 28-30,1984.

7. Jery, B., Brennen, C.E., Caughey, T.K., and Acosta, A.J., "Forces on Centrifugal Pump Impellers," "Second International Pump Symposium", Houston, Texas, April 29-May 2,1985.

8. Jery, B., "Experimental Study of Unsteady Hydrodynamic Force Matrices on Whirling Centrifugal Pump-Impellers", Ph. D. Thesis, Division of Engineering and Applied Science, California Institute of Technology, October 1985.

9. Rocketdyne Division, Rockwell, personal communication

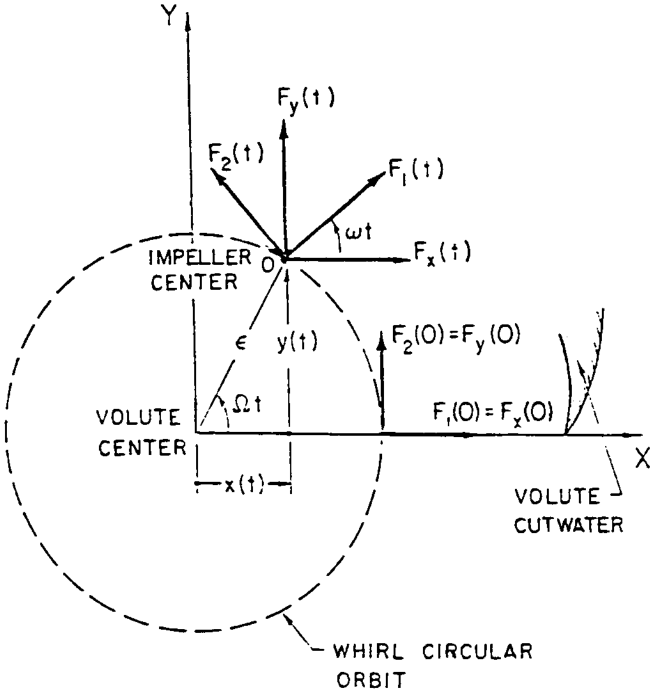
Y
$F_y(t)$
$F_2(t)$
$F_1(t)$
ωt
$F_x(t)$
IMPELLER CENTER
O
ϵ
y(t)
$F_2(O)=F_y(O)$
Ωt
VOLUTE CENTER
$F_1(O)=F_x(O)$
X
x(t)
VOLUTE CUTWATER
WHIRL CIRCULAR ORBIT

Figure 1 Schematic representation of the position of the impeller within the volute. The measured forces are indicated in the rotating dynamometer frame (as F_1, F_2) and in the stationary volute frame (as F_x, F_y).

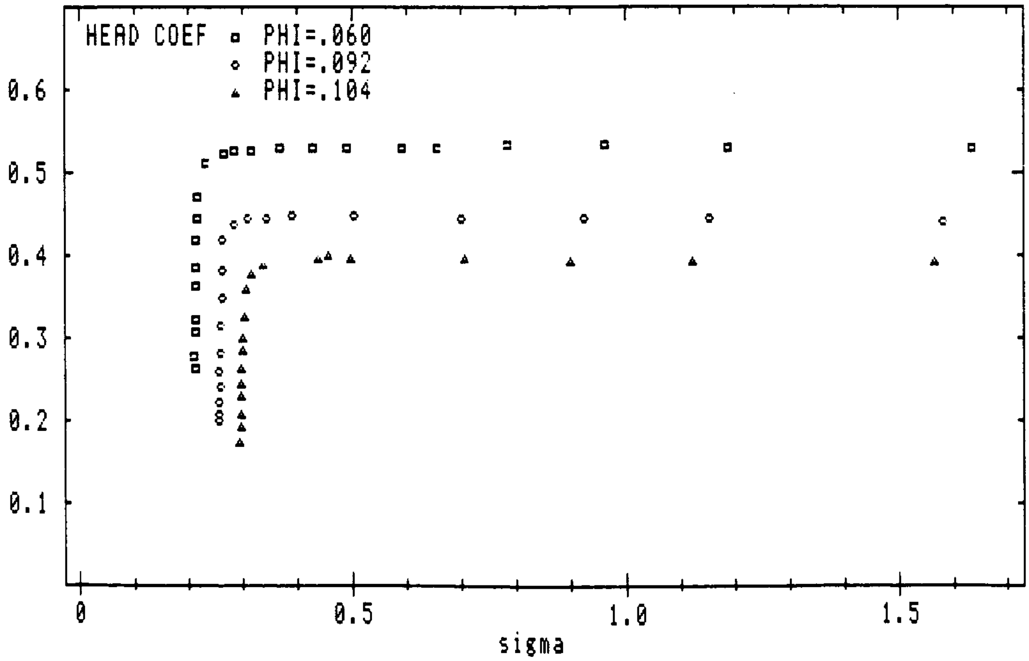

Figure 2 Cavitation performance curves for the three flow coefficients: ϕ=0.060 (below design), ϕ=0.092 (design) and ϕ=0.104 (above design), for volute A/impeller X at 3000 rpm.

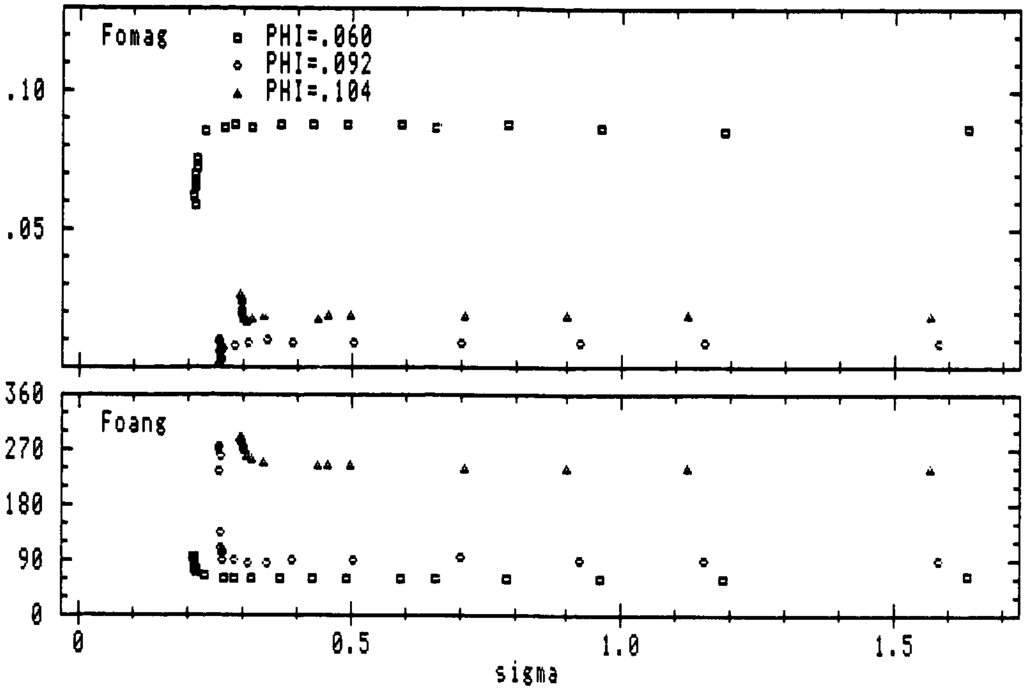

Figure 3 The dependence of the magnitude and direction of the volute force, $\{F_o\}$, on cavitation number for the three flow coefficients: ϕ=0.060, ϕ=0.092, ϕ=0.104, for volute A/impeller X at 3000 rpm.

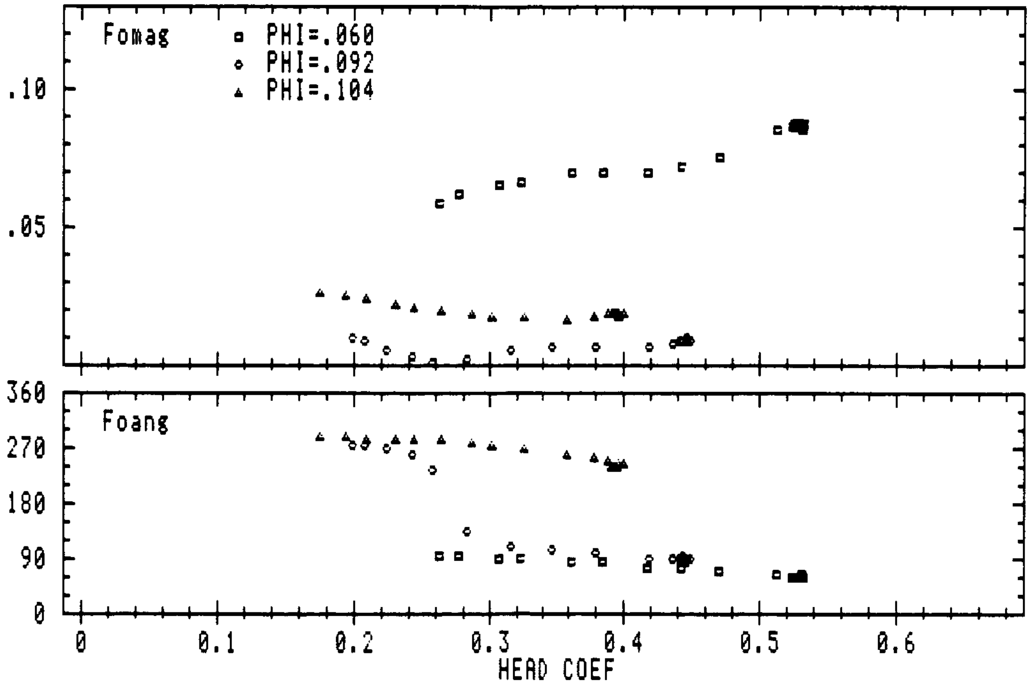

Figure 4 The dependence of the magnitude and direction of the volute force, $\{F_o\}$, on head coefficient for the three flow coefficients: ϕ=0.060, ϕ=0.092, ϕ=0.104, for volute A/impeller X at 3000 rpm.

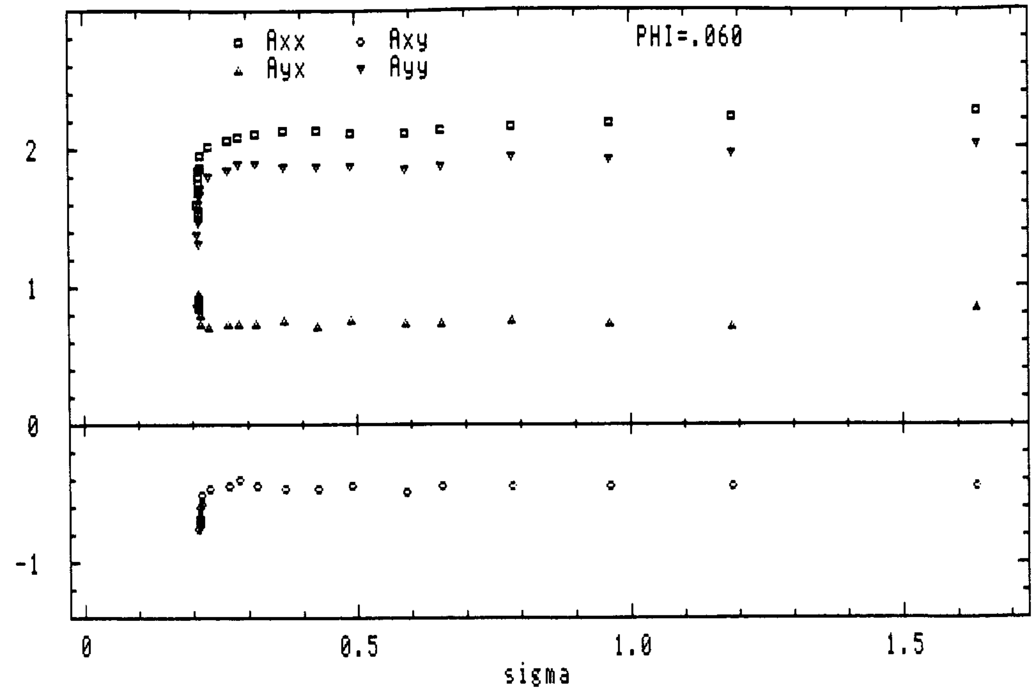

Figure 5 The dependence of the elements of the hydrodynamic force matrix, [A], on cavitation number for ϕ=0.060 (below design), for volute A/impeller X at 3000 rpm.

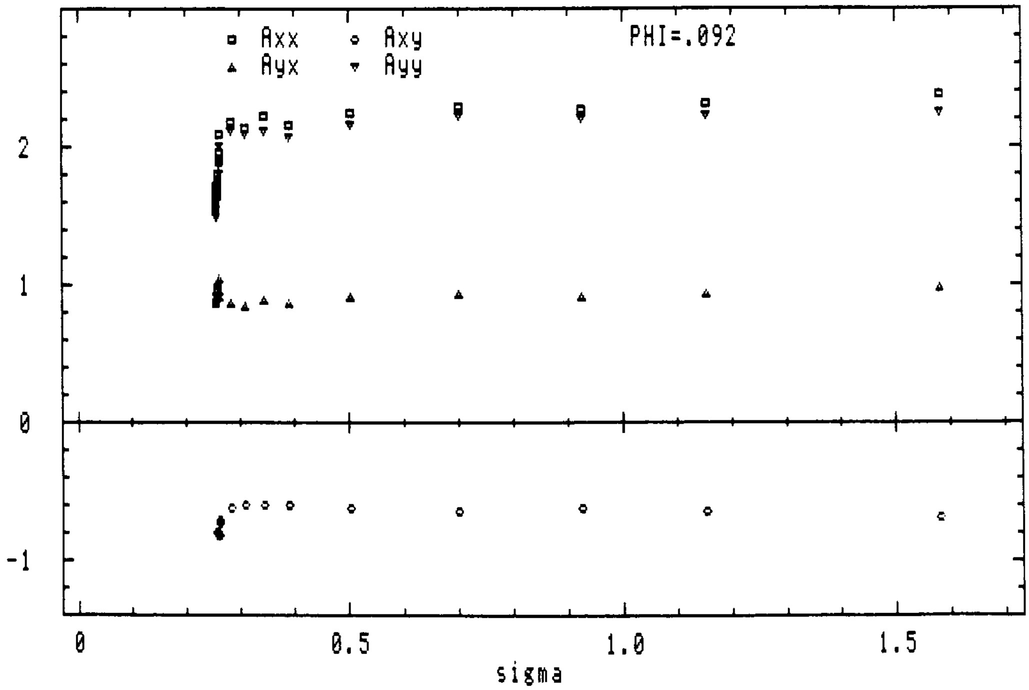

Figure 6 The dependence of the elements of the hydrodynamic force matrix, [A], on cavitation number for ϕ=0.092 (at design), for volute A/impeller X at 3000 rpm.

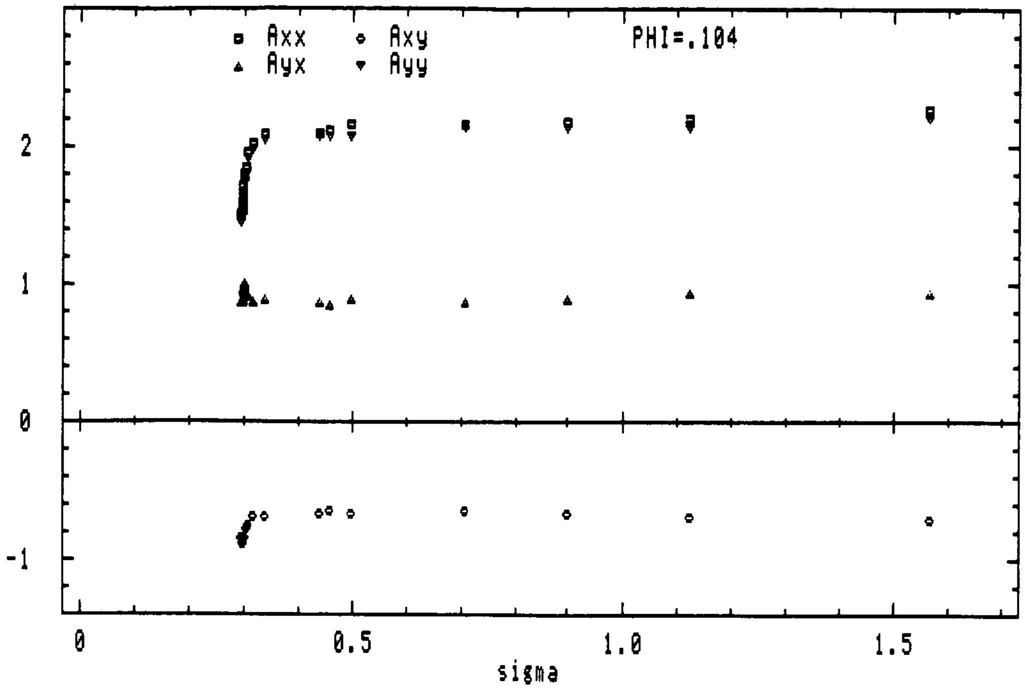

Figure 7 The dependence of the elements of the hydrodynamic force matrix, [A], on cavitation number for ϕ=0.104 (above design), for volute A/impeller X at 3000 rpm.

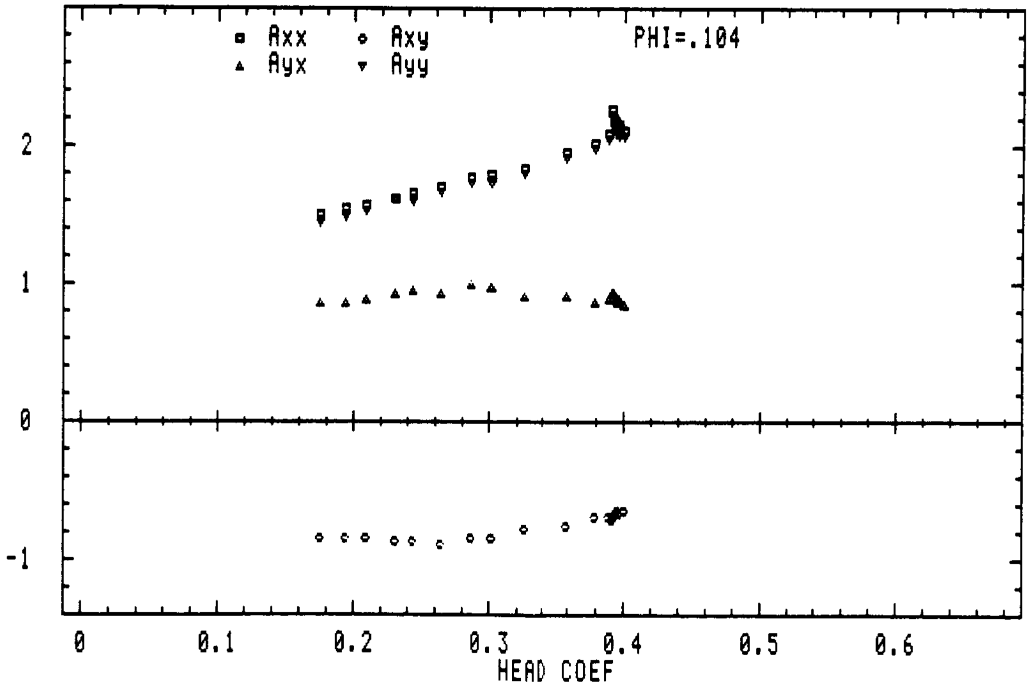

Figure 8 The dependence of the elements of the hydrodynamic force matrix, [A], on head coefficient for ϕ=0.104 (above design), for volute A/impeller X at 3000 rpm.

N87-22226

FORCE AND MOMENT ROTORDYNAMIC COEFFICIENTS FOR PUMP-IMPELLER SHROUD SURFACES

Dara W. Childs
Texas A&M University
College Station, Texas 77843

Governing equations of motion are derived for a bulk-flow model of the leakage path between an impeller shroud and a pump housing. The governing equations consist of a path-momentum, a circumferential-momentum, and a continuity equation. The fluid annulus between the impeller shroud and pump housing is assumed to be circumferentially symmetric when the impeller is centered; i.e., the clearance can vary along the pump axis but does not vary in the circumferential direction.

A perturbation expansion of the governing equations in the eccentricity ratio yields a set of zeroth and first-order governing equations. The zeroth-order equations define the leakage rate and the circumferential and path velocity distributions and pressure distributions for a centered impeller position. The first-order equations define the perturbations in the velocity and pressure distributions due to either a radial-displacement perturbation or a tilt perturbation of the impeller. Integration of the perturbed pressure and shear-stress distribution acting on the rotor yields the reaction forces and moments acting on the impeller face.

Introduction

Figure 1 illustrates an impeller stage of a multi-stage centrifugal pump. Leakage along the front side of the impeller, from impeller discharge to inlet, is restricted by a wear-ring seal, while leakage along the back side is restricted by either an interstage seal or a balance-discharge seal. Lomakin [1] originally recognized the major influence that seals have on the rotordynamic response of centrifugal pumps. Recent analysis and test results are provided by references [2-4].

More recently, various investigators have considered the forces developed by flow through the impeller and its interaction with either a volute or a vaned diffuser. Cal Tech researchers [5] have presented measured force coefficients for an impeller precessing in a volute. Ohashi and Shoji [6] also provide measured force coefficients for an impeller whirling in vaneless and vaned diffusers. More recently, Bolleter et al. [7] from Sulzer Brothers, Ltd. have also presented test results for an impeller in a vaned diffuser. The Cal Tech and Sulzer

PRECEDING PAGE BLANK NOT FILMED

test programs use conventional impellers in their test programs, but use a radial face seal to minimize or eliminate the forces which would normally be developed by the wear-ring seals. The face seals employed by these investigators sharply reduce the leakage flow down the front face of the impeller. The impeller tested by Ohashi et al. has flat, parallel, front and back shrouds. Test results from all these investigators suggest that impellers create relatively benign forces from a rotordynamic viewpoint. Ohashi concludes that impeller forces would damp forward whirling motion in most operating conditions. The Cal Tech and Sulzer researchers conclude that impellers would provide positive damping unless a rotor's running speed exceeded its critical speed by an approximate factor of 2.5. Hence impellers are predicted to yield smaller destabilizing forces than bearings or long seals which are predicted to yield destabilizing forces when the running speed exceeds twice the critical speed.

There is some contrary evidence from operating pump experience with respect to impeller forces. Specifically, Massey [8] cites experience with an 11-stage pump which was unstable and whirled at 80% of running speed; i.e., the pump was unstable when its running speed was only 1.25 times the critical speed. The HPOTP (High Pressure Oxygen Turbopump) of the SSME also whirled at 80% of running speed [9]. This evidence suggests that some unaccounted-for destabilizing force is present in pumps. The present analysis is aimed at investigating the forces and moments developed by impeller-shroud forces.

A bulk-flow analysis is employed similar to that of Childs and Kim [3]. However the analysis is extended to account for the changing geometry of impeller surface. In addition, the shear stress contribution to the reaction forces is accounted for, and the reaction-moment coefficients are calculated using the approach of reference [10]. Specifically, the following general model is used to define the reaction forces and moments which arise for small motion of a pump impeller about its centered position.

$$
-\begin{Bmatrix} F_X \\ F_Y \\ M_Y \\ M_X \end{Bmatrix} = \begin{bmatrix} K & k & k_{\varepsilon\alpha} & -k_{\varepsilon\alpha} \\ -k & K & -k_{\varepsilon\alpha} & -K_{\varepsilon\alpha} \\ K_{\alpha\varepsilon} & k_{\alpha\varepsilon} & K_{\alpha} & -k_{\alpha} \\ k_{\alpha\varepsilon} & -K_{\alpha\varepsilon} & K_{\alpha} & K_{\alpha} \end{bmatrix} \begin{Bmatrix} X \\ Y \\ \alpha_Y \\ \alpha_X \end{Bmatrix} + \begin{bmatrix} C & c & C & -c_{\varepsilon\alpha} \\ -c & C & -c_{\varepsilon\alpha} & -C_{\varepsilon\alpha} \\ C_{\alpha\varepsilon} & c_{\alpha\varepsilon} & C_{\alpha} & -{}_{\alpha} \\ c_{\alpha\varepsilon} & -C_{\alpha\varepsilon} & c_{\alpha} & C_{\alpha} \end{bmatrix} \begin{Bmatrix} \dot{X} \\ \dot{Y} \\ \dot{\alpha}_Y \\ \dot{\alpha}_X \end{Bmatrix} \tag{1}
$$

$$
+ \begin{bmatrix} M & 0 & M_{\varepsilon\alpha} & 0 \\ 0 & M & 0 & -M_{\varepsilon\alpha} \\ M_{\alpha\varepsilon} & 0 & M_{\alpha} & 0 \\ 0 & -M_{\alpha\varepsilon} & 0 & M_{\alpha} \end{bmatrix} \begin{Bmatrix} \ddot{X} \\ \ddot{Y} \\ \ddot{\alpha}_Y \\ \ddot{\alpha}_X \end{Bmatrix}
$$

where (F_X, F_Y), (X, Y) define the components of the impeller reaction forces and relative displacements, and (M_Y, M_X), (α_Y, α_X) define the components of the reaction moments and rotation (small-angles) vectors.

Geometry and Kinematics

Figure 1 illustrates the annular leakage paths along the front and back sides of a typical shrouded impeller of a multistage centrifugal pump. The present discussion concentrates on the flow and pressure fields within the forward annulus; however, the analysis also applies to the rear annulus. As illustrated in figure 2, the outer surface of the impeller is a surface of revolution formed by rotating the curve $R = R(Z)$ about the Z axis. A point on the surface may be located by the coordinates Z, $R(Z)$, θ. The length along the curve $R(Z)$ from the initial point R_i, Z_i to an arbitrary point R, Z is denoted by S and defined by

$$S = \int_{Z_i}^{Z} \sqrt{1 + \frac{dR}{dZ}^2}\, du = \int_{R_i}^{R} \sqrt{1 + \frac{dZ}{dR}^2}\, du \tag{2}$$

In the equations which follow, the path coordinate S and angular coordinate θ are used as independent spatial variables. The coordinates Z,R defining the impeller surface are be expressed as parametric functions of S, i.e., $Z(S)$, $R(S)$.

Trigonometric functions of the angle γ, illustrated in figure 3, are defined as follows

$$\begin{gathered}\tan\gamma = -\frac{dR}{dZ}\\ \cos\gamma = \frac{dZ}{dS}, \quad \sin\gamma = -\frac{dR}{dS}\end{gathered} \tag{3}$$

The clearance between the impeller and the housing is denoted as $H(S,\theta,t)$, with the time dependency introduced by impeller motion. In the centered position, the clearance function depends only on S and is denoted by $H_0(S)$. Displacement of the impeller in the X and Y directions obviously causes a change in the clearance function. The clearance function is also changed by pitching or yawing of the impeller as defined by rotations α_X, α_Y about the X and Y axes, respectively. For small displacements and rotations of the impeller the clearance function can be stated

$$\begin{aligned}H(S,\theta,t) = H_0(S) &- [(X + \alpha_Y Z)\cos\gamma - \alpha_Y R\sin\gamma]\cos\theta\\ &- [(Y - \alpha_X Z)\cos\gamma + \alpha_X R\sin\gamma]\sin\theta\end{aligned} \tag{4}$$

Observe in this equation that H_0, R, Z, $\cos\gamma$ and $\sin\gamma$ are solely functions of S, while X, Y, α_X, α_Y are functions only of t.

Governing Equations

Returning to figure 2, the path coordinate S and circumferential coordinate $R\theta$ are used to locate a fluid differential element of thickness $H(S,\theta,t)$ illustrated in figure 4. From the geometry of figure 4, the continuity equation can be stated

$$\frac{\partial H}{\partial t} + \frac{\partial}{\partial S}(U_s H) + \frac{1}{R}\frac{\partial}{\partial \theta}(U_\theta H) + \left(\frac{H}{R}\right)\frac{\partial R}{\partial S} U_s = 0$$

where U_s and U_θ are the path and circumferential bulk-velocity components, respectively.

Figure 5 illustrates the pressure and shear-stress components acting on the differential fluid element. The first subscripts (s,θ) in the shear-stress definitions (τ_{ss}, τ_{sr}), $(\tau_{\theta s}, \tau_{\theta r})$ denote path and θ directions, respectively; the second subscripts (s, r) denote stator and rotor surfaces, respectively. The path momentum equation can be stated

$$-H\frac{\partial P}{\partial S} = -\rho H \frac{U_\theta^2}{R}\frac{dR}{dS} + \tau_{ss} + \tau_{sr}$$

$$+ \rho H \left(\frac{\partial U_s}{\partial t} + \frac{\partial U_s}{\partial \theta}\frac{U_\theta}{R} + \frac{\partial U_s}{\partial S} U_s\right)$$

The circumferential-momentum equation can be stated

$$-\frac{H}{R}\frac{\partial P}{\partial \theta} = \tau_{\theta s} + \tau_{\theta r} + \rho H \left(\frac{\partial U_\theta}{\partial t} + \frac{\partial U_\theta}{\partial \theta}\frac{U_\theta}{R} + \frac{\partial U_\theta}{\partial S} U_s + \frac{U_\theta U_s}{R}\frac{\partial R}{\partial S}\right)$$

Following Hirs' approach [11], the wall shear-stress definitions in these equations can be stated

$$\tau_{ss} = \frac{ns}{2}\rho U_s^2 R_a^{ms}\left[1 + (U_\theta/U_s)^2\right]^{\frac{ms+1}{2}} \tag{5}$$

$$\tau_{sr} = \frac{nr}{2}\rho U_s^2 R_a^{mr}\left\{1 + \left[(U_\theta - R\omega)/U_s\right]^2\right\}^{\frac{mr+1}{2}}$$

$$\tau_{\theta s} = \frac{ns}{2}\rho U_s U_\theta R_a^{ms}\left[1 + (U_\theta/U_s)^2\right]^{\frac{ms+1}{2}}$$

$$\tau_{\theta r} = \frac{nr}{2}\rho U_s (U_\theta - R\omega) R_a^{mr}\left\{1 + \left[(U_\theta - R\omega)/U_s\right]^2\right\}^{\frac{mr+1}{2}}$$

where

$$R_a = 2H\,U_s/\nu \tag{6}$$

The empirical coefficients (ns, ms), (nr, mr) account for different surface roughnesses on the stator and rotor, respectively.

Impeller-Annulus Geometry

For this analysis, the assumption is made that the impeller is nominally centered in its housing. Hence, in the centered position, the clearance function $H_o(s)$ is only a function of the path coordinate S and does not depend on the azimuthal coordinate $R\theta$. The inlet-clearance function $H_o(0)$, the inlet path velocity $U_s(0)$, and the inlet radius $R(0)$ are denoted, respectively, by C_i, V_i, and R_i. In terms of these variables, leakage volumetric flowrate is defined by

$$\dot{Q} = 2\pi R_i C_i V_i \tag{7}$$

The length of the leakage path along the impeller face is defined by

$$L_s = \int_{Z_i}^{Z_i+L} \sqrt{1+\frac{dR}{dZ}^{2}}\;dZ \tag{8}$$

Nondimensionalization and Perturbation Analysis

The governing equations define the bulk-flow velocity components (U_s, U_θ) and the pressure P as a function of the coordinates $(R\theta, S)$ and time, t. They are conveniently nondimensionalized by introducing the following variables

$$\begin{aligned} u_s &= U_s/V_i,\; u_\theta = U_\theta/R_i\omega,\; p = P/\rho V_i^2 \\ h &= H/C_i,\; s = S/L_s,\; r = R/R_i \\ \tau &= \omega t,\; b = V_i/R_i\,\omega,\; T = L_s/V_i \end{aligned} \tag{9}$$

The objective of the present analysis is to examine the changes in (u_s, u_θ, p) due to changes in the clearance function $h(\theta, s, t)$ caused by small motion of the impeller within its housing. To this end, the governing equations are expanded in the perturbation variables

$$\begin{aligned} u_s &= u_{so} + \varepsilon u_{s1},\; h = h_o + \varepsilon h_1 \\ u_\theta &= u_{\theta o} + \varepsilon u_{\theta 1},\; p = p_o + \varepsilon p_1 \end{aligned} \tag{10}$$

were $\varepsilon = e/C_i$ is the eccentricity ratio. The following equations result:

Zeroth-Order Equations

(a) Path-Momentum Equation

$$\frac{dp_o}{ds} + u_{so}\frac{du_{so}}{ds} - \frac{1}{r}\left(\frac{dr}{ds}\right)(u_{\theta o}/b)^2 + \left(\frac{\sigma_s+\sigma_r}{2}\right)u_{so}^2 = 0 \tag{11a}$$

(b) Circumferential-Momentum Equation

$$2\frac{du_{\theta o}}{ds} + 2\frac{u_{\theta o}}{r}\frac{dr}{ds} + [\sigma_r(u_{\theta o} - r) + \sigma_s u_{\theta o}] = 0 \tag{11b}$$

(c) Continuity Equation

$$r\, h_o\, u_{so} = 1 \tag{11c}$$

observe that the continuity equation follows directly from Eq. (7)

First-Order Equations

(a) Path-Momentum Equation

$$\frac{\partial p_1}{\partial s} = h_1 A_{1s} - u_{\theta 1} A_{2s} - u_{s1} A_{3s} - \left[\omega T \frac{\partial u_{s1}}{\partial \tau} + \omega T \frac{u_{\theta o}}{r}\frac{\partial u_{s1}}{\partial \theta} + u_{so}\frac{\partial u_{s1}}{\partial s}\right] \tag{12a}$$

(b) Circumferential-Momentum Equation

$$b\frac{L_s}{Ri}\frac{1}{r}\frac{\partial p_1}{\partial \theta} = h_1 A_{1\theta} - u_{\theta 1} A_{2\theta} - u_{s1} A_{3\theta} - \left[\omega T \frac{\partial u_{\theta 1}}{\partial \tau} + \omega T \frac{u_{\theta o}}{r}\frac{\partial u_{\theta 1}}{\partial \theta} + u_{so}\frac{\partial u_{\theta 1}}{\partial s}\right] \tag{12b}$$

(c) Continuity Equation

$$\frac{\partial u_{s1}}{\partial s} + \frac{\omega T}{r}\frac{\partial u_{\theta 1}}{\partial \theta} + u_{s1}\left(\frac{1}{r}\frac{dr}{ds} + \frac{1}{h_o}\frac{dh_o}{ds}\right) = -\frac{h_1 u_{so}}{h_o^2}\cdot\frac{dh_o}{ds} - \frac{1}{h_o}\left(u_{so}\frac{\partial h_1}{ds} + \omega T\frac{u_{\theta o}}{r}\frac{\partial h_1}{\partial \theta} + \omega T\frac{\partial h_1}{\partial \tau}\right) \tag{12c}$$

Most of the parameters of these equations are defined in Appendix A. The quantities σ_s and σ_r are defined by

$$\sigma_s = (L_s/H_o)\,\lambda_s\,,\quad \sigma_r = (L_s/H_o)\lambda_r \tag{13}$$

where λ_s and λ_r are dimensionless stator and rotor friction factors defined by

$$\lambda_s = ns\, R_{ao}{}^{ms}\left[1 + (u_{\theta o}/bu_{so})^2\right]^{\frac{ms+1}{2}}$$

$$\lambda_r = nr\, R_{ao}^{mr} \left\{1 + \left[(u_{\theta o}-r)/bu_{so}\right]^2\right\}^{\frac{mr+1}{2}}$$

Zeroth-Order-Equation Solutions

The zeroth-order Eqs. (11) define the pressure and velocity distributions for a centered impeller position. For a known volumetric flowrate, the continuity equation completely defines u_{so}. The continuity equations can be used to solve for u_{so} to obtain

$$\frac{du_{so}}{ds} = - u_{so} \left(\frac{1}{h_o}\frac{dh_o}{ds} + \frac{1}{r}\frac{dr}{ds}\right)$$

substituting into Eq. (11a) yields

$$\frac{dp_o}{ds} - \frac{1}{r}\left(\frac{dr}{ds}\right)\frac{u_{\theta o}^2}{b^2} + \left[\left(\frac{\sigma_r+\sigma_s}{2}\right) - \frac{1}{h_o}\frac{dh_o}{ds} - \frac{1}{r}\frac{dr}{ds}\right] u_{so}^2 = 0$$

$$\frac{du_{\theta o}}{ds} + \frac{u_{\theta o}}{r}\frac{dr}{ds} + [\sigma_r(u_{\theta o}-r) + \sigma_s u_{\theta o}]/2 = 0 \tag{14}$$

Those equations are coupled and nonlinear and must be solved iteratively. The initial condition for $u_{\theta o}(0)$ is obtained from the exit flow condition of the impeller. The inlet and discharge pressure of the impeller are known and serve, respectively, as the exit (P_e) and supply (P_s) pressures for the leakage flow along the impeller face. The inlet conditions for p_o is obtained from the inlet relationship

$$P_s - P_o\,(0,\,\theta,\,t) = \rho\,(1+\xi)\,U_{so}^2(0,\,\theta,\,t)/2 \tag{15}$$

From this relationship, the zeroth-order pressure relationship is

$$p_o(0) = P_s/\rho V_i^2 - (1+\xi)\,u_{so}^2(0)/2 \tag{16}$$

The impeller exit may also include a restriction yielding a relationship of the form

$$P\,(L_s,\theta,t) - P_e = \frac{\rho}{2}\,C_{de}\,U_s^2\,(L_s,\theta,t) \tag{17}$$

The solution to the zeroth-order Eqs. (14) must be developed iteratively since all of the coefficients depend on the local path velocity U_{so}. In this study, the equations are solved by the following iterative steps:

(a) Guess or estimate V_i which then defines $u_{so}(s)$.
(b) Calculate $p_o(0)$ from Eq. (16), and use a specified $u_{\theta o}(0)$ as initial conditions to numerically integrate Eqs. (14) out to $s = 1$, i.e., the annulus exit.

(c) Based on the difference between a calculated exit pressure and the prescribed exit pressure, calculate a revised V_i and repeat the cycle until convergence is achieved.

First-order Equations Solutions

The first-order Eqs. (12) define the first-order perturbations u_{s1} (s,θ,τ), $u_{\theta 1}$ (s,θ,τ), and p_1 (s,θ,τ) resulting from the perturbed clearance function h_1. From Eqs. (4) and (9), h_1 can be stated

$$\begin{aligned}\varepsilon h_1 = & \left\{ -\left[x+\alpha_Y \left(\frac{L}{Ci}\right) z\right] \cos\gamma + \alpha_Y \left(\frac{Ri}{Ci}\right) r\sin\gamma \right\} \cos\theta \\ & + \left\{ -\left[y-\alpha_X \left(\frac{L}{Ci}\right) z\right] \cos\gamma - \alpha_X \left(\frac{Ri}{Ci}\right) r\sin\gamma \right\} \sin\theta \\ & = h_{1c}(s,\tau)\cos\theta + h_{1s}(s,\tau)\sin\theta\end{aligned} \tag{18}$$

The theta dependency of the dependent variables is eliminated by assuming the following, comparable solution format

$$\begin{aligned} u_{s1} &= u_{s1c}\cos\theta + u_{s1s}\sin\theta \\ u_{\theta 1} &= u_{\theta 1c}\cos\theta + u_{\theta 1s}\sin\theta \\ p_1 &= p_{1c}\cos\theta + p_{1s}\sin\theta \end{aligned}$$

Substituting into Eqs. (12) and equating like coefficients of $\cos\theta$ and $\sin\theta$ yields six equations in the independent variables s,τ. By introducing the complex variables

$$\begin{aligned} \underline{u}_{s1} &= u_{s1c} + j\,u_{s1s} , \quad \underline{u}_{\theta 1} = u_{\theta 1c} + j\,u_{\theta 1s} \\ \underline{p}_1 &= p_{1c} + jp_{1s} , \quad \underline{h}_1 = h_{1c} + j\,h_{1s} \end{aligned} \tag{19}$$

these real equations are reduced to the following three complex equations in s and τ.

$$\begin{aligned}\frac{\partial \underline{p}_1}{\partial s} = & \ \underline{h}_1 A_{1s} - \underline{u}_{\theta 1} A_{2s} - \underline{u}_{s1} A_{3s} \\ & - \left[\omega T \frac{\partial \underline{u}_{s1}}{\partial \tau} - j\,\omega T \frac{u_{\theta o}}{r} \underline{u}_{s1} + u_{so} \frac{\partial \underline{u}_{s1}}{\partial s}\right]\end{aligned} \tag{20a}$$

$$\begin{aligned}- j\,\frac{b}{r} \left(\frac{L_s}{R_i}\right) \underline{p}_1 = & \ \underline{h}_1 A_{1\theta} - \underline{u}_{\theta 1} A_{2\theta} - \underline{u}_{s1} A_{3\theta} \\ & - \left[\omega T \frac{\partial \underline{u}_{\theta 1}}{\partial \tau} - j\,\omega T \frac{u_{\theta o}}{r} \underline{u}_{\theta 1} + u_{so} \frac{\partial \underline{u}_{\theta 1}}{\partial s}\right]\end{aligned} \tag{20b}$$

$$\frac{\partial \underline{u}_{s1}}{\partial s} - j\frac{\omega T}{r}\,\underline{u}_{\theta 1} + \underline{u}_{s1}\left(\frac{1}{r}\frac{dr}{ds} + \frac{1}{h_o}\frac{dh_o}{ds}\right) =$$

$$\underline{h}_1\left[\frac{u_{so}}{h_o^2}\frac{dho}{ds} + j\frac{\omega T}{h_o}\frac{u_{\theta o}}{r}\right] - \frac{u_{so}}{h_o}\frac{\partial \underline{h}_1}{\partial s} - \frac{\omega T}{h_o}\frac{\partial \underline{h}_1}{\partial \tau} \qquad (20c)$$

From Eqs. (3) and (17), $\underline{h}_1$ can be stated

$$\varepsilon \underline{h}_1 = -q \left(\frac{L}{L_s}\right)\frac{dz}{ds} - \alpha\, G_o \qquad (21)$$

where

$$G_o = \left(\frac{L^2}{C_i L_s}\right) z \frac{dz}{ds} + \left(\frac{R_i{}^2}{C_i L_s}\right) r \frac{dr}{ds} \qquad (22)$$

$$q = x + jy \quad , \quad \alpha = \alpha_Y - j\alpha_X$$

From Eq. (21), the following additional result is obtained

$$\varepsilon \frac{\partial \underline{h}_1}{\partial s} = -\, q \left(\frac{L}{L_s}\right)\frac{d^2 z}{ds^2} - \alpha\, F_1 \qquad (23)$$

where

$$F_1 = \left(\frac{L^2}{C_i L_s}\right)\left[\left(\frac{dz}{ds}\right)^2 + z\frac{d^2 z}{ds^2}\right] + \left(\frac{R_i{}^2}{C_i L_s}\right)\left[\left(\frac{dr}{ds}\right)^2 + r\frac{d^2 r}{ds^2}\right] \qquad (24)$$

The time dependency of Eqs. (20) is eliminated by assuming harmonic seal motion of the form

$$q = q_o e^{jf\tau} \qquad \alpha = \alpha_o e^{jf\tau} \qquad h_1 = h_{1o} e^{jf\tau} \qquad (25)$$

$$f = \Omega/\omega$$

where Ω is the seal whirl frequency and q_o and α_o are real constants. The associated harmonic solution can then be stated

$$\underline{u}_{s1} = \overline{u}_{s1}\, e^{jf\tau} \qquad \underline{u}_{\theta 1} = \overline{u}_{\theta 1} e^{jf\tau}$$

$$\underline{p}_1 = \overline{p}_1\, e^{jf\tau} \qquad (26)$$

Substitution from Eqs. (25) and (26) into the governing complex partial differential equations yields the following three complex ordinary equations in s

$$\frac{d}{ds}\begin{Bmatrix}\bar{u}_{s1}\\ \bar{u}_{\theta 1}\\ p_1\end{Bmatrix} + [A]\begin{Bmatrix}\bar{u}_{s1}\\ \bar{u}_{\theta 1}\\ p_1\end{Bmatrix} = \left(\frac{q_o}{\varepsilon}\right)\begin{Bmatrix}g_1\\ g_2\\ g_3\end{Bmatrix} + \left(\frac{\alpha_o}{\varepsilon}\right)\begin{Bmatrix}g_4\\ g_5\\ g_6\end{Bmatrix} \tag{27}$$

where

$$[A] = \begin{bmatrix} \left(\frac{1}{r}\frac{dr}{ds} + \frac{1}{h_o}\frac{dh_o}{ds}\right) & -j\frac{\omega T}{r} & 0 \\ A_{3\theta}/u_{so} & (A_{2\theta} + j\Gamma T)/u_{so} & -j\frac{b}{ru_{so}}\left(\frac{L_s}{R_i}\right) \\ A_{3s} - u_{so}\left(\frac{1}{r}\frac{dr}{ds} + \frac{1}{h_o}\frac{dh_o}{ds}\right) + j\Gamma T & A_{2s} + j\omega T u_{so} & 0 \end{bmatrix} \tag{28}$$

$$\begin{Bmatrix}g_1\\ g_2\\ g_3\end{Bmatrix} = \left(\frac{L}{L_s}\right)\begin{Bmatrix} F_2 + j\frac{\Gamma T}{ho}\frac{dz}{ds} \\ -\left(\frac{A_{1\theta}}{u_{so}}\right)\frac{dz}{ds} \\ -A_{1s}\frac{dz}{ds} - u_{so}F_2 - ju_{so}\frac{\Gamma T}{h_o}\frac{dz}{ds}\end{Bmatrix} \tag{29}$$

$$\begin{Bmatrix}g_4\\ g_5\\ g_6\end{Bmatrix} = \begin{Bmatrix} F_3 + jG_o\,\Gamma T/h_o \\ -A_{1\theta}G_o/u_{so} \\ -G_oA_{1s} - u_{so}F_3 - jG_ou_{so}\,\Gamma T/h_o\end{Bmatrix} \tag{30}$$

and

$$\Gamma = \omega\,(f - u_{\theta o}/r)$$

$$F_2 = \frac{u_{so}}{ho}\left(\frac{d^2z}{ds^2} - \frac{1}{h_o}\frac{dh_o}{ds}\frac{dz}{ds}\right) \tag{31}$$

$$F_3 = \frac{u_{so}}{ho}\left(F_1 - \frac{G_o}{h_o}\frac{dh_o}{ds}\right)$$

The following three boundary conditions are specified for the solution of Eq. (27):

(a) The entrance-perturbation, circumferential velocity is zero, i.e.,

$$\bar{u}_{\theta 1}(0) = 0 \qquad (32.a)$$

(b) The entrance loss at the seal entrance is defined by Eq. (15), and the corresponding perturbation-variable relationship is

$$\bar{p}1\ (0) = -(1 + \xi)\ \bar{u}s1\ (0) \qquad (32.b)$$

(c) The relationship at the exit is provided by Eq. (17) and yields the following perturbation relationship

$$\bar{p}_1\ (1) = C_{de}\ u_{so}\ (1)\ \bar{u}_{s1}\ (1) \qquad (32.c)$$

The value for C_{de} depends on the wear-ring seal geometry. Solution of Eq. (27) for the boundary conditions of Eqs. (32) is relatively straightforward, involving successive solutions for displacement and rotation excitations. The complete solution is the sum of the homogeneous solution (which depends on the unknown initial conditions $\bar{p}_1$ (0), $\bar{u}_{s1}$ (0)) and the particular solutions which are proportional to either q_o or α_o. Complete solutions are developed separately for the two vectors on the right-hand side of Eq. (27), which satisfy the boundary conditions of Eqs. (32). By virtue of the problem's linearity, these two solutions may be added to obtain the complete system solution or employed separately to calculate the rotordynamic coefficients. The solution to Eq. (27), due to displacement perturbation, is obtained by setting $\alpha_o = 0$, and may be stated

$$\begin{Bmatrix} \bar{u}_{s1} \\ \bar{u}_{\theta 1} \\ \bar{p}_1 \end{Bmatrix} = \left(\frac{q_o}{\varepsilon}\right) \begin{Bmatrix} f_{1c} + j\ f_{1s} \\ f_{2c} + j\ f_{2s} \\ f_{3c} + j\ f_{3s} \end{Bmatrix} = \left(\frac{q_o}{\varepsilon}\right) \begin{Bmatrix} f_1 \\ f_2 \\ f_3 \end{Bmatrix} \qquad (33)$$

The soluton due to angular perturbations is obtained by setting $q_o = 0$ and may be stated

$$\begin{Bmatrix} \bar{u}_{s1} \\ \bar{u}_{01} \\ \bar{p}_1 \end{Bmatrix} = \left(\frac{\alpha_o}{\varepsilon}\right) \begin{Bmatrix} f_{4c} + j\ f_{4s} \\ f_{5c} + j\ f_{5s} \\ f_{6c} + j\ f_{6s} \end{Bmatrix} = \left(\frac{\alpha_o}{\varepsilon}\right) \begin{Bmatrix} f_4 \\ f_5 \\ f_6 \end{Bmatrix} \qquad (34)$$

Reaction Forces and Moments

From figure 5, the differential force components acting on a differential-impeller surface area can be stated

$$\begin{aligned} dF_X &= -(P\cos\Upsilon - \tau_{rs}\sin\Upsilon)\ R\ d\theta dS\ \cos\theta + \tau_{r\theta}\sin\theta\ R\ d\theta ds \\ dF_Y &= -(P\cos\Upsilon - \tau_{rs}\sin\Upsilon)\ R\ d\theta ds\ \sin\theta - \tau_{r\theta}\cos\theta\ R\ d\theta ds \qquad (35) \\ dF_Z &= -(P\sin\Upsilon + \tau_{rs}\cos\Upsilon)\ R\ d\theta ds \end{aligned}$$

The shear-stress contribution to these differential-force components has been neglected in prior analysis of seals. The X and Y components are used to define rotordynamic coefficients; the Z component defines the axial thrust. Taking moments of the differential force vector about the origin of the X, Y, Z system yields the following differential moment components.

$$
\begin{aligned}
dM_X &= \left\{ -[P(R\sin\Upsilon - Z\cos\Upsilon) + \tau_{rs}\,(R\cos\Upsilon + Z\sin\Upsilon)]\,\sin\theta + Z\,\tau_{r\theta}\cos\theta \right\} R\,d\theta ds \\
dM_Y &= \left\{ -[P(R\sin\Upsilon - Z\cos\Upsilon) + \tau_{rs}\,(R\cos\Upsilon + Z\sin\Upsilon)]\,\cos\theta + Z\,\tau_{r\theta}\sin\theta \right\} R\,d\theta ds \\
dM_Z &= -\tau_{r\theta}\,R^2\,d\theta ds
\end{aligned}
\tag{36}
$$

The X and Y components yield rotordynamic coefficients; the Z component defines the drag torque.

From Eqs. (35) and (36), the force and moment perturbations are stated

$$
\begin{aligned}
F_{X1} = &-\varepsilon\int_0^{L_s}\int_0^{2\pi} (P_1\cos\Upsilon - \tau_{rs1}\sin\Upsilon)\cos\theta\, R\, d\theta dS \\
&+\varepsilon\int_0^{L_s}\int_0^{2\pi} \tau_{r\theta 1}\sin\theta\, R\, d\theta dS
\end{aligned}
\tag{37a}
$$

$$
\begin{aligned}
F_{Y1} = &-\varepsilon\int_0^{L_s}\int_0^{2\pi} (P_1\cos\Upsilon - \tau_{rs1}\sin\Upsilon)\sin\theta\, R\, d\theta dS \\
&-\varepsilon\int_0^{L_s}\int_0^{2\pi} \tau_{r\theta 1}\cos\theta\, R\, d\theta dS
\end{aligned}
\tag{37b}
$$

$$
\begin{aligned}
M_{X1} = &-\varepsilon\int_0^{L_s}\int_0^{2\pi} \left[P_1(R\sin\Upsilon - Z\cos\Upsilon) + \tau_{rs1}\,(R\cos\Upsilon + Z\sin\Upsilon)\right] R\sin\theta\, d\theta dS \\
&+\varepsilon\int_0^{L_s}\int_0^{2\pi} \tau_{r\theta 1}\, ZR\cos\theta\, d\theta dS
\end{aligned}
\tag{37c}
$$

$$
\begin{aligned}
M_{Y1} = &\ \varepsilon\int_0^{L_s}\int_0^{2\pi} \left[P_1(R\sin\Upsilon - Z\cos\Upsilon) + \tau_{rs1}\,(R\cos\Upsilon + Z\sin\Upsilon)\right]\cos\theta\, R\, d\theta dS \\
&+\varepsilon\int_0^{L_s}\int_0^{2\pi} \tau_{r\theta 1}\, ZR\sin\theta\, d\theta dS
\end{aligned}
\tag{37d}
$$

From Eq. (5), the perturbation shear stresses can be stated

$$\begin{aligned} \tau_{sr1} &= \rho V_i^2 \, (B_{s1} \, u_{s1} + B_{s2} \, u_{\theta 1} + B_{s3} \, h_1) \\ \tau_{\theta r1} &= \rho V_i^2 \, (B_{\theta 1} \, u_{s1} + B_{\theta 2} \, u_{\theta 1} + B_{\theta 3} \, h_1) \end{aligned} \tag{38}$$

The coefficients of these equations are defined in the appendix. Successive substitutions from (a) Eqs. (9) and (18), (b) Eqs. (19), and (c) Eqs. (21), (24), and (26) into Eqs. (37) yields

$$\frac{F_r + jF_\theta}{F_o} = \frac{(F_{X1} + jF_{Y1})e^{-jf\tau}}{F_o} \tag{39a}$$

$$= -\frac{\epsilon\pi L_s}{C_d L} \int_0^1 \Bigg\{ \bar{p}_1 \left(\frac{L}{L_s}\right) \frac{dz}{ds} + \bar{u}_{s1} \left[\left(\frac{R}{L_s}\right) \frac{dr}{ds} B_{s1} + j \, B_{\theta 1} \right]$$

$$+ \bar{u}_{\theta 1} \left[\left(\frac{R}{L_s}\right) \frac{dr}{ds} B_{s2} + j \, B_{\theta 2} \right] + \bar{h}_1 \left[\left(\frac{R}{L_s}\right) \frac{dr}{ds} B_{s3} + j \, B_{\theta 3} \right] \Bigg\} r ds$$

$$\frac{M_\theta - jM_r}{F_o L} = \frac{(M_{Y1} - jM_{X1})e^{-jf\tau}}{F_o L} \tag{39b}$$

$$= -\frac{\epsilon\pi L_s}{C_d} \int_0^1 \Bigg\{ \bar{p}_1 \left[\left(\frac{R_i^2}{L L_s}\right) r \frac{dr}{ds} + \left(\frac{L}{L_s}\right) z \frac{dz}{ds} \right]$$

$$+ \bar{u}_{s1} \left[\left(\frac{R_i}{L_s}\right) \left(z \frac{dr}{ds} - r \frac{dz}{ds}\right) B_{s1} + j \, B_{\theta 1} \right]$$

$$+ \bar{u}_{\theta 1} \left[\left(\frac{R_i}{L_s}\right) \left(z \frac{dr}{ds} - r \frac{dz}{ds}\right) B_{s2} + j \, B_{\theta 2} \right]$$

$$+ \bar{h}_1 \left[\left(\frac{R_i}{L_s}\right) \left(z \frac{dr}{ds} - r \frac{dz}{ds}\right) B_{s3} + j \, B_{\theta 3} \right] \Bigg\} \; r ds$$

where

$$F_o = 2R_i L \Delta P \tag{40}$$

Note that

$$\Delta P = P_s - P_e = C_d \frac{\rho V_i^2}{2} \tag{41}$$

is the total pressure drop along the leakage path from impeller discharge to inlet.

Rotordynamic Coefficients for Displacement Perturbations

Eqs. (39) apply for simultaneous displacement and slope perturbations and are solved alternately for displacement and slope perturbations. For the displacement solution, α_o is set equal to zero, and Eqs. (21) and (33) yield

$$f_{rq} = \frac{F_r(f)}{q_oF_o} = -\frac{\pi}{C_d}\left(\frac{L_s}{L}\right)\int_o^1 \left[f_{3c}\left(\frac{L}{L_s}\right)\frac{dz}{ds} + f_{1c}\left(\frac{R_i}{L_s}\right)\frac{dr}{ds}B_{s1} - f_{1s}B_{\theta 1} + f_{2c}\left(\frac{R_i}{L_s}\right)\frac{dr}{ds}B_{s2} - f_{2s}B_{\theta 2} - \left(\frac{LR_i}{L^2{}_s}\right)\frac{dz}{ds}\frac{dr}{ds}B_{s3}\right] rds$$

$$f_{\theta q} = \frac{F_\theta(f)}{q_oF_o} = -\frac{\pi}{C_d}\left(\frac{L_s}{L}\right)\int_o^1 \left[f_{3s}\left(\frac{L}{L_s}\right)\frac{dz}{ds} + f_{1s}\left(\frac{R_i}{L_s}\right)\frac{dr}{ds}B_{s1} + f_{1c}B_{\theta 1} + f_{2s}\left(\frac{R_i}{L_s}\right)\frac{dr}{ds}B_{s2} + f_{2c}B_{\theta 2} - \left(\frac{L}{L_s}\right)\frac{dz}{ds}B_{\theta 3}\right] rds$$

$$m_{\theta q} = \frac{M_\theta(f)}{q_oF_oL} = \frac{\pi}{C_d}\left(\frac{Ls}{L}\right)\int_o^1 \left[f_{3s}E_1 + f_{1c}E_2B_{s1} - f_{1s}B_{\theta 1} + f_{2s}E_2B_{s2} - f_{2s}B_{\theta 2} - \left(\frac{L}{L_s}\right)E_2\frac{dz}{ds}B_{s3}\right] rds \tag{42}$$

$$m_{rq} = \frac{M_r(f)}{q_oF_oL} = \frac{\pi}{C_d}\left(\frac{Ls}{L}\right)\int_o^1 \left[f_{3c}E_1 + f_{1s}E_2B_{s1} + f_{1c}B_{\theta 1} + f_{2c}E_2B_{s2} + f_{2c}B_{02} - \left(\frac{L}{L_s}\right)\frac{dz}{ds}B_{\theta 3}\right] rds$$

where

$$E_1 = \left(\frac{R_i{}^2}{LL_s}\right) r\frac{dr}{ds} + \left(\frac{L^2}{L_s}\right) z\frac{dz}{ds}$$

$$E_2 = \left(\frac{R_i}{L_s}\right)\left(z\frac{dr}{ds} - r\frac{dz}{ds}\right) \tag{43}$$

The right-hand side of Eqs. (42) is only a function of the frequency-ratio, f, and can be evaluated for selected values of this parameter.

The comparable results from Eq. (1) are

$$
\begin{aligned}
f_{rq}(f) &= \frac{F_r(f)}{q_o F_o} = -(\tilde{K} + f\tilde{c} - f^2\tilde{M}) \\
f_{\theta q}(f) &= \frac{F_\theta(f)}{q_o F_o} = \tilde{k} - f\tilde{C} \\
m_{\theta q}(f) &= \frac{M_\theta(f)}{q_o F_o L} = -(\tilde{K}_{\alpha\varepsilon} + f\tilde{c}_{\alpha\varepsilon} - f^2\tilde{M}_{\alpha\varepsilon}) \\
-m_{rq}(f) &= \frac{M_r(f)}{q_o F_o L} = \tilde{K}_{\alpha\varepsilon} - f\tilde{C}_{\alpha\varepsilon} - f^2 m_{\alpha\varepsilon}
\end{aligned}
\qquad (44)
$$

Where the nondimensional coefficients are defined by

$$
\begin{aligned}
&\tilde{K} = KC_i/F_o,\ \tilde{k} = kC_i/F_o,\ \tilde{M} = MC_i\,\omega^2/F_o \\
&\tilde{C} = CC_i\omega/F_o,\ \tilde{c} = cC_i\omega/F_o \\
&\tilde{K}_{\alpha\varepsilon} = K_{\alpha\varepsilon}C_i/LF_o,\ \tilde{C}_{\alpha\varepsilon} = C_{\alpha\varepsilon}C_i\omega/LF_o,\ \tilde{M}_{\alpha\varepsilon} = M_{\alpha\varepsilon}C_i\omega^2/LF_o \\
&\tilde{k}_{\alpha\varepsilon} = k_{\alpha\varepsilon}C_i/LF_o,\ \tilde{c}_{\alpha\varepsilon} = c_{\alpha\varepsilon}C_i\omega/LF_o\ ,\ m_{\alpha\varepsilon}C_i\omega^2/LF_o
\end{aligned}
\qquad (45)
$$

The dynamic coefficients are obtained by equating the right-hand sides of Eqs. (42) and (44) and by carrying out a least-square curve fit on the results from Eq. (42).

Rotordynamic Coefficients for Slope Perturbations

Applying the procedure of the preceding section to Eqs. (42) with $q_o = 0$ yields

$$
\begin{aligned}
f_r\,(f) = \frac{F_r(f)}{\alpha_o F_o} = -\frac{\pi}{C_d}\left(\frac{L}{Ls}\right)\int_o^1 \Bigg[& f_{6c}\left(\frac{L}{Ls}\right)\frac{dz}{ds} + f_{4c}\left(\frac{Ri}{Ls}\right)\frac{dr}{ds}B_{s1} - f_{4s}B_{\theta 1} \\
& + f_{5c}\left(\frac{Ri}{Ls}\right)\frac{dr}{ds}B_{s2} - f_{5s}B_{\theta 2} - G_o\left(\frac{Ri}{Ls}\right)\frac{dr}{ds}B_{s3}\Bigg] r\,ds
\end{aligned}
$$

$$
f_\theta\,(f) = \frac{F_\theta(f)}{\alpha_o F_o} = -\frac{\pi}{C_d}\left(\frac{L}{Ls}\right)\int_o^1 \Bigg[f_{6s}\left(\frac{L}{Ls}\right)\frac{dz}{ds} + f_{4s}\left(\frac{Ri}{Ls}\right)\frac{dr}{ds}B_{s1} + f_{4c}B_{\theta 1}
$$

$$+ f_{5s} \left(\frac{Ri}{Ls}\right) B_{s2} + f_{5c} B_{\theta 2} - G_o B_{\theta 3}\Big] \, rds \tag{46}$$

$$m_{\theta\alpha}(f) = \frac{M_\theta(f)}{\alpha_o F_o L} = - \frac{\pi}{C_d} \left(\frac{L}{Ls}\right) \int_o^1 \Big[f_{6c} E_1 + f_{4c} E_2 B_{s1} - f_{4s} B_{\theta 1}$$

$$+ f_{5c} E_2 B_{s2} - f_{5c} B_{\theta 2} - G_o E_2 B_{s3}\Big] \, rds$$

$$m_{r\alpha}(f) = \frac{M_r(f)}{\alpha_o F_o L} = - \frac{\pi}{C_d} \left(\frac{L}{Ls}\right) \int_o^1 \Big[f_{6s} E_1 + f_{4s} E_2 B_{s1} + f_{4c} B_{\theta 1}$$

$$+ f_{5s} E_2 B_{s2} + f_{5c} B_{\theta 2} - G_o B_{\theta 3}\Big] \, rds$$

Eq. (1) yields the corresponding solution format

$$f_{r\alpha}(f) = \frac{F_r(f)}{\alpha_o F_o} = - (\tilde{K}_{\varepsilon\alpha} + f \, \tilde{c}_{\varepsilon\alpha} - f^2 \tilde{M}_{\alpha}) \tag{47}$$

$$f_{\theta\alpha}(f) = \frac{F_\theta(f)}{\alpha_o F_o} = (\tilde{k}_{\varepsilon\alpha} - f\tilde{C}_{\varepsilon\alpha} - \tilde{f}^2 m_{\varepsilon\alpha})$$

$$m_{\theta\alpha}(f) = \frac{M_\theta(f)}{\alpha_o F_o L} = (\tilde{k}_{\alpha} + f c_{\alpha} - f^2 M_{\alpha})$$

$$-m_{r\alpha}(f) = - \frac{M_r(f)}{\alpha_o F_o L} = \tilde{k}_{\alpha} - \tilde{f} C_{\alpha} - \tilde{f}^2 m_{\alpha}$$

where

$$\begin{aligned}
&\tilde{K}_{\varepsilon\alpha} = K_{\varepsilon\alpha}/F_o, \ \tilde{k}_{\varepsilon\alpha} = k_{\varepsilon\alpha}/F_o, \ \tilde{M}_{\varepsilon\alpha} = M_{\varepsilon\alpha}\omega^2/F_o \\
&\tilde{C}_{\varepsilon\alpha} = C_{\varepsilon\alpha}\omega/F_o, \ \tilde{c}_{\varepsilon\alpha} = c_{\varepsilon\alpha}\omega/F_o, \ \tilde{m}_{\varepsilon\alpha} = m_{\varepsilon\alpha}\omega^2/F_o \\
&\tilde{K}_{\alpha} = K_{\alpha}/F_oL, \ \tilde{k}_{\alpha} = k_{\alpha}/F_oL, \ \tilde{M}_{\alpha} = M_{\alpha}\omega^2/F_oL \\
&\tilde{C}_{\alpha} = C_{\alpha}\omega/F_oL, \ \tilde{c}_{\alpha} = c_{\alpha}\omega/F_oL, \ \tilde{m}_{\alpha} = m_{\alpha}\omega^2/F_oL
\end{aligned} \tag{48}$$

The rotordynamic coefficients are obtained by equating the right-hand side of Eqs. (46) and (47).

Predictions and Comparison to Experimental Results

Figures 6(a) and 6(b) illustrate, respectively, a nominal pump-impeller geometry with a conventional wear-ring seal and a modified pump impeller with a face seal. Bolleter et al. tested the face-seal impeller to eliminate the forces which would normally be generated by the wear-ring seal. Their tests were at best efficiency point (BEP) with the pump running at 2000 rpm, while developing 68m of head and 130 l/sec of flow rate. The impeller has seven blades and an impeller exit angle of 22.5°. The test fluid is water at 80°F.

The present analysis requires an estimate of the ΔP across the impeller versus the total head rise of the stage. At U. Bolleter's suggestion, the impeller ΔP was estimated to be 70% of the total ΔP of the pump. An estimate of the inlet tangential velocity is also required. Fortunately, pitot-tube measurements are available, indicating that the inlet tangential velocity is approximately 50% of the exit impeller surface velocity; i.e., $u_{\theta o}(o) \cong 0.5$. This is in contrast to a theoretically-predicted tangential velocity of $0.72\ R_i\omega$ based on the blade-exit angle. Adkins' measurements at Cal Tech [12] also show substantially lower exit tangential velocities than predicted from exit blade angles.

Both walls of the impeller were assumed to be smooth and represented by Yamada's [13] test data; mr = ms = -0.25, nr = ns = 0.079. The inlet loss for the impeller, ξ, was assumed to be 0.1. The discharge coefficient for the seal was calculated iteratively as follows. With an assumed C_{de}, Eqs. (14), (15), and (17) were used to calculate the leakage through the impeller annulus and the pressure and tangential-velocity upstream of the seal. The seal is then analyzed (with the same equations) using the calculated seal inlet pressure and tangential velocity to determine leakage and C_{de}. The iteration continues until the leakage predictions for the exit seal and the impeller annulus agree.

Figures 7(a) and (b) illustrate the predicted radial and tangential force coefficients f_{rq} and $f_{\theta q}$ versus the whirl frequency ratio $f = \Omega/\omega$ for the face-seal, impeller. Results are presented for $u_{\theta o}(0) = 0.5$, 0.6, and 0.7. The $u_{\theta o}(0) = 0.5$ data of these figures is generally consistent with expectations based on experience with seals except for a slight "dip" in f_{rq} and "bump" in $f_{\theta q}$. However, the peaks exhibited at higher value for $u_{\theta o}$ are quite unexpected. They arise primarily due to the centrifugal acceleration term in the path-momentum equation. If the term

$$\frac{2u_{\theta o}}{R}\frac{dr}{ds} / b^2,$$

is dropped from the A_{2s} definition of Appendix A, the "peaks" are substantially eliminated from the force predictions.

Figure 8(a) and (b) provide predictions for f_{rq} and $f_{\theta q}$ for the conventional wear-ring-seal impeller of figure 6(a). The predicitons are only for the impeller and do not include the exit wear-ring seal. The $f_{\theta q}$ results for the two impellers are quite similar; however, the f_{rq} values are generally larger for the face-seal impeller.

Table 1 below provides zeroth-order-solution results for the conventional-seal impeller of figure 6(b).

Observe that the leakage is reduced by increasing $u_{\theta o}(0)$. Also observe the relatively high seal-inlet-tangential velocity prediction for the exit seals, which will predictably lead to increased cross-coupled stiffness coefficients and decreased rotor stability. The Reynolds number values suggest that care should be taken in extrapolating impeller force data from one operating condition to another. Specifically, changes in temperature or operating media would be expected to yield significant changes in force data.

The freqency-dependency of f_{rq} and $f_{\theta q}$ exhibited in figures 7 and 8 for $u_{\theta o}(0)$ = 0.6, 0.7 can not be modeled by the rotordynamic-coefficient model on Eq. (1). Stated differently, The quadratic dependency of f_{rq} and $f_{\theta q}$ on f, which is specified in Eq. (44), is simply not true. A significantly more complicated dependency is clearly in order. While these results of figures 7 and 8 are surprising, recent data from the Cal Tech program by Franz and Arndt [14] are qualitatively similar.

The $u_{\theta o}(0)$ = 0.5 results of figure 7 are reasonably modeled by a quadratic dependency of f and can be modeled by rotordynamic coefficients. A comparison of predicted and measured coefficients is provided in Table 2.

Keeping in mind that the present theory does not account for the momentum flux exiting from the impeller or the pressure forces on the impeller exit, the comparison between theory and experiment of Table 1 is encouraging. The prediction of C and M are good. The results for k are consistent with Adkins [12] statement that the impeller annulus accounts for approximately one half of the measured stiffness values in Cal Tech test results. The results for K and c are obviously dissappointing; perhaps these coefficients depend more heavily on the impeller-diffuser interaction forces.

Conclusions and Extensions

An analysis has been developed for the forces on the shroud of an impeller. The "bulk-flow" nature of the analysis restricts its applicability to impellers having fairly small clearances between the impeller shroud and casing.

The results of the analysis are unexpected in that resonances of the fluid system are predicted at inlet tangential velocities which are higher than approximately 0.5 $R_i\omega$. Conventional rotordynamic-coefficient models are not an adequate representation of rotor forces if the resonances are present. The resonance phenomenon predicted by this analysis are in qualitative agreement with recent measurements from Cal Tech [14].

Rotordynamic-coefficients predictions from this analysis are in reasonable agreement with test results from Bolleter et al. [7], for the direct damping and cross-coupled stiffness coefficients, C and k.

The analysis which was developed in this paper for impeller shrouds can also be applied to seals and provides an expanded capability with respect to clearances as a function of axial or path coordinate. Prior analyses have been developed for either constant-clearance or convergent-tapered seals. The present analysis would apply for any continuously varying clearance function. This option can be directly used to account for elastic deformation of the seal bore due to pressure or other loading. It also provides possibilities for optimizing the clearance function to maximize stiffness, damping, etc.

The addition of shear-stress contributions in the present analysis made very little difference in seal calculations. As yet, no comparisons have been made on impeller force calculations with and without the shear-stress contributions.

The importance of the moment coefficients, which are defined by the represent analysis, are as yet undetermined. Current rotordynamic codes are not yet up to accept these coefficients; however, a code is under development at TAMU which will account for these coefficients and can be used to determine their importance.

The significance of the "resonance" phenomenon, which is predicted by the present analysis, on rotordynamics also remains unsettled. An analysis of the phenomenon is planned which will include curvefitting the $f_{rq}(f)$ and $f_{\theta q}(f)$ predictions and examining their influence on a Jeffcott rotor model.

The present analysis can be readily extended to account for axial force coefficients. An extension of this nature is projected for the coming year.

APPENDIX A

Perturbation Coefficients

$$A_{1s} = [\sigma_s(1-ms) + \sigma_r\,(1-mr)]\;u_{so}^2/2h_o$$

$$A_{2s} = -\frac{2u_{\theta o}}{r}\,\frac{dr}{ds}/b^2 + [\sigma_r\,(mr+1)\,\beta_o + \sigma_s\,(ms+1)\,\beta_1]\;u_{so}/2$$

$$A_{3s} = \frac{du_{so}}{ds} + [(2+mr)\,\sigma_r + (2+ms)\,\sigma_s]\;u_{so}/2$$

$$-[(1+mr)\,\sigma_r\,\beta_o\,(u_{\theta o}-r) + (1+ms)\,\sigma_s\,\beta_1\,u_{\theta o}]\;/2$$

$$2A_{1\theta} = u_{so}\,[(1-mr)\,(u_{\theta o}-r)\,\sigma_r + (1-ms)\,u_{\theta o}\,\sigma_s + 2\,\frac{u_{\theta o}}{r}\,\frac{dr}{ds}]/ho$$

$$2A_{2\theta} = u_{so}\,(\sigma_r+\sigma_s) + \sigma_r\,(mr+1)\,(u_{\theta o}-r)\,\beta_o + 2\,\frac{u_{so}}{r}\,\frac{dr}{ds}$$

$$+\;\sigma_s\,(ms+1)\,u_{\theta o}\,\beta_1$$

$$2A_{3\theta} = \sigma_r\ (u_{\theta o}-r)\ [mr - (1+mr)\ \beta o\ (u_{\theta o}-r)/u_{so}]$$
$$+\ \sigma_s\ u_{\theta o}\ [ms - (1+ms)\ \beta 1\ u_{\theta o}/u_{so}]$$

$$\beta_o = (u_{\theta o}-r)/b^2u_{so}\ \{1 + [(u_{\theta o}-r)\ /bu_{so}]^2\}$$

$$\beta_1 = u_{\theta o}/b^2u_{so}\ [1 + (u_{\theta o}/bu_{so})^2]$$

$\tau_{r\theta}$ Perturbation Coefficients

$$B_{\theta 1} = \lambda_r\ (1+mr)(u_{\theta o}-r)[1-\beta_o(u_{\theta o}-r)/u_{so}]/2b$$

$$B_{\theta 2} = \lambda_r\ [u_{so}+(1+mr)(u_{\theta o}-r)\beta o]/2b$$

$$B_{\theta 3} = \lambda_r\ mr\ (u_{\theta o}-r)u_{so}/2bh_o$$

τ_{rs} Perturbation Coefficients

$$B_{s1} = \lambda_r[(2+mr)\ u_{so} - (1+mr)\ \beta_o\ (u_{\theta o}\ -r)]/2$$

$$B_{s2} = \lambda_r(1+mr)\ \beta_o\ u_{so}/2$$

$$B_{s3} = \lambda_r m_r u_{so}{}^2/2h_o$$

REFERENCES

1. Lomakin, A., "Calculation of Critical Speed and Securing of the Dynamic Stability of the Rotor Hydraulic High Pressure Machines with Reference to Forces Arising in Seal Gaps," *Energomashinostroenie*, Vol. 4, 1958.

2. Childs, D., and Kim, C-H., "Test Results for Round-Hole-Pattern Damper Seals: Optimum Configurations and Dimensions for Maximum Net Damping," 85-Trib-16, ASME-ASLE Joint Lubrication Conference, Atlanta, GA, 8-10 October, 1985; also recommended for *ASME Trans., Jl. of Tribology Technology*.

3. Childs, D., and Kim, C-H., "Analysis and Testing for Rotordynamic Coefficients of Turbulent Annular Seals with Different Directionally Homogeneous Surface Roughness Treatment for Rotor and Stator Elements," *ASME Trans. Journal of Tribology Technology*, Vol. 107, July 1985, pp. 296-306.

4. von Pragenau, G. L., "Damping Seals for Turbomachinery," NASA Technical Paper 1987, 1982.

5. Jery, B., Acosta, A. J., Brennen, C. E., Caughey, T. K., "Hydrodynamic Impeller Stiffness, Damping and Inertia in the Rotordynamics of Centrifugal Pumps," Proceedings of Workshop on Rotordynamics Instability Problems in High Performance Turbomachinery, Texas A&M University, College Station, TX, NASA Conference Publication 2338, May 1984, pp. 137-160.

6. Ohashi, H., and Shoji, H., "Lateral Fluid Forces Acting on a Whirling Centrifugal Impeller in Vaneless and Vaned Diffuser," Proceedings of Workshop on Rotordynamics Instability Problems in High Performance Turbomachinery, Texas A&M University, College Station, Texas, NASA Conference Publication 2338, May 1984, pp. 109-122.

7. Bolleter, U., Wyss, A., Welte, I., and R. Sturchler, "Measurement of Hydrodynamic Matrices of Boiler Feed Pump Impellers," ASME Paper 85-DET-147, 10th Biennial Conference on Mechanical Vibration and Noise, Cincinnati, Ohio, 10-13 September 1985.

8. Massey, I. C.,, "Subsynchronous Vibration Problem in High Speed Multistage Centrifical Pumps," Proceedings of the 14th Turbomachinery Symposium, Turbomachinery Laboratories, Mechanical Engineering Dept., Texas A&M University, College Station, Texas, October 22-24, 1985, pp. 11-16.

9. Childs, D., and Moyer, D., "Vibration Characteristics of the HPOTP (High Pressure Oxygen Turbopump) of the SSME (Space Shuttle Main Engine)." ASME Trans. J. of Engineering for Gas Turbine, and Power, Vol. 107, January 1985, pp. 152-159.

10. Childs, D. W., "Rotordynamic Moment Coefficients for Finite-Length Turbulent Seals;" Proceedings IFTOMM Conference on Rotordynamic Problems in Power Plants, 28 September - 1 October 1981.

11. Hirs, G. G., "A Bulk-Flow Theory for Turbulence in Lubricant Film," ASME Journal of Lubrication Technology, April 1973, pp. 137-146.

12. Adains, D. R., "Analyses of Hydrodynamic Forces on Centrifugal Pump Impellers," Report Number 200.23, California Institute of Technology, 1985.

13. Yamada, Y., "Resistance of Flow Through Annulus with an Inner Rotating Cylinder," Bul. JSME, 1962, Vol. 5., No. 18, pp. 301-310.

14. Franz, R. and Arndt, N., "Measurement of Hydrodynamic Forces on the Impeller of HPOTP of the SSME, Report Number E249.2, California Institute of Technology, March 1986.

$U_{\theta o}(0)/R_i\ \omega$	0.5	0.6	0.7
$U_{\theta o}(1)/R(1)\omega$	0.884	0.947	0.996
$\dot{m}$(Kg/sec)	4.03	3.75	3.44
$R_{ao} = 2V_iC_i/\nu$	73,300	68,100	62,600

Table 1. Zeroth-order-solution results for the conventional-wear-ring impeller.

	Measured	Theory Face-Seal Impeller
K(N/m)	-.5×106	$-.042\times10^6$
k(N/m)	.6×106	$.288\times10^6$
C(N sec/m)	2570*	2020
c(N sec/m)	7610	2290
M (kg)	29.6	8.96
m (kg)	10.8	-0.009

*Combined viscous and hysteretic damping.

Table 2. Theory versus experiment for the face-seal impeller.

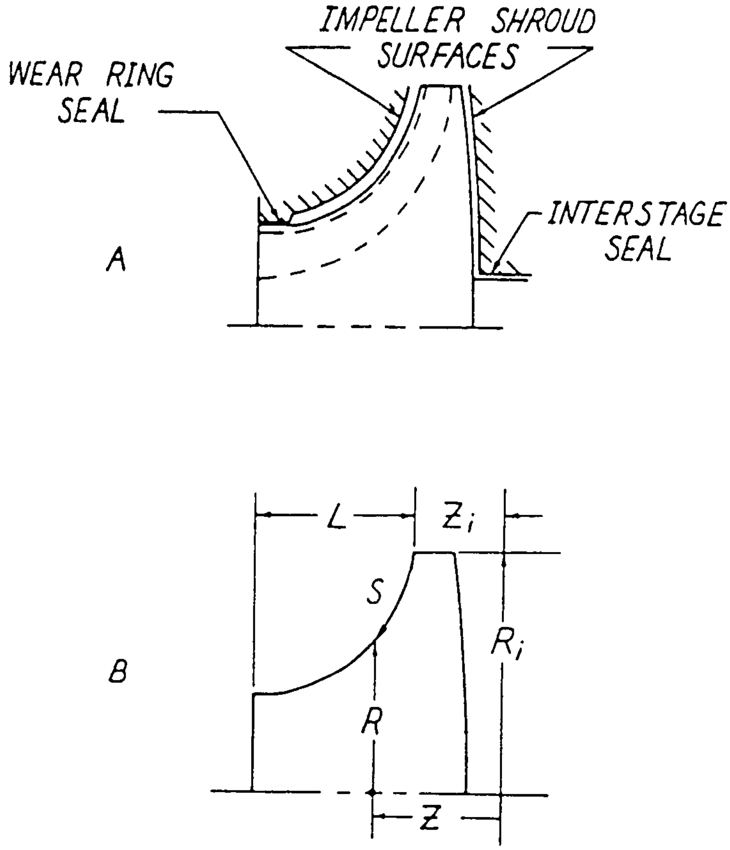
IMPELLER SHROUD SURFACES
WEAR RING SEAL
INTERSTAGE SEAL
A
L
Z$_i$
S
R_i
B
R
Z

Figure 1. Impeller stage.

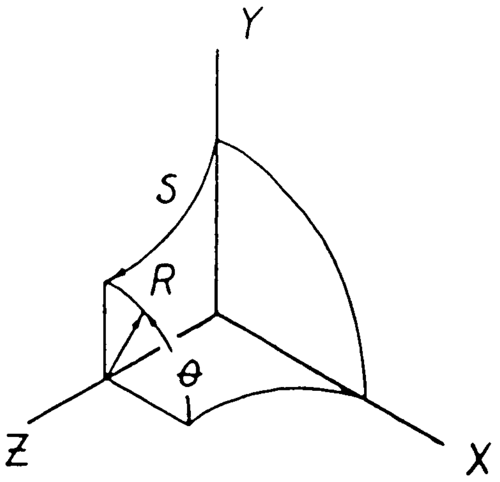

Figure 2. Impeller surface geometry.

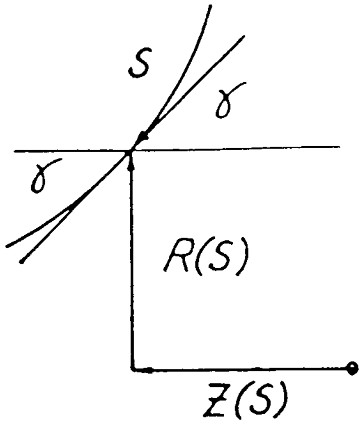

Figure 3. Local attitude angle of impeller surface.

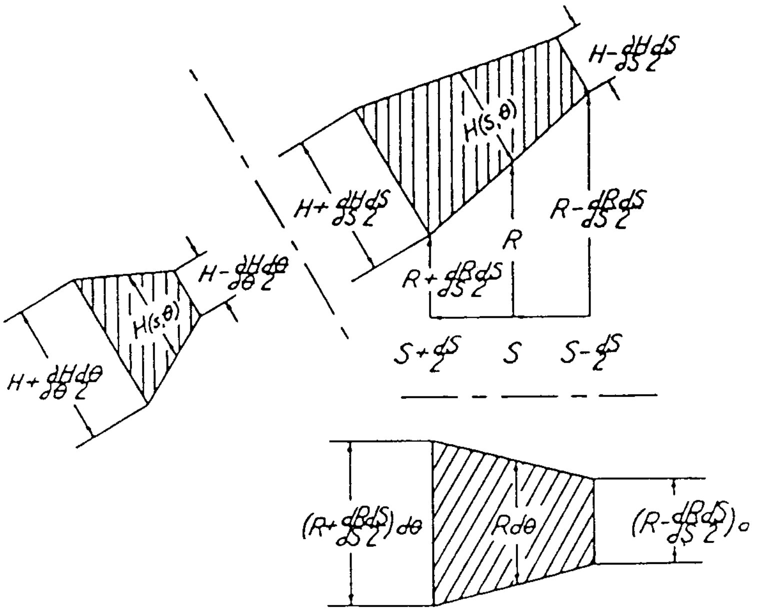
$H-\frac{\partial H}{\partial S}\frac{dS}{2}$
$H(S,\theta)$
$H+\frac{\partial H}{\partial S}\frac{dS}{2}$
$R-\frac{\partial R}{\partial S}\frac{dS}{2}$
R
$R+\frac{\partial R}{\partial S}\frac{dS}{2}$
$H-\frac{\partial H}{\partial \theta}\frac{d\theta}{2}$
$H(s,\theta)$
$H+\frac{\partial H}{\partial \theta}\frac{d\theta}{2}$
$S+\frac{dS}{2}$
S
$S-\frac{dS}{2}$
$(R+\frac{\partial R}{\partial S}\frac{dS}{2})d\theta$
$Rd\theta$
$(R-\frac{\partial R}{\partial S}\frac{dS}{2})d\theta$

Figure 4. Differential-fluid element.

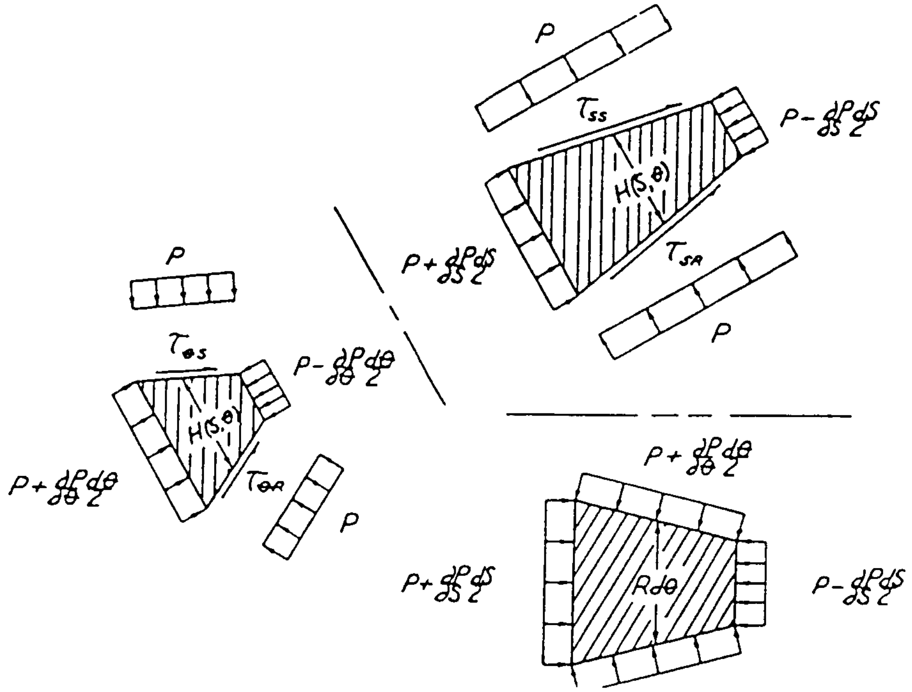
P
τ_{ss}
$P - \frac{\partial P}{\partial S}\frac{dS}{2}$
$H(S,\theta)$
τ_{sR}
$P + \frac{\partial P}{\partial S}\frac{dS}{2}$
P
P
$\tau_{\theta s}$
$P - \frac{\partial P}{\partial \theta}\frac{d\theta}{2}$
$H(S,\theta)$
$P + \frac{\partial P}{\partial \theta}\frac{d\theta}{2}$
$\tau_{\theta R}$
P
$P + \frac{\partial P}{\partial \theta}\frac{d\theta}{2}$
$P + \frac{\partial P}{\partial S}\frac{dS}{2}$
$R d\theta$
$P - \frac{\partial P}{\partial S}\frac{dS}{2}$

Figure 5. Free-body diagram for differential-fluid element.

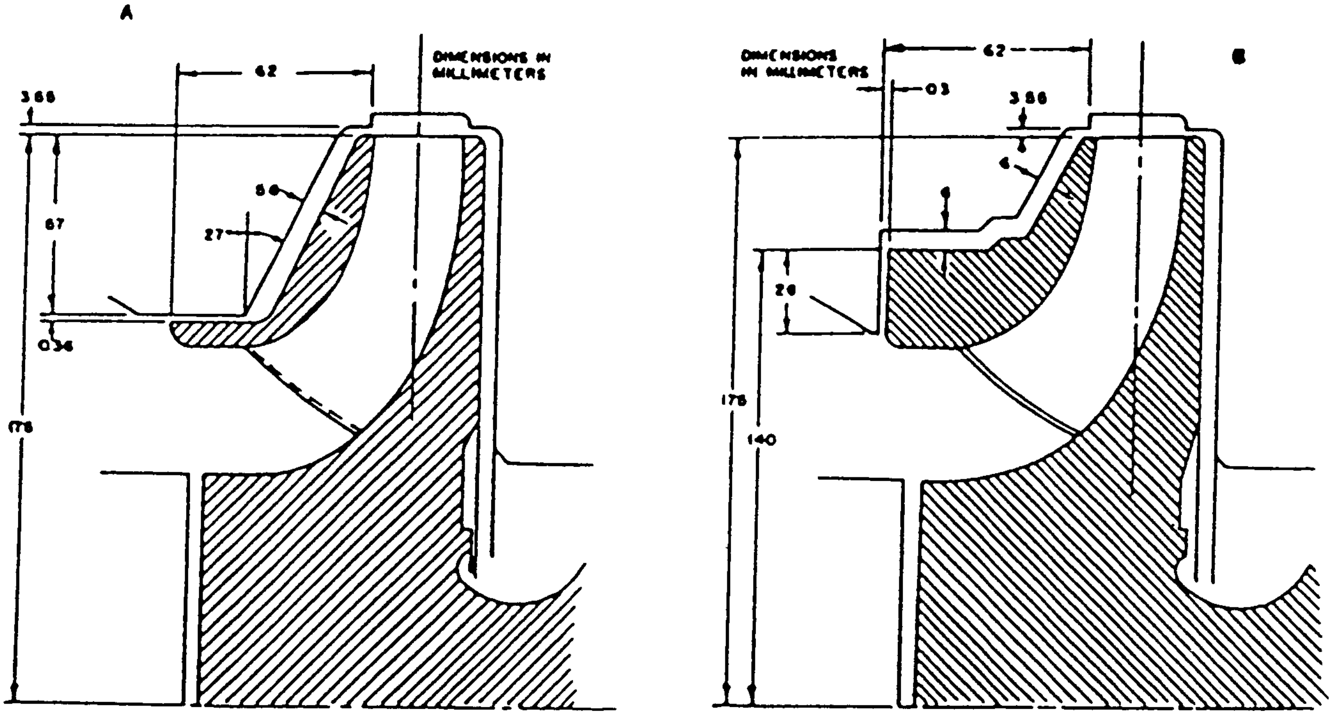
A
62
DIMENSIONS IN MILLIMETERS
3.66
67
56
27
0.36
178
DIMENSIONS IN MILLIMETERS
62
0.3
3.86
6
28
178
140
B

Figure 6. Nominal configuration of Sulzer test impeller [7] with conventional wear-ring seal.

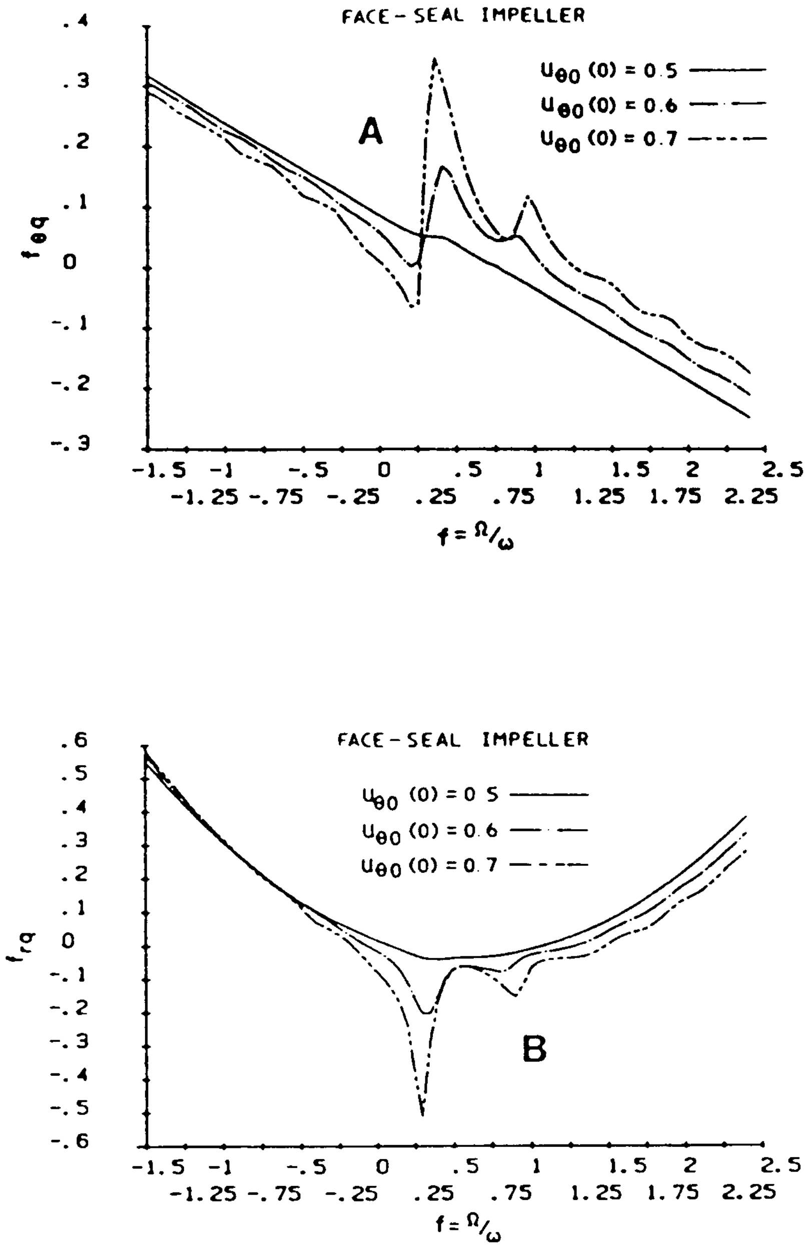

Figure 7. Nondimensional force coefficients for the face-seal impeller; A tangential-force coefficient, B radial-force coefficient.

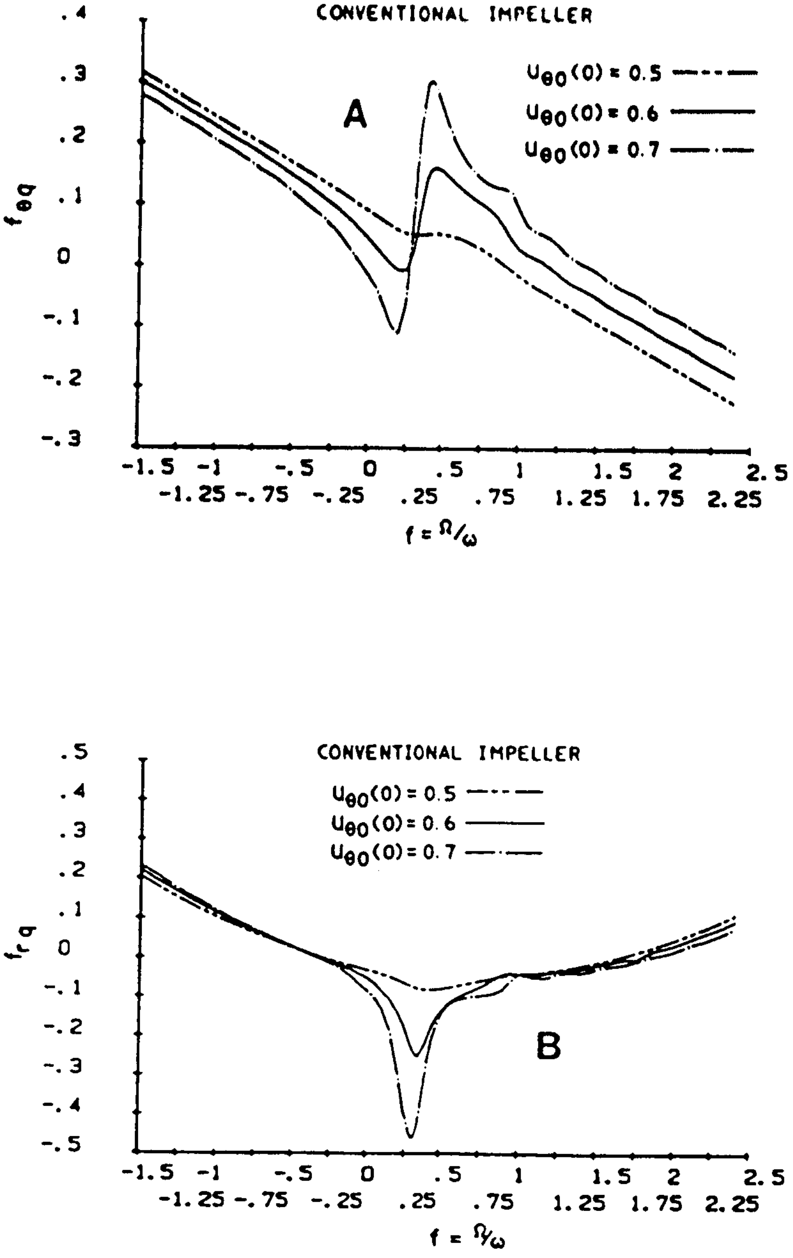

Figure 8. Nondimensional force coefficients for the conventional impeller; A tangential-force coefficient, B radial-force coefficient.

INFLUENCE OF TORSIONAL-LATERAL COUPLING ON STABILITY BEHAVIOR OF GEARED ROTOR SYSTEMS*

P. Schwibinger and R. Nordmann
University of Kaiserslautern
Kaiserslautern, Federal Republic of Germany

In high-performance turbomachinery trouble often arises because of unstable nonsynchronous lateral vibrations. The instabilities are mostly caused by oil-film bearings, clearance excitation, internal damping, annular pressure seals in pumps, or labyrinth seals in turbocompressors. In recent times the coupling between torsional and lateral vibrations has been considered as an additional influence. This coupling is of practical importance in geared rotor systems. The literature (refs. 1 and 2) describes some field problems in geared drive trains where unstable lateral vibrations occurred together with torsional oscillations. This paper studies the influence of the torsional-lateral coupling on the stability behavior of a simple geared system supported by oil-film bearings. The coupling effect is investigated by parameter studies and a sensitivity analysis for the uncoupled and coupled systems.

INTRODUCTION

The dynamic behavior of many rotating machines (e.g., turbines and compressor pumps) is influenced by the stiffness and damping characteristics of nonconservative effects such as oil-film forces, forces in seals, and clearing excitation forces. Besides the forced unbalance vibrations, unstable nonsynchronous vibrations caused by such self-exciting mechanisms may also occur. Usually the stability analysis for this turbomachinery is limited to a lateral rotor dynamic analysis that is carried out independently from the torsional vibration analysis. However, for geared rotor systems - that is, compressor or turbogenerator sets (fig. 1) - the torsional and lateral vibrations are coupled because of the offset centerlines of the geared rotors. Previously we did not know how much this coupling affected the stability of the machine.

In the literature we find several publications concerning torsional-lateral coupling in high-performance turbomachinery with gears. Wachel and Szenasi (ref. 1) describe a field problem in a geared system where unstable lateral vibrations occurred together with torsional oscillations. The authors do not describe the coupling mechanisms, but they point out the importance of gears for the exchange of energy between torsional and lateral vibrations. Similar instability phenomena were observed on different units. Yamada and Mitsui (ref. 2) deal with a two-stage ship gear supported by oil-film bearings. During operation with partial load the pinion ran unstably. A coupled torsional-lateral analysis limited to the gear stage shows that the oil-film

---

*This research work was supported by Deutsche Forschungsgemeinschaft, German Federal Republic.

bearings are the source of instability, but the stability threshold is decisively influenced by the torsional stiffness of the rotor system. Iannuzzelli and Elward (ref. 3) point out that certain measured eigenfrequencies of a compressor train can be verified only by an analytical model that considers the torsional-lateral coupling in a gear stage. Simmons and Smalley (ref. 4) found by experimental and analytical investigations of a gas turbine/compressor train that torsional modes (i.e., coupled torsional-lateral modes) with a superposed bending component at the gear wheel can be damped significantly by the oil-film bearings.

This paper investigates the influence of the torsional-lateral coupling in the gear on the stability behavior of a simple geared system (fig. 2). The coupling effect is analyzed by means of parameter studies and a sensitivity analysis for the uncoupled and coupled systems.

NATURAL VIBRATIONS OF GEARED ROTOR SYSTEM

Mechanical Model

Figure 1 shows a typical turbomachine consisting of two elastic shafts connected by a reduction gear. The rotors run in oil-film bearings. Usually the lateral vibration analysis (including a stability analysis) is carried out for both shafts separately and independently from the torsional rotor dynamics analysis. But in fact torsional and lateral vibrations of both rotors are coupled by the gear. To study whether this coupling may really be ignored in a stability analysis, we first consider a simple geared rotor system. Figures 2 and 3 show the model with two elastic shafts connected by a gear. The axes of the shafts are offset by the angle of mesh so that the tooth force acts in the vertical plane on the gear wheels. Both shafts are elastic for torsion and bending. Shaft 1 runs in two identical oil-film bearings that are the only source of instability in the system. Shaft 2 is supported rigidly. Note that not all the effects of the real machine can be investigated with the simple model. We concentrate on the coupling effect in the gear stage and its interaction with the self-excited vibrations of the vibration system.

In a gear a strong torsional-lateral coupling exists naturally because of the mechanism of power transmission. The torsional moment fed into the gear is transmitted by tooth forces. For that reason transverse forces and bending moments result from the torsional moment. Also the torsional and lateral displacements of the gear wheels are coupled kinematically (fig. 4), provided that both wheels maintain contact during operation. Without the lateral displacement of the gear wheels the kinematic relation in a gear stage is

$$r_1 q_1 = r_2 q_2 \tag{1}$$

This is the model commonly used in rotor dynamics analysis. If we allow lateral movement of the gear wheels, the geometric equation

$$r_1 q_1 + q_3 = r_2 q_2 + q_4 \tag{2}$$

implies a coupling of the torsional and lateral degrees of freedom.

From the theoretical considerations it is known that, for small vibrations of the journal bearings around a static equilibrium position, there is a linear force motion relation for the oil film (fig. 5):

$$\begin{bmatrix} \Delta f_1 \\ \Delta f_2 \end{bmatrix} = -\begin{bmatrix} c_{11} & c_{12} \\ c_{21} & c_{22} \end{bmatrix} \cdot \begin{bmatrix} \dot{q}_1 \\ \dot{q}_2 \end{bmatrix} - \begin{bmatrix} k_{11} & k_{12} \\ k_{21} & k_{22} \end{bmatrix} \begin{bmatrix} q_1 \\ q_2 \end{bmatrix} \tag{3}$$

where

k_{ik} stiffness coefficients of bearings

c_{ik} damping coefficients of bearings

The stiffness and damping coefficients depend on the rotational speed and the static load on the bearing. The resulting static equilibrium position of the shaft in the journal bearing is characterized by the dimensionless Sommerfeld number. In addition, the bearing coefficients depend on the load direction, which must be taken into consideration for geared rotors, where the gear transmission forces often make up an appreciable part of the bearing load. Available data for these coefficients assume a specific load direction (gravity load direction), but in a geared rotor system the load direction may be different because it is governed by the gear mesh forces. Hence, if the bearing geometry is such that the coefficients are sensitive to load direction, they must be calculated by solving the lubrication equation or by using an approximate formula (refs. 5 and 6). As the coefficients normally are obtained in a bearing coordinate system that does not coincide with the chosen system for the geared rotor, a transformation must be performed. Besides being anisotropic, the stiffness cross-coupling terms are generally unequal. This asymmetry is the reason for self-excited shaft vibrations.

For the statically indeterminate supported shaft in journal bearings, the calculation of the static load in the bearings leads to a nonlinear problem that has to be solved numerically. The reason for this is the nonlinear force-motion relation in the journals. In our study the static bearing loads due to the transmitted power and rotor weight are estimated with the rigidly supported shaft system.

An energy-flow diagram demonstrates how self-excited bending vibrations in a geared system may exchange energy with torsional oscillations by means of the gear mechanism (fig. 6). The main energy flows from the motor to the generator to transmit the required power for the unit. Because of shear forces in the oil film of the journal bearing, energy branches off from the main flow to the bearing, where it may dissipate from oil-film friction or may excite bending vibrations in the shaft and the gear. Because torsional and bending displacements are coupled in the gear stage, torsional oscillations of the geared rotor train also are excited. It is clear from these considerations that the stability behavior is affected by this energy exchange between the torsional and the lateral system.

Equations of Motion

To obtain the equations of motion for the simple shaft system (fig. 2) with N degrees of freedom, we apply the principle of virtual work. Using static deflection functions for the approximation of the displacements, we can discretize the model with continuous mass and stiffness distribution into disk, shaft, and bearing elements connected at their nodes. The resulting energy equation expresses that the sum of the virtual work done by the inertia, damping, stiffness, and external forces is equal to zero:

$$\delta\underline{q}^T \{ \underline{M}\,\underline{\ddot{q}} + \underline{D}\,\underline{\dot{q}} + \underline{K}\,\underline{q} - \underline{f}(t) \} = 0 \tag{4}$$

where

$\underline{M}$ (N x N)	mass matrix
$\underline{D}$ (N x N)	damping matrix
$\underline{K}$ (N x N)	stiffness matrix
$\underline{q}$ (N x 1)	vector of displacements
$\underline{f}$ (N x 1)	vector of external forces

To connect both shafts, we introduce the kinematic relation of equation (1) for the uncoupled system and of equation (2) for the torsional-lateral-coupled system by the matrix equation

$$\underline{q} = \underline{T} \cdot \underline{\tilde{q}} \tag{5}$$

where

$$\underline{q} = \left[\begin{array}{c} \cdot \\ \cdot \\ q_1 \\ q_2 \\ q_3 \\ q_4 \\ \cdot \\ \cdot \end{array}\right] \begin{array}{c} 1 \\ \cdot \\ \cdot \\ \cdot \\ \cdot \\ \cdot \\ \cdot \\ N \end{array} \quad \text{and} \quad \underline{\tilde{q}} = \left[\begin{array}{c} \cdot \\ \cdot \\ q_1 \\ q_3 \\ q_4 \\ \cdot \\ \cdot \end{array}\right] \begin{array}{c} 1 \\ \cdot \\ \cdot \\ \cdot \\ \cdot \\ \cdot \\ \tilde{N} \end{array}$$

and for the torsion-bending uncoupled case

$$\underline{T} = \begin{array}{c|c|c|c} & q_1 & & \\ \hline & \underline{E} \;\vdots & \underline{0} & 1 \\ \hline q_2 & \cdots\ \frac{r_1}{r_2}\ \cdots & & \vdots \\ \hline & \underline{0} & \underline{E} & N \\ \hline & 1 \;\ldots\ldots & \tilde{N} & \end{array}$$

and for the torsion-bending coupled case

$$\text{resp.} \quad \underline{T} = \begin{array}{c|c|c|c} & q_1 \quad q_2 & q_3 & 1 \\ \hline & \underline{E} \;\vdots & \vdots\ \underline{0}\ \vdots & \vdots \\ \hline q_2 & \cdots\ \frac{r_1}{r_2} & \frac{1}{r_2}\ \ -\frac{1}{r_2}\ \cdots & \vdots \\ \hline & \underline{0} & \underline{E} & N \\ \hline & 1 \;\ldots\ldots & \ldots\ldots\tilde{N} & \end{array}$$

where

$\tilde{N} = N - 1$ reduced number of degrees of freedom

$\tilde{\underline{q}}$ $(\tilde{N} \times 1)$ reduced vector of displacements

T $(N \times \tilde{N})$ coupling matrix

$\underline{E}$ matrix of unity

The application of the constraint equation (5) to equation (4) eliminates the torsional degree of freedom at one gear wheel (fig. 4) and yields the equation of motion for the coupled system:

$$\underbrace{\underline{T}^T \underline{M}\,\underline{T}\,\ddot{\tilde{\underline{q}}}}_{\tilde{\underline{M}}\,\ddot{\tilde{\underline{q}}}} + \underbrace{\underline{T}^T \underline{D}\,\underline{T}\,\dot{\tilde{\underline{q}}}}_{\tilde{\underline{D}}\,\dot{\tilde{\underline{q}}}} + \underbrace{\underline{T}^T \underline{K}\,\underline{T}\,\tilde{\underline{q}}}_{\tilde{\underline{K}}\,\tilde{\underline{q}}} = \underbrace{\underline{T}^T \underline{f}(t)}_{\tilde{\underline{f}}(t)} \tag{6}$$

The matrices $\tilde{\underline{K}}$ and $\tilde{\underline{D}}$ contain stiffness and damping terms for the bearings. They are asymmetric and depend on the running speed of the rotor and on the transmitted load. The external load may be caused by unbalance or by gear-mesh errors. Because our study is restricted to a stability analysis, we consider only the homogeneous equations of motion ($\tilde{\underline{f}} = 0$).

Lund (ref. 7) introduced a similar model for a geared train of rotors and mentioned the influence torsional-lateral coupling may have on the critical speeds, stability, and unbalance response of the system. But he focused more on the solution algorithm, which is a modified transfer matrix method, than on the discussion of the stability behavior.

Natural Vibrations - Eigenvalues and Natural Modes

The natural vibrations can be calculated from the homogeneous equations of motion ($\underline{\tilde{f}} = 0$).

Assuming a solution of the form $\underline{\tilde{q}}(t) = \underline{r} \cdot e^{\lambda t}$, we obtain the quadratic eigenvalue problem

$$(\lambda^2 \underline{\tilde{M}} + \lambda \underline{\tilde{D}} + \underline{\tilde{K}})\ \underline{r} = \underline{0} \tag{7}$$

with $2\tilde{N}$ eigenvalues λ_j and corresponding eigenvectors $\underline{r}_j$. In most cases eigenvalues as well as eigenvectors occur in conjugate complex pairs:

$$\begin{aligned} &\text{Eigenvalues} - \lambda_j = \alpha_j + i\omega_j \qquad && \bar{\lambda}_j = \alpha_j - i\omega_j \\ &\text{Eigenvectors} - \underline{r}_j = \underline{s}_j + i\underline{t}_j \qquad && \bar{\underline{r}}_j = \underline{s}_j - i\underline{t}_j \end{aligned} \tag{8}$$

We consider only the part of the solution that belongs to a conjugate complex pair:

$$\underline{\tilde{q}}_j(t) = B_j e^{\alpha_j t} \{\underline{s}_j \sin(\omega_j t + \gamma_j) + \underline{t}_j \cos(\omega_j t + \gamma_j)\} \tag{9}$$

where ω_j is the circular natural frequency of this part and α_j the damping constant. If the damping constant $\alpha_j > 0$, the natural vibrations increase and make the system unstable, if $\alpha_j < 0$, the natural vibrations decrease and the system runs stably.

For the torsional-lateral-coupled system the eigenvalues are composed of torsional-lateral-coupled damping constants and eigenfrequencies. The corresponding modes are set up by torsional and lateral components. We define the expression in braces of equation (9) as the natural mode. In contrast to conservative systems there is no constant modal shape: proportions and relative phasing generally vary from point to point at the shaft. The lateral components of one natural mode represent a time-dependent curve in space. The plane of motion of one point of the shaft has an elliptical orbit. The torsional components of one natural mode also twist the shaft along its axis.

If we transpose the matrices $\underline{\tilde{M}}$, $\underline{\tilde{D}}$, and $\underline{\tilde{K}}$, we obtain the so-called left-hand eigenvalue problem

$$\{\lambda^2 \underline{\tilde{M}}^T + \lambda \underline{\tilde{D}}^T + \underline{\tilde{K}}^T\}\ \underline{l} = \underline{0} \tag{10}$$

which has the same eigenvalues λ but different eigenvectors $\underline{l}$. Both eigenvector sets are needed to decouple the system matrices for the sensitivity analysis of the eigenvalues.

First the eigenfrequencies and modes for the rigidly supported system are calculated in the manner described. A similar system was studied by Iida (ref. 8). Because of its geometry (fig. 3), for bending purposes shaft 2 is very stiff as compared with shaft 1. Figure 7 shows the natural modes of vibration where the torsional displacement of shaft 1 is multiplied by the radius of gear wheel 1 and the twisting of shaft 2 is multiplied by the radius of gear wheel 2 to match the dimension with the bending. With this normalization the kinematic constraint equation (1) equation (2) can be verified at once from the plot of the eigenvectors, because the sum of torsional and lateral displacement at shaft 1 and shaft 2 must be equal at the gear mesh.

In the first mode the torsional displacement is rather predominant, but in the second and fourth modes it is comparable to the flexural displacement. In these two modes the eigenfrequencies of the torsional-lateral-coupled system differ about 15 and 5 percent, respectively, from the solutions of the uncoupled system. The third eigenvector lies in the x-y plane, which is perpendicular to the direction of the tooth force. Therefore for the rigidly supported system it is a completely decoupled bending mode.

When the coupling effect has such a strong influence on the eigenfrequencies, how does it affect the damping constants of the eigenvalues for the oil-film-supported system in figure 2? To answer this question, we calculate the eigenvalues for the uncoupled and coupled systems. Because the bearing coefficients depend on both the rotational speed and the static load on the journal, the eigenvalues change with the running speed and the transmitted load.

In figure 8, for the six lowest eigenvalues, the eigenfrequencies ($f = \omega/2\pi$ rpm) and damping coefficients ($a = \alpha/2\pi$ rpm) are plotted as a function of the rotational speed of shaft 1 for the uncoupled system (– – –) and for the torsional-lateral-coupled system (_____). In this diagram the static load on the bearings remains constant during the alteration of shaft speed. Static load is determined by the weight of the shaft and the transmitted moment M_M or M_G (fig. 3).

It is obvious that most of the eigenfrequencies change only little and that they almost coincide with the solutions for the rigidly supported system. The reason for this is that the oil-film bearings in the investigated speed range are relatively stiff as compared with the elasticity of the shaft. Exceptions are the two whirling frequencies, which grow linearly with the rotor speed. Their frequency is approximately one-half the speed of shaft 1. They belong to highly damped modes where the movement of the oil-film-supported shaft represents a conical whirl in one of the two bearings.

In some modes the frequencies for the uncoupled and torsional-lateral-coupled systems differ essentially (e.g., the second frequency of the coupled system is about 15 percent lower than that for the uncoupled system). Figure 9 shows the strong torsional-lateral coupling in the corresponding eigenmode in contrast to the first eigenvector, which remains an almost pure torsional mode even in the coupled model.

The coupling affects not only the eigenfrequencies and modes but also the damping constants (fig. 8). The zero passage of one damping coefficient indicates the stability threshold of the system. In the uncoupled system all the damping constants for the bending modes are negative up to a threshold speed of 3745 rpm, where the first bending mode (f_2 = 2157 rpm) becomes unstable. It proves that the dangerous positive damping constants occur at the lower bending eigenvalues. Because we have not introduced additional torsional damping, the damping constants for the torsional modes (f_1 = 821 rpm, f_4 = 4370 rpm) are equal to zero.

In the torsional-lateral-coupled system the lateral motion of the shaft in the journals may contribute additional damping to the torsional modes (fig. 6). An additional negative damping is in general desirable, but a positive damping, which may destabilize the torsional modes, is also possible. Figure 8 indeed shows that the first weakly coupled torsional eigenvalue (f_1 = 812 rpm) becomes slightly unstable at 1740 rpm. Obviously the instability whirl tends to lock in at the lowest system frequency, which in the coupled case may be a bending or a torsional mode. Because negative torsional damping is always present in real machines (material damping, damping of the surrounding media), the slight torsional instability of our coupled model would not occur in practice. The next eigenvalue, which becomes clearly unstable at 3510 rpm, belongs to the second strongly torsional-lateral-coupled mode (f_2 = 1871 rpm). Its threshold speed is 7 percent lower than in the uncoupled case. In addition, the third eigenvalue, which remains stable in the uncoupled case, becomes unstable at a rotational speed of 4150 rpm in the torsional-lateral-coupled model. The corresponding eigenfrequency and eigenvector (an almost pure bending mode lying in the x-y plane, which is perpendicular to the plane of tooth force action) nearly coincide with the solutions of the uncoupled system (fig. 7). Therefore we conclude that although we cannot recognize a strong torsional-lateral coupling in the frequencies and modes, the coupling may still affect the stability behavior. This effect is due to the energy exchange between the torsional and bending vibrations at the gear mesh (fig. 6).

It is important to note that the instability onset speed of the uncoupled and the torsional-lateral-coupled systems are not equal. The coupling mechanism in gears may essentially lower the threshold speed. Classical uncoupled stability analysis indicates that the system becomes unstable at the lowest lateral threshold speed of the individual rotors. In a coupled analysis the actual stability threshold may occur in a torsional or a strongly torsional-lateral-coupled mode of the complete system.

DISCUSSION OF STABILITY BEHAVIOR

In a classical vibration analysis, which ignores the coupling between torsional and lateral vibrations in gears, the torsional critical speeds are only sensitive to torsional system parameters whereas the lateral eigenvalues of an individual rotor depend only on its bending parameters. We use the expression "torsional parameter" in this context for rotary inertia or torsional stiffness and "bending parameters" for quantities such as mass or flexural stiffness. If we consider torsional and bending vibrations as coupled in the gear, an eigenvalue is generally sensitive to torsional and bending parameters of all shafts. The effect of the coupling on the stability behavior of the complete rotor system can therefore be studied by answering the questions

(1) How do modifications of torsional and bending system parameters change the stability threshold? (Parameter study)

(2) How do changes of torsional and bending system parameters affect the damping constant of the eigenvalues? (Sensitivity analysis)

Parameter Studies

For the parameter study two torsional parameters and two bending parameters of the simple shaft system were selected (fig. 10). Figures 11 and 12 show how the stability threshold speed due to the zero passage of the second eigenvalue (real part) changes when the chosen system parameters are varied. As a reference model we take the torsional-lateral-coupled model with the data of figure 3. Its second eigenvalue becomes unstable at a speed of 3510 rpm. The question is now: How do respective torsional bending parameters affect this instability onset speed?

Figure 11 shows the influence of the torsional stiffness $\hat{k}_2$ and rotary inertia Θ_2 of shaft 2. Of course the torsional parameters do not change the stability threshold in the uncoupled model. In the coupled case, the rise of the torsional stiffness $\hat{k}_2$ stabilizes the second eigenvalue, but a higher rotary inertia Θ_2 destabilizes it. At first sight (fig. 11) it appears that a torsionally stiffer shaft 2 would make the system more stable. But when the second eigenvalue becomes more stable, the first eigenvalue is destabilized; therefore the stability threshold of the coupled system is lowered by an increased torsional stiffness. Decreasing the rotary inertia Θ_2 produces similar results. This effect is ignored in figure 11 because only the real part of the second eigenvalue is considered.

Figure 12 shows that the influence of the bending parameters on the threshold speed for the second eigenvalue is much stronger than the influence of the torsional parameters. It is again interesting to note that the instability onset speed essentially depends on whether an uncoupled or a torsional-lateral-coupled model is used. In our case a stiffer shaft 1 (k_1) with a smaller mass m_1 makes the system more stable. In both cases the stability threshold for the coupled model is lower than for the uncoupled one.

We conclude from this study that the stability threshold speed is substantially influenced (1) by the model used in the coupled or uncoupled case and (2) by the torsional and bending system parameters in the coupled case. This fact indicates a strong torsional-lateral coupling relation to the stability behavior.

Sensitivity Analysis

As a second tool to investigate the influence of the torsional-lateral coupling, we used a sensitivity analysis of the eigenvalues. This method yields so-called influence coefficients, which describe the change of an eigenvalue λ_n caused by a small modification of a system parameter p_k. The influence coefficients for the real parts of the eigenvalues express how sensitive the stability of the system is to parameter changes. The stability threshold of an uncoupled model is only affected by the bending parameters of the individual rotors. In contrast to that for the torsional-lateral-coupled system, an eigenvalue is generally influenced by torsional and bending parameters of all shafts. Therefore by the aid of the sensitivities of the real eigenvalue parts for the uncoupled and coupled systems, the influence of the torsional-lateral coupling on the stability behavior can be discussed.

This sensitivity analysis is based on an expansion of the eigenvalues in terms of the generalized system parameters p_k, where the p_k may be mass, damping, stiffness, or even physical parameters, for example, bearing clearance (ref. 8):

$$\lambda_n = \lambda_{n,o} + \frac{\partial\lambda_n}{\partial p_{1/o}} \cdot \Delta p_1 + \frac{\partial\lambda_n}{\partial p_{2/o}} \cdot \Delta p_2 + \ldots \frac{\partial\lambda_n}{\partial p_{k/o}} \cdot \Delta p_k \tag{11}$$

Truncation of Taylor's expansion after the first derivatives leads to a linear approximate formula. It is shown in references 8 to 10 that the eigenvalue derivatives can be expressed by the eigenvalues, by the left- and right-hand eigenvectors of the original system (subscript o), and by derivatives of the system matrices $\underline{\tilde{M}}$, $\underline{\tilde{D}}$, and $\underline{\tilde{K}}$ to the parameters p_k (subscript k).

$$\frac{\partial\lambda_n}{\partial p_{k/o}} = -\underline{l}_n^T \left(\lambda_n^2 \cdot \underline{\tilde{M}}_{,k} + \lambda_n \underline{\tilde{D}}_{,k} + \underline{\tilde{K}}_{,k}\right) \underline{r}_{n/o} = g_{n,k} \tag{12}$$

The eigenvectors must be normalized in a special way (ref. 10). The derivatives are also called influence coefficients.

For the simple gear model we start from a point near the stability threshold speed and investigate how particular parameters affect the stability behavior. Figure 13 shows the influence of the torsional stiffness $\hat{k}_2$ on the real and the imaginary part of the second eigenvalue. It can be seen that increasing the torsional stiffness has a stabilizing effect on the second eigenvalue. The corresponding influence coefficient calculated with the given linear formula is indicated by the tangent to the curve.

Figure 14 contains influence coefficients for the elements used in our gear model such as disks, journal bearings, and beams. The influence coefficients in equation (12) represent an absolute measure for the changes of the complex eigenvalues $\lambda_n = \alpha_n + i\omega_n$ caused by parameter modifications.
By means of these coefficients a relative measure, the nondimensional sensitivity, can be defined:

$$\begin{aligned} \frac{\Delta\alpha_n/|\alpha_n|}{\Delta p_k/p_k} &= S_{n,k}^{\alpha} = \mathrm{Re}(g_{n,k}) \cdot \frac{p_k}{\alpha_n} \\ \frac{\Delta\omega_n/\omega_n}{\Delta p_k/p_k} &= S_{n,k}^{\omega} = \mathrm{Im}(g_{n,k}) \frac{p_k}{\omega_n} \end{aligned} \tag{13}$$

where $S_{n,k}^{\alpha}$ is the nondimensional sensitivity of the damping coefficient and $S_{n,k}^{\omega}$, of the natural frequency. This presentation has the great advantage that the influence of several parameters on different modes can be compared immediately.

To show the influence of torsional and bending system parameters on the stability behavior of our rotor system, relative sensitivities for the real part of the second eigenvalue were calculated near the threshold speed of the uncoupled and coupled models (n_1 = 3680 rpm) and are plotted in figure 15. It is important to note that the values of the relative sensitivities for the uncoupled and coupled models are different.

Of course in the uncoupled model the torsional parameters do not affect the real part of the second eigenvalue, which belongs to a pure bending mode. The corresponding sensitivities are therefore equal to zero.

Nevertheless in the uncoupled model changes of the bending parameters of shaft 1 have a strong influence on the real part of the second eigenvalue. Because the oil-film bearings are relatively stiff as compared with the bending stiffness of shaft 1, the changes of the shaft parameters (e.g., bending stiffness, mass of the pinion) have a much stronger effect on the damping constant than do the bearing parameters (e.g., clearance Ψ). In the uncoupled case the bending of the rigidly supported shaft 2 is not related to the oil-film-supported shaft 1, which becomes unstable. Therefore the bending parameters of shaft 2 have no influence on the stability behavior.

In the coupled model it is obvious that changes of the torsional parameters can have a strong influence on the real part of the second eigenvalue. A comparison of the different torsional parameters points out that the main influence is from the torsional parameters of shaft 2. Their relative sensitivities are much greater than those of the torsional parameters of shaft 1. A look at the torsional components of the corresponding second mode makes the reasons clear: shaft 2 shows a maximum displacement because of torsion at the gear wheel and is much more twisted than shaft 1.

The sensitivity of the torsional stiffness has a negative sign. An increasing stiffness stabilizes the rotor system, as we have already seen in the parameter study (figs. 11 and 13). The rotatory inertia of the second gear wheel and of the generator have a positive sensitivity. Increasing values of this parameter have a destabilizing effect (fig. 11).

Changes of the bending parameters have a stronger effect on the real part of the second eigenvalue than do the torsional parameters. Because the bending of shaft 2 is for the coupled model connected to the oil-film-supported shaft 1 by the coupling equation (2), its parameters also influence the stability behavior of our model. But as shaft 2 is almost too rigid to bend in the second mode the influence coefficients of its parameters (e.g., mass of the wheel and lateral stiffness) are relatively small.

Obviously the dimensionless sensitivities of the bending parameters of shaft 1 differ essentially from the values of the uncoupled model. For example, the influence coefficient of the clearance for the right bearing in the coupled case is of about the same magnitude as that in the uncoupled case but has the opposite sign. The sensitivities of the bending stiffness and the mass of the pinion are essentially smaller than those in the uncoupled model.

The results show that the stability behavior of our model is particularly influenced by the bending parameters of shaft 1 and the torsional parameters of shaft 2. The differences in the solutions for the sensitivities in the uncoupled and coupled models indicate that the torsional-lateral coupling must not be neglected in discussing the stability behavior of geared rotors.

CONCLUSIONS

In this paper a study of the stability behavior is given for a simple geared shaft system. It is shown that the classical eigenvalue analysis, which ignores the coupling of torsional and lateral vibrations in gears, may lead to serious errors in the prediction of the stability onset speed, the critical speeds, and the natural modes. Also it does not account for the damping of the torsional modes, which is attributed to the lateral motions in the journals.

The strong relation of torsional-lateral coupling to stability behavior is proven by parameter studies and sensitivity analysis, which show the influence of torsional and bending system parameters on the stability threshold and damping constants.

The analytical results for the simple geared model remain to be verified by experimental investigations and extended to more complex rotor systems.

REFERENCES

1. Wachel, J.C.; and Szenasi, F.R.: Field Verification of Lateral-Torsional Coupling Effects on Rotor Instabilities in Centrifugal Compressors. NASA CP-2147, 1980.

2. Yamada, T.; and Mitsui, J.: A Study on the Unstable Vibration Phenomena of a Reduction Gear system, Including the Lightly Loaded Journal Bearings for a Marine Steam Turbine. Bull. JSME, Vol. 22, No. 163, 1979.

3. Iannuzzelli, R.J.; and Elward, R.M.: Torsional-Lateral Coupling in Geared Rotors. ASME No. 84-GT-71, 1984.

4. Simmons, H.R.; and Smalley, A.J.: Lateral Gear Shaft Dynamics Control Torsional Stresses in Turbine Driven Compressor Train. ASME No. 84-GT-28, 1984.

5. Dubois, G.B.; and Ocvirk, F.W.: Analytical Derivation and Experimental Evaluation of Short-Bearing Approximation for Full Journal Bearings. NACA Report 1157, 1953.

6. Ott, H.H.: Zylindrisches Gleitlager bei instationärer Belastung. Dissertation ETH Zurich, 1948.

7. Lund, J.W.: Critical Speeds, Stability and Response of a Geared Train of Rotors. ASME No. 77-DET-30, 1977.

8. Iida, H.; Tamura, A.; Kikuch, K; and Agata, H.: Coupled Torsional-Flexural Vibration of a Shaft in a Geared System of Rotors. Bull. JSME, Vol. 23, No. 1986, Dec. 1980.

9. Glienicke, J.: Feder- und Dampfungskonstanten von Gleitlagern und deren Einfluss auf das Schwingungsverhalten eines einfachen Rotors. (Stiffness and Damping Coefficients in Journal Bearings). Thesis TH Karlsruhe, 1966.

10. Fritzen, C.P.; and Nordmann, R.: Influence of Parameter Changes to the Stability Behavior of Rotors. Rotordynamic Instability Problems in High-Performance Turbomachinery. NASA CP-2250, 1982.

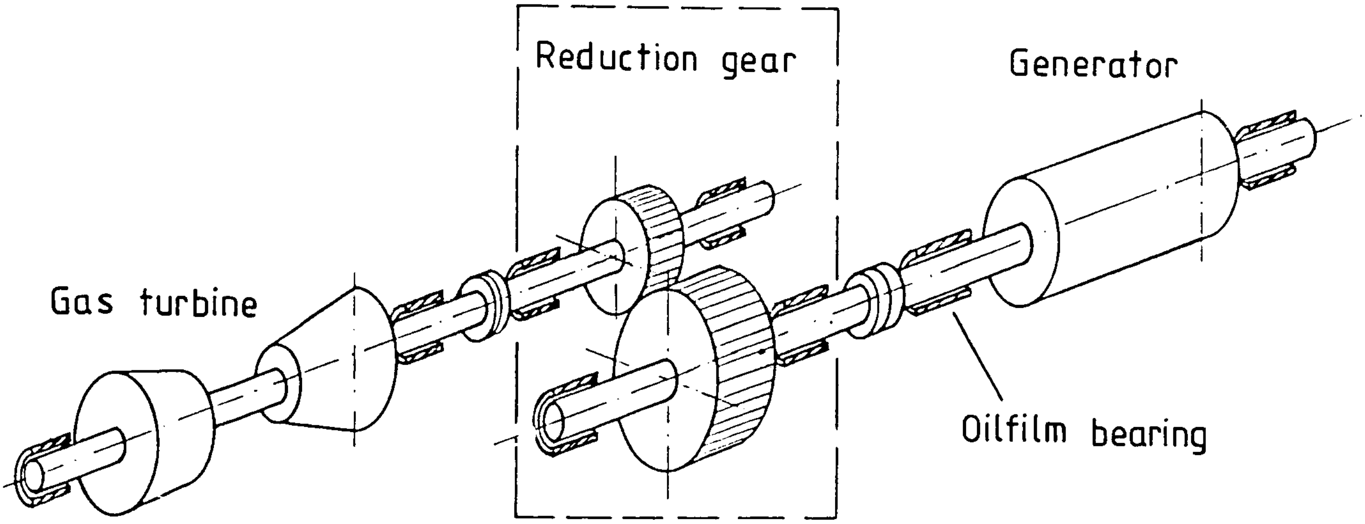
Reduction gear
Generator
Gas turbine
Oilfilm bearing

Figure 1. - Reduction gear in a turbogenerator set.

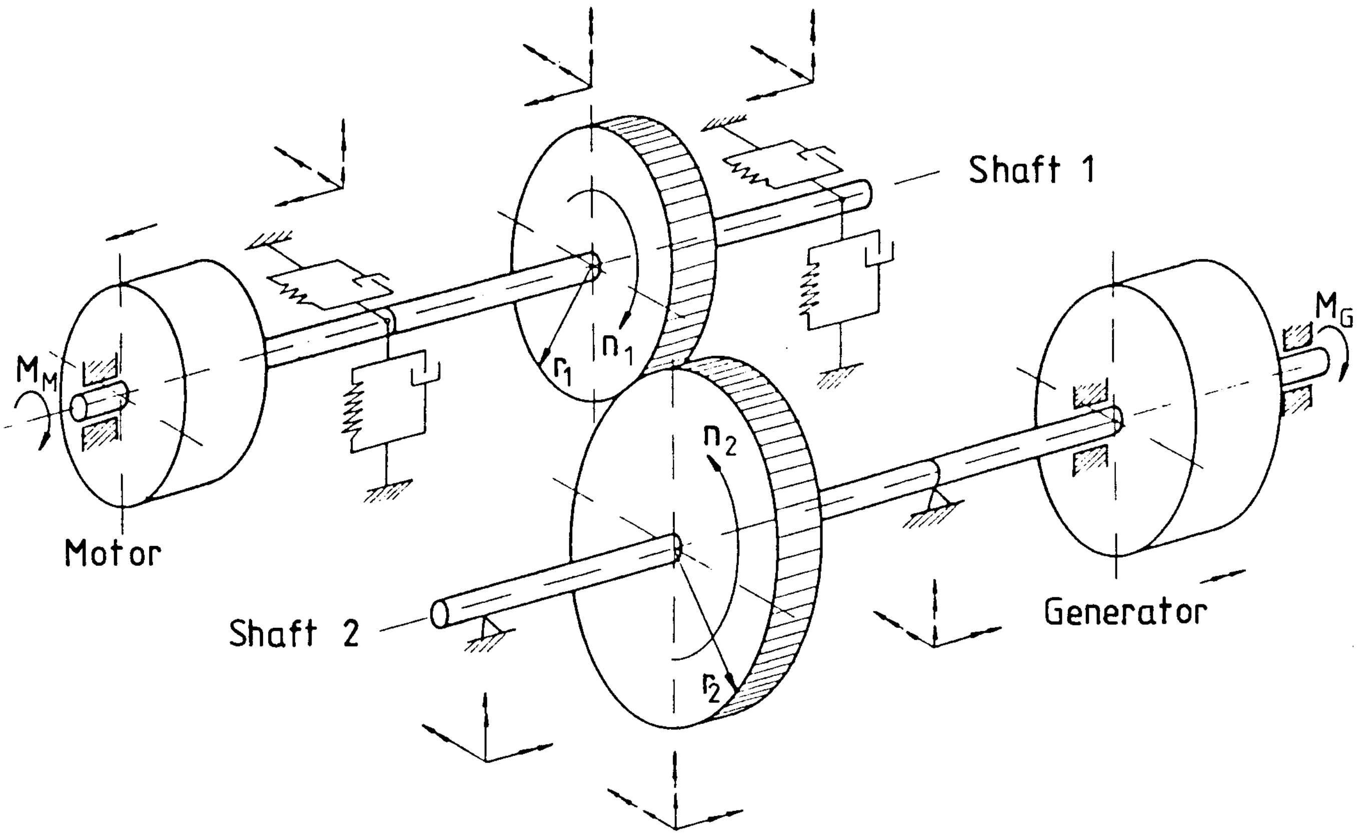
Shaft 1
M_M
M_G
r_1
n_1
n_2
r_2
Motor
Shaft 2
Generator

Figure 2. - Model of a geared rotor system.

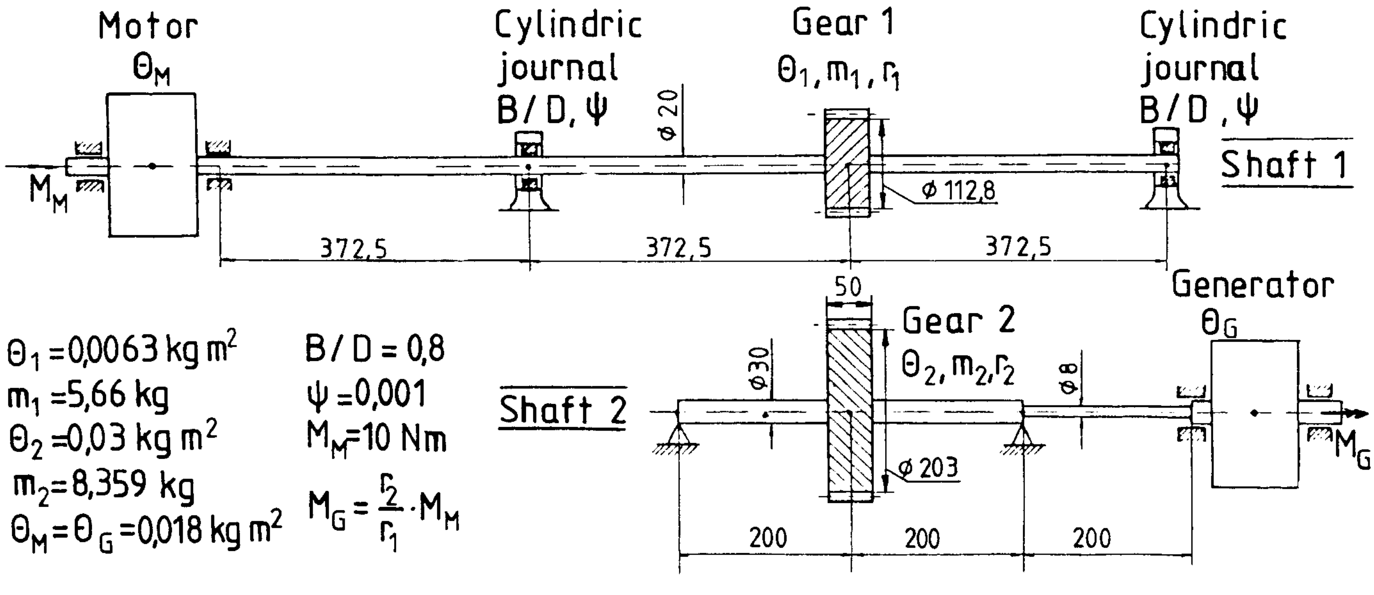
Motor
Θ_M
Cylindric journal
B/D, ψ
ϕ 20
Gear 1
Θ_1, m_1, r_1
Cylindric journal
B/D, ψ
Shaft 1
M_M
ϕ 112,8
372,5
372,5
372,5
50
Generator
Θ_G
Gear 2
Θ_2, m_2, r_2
ϕ30
ϕ8
Shaft 2
ϕ 203
M_G
200
200
200
$\Theta_1 = 0{,}0063$ kg m²
$m_1 = 5{,}66$ kg
$\Theta_2 = 0{,}03$ kg m²
$m_2 = 8{,}359$ kg
$\Theta_M = \Theta_G = 0{,}018$ kg m²
B/D = 0,8
ψ = 0,001
$M_M = 10$ Nm
$M_G = \frac{r_2}{r_1} \cdot M_M$

Figure 3. - Data for the geared rotor system.

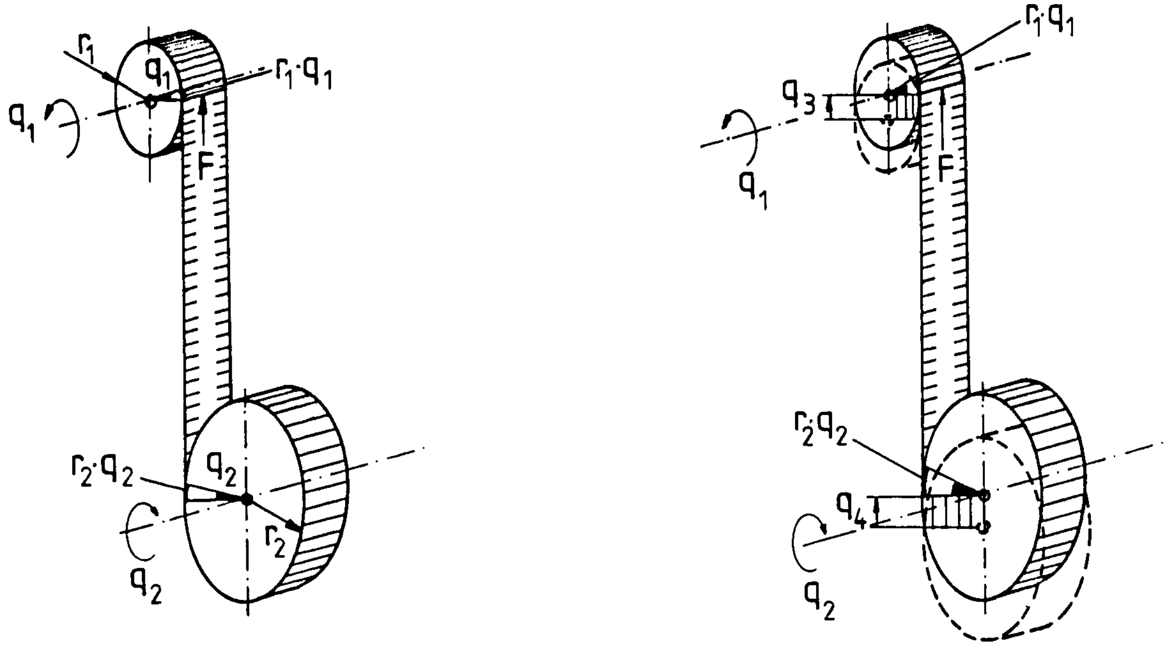
r1
q1
r1·q1
q1
F
r2·q2
q2
r2
q2
r1·q1
q3
q1
F
r2·q2
q4
q2

Kinematic constraint without lateral displacement of gear wheels

$\boxed{r_1 q_1 = r_2 q_2}$

Kinematic constraint with lateral displacement of gear wheels

$\boxed{r_1 q_1 + q_3 = r_2 q_2 + q_4}$

Figure 4. - Kinematic constraints in a gear stage.

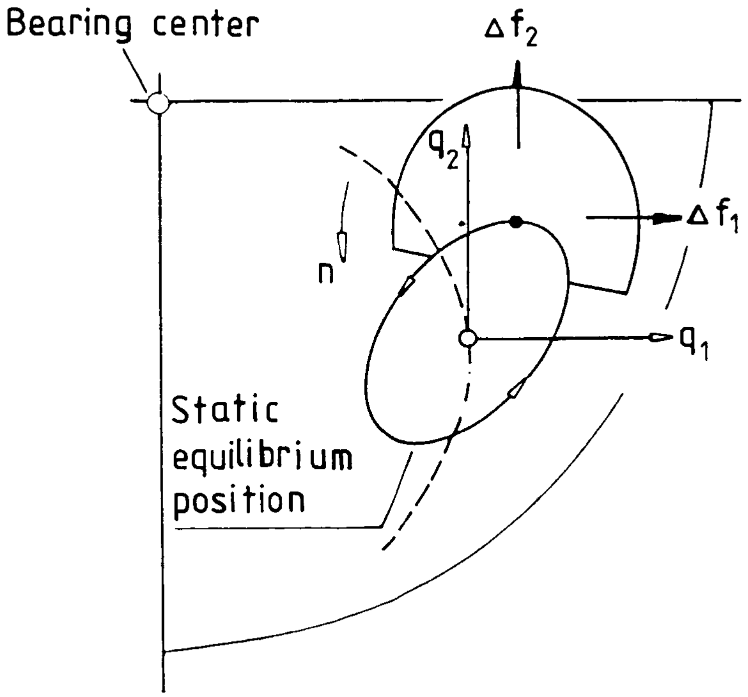
Bearing center
Δf2
q2
Δf1
n
q1
Static equilibrium position

Figure 5. - Vibrations of the journal.

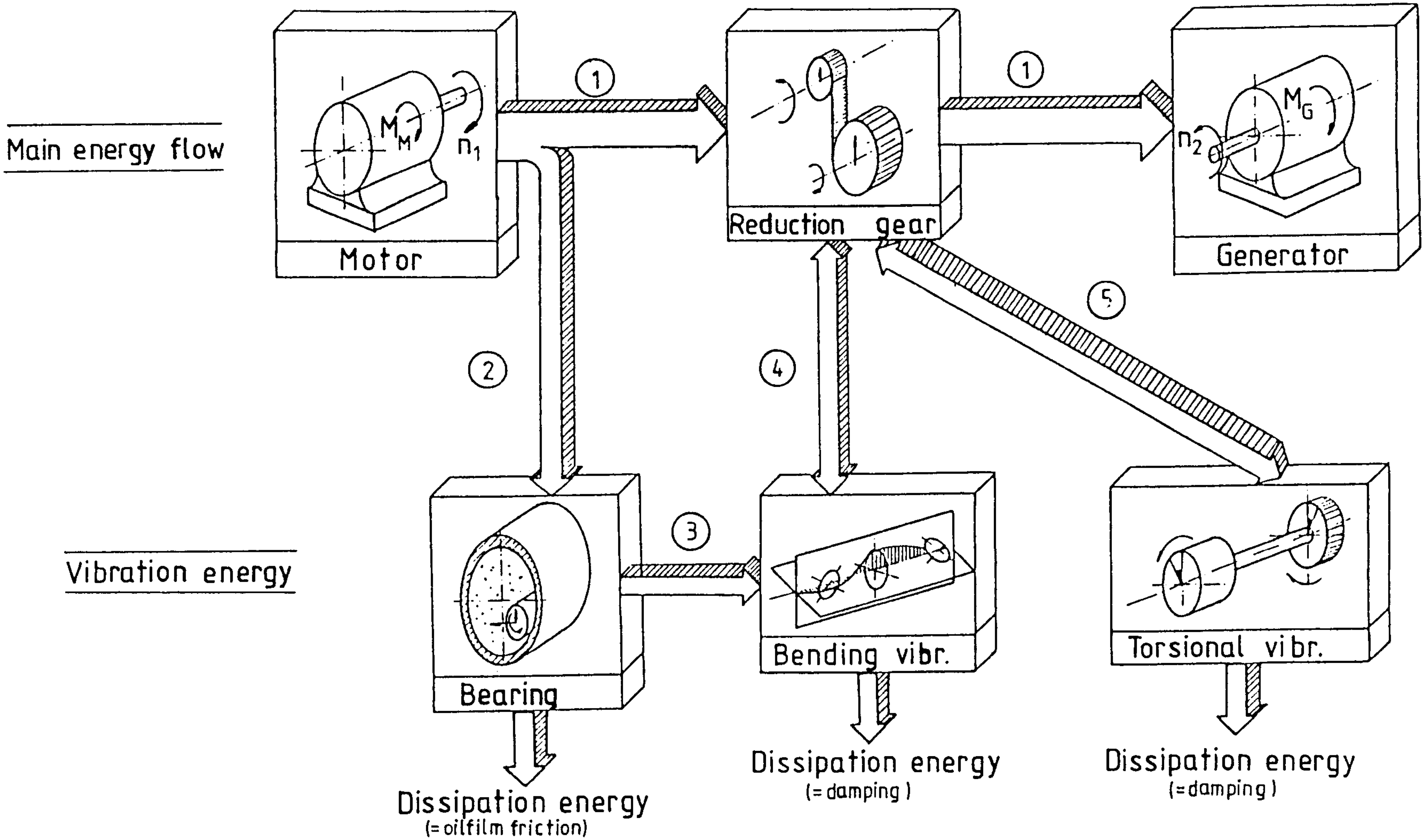
Main energy flow
Vibration energy
Motor
M_M
n_1
①
Reduction gear
①
Generator
M_G
n_2
②
④
⑤
③
Bearing
Bending vibr.
Torsional vibr.
Dissipation energy
(=oilfilm friction)
Dissipation energy
(=damping)
Dissipation energy
(=damping)

① Main energy flow from motor to generator.

② Energy flow branching off the main flow due to shear forces in the oilfilm.

③ Energy flowing from the oilfilm to the shaft bending vibrations.

④ Energy flowing from bending vibrations in the gear mechanism and back.

⑤ Energy flowing from the lateral excited gear wheels to the torsional motion and back, due to torsional-lateral coupling.

Figure 6. - Energy flow in a geared system with oilfilm excited torsional- lateral vibrations (schematic).

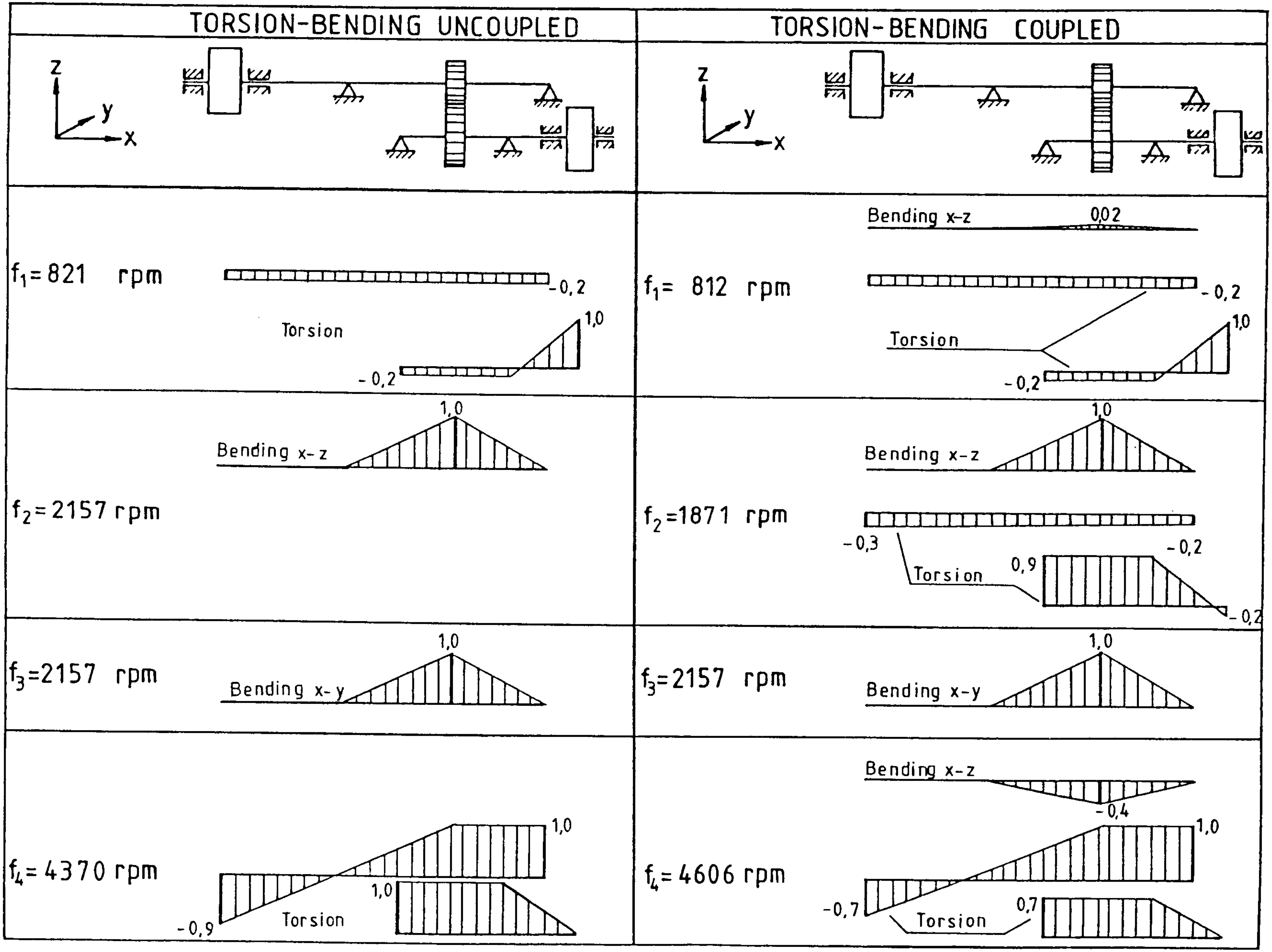
TORSION-BENDING UNCOUPLED
TORSION-BENDING COUPLED
z
y
x
f_1= 821 rpm
-0,2
Torsion
1,0
-0,2
f_2= 2157 rpm
Bending x-z
1,0
f_3=2157 rpm
Bending x-y
1,0
f_4= 4370 rpm
1,0
-0,9
Torsion
1,0
f_1= 812 rpm
Bending x-z
0,02
-0,2
Torsion
1,0
-0,2
f_2=1871 rpm
Bending x-z
1,0
-0,3
Torsion
0,9
-0,2
-0,2
f_3=2157 rpm
Bending x-y
1,0
f_4= 4606 rpm
Bending x-z
-0,4
1,0
-0,7
Torsion
0,7

Figure 7. - Eigenfrequencies and eigenvectors of the rigidly supported gear system (ref. 9).

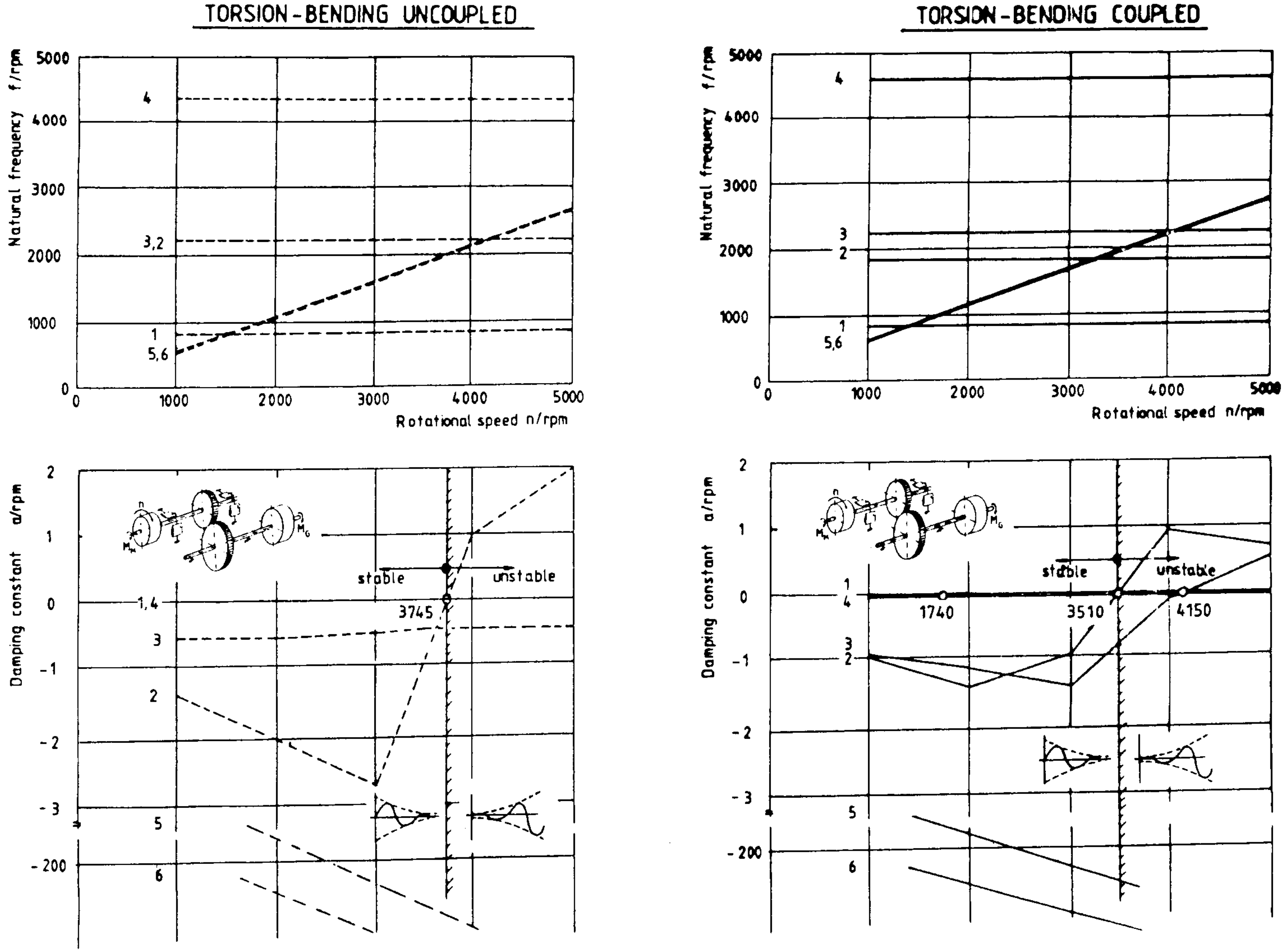

Figure 8. - Eigenfrequencies and damping for the uncoupled and torsional-lateral coupled system.

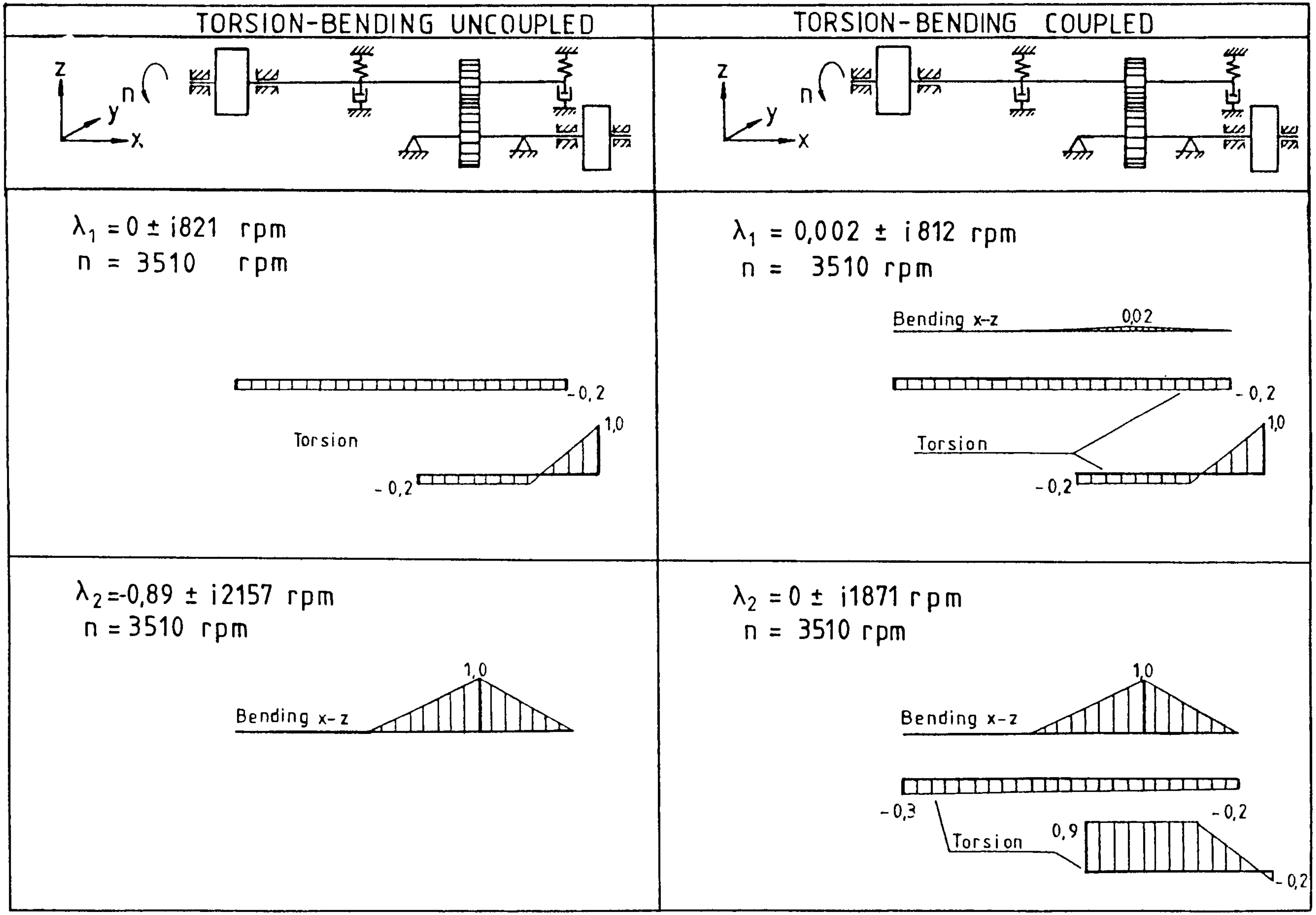
TORSION-BENDING UNCOUPLED
TORSION-BENDING COUPLED
z
y
x
n
λ1 = 0 ± i821 rpm
n = 3510 rpm
-0,2
1,0
Torsion
-0,2
λ1 = 0,002 ± i812 rpm
n = 3510 rpm
Bending x-z
0,02
-0,2
1,0
Torsion
-0,2
λ2 = -0,89 ± i2157 rpm
n = 3510 rpm
1,0
Bending x-z
λ2 = 0 ± i1871 rpm
n = 3510 rpm
1,0
Bending x-z
-0,3
-0,2
Torsion
0,9
-0,2

Figure 9. - First and second eigenvector of the uncoupled and torsional-lateral coupled system at the stability threshold (in the moment of maximum lateral displacement).

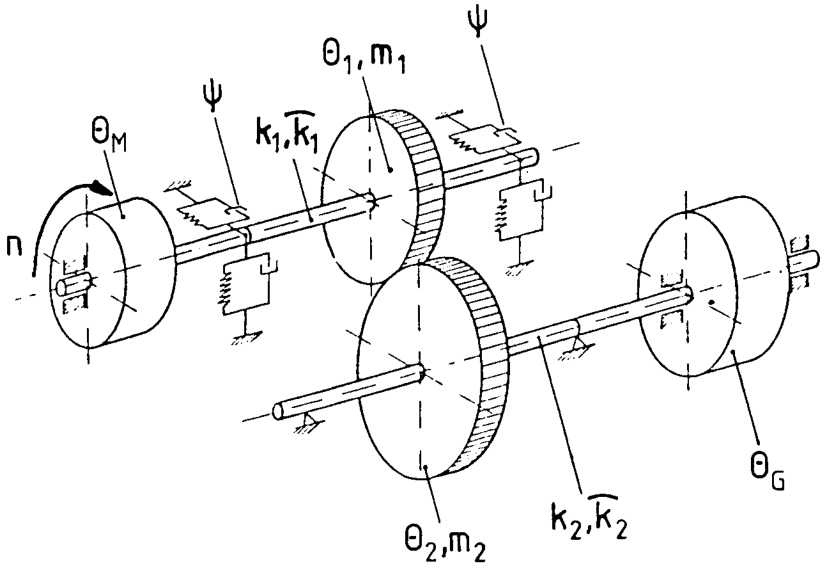
ψ
Θ_1, m_1
ψ
Θ_M
$k_1, \overline{k}_1$
n
Θ_G
Θ_2, m_2
$k_2, \overline{k}_2$

	Bending	Torsion
m_1	●	
m_2	○	
Θ_M		○
Θ_1		○
Θ_2		●
Θ_G		○
ψ	○	
k_1	●	
k_2	○	
$\overline{k}_1$		○
$\overline{k}_2$		●

● Varied parameters

Figure 10. - Variation of parameters.

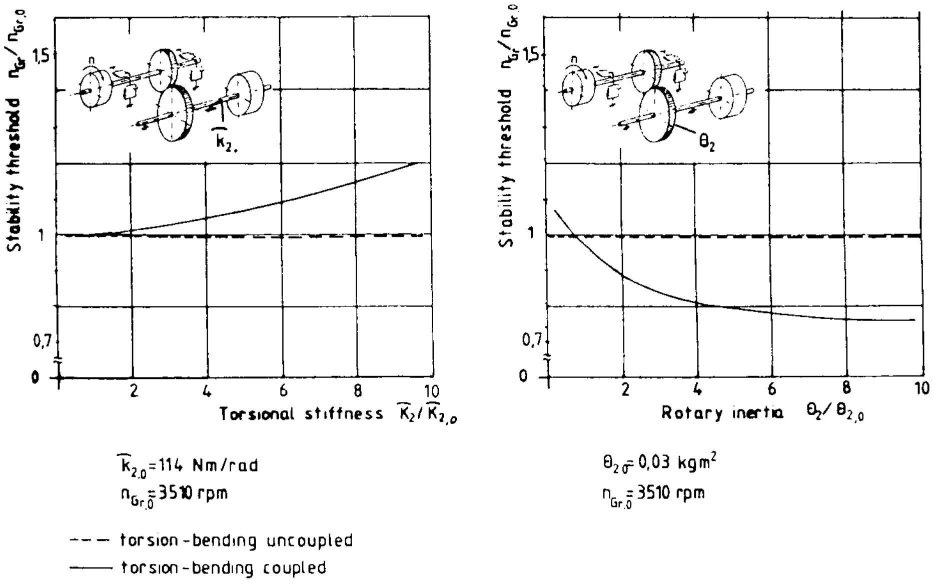

Figure 11. - Influence of torsional parameters on the stability threshold.

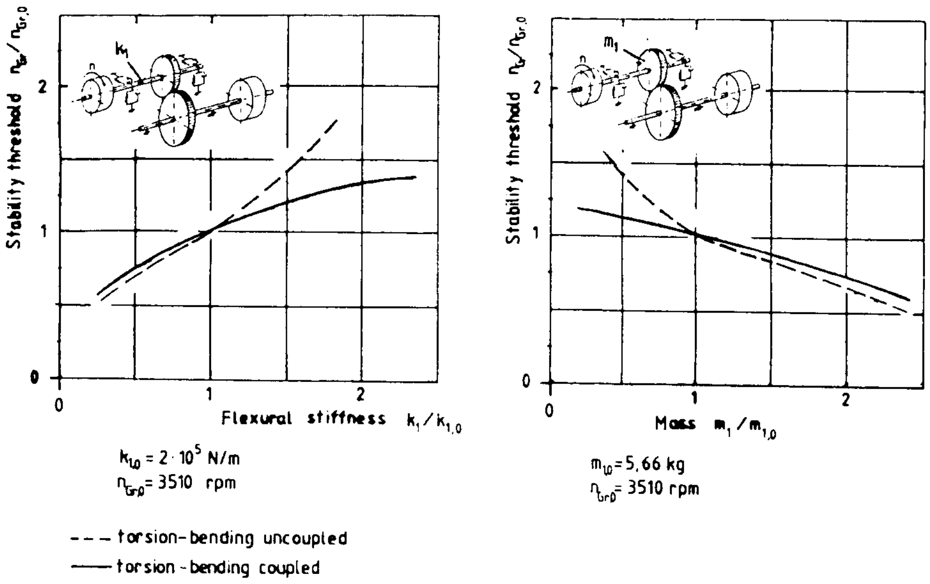

Figure 12. - Influence of bending parameters on the stability threshold.

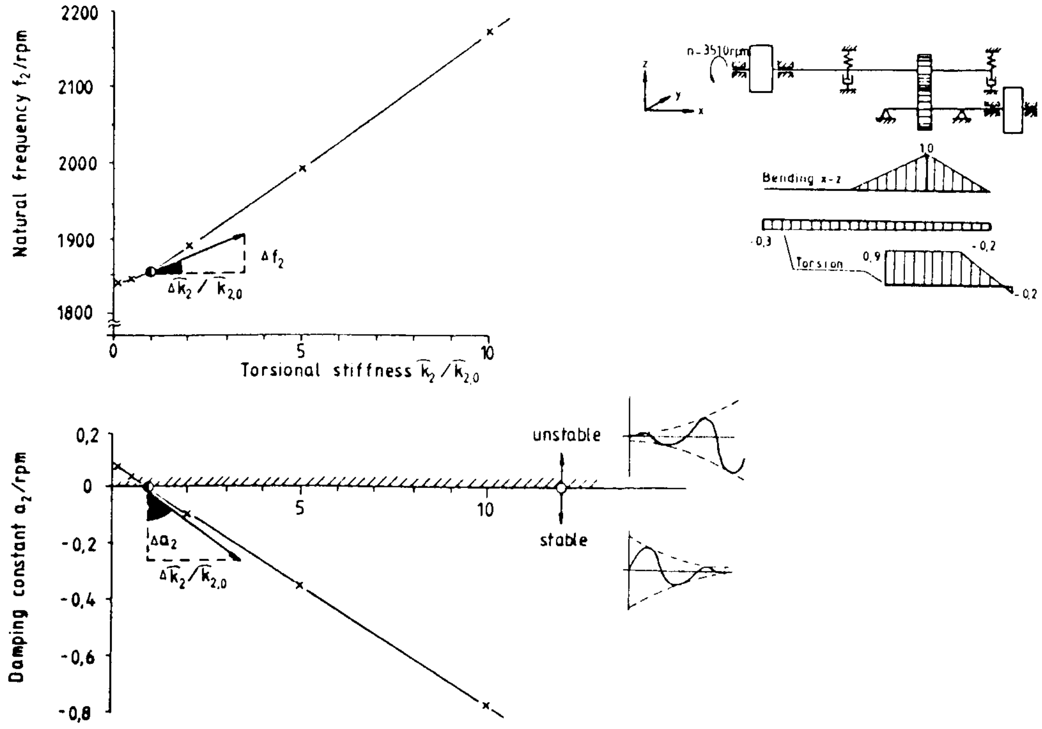

Figure 13. - Effect of change in torsional stiffness $\hat{k}_2$ to the second eigenvalue for the torsional-lateral coupled system.

Element	Force-Motion-Relation	Influence-Coefficient g_{nk}
Disk 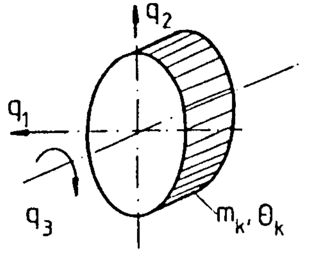	Bending: $\begin{bmatrix} F_1 \\ F_2 \end{bmatrix} = \begin{bmatrix} m_k & 0 \\ 0 & m_k \end{bmatrix} \begin{bmatrix} q_1 \\ q_2 \end{bmatrix}$ Torsion: $F_3 = \Theta_k \cdot \ddot{q}_3$	Bending: $g_{n,k} = \frac{\partial \lambda_n}{\partial m_k} = -\lambda_n^2 (l_1 r_1 + l_2 r_2)_n$ Torsion: $g_{n,k} = \frac{\partial \lambda_n}{\partial \Theta_k} = -\lambda_n^2 (l_3 r_3)_n$
Journal Bearing 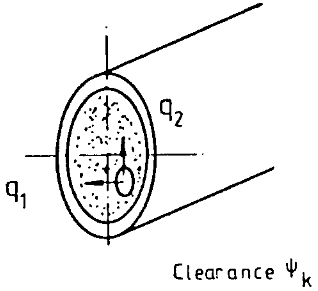	$\begin{bmatrix} F_1 \\ F_2 \end{bmatrix} = \begin{bmatrix} c_{11} & c_{12} \\ c_{21} & c_{22} \end{bmatrix} \begin{bmatrix} \dot{q}_1 \\ \dot{q}_2 \end{bmatrix} + \begin{bmatrix} k_{11} & k_{12} \\ k_{21} & k_{22} \end{bmatrix} \begin{bmatrix} q_1 \\ q_2 \end{bmatrix}$	Bending: $g_{n,\psi} = \frac{\partial \lambda_n}{\partial \psi_k} = \sum_{i=1}^{2} \sum_{j=1}^{2} \frac{\partial \lambda_n}{\partial c_{ij}} \cdot \frac{\partial c_{ij}}{\partial \psi_k} + \frac{\partial \lambda_n}{\partial k_{ij}} \cdot \frac{\partial k_{ij}}{\partial \psi_k}$ $= \sum_{i=1}^{2} \sum_{j=1}^{2} -\lambda_n (l_i r_j)_n \frac{\partial c_{ij}}{\partial \psi_k} - (l_i r_j)_n \frac{\partial k_{ij}}{\partial \psi_k}$
Beam 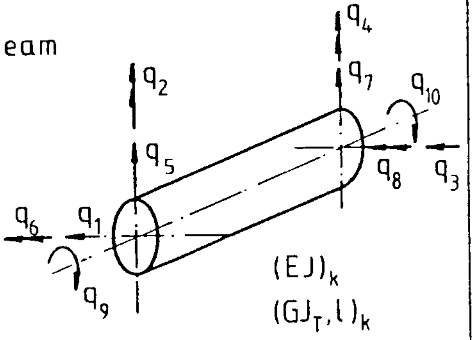 q_1 q_2 q_3 q_4 q_5 q_6 q_7 q_8 q_9 q_{10} $(EJ)_k$ $(GJ_T, l)_k$	Bending: $\begin{bmatrix} F_1 \\ \vdots \\ F_8 \end{bmatrix} = EJ \begin{bmatrix} K_{11} & \cdots & K_{18} \\ \vdots & \ddots & \vdots \\ K_{81} & \cdots & K_{88} \end{bmatrix}_k \begin{bmatrix} q_1 \\ \vdots \\ q_8 \end{bmatrix}$ Torsion: $\begin{bmatrix} F_9 \\ F_{10} \end{bmatrix} = \frac{GJ_T}{l} \begin{bmatrix} 1 & -1 \\ -1 & 1 \end{bmatrix}_k \begin{bmatrix} q_9 \\ q_{10} \end{bmatrix}$	Bending: $g_{n,k} = \frac{\partial \dot{\lambda}_n}{\partial (EJ)_k} = -[l_1 \cdots l_8]_n \begin{bmatrix} K_{11} & \cdots & K_{18} \\ \vdots & \ddots & \vdots \\ K_{81} & \cdots & K_{88} \end{bmatrix}_k \begin{bmatrix} r_1 \\ \vdots \\ r_8 \end{bmatrix}_n$ Torsion: $g_{n,k} = \frac{\partial \lambda_n}{\partial \left(\frac{GJ_T}{l}\right)_k} = -[l_9, l_{10}]_n \begin{bmatrix} 1 & -1 \\ -1 & 1 \end{bmatrix}_k \begin{bmatrix} r_9 \\ r_{10} \end{bmatrix}_n$

Figure 14. - Influence coefficients for the disk, journal bearing, and beam elements.

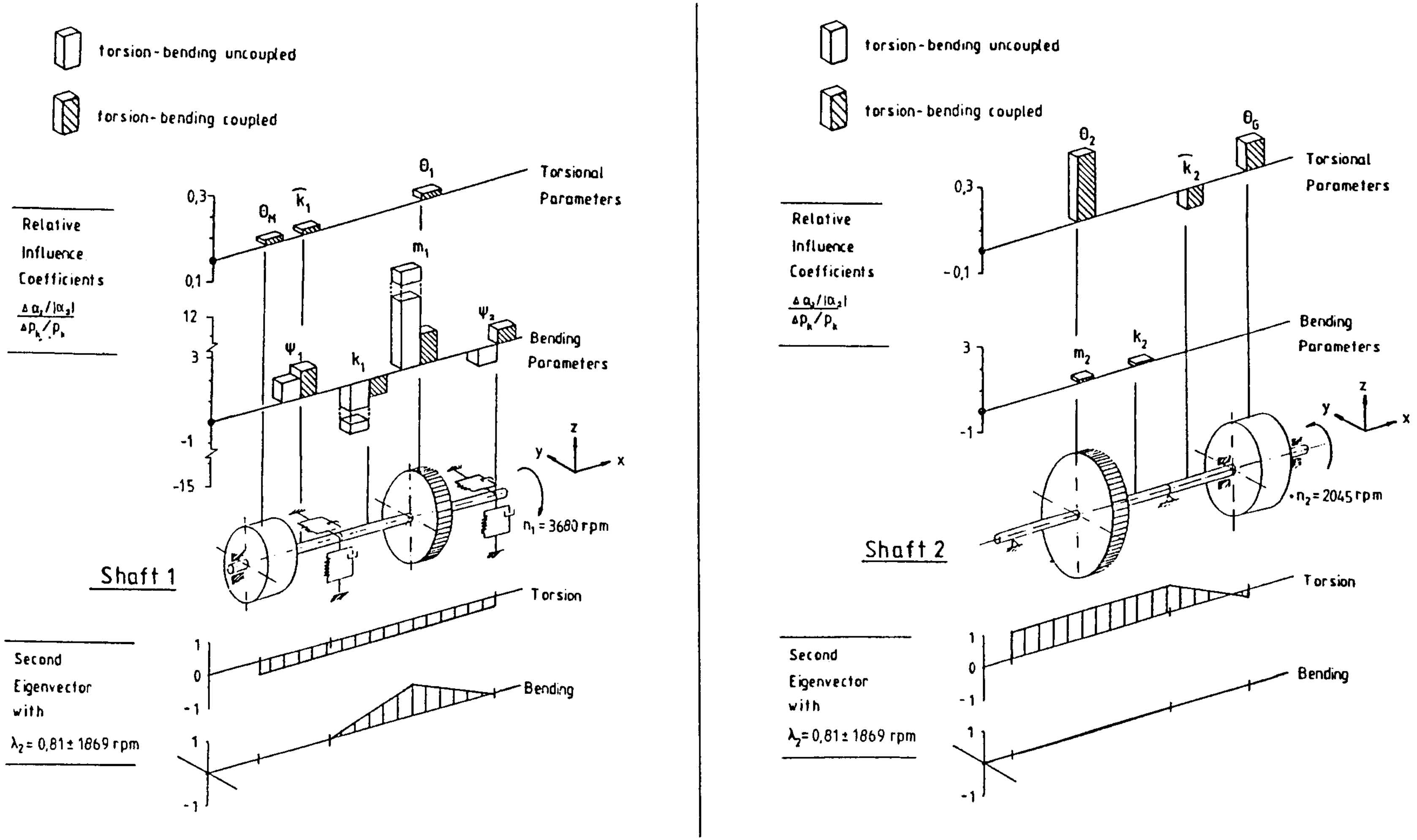
torsion-bending uncoupled
torsion-bending coupled
Relative
Influence
Coefficients
$\frac{\Delta\alpha_2/|\alpha_2|}{\Delta p_k/p_k}$
0,3
0,1
12
3
-1
-15
Θ_M
$\tilde{k}_1$
Θ_1
Torsional
Parameters
m_1
ψ_1
k_1
ψ_2
Bending
Parameters
z
y
x
$n_1 = 3680$ rpm
Shaft 1
Torsion
Second
Eigenvector
with
$\lambda_2 = 0{,}81 \pm 1869$ rpm
1
0
-1
Bending
1
-1
torsion-bending uncoupled
torsion-bending coupled
Relative
Influence
Coefficients
$\frac{\Delta\alpha_2/|\alpha_2|}{\Delta p_k/p_k}$
0,3
-0,1
3
-1
Θ_2
$\tilde{k}_2$
Θ_G
Torsional
Parameters
m_2
k_2
Bending
Parameters
z
y
x
$n_2 = 2045$ rpm
Shaft 2
Torsion
Second
Eigenvector
with
$\lambda_2 = 0{,}81 \pm 1869$ rpm
1
0
-1
Bending
1
-1

Figure 15. - Sensitivities of the second eigenvalue.

1. Report No.
NASA CP-2443

2. Government Accession No.

3. Recipient's Catalog No.

4. Title and Subtitle
Rotordynamic Instability Problems in High-Performance Turbomachinery - 1986

5. Report Date
January 1987

6. Performing Organization Code
553-13-00

7. Author(s)

8. Performing Organization Report No.
E-3136

10. Work Unit No.

9. Performing Organization Name and Address
National Aeronautics and Space Administration
Lewis Research Center
Cleveland, Ohio 44135

11. Contract or Grant No.

12. Sponsoring Agency Name and Address
National Aeronautics and Space Administration
Washington, D.C. 20546

13. Type of Report and Period Covered
Conference Publication

14. Sponsoring Agency Code

15. Supplementary Notes
The workshop was sponsored by Texas A&M University, College Station, Texas; the U.S. Army Research Office, Durham, North Carolina; and the Aeropropulsion Laboratory, Wright-Patterson Air Force Base, Ohio, and held at Texas A&M University on June 2-4, 1986.

16. Abstract
The first rotordynamics workshop proceedings (NASA CP-2133, 1980) emphasized a feeling of uncertainty in predicting the stability of characteristics of high-performance turbomachinery. In the second workshop proceedings (NASA CP-2250, 1982) these uncertainties were reduced through programs established to systematically resolve problems, with emphasis on experimental validation of the forces that influence rotordynamics. In the third proceedings (NASA CP-2338, 1984) many programs for predicting or measuring forces and force coefficients in high-performance turbomachinery produced results. Data became available for designing new machines with enhanced stability characteristics or for upgrading existing machines. The present workshop proceedings illustrates a continued trend toward a more unified view of rotordynamic instability problems and several encouraging new analytical developments. The intent of the workshop and this proceedings is to provide a continuing impetus for an understanding and resolution of these problems.

17. Key Words (Suggested by Author(s))
Rotordynamics
Turbomachinery
Instability

18. Distribution Statement
Unclassified - unlimited
STAR Category 37

19. Security Classif. (of this report)	20. Security Classif. (of this page)	21. No. of pages	22. Price*
Unclassified	Unclassified	562	A24

*For sale by the National Technical Information Service, Springfield, Virginia 22161